Non-equilibrium dynamics in atom-cavity systems and particle-hole symmetric superfluids

Dissertation
zur Erlangung des Doktorgrades
an der Fakultät für Mathematik, Informatik und Naturwissenschaften
Fachbereich Physik
der Universität Hamburg

vorgelegt von

Jim Peter Skulte

Hamburg

2024

Gutachter der Disputation: Prof. Dr. Ludwig Mathey
                                                            Prof. Dr. Andreas Hemmerich

Zusammensetzung der Prüfungskomission: Prof. Dr. Ludwig Mathey
                                                            Prof. Dr. Andreas Hemmerich
                                                            Dr. Christoph Becker
                                                            Prof. Dr. Michael Potthoff
                                                            Prof. Dr. Roman Schnabel

Vorsitzender der Prüfungskimission: Prof. Dr. Roman Schnabel

Datum der Disputation: 01.11.2024

Vorsitzender des Fach-Promotionsausschusses PHYSIK: Prof. Dr. Markus Drescher
Leiter des Fachbereichs PHYSIK: Prof. Dr. Wolfgang J. Parak
Dekan der Fakultät MIN: Prof. Dr.-Ing. Norbert Ritter

Contents

Preface

The following work, presented in this cumulative thesis, has been conducted from October 2020 until May 2024 at the Center for Optical Quantum Technologies. It is based on the publications I-XI presented in the chapters 2 and 3. My work has been funded by the German Academic Scholarship Foundation and the Cluster of Excellence "Advanced Imaging of Matter" (EXC 2056), Project No. 390715994. The work was supervised by Prof. Ludwig Mathey and as secondary supervisor by Prof. Andreas Hemmerich.

Quote

"A process cannot be understood by stopping it. Understanding must move with the flow of the process, must join it and flow with it." - Frank Herbert, Dune

Zusammenfassung

Neue Funktionalitäten können entstehen, wenn ein System aus dem Gleichgewichtszustand gebracht wird.

Wir haben Nicht-Gleichgewichts-Eigenschaften von Licht-Materie gekoppelten Systemen mittels einer statischen Pumpe oder periodischem Treiben untersucht. Als primäres Beispiel haben wir die Eigenschaften von sogenannten Zeitkristallen erforscht. Zeitkristalle brechen spontan die Zeit-Translations-Symmetrie (ZTS) und sind robust gegenüber lokalen Störungen. Wenn das System eine zugrunde liegende kontinuierliche ZTS hat, die gebrochen wird, nennt man die Phase einen kontinuierlichen Zeitkristall. Liegt dem System nur eine diskrete Zeit-Translations-Symmetrie zugrunde, so wird die entstehende Phase als diskreter Zeitkristall bezeichnet. In der zugrunde liegenden Thesis haben wir in Veröffentlichung [1] die Robustheit eines diskreten Zeitkristalls gegenüber Molekularfeld brechenden Termen wie Kontaktwechselwirkungen und räumlicher Beschränkung untersucht und in Veröffentlichung [2] die Rolle des dissipativen Kanals im offenen Dicke-Modell erforscht. Des Weiteren haben wir das Dicke-Modell in den Veröffentlichung [3–5] um ein drittes Energieniveau erweitert. Durch das Hinzufügen des dritten atomaren Niveaus im Vergleich zum Standard Dicke-Model, welches aus zwei Energieniveaus besteht, haben wir in Veröffentlichung [3] das Auftreten eines inkommensurablen Zeitkristalls theoretisch erklärt und haben explizit gezeigt wie ein Atom-Hohlraumresonator-System auf das von uns vorgeschlagene drei-Niveau Dicke-Modell abgebildet werden kann. Wir haben diese Vorhersage in Zusammenarbeit mit der Gruppe von Andreas Hemmerich in der Veröffentlichung [4] experimentell bestätigt. Im Anschluss an diese Arbeit haben wir in Veröffentlichung [5] numerisch und experimentell gezeigt, wie das Bose-Einstein-Kondensat (BEC) mit dem gleichen Schema, aber stärkerem Treiben als zuvor, in einen dunklen Zustand des Lichtfeldes gebracht werden kann.

In den Veröffentlichungen [6] und [7] haben wir einen kontinuierlichen Zeitkristall in einem Hohlraumresonator-BEC-System untersucht. In Zusammenarbeit mit der experimentellen Gruppe von Andreas Hemmerich konnten wir Grenzzyklen in einem Quantengasexperiment beobachten. Indem wir numerisch und experimentell die Robustheit gegenüber zeitlichem Rauschen in der Licht-Materie-Kopplungsstärke sowie Fluktuationen in der Teilchenzahl und den Quantenkorrekturen niedrigster Ordnung unter Verwendung der Methode der "truncated Wigner approximation" (TWA) Methode nachgewiesen haben, konnten wir die Realisierung des ersten kontinuierlichen Zeitkristall vermelden. In der darauf folgenden Veröffentlichung [7] haben wir ein allgemeines Minimalmodell vorgeschlagen, das Grenzzyklen in einem Licht-Materie-System beherbergt, und das Experiment auf dieses Modell abgebildet. Wir haben die Existenz von Grenzzyklen sowohl für repulsive als auch für attraktive Potentiale vorhergesagt und experimentell bestätigt. Darüber hinaus haben wir die Existenz einer zugrundeliegenden Hopf-Bifurkation gezeigt,

die zu dieser Dynamik führt, indem wir die Eigenwerte der Jacobi-Matrix sowie das einhergehende Skalierungsverhalten bestimmt haben. In der Veröffentlichung [8] haben wir, wiederum in Zusammenarbeit mit der Gruppe von Andreas Hemmerich, den Übergang von einem kontinuierlichen zu einem diskreten Zeitkristall untersucht, indem wir den zuvor entdeckten kontinuierlichen Zeitkristall periodisch getrieben haben. In der Sprache der nichtlinearen Dynamik kann dies als die erste Beobachtung von "Entrainment" und "Sub-Entrainment" in einem Quantengasexperiment angesehen werden.

Wir haben die Plattform, bestehend aus einem Hohlraumresonator und einem BEC, die wir bereits ausgiebig untersucht haben, genutzt, um einen Rotationssensor vorzuschlagen, der den offenen Charakter des Systems für eine verbesserte Nutzbarkeit verwendet. Die Idee besteht darin, das aus dem Hohlraum austretende Lichtfeld als Fenster in die Dynamik des Systems zu nutzen, um die Eigenschaften der Atomtronik und der Echtzeitauslesung zu kombinieren. Um diese Idee als Sensor zu nutzen, haben wir die Abhängigkeit zwischen der angelegten externen Drehung und der Anzahl der aus dem Hohlraum austretenden Photonen gezeigt, die wiederum als Signal für den Sensor verwendet werden. Der theoretische Vorschlag wird in der Veröffentlichung [9] vorgestellt.

Wir haben außerdem die Kontrolle einer aktiven Raman-Mode durch Kopplung mit einer Hohlraummode in Veröffentlichung [10] untersucht. Mithilfe von analytischen Werkzeugen und TWA haben wir gezeigt, dass die Raman-Mode stark eingegrenzt werden kann, wenn sie auf Resonanz mit der doppelten Hohlraumfrequenz abgestimmt ist.

Wir haben die Dynamik von topologischen Defekten wie "Vortices" in Supraflüssigkeiten in der Veröffentlichung [11] untersucht. Dazu haben wir die Ergebnisse für die Gross-Pitaevskii (GP)-Gleichung, die nicht Teilchen-Loch-symmetrisch ist, und die nichtlineare Klein-Gordon (NLKG)-Gleichung, die eine Teilchen-Loch-Symmetrie aufweist, verglichen. Wir konnten auf das Fehlen der Magnus-Kraft für die Klein-Gordon-Flüssigkeit hinweisen und Protokolle zur Messung dieser Effekte in modernen Experimenten voraussagen. In einem gemeinsamen Manuskript mit der Gruppe von Henning Moritz, das in Vorbereitung ist und bald veröffentlicht wird, haben wir das Modell auf den berühmten Übergang vom Bardeen-Cooper-Schrieffer-Zustand von Paaren aus Fermionen zum Bose-Einstein-Kondensat von zweiatomigen Molekülen angewendet (BEC-BCS-Übergang). Wir haben explizit gezeigt, wie die effektiven Parameter durch die Verwendung von Quanten-Monte-Carlo-Daten (QMC) bestimmt werden können. Wir haben die numerisch beobachteten kollektiven Moden, die durch einen räumlichen Einschluss verschoben sind, mit experimentellen Daten der Gruppe von Henning Moritz verglichen und eine große Übereinstim-

mung festgestellt. Wir haben gezeigt, wie sich der Charakter der am tiefsten liegenden kollektiven Mode von einer "breathing" Mode auf der BEC-Seite zur Higgs-Mode auf der BCS-Seite für ein System mit starkem räumlichen Einschluss ändert.

Abstract

New functionalities can emerge if a system is pushed away from its equilibrium. We study non-equilibrium properties of light-matter systems by applying either a static or a periodic drive. As a prime example we investigate properties of so-called time crystals. Time crystals (TC) spontaneously break the time translational symmetry (TTS) and are robust against local perturbations. If the system has an underlying continuous TTS that becomes broken, the phase is called a continuous time crystal (CTC). If the system only has an underlying discrete time translational symmetry, then the emerging phase is called a discrete time crystal (DTC). In this thesis, we have studied the robustness of a DTC against mean-field breaking terms such as contact interactions and confinement in publication [1] and have studied the role of the dissipative channel in the open Dicke model in publication [2]. We have also extended the Dicke model to the three-level Dicke model in the publications [3–5]. By adding a third atomic level to the standard two-level Dicke model, we theoretically explain the emergence of an incommensurate time crystal (ITC) in publication [3] and explicitly show the mapping of an atom-cavity system to the proposed three-level Dicke model. We confirmed this prediction experimentally in collaboration with the group of Andreas Hemmerich in publication [4]. Following this work, we highlight theoretically as well as in the experiment, how the same driving scheme can be used with a stronger driving amplitude to push the Bose-Einstein-condensate (BEC) into a dark state of the light field [5].

In publications [6] and [7] we studied a CTC in a cavity-BEC system. In collaboration with the experimental group of Andreas Hemmerich, we have been able to observe limit cycles in a quantum gas experiment. By showing numerically and experimentally the robustness against temporal noise in the light-matter coupling strength, as well as against fluctuations in the particle number and against the lowest order quantum corrections using the truncated Wigner approximation method (TWA), we have been able to report the realisation of the first CTC. In the follow-up publication [7], we have proposed a general minimal model, which hosts limit cycles in a light-matter system, and mapped the atom-cavity experiment onto it. We have predicted and confirmed the existence of limit cycles for both repulsive as well as attractive potentials. Further, we have shown the existence of an underlying Hopf bifurcation leading to this dynamics by computing the eigenvalues of the Jacobian as well as by means of scaling laws. In publication [8] we have studied, again in collaboration with the group of Andreas Hemmerich, the transition from a CTC to a DTC by periodically driving the previously discovered CTC. In the language of nonlinear dynamics this can be seen as the first observation of entrainment and sub-entrainment in a quantum gas experiment.

We have used the atom-cavity platform, which we have extensively studied before, to propose a rotational sensor that exploits the open character of the system for improved

usability. The idea is to use the light-field leaking out of the cavity as a window into the dynamics of the system to combine the features of atomtronics and real-time read out. To use this idea as a sensor, we show the dependence between the external rotation applied and the number of photons leaking out of the cavity, which is in return used as the signal for the sensor. The theoretical proposal is reported in publication [9].

We also studied the control of an active Raman mode by coupling it to a cavity mode in publication [10]. We have shown, by use of analytical tools as well as TWA, that the Raman mode can be strongly confined, if tuned to resonance with twice the cavity frequency.

We studied the dynamics of topological defects such as vortices in superfluids in publication [11]. We compared the results for the Gross-Pitaevskii (GP) equation, which is not particle-hole symmetric, and the nonlinear Klein-Gordon (NLKG) equation, hosting a particle-hole symmetry. We point out the absence of the Magnus force for the Klein-Gordon fluid and predict protocols to measure these effects in state-of-the-art experiments. In a joint manuscript with the group of Henning Moritz, that is in preparation and will be published soon, we have applied the model to the famous crossover from the Bardeen–Cooper–Schrieffer state of pairs of fermions to the Bose–Einstein-condensate of diatomic molecules (BEC-BCS crossover). We have explicitly demonstrated how the effective parameters can be fixed by the use of quantum Monte Carlo (QMC) data. We compared the numerically observed collective modes including a spatial confinement and experimental data of the group of Henning Moritz and find great agreement. We show how the character of the lowest lying collective mode changes from a breathing mode on the BEC side to the Higgs mode on the BCS side for a system with strong spatial confinement.

List of Publications

This cumulative dissertation is based on the publications listed below.

- **Publication I**: R.J.L. Tuquero, <u>J. Skulte</u>, L. Mathey and J.G. Cosme, *Dissipative time crystal in an atom-cavity system: Influence of trap and competing interactions*, Phys. Rev. A 105, 043311 (2022)

- **Publication II**: J.G. Cosme, <u>J. Skulte</u>, and L. Mathey, *Bridging closed and dissipative discrete time crystals in spin systems with infinite-range interactions*, Phys. Rev. B 108, 024302 (2023)

- **Publication III**: <u>J. Skulte</u>, P. Kongkhambut, H. Keßler, A. Hemmerich, L. Mathey and J.G. Cosme, *Parametrically driven dissipative three-level Dicke model*, Phys. Rev. A 104, 063705 (2021)

- **Publication IV**: P. Kongkhambut, H. Keßler, <u>J. Skulte</u>, L. Mathey, J.G. Cosme A. Hemmerich, *Realization of a Periodically Driven Open Three-Level Dicke Model*, Phys. Rev. Letters 127, 253601 (2021)

- **Publication V**: <u>J. Skulte</u>, P. Kongkhambut, S. Rao, L. Mathey, H. Keßler, A. Hemmerich and J.G. Cosme, *Condensate Formation in a Dark State of a Driven Atom-Cavity System*, Phys. Rev. Letters 130, 163603 (2023)

- **Publication VI**: P. Kongkhambut, <u>J. Skulte</u>, L. Mathey, J.G. Cosme, A. Hemmerich and H. Keßler, *Observation of a continuous time crystal*, Science 377, 670-673 (2022)

- **Publication VII**: <u>J. Skulte</u>, P. Kongkhambut, H. Keßler, A. Hemmerich, L. Mathey and J.G. Cosme, *Realizing limit cycles in dissipative bosonic systems*, accepted to Physical Rev. A (2024)

- **Publication VIII**: P. Kongkhambut, J.G. Cosme, <u>J. Skulte</u>, Michelle A. Moreno Armijo, L. Mathey, A. Hemmerich, and H. Keßler, *Observation of a phase transition from a continuous to a discrete time crystal*, submitted to Reports on Progress in Physics: Original Research (2024)

- **Publication IX**: <u>J. Skulte</u>, J.G. Cosme and L. Mathey, *Quantum rotation sensor with real-time readout based on an atom-cavity system*, submitted to Phys. Rev. Letters (2023)

- **Publication X**: H. P. Ojeda Collado, Marios H. Michael, <u>J. Skulte</u>, Angel Rubio and L. Mathey, *Equilibrium parametric amplification in Raman-cavity hybrids*, submitted to Phys. Rev. Letters (2023)

- **Publication XI**: <u>J. Skulte</u>, L. Broers, J.G. Cosme and L. Mathey, *Vortex and soliton dynamics in particle-hole-symmetric superfluids*, Phys. Rev. Res. 3, 043109 (2021)

1 Introduction

Life is in perpetual motion. This ranges from the branches of a tree, experiencing a mild breeze, predator-prey communities, our daily body temperature changes, our sleep cycle, to the ongoing beating of our heart [12–15]. It is crucial to understand the underlying laws of nature that lead to these complex systems with its nontrivial dynamics. Before attempting to understand these phenomena in such large systems, the goal is to understand its ingredients individually on the small scale before putting everything back together. In order to do this, quantum simulators can be used as first proposed by Richard Feynman [16]. The underlying idea is that as the world is quantum on its smallest length and energy scales, we need to use quantum devices to simulate it. One of the most used platforms to do so are ultracold atoms [17]. These platforms have become available after the first realisations of Bose-Einstein condensates (BEC) [18, 19] in the 90s. These experiments offer high controllability, stability and reproducibility. Later, by the means of laser light, optical lattices could be applied to the BECs, which allowed to simulate quantum solid state physics at slower time scales and without defects [20–23]. The great controllability has allowed studying phase transitions in a controlled way by changing system parameters [24]. The understanding of phase transitions and the associated properties is crucial to understand the dynamics and response of the system to perturbations.

Hence, the study of phase transitions and the associated changes in material properties are of great interest and at the heart of solid state physics [25]. During a phase transition, a symmetry is spontaneously broken [25–27]. A symmetry is said to be broken if the ground state possesses a lower symmetry class then the underlying equations governing the dynamics. One of the standard examples is the transition from liquid water to ice. While for water, the density of molecules has a continuous translational symmetry, as it freezes into a solid, a spatial pattern occurs. The water molecules arrange in a fixed spatial pattern leading to a reduced discrete symmetry for the density of water.

A scope of modern physics is to first understand the mechanisms behind non-equilibrium dynamics and ultimately to design new phases of matter with new functionalities and applications. The idea is to not to just use ultracold atom platforms to study ground state or steady state properties of the emulated solid state systems, but also to quantum simulate the dynamics of more complex systems. This can either be done by changes in the environment due to variations in light-matter interactions of the physical system in question [28–30] or by applying an external periodic drive [31–34]. This will either renormalise properties of the system or can even push it into a new phase of matter with possibly new properties that are forbidden in equilibrium.

As a particular example of non-equilibrium physics, we have been interested in so-called time crystal. This phase of matter spontaneously breaks the time translational symme-

try. The phenomenon was first coined in biology by Winfree [13,35] and later rediscovered and translated into the language of physics by Wilczek and Shapere in 2012 [36,37]. It can be seen as the analog of a space crystal, were the atoms spontaneously break the translational symmetry to form a crystal, but in the time domain. Time crystals allow to study the stability and the underlying structure of such non-equilibrium phases in a very controlled way.

The quantum simulator we are interested combines the physics of using BECs in optical lattices with the controllability of the light-matter coupling. For further readings on various implementations of strong light-matter couplings we refer the reader to [38–44]. The majority of the systems considered in this PhD thesis correspond to atom-cavity systems. Atom-cavity systems [43–49] allow to study the interactions between ultracold quantum gases and electromagnetic fields at strong couplings. Further, the controllability of this platform makes it especially useful to study nonlinear physics and dissipative effects due to light leaking out of the cavity. Due to the light-field leaking out of the cavity the dynamics can be *in-situ* observed. Hence, with a single experimental trace a time series can be measured without destructive measurements of the atoms. The cavity-BEC platform allows to measure the photon number as well as the relative phase of a pump laser and the light-field leaking out of the cavity. In addition to these in-situ measurements, a destructive time-of-flight measurement can be done to extract direct information on the momentum states of the BECs.

In this thesis, we have studied the stability of discrete and continuous time crystals [1–9] including the first demonstration of a continuous time crystal [6]. One key aspect of these results is the so-called recoil-resolved atom-cavity system. This means that the timescale of the dynamics of the atoms as well as of the light-field are comparable and none of those two can be adiabatically eliminated. This particular case allows for the extended stability of discrete time crystals [1–5] as well as the emergence of limit cycles [6–8]. We have contributed to atomtronics in the form of a rotation sensor [9] as well as cavity enhanced localisation of a Raman mode [10].

We have shown how symmetries, such as particle-hole symmetry, can drastically change the dynamics of superfluids. Furthermore, we have first used this to show the absence of the Magnus force for nonlinear Klein-Gordon fluids [11] and also have been able to use this theory to map it on the BEC-BCS crossover as is implemented in the experiment done in the group of Henning Moritz. Additionally, we have used this to predict the lowest relevant collective modes during the BEC-BCS crossover including a spatial confinement. A joint manuscript with the group of Henning Moritz is in preparation. This thesis is structured as follows:

Overview

- Chapter 2 introduces the atom-cavity system, shows the mapping to the toy models considered, and briefly discusses the numerical as well as analytical tools used. The chapter further gives a short introduction to the field of time crystals and discuss to some extent the basics of bifurcation theory. The chapter includes publication [1], where the stability of a dissipative time crystal is discussed for varying

mean-field breaking terms such as inhomogeneous trapping potentials and contact interactions. Publication [2] discusses the connection between the dissipative time crystal found in open systems with infinite-range interactions, namely the open Dicke model and the Lipkin-Meshkov-Glick model. Publication [3] introduces the three-level Dicke model and shows how this model can be realised using phase-modulation in an atom-cavity system. Publication [4] shows the experimental realisation of the model proposed in publication [3] and shows the realisation of an incommensurate time crystal. Publication [5] follows up on publication [3] and publication [4], but uses a stronger drive to realise the condensation in a dark state of the atom-cavity system by a transfer due to the cavity. Publication [6] presents the first experimental realisation of a continuous time crystal. Here, a blue-detuned atom-cavity system is used. Publication [7] provides the theoretical framework to understand the mechanism that lead to the limit-cycle in publication [6]. It further generalises the mechanism to also include attractive light potentials and further provides an experimental realisation for such attractive light potentials. Publication [8] shows the entrainment of a continuous time crystal. It is highlighted that this can be understood as a phase transition from a continuous to a discrete time crystal. In publication [9] we propose to use a version of a Dicke-Hubbard model of the atom-cavity system to use it as a rotational sensor. We discuss the sensitivity of the sensor and its dependencies on the different parameters. Publication [10] proposes the use of a cavity to control and manipulate the equilibrium properties of Raman modes.

- Chapter 3 discusses the dynamical properties of particle-hole symmetric superfluids. It includes a derivation of the conserved quantities, the mode structure and presents a simplified model to partially describe the experimental results found in the group of Henning Moritz. For this collaboration the manuscript is in preparation and not included in this thesis. The chapter includes publication [11], which discusses the dynamics of topological defects like vortices and solitons.

- Chapter 4 concludes and briefly discusses an outlook for future work.

2 Atom-cavity systems

Large parts of my research during my PhD have been focused on atom-cavity systems. In publications [1–9] we focus on cavity-BEC systems or atom-cavity systems, where a BEC is placed inside a high-finesse cavity and is transversely pumped by external laser beams. For an introduction to this particular setup including many examples, we refer to [50]. In publication [10] we study a generic model of atom-cavity systems, where a Raman-mode is coupled to a high-finesse cavity, which leads to Raman-cavity hybrid modes.
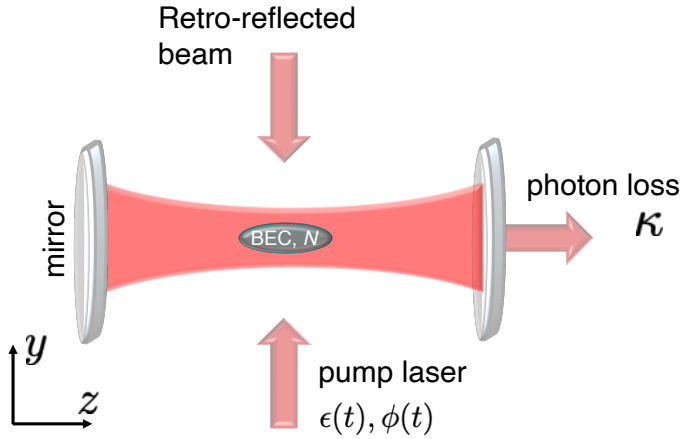
2.1 Cavity-BEC system

Figure 2.1: Sketch of the atom-cavity setup. A BEC consisting of N atoms is placed inside a high-finesse cavity and is transversely pumped by a laser beam with wavelength λ that is retro reflected such that it forms a standing wave potential. The pump laser strength is given by ϵ and the phase of the standing wave potential by ϕ. Light inside the cavity is leaking out of the cavity with the loss rate κ.

The full effective atom-cavity Hamiltonian can be decomposed into an atomic, a cavity and a light-matter interaction part [50–52]. We assume to be in the dispersive regime, such that the excited states can be adiabatically eliminated. A sketch of the setup is shown in Fig. 2.1. We consider a two-dimensional setup with the pump beam aligned with the y-direction and the cavity aligned along the z-direction. A BEC consisting of N atoms is placed inside two mirrors that form a cavity with a photon loss rate κ. The

atoms are transversely pumped by a laser beam with wavelength λ that is retro-reflected such that it forms a standing wave potential for the atoms. The strength of the laser beam is given by ϵ, which can be periodically modulated, and the phase of the standing wave potential is given by ϕ, which can also be periodically driven by applying an electro-optic modulator to the laser beam. Depending on the wavelength of the pump laser, the atoms can either feel an attractive or repulsive light potential. The total Hamiltonian decomposed into different contributions then reads

$$\hat{H} = \hat{H}_C + \hat{H}_A + \hat{H}_{AC}. \tag{2.1}$$

The single-mode cavity light field has a mode function of $\cos(kz)$ and a resonance frequency of ω_C. The pump laser frequency is given by ω and the system is described within the rotating frame of the pump laser, and we define the detuning as $\delta_C = \omega_P - \omega_C$ with ω_P the frequency of the pump laser. The cavity Hamiltonian is given by

$$\hat{H}_C/\hbar = -\delta_C \hat{a}^\dagger \hat{a} \tag{2.2}$$

with the cavity mode annihilation and creation operators $\hat{a}^\dagger$ and $\hat{a}$, respectively. The atomic Hamiltonian is given by

$$\hat{H}_A/\hbar = \int dydz \hat{\Psi}^\dagger(y,z) \left[-\frac{\hbar}{2m}\nabla^2 - \omega_{\mathrm{rec}}\epsilon_{\mathrm{p}}\cos^2(ky) \right] \hat{\Psi}(y,z), \tag{2.3}$$

where $\hat{\Psi}^\dagger$ and $\hat{\Psi}$ are the bosonic annihilation and creation field operators for the atoms, $k = 2\pi/\lambda$ describes the wave number of the pump light field, and $\epsilon_p = \epsilon/\omega_{\mathrm{rec}}$ is the corresponding pump strength. It is quantified in terms of the maximal energy depth of the pump lattice in units of the recoil energy $E_{\mathrm{rec}} = \hbar\omega_{\mathrm{rec}}$ with the recoil frequency $E_{\mathrm{rec}} = \hbar^2 k^2/2m$, where m is the atomic mass. Finally, the atom-cavity interaction is given by

$$\hat{H}_{AC}/\hbar = \int dydz \hat{\Psi}^\dagger(y,z) \Big[U_0 \hat{a}^\dagger \hat{a} \cos^2(kz)$$
$$+ \mathrm{sign}(U_0)\sqrt{\omega_{\mathrm{rec}}|U_0|\epsilon_{\mathrm{p}}}\cos(ky)\cos(kz)(a^\dagger + a) \Big] \hat{\Psi}(y,z), \tag{2.4}$$

where U_0 is the maximal light-shift per single atom, which can be positive or negative depending on whether a blue- or red-detuned pump laser with respect to the relevant atomic transition is used. As depicted in Fig. 2.2, the system exhibits a normal-superradiant phase transition. In the so-called normal phase (NP) below the phase transition the atoms acquire a density modulation from the applied standing wave potential. However, photons scattered from the pump beam will, due to the density of the atoms, deconstructively interfere with each other such that there is no net light field in the cavity and no light is leaking out of the cavity as shown in Fig. 2.2(a). As the intensity of the laser beam is increased the critical pump strength ϵ_{crit} is reached and the system undergoes the superradiant phase transition. The atoms spontaneously self-organise in one of the two degenerate checkerboard patterns as depicted in Fig. 2.2(b). The atoms
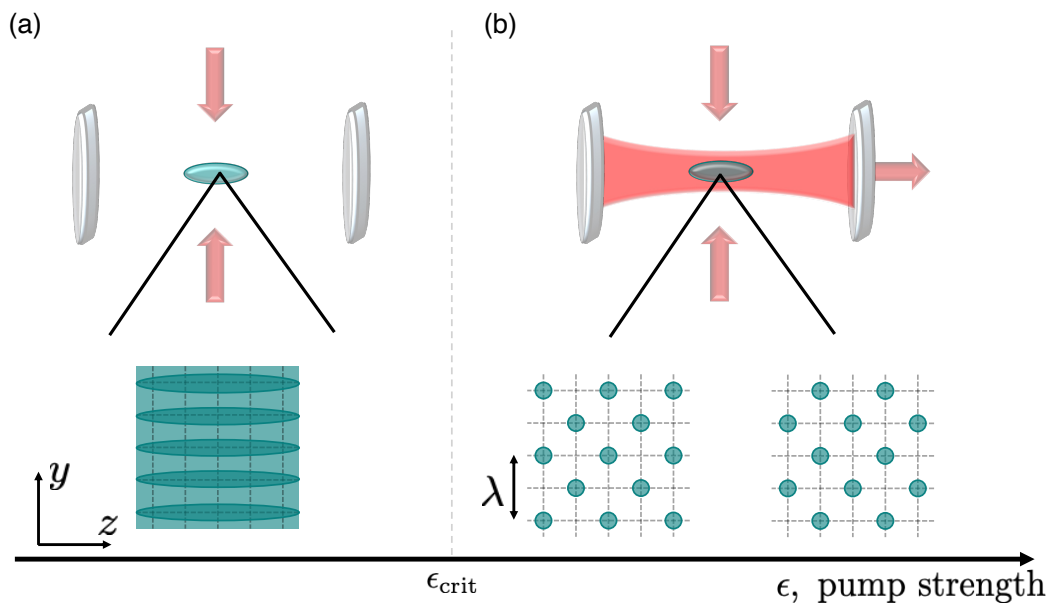
Figure 2.2: Sketch of the cavity-BEC setup below and above the superradiant phase transition. (a) For a pump strength below the critical value, atoms can scatter photons from the standing wave potential into the cavity. However, the atom density is homogeneous plus a small modulation due to the standing wave along the y-direction with the periodicity of $\lambda/2$. This means that for every scattered photon a second photon is scattered exactly with the opposite phase and there is no light field inside the cavity. (b) Above the critical pump strength, the atoms spontaneously self-organise in one of the two possible checkerboard patterns with spacing λ. The atoms fulfill the Bragg condition and scatter light into the cavity. This can be measured by the light field emitted from the cavity.

now perfectly fulfill the Bragg condition and the photons are constructively scattered into the cavity. Photons leaking out of the cavity can be detected and the $\mathcal{Z}_2$ symmetry breaking can be inferred by measuring the phase of the cavity photons compared to the pump beam. In the superradiant phase it is energetically favorable to acquire kinetic energy as this new pattern reduces the light-matter-coupling energy.

The focus of our research is related to the dynamics of the experiment in the group of Andreas Hemmerich in Hamburg. The experiment operates in the recoil-resolved regime [53, 54], this means that the dynamics of the light-field and the atoms evolve at the same timescale and the usual adiabatic elimination of the cavity dynamics employed in the extremely lossy cavity regime is not justified. Hence, in our numerics we solve the equations of motion for both the light field and the atomic sector simultaneously.

Typical parameters implemented in both the experiment and our numerics are $\kappa = 2\pi \times 4$ kHz, the total particle number $N_A = 60 \times 10^3$ and U_0 in the order of Hz.

Variations of this Hamiltonian have been used in publications [1, 3–9].

2.1.1 Methods

In the following, we briefly discuss the main methods we have repeatedly used and point towards further literature for a more in depth introduction.

Truncated Wigner approximation (TWA)

In publications [1,2,5,6,8–10] we have used the semiclassical TWA to include the leading-order quantum corrections to the mean-field effects [55, 56]. Roughly speaking, the idea is to sample over the initial Wigner distribution and to average over all trajectories to estimate the observable of interest. This method is well established in its continuous version [52, 55–59] as well as for spin models [2, 60–64]. In our case, we use a modified version of the TWA for open systems. Meaning, that we additionally consider the stochastic noise ξ associated to the dissipation of photons out of the cavity, which is defined as $\langle \xi^*(t')\xi(t)\rangle = \kappa\delta(t - t')$ [52, 65].
For a review we refer to [56]. There, the Wigner distribution is derived for the special cases of Fock states and coherent states in the initial state as well as an explicit recipe on how to derive the equations of motion. In our atom-cavity system we initiate the light field as well as the atoms as coherent states.

Schwinger-boson mapping

The Schwinger-boson mapping [66–68], sometimes called the Jordan–Schwinger map, is used to connect M bosonic N-level systems represented by the states $|1\rangle^{(i)},...,|N\rangle^{(i)}$ with $i \in \{1, ..., M\}$ to $SU(N)$ spin models. Therefore, the operators $\hat{A}_r^s = \sum_{i=1}^{M} = |r\rangle^{(i)}\langle s|$ are introduced [68]. In our studies we have primarily focused on the case that $N = 3$ and $N = 2$ leading to $SU(3)$ and $SU(2)$ spin models. For details, we refer to the appendix of publication [3], where we discuss this in great detail and explicitly show the mapping for a three-level system. We note that this mapping is just a rewriting of the same systems and no approximation is done during this mapping. Fig. 2.3(b)-(c) depict how this mapping is done after the low mode approximation of the full atom-cavity system to go from two-level systems to the Dicke model.

Holstein-Primakoff (HP) transformation

As the name suggests, the HP transformation is a priori no approximation [69–71]. However, the method is often used for large spin systems after the Schwinger-boson mapping such that an expansion in the large spin number can be done by the use of a Taylor expansion. In our case, we are often interested in the HP transformation, if we take the thermodynamic limit, meaning that the large spin number $N \to \infty$ [72, 73]. In the following we represent the HP transformation for $SU(3)$ spins, which we obtained

using the Schwinger-boson mapping above. The transformation is given by

$$\hat{J}_z^{12} = \hat{a}_{12}^\dagger \hat{a}_{12} - N_a/2$$

$$\hat{J}_+^{12} = \hat{a}_{12}^\dagger \sqrt{N_a - \left(\hat{a}_{12}^\dagger \hat{a}_{12} + \hat{a}_{13}^\dagger \hat{a}_{13}\right)}$$

$$\hat{J}_-^{12} = \sqrt{N_a - \left(\hat{a}_{12}^\dagger \hat{a}_{12} + \hat{a}_{13}^\dagger \hat{a}_{13}\right)}\ \hat{a}_{12}$$

$$\hat{J}_z^{13} = \hat{a}_{13}^\dagger \hat{a}_{13} - N_a/2$$

$$\hat{J}_+^{13} = \hat{a}_{13}^\dagger \sqrt{N_a - \left(\hat{a}_{12}^\dagger \hat{a}_{12} + \hat{a}_{13}^\dagger \hat{a}_{13}\right)}$$

$$\hat{J}_-^{13} = \sqrt{N_a - \left(\hat{a}_{12}^\dagger \hat{a}_{12} + \hat{a}_{13}^\dagger \hat{a}_{13}\right)}\ \hat{a}_{13}$$

$$\hat{J}_+^{23} = \hat{a}_{12}^\dagger \hat{a}_{13}$$

$$\hat{J}_-^{23} = \hat{a}_{13}^\dagger \hat{a}_{12}. \tag{2.5}$$

At this level there is no approximation, and we note that while the number of 8 spin operators are reduced to 3 bosonic modes, the system is now highly non-linear in bosonic mode. The approximation can now be done, if N is large. We Taylor expand the square roots to obtain a linear theory again. We discuss this in greater detail in the appendix of publication [3]. The approximation step is sketched in Fig. 2.3(c)-(d).
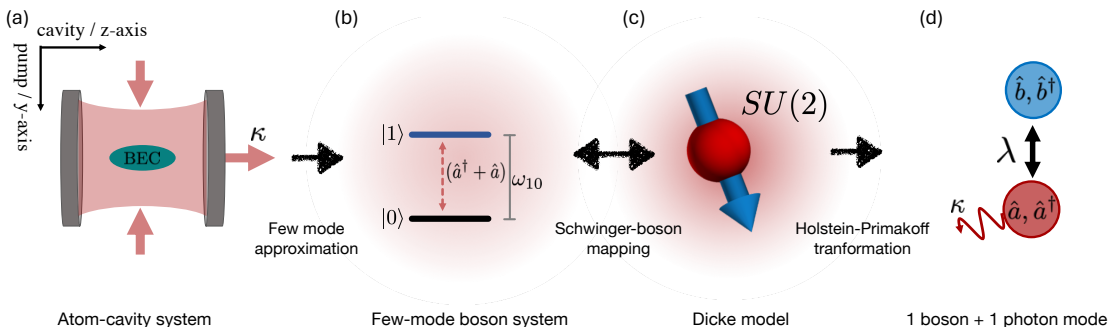

Figure 2.3: Sketch of the different levels of approximations starting from the full atom-cavity system for the example of the mapping to the Dicke model. (a) A BEC is transversely pumped by a retro reflected laser beam along the y-direction to form a standing wave potential. Light can be scattered into a high-finesse cavity with a photon loss rate κ and is oriented along the z-direction. (b) By employing a few-mode approximation, a few-mode boson model is obtained. (c) The system in (b) can be mapped, using a Schwinger-boson mapping, onto $SU(2)$ spins, which can be written as the Dicke model. (d) By applying a Holstein-Primakoff transformation and by only taking the lowest order contributions we obtain a system of two coupled oscillators.

2.1.2 Toy models

In the following we discuss the relevant toy models we have studied in the publications [2–7, 9]. We start with the full-atom cavity system and first apply a low-mode expansion. This is done by considering the relevant spatial modes, see Fig. 2.3. During my PhD the relevant spatial modes changed depending on whether we used amplitude driving to study the system, see publications [1, 2, 8], phase shaking of the pump beam, see publications [3–5] or whether we studied effects for stronger light-matter couplings as in publication [7]. To map these few-boson systems to spin systems we used the Schwinger-Boson mapping, see Fig. 2.3(b)-(c). Finally, for these simple models we used the Holstein-Primakoff approximation to either gain further analytical insights or to arrive at the model in question as in publication [10], see Fig. 2.3(c)-(d). Fig. 2.3 sketches these steps for the case of only two relevant spatial modes, leading to the standard Dicke model.

Dicke model

The Dicke model is a standard model in quantum optics that captures a wide class of light-matter systems. It describes N two-level systems coupled to a single quantised light mode. The model is called open Dicke model if any loss channels are included, usually in the form of a loss in the light mode. By applying a rotating wave approximation, the Dicke model reduces to the Tavis-Cummings model [74]. The limit of one two-level system coupled to a single quantised light mode is captured by the quantum Rabi model. Taking both limits of the rotating wave approximation and taking the number of two-level systems to one reproduces the Jaynes-Cummings model [74].

The Dicke model was first introduced in the context of a superradiant burst [75]. Here, N inverted two-level systems collectively emit light in a single mode with an intensity scaling as $\propto N^2$. This emission is enhanced compared to the emission due to spontaneous emission which scales as $\propto N$. Hence, this effect was dubbed superradiance. The study of superradiant bursts in free space [76], in special geometries of atoms [77–81] as well as in superradiant lasers [82–88] is still an active field of research. However, these phenomena are not discussed in this thesis.

Later, the Dicke model was introduced with the superradiant phase as a steady state phenomenon, which we have studied during my PhD. It was first pioneered in the 70s [89–93] and has been extensively studied including extensions and further generalisations in [3, 68, 73, 94–101]. However, soon after the first proposals, no-go theorems have been put forth, which have shown that this transition cannot occur for bare atomic levels due to the fact that the term $\vec{A}^2$, with $\vec{A}$ being the electromagnetic vector potential, cannot be dropped as it is done for the derivation of the Dicke model with minimal coupling [102–105].

However, scientists have found ways to circumvent these no-go theorems by using effective levels instead of the bare atomic levels. The first experimental proposals using ultracold atoms coupled to an open cavity have been discussed in [106–108] and the following first experimental realisations have been reported in [43–46, 95, 109–111]. For further reading we suggest to start with the following papers [72, 73, 112–114]. The Dicke

model can be defined as

$$\frac{\hat{H}_{\text{Dicke}}}{\hbar} = \omega_p \hat{a}^\dagger \hat{a} + \omega_0 \sum_{\ell=1}^{N} \sigma_\ell^z + \frac{2\lambda}{\sqrt{N}} \sum_{\ell=1}^{N} (\hat{a} + \hat{a}^\dagger) \sigma_\ell^x, \tag{2.6}$$

where we have introduced the individual spin operators σ_ℓ^μ obeying the $SU(2)$ algebra, and the bosonic operators $\hat{a}$ and $\hat{a}^\dagger$ annihilate and create a photon in the quantised light mode, respectively. ω_p is the frequency of the light mode, ω_0 the spacing of the individual spins, N the total number of spins and λ the light-matter coupling strength. Due to the collective coupling, we can further introduce collective spin operators as $\hat{J}_\mu = \sum_\ell \sigma_\ell^\mu$ with $\mu \in x, y, z$ and obtain

$$\frac{\hat{H}_{\text{Dicke}}}{\hbar} = \omega_p \hat{a}^\dagger \hat{a} + \omega_0 \hat{J}_z + \frac{2\lambda}{\sqrt{N}} (\hat{a} + \hat{a}^\dagger) \hat{J}_x. \tag{2.7}$$

As mentioned before, the Dicke model contains a superradiant phase transition. If a critical light-matter coupling strength is crossed, the system spontaneously acquires a finite light-field occupation. The transition is a so-called $\mathbb{Z}_2$ breaking pitchfork bifurcation as the superradiant phase has two degenerate ground states with different light phases, as is discussed for the full atom-cavity system. We discuss bifurcation to greater detail later in this chapter. Pitchfork describes the form of the stationary fixed points of the system. In the normal phase with a vanishing light-field, the only fixed point is $\langle \hat{a} \rangle = 0$. If the critical point at λ_{crit} is crossed, the fixed point becomes unstable and the new two stable fixed points are given by $\langle \hat{a} \rangle \propto \pm \sqrt{\lambda - \lambda_{\text{crit}}}$. This shape of the fixed points for varying λ leads to the name pitchfork bifurcation. To map the full atom-cavity Hamiltonian to the Dicke model a two-mode approximation is carried out as sketched in Fig. 2.3. The atomic field operator is expanded as

$$\Psi(y, z) = \hat{c}_0 + \frac{\hat{c}_1}{\sqrt{2}} \cos(ky) \cos(kz) \tag{2.8}$$

with $\hat{c}_i$ as bosonic annihilation operators. Below and closely above the superradiant phase transition this approximation is valid and the Dicke model is obtained, details can be found in [43]. We study the open periodically driven Dicke model in publication [2].

Lipkin-Meshkov-Glick model

The Lipkin-Meshkov-Glick (LMG) model can be obtained from the Dicke model by adiabatic elimination of the light-field in the limit $\kappa \to \infty$ [74, 112]. First, the LMG model was introduced in the context of nuclear spins [115–117] and was applied to fully connected spin models later [118–120]. Recently, it attracted interests from the time crystal community due to its strong all-to-all coupling, which in return can stabilise the time crystalline phase [2, 121–123]. The Hamiltonian is given by

$$\frac{\hat{H}_{\text{LMG}}}{\hbar} = \omega_0 \hat{J}_z - \Lambda \hat{J}_x^2 \tag{2.9}$$

with $\Lambda = 4\lambda^2 \omega_p / \left(N \left(\kappa^2 + \omega_p^2 \right) \right)$. We have studied the connection between the open Dicke model and the LMG for dissipative time crystals in publication [2].

Three-level Dicke model

One natural extension of the Dicke model, which as discussed above describes N two-level systems coupled to a single quantised light mode, is to study N three-level systems coupled to a single quantised light-mode. Variations of this model have been studied in [3–5, 124–130]. Using large spin operators the three-level Dicke model can be defined as

$$\frac{\hat{H}_{\text{three-level}}}{\hbar} = \omega_p \hat{a}^\dagger \hat{a} + \omega_{12} \hat{J}_z^{12} + \omega_{13} \hat{J}_z^{13} + \frac{2}{\sqrt{N}} \left(\hat{a}^\dagger + \hat{a} \right) \left(\lambda_{12} \hat{J}_x^{12} + \lambda_{13} \hat{J}_x^{13} \right). \quad (2.10)$$

To obtain such Hamiltonian from the atom-cavity system a third spatial mode needs to be considered. We have shown that a third spatial mode can alter the dynamics drastically by considering a dark spatial mode $\sin(ky)\cos(kz)$. This mode is a dark state relative to the cavity as the mode functions do not fit in the field produced by constructive interference of the pump and cavity field. We couple to this mode dynamically by phase shaking of the pump laser beam. We have shown the condensation in this dark state of the system in publication [5]. Furthermore, we have also shown that the density wave that builds up along the cavity direction $\cos(2kz)$ can destabilise, due to the back action on the effective light-field detuning stemming from the localisation of atoms. This effect becomes important for stronger light-matter coupling deep into the superradiant phase leading to limit cycle oscillations as have been observed in publication [6] and further studied in publication [7] and [8].

Dicke-Hubbard model

If an optical lattice is added to the full atom-cavity Hamiltonian and assuming that the optical lattice is sufficiently deep, we can expand our wavefunction into Wannier functions [5, 50, 131–133]

$$\Psi(y, z) = \sum_{n,m} w(y - y_n) w(z - z_m) \hat{b}_{nm} \quad (2.11)$$

with $y_n = \lambda/2 \times n$, $z_m = \lambda/2 \times m$ and $n, m \in \mathbb{Z}$. By regrouping the terms we can arrive at the Dicke-Hubbard Hamiltonian, where we neglected overall energy shifts due to the pump lattice and the shift due to the dynamical cavity lattice

$$\frac{\hat{H}_{\text{DH}}}{\hbar} = \omega_p \hat{a}^\dagger \hat{a} - J \sum_{\langle e,o \rangle} \left(\hat{b}_e^\dagger \hat{b}_o + \text{h.c.} \right) + U \sum_{i,j} \hat{n}_{n,m} \left(\hat{n}_{n,m} - 1 \right) - g \left(\hat{a}^\dagger + \hat{a} \right) \left(\sum_e \hat{n}_e - \sum_o \hat{n}_o \right) \quad (2.12)$$

with J the tunneling amplitude, $\langle .,. \rangle$ denoting nearest neighbor hopping and e/o denoting even and odd sites. A site is called even if the indices $(-1)^{n+m} = 1$ and odd if $(-1)^{n+m} = -1$. $\hat{b}_{n,m}$ and $\hat{b}_{n,m}^\dagger$ are the bosonic annihilation and creation operators at the site (n, m), $\hat{n}_{n,m}$ is defined as $\hat{b}_{n,m}^\dagger \hat{b}_{n,m}$ and g denotes the effective light-matter coupling. In our publication [7] we used the Dicke-Hubbard Hamiltonian to model the

system. For simplicity, we neglected shifts due to the pump-beam and have set the contact interaction U to zero. A derivation of the Dicke-Hubbard model from the full atom-cavity Hamiltonian can be found in [133].
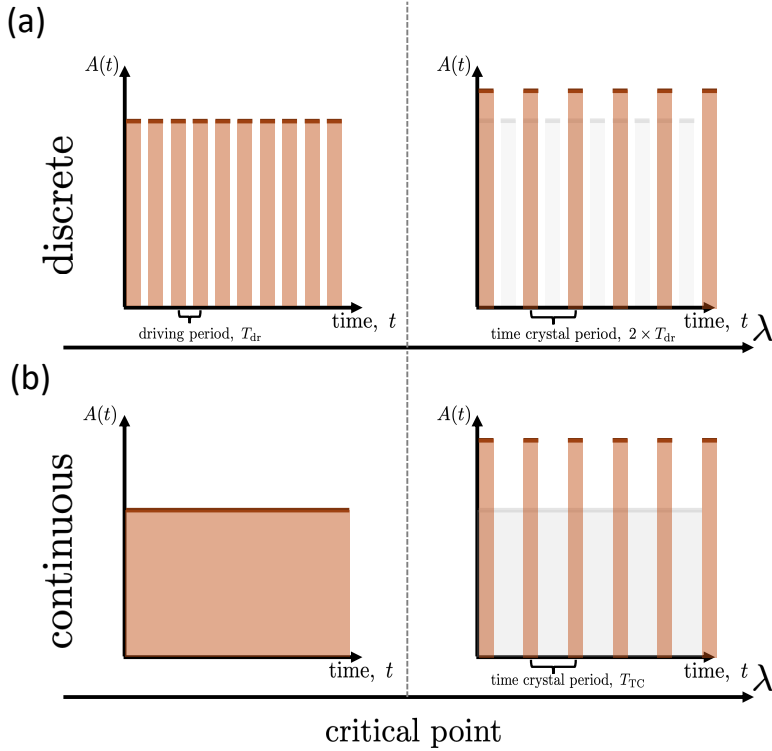
2.2 Time crystals

Figure 2.4: Sketch of the different kinds of time crystal. (a) Sketch of a discrete time crystal. A periodic drive is applied to the system and some observable $A(t)$ oscillates with the driving period T_{dr}. As some tuning parameter λ is tuned a critical point occurs and the system undergoes a phase transition into a discrete time crystal. The observable $A(t)$ oscillates at a subharmonic responds of the driving period. Here, the case of period doubling is depicted with $T_{TC} = 2 \times T_{dr}$. (b) Sketch of a continuous time crystal. Below the transition the observable is time independent. As the tuning parameter λ is increased the system spontaneously starts to oscillate at a period T_{TC}. In both cases, the dynamics of the observable before the phase transition is shown as a light gray background.

As the publications [1–4, 6–8] use the term "time crystals" to describe non-equilibrium dynamics, we will give a short introduction to this topic.

The concept of symmetry breaking is vital in physics [25, 27]. It ranges from the spatial

symmetry breaking as can be found in crystals [27] to the breaking of gauge symmetries as is done in the Higgs mechanism [26].

In physics, this concept was taken to the time domain by Wilczek and Shapere in 2012 [36,37]. They proposed that some observable $\hat{A}$ could spontaneously start to oscillate in the ground state of the system, which would be the analogue to spatial crystals. However, it was quickly shown that such phases cannot exist due to energy conservation [134–136]. Despite this drawback, the initial proposal sparked so much attention that people have shown ways to circumvent these no-go theorems. First, this has been done in periodically driven closed systems [137–142] and by studying so-called discrete time crystal, later discrete time crystal have been studied in open systems [143,144] and recently, continuous time crystal have been proposed [145–148] and observed [6,149–152].

Discrete time crystal (DTC)

A pictorial sketch of a discrete time crystal is shown in Fig. 2.4(a). For this class of time crystals, the system is periodically driven, which already breaks the continuous time translation symmetry and the system is left with a discrete time translational symmetry. On the level of the Hamiltonian, this translates to $\hat{H}(t) = \hat{H}(t + nT_{\mathrm{dr}})$ with $n \in \mathbb{N}$ and T_{dr} the driving period such that all observables also oscillate with this frequency. As some tuning parameter is changed the system spontaneously breaks this discrete symmetry such that $A(t) \neq A(t + nT_{\mathrm{dr}})$ for some observable A. The observable starts to oscillate with some subharmonic frequency of the drive $A(t) = A(t + T_{\mathrm{dr}}/m)$ with $m > 1 \in \mathbb{R}$, see Fig. 2.4. Quickly after the first theoretical proposals [137–140] the first period-doubling DTCs have been observed in spin systems [141, 142]. In [52] we have proposed an incommensurate time crystal, meaning that the TC frequency is not a multiple integer of the drive. We have further investigated this in publications [3–5].

Continuous time crystal (CTC)

In contrast to DTCs, CTCs are thought to break the continuous time translation symmetry. As sketched in Fig. 2.4(b), before the transition, the system is in a steady state without any temporal dependence. After the transition point, the system spontaneously starts to oscillate at an intrinsic frequency T_{TC}. This phenomenon can often be linked to a Hopf bifurcation leading to a limit cycle as is discussed in the following section.

After the first theoretical proposals [145–148], the first CTC has been experimentally observed in 2022 [6] and many experimental realisations have followed since then [149–152]. Today, DTCs and CTCs have been studied in a wide range of physical systems ranging from spin systems [121, 123, 137, 138, 153–162] to bosonic platforms [1–4, 6, 52, 143, 144, 148, 150, 163–169] to superconductors [10, 170, 171]. Recently, it has been proposed to use CTCs for sensing [172]. For extended reviews on this topic we refer the reader to [173–176].

2.3 Raman-Cavity coupling

In publication [10] we have studied the hybridization of a Raman and a cavity mode [10]. In the following we discuss the basic coupling of Raman active modes and how to derive the toy model we have studied analytically and numerically using TWA.

Raman active modes can be found in phonon systems [177, 178], as molecular vibrations [179] and as the Higgs mode in superconductors [180–182]. For an extensive discussion of examples and methods that rely on Raman modes we refer to [183].

We can define the induced electric dipole moment μ_{in} as [183]

$$\mu_{\text{in}} = \alpha \mathbf{E} \tag{2.13}$$

with $\mathbf{E}$ the electric field and α is the electronic polarizability tensor with its 9 components. The polarizability depends on the electric charge distribution of the system. Hence, we can expand α for small displacements of the nuclei in a normal coordinate Q and obtain

$$\alpha_{ij} = (\alpha_{ij})_0 + \sum_k \left(\frac{\partial \alpha_{ij}}{\partial Q_k} \right) Q_k \ . \tag{2.14}$$

The first term $(\alpha_{ij})_0$ is simply the often considered part of the polarizability tensor and the second term $\left(\frac{\partial \alpha_{ij}}{\partial Q_0} \right) Q_0$ leads to the first order Raman-effect [183]. Hence, if we neglect the contribution from $(\alpha_{ij})_0$, the light-matter interaction U is given by $U = \mu_{\text{in}} \mathbf{E} \approx \mathbf{E}^2 Q_0$, which is the typical form for a Raman coupling.

Our model studied in publication [10] can be derived by taking the HP approximation for the two-Photon Dicke model [184, 185]. With this we obtain the light-Raman coupling in the form of $\left(\hat{a} + \hat{a}^\dagger \right)^2 \left(\hat{b} + \hat{b}^\dagger \right)$ as expected for a Raman mode coupled to the light field.

2.4 Bifurcation theory

Most systems that can be found in nature are complex and highly nonlinear. However, solving nonlinear equations analytically is only in special cases possible. Due to this fact, many physical systems are approximated into a linear regime. A famous example is that of a swinging pendulum. Even though this example is very simple, the equations are nonlinear and finding an analytical solution is very difficult. Though, for small excitations, or if one is only interested in the low energy dynamics of the system, approximations can be done and the system can be described by the famous harmonic oscillator, which is easy to solve.

If one does not want to be limited to low-energy excitations, the nonlinearities have to be included and cannot be neglected. We know that a pendulum is swinging back and forth for low energies. We also know that for high energies the solution is simple again. The pendulum simply swirls over the top. The goal of bifurcation theory is now to find a framework that allows to predict points in parameter space, where the dynamics drastically changes. We want to predict the transition from swinging back and forth to the swirling over the top. In other words, we want to classify the *dynamics* of the system, whether it settles into an equilibrium, follows a drive, enters an oscillating regime, or exhibits chaotic behavior.

In our discussion we follow the book 'Nonlinear dynamics and Chaos' by Strogatz [12]. For any further readings and more examples we refer the reader to this book.

Fixed points and bifurcations

We are considering an equation of the form

$$\partial_t x = f(x), \tag{2.15}$$

where we have introduced the shorthand notation $\frac{\partial}{\partial a} r \equiv \partial_a r$ and with $f(x)$ some function of x. Starting from an initial point x_0, we can use this equation to propagate x and obtain $x(t)$. This function is then called a *trajectory* for the initial state x_0. If we plot all qualitatively distinct trajectories for different initial points, we obtain the *phase portrait*. We use a phase portrait in publication [7]. Points, where trajectories flow to and stagnate, are called *fixed points*. These fulfil the condition $f(x^*) = 0$. Fixed points represent equilibrium solutions. They can either be called *stable* fixed points, if all small perturbations away from the point decay or can be classified as *unstable* fixed points, if small perturbations grow in time away from the fixed point. Bifurcation theory is considering the change of the fixed points of the system as a parameter is changed. The points with this qualitative change in the dynamics due to the changed fixed points structure are called *bifurcation points*. As the most simple example we consider the buckling of a metal beam due to a weight placed on top of the beam. Fig. 2.5 shows the two scenarios. If the weight is small enough, the beam will remain vertical. The fixed point would be no deflection of the beam. If we increase the weight, at some point, the system will suddenly change and the beam will start to buckle. The deflection becomes finite, and we obtain two finite fixed points as the beam can buckle to the left or right.

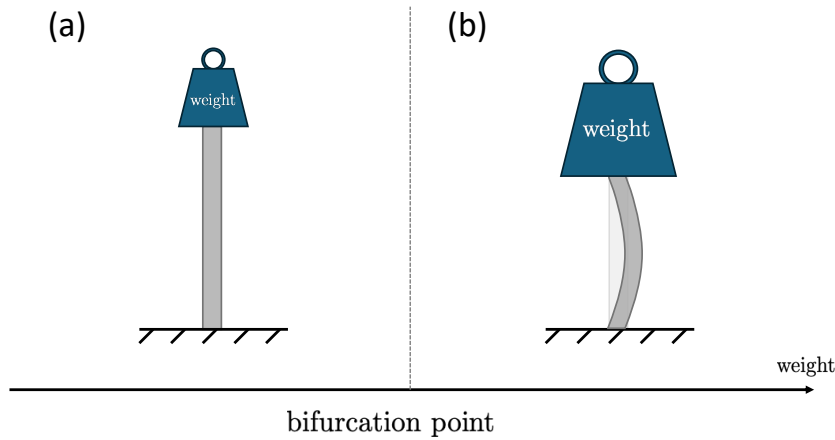This mean this scenario can be understood as a pitchfork bifurcation.

Figure 2.5: Sketch of a bifurcation. A weight is placed on a beam. For sufficiently small weights, the beam is not buckling, and the vertical displacement is zero, see (a). (b) As the weight increases the system passes a bifurcation point and the beam buckles, while acquiring a finite horizontal displacement.

2.4.1 Limit cycles

After having discussed what a bifurcation is, we want to use this framework to describe the particular class of oscillating phases. These are of particular interest as one can observe the following: 'Life is not standing still'. We can observe this in our daily life by our daily rhythm in body temperature, our sleep cycle and by the ongoing beating of our heart [12, 13, 15]. In neurosciences, we find that pace-maker neurons fire in a periodic fashion [186]. In biological systems such as the membrane potential of the frog hair cells in the low-frequency hearing organ oscillates in time already before any signal is received [187, 188], or we observe that almost all predator-prey models have oscillating solutions [14].

While these examples all appear in very different setups, what they all have in common is that the system spontaneously oscillates without an external periodic drive. These oscillations occur in complex, non-linear systems and are called *limit cycles*. Limit cycles can be described using effective models containing the relevant few degrees of non-linear systems, which contain oscillating solutions. A limit cycle can be defined as an isolated closed trajectory. Isolated means that all trajectories nearby either spiral away or towards the limit cycle and are not closed. If all neighboring trajectories spiral towards the limit cycle trajectory, the limit cycle is called stable. This means that all local perturbations will decay, and the trajectory will flow towards the limit cycle trajectory. In contrast, if the nearby trajectories spiral away, the limit cycle is called unstable, as any perturbation will take the dynamics away from the limit cycle. Limit cycles can only occur in *nonlinear* systems. While there can be closed trajectories in

linear systems, as for the harmonic oscillator with some initial state, these trajectories are never isolated. Intuitively this can be understood by the following reasoning. Assume we have found some periodic solution $cx(t)$. As the systems is linear, we know that $(c + \epsilon)x(t)$ is a solution as well. As $\epsilon \to 0$ any perturbation will lead us to this closed trajectory without any trajectories that are not closed in between [12].

For two-dimensional systems there are four classes of limit cycles, which all have different scaling laws for the amplitude of the limit cycle as well as the period of the limit cycle. Namely, the *saddle-node*, *Infinite-period*, *Homoclinic* and *Hopf*-bifurcation. Here, we will only focus on the Hopf bifurcation. We refer to the book by Strogatz [12] for details on the other types of limit cycles.

Hopf bifurcations

Framework

Here, we will briefly discuss the theoretical framework we have used to study limit cycles in publication [7]. The recipe allows studying Hopf bifurcations analytically, as well as numerically if needed. Extended discussion can be found in [7, 12, 189–191]. We assume that we have some equations of motion in the form of

$$\partial_t \mathbf{X} = \mathbf{F}(\mathbf{X}). \tag{2.16}$$

First, we compute the fixed points $\mathbf{X}_0$ by solving for $\mathbf{F}(\mathbf{X}_0) = 0$. Next, a Taylor series expansion around those fixed points leads to

$$\partial_t \delta_{\mathbf{X}} = \mathbf{J}_0 \delta_{\mathbf{X}} \tag{2.17}$$

with $\delta_{\mathbf{X}} = \mathbf{X}_0 - \mathbf{X}$ and $\mathbf{J}_0 = \left. \frac{\partial \mathbf{F}(\mathbf{X})}{\partial \mathbf{X}} \right|_{\mathbf{X}_0}$ the Jacobian stability matrix. To consider the stability of the fixed points we compute the eigenvalues (EV) of the Jacobian $\omega_{\mathrm{EV},i}$. Around the fixed points the dynamics of $\delta_{\mathbf{X}}$ is proportional to $\exp(\omega_{\mathrm{EV},i}t)$. Hence, only if the real part of all EVs are negative the fixed point will be stable. A Hopf bifurcation now occurs, if a conjugate pair of EVs crosses from negative to positive real parts, while having a finite imaginary part. The resulting limit cycle frequency will be approximately the imaginary value. In contrast, for the previously mentioned pitchfork bifurcation the imaginary parts are zero, while the real part crosses the imaginary axis [12].

In publication [7], our equations of motions are highly nonlinear, and we solve for the fixed points and for the EVs numerically.

Examples

A simple limit cycle

To showcase the basic tools we have introduced above, we will briefly discuss a simple example.

18

The equation of motion describing a radial and angular direction, r and θ, are given by:

$$\partial_t r = \mu r - r^3$$
$$\partial_t \theta = \omega + br^2. \tag{2.18}$$

As we will see the parameter μ is controlling the stability of the fixed points, ω describes the oscillation frequency and b relates the dependence of the frequency on the amplitude of the oscillations. We want to discuss the appearance of a Hopf bifurcation as we tune the parameter μ. It can be quickly seen that for $\mu < 0$ the only fixed point is given by $r = 0$. All trajectories spiral towards the origin. The sign of ω determines the direction of the spirals. We will use the framework developed above to determine the character of transition as μ becomes positive. To compute the Jacobian it is convenient to convert the equations back into Cartesian coordinates, and we find for the Jacobian [12]

$$\begin{pmatrix} \mu & -\omega \\ \omega & \mu \end{pmatrix} \tag{2.19}$$

with its eigenvalues $\lambda_\pm = \mu \pm i\omega$. Fig. 2.6 sketches the phase portrait below and above the Hopf bifurcation. Below the transition all trajectories spiral to the single fixed point. Above the transition a limit cycle occurs.
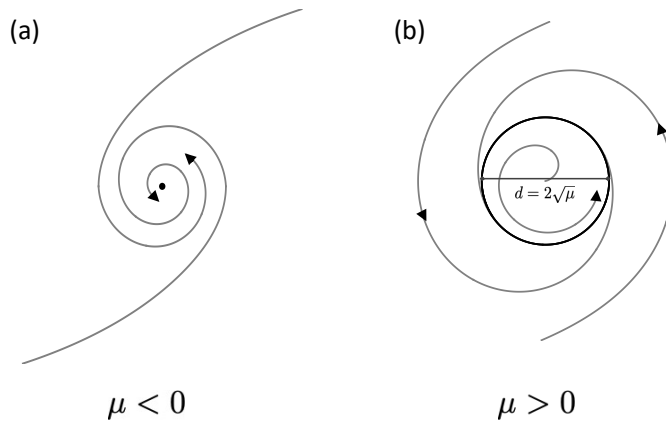

Figure 2.6: Sketch of the phase portrait below $\mu < 0$ and above $\mu > 0$ the Hopf bifurcation. (a) All trajectories spiral towards the fixed point in the centre. (b) All trajectories are attracted towards the stable limit cycle with radius $\sqrt{\mu}$.

Van der Pol oscillator

The van der Pol oscillator is undoubtedly the most famous example model hosting a limit cycle and still plays a great role in developing new tools for nonlinear dynamics and subject of research in quantum mechanical systems [192–196]. The van der Pol equation was historically first used to describe nonlinear electrical circuits in radios and

is given by

$$\partial_{tt}x + \mu\left(x^2 - 1\right)\partial_t x + x = 0 \tag{2.20}$$

with $\mu \geq 0$. For $\mu = 0$ the equation reduces to the equation of a simple harmonic oscillator. However, for finite μ a nonlinear damping term is added. Without further analysis it can be seen that for large x ($|x| > 1$) this term acts as an ordinary positive damping term, while for small x ($|x| < 1$) it acts a negative damping term. This means the dissipation effectively pumps energy into the system in this case. Intuitively, it becomes clear why limit cycle can appear. Limit cycle will occur if over one complete cycle the dissipation balances between the energy lost for positive damping and negative damping. As a remark, we note that this example does not fit into the standard classification of limit cycles, but the bifurcation is akin to the degenerate Hopf bifurcation. This is due to the degenerate case $\mu = 0$. Details on this extra complications, if there are additional symmetries, are also found in the book by Strogatz [12].

2.4.2 Entrainment and synchronisation

Previously we discussed what a limit cycle is. Here, we will briefly discuss which phenomena can occur if many limit cycle interact and *synchronise*. One of the most famous examples of synchronisation, and maybe even one of the most beautiful examples, due to its simplicity and complexity at the same time, in nature is the unison flashing of fireflies as can be observed in Southeast Asia [12]. Essentially the male fireflies gather in trees and flash on and off to attract the female fireflies. The male fireflies interact with each other and slow down or speed up the flashing until they are flashing in unison. To appreciate the beauty of this spectacle, we highly recommend the reader to see the episode 'Talking to Strangers' by David Attenborough's television series 'The Trials of Life' from 1992.

Entrainment vs synchronisation

In this thesis we will distinguish between entrainment and synchronisation. We will refer to entrainment if a limit cycle is externally forced by some oscillator and there is no back action from the limit cycle to the external oscillator. We will refer to synchronisation if the system consists of many limit cycles that are all coupled to each other and interact. A sketch of these two different kinds of interaction structures can be found in Fig. 2.7. In this thesis we will not discuss the phenomenon of synchronisation further. However, we note that there are many interesting questions to ask and potentially answered with the models and platforms we have discussed in this thesis and suggest this for future work.

Entrainment

Fireflies cannot only synchronise, they can also be entrained by a torch [197]. Another example is the entrainment of the cardiac system, namely the heart [198] or the injection
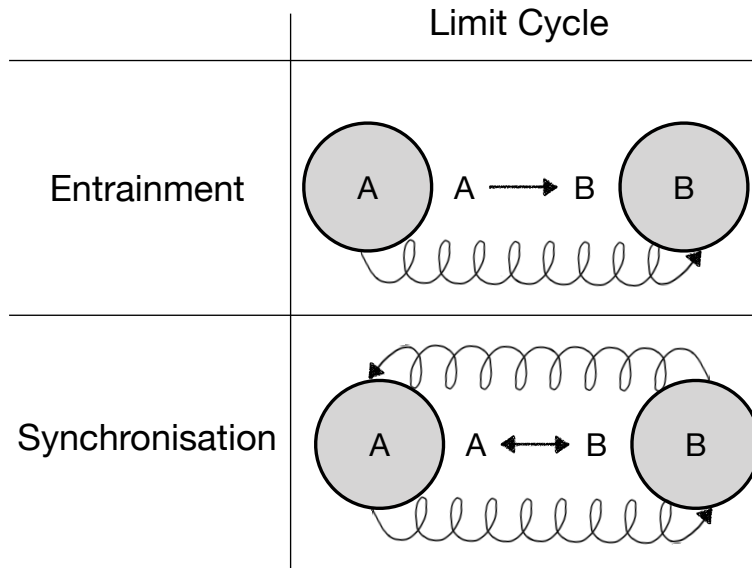
Figure 2.7: Sketch of entrainment vs synchronisation. Curly lines denote interaction and the arrows the direction of the interaction. While for entrainment only limit cycle A influences limit cycle B and not the other way around, for synchronisation limit cycle A and B interact and influence each other.
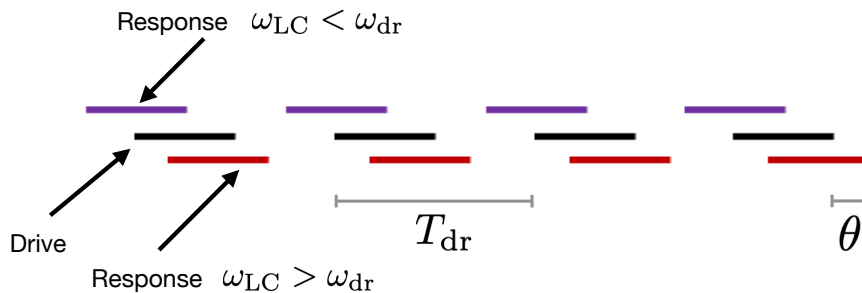

Figure 2.8: Sketch of the phase relation between the drive and the response of the limit cycle. Solid lines denote times when $\cos(\omega t) > 0$. θ denotes the phase difference between the drive and the entrained limit cycle.

locking of laser [199]. While this phenomenon occurs in very different settings, they all have in common that the central idea is that an external drive is applied to a limit cycle. Now depending on whether the external frequency is slower or faster than the limit cycle frequency, the limit cycle will speed up or will slow down to have the same frequency of the drive. This will only be possible for a symmetric range around the limit cycle frequency. For a toy model capturing these findings and more details we refer to the book by Strogatz [12].

Here, we will briefly focus on the phase relation of the drive and the response [12] as

this has been used in publication [8]. Fig. 2.8 depicts this relation. The solid black line denotes the times when the drive $\propto \cos(\omega_{\mathrm{dr}} t)$ is larger than 0. The corresponding response for a limit cycle with a smaller frequency than the drive is depicted in purple and for a limit cycle frequency larger than the drive in red. It can be seen that the phase difference θ is negative for $\omega_{\mathrm{LC}} < \omega_{\mathrm{dr}}$, 0 if $\omega_{\mathrm{LC}} = \omega_{\mathrm{dr}}$ and becomes positive if $\omega_{\mathrm{LC}} > \omega_{\mathrm{dr}}$. We note that this only occurs for entrained limit cycle, for a simple periodically driven harmonic oscillator (HO) this is not the case. Here, for slow driving the HO can follow the drive and both are in phase as the HO is not oscillating preciously to the drive. As the driving becomes faster

exactly out of phase with

In publication [8] we were

the definition of the phase

frequencies in Fig. 2.9. We choose θ such that for the resonant case of $\omega_{\mathrm{dr}} = 2\omega_{\mathrm{LC}}$ the phase is zero. More detailed and numerical results for subharmonic entrainment can be found in the supplemental material of publication [8]. We note that subharmonic entrainment is an example of a discrete time crystal.

Figure 2.9: Sketch of the phase relation between the drive and the response of the limit cycle for subharmonic entrainment. Solid lines denote times when $\cos(\omega t) > 0$. θ denotes the phase difference entrained limit cycle if $\omega_{\mathrm{dr}} = 2\omega_{\mathrm{LC}}$ and the entrained limit cycle with a different driving frequency.

2.5 Atomtronics

In publication [9] we proposed an atom-cavity based rotation sensor. In this section, we briefly discuss the field of atomtronics and atom interferometry and discuss one of the relevant quantities to compare sensors. Atomtronics is a subfield of the wider research field of quantum technologies [202]. Quantum technologies are promised to enable important innovations in areas as communication, sensing, simulation and computing [202, 203] within the next decades.
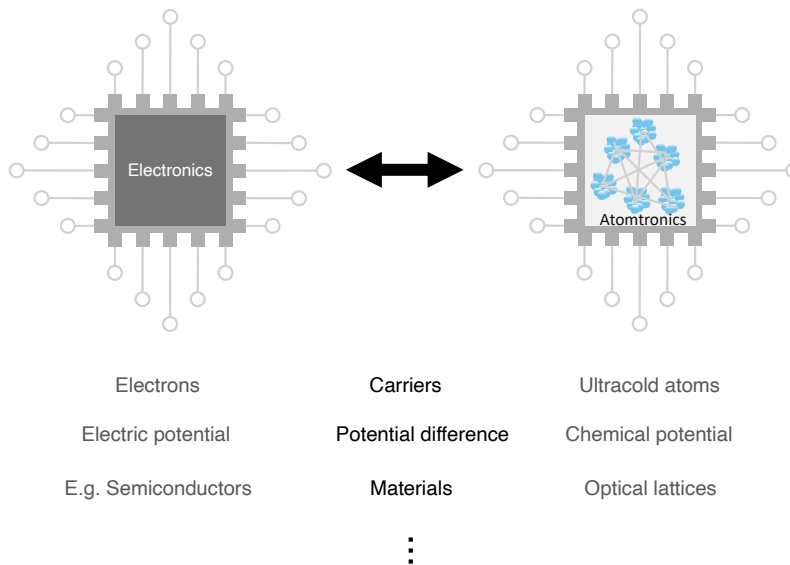
2.5.1 Atom-interferometry

Figure 2.10: Sketch of a circuit from electronics and atomtronics. While in electronics the electrons are carrying the charge, in atomtronics this is done by atoms. The electric potential is replaced by the chemical potential and instead of using a semiconductor device an optical lattice might be used. Adapted from [204].

Atomtronics realises matter-wave circuits based on ultracold atoms, see the sketch in Fig. 2.10. Due to the analogy between these circuits consisting of cold atoms and those formed by electron circuits of conductors the name *atomtronics* was coined. To just name a few examples, the role of the carriers of the electronic charge are electrons in electronics and in atomtronics the atoms carry the charge. Further, the electric potential is mimicked by the chemical potential and so on. This mapping from parameter and concepts from electronics to atomtronics is shown in Fig. 2.10. However, it is important to stress that atomtronics has not just the goal of copying and maybe improve parts of electronics by some previously defined goals, but also to be used for different tasks such as sensors, optical devices and so on. This is sketched in Fig. 2.11, but is by no means
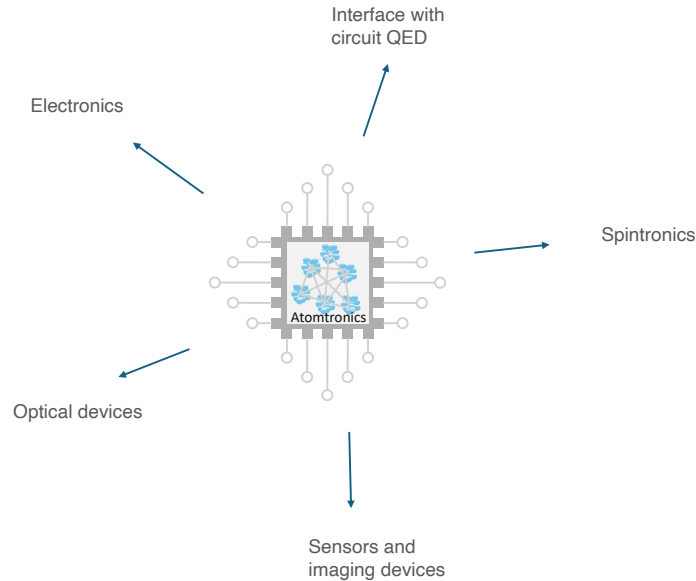
23

Figure 2.11: Sketch of fields of application of atomtronics. This can range from building better electronics, to better sensors, to spintronic devices to optical devices. Adapted from [204].

a complete list of fields of application. So it is really an effort to go beyond electronics and use these platform for a larger set of tasks.

Atomtronics promises to utilise the accuracy and long-time stability of ultracold atoms platforms. As an example, current technologies use laser interferometry based on optical Sagnac interferometers for rotational sensing, however these can fall short due to its limited sensitivity and long-term stability [205]. To overcome these obstacles, atom interferometers can combine the benefits of atomtronics and the setup of interferometer. Atom interferometry allows building high precision rotation and acceleration sensors [206–211] with applications ranging from fundamental physics [212–214], absolute gravimetry [215, 216] to inertial navigation [217–219]. For a review of atomtronics and atom-interferometry we refer to [202].

Inertial navigation

For inertial navigation it is crucial to have a high repetition rate in the measurements [219, 220], which can be challenging, if the frequency of interest is large. We propose to overcome this constraint by the use of an open system that allows for measurements of fast time-varying signals due to the light leaking out of the system that allows to trace back the dynamics inside the sensor [9].

(a)

$|\alpha|^2_{\text{steady}} \times 10^3$

0   5   10   15

(b)

$\log_{10}(RW)\ [^{\circ}/\sqrt{\text{hr}}]$
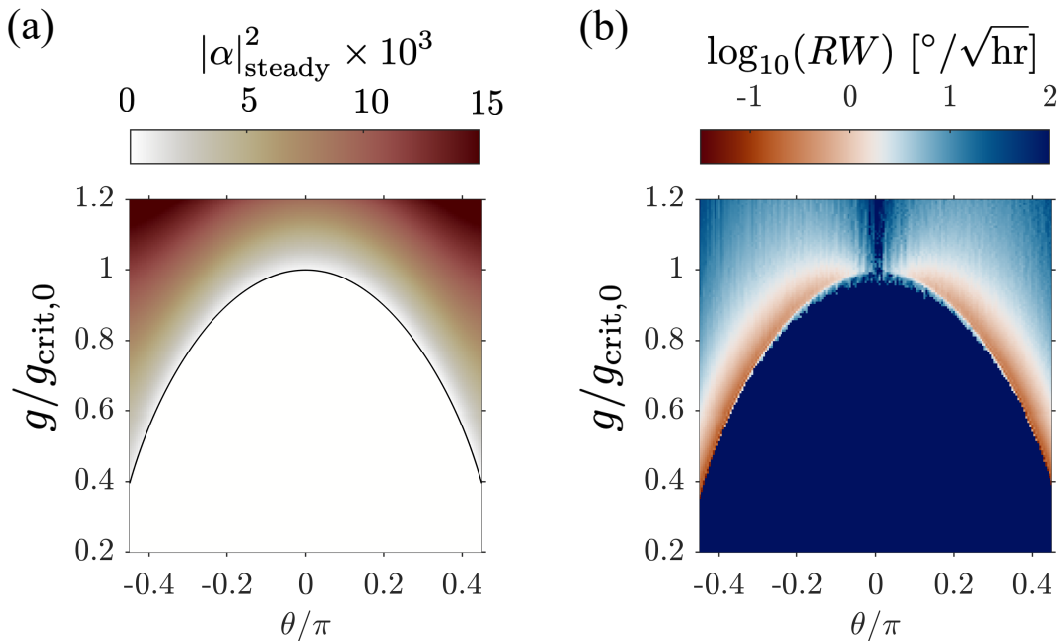
-1   0   1   2

Figure 2.12: (a) The steady state light field intensity $|\alpha|^2$ obtained using TWA simulations as a function of the external rotation frequency and light-matter coupling strength. The light-matter coupling strength is rescaled by the critical value for the non-rotating case. The red curve corresponds to the analytically derived phase boundary. (b) The random walk RW on a logarithmic scale using the same axis and method as in (a). For each data point, we average over 10^2 TWA trajectories.

Sensitivity

To quantify the sensitivity of our proposed sensor we define the Allan deviation as $\sigma(T_i)$ with T_i the interrogation time as

$$\sigma(T_i) = \frac{\langle N_p^2 \rangle}{dN_p/d\Omega} \tag{2.21}$$

with Ω the external rotation frequency and N_p the photon number leaking out of the cavity. The number of photons can be obtained from the atom-cavity system via $N_p = \kappa T_i |\alpha|^2$. We present a numerically obtained phase diagram by the use of TWA in Fig. 2.12(a) for different Peierls phases of θ, which is directly proportional to the externally applied external rotation Ω and for different light-matter coupling strength g. We rescale g by the critical light-matter strength required to enter the superradiant phase without any external rotation applied. We observe a strong dependence of the photon number on the external rotations applied as can be seen for fixed light-matter coupling strength g. Furthermore, we also observe that the critical light-matter coupling is strongly lowered as an external rotation is applied. This happens as the external

rotations effectively decreases the real part of the tunneling amplitude. To enter the superradiant phase it is a competition between the cost of the light-matter energy and tunneling energy. By changing the tunneling energy, due to the external rotation, we can change the critical light-matter coupling strength needed to enter the superradiant phase. This is the key mechanism to use the system as a rotation sensor as changes in external rotations are translated into changes in the photon number detected. We note that the system can even be pushed from the normal to superradiant phase and vice versa due to changes in the external rotation. We use the same parameter as for the atom-cavity system and for the tunneling amplitude $J = 2$ kHz. Intuitively, the quantity describes the ratio between the standard deviation of the photon number and the change in the photon number by change of the external rotation frequency. In simple words, how much does the rotation frequency need to change to be not hidden in the fluctuations. Using a mean-field ansatz and the model obtained in publication [9] we can compute this quantity to be

$$\sigma(T_i) = \frac{2\omega_{\text{rec}}}{n_s \pi^2} \sqrt{\frac{\delta_C^3}{T_i \kappa N_{\text{A}} J \left(\delta_C^2 + \kappa^2\right)}} \frac{x^2 \sqrt{x^2 - \frac{\cos(\theta)^2}{x^2}}}{\cos(\theta) \sin(\theta)} \quad (2.22)$$

$$\propto \frac{\omega_{\text{rec}}}{n_s \sqrt{N_{\text{A}}}} \sqrt{\frac{\delta_C^3}{\left(\delta_C^2 + \kappa^2\right) T_i \kappa J}}$$

with $x = g/g_{\text{crit},0}$, $g_{\text{crit},0}$ the critical light-matter coupling without external rotations, J the tunneling amplitude between neighboring sites, δ_C the effective light-field detuning, κ the loss rate of the cavity, n_s the number of sites, N_{A} the number of atoms and θ the Peierls phase obtained via the externally applied rotation. We deduct that the sensitivity can be increased by adding more atoms, by increasing the number of sites or if the interrogation time is increased. The Allan deviation scales with $T_i^{-1/2}$, which is as expected for systems with white Gaussian noise. A further path to increase the sensitivity is to reduce δ_C, while keeping the loss rate κ constant or by further increasing κ. However, one should note that the system can become unstable in this limit as back action on the light-field frequency due to the localisation of the atoms becomes relevant. Another relevant quantity is the so-called random walk parameter RW. This quantity can be obtained by from the Allan deviation via $RW = \sigma(T_i)\sqrt{T_i}$ and is independent of the interrogation time. We obtain for the random walk

$$RW = \sigma(T_i)\sqrt{T_i} \propto \frac{\omega_{\text{rec}}}{n_s \sqrt{N_{\text{A}}}} \sqrt{\frac{\delta_C^3}{\left(\delta_C^2 + \kappa^2\right) \kappa J}}. \quad (2.23)$$

This quantity measures the accumulated drift over time in the measure angle due to the noise in the time-integrated signal and is usually presented in deg/$\sqrt{\text{hr}}$. In Fig. 2.12(b) we present the numerical TWA results for the RW again for varying θ and g on the same range of parameters as for the photon number. As expected, the sensitivity is increased as the sensor operates closer to the phase transition. It is beneficial to operate the sensor with an initial offset rotation, which lowers the critical light-matter coupling and expands

the area in the phase diagram in which we achieve the best sensitivities. However, we note that it is crucial to be close to the phase transition. This might be challenging in an experiment as this requires high stability in the number of atoms, which ideally should saturate the fluctuations of the atom number as expected for coherent states. With realistic parameter, we find for values down to $10^{-1.5}$ for the RW in units if $°/\sqrt{\text{hr}}$. To further reduce this value the same parameter need to be changed as for the Allan deviation. We find the numerically by the use of TWA that the emitted light field of the cavity is phase squeezed. This increases the variance of the photon number, which we assume to be in a coherent state for our analytical prediction. If one is able to push the light field into being amplitude squeezed, one could highly increase the sensitivity of the sensor. For more details we refer to the publication [9], which will be updated soon.

2.6 Publication I: Dissipative time crystal in an atom-cavity system: Influence of trap and competing interactions

R.J.L. Tuquero, <u>J. Skulte</u>, L. Mathey and J.G. Cosme — **Physical Rev. A 105, 043311 (2022)**

Motivation

This work was motivated by the first realisation of a dissipative discrete time crystal (DTC) in a laser-pumped atom-cavity system in the group of Andreas Hemmerich. The goal of this project was to analyse in detail the long-time stability of this new non-equilibrium phase against contact interactions and a confining potential as they are present in the experiment.

Main findings

In this work, first-authored by Richelle J.L. Tuquero, we have investigated the stability of the DTC adding mean-field breaking terms as can be found in the experiment in Hamburg on time scales that cannot be realised in experiments today. We have mapped out the dynamical phase diagram for various strength of contact interactions and harmonic trapping confinements. We have found regimes in which the DTC is indeed long-lived despite the mean-field breaking terms we have added.
Furthermore, we have found regimes in which metastable DTCs can emerge. These can either exist with prethermalization plateaus for tight harmonic potentials or without prethermalization plateaus for sufficient strong contact interactions.

Contribution

My contribution to this work consisted of adding analytical calculations. RJLT performed the numerical studies under the supervision of JGC. All authors contributed to the discussion and interpretation of the results, as well as to writing the manuscript.

Dissipative time crystal in an atom-cavity system: Influence of trap and competing interactions

Richelle Jade L. Tuquero [1], Jim Skulte [2,3] Ludwig Mathey,[2,3] and Jayson G. Cosme [1]

[1]*National Institute of Physics, University of the Philippines, Diliman, Quezon City 1101, Philippines*
[2]*Zentrum für Optische Quantentechnologien und Institut für Laser-Physik, Universität Hamburg, 22761 Hamburg, Germany*
[3]*The Hamburg Center for Ultrafast Imaging, Luruper Chaussee 149, 22761 Hamburg, Germany*

While the recently realized dissipative time crystal in a laser-pumped atom-cavity system in the experiment of Keßler *et al.* [Phys. Rev. Lett. **127**, 043602 (2021)] is qualitatively consistent with a theoretical description in an idealized limit, here, we investigate the stability of this dissipative time crystal in the presence of an inhomogeneous potential provided by a harmonic trap, and competing short- and infinite-range interactions. We note that these features are ubiquitous in any realization of atom-cavity systems. By mapping out the dynamical phase diagram and studying how it is modified by the harmonic trap and short-range interactions, we demonstrate the persistence of long-lived dissipative time crystals beyond the idealized limit. We show the emergence of metastable dissipative time crystals with and without prethermalization plateaus for tight harmonic confinement and strong contact interaction, respectively.

I. INTRODUCTION

Time crystals are nonequilibrium many-body phases, in which time-translation symmetry is spontaneously broken [1–5]. Time crystals that are induced by periodic driving exhibit a robust subharmonic response in relation to the driving frequency. Isolated systems under periodic driving, however, continuously heat up, in general, causing the time crystalline order to "melt" into a featureless state. One approach to stabilize periodically driven time crystals, also known as Floquet time crystals, consists of adding strong disorder to push the system into a many-body localized phase [6–8]. This has enabled the experimental observation of discrete time crystals in various periodically driven systems [9–13]. Discrete time crystals, which do not rely on many-body localization, have been realized in other experimental platforms [14–16]. Alternative strategies to stabilize time crystals include coupling the system to an environment [17–21] or including long-range interaction [22–26].

Dissipation, in particular, has been utilized to create a dissipative time crystal (DTC) in an atom-cavity system [27]. Due to the approximation of the atom-cavity system via the Dicke model [28], this paradigmatic DTC can be regarded as a realisation of the Dicke time crystal [18]. The open Dicke model describes an ensemble of two-level systems interacting with photons in a leaky cavity [29]. Note that the standard Dicke model does not have any notion of spatial dimension as it is a zero-dimensional model. That is, it excludes spatially dependent potential for the atoms. More importantly, it only captures the all-to-all photon-mediated coupling between the atoms. These approximations provide an idealized limit, in which the spatial $\mathbb{Z}_2$ symmetry breaking in the superradiant phase is intimately tied to the temporal $\mathbb{Z}_2$ symmetry breaking of the period-doubled Dicke time crystal. Moreover,

the infinite-range nature of the cavity-mediated interaction makes this approximate description mean-field solvable and, in fact, exactly solvable in the thermodynamic limit [18,30]. The absence of an inhomogeneous potential and other forms of interaction distinguishes the Dicke model from an atom-cavity system in Ref. [27] and any other realisations, where an external harmonic trap and inherent collisional interactions between the atoms are present. These subtle yet important distinctions pose the question about the stability of DTCs, or any prediction based on the Dicke approximation, in realistic atom-cavity setups, in addition to the finite lifetime of Bose-Einstein condensates. On the one hand, inhomogeneous potentials, such as a harmonic trap, break the spatial symmetry, which could affect the $\mathbb{Z}_2$ symmetry broken states responsible for the period-doubling response. On the other hand, short-range interactions break the mean-field solvability of the Dicke model [30]. Given that these features are ubiquitous in any atom-cavity system, it is imperative to point out their influence. In the absence of dissipation, beyond mean-field effects on discrete time crystals in a spin model with competing short- and long-range interactions are studied in Ref. [31].

In this work, we investigate the influence of harmonic confinement and short-range interaction on the DTC found in a periodically driven atom-cavity system. We show that a DTC remains stable in the presence of weak perturbations that explicitly break spatial symmetry and mean-field solvability of the model. This is in contrast to the absence of a stable period-doubling response predicted in a similar atom-cavity setup but for the bad cavity limit, wherein the cavity dynamics is orders of magnitude faster than the atomic dynamics [32]. While it was mentioned in Ref. [27] that strong contact interaction may lead to a DTC with finite lifetime, similar to a metastable Dicke time crystal [30], a detailed analysis of
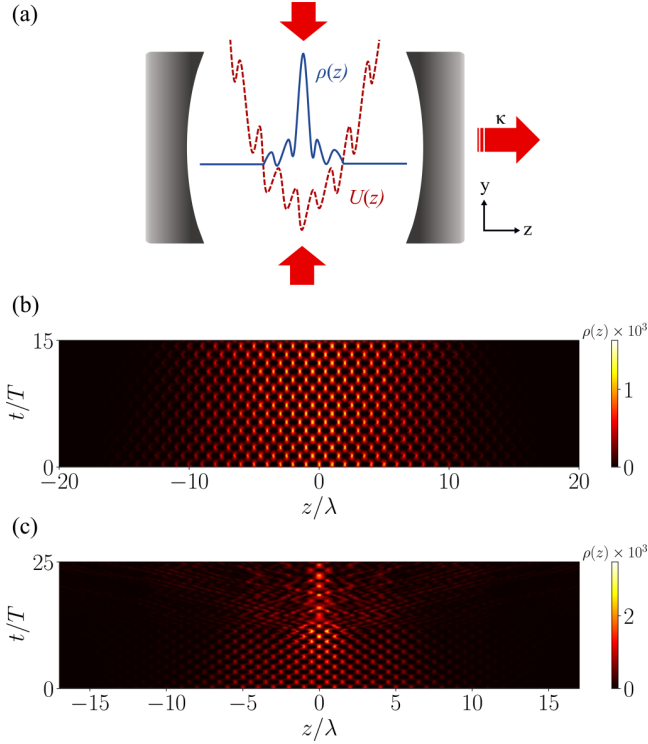
FIG. 1. (a) Schematic diagram of the atom-cavity system consisting of a Bose-Einstein condensate with a harmonic trap inside a high-finesse optical resonator. The solid curve denotes the particle distribution $\rho(z)$ in the self-organized density wave phase and the dashed curve denotes the combined dipole potential $U(z)$ due to the cavity field and the harmonic trap. The cavity photon loss rate is κ. The pump and cavity wavelength is λ. Dynamics of the atomic density for a (b) stable and (c) metastable dissipative time crystal with harmonic trap frequency $\omega = \hbar/m(3.5\lambda)^2$ and short-range interaction energy $E_{\mathrm{int}}/E_{\mathrm{rec}} = 0.26$ with E_{int} as defined Sec. IV. In (b), the driving strength is $f_{\mathrm{d}} = 0.7$ and the driving frequency is $\omega_{\mathrm{d}}/2\pi = 5\,\mathrm{kHz}$. While in (c), $f_{\mathrm{d}} = 0.5$ and $\omega_{\mathrm{d}}/2\pi = 3.5\,\mathrm{kHz}$.

this phase, which we call metastable DTC, is still lacking. Aside from the Dicke time crystal, other dynamical phases in dissipative systems are found to exhibit metastability when pushed out of the idealized limit [33,34]. Here, we show that metastable DTCs may emerge not only because of short-range interaction competing with the infinite-range interaction but also due to the influence of harmonic confinement.

This work is organized as follows. We discuss the system, the method for simulating the dynamics, and the driving protocol in Sec. II. The properties of the stable DTC in the ideal atom-cavity system is reviewed in Sec. III. In Sec. IV, we map out and analyze the dynamical phase diagram for different combinations of contact interaction strength and harmonic trap frequency. In Sec. V, we further study the metastable dissipative time crystal and its lifetime. Finally, we conclude this paper in Sec. VI

II. SYSTEM

We consider an atom-cavity system with a Bose-Einstein condensate (BEC) of ^{87}Rb atoms as depicted in Fig. 1(a). An

external laser is applied along the y direction, which is perpendicular to the cavity axis aligned in the z direction. Photons leak out of the cavity at a rate of κ. The cavity wavelength is λ. An external harmonic trap is present along the z direction. In the following, we consider the one-dimensional limit of the system and investigate only the dynamics along the cavity axis.

We vary the pump intensity ϵ to investigate the dynamical response of the system. The transversely pumped atom-cavity system hosts a self-organisation phase transition [35]. Above a critical value ϵ_{crit}, it becomes energetically favourable for the atoms to self-organise into a chequerboard density wave (DW) phase to scatter photons from the pump into the cavity [36,37]. This self-organisation phase transition is as an approximate emulation of the superradiant phase transition in the Dicke model [29]. In the density wave phase, the system breaks the $\mathbb{Z}_2$ symmetry as the atoms spontaneously localise either in the odd or even sites of the emergent standing wave formed by the cavity photons. These two symmetry broken states can be distinguished by the sign of the density wave order parameter $\Theta = \langle \cos(kz) \rangle$ where $k = 2\pi/\lambda$. That is, a non-zero positive (negative) value for Θ corresponds to an even (odd) DW state [35–38].

The Hamiltonian for the system is a combination of the cavity and the atom Hamiltonian, as well as the short-range atom-atom interaction and the atom-cavity interaction, i.e.,

$$\hat{H} = \hat{H}_{\mathrm{C}} + \hat{H}_{\mathrm{A}} + \hat{H}_{\mathrm{AA}} + \hat{H}_{\mathrm{AC}}. \tag{1}$$

The Hamiltonian for the cavity with a mode function $\cos(kz)$ is given by

$$\hat{H}_{\mathrm{C}} = -\hbar \delta_{\mathrm{C}} \hat{\alpha}^\dagger \hat{\alpha}. \tag{2}$$

where δ_{C} is the pump-cavity detuning and $\hat{\alpha}^\dagger$ ($\hat{\alpha}$) is the creation (annihilation) operator for the cavity photon. We include a harmonic trap for the atoms with trap frequency ω. The single-particle Hamiltonian for the atoms is

$$\hat{H}_{\mathrm{A}} = \int \hat{\Psi}^\dagger(z) \left[-\frac{\hbar^2}{2m} \frac{d^2}{dz^2} + \frac{1}{2} m \omega^2 z^2 \right] \hat{\Psi}(z)\, dz \tag{3}$$

where m is the mass of a ^{87}Rb atom and $\Psi(z)$ is the bosonic field operator associated with the BEC. We are interested in the interplay between the infinite-range cavity-mediated interaction and the inherent short-range collisional interaction between the atoms. The short-range interaction is described by

$$\hat{H}_{\mathrm{AA}} = \frac{g_{\mathrm{aa}}}{2} \int \hat{\Psi}^\dagger(z) \hat{\Psi}^\dagger(z) \hat{\Psi}(z) \hat{\Psi}(z) dz. \tag{4}$$

where g_{aa} is the contact interaction strength. On the other hand, the atom-cavity interaction, which gives rise to a dynamical infinite-range interaction between the atoms, is modeled by

$$\hat{H}_{\mathrm{AC}} = \int \hat{\Psi}^\dagger(z) \hbar U_0 [\cos^2(kz) \hat{\alpha}^\dagger \hat{\alpha}$$

$$+ \sqrt{\frac{\epsilon}{\hbar |U_0|}} \cos(kz)(\hat{\alpha}^\dagger + \hat{\alpha})] \hat{\Psi}(z)\, dz. \tag{5}$$

The pump frequency is red-detuned with respect to the atomic transition frequency leading to a negative light shift per

photon $U_0 < 0$. Note that the atom-cavity interaction strength depends on U_0 and the pump intensity ϵ.

The dynamics of the system is captured by the following Heisenberg-Langevin equations

$$\frac{\partial}{\partial t}\hat{\Psi} = \frac{i}{\hbar}[\hat{H}, \hat{\Psi}] \qquad (6)$$

$$\frac{\partial}{\partial t}\hat{\alpha} = \frac{i}{\hbar}[\hat{H}, \hat{\alpha}] - \kappa\hat{\alpha} + \xi, \qquad (7)$$

where ξ is the stochastic noise due to the cavity dissipation with $\langle\xi^*(t)\xi(t')\rangle = \kappa\delta(t - t')$ [35]. We employ the truncated Wigner approximation (TWA) to simulate the quantum dynamics [39,40]. The TWA goes beyond the mean-field approximation through the inclusion of quantum noise from the initial state and the fluctuations corresponding to the dissipation in the cavity. This method treats the quantum operators as c numbers and it is applicable for large number of atoms and weak coupling. For the initial states, we choose coherent states for the BEC and the empty cavity mode. We then propagate an ensemble of initial states, which samples the initial Wigner distributions, according to the coupled stochastic differential equations in Eq. (6). The TWA has been used to confirm robustness of dissipative time crystals [41–43] and in comparison with experiment [27,44].

We assume the initial state of the BEC to be homogeneous in the absence of a harmonic trap. When a harmonic trap is present, we use imaginary time propagation to initialize the system in the ground state (see Appendix A for details). We consider the pump protocol depicted in Fig. 2(a). The pump intensity is linearly increased for 2.5 ms until it reaches $\epsilon_0 = 1.02\epsilon_{\text{crit}}$, where ϵ_{crit} is the critical pump intensity for self-organisation for a given contact interaction strength and harmonic oscillator frequency. Next, ϵ is held constant until 30 ms allowing the system to relax to the corresponding DW state. Finally, the pump intensity is periodically modulated according to

$$\epsilon(t) = \epsilon_0(1 + f_d\sin(\omega_d t)), \qquad (8)$$

where f_d is the driving strength and ω_d is the driving frequency. The driving period is $T = 2\pi/\omega_d$.

In the following, we use realistic parameters according to the experimental set-up in Ref. [27]. The particle number is $N_a = 65 \times 10^3$ atoms, recoil frequency $\omega_{\text{rec}} = 2\pi^2\hbar/m\lambda^2 = 2\pi \times 3.55$ kHz, decay rate $\kappa = 2\pi \times 4.55$ kHz, $U_0 = -2\pi \times 0.36$ Hz, and effective pump detuning $\delta_{\text{eff}} = \delta_C - N_a U_0/2 = -2\pi \times 18.5$ kHz. We simulate the dynamics for 200 driving cycles.

III. IDEAL DISSIPATIVE TIME CRYSTAL

In this section, we recall the defining properties of a DTC in the ideal limit when both contact interaction and harmonic trap are absent, as a preparational step to determine their influence in Sec. IV. In this limit, the atom-cavity system maps approximately onto the Dicke model if inhomogeneous trap and contact interactions are neglected, and thus, the DTC observed here is equivalent to the paradigmatic Dicke time crystal [18].

Modulation of the pump intensity leads to the formation of a DTC in the atom-cavity system, for a specific regime of
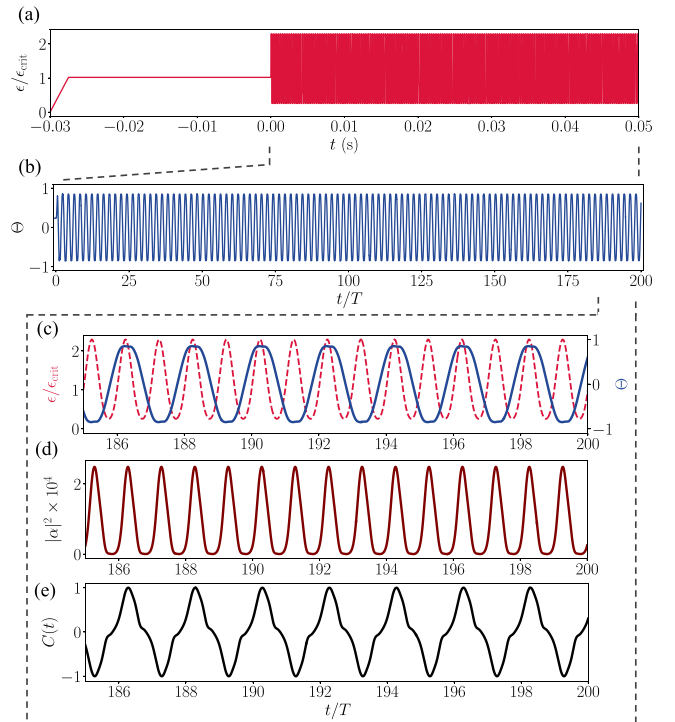

FIG. 2. (a) Protocol for the pump intensity. Dynamics of a single TWA trajectory for the (b) order parameter during periodic modulation. Zoom-in of the dynamics for the (c) order parameter, (d) intracavity photon number $|\alpha|^2$, and (e) the correlation function $C(t)$. The driving parameters are $f_d = 0.5$ and $\omega_d/2\pi = 4$ kHz in the absence of a harmonic trap and contact interactions.

driving strength and frequency [27,41]. This dynamical phase is characterized by a period-doubled switching between the symmetry broken DW states. The mean-field approximation of the ideal DTC is depicted in Fig. 2(b)–2(c). The periodic switching of the sign of the order parameter in Fig. 2(c) underpins how the system switches between the odd and even DW states. Moreover, the switching occurs at twice the driving period as seen in Fig. 2(c). Another important characteristic of a DTC is seen from the dynamics of the cavity mode occupation $|\alpha|^2$, which exhibits pulsating behavior at the driving frequency, see Fig. 2(d). This means that the DTC rely on the presence of cavity photons, which mediate an infinite-range interaction between the atoms, and thus highlights the many-body nature of the DTC phase.

To quantify the behavior of the time crystal using the TWA, we obtain the two-point temporal correlation function

$$C(t) = \text{Re}\{\langle\hat{\alpha}^\dagger(t)\hat{\alpha}(t_0)\rangle\}/\langle\hat{\alpha}^\dagger(t_0)\hat{\alpha}(t_0)\rangle, \qquad (9)$$

where t_0 is the time before modulation is switched on. In Fig. 2(e), we present an example of the dynamics of $C(t)$ in a ideal DTC. Note that it closely follows the behavior of the order parameter Θ. In the following, we use $C(t)$ instead of Θ, which averages out in TWA due to the $\mathbb{Z}_2$ symmetry breaking response of the DTC.
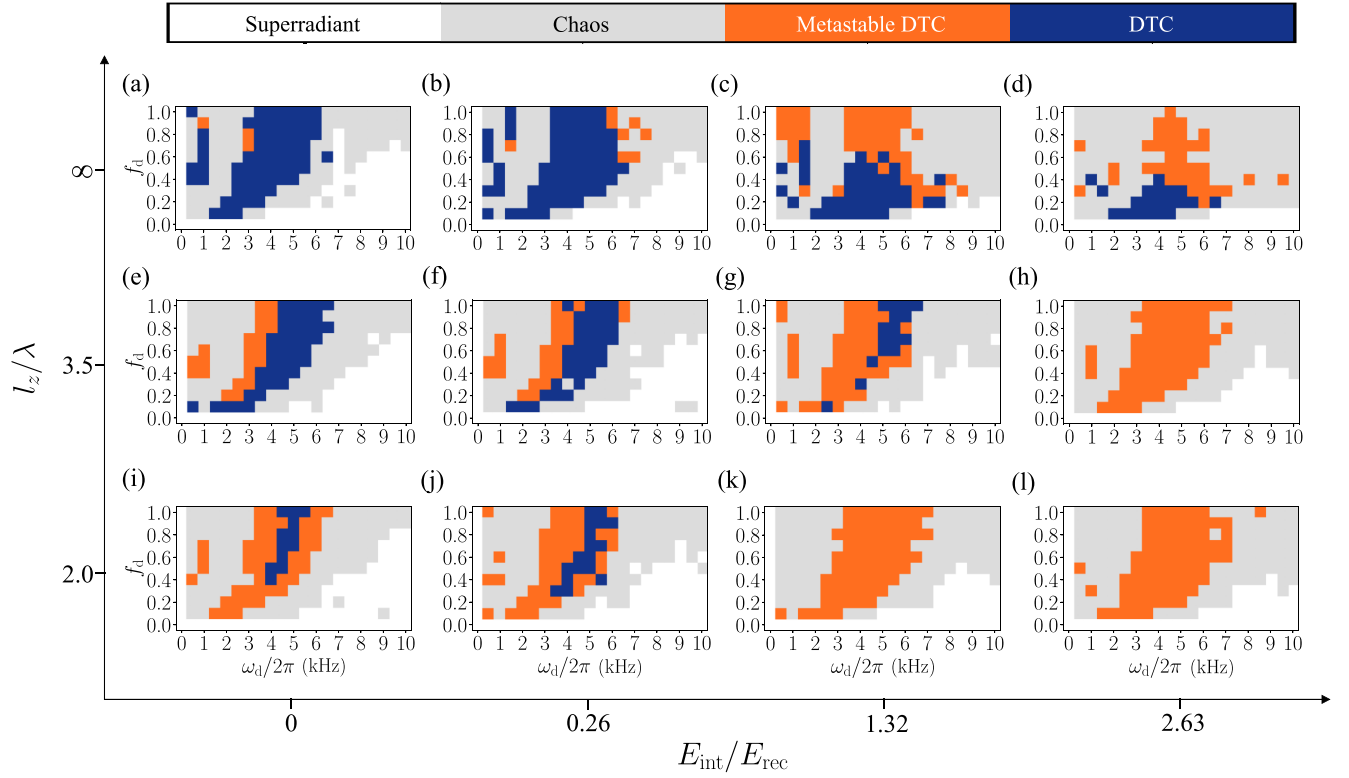
FIG. 3. Gallery of dynamical phase diagrams for increasing contact interaction strength, from left (zero contact interaction) to right, and increasing harmonic oscillator trap frequency, from top (no harmonic trap, $\omega = 0$) to bottom. The oscillator strengths in units of recoil energy from top to bottom are $E_{\mathrm{osc}}/E_{\mathrm{rec}} = \{0, 0.004, 0.013\}$.

IV. DYNAMICAL PHASE DIAGRAMS

We now explore the influence of harmonic confinement and short-range interactions between the atoms on the stability of the DTC. The harmonic trap frequency ω is related to the oscillator length l_z via $\omega = \hbar/(l_z^2 m)$. Alternatively, we measure the confinement strength by comparing $E_{\mathrm{osc}} = \hbar\omega$ with the recoil energy $E_{\mathrm{rec}} = \hbar\omega_{\mathrm{rec}}$ We quantify the contact interaction via the mean-field interaction energy $E_{\mathrm{int}} = g_{\mathrm{aa}} N_a/\lambda$, where $g_{\mathrm{aa}} > 0$ is the repulsive contact interaction strength.

We use $C(t)$ to classify the phases in the dynamical phase diagrams shown in Fig. 3. Specifically, we classify a stable or persistent DTC if $C(t)$ perfectly switches sign every driving cycle for the final 100 driving periods. We also observe the emergence of a metastable DTC phase. On the level of a single TWA trajectory, we define a metastable DTC by having a $C(t)$ that switches sign at least six consecutive times (or equivalently three consecutive period doubling) during the initial stage of driving, $t \in [0, 6T]$, before eventually becoming chaotic, in which $C(t)$ does not change sign over multiple driving periods with irregular intervals. We identify a completely chaotic phase by the lack of consecutive period doubling over $t \in [0, 6T]$ in addition to the obvious irregular dynamics of $C(t)$ (see Appendix B for an example). In Fig. 3, the dynamical phase diagrams are arranged in increasing contact interaction strength from left to right and increasing harmonic oscillator frequency from top to bottom. The resonant nature of DTCs in atom-cavity systems [27,45,46] is evident from the fact that both stable and metastable DTCs

are only found in some range of the driving frequency in Fig. 3.

The dynamical phase diagram in the ideal scenario, in which both harmonic trap and contact interaction are neglected is shown in Fig. 3(a). A stable DTC can be found in a large area of the driving parameter space, specifically for $\omega_d/2\pi \in [1, 6]$ kHz. We also observe a DTC in a much smaller region of the parameter space for low driving frequencies, $\omega_d/2\pi < 1.0$ kHz. This phase is distinct from the usual DTC phase due to the presence of faster but subdominant oscillations in the order parameter corresponding to third harmonics as exemplified in Appendix C. While this phase is robust against the quantum noise included in TWA, it is noticeably less robust against contact interaction and harmonic confinement as inferred from the gradual disappearance of the relevant region in Fig. 3.

We find stable DTC in the presence of inhomogeneous trapping and short-range interaction. This suggests that indeed a stable DTC phase can form in the atom-cavity system with harmonic trap and inherent collisional interaction, and thus supports the experimental observation of a DTC in Ref. [27]. Moreover, the presence of both short-range collisional interaction and infinite-range cavity-mediated interaction between the atoms implies the departure of the DTC from the mean-field regime. This persistence of the DTC phase agrees with the prediction of a long-lived Dicke time crystal despite the presence of short-range interaction, which breaks the mean-field solvability of the Dicke model [30]. Typical dynamics of

the atomic distribution in the stable DTC phase in the nonideal limit is demonstrated in Fig. 1(b), which shows the system periodically switching between the odd and even DW states.

The parameter regime with a stable DTC phase decreases with increasing short-range interaction strength and harmonic confinement as seen in Fig. 3. The stable DTC is replaced by either a chaotic phase or a metastable DTC. In general, the region of the chaotic phase expands with increasing E_{int}, which is a consequence of the nonlinear nature of the short-range interaction that couples the periodic motion to a continuum of excitations of the atomic cloud. Strong driving enables a DTC with large photon number and deep intracavity field, thereby forming large density modulations in the atomic distribution (see Appendix D). The energy associated with the collisional interaction is large for a distribution with large density modulation, which means that repulsive contact interaction penalizes its formation. As demonstrated in Figs. 3(a)–3(d), this leads to the suppression of stable DTCs in the strong driving regime, $f_d > 0.5$, for increasingly strong contact interaction.

In addition to contact interaction, strong harmonic confinement can also destabilize a DTC due to trap-induced coupling between relevant momentum modes becoming dominant over cavity-induced coupling, see Appendix E. Note that strong harmonic confinement increases the density at the center of the trap, while strong contact interaction reduces it. These two system properties therefore have competing influence on the density. This explains how strong harmonic confinement "melts" the DTCs with small density modulation corresponding to weak driving strength f_d, as demonstrated in Fig. 3(i), which is in contrast to the effect of contact interaction shown in Fig. 3(c). Because of their competing effect on the particle density, one may have naively expected that the contact interaction may be tuned appropriately to cancel the effect of the harmonic trap and therefore stabilize the DTC phase. However, we highlight in Figs. 3(e)–3(h) and 3(i)–3(l) that this is not the case and, in fact, increasing the contact interaction strength leads to further destabilisation of the DTC. Similarly, for a fixed contact interaction strength, tightening the trap in an attempt to counteract the repulsive interaction shrinks the area in the phase diagram where a stable DTC persists, as seen in Figs. 3(b), 3(f), and 3(j). The harmonic trap or any inhomogeneous potentials, in general, will couple various momentum modes. Such a coupling may significantly deplete the momentum modes that are important for the $\mathbb{Z}_2$ symmetry broken states participating in the DTC phase, namely the $|\mathbf{k} = 0\rangle$ and $|\mathbf{k} = 2\pi/\lambda\rangle$ momentum modes. Thus, we demonstrate the importance of ensuring a weak inhomogeneous trap to obtain a stable DTC.

V. METASTABLE DISSIPATIVE TIME CRYSTAL

We now further investigate the metastable dissipative time crystal, the predominant nontrivial dynamical phase for large oscillator frequency and large contact interaction strength, as seen in the phase diagrams in Fig. 3. The metastable DTC exhibits a period-doubled response on a time scale larger than the oscillation period before the dynamics become irregular as shown in Fig. 1(c), for example.

We first focus on the case without a harmonic trap but with a nonzero short-range interaction. In the metastable DTC phase, the irregularity in the dynamics for a single trajectory translates into an exponentially decaying oscillations of the temporal correlation $C(t)$ after averaging over multiple trajectories in TWA as shown in Fig. 4(a). Moreover, we obtain the stroboscopic correlation function $\overline{C}(t)$ defined as the envelope of the oscillations in the correlation function. A metastable DTC is characterized by having a finite lifetime, τ, which we extract by fitting an exponential decay $\sim \exp(-t/\tau)$ to the corresponding stroboscopic correlation function $\overline{C}(t)$, as depicted in Fig. 4(b). We demonstrate in Fig. 4(c) that the lifetime decreases with the contact interaction strength. Similar to the metastable Dicke time crystal [30], we emphasise that the metastable DTC for $E_{int} > 0$ without harmonic confinement is distinct from the prethermal discrete time crystals, which rely on high driving frequency to increase the relaxation time towards a featureless thermal state [16,47,48]. Unlike in a prethermal discrete time crystal, there is no visible prethermalization plateaus in Fig. 4(b) for the metastable DTCs induced by contact interaction.

Next, we present in Fig. 4(d) the representative dynamics of $C(t)$ when there is a harmonic confinement but short-range interaction is ignored. The fluctuation in the oscillation amplitude of $C(t)$ is more pronounced during the initial dynamics, $t/T \in [0, 20]$, but it stabilizes in the long-time limit for a stable DTC under weak confinement. The fluctuating oscillation amplitude is highlighted in the relatively noisy dynamics of the stroboscopic correlation functions shown in Fig. 4(e). The oscillations inferred from Fig. 4(b) are more stable compared to those in Fig. 4(e), which corroborates the role of the harmonic trap in introducing small irregularity in the period-doubling response and the photon number dynamics observed in the experiment [27]. In Fig. 4(f), we find that the lifetime of a metastable DTC decreases with increasing harmonic oscillator frequency similar to the effect of the short-range interaction. Both energy scales Figs. 4(c) and 4(f) are in relation to the recoil energy, i.e. E_{osc}/E_{rec}, and E_{int}/E_{rec}. We further observe that the typical lifetime of metastable DTCs with harmonic confinement is shorter by an order of magnitude than those without the trap but with contact interaction, as inferred from comparing Figs. 4(c) and 4(f). This implies that an inhomogeneous potential, such as the harmonic trap, has a more detrimental effect on the stability of dissipative time crystals that rely on states with spatial long-range order, like the DW phase in the atom-cavity system.

A different kind of metastable DTC emerges for strong harmonic confinement without contact interaction. We observe in Fig. 4(e) the appearance of prethermalization plateaus, wherein the amplitude of the period-doubling response is fixed, reminiscent of those found in prethermal discrete time crystals [16,47,48]. This behavior is different from the exponential decay observed as soon as the periodic driving starts in the *standard* metastable DTCs for strong contact interactions and without harmonic trap, see Fig. 4(b). Thus, we propose a second kind of metastable DTC, a prethermal dissipative time crystal (PDTC). This phase can be understood in the paradigm of prethermalization arising from fast driving. In the presence of a harmonic trap, the energy of the system can be rescaled by the oscillator frequency ω. Then, the ratio
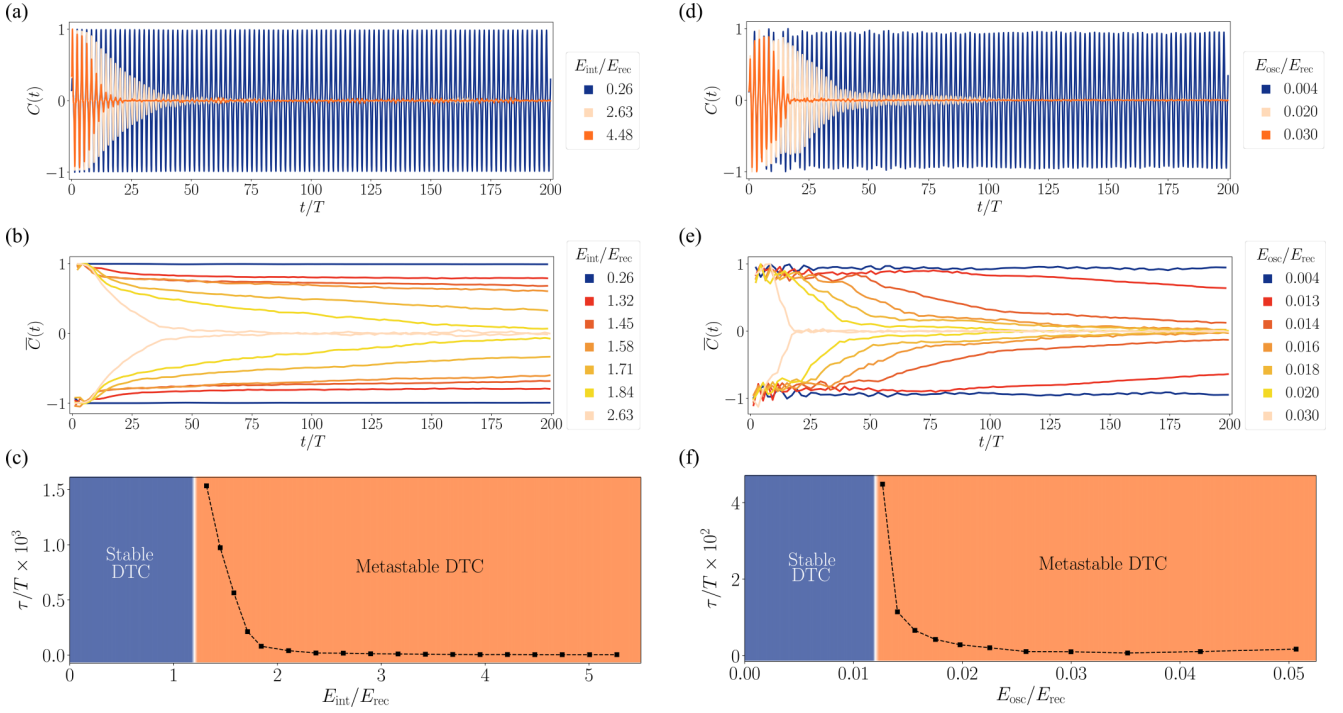
FIG. 4. (a)-(c) Behaviour of the correlation function for varying contact interaction strength ($E_{int} > 0$) and zero oscillator frequency ($E_{osc} = 0$) obtained using TWA with 10^3 trajectories. (a) Exemplary dynamics of $C(t)$. (b) Stroboscopic correlation function $\bar{C}(t)$ for different contact interaction strength. (c) Dependence of the lifetime τ on the harmonic oscillator frequency. The driving parameters are $f_d = 0.5$ and $\omega_d/2\pi = 4$ kHz. (d)-(f) Similar to (a)-(c) but for varying harmonic trap frequency ($E_{osc} > 0$) and zero contact interaction ($E_{int} = 0$).

between the driving frequency and the oscillator frequency becomes the relevant energy scale for defining the "fast-driving regime", $\omega_d/\omega \gg 1$. Similar to a prethermal discrete time crystal [16,47,48], the relaxation time in the PDTC can be increased by increasing the relative driving frequency, ω_d/ω, which is effectively achieved by decreasing the oscillator frequency as demonstrated in Fig. 4(e). This point of view is consistent with the infinitely long-lived DTC found in the mean-field limit $\omega = 0$, in which $\omega_d/\omega \to \infty$.

VI. CONCLUSIONS

In conclusion, we have investigated the properties of dissipative time crystals under realistic conditions of the atom-cavity system. Specifically, we included a harmonic confining potential and short-range interactions that compete with the infinite-range interaction mediated by the cavity photons. Our results demonstrate that the DTC phase is robust for a nonzero harmonic potential and contact interaction strength, consistent with the observation of a DTC in a similar setup [27]. We also show that the irregular amplitude of oscillations observed in the experiment [27] can be attributed to the harmonic trap. We point out that for the bad cavity $\kappa \gg \omega_{rec}$, and similar conditions, there seems to be no evidence for a stable DTC phase [32], which may hint at the importance of having recoil resolution $\kappa \sim \omega_{rec}$ as considered in this work and in the experimental setup in Ref. [27].

For sufficiently strong harmonic confinement and contact interaction, a DTC may become unstable towards the formation of two kinds of metastable DTC. Strong contact in-

teractions lead to an exponentially decaying period-doubling response. On the other hand, strong harmonic trap gives rise to prethermal DTC with prethermalization plateaus, during which the correlation function exhibits subharmonic response at a fixed amplitude. Our work sheds light on the crucial role of trapping on the stability of a DTC, which we expect to apply to inhomogeneous potentials, in general. The metastable DTCs are a genuine many-body phase produced by the interplay between driving, dissipation, and mean-field breaking effects, such as competing range of interaction and inhomogeneity in space. We provide not only a strategy for stabilising DTC but also a route for systematic realization of a standard metastable DTC and a prethermal DTC. As an outlook, the transition from a stable to a metastable DTC can be experimentally explored using a combination of Feshbach resonance for tuning the contact interaction strength [49] and digital micromirror device for creating arbitrary potential for the atoms [50]. Finally, we emphasise all atom-cavity systems have a confining potential and atomic interactions. Our study demonstrates a general strategy to determine the influence of these inevitable features on any many-body state that is created in these systems.
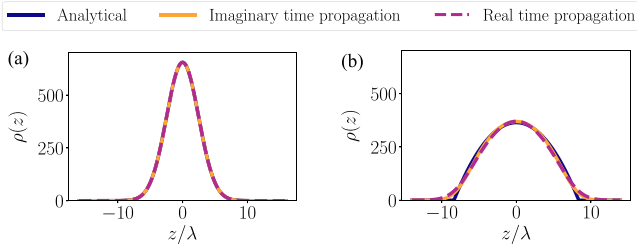
FIG. 5. Density profile according to the analytical prediction, imaginary time propagation, and real time propagation for $l_z/\lambda = 3.5$ with (a) zero short-range contact interaction and (b) $E_{int}/E_{rec} = 0.2634$. In (a), the analytical density profile is Gaussian function, while in (b) it follows from Thomas-Fermi approximation.

APPENDIX A: INITIAL GROUND STATE

We use imaginary time propagation $t \to -it$ in the underlying equations of motion to initialize the system in the ground state with harmonic trap and contact interaction. To check if our scheme works, we also propagate the system in real time with the same harmonic trap and contact interaction, which in principle should render the density profile unchanged. As an initial guess for the case when there is only a harmonic trap, we use the exact ground state of the quantum harmonic oscillator, which is a Gaussian function. Fig. 5(a) confirms the validity of the imaginary time propagation as the exact analytical ground state matches both the density profiles obtained from the imaginary and real time propagation methods. On the other hand, for nonzero contact interaction, the appropriate initial guess is the density profile according to the Thomas-Fermi approximation [51]. Fig. 5(b) displays good agreement between the three methods.

APPENDIX B: CHAOTIC PHASE

The chaotic phase is characterized by intermittent dynamics as the system gets stuck in one of the DW states randomly in time. In Fig. 6, we show the dynamics of the order parameter in the chaotic phase.

APPENDIX C: DTC FOR LOW DRIVING FREQUENCY

In Fig. 7, we present an example of a DTC found in low driving frequencies and large driving strength. As briefly discussed in the main text, this unique DTC phase is marked by subdominant third harmonic oscillations of the period-doubling response.
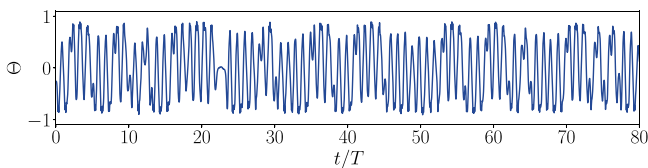

FIG. 6. Time evolution of the order parameter Θ in the chaotic phase. The driving parameters are $f_d = 0.8$ and $\omega_d/2\pi = 2.5\,\text{kHz}$.
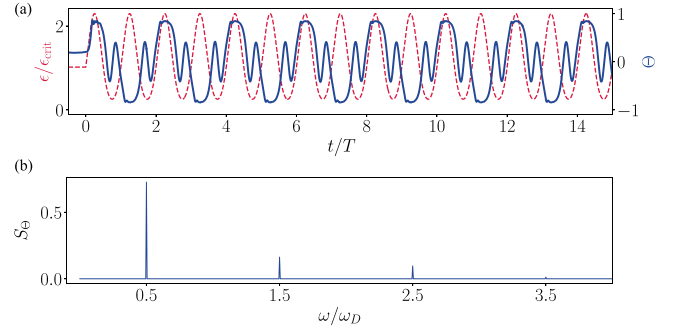

FIG. 7. (a) Dependence of pump intensity and order parameter Θ on time for $\omega = 0$ and $E_{int} = 0$. The driving parameters are $f_d = 0.5$ and $\omega_d/2\pi = 1\,\text{kHz}$. (b) Corresponding power spectrum of Θ in (a).

APPENDIX D: DTC FOR VARYING DRIVING STRENGTH

We show in Fig. 8 the dependence of the DTC on the driving strength for an ideal atom-cavity system, where both short-range interaction and harmonic trap are neglected. The amplitude of oscillations in the intracavity field dynamics increases with f_d suggesting that the density modulations in the DW phase becomes more prominent, see Fig. 8(b).

APPENDIX E: COUPLING OF MOMENTUM STATES DUE TO THE HARMONIC TRAP

An inhomogeneous single-particle potential leads to coupling of various single-particle momentum states. In the case of the harmonic trap considered here, this can be seen by going to the momentum space for the following single-particle Hamiltonian

$$\hat{H}_{\text{HO}} = \int dz \hat{\Psi}^\dagger(z) V(z) \hat{\Psi}(z), \tag{E1}$$

where the potential is

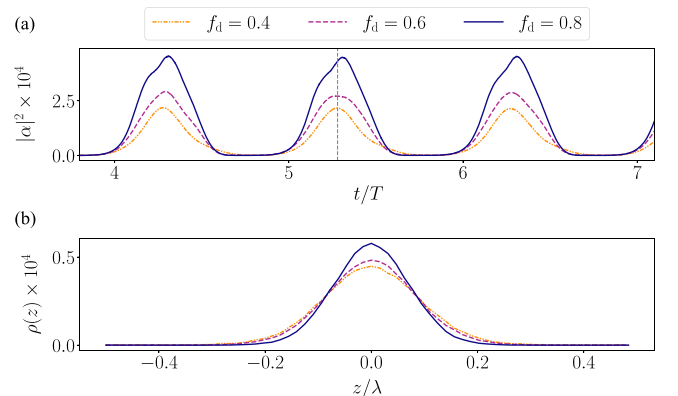$$V(z) = \frac{m\omega_{\text{rec}}^2 b^2 z^2}{2}. \tag{E2}$$

FIG. 8. (a) Time evolution of the intracavity photon number for varying driving strength f_d. (b) Snapshots of the single-particle density distribution of the atoms over a unit cell of the density wave. The snapshots are taken at the time denoted by the vertical dashed line in (a). The driving frequency is $\omega_d/2\pi = 4\,\text{kHz}$.
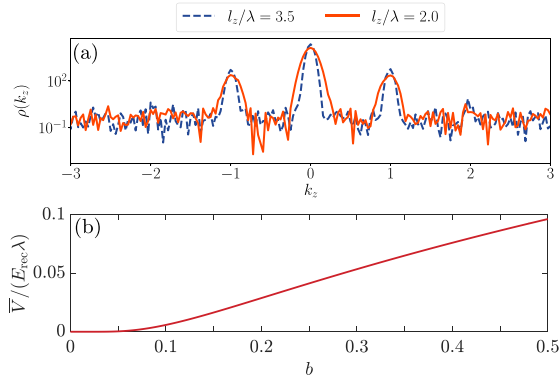
FIG. 9. (a) Snapshots of the momentum distributions for a stable DTC ($f_d = 0.3$) and a metastable DTC ($f_d = 0.6$). The remaining parameters $l_z/\lambda = 3.5$, $\omega_d/2\pi = 3.5\,$kHz, and zero contact interaction, $E_{int} = 0$. (b) Effective coupling induced by the harmonic trap for momentum states with difference of $\Delta k = \pi/\lambda$ as a function of the unitless trap frequency b.

The harmonic trap frequency relative to the recoil frequency is given by $b = \lambda^2/(2\pi^2 l_z^2)$, which follows from $\omega = \hbar/(l_z^2 m)$ and $\omega_{rec} = 2\pi^2\hbar/(m\lambda^2)$. We expand the field operators according to $\hat{\Psi}(z) = \sum_k \exp(ikz)\hat{a}_k$ and obtain

$$\hat{H}_{HO} = \sum_{k_1, k_2} V(k_1 - k_2)\hat{a}_{k_1}^\dagger \hat{a}_{k_2}, \qquad (E3)$$

where

$$V(k) = \int dz \exp(ikz)V(z). \qquad (E4)$$

We can infer from Eq. (E3) that different pairs of momentum states can be coupled depending on the potential Eq. (E4). To gain further analytical insight, we approximate the harmonic potential via

$$V_{eff}(z) = \hbar\omega_{rec}b\left(1 - \exp\left(-\frac{z^2}{2l_z^2}\right)\right) \qquad (E5)$$

$$= V(z) + \mathcal{O}(z^4). \qquad (E6)$$

Note that this effective potential underestimates the effect of the actual harmonic potential which leads to an underestimation of the coupling strength between the momentum modes. Nevertheless, we will use this Gaussian potential to obtain an analytical expression for $V(k)$. Taking the Fourier transform of $V_{eff}(z)$ yields

$$V(\Delta k) = \hbar\omega_{rec}\lambda\frac{\sqrt{b}}{\pi\sqrt{2}}\exp(-(\Delta k)^2 l_z^2/2), \qquad (E7)$$

The presence of the harmonic trap creates additional momentum excitations and it broadens the distribution around the relevant ones, namely $|k_0\rangle \equiv |\mathbf{k} = 0\rangle$ and $|k_1\rangle \equiv |\mathbf{k} = \pm 2\pi/\lambda\rangle$, as demonstrated in Fig. 9(a). The coupling between these two modes is crucial in the formation of both DW and DTC phases. If other momentum modes become significantly coupled to these two modes, then the DTC phase may become unstable as atoms occupy other momentum modes. To get an order of magnitude estimate for the strength of harmonic confinement that may lead to instability of the DTC phase, we calculate the effective coupling strength between the relevant momentum modes and a momentum state between them, i.e., $\Delta k = (k_1 - k_0)/2 = \pi/\lambda$. Using Eq. (E7), we get

$$\overline{V} \equiv V(\Delta k = \pi/\lambda) = \hbar\omega_{rec}\lambda\frac{\sqrt{b}}{\pi\sqrt{2}}\exp(-1/4b). \qquad (E8)$$

In Fig. 9(b), we show the dependence of the trap-induced coupling between $|k_0\rangle$ and $|k_1\rangle$ on b. The coupling is negligible for $b < 0.05$, which corresponds to a ratio between the pump wavelength and oscillator length of $\lambda/l_z < 1$. We then get an order of magnitude condition $l_z > \mathcal{O}(\lambda)$ for which the momentum modes $|k_0\rangle$ and $|k_1\rangle$ are mainly coupled by the cavity and the effect of the trap remains minimal. That is, we do not expect to observe any stable DTC for $l_z < \mathcal{O}(\lambda)$ when the trap-induced coupling becomes significant.

[1] F. Wilczek, Quantum Time Crystals, Phys. Rev. Lett. **109**, 160401 (2012).

[2] A. Shapere and F. Wilczek, Classical Time Crystals, Phys. Rev. Lett. **109**, 160402 (2012).

[3] K. Sacha, *Time Crystals* (Springer, Cham, 2020).

[4] D. V. Else, C. Monroe, C. Nayak, and N. Y. Yao, Discrete time crystals, Annu. Rev. Condens. Matter Phys. **11**, 467 (2020).

[5] V. Khemani, R. Moessner, and S. L. Sondhi, A brief history of time crystals, arXiv:1910.10745.

[6] D. V. Else, B. Bauer, and C. Nayak, Floquet Time Crystals, Phys. Rev. Lett. **117**, 090402 (2016).

[7] N. Y. Yao, A. C. Potter, I.-D. Potirniche, and A. Vishwanath, Discrete Time Crystals: Rigidity, Criticality, and Realizations, Phys. Rev. Lett. **118**, 030401 (2017).

[8] V. Khemani, A. Lazarides, R. Moessner, and S. L. Sondhi, Phase Structure of Driven Quantum Systems, Phys. Rev. Lett. **116**, 250401 (2016).

[9] J. Zhang, P. W. Hess, A. Kyprianidis, P. Becker, A. Lee, J. Smith, G. Pagano, I.-D. Potirniche, A. C. Potter, A. Vishwanath, N. Y. Yao, and C. Monroe, Observation of a discrete time crystal, Nature (London) **543**, 217 (2017).

[10] S. Choi, J. Choi, R. Landig, G. Kucsko, H. Zhou, J. Isoya, F. Jelezko, S. Onoda, H. Sumiya, V. Khemani, C. von Keyserlingk, N. Y. Yao, E. Demler, and M. D. Lukin, Observation of discrete time-crystalline order in a disordered dipolar many-body system, Nature (London) **543**, 221 (2017).

[11] J. Rovny, R. L. Blum, and S. E. Barrett, Observation of Discrete-Time-Crystal Signatures in an Ordered Dipolar Many-Body System, Phys. Rev. Lett. **120**, 180603 (2018).

[12] J. Randall, C. E. Bradley, F. V. van der Gronden, A. Galicia, M. H. Abobeih, M. Markham, D. J. Twitchen, F. Machado, N. Y. Yao, and T. H. Taminiau, Many-body–localized discrete time crystal with a programmable spin-based quantum simulator, Science **374**, 1474 (2021).

[13] X. Mi, M. Ippoliti, C. Quintana, A. Greene, Z. Chen, J. Gross, F. Arute, K. Arya, J. Atalaya, R. Babbush, J. C. Bardin, J. Basso, A. Bengtsson, A. Bilmes, A. Bourassa, L. Brill, M. Broughton, B. B. Buckley, D. A. Buell, B. Burkett *et al.*, Time-crystalline eigenstate order on a quantum processor, Nature (London) **601**, 531 (2022).

[14] J. Smits, L. Liao, H. T. C. Stoof, and P. van der Straten, Observation of a Space-Time Crystal in a Superfluid Quantum Gas, Phys. Rev. Lett. **121**, 185301 (2018).

[15] S. Autti, V. B. Eltsov, and G. E. Volovik, Observation of a Time Quasicrystal and Its Transition to a Superfluid Time Crystal, Phys. Rev. Lett. **120**, 215301 (2018).

[16] A. Kyprianidis, F. Machado, W. Morong, P. Becker, K. S. Collins, D. V. Else, L. Feng, P. W. Hess, C. Nayak, G. Pagano, N. Y. Yao, and C. Monroe, Observation of a prethermal discrete time crystal, Science **372**, 1192 (2021).

[17] D. V. Else, B. Bauer, and C. Nayak, Prethermal Phases of Matter Protected by Time-Translation Symmetry, Phys. Rev. X **7**, 011026 (2017).

[18] Z. Gong, R. Hamazaki, and M. Ueda, Discrete Time-Crystalline Order in Cavity and Circuit QED Systems, Phys. Rev. Lett. **120**, 040404 (2018).

[19] F. Iemini, A. Russomanno, J. Keeling, M. Schirò, M. Dalmonte, and R. Fazio, Boundary Time Crystals, Phys. Rev. Lett. **121**, 035301 (2018).

[20] B. Buča, J. Tindall, and D. Jaksch, Non-stationary coherent quantum many-body dynamics through dissipation, Nat. Commun. **10**, 1730 (2019).

[21] M. Hajdušek, P. Solanki, R. Fazio, and S. Vinjanampathy, Seeding Crystallization in Time, Phys. Rev. Lett. **128**, 080603 (2022).

[22] A. Russomanno, F. Iemini, M. Dalmonte, and R. Fazio, Floquet time crystal in the Lipkin-Meshkov-Glick model, Phys. Rev. B **95**, 214307 (2017).

[23] V. K. Kozin and O. Kyriienko, Quantum Time Crystals from Hamiltonians with Long-Range Interactions, Phys. Rev. Lett. **123**, 210602 (2019).

[24] S. P. Kelly, E. Timmermans, J. Marino, and S.-W. Tsai, Stroboscopic aliasing in long-range interacting quantum systems, SciPost Phys. Core **4**, 21 (2021).

[25] A. Pizzi, A. Nunnenkamp, and J. Knolle, Classical Prethermal Phases of Matter, Phys. Rev. Lett. **127**, 140602 (2021).

[26] B. Ye, F. Machado, and N. Y. Yao, Floquet Phases of Matter Via Classical Prethermalization, Phys. Rev. Lett. **127**, 140603 (2021).

[27] H. Keßler, P. Kongkhambut, C. Georges, L. Mathey, J. G. Cosme, and A. Hemmerich, Observation of a Dissipative Time Crystal, Phys. Rev. Lett. **127**, 043602 (2021).

[28] F. Mivehvar, F. Piazza, T. Donner, and H. Ritsch, Cavity QED with quantum gases: new paradigms in many-body physics, Adv. Phys. **70**, 1 (2021).

[29] P. Kirton, M. M. Roses, J. Keeling, and E. G. Dalla Torre, Introduction to the Dicke model: From equilibrium to nonequilibrium, and vice versa, Adv. Quantum Technol. **2**, 1800043 (2019).

[30] B. Zhu, J. Marino, N. Y. Yao, M. D. Lukin, and E. A. Demler, Dicke time crystals in driven-dissipative quantum many-body systems, New J. Phys. **21**, 073028 (2019).

[31] A. Pizzi, J. Knolle, and A. Nunnenkamp, Higher-order and fractional discrete time crystals in clean long-range interacting systems, Nat. Commun. **12**, 2341 (2021).

[32] P. Molignini, L. Papariello, A. U. J. Lode, and R. Chitra, Superlattice switching from parametric instabilities in a driven-dissipative Bose-Einstein condensate in a cavity, Phys. Rev. A **98**, 053620 (2018).

[33] S. Sarkar and Y. Dubi, Signatures of discrete time-crystallinity in transport through quantum dot arrays, arXiv:2107.04214.

[34] K. Seetharam, A. Lerose, R. Fazio, and J. Marino, Correlation engineering via nonlocal dissipation, Phys. Rev. Research **4**, 013089 (2022).

[35] H. Ritsch, P. Domokos, F. Brennecke, and T. Esslinger, Cold atoms in cavity-generated dynamical optical potentials, Rev. Mod. Phys. **85**, 553 (2013).

[36] K. Baumann, C. Guerlin, F. Brennecke, and T. Esslinger, Dicke quantum phase transition with a superfluid gas in an optical cavity, Nature (London) **464**, 1301 (2010).

[37] J. Klinder, H. Keßler, M. Wolke, L. Mathey, and A. Hemmerich, Dynamical phase transition in the open Dicke model, Proc. Natl. Acad. Sci. USA **112**, 3290 (2015).

[38] D. Nagy, G. Szirmai, and P. Domokos, Self-organization of a Bose-Einstein condensate in an optical cavity, Eur. Phys. J. D **48**, 127 (2008).

[39] A. Polkovnikov, Phase space representation of quantum dynamics, Ann. Phys. **325**, 1790 (2010).

[40] I. Carusotto and C. Ciuti, Quantum fluids of light, Rev. Mod. Phys. **85**, 299 (2013).

[41] J. G. Cosme, J. Skulte, and L. Mathey, Time crystals in a shaken atom-cavity system, Phys. Rev. A **100**, 053615 (2019).

[42] H. Keßler, J. G. Cosme, M. Hemmerling, L. Mathey, and A. Hemmerich, Emergent limit cycles and time crystal dynamics in an atom-cavity system, Phys. Rev. A **99**, 053605 (2019).

[43] H. Keßler, J. G. Cosme, C. Georges, L. Mathey, and A. Hemmerich, From a continuous to a discrete time crystal in a dissipative atom-cavity system, New J. Phys. **22**, 085002 (2020).

[44] P. Kongkhambut, J. Skulte, L. Mathey, J. G. Cosme, A. Hemmerich, and H. Keßler, Observation of a continuous time crystal, arXiv:2202.06980.

[45] J. Skulte, P. Kongkhambut, H. Keßler, A. Hemmerich, L. Mathey, and J. G. Cosme, Parametrically driven dissipative three-level Dicke model, Phys. Rev. A **104**, 063705 (2021).

[46] P. Kongkhambut, H. Keßler, J. Skulte, L. Mathey, J. G. Cosme, and A. Hemmerich, Realization of a Periodically Driven Open Three-Level Dicke Model, Phys. Rev. Lett. **127**, 253601 (2021).

[47] F. Machado, G. D. Kahanamoku-Meyer, D. V. Else, C. Nayak, and N. Y. Yao, Exponentially slow heating in short and long-range interacting floquet systems, Phys. Rev. Research **1**, 033202 (2019).

[48] A. Pizzi, A. Nunnenkamp, and J. Knolle, Classical approaches to prethermal discrete time crystals in one, two, and three dimensions, Phys. Rev. B **104**, 094308 (2021).

[49] C. Chin, R. Grimm, P. Julienne, and E. Tiesinga, Feshbach resonances in ultracold gases, Rev. Mod. Phys. **82**, 1225 (2010).

[50] G. Gauthier, I. Lenton, N. M. Parry, M. Baker, M. J. Davis, H. Rubinsztein-Dunlop, and T. W. Neely, Direct imaging of a digital-micromirror device for configurable microscopic optical potentials, Optica **3**, 1136 (2016).

[51] C. J. Pethick and H. Smith, *Bose-Einstein Condensation in Dilute Gases*, 2nd ed. (Cambridge University Press, Cambridge, 2008).

2.7 Publication II: Bridging closed and dissipative discrete time crystals in spin systems with infinite-range interactions

J.G. Cosme, <u>J. Skulte</u>, and L. Mathey — **Phys. Rev. B 108, 024302 (2023)**

Motivation

This work was motivated by the first realisation of a dissipative discrete time crystal (DTC) in a laser-pumped atom-cavity system in the group of Andreas Hemmerich, the previous work on the stability of such DTCs and the findings of DTCs in the closed Dicke and the closed Lipkin-Meshkov-Glick (LMG) model. These model connect as the under- and overdamped limit of the Dicke model, on which the atom-cavity DTC can be mapped on. Our goal was to understand the role of the dissipation strength κ on the stability of the DTCs.

Main findings

In this work, first-authored by Jayson G. Cosme, we have investigated the role of the dissipation strength in a bosonic mode on the presence and stability on sub-harmonic oscillations, which are classified as DTCs, in the periodically driven Dicke model. In the limit of strong dissipation κ we studied an effective atom-only description and in the limit of $\kappa \to \infty$ the closed LMG model. For vanishing dissipation, we studied the closed Dicke model. This allowed us to compare phase diagrams of the open Dicke model for dissipation strengths ranging effectively from 0 to infinity and varying driving strengths. In our driving protocol we considered varying strength and duty cycle, which is defined as the 'bright' time in one periodic cycle, for a 'bang-bang-protocol'. For all dissipation strength we found stable TCs in the closed, as well as DTCs in the open regime. However, we found that the DTC regime grows for dissipation strengths on time scales similar to the intrinsic time scales and in general that DTCs are more robust against fluctuations in the initial state and random noise in the drive. We further analysed scaling effects for finite particle numbers by comparing discrete truncated Wigner approximation (DTWA) and full quantum simulations for varying interaction strengths and number of spins.

Contribution

I performed the full-quantum simulations under the supervision of JGC and LM. JGC performed the semi-classical simulations. All authors contributed to the discussion and interpretation of the results, as well as to writing the manuscript.

Bridging closed and dissipative discrete time crystals in spin systems with infinite-range interactions

Jayson G. Cosme [*]

National Institute of Physics, University of the Philippines, Diliman, Quezon City 1101, Philippines

Jim Skulte and Ludwig Mathey

Zentrum für Optische Quantentechnologien und Institut für Laser-Physik, Universität Hamburg, 22761 Hamburg, Germany
and The Hamburg Center for Ultrafast Imaging, Luruper Chaussee 149, 22761 Hamburg, Germany

We elucidate the role that the dissipation in a bosonic channel plays in the prevalence and stability of time crystals (TCs) in a periodically driven spin-boson system described by the Dicke model. Here, the bosons are represented by photons, and they mediate the infinite-range interactions between the spin systems. For strong dissipation, we study the dynamics using an effective atom-only description and the closed Lipkin-Meshkov-Glick model. By mapping out the phase diagrams for varying dissipation strengths, ranging from zero to infinitely strong, we demonstrate that the area in the phase diagram, where a TC exists, grows with the dissipation strength but only up to an optimal point, beyond which most of the TCs become unstable. We find TCs in both closed-system and dissipative regimes, but dissipative TCs are shown to be more robust against random noise in the drive and are only weakly affected by the choice of initial state. We present the finite-sized behavior and the scaling of the lifetime of the TCs with respect to the number of spins and the interaction strength within a fully quantum mechanical description.

I. INTRODUCTION

A time crystal (TC) is a nonequilibrium phase of matter signified by the spontaneous breaking of time-translation symmetry [1–5]. This characteristic behavior manifests itself in the emergence of a periodic pattern in time distinct from the underlying temporal symmetry of the system. For example, a TC in a system described by the periodically driven Hamiltonian $H(t) = H(t + T_d)$, where T_d is the driving period, will display an observable $\hat{O}$ oscillating at a lower frequency or higher period, i.e., $\langle \hat{O}(t) \rangle = \langle \hat{O}(t + nT_d) \rangle$ with $n > 1$. TCs are formed through an interplay between periodic driving, many-body interactions, and possibly dissipation. Initial predictions and subsequent realizations of TCs involve closed systems, wherein tailored interactions and strong disorder prevent heating dynamics that would otherwise destabilize a TC [6–23]. Controlled dissipation has also been demonstrated as an alternative strategy for stabilizing TCs [24–40]. In most of these physical systems, time-crystalline dynamics can be understood using the spin language [6–20,24–35].

Focusing on fully connected spin systems or, equivalently, spins with all-to-all interactions, time-crystalline phases have been studied both for closed and dissipative systems through the Lipkin-Meshkov-Glick (LMG) model and the open Dicke model (DM), respectively. Introduced in the context of nuclear physics [41–43], the LMG model describes N fully connected spin-$\frac{1}{2}$ particles in a transverse field [44,45]. A similar model

for photon-mediated interactions is the DM [46]. The DM typifies a spin-boson system, wherein the bosons, specifically, photons in a single mode, mediate the all-to-all interactions between the spins [47,48]. The open version of the DM includes a dissipation channel via the photon decay. On the one hand, discrete TCs and the related subharmonic response are predicted to exist in the periodically driven closed LMG model [9,10,49]. We note that direct experimental observation of a TC in such an infinite-range interacting closed system remains elusive, even though existing platforms could in principle simulate the LMG model, for example, in Refs. [50–53]. On the other hand, the paradigmatic discrete TC in open systems is proposed in the driven-dissipative DM [24,25]. Using a cavity-quantum-electrodynamics (QED) platform as a quantum simulator of the open DM, indeed, a Dicke TC has been realized experimentally [39], despite the mean-field breaking terms in cavity-QED systems that compete with the infinite-range interactions necessary for emulating the DM [54].

In the limit of an extremely strong photon decay rate $\kappa \to \infty$, adiabatic elimination of the rapidly evolving photon field will map the open DM onto the closed LMG model, which establishes the relation between these two fully connected models [45,48,55]. However, it has been suggested for selected parameters that too strong dissipation could be detrimental to the stability of TCs in the open DM [24,25], which then poses the question of how this relates to the TC phenomenology in the closed LMG model [9,10]. As we will show later, the precise form of driving and the choice of the initial state become crucial in the closed-system limits of
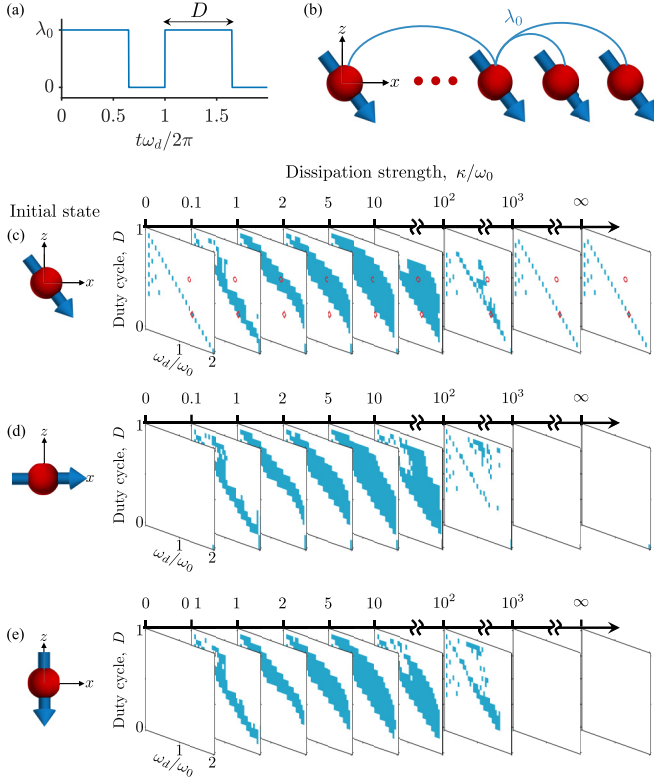
---

*jcosme@nip.upd.edu.ph

FIG. 1. (a) Driving protocol. The duty cycle D is the duration of the bright time in one Floquet cycle. (b) During the bright times, photons mediate the all-to-all interactions between the spins. (c)–(e) Dynamical phase diagrams as a function of D and driving frequency ω_d for varying dissipation strengths κ. The light-matter coupling is fixed at $\lambda_0 = 1.1\lambda_{\rm cr}$, and the photon frequency is $\omega_p = \omega_0$. As depicted in the left-most panels of (c)–(e), three types of initial product states are considered: (c) one of the $\mathbb{Z}_2$-symmetry broken states, (d) spins polarized along the positive x direction, and (e) spins polarized along the negative z direction. The dark areas in each phase diagram denote the period-doubling time crystalline phases. We use the Dicke model (DM) for $\kappa/\omega_0 \leqslant 10^3$, the atom-only DM for $10^3 \leqslant \kappa/\omega_0 < \infty$, and the Lipkin-Meshkov-Glick (LMG) model for $\kappa = \infty$.

vanishing and infinitely strong dissipation rates. In contrast, we will demonstrate that the time-crystalline dynamics occur more ubiquitously in the dissipative regime.

In this paper, we present a thorough investigation of TCs in the transition from closed-system to dissipative limits, or vice versa, for spin systems with infinite-range interactions mediated by photons. By doing so, we shed light on the precise roles of dissipation and the form of driving on the emergence of TCs in infinite-range interacting systems, such as the cavity-QED setup used in the realization of the dissipative Dicke TC [34]. To describe the system, we use the open DM for weak and intermediate dissipations and an effective atom-only description and the LMG model for strong dissipations in which the photons are adiabatically eliminated. We consider a binary drive wherein the system periodically switches between interacting and noninteracting Hamiltonians as shown in Fig. 1(a). Mapping out the phase diagrams for a range of dissipation strengths $\kappa \in [0, \infty)$, we connect the TCs in the closed and dissipative regimes and demonstrate that

the areas in the phase diagram with TCs and time quasicrystals (TQCs) expand with increasing dissipation but only up to an optimal value, as depicted in Figs. 1(c) and 1(d). We also find numerical evidence suggesting that the mechanism for generating TCs in the dissipative system is a period-doubling instability arising from a parametric resonance, and therefore, we generalize the conditions first proposed in Ref. [24]. Furthermore, the TCs in the open DM are found to be more robust against random errors in the drive and are less sensitive to the choice of initial states than their counterparts in the closed-system limits, $\kappa = 0$ and $\kappa \to \infty$. Nevertheless, the TCs in the closed LMG model display enhanced stability for few spins, wherein quantum effects dominate, as their lifetimes can be increased by simply increasing the interaction strength without changing the number of spins, and they have longer lifetimes than the TCs in the open DM in general.

This paper is organized as follows. In Sec. II, we introduce the relevant physical models, namely, the DM, its atom-only description, and the LMG model, and the driving protocol. In Sec. III, we explore using mean-field theory, the dynamical phase diagrams for varying dissipation strengths, and the robustness of TCs against noises in the drive and choices of initial states. In Sec. IV, we investigate the properties of TCs for both closed-system and dissipative limits in the quantum regime of few spins. Finally, we conclude in Sec. V.

II. MODELS AND DRIVING PROTOCOL

The Hamiltonian for the open DM is [47]

$$\frac{\hat{H}}{\hbar} = \omega_p \hat{a}^\dagger \hat{a} + \omega_0 \hat{J}_z + \frac{2\lambda}{\sqrt{N}}(\hat{a}^\dagger + \hat{a})\hat{J}_x, \qquad (1)$$

where N is the total number of spins, $\hat{a}$ ($\hat{a}^\dagger$) is the bosonic annihilation (creation) operator for the photons, and $\hat{J}_\mu = \sum_{i=1}^N \sigma_i^\mu$ ($\mu = x, y, z$) are the collective spin operators. The light-matter coupling strength is λ, the photon frequency is ω_p, and the transition frequency of the two-level atoms represented by the spins operators is ω_0. In the presence of photon losses, the dynamics of the system can be described by the Lindblad master equation [56]:

$$\partial_t \hat{\rho} = -i\left[\frac{\hat{H}}{\hbar}, \hat{\rho}\right] + \kappa D[\hat{a}]\hat{\rho}, \qquad (2)$$

where $D[\hat{a}]\hat{\rho} = 2\hat{a}\hat{\rho}\hat{a}^\dagger - (\hat{a}^\dagger\hat{a}\hat{\rho} + \hat{\rho}\hat{a}^\dagger\hat{a})$. The rate of photon emission is characterized by the photon decay rate or dissipation strength κ.

An effective atom-only description can be obtained for large but finite dissipation strength $\infty > \kappa \gg \omega_0$ [57,58], which in this paper will be called the atom-only DM (ADM). The ADM Hamiltonian is [58]

$$\frac{\hat{H}_{\rm ADM}}{\hbar} = \omega_0 \hat{J}_z - \left[\frac{4\lambda^2\omega_p}{N(\kappa^2 + \omega_p^2)}\right]\hat{J}_x^2 - \left[\frac{4\lambda^2\kappa\omega_p\omega_0}{N(\kappa^2 + \omega_p^2)^2}\right]\{\hat{J}_x, \hat{J}_y\}$$

$$- \left[\frac{2\lambda^2\omega_0(\omega_p^2 - \kappa^2)}{N(\kappa^2 + \omega_p^2)}\right]\hat{J}_z. \qquad (3)$$

In the thermodynamic limit, the ADM Hamiltonian yields the correct set of equations of motion obtained in Ref. [57].

In the limit of $\kappa \rightarrow \infty$, the photonic mode can be adiabatically eliminated to obtain a Hamiltonian that depends only on the spins, equivalent to the anisotropic LMG model [41–43,59]:

$$\frac{\hat{H}_{\mathrm{LMG}}}{\hbar} = \omega_0 \hat{J}_z - \left[\frac{4\lambda^2 \omega_p}{N(\kappa^2 + \omega_p^2)} \right] \hat{J}_x^2. \qquad (4)$$

The last term in Eq. (4) reveals that indeed the photons mediate the effective all-to-all interactions between the spins. In addition to the light-matter coupling strength λ, the parameters related to the photonic degree of freedom, namely, the photon frequency ω_p and dissipation rate κ, also contribute to the strength of the effective spin-spin interactions.

In the thermodynamic limit, we rescale $a = \langle \hat{a} \rangle / \sqrt{N}$ and $j_{\mu \in \{x,y,z\}} = \langle \hat{J}_\mu \rangle / N$. The three models described above all possess a symmetry-breaking phase transition at a critical value of the coupling strength given by [45,47,56,57]

$$\lambda_{\mathrm{cr}} = \frac{1}{2} \sqrt{\frac{\omega_0}{\omega_p} (\omega_p^2 + \kappa^2)}. \qquad (5)$$

Below the critical coupling strength, the stable phase or steady state corresponds to all the spins pointing in the negative z direction $\{j_x, j_y, j_z\} = \{0, 0, -\frac{1}{2}\}$. This phase is sometimes referred to as the normal phase (NP) and for the DM. Another defining feature of the NP is the absence of photons $a = 0$. Above the critical coupling strength, the system undergoes a quantum phase transition as it spontaneously breaks the $\mathbb{Z}_2$ symmetry, $\{\hat{a}, \hat{J}_x\} \rightarrow \{-\hat{a}, -\hat{J}_x\}$. The steady state in the symmetry-broken phase has a spin configuration of [56]

$$\{j_x, j_y, j_z\} = \frac{1}{2} \left\{ \pm \sqrt{1 - \left(\frac{\lambda_{\mathrm{cr}}^2}{\lambda^2}\right)^2}, 0, -\frac{\lambda_{\mathrm{cr}}^2}{\lambda^2} \right\}. \qquad (6)$$

In the DM, the photon mode is occupied in the symmetry-broken phase, also known as the superradiant phase. The corresponding steady-state photon amplitude is

$$a = \mp \frac{\lambda}{\omega - i\kappa} \sqrt{1 - \left(\frac{\lambda_{\mathrm{cr}}^2}{\lambda^2}\right)^2}. \qquad (7)$$

We are interested in a binary Floquet drive or bang-bang protocol wherein the interactions periodically switch according to

$$\lambda(t) = \begin{cases} \lambda_0, & nT_d \leqslant t < (n+D)T_d \\ 0, & (n+D)T_d \leqslant t < (n+1)T_d, \end{cases} \qquad (8)$$

where $n \in [0, 1, 2, \dots]$, T_d is the driving period related to the driving frequency via $\omega_d = 2\pi/T_d$, and $D \in [0, 1]$ is a unitless quantity called the duty cycle. The duty cycle controls the duration of the dark ($\lambda = 0$) and bright ($\lambda = \lambda_0$) times in a driving cycle. For $D = 0$, the the light-matter coupling is always off, while for $D = 1$, the light-matter coupling has a constant nonzero value λ_0 for all times. This binary driving protocol has been shown to host a period-doubling dissipative TC for $D = 0.5$ [24,25]. We note that, for $D \rightarrow 1$, this protocol is not identical to the kicking protocol considered in Ref. [9] because, there, the spins are flipped using a π pulse along the x direction during the kicking times, i.e., the transverse field ω_0 is driven. Instead of applying a spin-flip

operation, we allow the spins to rotate freely according to the coherent time evolution during the dark times, at least for the closed-system or nondissipative regimes.

III. MEAN-FIELD RESULTS

We first consider the thermodynamic or mean-field limit of a large number of spins N. In the limit of a large number of spins, cavity-QED systems based on quantum gases [60,61] are ideal platforms for quantum simulations since the typical number of atoms, emulating the two-level systems, reaches $N \sim 10^5$. In fact, various phenomena predicted in the DM ranging from the normal-superradiant phase transition [50,62] to the formation of dissipative discrete TCs [34] have been observed using quantum-gas-cavity systems.

The mean-field dynamics can be obtained by solving the corresponding semiclassical equations of motion. Depending on the value of κ, we use the appropriate model, i.e., the DM for $\kappa/\omega_0 < 10^3$, the ADM for $10^3 \leqslant \kappa/\omega_0 < \infty$, and the LMG model for $\kappa = \infty$. The semiclassical equations of motion for the three models are presented in Appendix A. In the following, we numerically integrate the equations of motion and mainly focus on the dynamical behavior of the expectation value of the total magnetization along the x component j_x. We consider a total driving time of $t_f = 100T_d$ in accordance with the typical time scales in state-of-the-art experiments on closed and dissipative discrete TCs [15–17,19,39].

In Secs. III A and III B, we choose as the initial state one of the $\mathbb{Z}_2$-symmetry-broken states amounting to all spins having a nonzero component in the positive x direction, which is denoted by the upper sign solution in Eq. (6). For the DM, the additional initial condition for the photon amplitude is given by Eq. (7). In Sec. III C, we investigate other types of initial states, namely, spins that are fully polarized either along the positive x direction or the negative z direction. We fix the light-matter coupling to $\lambda_0 = 1.1\lambda_{\mathrm{cr}}$ and the photon frequency to $\omega_p = \omega_0$. Fixing $\lambda_0/\lambda_{\mathrm{cr}}$ makes the results for the LMG model independent of ω_p and κ since the interaction strength in the LMG Hamiltonian Eq. (4) only depends on this ratio. In Appendix C, we show similar results for other choices of λ and ω_p.

A. Dynamical phases

A generic many-body system with periodic driving, especially in the absence of dissipation, is expected to inevitably heat up and approach a featureless state [63,64]. TCs in closed systems are particularly interesting since they are exceptions to this. To distinguish between nontrivial phases and a thermal or chaotic phase, we define the decorrelator:

$$d = \frac{1}{(t_f - t_i)} \sum_{t=t_i}^{t_f} [|j_x(t)| - |j_x'(t)|], \qquad (9)$$

where $j_x'(t)$ is the dynamics of a slightly perturbed initial state relative to $j_x(t)$. Specifically, we choose $j_x'(0) = j_x(0) - 0.5 \times 10^{-3}$, $j_y'(0) = 0$, and $j_z'(0) = -\sqrt{1 - |j_x'(0)|^2}/2$. The decorrelator provides a measure for the distance between the time-evolving observables to probe the emergence of chaos [65,66]. A large decorrelator $d \sim 1$ signifies sensitivity to initial conditions consistent with classical chaos. We obtain
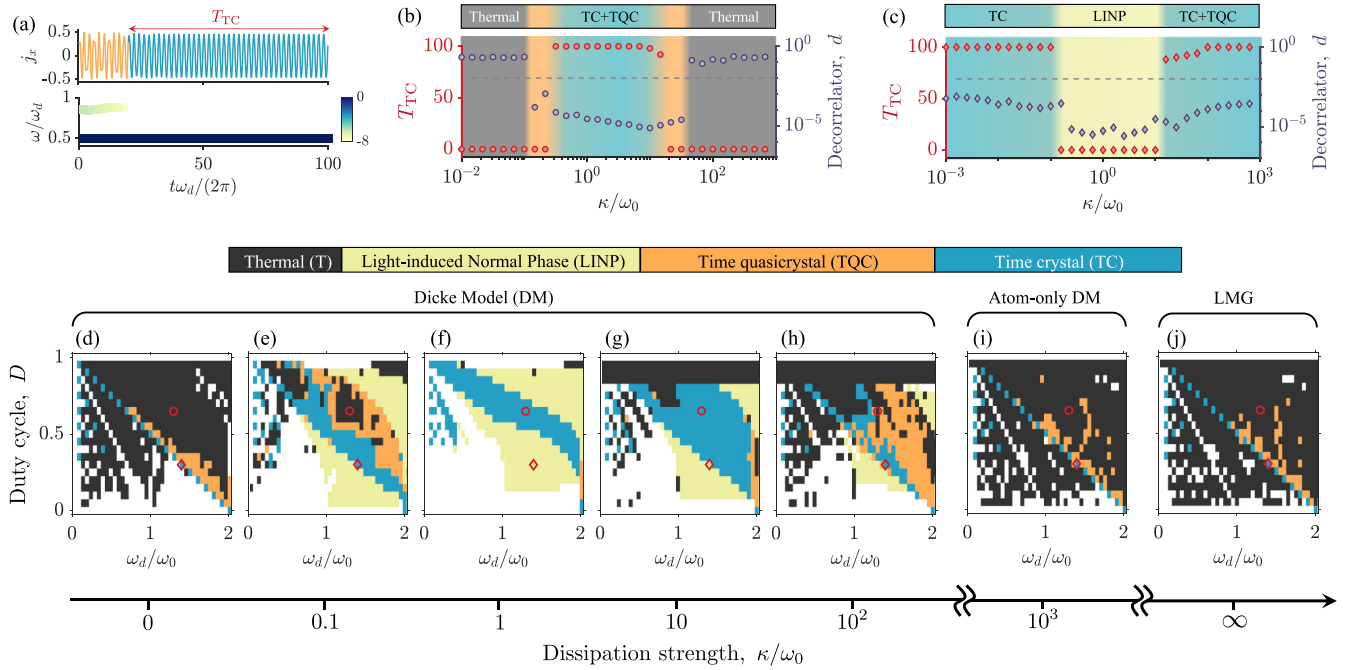
FIG. 2. (a) (Top panel) Exemplary dynamics of j_x for $\kappa/\omega_0 = 20$ with driving parameters $\{D, \omega_d\} = \{0.3, 1.4\omega_0\}$. These driving parameters are denoted as a circle in (d)–(j). The dark curve with duration T_{TC} denotes the period-doubling response, while the light curve corresponds to the transient quasi-period-doubling behavior. (Bottom panel) Corresponding time-frequency power spectrum of j_x in log scale for the two highest peaks. (b) and (c) Dependence of T_{TC} and the decorrelator d on the dissipation strength κ for driving parameters marked by (b) circles and (c) diamonds in (d)–(j). The driving parameters are (b) $\{D, \omega_d\} = \{0.65, 1.3\omega_0\}$ and (c) $\{D, \omega_d\} = \{0.3, 1.4\omega_0\}$. The horizontal dashed lines denote $d = 0.01$, which is the threshold used to distinguish between thermal and nonthermal phases. (d)–(j) Various phases identified for different driving parameters D and ω_d. Each panel corresponds to a specific value of κ. Harmonic, superharmonic, and n-tupling dynamics are all represented in the white areas. For the results shown here, the photon frequency and light-matter coupling strength are fixed to $\omega_p = \omega_0$ and $\lambda_0 = 1.1\lambda_{cr}$, respectively.

the decorrelator for a time window spanned by $t_i = 50T_d$ and $t_f = 100T_d$. To classify thermal phases, we set a threshold of $d \geqslant 0.01$.

In the top panel of Fig. 2(a), we show an exemplary dynamics exhibiting both a TQC for transient times and a period-doubling TC for long times. To quantify the lifetime of the TC T_{TC}, we calculate a time-frequency power spectrum according to $P(\omega, t) = |\mathcal{F}(\omega, t)|^2 / \sum_{i=1}^{N_f} |\mathcal{F}(\omega, t)|^2$, where $\mathcal{F}(\omega, t)$ is the Fourier transform of j_x for the time window starting at time t and ending at $t_f = 100T_d$. The total number of discrete frequencies resolved by the Fourier transform is N_f. To demonstrate how we obtain T_{TC} using $P(\omega, t)$, we present in the bottom panel of Fig. 2(a) an example of the time-frequency power spectrum. A TQC is marked by the appearance of a secondary peak in the power spectrum in addition to the primary peak associated with the period-doubling response [65]. We then use the appearance of a secondary peak in the power spectrum with $\ln P(\omega, t') > -8$ as a criterion for detecting TQC phases. That is, the lifetime of the TC phase for simulation times considered here is $T_{TC} = 100T_d - t'$. In Fig. 2(a), we indeed find a secondary peak around $t' \approx 20T_d$ consistent with a visual inspection of the dynamics shown in the top panel. Thus, for this example, the system is in a time-quasicrystalline phase for $t < t'$, and the TC emerging for $t > t'$ has a lifetime of at least $T_{TC} = 80T_d$.

The lifetime T_{TC} and the decorrelator d as a function of the dissipation strength κ are shown in Figs. 2(b) and 2(c), which correspond to driving parameters $\{D, \omega_d\} = \{0.65, 1.3\omega_0\}$ and $\{D, \omega_d\} = \{0.3, 1.4\omega_0\}$, respectively. In Fig. 2(b), the values of the decorrelator d for thermal phases are several orders of magnitude larger than those for nonthermal phases. We set $T_{TC} = 0$ for thermal phases, regardless of whether a transient TQC is found for early times or a time-crystalline signal is detected for a single mean-field trajectory.

For time-translation symmetry-breaking responses, we find the following phases: (i) pure TC, (ii) pure TQC, and (iii) mixed TC and TQC. A pure TC is characterized by having period-doubling dynamics for the entire duration of the simulation $T_{TC} = 100T_d$, as exemplified by $\kappa/\omega_0 = 1$ in Fig. 2(b) and $\kappa/\omega_0 = 10^{-3}$ in Fig. 2(c). On the other hand, a pure TQC, while insensitive to initial conditions $d < 0.01$, still has $T_{TC} = 0$ since its spectrum has at least one additional subharmonic frequency peak, which in general is incommensurate with the driving frequency for the entire simulation time. An example of the dynamics and the power spectrum for a pure TQC is $\kappa/\omega_0 = 21$ shown in Appendix B. Lastly, a mixed TC and TQC phase is denoted by a transient TQC at early times and a TC at long times, as shown in Fig. 2(a), for example. We label the pure TC phase and mixed TC-and-TQC phase as simply TC for the rest of the paper since both have long-time period-doubling behavior.

The results presented in Figs. 2(b) and 2(c) highlight one of the key findings of this paper, which is the nonmonotonic behavior in the presence and lifetime of TCs as a function of the dissipation strength. The optimal dissipation strength will strongly depend on the specific choice of driving parameters. This is illustrated by the absence of TCs for $\kappa/\omega_0 < 10^{-1}$ and $\kappa/\omega_0 > 10^2$ in Fig. 2(b), while they are present in Fig. 2(c) for the same regimes of dissipation strength. In fact, for intermediate dissipation strengths $10^{-1} < \kappa/\omega_0 < 10^2$, wherein TCs are seen in Fig. 2(b), the driving parameters in Fig. 2(c) push the system into a light-induced NP, which is a NP dynamically stabilized by the drive and is defined by having zero photon number despite $\lambda_0 > \lambda_{cr}$ [30] (see also Appendix B).

In Figs. 2(d)–2(j), the dynamical phase diagrams as a function of the driving parameters are shown, wherein each panel corresponds to a particular choice of dissipation strength κ. That is, we demonstrate in Figs. 2(d)–2(j) how the dynamical phase diagram changes with the dissipation strength. In the following, we will not discuss harmonic, superharmonic, and n-tupling dynamics, which are all indicated by the white areas in the dynamical phase diagrams. Instead, we concentrate on the influence of dissipation on the thermal, time-crystalline, and time-quasicrystalline phases.

1. Closed systems

We find TC and TQC phases in the closed-system limits, namely, the closed DM ($\kappa = 0$), the ADM ($\kappa/\omega_0 = 10^3$), and the LMG model ($\kappa \to \infty$), albeit only in a relatively narrow region of the driving parameter space. The dynamical phase diagrams for closed systems in Figs. 2(d), 2(i), and 2(j) share a strong similarity with each other, especially in the location of the TC phases. The qualitative agreement between the ADM and LMG phase diagrams implies the applicability of the LMG model for dynamical states, such as a TC, which is in contrast to the limitation of the LMG model in describing steady states [57,58].

The apparent period-doubling response seen for $D = 0$, as illustrated in Fig. 3(a), can be considered trivial since this simply corresponds to a sudden quench at $t = 0$ from $\lambda = 1.1\lambda_{cr}$ to 0. Within the LMG model, this leads to a coherent dynamics of the spins precessing around the z axis at a frequency ω_0, i.e., a precession period of $T_0 = 2\pi/\omega_0$. For a driving frequency of $\omega_d = 2\omega_0$, such a response will seemingly appear as subharmonic even though the periodic drive is actually absent for $D = 0$, as illustrated in Fig. 3(a).

Based on the location of the TC phases in the phase diagrams in Figs. 2(d), 2(i), and 2(j), for the closed DM, ADM, and LMG model, we identify that a period-doubling instability emerges for bang-bang protocols when the duty cycle follows

$$D_{\text{ins}} = 1 - \frac{\omega_d}{2\omega_0}. \quad (10)$$

The above condition appears as a line in the phase diagram, and it can be analytically understood as follows. The magnetization j_x for the noninteracting limit will have the same magnitude but opposite sign as its initial value every $(n + 1/2)T_0$, where n is an integer. Hence, for the driven system, the dark time must be exactly half the precession period in the absence of spin interactions $t_{\text{dark}} = T_0/2$. The instability
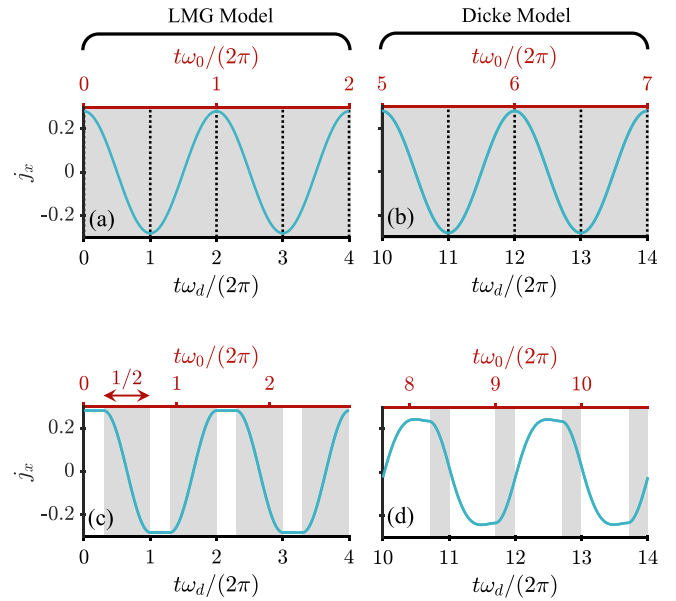

FIG. 3. Dynamics of j_x in the (left panels) Lipkin-Meshkov-Glick (LMG) model and (right panels) Dicke model with $\kappa/\omega_0 = 1$. (a) and (b) In the absence of driving and for a sudden quench $D = 0$, the spins precess around the z direction due to the first term in the Hamiltonian in Eq. (4). The top axis displays time in units of the precession period $T_0 = \omega_0/(2\pi)$, while the bottom axis shows time in units of the driving period $T_d = \omega_d/(2\pi)$. This apparent period doubling is trivial as the periodic driving is absent. (c) and (d) Time crystals for the periodically driven systems with parameters (c) $\{D, \omega_d\} = \{0.3, 1.4\omega_0\}$ and (d) $\{D, \omega_d\} = \{0.7, 1.3\omega_0\}$. The shaded areas indicate the dark time when the spin interactions are switched off. The arrow in (c) indicates that the dark time is $t_{\text{dark}} = T_0/2$. The remaining parameters are the same as in Fig. 2.

condition Eq. (10) precisely satisfies this:

$$t_{\text{dark}} = (1 - D_{\text{ins}})T_d = \frac{2\pi}{2\omega_0} = \frac{T_0}{2}. \quad (11)$$

The state at times $t = (n + 1/2)T_0$ is the symmetry-broken partner of the initial state, which is chosen to be an eigenstate of the Hamiltonian with spin-spin interactions. As such, the states do not change during the bright times of each driving cycle, as depicted in the white areas in Fig. 3(c), which then yields the apparent period-doubling response for the bang-bang protocol. Therefore, the emergence of a period-doubling response in the absence of dissipation strongly hinges on the appropriate timing of when the interactions are switched on and off. This interplay between the internal dynamics of the spins and the timing of the external drive is also argued to be important for the n-tupling response in a variable-range interacting spin model with binary driving [49].

We remark that the equivalence of the dynamics in the ADM and the LMG model for a TC is solely attributed to the specific form of the binary drive. For both models, during the bright times, the state of the system is the same initially prepared symmetry-broken phase defined by Eq. (6). During the dark times, the additional terms in the ADM Hamiltonian [last two lines in Eq. (3)] are also set to zero, which means that the resulting equations of motion are the same for both

models. Thus, the spins in the ADM will simply precess in the same way as they would in the LMG model during the dark times.

In general, for an integer m, the period doubling arises if $t_{\text{dark}} = (m + 1/2)T_0$. The driving parameters for the isolated islands of TCs in Figs. 2(d), 2(i), and 2(j) and more clearly in Fig. 1(c) for $\kappa/\omega_0 = \{0, 10^3, \infty\}$ satisfy this general condition for the period doubling instability. We emphasize that the arguments discussed so far hold only if the initial state is an eigenstate of the Hamiltonian during the bright times. Otherwise, the system will dephase, and a clean period-doubling dynamics will not be observed. This will be discussed further in Sec. III C. Moreover, Eqs. (10) and (11) only apply to binary drives, in which the system becomes noninteracting at well-defined times. For smooth sinusoidal driving, we do not find any clean period-doubling response for all relevant types of initial states in the absence of dissipation, as shown in Appendix D. This underscores the sensitivity to the specific driving protocol of the TC in the closed-system limit.

2. Open systems

We now discuss the results for the open DM with dissipation strength $0 < \kappa/\omega_0 < 10^3$. For $D = 0$, the photonic and spin degrees of freedom decouple, leading to a spin dynamics equivalent to the $D = 0$ case in the LMG model. The initially nonzero photon number eventually vanishes due to dissipation. The magnetization j_x oscillates at a frequency ω_0 around zero, as seen in Fig. 3(b), and the apparent period doubling for $D = 0$ is trivial since the periodic driving is in fact absent. We show an example of a dissipative TC in the DM in Fig. 3(d), in which the specific driving parameters yield bright and dark times that are both incommensurate to the precession period, $t_{\text{bright}} \approx 0.5385T_0$ and $t_{\text{dark}} \approx 0.2308T_0$, respectively. This demonstrates that the period-doubling instability conditions for the nondissipative limits based on Eqs. (10) and (11) are no longer applicable, in general, when dissipation is present.

Going from $\kappa = 0$ to $\kappa/\omega_0 = 0.1$ [Figs. 2(d) and 2(e)], we see that, while time-crystalline phases remain along the line defined by Eq. (10), new TCs start to emerge in other parts of the phase diagram associated with driving parameters that would otherwise lead to thermal phases in the closed DM. Moreover, some of the thermal phases for $\kappa = 0$ are converted to not only TCs but also TQCs after dissipation is introduced. Thus, we provide a concrete demonstration of dissipation, the photon decay, counteracting the heating induced by the periodic drive. Increasing the dissipation strength pushes the TCs away from the instability line in the closed-system limit, as seen from the change in the phase diagram from $\kappa/\omega_0 = 0.1$ to $\kappa/\omega_0 = 1$, see Figs. 2(e) and 2(f). Further increase in the dissipation strength leads to an expansion of the area in the phase diagram with TCs, as demonstrated in Figs. 1(c) and 2(d) for $\kappa/\omega_0 \in [1, 10]$.

Note, however, that the dissipation-induced enhancement of TC in the phase diagram only applies up to a certain value of κ. In Fig. 1(c), comparing the area of the time-crystalline phase in $\kappa/\omega_0 = 5$ and $\kappa/\omega_0 = 10$, we find that the TC area decreases for $\kappa/\omega_0 > 5$. While the overall shape of the area with both TC and TQC is not significantly changed from

$\kappa/\omega_0 = 10$ to $\kappa/\omega_0 = 10^2$, as displayed in Figs. 2(g) and 2(h), there are more TQCs in the phase diagram for $\kappa/\omega_0 = 10^2$ than for $\kappa/\omega_0 = 10$, which implies that the TCs are converted to TQCs with increasing dissipation strength. This can also be inferred from the expansion of the TQC domain as the dissipation strength increases from $\kappa/\omega_0 = 10$ to $\kappa/\omega_0 = 21$ in Appendix B.

We have seen that, for the ADM and LMG model, the TCs are restricted along the instability line Eq. (10). The question remains whether the phase diagrams for dissipative systems will change gradually or suddenly as κ increases to large enough values, such that the adiabatic approximation and thus the ADM and LMG model can be applied. To address this issue, we consider even stronger dissipation strengths on the order of $\kappa/\omega_0 \sim 10^2$ while still solving the full semiclassical equations including the photon dynamics. For even stronger dissipation beyond the optimal value, we find that the dynamical phase diagram gradually develops features that resemble its closed-system counterpart, as seen in Figs. 1(c) and 2(d) for $\kappa/\omega_0 = 10^2$. Comparing $\kappa/\omega_0 = 10^2$ and $\kappa/\omega_0 = \{10^3, \infty\}$, some of the TQCs, which were previously TCs for weaker dissipation, turn into thermal phases in the closed-system models. Moreover, going from $\kappa/\omega_0 = 10$ to $\kappa/\omega_0 = 10^2$, the time-crystalline phases start to gather toward the instability line Eq. (10) for closed systems.

To summarize Sec. III A, we identify the condition for creating TCs in the closed-system limit with a periodic binary drive or bang-bang protocol. We also demonstrate that dissipation, in general, leads to the expansion of the TC and TQC areas in the phase diagram. The two limits $\kappa = 0$ and $\kappa \to \infty$ are smoothly connected by the gradual change of the phase diagram as dissipation is increased.

B. Robustness against random driving errors

We will now investigate the role of dissipation on the robustness of TCs against temporal noise. To this end, we introduce a random driving error in the duty cycle for every Floquet drive:

$$\lambda(t) = \begin{cases} \lambda_0, & nT_d \leqslant t < (n + D_n)T_d \\ 0, & (n + D_n)T_d \leqslant t < (n + 1)T_d, \end{cases} \quad (12)$$

where $D_n = D + \Delta D_n$, and ΔD_n is a random number drawn from a box distribution $\Delta D_n \in [-\Delta D, \Delta D]$. A single realization of this disordered drive is depicted in Fig. 4(a) [see also the inset of Fig. 4(c)]. We also consider another kind of temporal perturbation, namely, in the light-matter coupling strength such that

$$\lambda(t) = \begin{cases} \lambda_0 + \lambda_n, & nT_d \leqslant t < (n + D)T_d \\ 0, & (n + D)T_d \leqslant t < (n + 1)T_d, \end{cases} \quad (13)$$

where $\lambda_n/\lambda_0 \in [-\Delta\lambda_0, \Delta\lambda_0]$. An example of a periodic drive with this disorder is shown in the inset of Fig. 4(e).

In the following, we use driving parameters corresponding to the circles and diamonds in Fig. 2, where TCs exist for clean driving or in the absence of temporal disorder. We take 100 disorder realizations when calculating the dynamics of j_x and the crystalline fraction Ξ, which we define as the average of the power spectrum of j_x at $\omega_d/2$. We present in Fig. 4(b) the disorder-averaged dynamics of j_x for a noisy duty cycle,
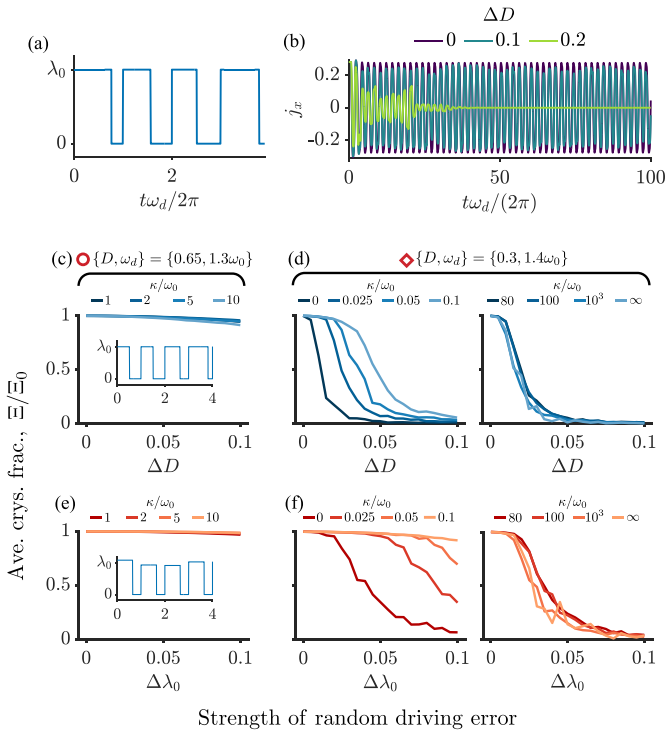
FIG. 4. (a) One realization of the disordered drive. (b) Dynamics of the total magnetization along the x direction j_x for different disorder strengths ΔD as indicated in the legend. The driving parameters are $\{D, \omega_d\} = \{0.65, 1.3\omega_0\}$, and the dissipation strength is $\kappa/\omega_0 = 1$. The initial state is a $\mathbb{Z}_2$-symmetry broken phase for $\lambda_0 = 1.1\lambda_{\mathrm{cr}}$. (c) and (d) Dependence of the relative crystalline fraction Ξ/Ξ_0 on the strength of the random driving error or temporal disorder ΔD. (e) and (f) Like (c) and (d) but for a noisy light-matter coupling with disorder strength $\Delta\lambda$. Insets: One realization of the disordered drive.

Eq. (12). As the disorder strength increases, the oscillation amplitude of j_x deviates from being a constant as the TC becomes unstable. This is expressed in the reduction of the relative crystalline fraction Ξ/Ξ_0, where Ξ_0 is the crystalline fraction in the clean case, for increasing disorder strength ΔD, as shown in Figs. 4(c) and 4(d). Additional frequencies introduced by the noise broaden the power spectrum of j_x and thereby decrease the crystalline fraction. More importantly, Figs. 4(c) and 4(d) demonstrate another key finding of this paper, which is the role of dissipation in making a TC more robust against temporal noise. For the nondissipative cases $\kappa/\omega_0 = \{0, 10^3, \infty\}$ in Fig. 4(d), the crystalline fraction decays rapidly with ΔD. In contrast, the decay is slower when dissipation is introduced, i.e., the crystalline fraction remains large over a wide range of disorder strengths. This is evident in Fig. 4(c) for intermediate dissipation strengths, wherein the crystalline fraction is found to slowly decrease with ΔD.

The dissipation-induced robustness against temporal noise can be understood as a consequence of the dissipation-induced expansion of the TC area in the phase diagram discussed in the previous subsection. In the phase diagram for $\kappa/\omega_0 = 10$ in Fig. 2(g), the TC corresponding to the driving parameters marked by the circle is surrounded by other period-doubling TCs, and thus, a perturbation in D, ω_d, and ω_0 will not easily push the system into a different dynamical phase. On the other

hand, for closed systems, we see in Figs. 2(d), 2(i), and 2(j) that, for driving parameters marked by the diamonds, a slight variation in D away from the instability condition Eq. (10) will take the system to a different dynamical phase other than a period-doubling TC. This leads to a TC that is less robust against temporal perturbations of the driving parameters D and ω_d. This also explains the relatively weak robustness observed for strong dissipation in the right panel of Fig. 4(d) since the TC area is relatively small and highly fragmented for dissipation strengths of this order of magnitude, as seen for $\kappa/\omega_0 = 10^2$ in Fig. 1(c). In Figs. 4(e) and 4(f), we observe similar findings for a drive with noisy light-matter coupling. Both dissipative and nondissipative models appear to be more robust against this type of noise, as seen from the larger plateaus in the crystalline fractions in Fig. 4(f) than those in Fig. 4(d). This can be attributed to the presence of TCs even for higher values of λ_0, as seen in Appendix C.

C. Initial fully polarized states

For potential applications and experimental realizations, we discuss how close the initial state must be to the desired state to create a TC. So far, we have considered one of the symmetry-broken states as the initial state. In Ref. [9], robustness against the choice of initial state for TCs in the kicked LMG model has been demonstrated but only for initial symmetry-broken states corresponding to an interaction strength different from the one in the Hamiltonian, i.e., $\lambda(t = 0) \neq \lambda_0$. Here, we explore other types of initial states, namely, fully polarized states either along the positive x direction $\{j_x, j_y, j_z\} = \{1/2, 0, 0\}$ or negative z direction $\{j_x, j_y, j_z\} = \{0, 0, -1/2\}$, which we label as $|\Rightarrow\rangle$ or $|\Downarrow\rangle$, respectively. A symmetry-broken state interpolates between these two limits. For the DM, we include a small fluctuation in the photon mode, such that $a(t = 0) = 0.01$.

We present in Figs. 5(a) and 5(b) the evolution of the phase diagrams as a function of the dissipation strength for initial fully polarized states $|\Rightarrow\rangle$ and $|\Downarrow\rangle$, respectively. Crucially, we find that, for both types of fully polarized initial states, time-crystalline phases are absent in the closed system models $\kappa/\omega_0 = \{0, 10^3, \infty\}$, and the phase diagrams are dominated by thermal phases, see also Figs. 1(d) and 1(e). The behavior is strikingly different for dissipative cases, as seen in Fig. 5 for $\kappa/\omega_0 = \{1, 10\}$. The choice of initial state between $|\Rightarrow\rangle$ and $|\Downarrow\rangle$ does not significantly alter the area in the phase diagram with TCs. This is further emphasized if we include the initial symmetry-broken state in the comparison as evidenced by the results for $\kappa/\omega_0 \in [1, 10]$ in Figs. 1(c)–1(e). This implies that dissipation allows for flexibility in the fidelity of the initial state preparation. In Appendix D, we observe similar results for a smooth sinusoidal or continuous driving protocol, which further corroborates the positive role of controlled dissipation for infinite-range interacting spin systems.

The results for the ADM and LMG model $\kappa/\omega_0 = \{10^3, \infty\}$, shown in Fig. 5(b), exhibit resonance lobes reminiscent of parametric resonances that appear when the driving frequency satisfies $\omega_d/\omega_0 = 2/n$, where $n \in \mathbb{Z}^+$. Notice that, in Fig. 5(b), the shape of the TC area for $\kappa/\omega_0 = 10$ is like that of the primary resonance lobe ($\omega_d/\omega_0 = 2$) for $\kappa/\omega_0 = \{10^3, \infty\}$. This points to a period-doubling instability arising
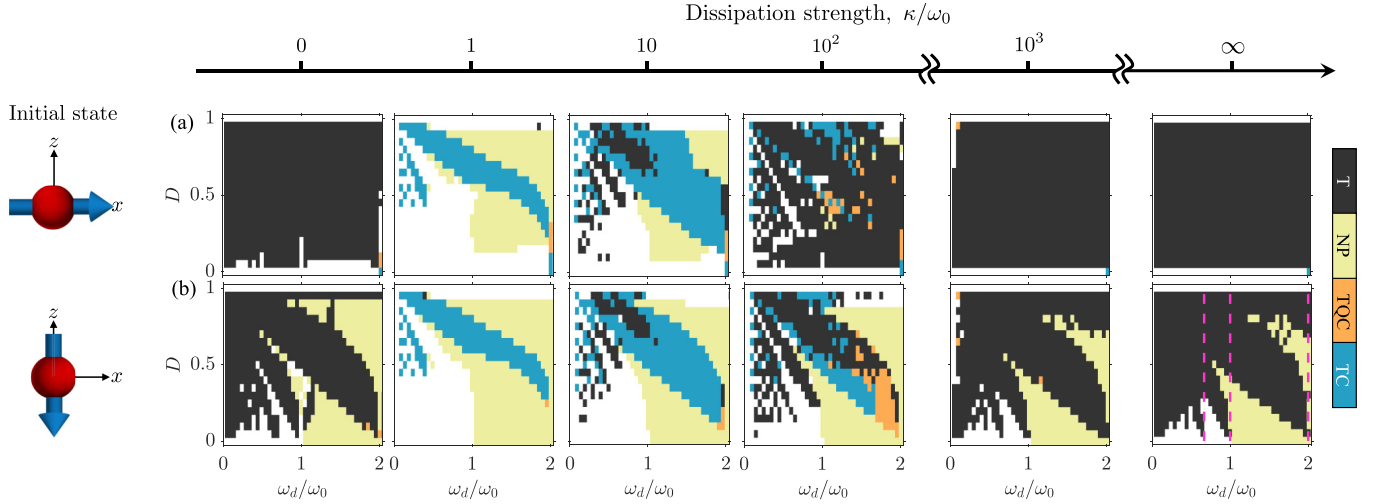
FIG. 5. Dynamical phase diagrams like Fig. 2 but for initial fully polarized states (a) $| \Rightarrow \rangle$ and (b) $| \Downarrow \rangle$ as schematically illustrated in the leftmost panels. The dashed vertical lines in $\kappa = \infty$ denote the parametric resonance condition $\omega_d/\omega_0 = 2/n$, where $n = \{1, 2, 3\}$. The system parameters are the same as in Fig. 2.

from a parametric resonance as the main mechanism behind the formation of dissipative TCs with binary driving, like the smooth sinusoidal driving in Refs. [34,67]. Note that the parametric resonance also applies to initial symmetry-broken states as evinced by the shape of the thermal region, including the TC and TQC phases, in Fig. 2(d) for $\kappa = 0$. There, the absence of dissipation heats up the system, resulting in a more prominent thermal phase except at the special points along the instability line for initial symmetry-broken states, Eq. (10).

IV. QUANTUM RESULTS

We now study the TCs in the limit of a small number of spins, wherein quantum effects and many-body correlations become dominant. Platforms for physical implementations of a relatively small number of artificial or effective spins include circuit QED systems based on superconducting qubits [24,68–72] and ion chains [51–53]. In the following, we obtain the full quantum results using the QuantumOptics.jl library [73], and we employ the discrete truncated Wigner approximation (DTWA) [74,75] for a larger number of spins beyond the reach of full quantum mechanical simulations.

We focus on the initial fully polarized state along the positive x direction $| \Rightarrow \rangle = \bigotimes_N | \rightarrow \rangle$, which in the mean-field regime corresponds to $\{j_x, j_y, j_z\} = \{\frac{1}{2}, 0, 0\}$, to gain insights into the features of TCs in the quantum regime. By comparing exact quantum and DTWA results, we will also assess the applicability of DTWA in capturing the time-crystalline dynamics for periodically driven infinite-range interacting spins. For the DM, the photon mode is initialized in the vacuum state $|0\rangle$, such that the initial state of the system is $|\psi(t = 0)\rangle = | \Rightarrow \rangle \otimes |0\rangle$.

The results for the LMG model with $N = 8$ spins and driving parameters $\{D, \omega_d\} = \{0.3, 1.4\omega_0\}$ are depicted in Fig. 6. In Fig. 6(a), for $\lambda_0 = 1.1\lambda_{cr}$, the system is in the thermal phase even in the mean-field limit of $N \rightarrow \infty$. This again exemplifies the importance of initializing the system in a symmetry-broken eigenstate to create a TC in the closed-system limit. In the quantum regime, the irregular mean-field

dynamics translate into a beating of the oscillations in the expectation value of the total magnetization $\langle \hat{J}_x \rangle/N$ like the behavior found in the kicked LMG model [9]. The full quantum mechanical and DTWA results agree on the overall qualitative behavior of the dynamics. While we find excellent agreement between the exact and DTWA results for short times, quantitative deviations appear in the long-time dynamics, which is expected in simulations of closed system quantum dynamics using phase-space methods [76].

For stronger interactions, e.g., $\lambda_0 = 4\lambda_{cr}$ in Fig. 6(b), a TC is formed, and interestingly, the mean-field, exact quantum, and DTWA results agree for the entire simulation time of 100 driving cycles, which is noteworthy, considering the relatively small number of spins $N = 8$. This also hints at the ability of the DTWA to capture the dynamics of TCs even for long times, provided that the interactions in a fully connected
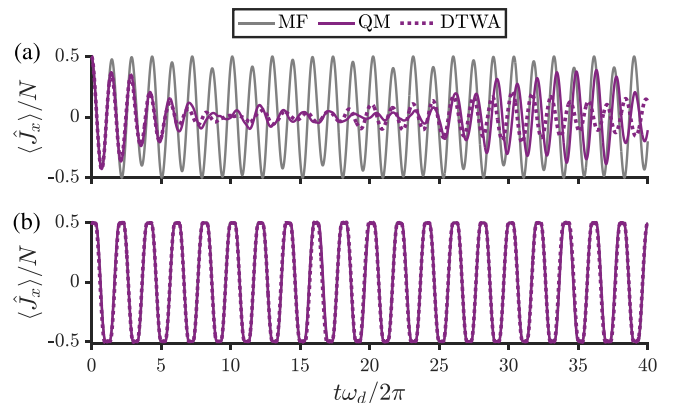
FIG. 6. Dynamics of the expectation value of the total magnetization along the x direction for an initial fully polarized state $| \Rightarrow \rangle$ in the Lipkin-Meshkov-Glick (LMG) model. The interaction strengths are (a) $\lambda_0 = 1.1\lambda_{cr}$ and (b) $\lambda_0 = 4.0\lambda_{cr}$. For the exact quantum mechanical (QM) results and discrete truncated Wigner approximation (DTWA), the number of spins is $N = 8$. The driving parameters are $D = 0.3$ and $\omega_d = 1.4\omega_0$.
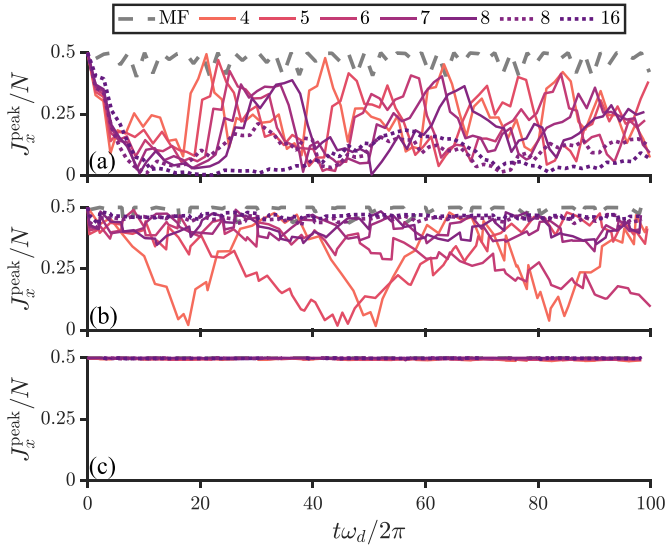
FIG. 7. Dynamics of the peaks in the total magnetization in the Lipkin-Meshkov-Glick (LMG) model for an initial state of $|\Rightarrow\rangle$. The solid (dotted) curves denote the full quantum [discrete truncated Wigner approximation (DTWA)] results. The interaction strengths are (a) $\lambda_0 = 1.1\lambda_{\text{cr}}$, (b) $\lambda_0 = 2.0\lambda_{\text{cr}}$, and (c) $\lambda_0 = 4.0\lambda_{\text{cr}}$. The driving parameters are the same as in Fig. 6.
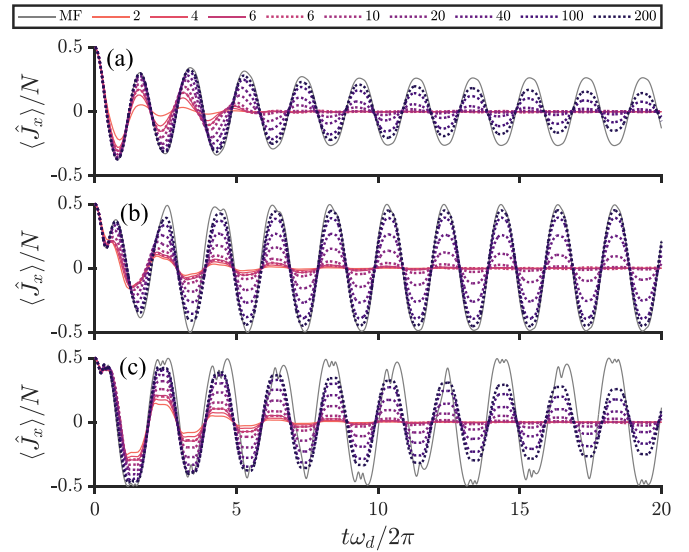

FIG. 8. Like Fig. 6 but for the open Dicke model with $\kappa = \omega_0$. The light-matter coupling strengths are (a) $\lambda_0 = 1.1\lambda_{\text{cr}}$, (b) $\lambda_0 = 2.0\lambda_{\text{cr}}$, and (c) $\lambda_0 = 4.0\lambda_{\text{cr}}$. The photon frequency is $\omega_p = \omega_0$. The driving parameters are $D = 0.5$ and $\omega_d = 1.6\omega_0$.

model are sufficiently strong. We note that the overlap of a symmetry-broken eigenstate with the fully polarized state along the x direction increases with the interaction strength, which can also be inferred from the mean-field steady-state solution in Eq. (6). This explains the appearance of a TC in Fig. 6(b) despite the initial state not being a symmetry-broken eigenstate for $\lambda_0 = 4\lambda_{\text{cr}}$. Thus, we propose utilizing large interaction strengths for creating TCs in fully connected systems with few spins if, for a given platform, it is easier to prepare an initial fully polarized state.

Next, we study the dependence of the beating oscillations on the number of spins in the LMG model. To this end, we obtain the peaks in the oscillatory dynamics of the magnetization J_x^{peak}, which is directly related to the envelope of the oscillations in $\langle \hat{J}_x \rangle$. In Fig. 7, we display the dynamics of J_x^{peak} for different N including the mean-field limit. For weak interactions, the chosen driving parameters in Fig. 7 lead to irregular and therefore non-time-crystalline dynamics. The convergence toward the mean-field limit for increasing N is slow and can only be seen at short times due to the irregularity of the long-time dynamics. The tendency toward the mean-field prediction becomes more clear for stronger interactions, as seen in Fig. 7(b) for $\lambda_0 = 2\lambda_{\text{cr}}$. We observe that the beat period increases with N, implying that it becomes infinitely large as $N \rightarrow \infty$, consistent with the mean-field prediction of an infinitely long-lived TC. This behavior is more apparent if the system is initialized in a symmetry-broken eigenstate, as shown in Appendix E. For sufficiently strong interactions represented by $\lambda_0 = 4\lambda_{\text{cr}}$ in Fig. 7(b), we recover results consistent with Fig. 6(b), especially the emergence of long-lived period-doubling response for a relatively small number of spins ($N \sim 4$).

We present in Fig. 8 the quantum dynamics in the open DM for $\kappa = \omega_0$. In Fig. 8(a), the driving parameters

correspond to a TC in the mean-field limit. For few spins, the period-doubling oscillations rapidly decay, and for $N < 10$, the time-translation symmetry-breaking response only survives for short times, typically around five driving cycles $t \approx 5T_d$. These exponentially decaying oscillations are analogous to the beating oscillations in the closed-system limit. However, unlike the beat period in the LMG model, the decay constant characterizing the exponential suppression of oscillations in the open DM does not monotonously depend on the interaction strength. This is evident from the longer-lived oscillations in Fig. 8(b) compared with those in Fig. 8(c), even though λ_0 is larger in Fig. 8(c). This means that using the interaction strength to prolong the lifetime of a TC in the open DM is not as efficient as in closed systems, if the driving parameters are fixed. Alternatively, increasing the number of spins could also increase the lifetime of a dissipative TC [26,28,77]. Indeed, we find in Fig. 8 that the decay slows down with N, irrespective of the interaction strength. In contrast to the LMG model, in which as few as $N = 4$ spins generate a period-doubling signal lasting for $t > 10T_d$, the number of spins needed for the open DM for the same time scale is $N > 20$.

We point out that, in Fig. 8(c), despite the mean-field dynamics showing irregular or chaotic behavior, both full quantum and DTWA simulations predict periodic albeit decaying oscillations. This apparent inconsistency between mean-field and quantum approaches, regarding the presence or absence of a transition to a chaotic phase, is also reported in a driven-dissipative LMG or fully connected Ising model [78]. Lastly, we note that, for $N = 6$, in Fig. 8, DTWA is in good agreement with the numerical data obtained from the full quantum mechanical treatment, thereby suggesting that, in dissipative scenarios, DTWA can capture time-crystalline dynamics even for small N. This stabilizing effect of dissipation on the performance of DTWA as a method is like that

TABLE I. Summary of the properties of the period-doubling TCs in infinite-range interacting spins.

	Closed (LMG model)	Open (DM)
Mean-field		
Robust against:		
Random errors in the drive	Weak	Strong
Choice of initial state	Weak	Strong
Choice of driving protocol	Weak	Strong
Variation in system parameters	Strong[a]	Strong[b]
Quantum		
Oscillations	Beating	Exponential decay
Lifetime increases with	Interaction strength	Number of spins

[a]In the LMG model, strong means that it is strongly robust only for variations and random errors in the interactions strength.

[b]In the open DM, strong means strong robustness only within the resonance area in the phase diagram.

found in the positive-P approach for driven-dissipative bosons [79].

V. SUMMARY AND DISCUSSION

In this paper, we have extensively studied the influence of dissipation on TCs in a spin system with infinite-range interactions with binary driving. We have employed both mean-field and quantum mechanical treatments of the dynamics in the open DM for different dissipation strengths. For large dissipation strengths $\kappa > 10^2$, we approximate the system as closed using the ADM and LMG model. In Table I, we summarize the key properties of TCs, specifically, robustness in the thermodynamic limit and dynamical features in the quantum limit, for the closed-system and dissipative regimes.

From our mean-field approach, we have identified a simple but finely tuned set of conditions, involving the driving parameters and initial state, for creating a period-doubling response in the closed-system limit. We have demonstrated that dissipation expands this instability line to include larger areas in parameter space. Thus, we connect the TC phenomenology in the open- and closed-system limits of the infinite-range interacting spins. Moreover, we have observed that the presence and lifetime of TCs do not monotonously depend on the dissipation strength. This implies the existence of an optimal dissipation strength for realizing TCs, like dissipative-driven Heisenberg chains [33]. However, here, we show that the optimal dissipation depends strongly on the specific choice of driving parameters, and in certain cases, the absence of dissipation, $\kappa = 0$ or $\kappa \to \infty$, could in fact be the optimal choice, if one is only interested in generating a period-doubling response. If the goal, however, is to create a TC that is also robust against unwanted errors in the drive and imperfect preparation of the initial state, we ascertain that controlled dissipation is helpful. We find that the TC area in the phase diagram becomes relatively large for intermediate dissipation strengths $\kappa \sim \omega_0$. A large TC area in the phase

diagram contributes to the robustness not only against variations in system parameters but also against noise in the drive. Furthermore, we demonstrate that dissipation can form TCs, which are insensitive to the choice of initial state. We also attribute the formation of dissipative TCs using a binary drive to a period-doubling instability of a parametric resonance, and thus, we generalize the mechanism and conditions proposed in Ref. [24].

Our quantum results for finite N obtained using numerically exact calculations and the DTWA indicate an exponential decay of the period-doubling oscillations when dissipation is present. On the other hand, in the two extremes $\kappa = 0$ or $\kappa \to \infty$, the TCs exhibit beating behavior, the period of which increases with the number of spins, consistent with Ref. [9]. The scaling with the interaction strength of the lifetime of closed-system TCs is more favorable than the scaling with the number of spins for open-system TCs. This suggests a possible advantage of TCs in the closed-system limits if the underlying platform operates with few spins, albeit the driving parameters must be finely tuned according to Eq. (10).

Finally, we remark on the apparent lack of experimental evidence for TCs in the closed fully connected spin systems. As we have shown in this paper, the period-doubling instability in the LMG model and the closed DM strongly depends on the specific driving protocol. For sinusoidal driving, which was utilized for the realization of dissipative TC in the small-κ regime of a cavity-QED system [34], the DM with $\kappa = 0$ and $\kappa \to \infty$ does not host any TCs as shown in Appendix D. Instead, a binary drive according to Eq. (8) is required to induce a period-doubling response but only in a narrow region in the phase diagram spanned by the driving parameters, i.e., they must follow Eq. (10). It remains to be seen whether alternative schemes that periodically drive the transverse field (as in Refs. [9,10]), instead of the spin-spin interaction strength (as done here), would yield a larger TC area in the relevant phase diagram. Assuming a binary drive, high-fidelity state preparation is still required, i.e., the initial state should not veer too far from the symmetry-broken state of the Hamiltonian during the bright times. For the cavity-QED system operating in the regime that emulates the ADM and LMG models, which is realized for dissipation strengths that are several orders of magnitude larger than the atomic transition frequency $\kappa \gg \omega_0$ [50], the above considerations for the driving protocol and initial state preparation may not be an issue. However, for this system, authors of future studies need to address whether the large bandwidth of the cavity would cause higher momentum modes to participate in the dynamics. If so, this leads to a breakdown of the two-level approximation of the atoms and therefore the mapping onto effective spin-$\frac{1}{2}$ particles.

APPENDIX A: EQUATIONS OF MOTION

For a Hamiltonian $\hat{H}$ and the type of dissipator in Eq. (2), the dynamics of the expectation value of an operator $\hat{O}$ is

$$\partial_t \langle \hat{O} \rangle = \frac{i}{\hbar} \langle [\hat{H}, \hat{O}] \rangle + \kappa \langle (2\hat{a}^\dagger \hat{O} \hat{a} - \hat{a}^\dagger \hat{a} \hat{O} - \hat{O} \hat{a}^\dagger \hat{a}) \rangle. \quad \text{(A1)}$$

Within mean-field theory, we approximate $\langle \hat{a} \hat{J}_\mu \rangle \approx \langle \hat{a} \rangle \langle \hat{J}_\mu \rangle$. We present the equations of motion for collective and individual spins, as the former is used in the mean-field treatment, while the latter is used in DTWA.

1. DM

The equations of motion for the DM are

$$\partial_t a = -(i\omega_p + \kappa)a - i2\lambda j_x, \quad \text{(A2)}$$

$$\partial_t j_x = -\omega_0 j_y, \quad \text{(A3)}$$

$$\partial_t j_y = \omega_0 j_x - 2\lambda(a + a^*)j_z, \quad \text{(A4)}$$

$$\partial_t j_z = 2\lambda(a + a^*)j_y. \quad \text{(A5)}$$

If we decompose j_μ in terms of individual spins, we obtain

$$\partial_t a = -(i\omega_p + \kappa)a - i\lambda \frac{1}{\sqrt{N}} \sum_i s_i^x, \quad \text{(A6)}$$

$$\partial_t s_i^x = -\omega_0 s_i^y, \quad \text{(A7)}$$

$$\partial_t s_i^y = \omega_0 s_i^x - 2\lambda \frac{1}{\sqrt{N}}(a + a^*)s_i^z, \quad \text{(A8)}$$

$$\partial_t s_i^z = 2\lambda \frac{1}{\sqrt{N}}(a + a^*)s_i^y. \quad \text{(A9)}$$

For beyond mean-field approaches, a fluctuation or stochastic term associated with the dissipation must be included in the equations of motion [60,75]. In our implementation of the equations of motion governing the trajectories in the DTWA, we separate the real and imaginary components of the photon field $a = a_R + ia_I$, which yields

$$da_R = (-\kappa a_R + \omega_p a_I)dt + \sqrt{\frac{\kappa}{2}} dW_1, \quad \text{(A10)}$$

$$da_I = \left(-\omega_p a_R - \kappa a_I - \frac{\lambda}{\sqrt{N}} \sum_j s_j^x \right) dt + \sqrt{\frac{\kappa}{2}} dW_2, \quad \text{(A11)}$$

$$\partial_t s_i^x = -\omega_0 s_i^y, \quad \text{(A12)}$$

$$\partial_t s_i^y = \omega_0 s_i^x - 4\lambda \frac{1}{\sqrt{N}} a_R s_i^z, \quad \text{(A13)}$$

$$\partial_t s_i^z = 4\lambda \frac{1}{\sqrt{N}} a_R s_i^y. \quad \text{(A14)}$$

The two independent Wiener processes W_1 and W_2 account for the stochastic noise, and they satisfy $\langle dW_i \rangle = 0$ and $\langle dW_i dW_j \rangle = \delta_{i,j} dt$.

2. ADM

Next, for the ADM in the thermodynamic limit, the equations of motion are [57,58]

$$\partial_t j_x = -\omega_0 j_y, \quad \text{(A15)}$$

$$\partial_t j_y = \omega_0 j_x + \frac{8\lambda^2 \omega_p}{(\kappa^2 + \omega_p^2)} j_x j_z + \frac{16\lambda^2 \kappa \omega_p \omega_0}{(\kappa^2 + \omega_p^2)^2} j_y j_z, \quad \text{(A16)}$$

$$\partial_t j_z = -\frac{8\lambda^2 \omega_p}{(\kappa^2 + \omega_p^2)} j_x j_y - \frac{16\lambda^2 \kappa \omega_p \omega_0}{(\kappa^2 + \omega_p^2)^2} (j_y)^2. \quad \text{(A17)}$$
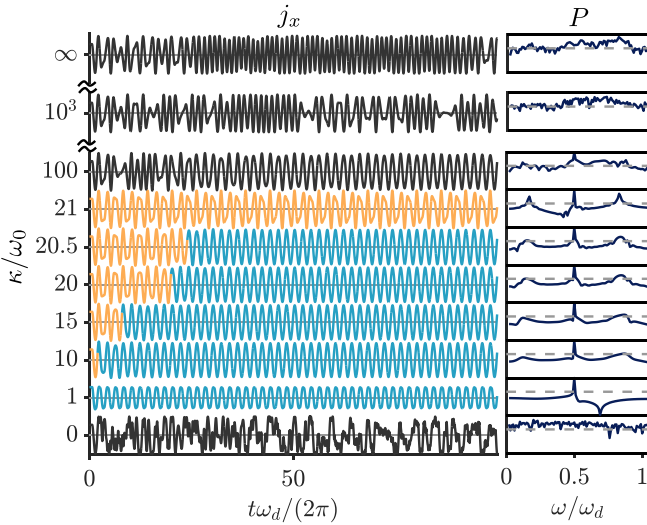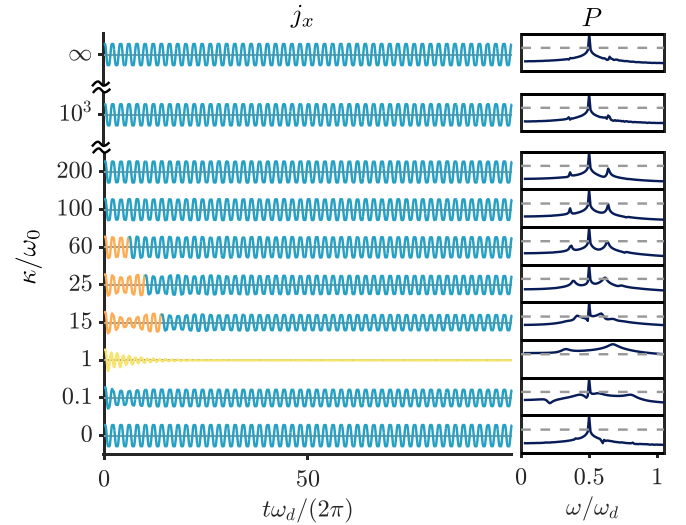
FIG. 9. Exemplary dynamics for different dissipation strengths κ with fixed driving parameters denoted by circles and diamonds in Figs. 2(d)–2(j). The left panels depict the dynamics of j_x, and the right panels show the corresponding power spectrum $\ln P$. The y axis range of each plot is $[-0.5, 0.5]$ for j_x and $[-22, 0]$ for $\ln P$. The horizontal line in the power spectrum plots denote the threshold used for identifying the presence of a time quasicrystal (TQC), which is $\ln P = -8$. The remaining parameters are the same as in Fig. 2.
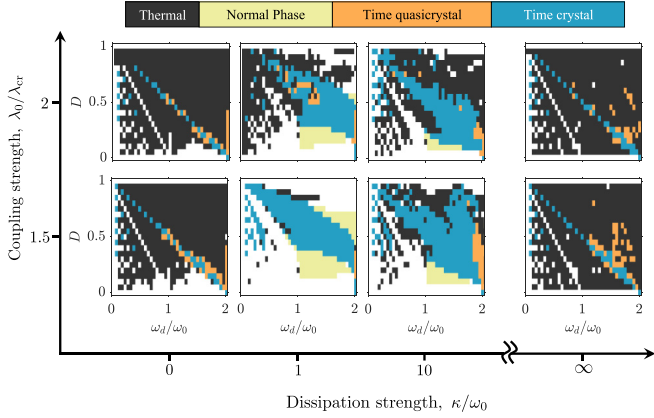
FIG. 10. Dynamical phase diagrams for different dissipation strengths. Along the vertical axis, we vary the the coupling strength and fix the frequency to $\omega_p = \omega_0$.
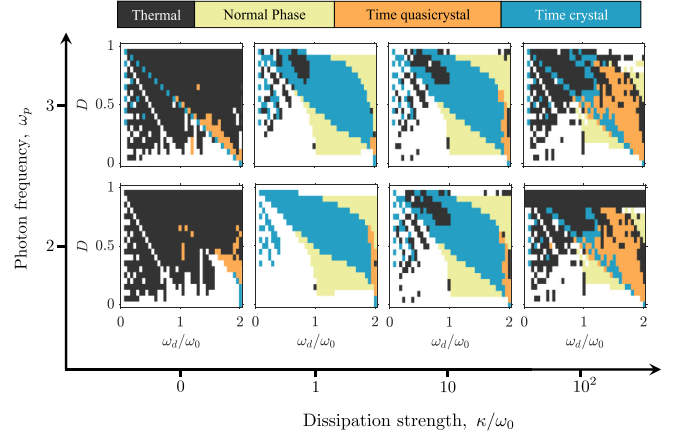
FIG. 11. Like Fig. 10 but for varying photon frequency along the vertical axis and fixed coupling strength $\lambda_0 = 1.1\lambda_{cr}$.

The corresponding equations for the individual spins are

$$\partial_t s_j^x = -\left\{ \omega_0 - \left[\frac{2\lambda^2\omega_0(\omega_p^2 - \kappa^2)}{N(\kappa^2 + \omega_p^2)} \right] \right\} s_j^y, \quad (A18)$$

$$\partial_t s_j^y = \omega_0 s_j^x + \frac{4\lambda^2\omega_p}{N(\kappa^2 + \omega_p^2)} s_j^z \sum_{i=1}^{N} s_i^x$$

$$+ \frac{8\lambda^2\kappa\omega_p\omega_0}{N(\kappa^2 + \omega_p^2)^2} s_j^z \sum_{i=1}^{N} s_i^y, \quad (A19)$$

$$\partial_t s_j^z = -\frac{4\lambda^2\omega_p}{N(\kappa^2 + \omega_p^2)} s_j^y \sum_{i=1}^{N} s_i^x$$

$$- \frac{8\lambda^2\kappa\omega_p\omega_0}{N(\kappa^2 + \omega_p^2)^2} s_j^y \sum_{i=1}^{N} s_i^y. \quad (A20)$$

3. LMG model

Finally, for the LMG model, we have [44,45]

$$\partial_t j_x = -\omega_0 j_y, \quad (A21)$$

$$\partial_t j_y = \omega_0 j_x + \frac{8\lambda^2\omega_p}{(\kappa^2 + \omega_p^2)} j_x j_z, \quad (A22)$$

$$\partial_t j_z = -\frac{8\lambda^2\omega_p}{(\kappa^2 + \omega_p^2)} j_x j_y. \quad (A23)$$

For the individual spins, we have

$$\partial_t s_j^x = -\omega_0 s_j^y, \quad (A24)$$

$$\partial_t s_j^y = \omega_0 s_j^x + \frac{4\lambda^2\omega_p}{N(\kappa^2 + \omega_p^2)} s_j^z \sum_{i=1}^{N} s_i^x, \quad (A25)$$

$$\partial_t s_j^z = -\frac{4\lambda^2\omega_p}{N(\kappa^2 + \omega_p^2)} s_j^y \sum_{i=1}^{N} s_i^x. \quad (A26)$$

APPENDIX B: EXEMPLARY DYNAMICS FOR DIFFERENT DISSIPATION STRENGTHS

We display in Fig. 9 the exemplary dynamics for different values of dissipation strength as indicated by the labels along the vertical axis. The left panels depict the mean-field results for the time evolution of j_x for driving parameters as indicated in the figure. For the specific choice of driving parameters in Fig. 9(a), the optimal dissipation strength, identified by a response that is mostly dominated by a clean period doubling, appears to be in the intermediate range $\kappa \sim \omega_0$. As we further increase the dissipation strength, time-quasicrystalline dynamics permeate during the early times, which is signified by the appearance of extra peaks in the power spectrum. The lifetimes of the TQCs increase with the dissipation rate, as seen in Fig. 9 for $\kappa/\omega_0 \in [10, 21]$. The system is in a thermal phase for zero- and strong-dissipation limits $\kappa/\omega_0 = \{0, 10^2, 10^3, \infty\}$.

In Fig. 9(b), we show the dynamics for a set of driving parameters along the instability line defined by Eq. (10). Here, we find period-doubling response in the nondissipative regimes and a light-induced NP for an intermediate dissipation strength $\kappa = \omega_0$.
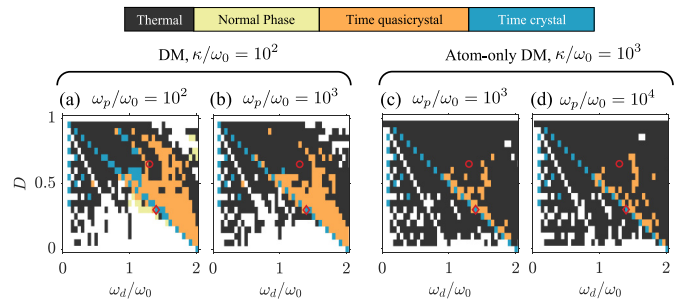

FIG. 12. Dynamical phase diagrams according to the (a) and (b) Dicke model (DM) and (c) and (d) atom-only Dicke model (ADM) for large dissipation strength and photon frequency as indicated. The coupling strength is fixed at $\lambda_0 = 1.1\lambda_{cr}$.
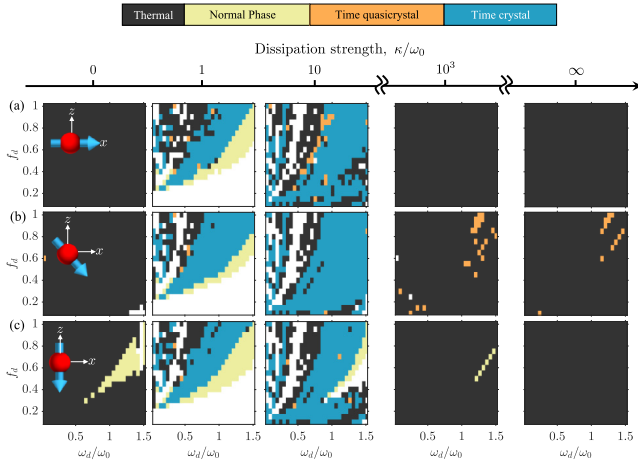
FIG. 13. Dynamical phase diagrams for a smooth sinusoidal drive and varying dissipation strengths. The remaining parameters are the same as in Fig. 2. The insets in the leftmost panels depict the initial state, namely, (a) fully polarized along the positive x direction, (b) one of the symmetry-broken states, and (c) fully polarized along the negative z direction.

FIG. 14. Dynamics in the Lipkin-Meshkov-Glick (LMG) model for an initial symmetry-broken eigenstate. The interaction strengths are (a) $\lambda_0 = 1.1\lambda_{cr}$, (b) $\lambda_0 = 2.0\lambda_{cr}$, and (c) $\lambda_0 = 4.0\lambda_{cr}$. The driving parameters are $D = 0.3$ and $\omega_d = 1.4\omega_0$.

APPENDIX C: DEPENDENCE ON THE LIGHT-MATTER COUPLING STRENGTH AND PHOTON FREQUENCY

The phase diagrams for varying dissipations strengths and coupling strengths λ are depicted in Fig. 10. We find similar results as discussed in the main text. More importantly, we demonstrate in Fig. 10 that the TCs persist for larger coupling strengths.

The results for other choices of photon frequency ω_p are shown in Fig. 11. We find that the phase diagrams for the dissipative scenarios are weakly affected by ω_p. Motivated by the typical values of the photon frequency in Ref. [50], we present in Fig. 12 the results for photon frequencies ω_p that are comparable with or larger than the dissipation strength κ. The phase diagrams for both DM and ADM corroborate our claim that the regions with TCs do not significantly change with ω_p. In fact, the number of thermal phases increases with ω_p.

APPENDIX D: CONTINUOUS SINUSOIDAL DRIVING

We briefly consider a different driving protocol given by a smooth sinusoidal drive of the light-matter coupling strength:

$$\lambda(t) = \lambda_0[1 + f_d \sin(\omega_d t)], \qquad (D1)$$

where f_d is the modulation or driving strength. This protocol has been implemented to experimentally observe the Dicke TC in the cavity-QED platform composed of Bose-Einstein condensates inside a high-finesse optical cavity pumped in the transverse direction by an optical standing wave [34].

In Fig. 13, we present the dynamical phase diagrams for such a continuous driving scheme. In addition to varying the dissipation strength, we also consider different initial states as sketched in the insets of Fig. 13. In the dissipative cases $\kappa/\omega_0 = \{1, 10\}$, time-crystalline phases appear within the resonance lobes, which have similar shape as those found in the cavity-QED simulator for the DM [34,54]. Contrary to the binary drive, we do not observe any TCs in the closed-system limits $\kappa/\omega_0 = \{0, 10^3, \infty\}$, irrespective of the initial state, for a sinusoidal drive as depicted in Fig. 13.

APPENDIX E: QUANTUM RESULTS FOR AN INITIAL SYMMETRY-BROKEN STATE IN THE LMG MODEL

The results obtained using full quantum simulations for an initial symmetry-broken eigenstate are shown in Fig. 14. The driving parameters are chosen such that the system is in a time-crystalline phase in the thermodynamic limit for the interaction strengths considered in Fig. 14. The beat period clearly increases with number of spins N, see Fig. 14(b). Furthermore, the dynamics shown in Fig. 7(b) appear to fluctuate around the dynamics in Fig. 14(b).

[1] F. Wilczek, Quantum Time Crystals, Phys. Rev. Lett. **109**, 160401 (2012).

[2] K. Sacha, Modeling spontaneous breaking of time-translation symmetry, Phys. Rev. A **91**, 033617 (2015).

[3] V. Khemani, R. Moessner, and S. L. Sondhi, A brief history of time crystals, arXiv:1910.10745 (2019).

[4] D. V. Else, C. Monroe, C. Nayak, and N. Y. Yao, Discrete time crystals, Annu. Rev. Condens. Matter Phys. **11**, 467 (2020).

[5] K. Sacha, *Time Crystals* (Springer, Cham, 2020).

[6] D. V. Else, B. Bauer, and C. Nayak, Floquet Time Crystals, Phys. Rev. Lett. **117**, 090402 (2016).

[7] N. Y. Yao, A. C. Potter, I.-D. Potirniche, and A. Vishwanath, Discrete Time Crystals: Rigidity, Criticality, and Realizations, Phys. Rev. Lett. **118**, 030401 (2017).

[8] V. Khemani, A. Lazarides, R. Moessner, and S. L. Sondhi, Phase Structure of Driven Quantum Systems, Phys. Rev. Lett. **116**, 250401 (2016).

[9] A. Russomanno, F. Iemini, M. Dalmonte, and R. Fazio, Floquet time crystal in the Lipkin-Meshkov-Glick model, Phys. Rev. B **95**, 214307 (2017).

[10] A. Pizzi, J. Knolle, and A. Nunnenkamp, Higher-order and fractional discrete time crystals in clean long-range interacting systems, Nat. Commun. **12**, 2341 (2021).

[11] R. E. Barfknecht, S. E. Rasmussen, A. Foerster, and N. T. Zinner, Realizing time crystals in discrete quantum few-body systems, Phys. Rev. B **99**, 144304 (2019).

[12] M. P. Estarellas, T. Osada, V. M. Bastidas, B. Renoust, K. Sanaka, W. J. Munro, and K. Nemoto, Simulating complex quantum networks with time crystals, Sci. Adv. **6**, eaay8892 (2020).

[13] A. Pizzi, A. Nunnenkamp, and J. Knolle, Classical Prethermal Phases of Matter, Phys. Rev. Lett. **127**, 140602 (2021).

[14] B. Ye, F. Machado, and N. Y. Yao, Floquet Phases of Matter via Classical Prethermalization, Phys. Rev. Lett. **127**, 140603 (2021).

[15] J. Zhang, P. W. Hess, A. Kyprianidis, P. Becker, A. Lee, J. Smith, G. Pagano, I.-D. Potirniche, A. C. Potter, A. Vishwanath *et al.*, Observation of a discrete time crystal, Nature (London) **543**, 217 (2017).

[16] S. Choi, J. Choi, R. Landig, G. Kucsko, H. Zhou, J. Isoya, F. Jelezko, S. Onoda, H. Sumiya, V. Khemani *et al.*, Observation of discrete time-crystalline order in a disordered dipolar many-body system, Nature (London) **543**, 221 (2017).

[17] J. Rovny, R. L. Blum, and S. E. Barrett, Observation of Discrete-Time-Crystal Signatures in an Ordered Dipolar Many-Body System, Phys. Rev. Lett. **120**, 180603 (2018).

[18] A. Kyprianidis, F. Machado, W. Morong, P. Becker, K. S. Collins, D. V. Else, L. Feng, P. W. Hess, C. Nayak, G. Pagano *et al.*, Observation of a prethermal discrete time crystal, Science **372**, 1192 (2021).

[19] J. Randall, C. E. Bradley, F. V. van der Gronden, A. Galicia, M. H. Abobeih, M. Markham, D. J. Twitchen, F. Machado, N. Y. Yao, and T. H. Taminiau, Many-body–localized discrete time crystal with a programmable spin-based quantum simulator, Science **374**, 1474 (2021).

[20] M. H. Muñoz Arias, K. Chinni, and P. M. Poggi, Floquet time crystals in driven spin systems with all-to-all *p*-body interactions, Phys. Rev. Res. **4**, 023018 (2022).

[21] J. Smits, L. Liao, H. T. C. Stoof, and P. van der Straten, Observation of a Space-Time Crystal in a Superfluid Quantum Gas, Phys. Rev. Lett. **121**, 185301 (2018).

[22] S. Autti, V. B. Eltsov, and G. E. Volovik, Observation of a Time Quasicrystal and Its Transition to a Superfluid Time Crystal, Phys. Rev. Lett. **120**, 215301 (2018).

[23] B. Huang, Y.-H. Wu, and W. V. Liu, Clean Floquet Time Crystals: Models and Realizations in Cold Atoms, Phys. Rev. Lett. **120**, 110603 (2018).

[24] Z. Gong, R. Hamazaki, and M. Ueda, Discrete Time-Crystalline Order in Cavity and Circuit QED Systems, Phys. Rev. Lett. **120**, 040404 (2018).

[25] B. Zhu, J. Marino, N. Y. Yao, M. D. Lukin, and E. A. Demler, Dicke time crystals in driven-dissipative quantum many-body systems, New J. Phys. **21**, 073028 (2019).

[26] F. Iemini, A. Russomanno, J. Keeling, M. Schirò, M. Dalmonte, and R. Fazio, Boundary Time Crystals, Phys. Rev. Lett. **121**, 035301 (2018).

[27] B. Buča, J. Tindall, and D. Jaksch, Non-stationary coherent quantum many-body dynamics through dissipation, Nat. Commun. **10**, 1730 (2019).

[28] F. M. Gambetta, F. Carollo, M. Marcuzzi, J. P. Garrahan, and I. Lesanovsky, Discrete Time Crystals in the Absence of Manifest Symmetries or Disorder in Open Quantum Systems, Phys. Rev. Lett. **122**, 015701 (2019).

[29] J. O'Sullivan, O. Lunt, C. W. Zollitsch, M. L. W. Thewalt, J. J. L. Morton, and A. Pal, Signatures of discrete time crystalline order in dissipative spin ensembles, New J. Phys. **22**, 085001 (2020).

[30] J. Skulte, P. Kongkhambut, H. Keßler, A. Hemmerich, L. Mathey, and J. G. Cosme, Parametrically driven dissipative three-level Dicke model, Phys. Rev. A **104**, 063705 (2021).

[31] M. Hajdušek, P. Solanki, R. Fazio, and S. Vinjanampathy, Seeding Crystallization in Time, Phys. Rev. Lett. **128**, 080603 (2022).

[32] A. Cabot, F. Carollo, and I. Lesanovsky, Metastable discrete time-crystal resonances in a dissipative central spin system, Phys. Rev. B **106**, 134311 (2022).

[33] D. D. Vu and S. Das Sarma, Dissipative Prethermal Discrete Time Crystal, Phys. Rev. Lett. **130**, 130401 (2023).

[34] H. Keßler, P. Kongkhambut, C. Georges, L. Mathey, J. G. Cosme, and A. Hemmerich, Observation of a Dissipative Time Crystal, Phys. Rev. Lett. **127**, 043602 (2021).

[35] X. Nie and W. Zheng, Mode softening in time-crystalline transitions of open quantum systems, Phys. Rev. A **107**, 033311 (2023).

[36] H. Keßler, J. G. Cosme, C. Georges, L. Mathey, and A. Hemmerich, From a continuous to a discrete time crystal in a dissipative atom-cavity system, New J. Phys. **22**, 085002 (2020).

[37] H. Alaeian and B. Buča, Exact multistability and dissipative time crystals in interacting fermionic lattices, Commun. Phys. **5**, 318 (2022).

[38] T. L. Heugel, M. Oscity, A. Eichler, O. Zilberberg, and R. Chitra, Classical Many-Body Time Crystals, Phys. Rev. Lett. **123**, 124301 (2019).

[39] P. Kongkhambut, J. Skulte, L. Mathey, J. G. Cosme, A. Hemmerich, and H. Keßler, Observation of a continuous time crystal, Science **377**, 670 (2022).

[40] H. Taheri, A. B. Matsko, L. Maleki, and K. Sacha, All-optical dissipative discrete time crystals, Nat. Commun. **13**, 848 (2022).

[41] H. J. Lipkin, N. Meshkov, and A. J. Glick, Validity of many-body approximation methods for a solvable model. (I). Exact solutions and perturbation theory, Nucl. Phys. **62**, 188 (1965).

[42] N. Meshkov, A. J. Glick, and H. J. Lipkin, Validity of many-body approximation methods for a solvable model. (II). Linearization procedures, Nucl. Phys. **62**, 199 (1965).

[43] A. J. Glick, H. J. Lipkin, and N. Meshkov, Validity of many-body approximation methods for a solvable model. (III). Diagram summations, Nucl. Phys. **62**, 211 (1965).

[44] J. Vidal, G. Palacios, and C. Aslangul, Entanglement dynamics in the Lipkin-Meshkov-Glick model, Phys. Rev. A **70**, 062304 (2004).

[45] S. Morrison and A. S. Parkins, Dynamical Quantum Phase Transitions in the Dissipative Lipkin-Meshkov-Glick Model with Proposed Realization in Optical Cavity QED, Phys. Rev. Lett. **100**, 040403 (2008).

[46] R. H. Dicke, Coherence in spontaneous radiation processes, Phys. Rev. **93**, 99 (1954).

[47] P. Kirton, M. M. Roses, J. Keeling, and E. G. Dalla Torre, Introduction to the Dicke model: From equilibrium to nonequilibrium, and vice versa, Adv. Quantum Technol. **2**, 1800043 (2019).

[48] J. Larson and T. Mavrogordatos, *The Jaynes-Cummings Model and Its Descendants* (IOP Publishing, Bristol, 2021).

[49] S. P. Kelly, E. Timmermans, J. Marino, and S.-W. Tsai, Stroboscopic aliasing in long-range interacting quantum systems, SciPost Phys. Core **4**, 021 (2021).

[50] K. Baumann, C. Guerlin, F. Brennecke, and T. Esslinger, Dicke quantum phase transition with a superfluid gas in an optical cavity, Nature (London) **464**, 1301 (2010).

[51] S. Korenblit, D. Kafri, W. C. Campbell, R. Islam, E. E. Edwards, Z. X. Gong, G. D. Lin, L. M. Duan, J. Kim, K. Kim *et al.*, Quantum simulation of spin models on an arbitrary lattice with trapped ions, New J. Phys. **14**, 095024 (2012).

[52] P. Jurcevic, H. Shen, P. Hauke, C. Maier, T. Brydges, C. Hempel, B. P. Lanyon, M. Heyl, R. Blatt, and C. F. Roos, Direct Observation of Dynamical Quantum Phase Transitions in an Interacting Many-Body System, Phys. Rev. Lett. **119**, 080501 (2017).

[53] C. Monroe, W. C. Campbell, L.-M. Duan, Z.-X. Gong, A. V. Gorshkov, P. W. Hess, R. Islam, K. Kim, N. M. Linke, G. Pagano *et al.*, Programmable quantum simulations of spin systems with trapped ions, Rev. Mod. Phys. **93**, 025001 (2021).

[54] Richelle Jade L. Tuquero, J. Skulte, L. Mathey, and J. G. Cosme, Dissipative time crystal in an atom-cavity system: Influence of trap and competing interactions, Phys. Rev. A **105**, 043311 (2022).

[55] J. Keeling, M. J. Bhaseen, and B. D. Simons, Collective Dynamics of Bose-Einstein Condensates in Optical Cavities, Phys. Rev. Lett. **105**, 043001 (2010).

[56] F. Dimer, B. Estienne, A. S. Parkins, and H. J. Carmichael, Proposed realization of the Dicke-model quantum phase transition in an optical cavity QED system, Phys. Rev. A **75**, 013804 (2007).

[57] F. Damanet, A. J. Daley, and J. Keeling, Atom-only descriptions of the driven-dissipative Dicke model, Phys. Rev. A **99**, 033845 (2019).

[58] S. B. Jäger, T. Schmit, G. Morigi, M. J. Holland, and R. Betzholz, Lindblad Master Equations for Quantum Systems Coupled to Dissipative Bosonic Modes, Phys. Rev. Lett. **129**, 063601 (2022).

[59] G. Engelhardt, V. M. Bastidas, C. Emary, and T. Brandes, ac-driven quantum phase transition in the Lipkin-Meshkov-Glick model, Phys. Rev. E **87**, 052110 (2013).

[60] H. Ritsch, P. Domokos, F. Brennecke, and T. Esslinger, Cold atoms in cavity-generated dynamical optical potentials, Rev. Mod. Phys. **85**, 553 (2013).

[61] F. Mivehvar, F. Piazza, T. Donner, and H. Ritsch, Cavity QED with quantum gases: New paradigms in many-body physics, Adv. Phys. **70**, 1 (2021).

[62] J. Klinder, H. Keßler, M. Wolke, L. Mathey, and A. Hemmerich, Dynamical phase transition in the open Dicke model, Proc. Natl. Acad. Sci. USA **112**, 3290 (2015).

[63] L. D'Alessio and M. Rigol, Long-time Behavior of Isolated Periodically Driven Interacting Lattice Systems, Phys. Rev. X **4**, 041048 (2014).

[64] M. Bukov, L. D'Alessio, and A. Polkovnikov, Universal high-frequency behavior of periodically driven systems: From dynamical stabilization to Floquet engineering, Adv. Phys. **64**, 139 (2015).

[65] A. Pizzi, J. Knolle, and A. Nunnenkamp, Period-n Discrete Time Crystals and Quasicrystals with Ultracold Bosons, Phys. Rev. Lett. **123**, 150601 (2019).

[66] A. Pizzi, A. Nunnenkamp, and J. Knolle, Classical approaches to prethermal discrete time crystals in one, two, and three dimensions, Phys. Rev. B **104**, 094308 (2021).

[67] R. Chitra and O. Zilberberg, Dynamical many-body phases of the parametrically driven, dissipative Dicke model, Phys. Rev. A **92**, 023815 (2015).

[68] A. Blais, J. Gambetta, A. Wallraff, D. I. Schuster, S. M. Girvin, M. H. Devoret, and R. J. Schoelkopf, Quantum-information processing with circuit quantum electrodynamics, Phys. Rev. A **75**, 032329 (2007).

[69] J. A. Mlynek, A. A. Abdumalikov, C. Eichler, and A. Wallraff, Observation of Dicke superradiance for two artificial atoms in a cavity with high decay rate, Nat. Commun. **5**, 5186 (2014).

[70] M. Bamba, K. Inomata, and Y. Nakamura, Superradiant Phase Transition in a Superconducting Circuit in Thermal Equilibrium, Phys. Rev. Lett. **117**, 173601 (2016).

[71] P. Forn-Díaz, J. J. García-Ripoll, B. Peropadre, J. L. Orgiazzi, M. A. Yurtalan, R. Belyansky, C. M. Wilson, and A. Lupascu, Ultrastrong coupling of a single artificial atom to an electromagnetic continuum in the nonperturbative regime, Nat. Phys. **13**, 39 (2017).

[72] F. Yoshihara, T. Fuse, S. Ashhab, K. Kakuyanagi, S. Saito, and K. Semba, Superconducting qubit-oscillator circuit beyond the ultrastrong-coupling regime, Nat. Phys. **13**, 44 (2017).

[73] S. Krämer, D. Plankensteiner, L. Ostermann, and H. Ritsch, QuantumOptics.jl: A Julia framework for simulating open quantum systems, Comput. Phys. Commun. **227**, 109 (2018).

[74] J. Schachenmayer, A. Pikovski, and A. M. Rey, Many-Body Quantum Spin Dynamics with Monte Carlo Trajectories on a Discrete Phase Space, Phys. Rev. X **5**, 011022 (2015).

[75] J. Huber, A. M. Rey, and P. Rabl, Realistic simulations of spin squeezing and cooperative coupling effects in large ensembles of interacting two-level systems, Phys. Rev. A **105**, 013716 (2022).

[76] A. Polkovnikov, Phase space representation of quantum dynamics, Ann. Phys. **325**, 1790 (2010).

[77] K. Tucker, B. Zhu, R. J. Lewis-Swan, J. Marino, F. Jimenez, J. G. Restrepo, and A. M. Rey, Shattered time: Can a dissipative time crystal survive many-body correlations? New J. Phys. **20**, 123003 (2018).

[78] N. Zhihao, Q. Wu, Q. Wang, G. Xianlong, and P. Wang, The failure of semiclassical approach in the dissipative fully-connected Ising model, arXiv:2302.04381 (2023).

[79] P. Deuar, A. Ferrier, M. Matuszewski, G. Orso, and M. H. Szymańska, Fully quantum scalable description of driven-dissipative lattice models, PRX Quantum **2**, 010319 (2021).

2.8 Publication III: Parametrically driven dissipative three-level Dicke model

J. Skulte, P. Kongkhambut, H. Keßler, A. Hemmerich, L. Mathey and J.G. Cosme
— **Phys. Rev. A 104, 063705 (2021)**

Motivation

This work was motivated by the previous proposal to study incommensurate time crystal (ITC) in an atom-cavity system during my Bachelor's project, which was motivated by the proposal of time crystal by Frank Wilczek. Our goal was to find a simplified model to study this phenomena, allowing for analytical insights into the mechanism.

Main findings

In this work, we studied the open three-level Dicke model, which describes one of the most fundamental class of light-matter systems. We assumed dissipation of the light mode stemming from photon losses. Furthermore, we mapped out the phase diagram for varying coupling strengths between the ground level and the two excited level. By applying a periodical drive to the coupling between the ground state and the highest excited state, while keeping the coupling between the ground state and the first excited state constant, we found an ITC. Using both numerical and analytical methods, we mapped out the phase diagram and characterized the ITC. We found the phenomena emerges due to a sum resonance between the hybrid polaron mode of atomic and light field and the energy difference between the ground and highest excited state. While we found the ITC emerging for blue detuned driving compared to the sum resonance, we found for red detuned driving a light induced and light enhanced superradiant phase depending on the initial state being in the normal phase or superradiant phase. We showed that by driving the phase of the pump beam of an atom-cavity system, the system can be approximated via the parametrically driven dissipative three-level Dicke model, which we discussed before.

Contribution

JGC, LM and I conceptualized the work. I performed the analytical calculations supported by JGC and supervised by LM. JGC and I performed the numerical simulations, supervised by LM. PK, HK and AH provided experimental insights on the system. All authors contributed to the discussion and interpretation of the results, as well as to writing the manuscript.

Parametrically driven dissipative three-level Dicke model

Jim Skulte [1,2] Phatthamon Kongkhambut,[1] Hans Keßler [1] Andreas Hemmerich [1,2]
Ludwig Mathey,[1,2] and Jayson G. Cosme [3]

[1]*Zentrum für Optische Quantentechnologien and Institut für Laser-Physik, Universität Hamburg, 22761 Hamburg, Germany*
[2]*The Hamburg Center for Ultrafast Imaging, Luruper Chaussee 149, 22761 Hamburg, Germany*
[3]*National Institute of Physics, University of the Philippines, Diliman, Quezon City 1101, Philippines*

We investigate the three-level Dicke model, which describes a fundamental class of light-matter systems. We determine the phase diagram in the presence of dissipation, which we assume to derive from photon loss. Utilizing both analytical and numerical methods we characterize the incommensurate time crystalline, light-induced, and light-enhanced superradiant states in the phase diagram for the parametrically driven system. As a primary application, we demonstrate that a shaken atom-cavity system is naturally approximated via a parametrically driven dissipative three-level Dicke model.

I. INTRODUCTION

The Dicke model is a paradigmatic model capturing the physics of a fundamental class of light-matter systems [1]. The standard two-level Dicke model describes the interaction between N two-level systems and a quantized single-mode light field. The dissipative or open standard Dicke model was first realized by using an atom-cavity setup allowing for an approximate description, in which the intracavity light field is adiabatically eliminated [2]. Later, it was also implemented in the recoil-resolved regime, which requires independent dynamical descriptions of the cavity and the matter field [3]. Meanwhile, extensions of the two-level Dicke models [4–11] and variations of the transversely pumped atom-cavity systems [12–19] have been studied.

An important class of quantum optical phenomena derive from three-level systems interacting with light. These phenomena include electromagnetically induced transparency (EIT) [20,21] and lasing without inversion (LWI) [22,23], as well as methods such as stimulated Raman adiabatic passage (StiRAP) [24,25]. They are based primarily on three-level systems in a λ or a V configuration. These three-level system configurations occur naturally in numerous physical systems, which is the origin of the universality of the phenomena that derive from them. In the context of the Dicke model, its generalization to three-level atoms interacting with a multi-mode photonic field has been proposed in Ref. [26]. A similar three-level model has been used to demonstrate subradiance [27–30].

In this work, we study a system of three-level atoms coupled to a photonic mode modeled by a three-level Dicke mode, in which the three-level system forms a V configuration, as depicted in Fig. 1(a). The three-level system can be described by using pseudospin operators following the algebra of the SU(3) group. Our representation maps onto the standard SU(3) basis, the Gell-Mann matrices [31], spanning the Lie

algebra in the defining representation of the SU(3) group. The Gell-Mann matrices are commonly used in particle physics to explain color charges [32,33]. We obtain the equilibrium phase diagram of the three-level Dicke model in the presence of dissipation due to photon loss. Moreover, we show that periodic driving of the light-matter interaction strength may lead to the emergence of new nonequilibrium phases, such as an incommensurate time crystal (ITC), light-induced superradiance (LISR), and light-enhanced superradiance (LESR).

Here, we present a comprehensive discussion of a parametrically driven three-level Dicke model. We discuss its dynamical phase diagram including the incommensurate crystalline phase, predicted by us in Ref. [34] and experimentally implemented in Ref. [35]. We show that this phase is a characteristic signature of the driven three-level Dicke model. We give a detailed account of how this model can be approximately implemented by a light-driven atom-cavity system.

This work is organized as follows: In Sec. II, we introduce the three-level Dicke model and discuss its phase diagram. We explore the dynamical phase diagram of the driven three-level Dicke model in Sec. III. The mapping of a shaken atom cavity system onto the periodically driven three-level Dicke model is presented in Sec. IV. In Sec. V, we conclude this paper.

II. THREE-LEVEL DICKE MODEL

We are interested in the properties of the three-level Dicke model for a system of N three-level atoms interacting with a quantized light mode, as schematically shown in Fig. 1(a). Each atom has three energy states $|1\rangle$, $|2\rangle$, and $|3\rangle$. We define the three-level Dicke model by the Hamiltonian

$$H/\hbar = \omega \hat{a}^\dagger \hat{a} + \omega_{12}\hat{J}_z^{12} + \omega_{13}\hat{J}_z^{13}$$
$$+ \frac{2}{\sqrt{N}}(\hat{a}^\dagger + \hat{a})(\lambda_{12}\hat{J}_x^{12} + \lambda_{13}\hat{J}_x^{13}), \quad (1)$$
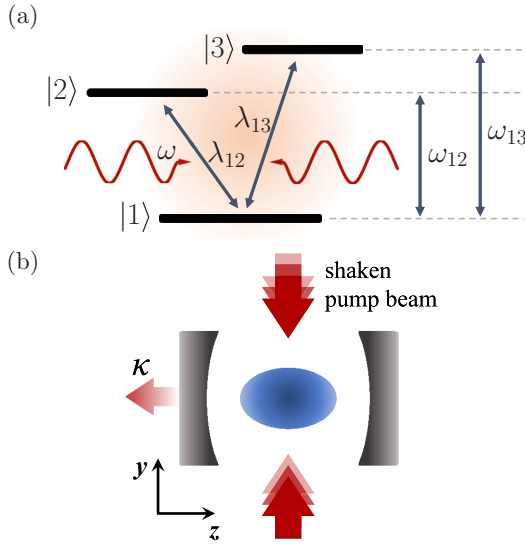
FIG. 1. (a) Three-level system coupled to a single light mode. (b) Schematic diagram of the shaken atom-cavity system. The cavity photon loss rate is κ. This atom-cavity configuration can emulate the driven dissipative three-level Dicke model.

FIG. 2. Long-time average of the mean-field dynamics of the (a) cavity mode occupation $|a|^2$, (b) $|j_x^{12}|^2$, and (c) $|j_x^{13}|^2$ for $\omega = \omega_{12} = \omega_{13} = \kappa$. The black curve denotes the critical line separating the normal and superradiant phases in the thermodynamic limit.

where ω is the photon frequency, ω_{nm} is the detuning between states $|m\rangle$ and $|n\rangle$, and λ_{nm} is the light-matter interaction strength associated with the photon-mediated coupling between states $|n\rangle$ and $|m\rangle$. The bosonic operators $\hat{a}$ and $\hat{a}^\dagger$ annihilate and create a photon in the quantized light mode, respectively. There are three classes of pseudospin operators $\hat{J}_\mu^{12}$, $\hat{J}_\mu^{13}$, and $\hat{J}_\nu^{23}$ with $\mu \in \{z, \pm\}$ and $\nu \in \{\pm\}$, corresponding to the transitions $|1\rangle \leftrightarrow |2\rangle$, $|1\rangle \leftrightarrow |3\rangle$, and $|2\rangle \leftrightarrow |3\rangle$, respectively. These operators obey the commutation relation of the SU(3) algebra (see Appendix A). The x and y components of the pseudospins are defined as $\hat{J}_x^\ell = (\hat{J}_+^\ell + \hat{J}_-^\ell)/2$ and $\hat{J}_y^\ell = (\hat{J}_+^\ell - \hat{J}_-^\ell)/2i$, respectively, with $\ell \in \{12, 13, 23\}$.

Note that, in principle, there is a light-matter coupling term proportional to $\hat{J}_x^{23}$ in Eq. (1) [26]. However, this term is neglected here since we are only interested in the case when $\omega_{12} \approx \omega_{13}$. This leads to a negligibly small λ_{23} since the light-matter coupling strength is proportional to the energy difference between the relevant states [36,37]. Moreover, we could also use the Gell-Mann matrices as the representation of the SU(3) group in our system. To retain a form of the Hamiltonian reminiscent of the standard two-level Dicke model, which is often written using a representation of the SU(2) group, we instead use the pseudospin operators as described above. Nevertheless, the Gell-Mann matrices can be obtained from appropriate superpositions of the pseudospin operators (see Appendix A).

The Hamiltonian in Eq. (1) is superficially similar to the two-component Dicke model [9,10,16,17] (see also Appendix B for a brief discussion). However, we emphasize that, unlike in the two-component Dicke model, which describes two types of two-level systems coupled through the light field, the pseudospin operators introduced in Eq. (1) obey the SU(3) algebra resulting from the use of three-level systems. This fundamentally changes the dynamics of the parametrically driven system out of equilibrium since new
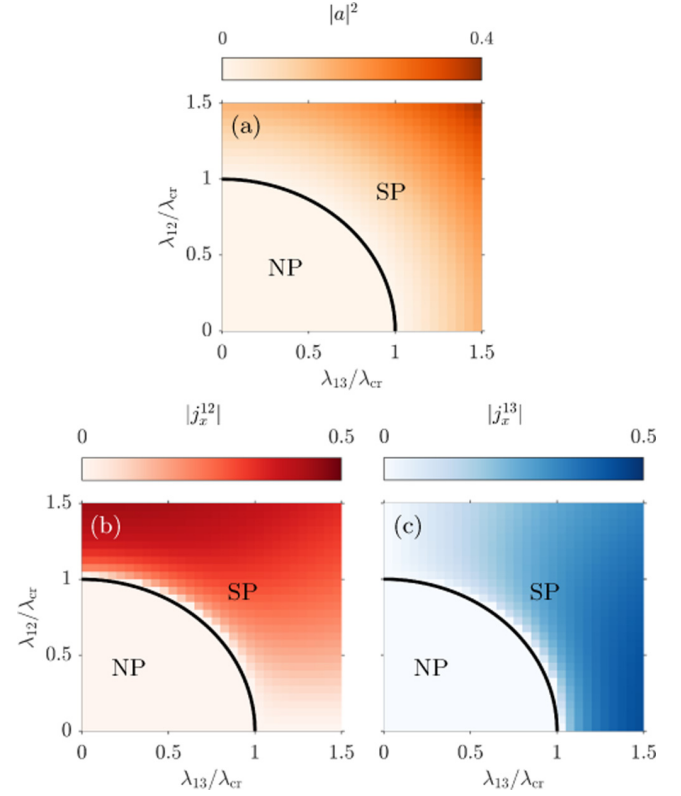
terms corresponding to additional spin operators are now present in the equations of motion.

A. Holstein-Primakoff transformation

To obtain analytical predictions of the phase boundaries, we employ a Holstein-Primakoff (HP) approximation in the thermodynamic limit, i.e., $N \to \infty$. This leads to the following Hamiltonian:

$$H/\hbar = \omega \hat{a}^\dagger \hat{a} + \omega_{12} \hat{a}_{12}^\dagger \hat{a}_{12} + \omega_{13} \hat{a}_{13}^\dagger \hat{a}_{13}$$
$$+ (\hat{a}^\dagger + \hat{a})[\lambda_{12}(\hat{a}_{12}^\dagger + \hat{a}_{12}) + \lambda_{13}(\hat{a}_{13}^\dagger + \hat{a}_{13})]. \quad (2)$$

We obtain an elliptic equation for the critical light-matter coupling from the stability matrix (see Appendix C for details):

$$\frac{(\kappa^2 + \omega^2)}{4\omega} = \left(\frac{\lambda_{12}^2}{\omega_{12}} + \frac{\lambda_{13}^2}{\omega_{13}}\right). \quad (3)$$

In the standard open Dicke model, $\lambda_{13} = 0$, the critical light-matter coupling, $\lambda_{cr} = [(\kappa^2 + \omega^2)(\omega_{12}/\omega)]^{1/2}/2$, is recovered [38]. To illustrate the resulting phases, we consider the case $\omega = \omega_{12} = \omega_{13}$. Then, the critical line in Eq. (5) defines a circle in the parameter space spanned by λ_{12} and λ_{13}, as seen in Fig. 2. For combinations of light-matter coupling strengths $\{\lambda_{12}, \lambda_{13}\}$ within the area enclosed by Eq. (5), the stable phase corresponds to a normal phase (NP), while those outside the area will lead to an instability towards the formation of a superradiant phase (SP).

B. Phase diagram

Next, we employ a mean-field approximation $\langle \hat{a}\hat{J}_\mu^\ell \rangle \approx \langle \hat{a} \rangle \langle \hat{J}_\mu^\ell \rangle$ starting from Eq. (1) to obtain the dynamics of the system in a semiclassical approximation (see Appendix D for details). This approximation becomes exact in the thermodynamic limit $N \to \infty$ in or near the steady state. Furthermore, we introduce the rescaled c numbers $a \equiv \langle \hat{a} \rangle / \sqrt{N}$ and $j_\mu^\ell \equiv \langle \hat{J}_\mu^\ell \rangle / N$. The resulting mean-field equations of motion that we simulate are shown in Appendix E. We further note that the SU(3) group inherits two Casimir charges, a quadratic C_1 and a cubic C_2. In contrast with this, the group SU(2) has only one quadratic Casimir charge, namely, the total spin $J^2 = (J_x)^2 + (J_y)^2 + (J_z)^2$. The expressions for the charges are shown in Appendix A. We track these quantities when solving the equations of motion to ensure convergence of our numerical results. In our simulations, we initialize in the normal phase $j_\mu^\ell = 0$, except for $j_z^{12} = j_z^{13} = -1/2$. This amounts to all the atoms initially occupying the lowest energy state $|1\rangle$. We initialize the cavity field as $a = 10^{-2}$.

An observable of interest is the occupation of the photonic mode $|a|^2$ because this differentiates the normal ($|a|^2 \to 0$ for $N \to \infty$) and superradiant ($|a|^2 > 0$) phases. Moreover, we are interested in the magnitude of the x component of the collective spin operators corresponding to the transition $|1\rangle \leftrightarrow |2\rangle$ and $|1\rangle \leftrightarrow |3\rangle$, which are $|j_x^{12}|$ and $|j_x^{13}|$, respectively. In Fig. 2, we present the long-time average of $|a|^2$, $|j_x^{12}|$, and $|j_x^{13}|$, calculated by numerically solving the equations of motion. Similar to the standard two-level Dicke model [39], the photonic mode occupation or the x component of the pseudospin operators can be regarded as order parameters because they are zero in the NP and are nonzero in the SP. Furthermore, we demonstrate in Fig. 2 that the onset of superradiance according to our mean-field dynamics agrees with the analytical critical line defined by Eq. (5). In the superradiant phase, $|j_x^{12}| > |j_x^{13}|$ for $\lambda_{12} > \lambda_{13}$ and $|j_x^{12}| < |j_x^{13}|$ for $\lambda_{12} < \lambda_{13}$, as inferred from Figs. 2(b) and 2(c).

III. PARAMETRICALLY DRIVEN OPEN THREE-LEVEL DICKE MODEL

We now explore the parametrically driven three-level Dicke model by the Hamiltonian

$$H/\hbar = \omega \hat{a}^\dagger \hat{a} + \omega_D \hat{J}_z^D + \omega_B \hat{J}_z^B + 2\phi(t)(\omega_B - \omega_D)\hat{J}_x^{DB} + \frac{2\lambda}{\sqrt{N}}(\hat{a}^\dagger + \hat{a})(\hat{J}_x^D - \phi(t)\hat{J}_x^B). \quad (4)$$

This particular choice of the Hamiltonian is motivated by its connection to the shaken atom-cavity system, which we demonstrate and explore in more detail later. Comparing with the undriven case in Eq. (1), it can be seen that $\omega_{12} = \omega_D$, $\omega_{13} = \omega_B$, $\hat{J}_\mu^{12} = \hat{J}_\mu^D$, $\hat{J}_\mu^{13} = \hat{J}_\mu^B$, $\lambda_{12} = \lambda$. We define $\phi(t) = f_0 \sin(\omega_{dr}t)$, which then means that $\lambda_{13} = -f_0 \sin(\omega_{dr}t)\lambda$. This labeling is motivated by the association of the pseudospins with the density wave states in the atom-cavity setup discussed later in Sec. IV. For now, we simply note that the photonic mode corresponds to a single cavity mode while the operators $\hat{J}_\mu^D$ and $\hat{J}_\mu^B$ are associated with the density wave (DW) and bond-density wave (BDW) states in the shaken atom-cavity system, respectively [34]. A small term

proportional to $\hat{J}_x^{23} \equiv \hat{J}_x^{DB}$ is included in Eq. (6) since this will appear later when we show how the atom-cavity system can be mapped onto the specific form of the parametrically driven three-level Dicke model Eq. (6).

A. Holstein-Primakoff transformation

In Sec. II A, we have applied the HP transformation to the undriven system described by Eq. (3). We now extend this analysis to include the driving term. Applying the transformation and identifying $\hat{d} \equiv \hat{a}_{12}$ and $\hat{b} \equiv \hat{a}_{13}$, we obtain a HP Hamiltonian shown in Eq. (F3) of Appendix F. In particular, we are interested in $d \equiv \langle \hat{d} \rangle$ and $b \equiv \langle \hat{b} \rangle$.

We recall that, for a quantum harmonic oscillator, $\hat{f}^\dagger = \sqrt{\omega_F/\hbar}[x_F - (i/\omega_F)p_F]$ and $\hat{f} = \sqrt{\omega_F/\hbar}[x_F + (i/\omega_F)p_F]$. Then, we can express the corresponding HP Hamiltonian in momentum-position representation as

$$H = \frac{\omega^2}{2}\hat{x}^2 + \frac{\hat{p}^2}{2} + \frac{\omega_D^2}{2}\hat{x}_D^2 + \frac{\hat{p}_D^2}{2} + \frac{\omega_B^2}{2}\hat{x}_B^2 + \frac{\hat{p}_B^2}{2}$$
$$+ 2\lambda\sqrt{\omega\omega_D}\hat{x}\hat{x}_D - 2\phi(t)\lambda\sqrt{\omega\omega_B}\hat{x}\hat{x}_B$$
$$+ \phi(t)(\omega_B - \omega_D)\sqrt{\omega_D\omega_B}\left(\hat{x}_D\hat{x}_B + \frac{\hat{p}_D\hat{p}_B}{\omega_D\omega_B}\right). \quad (5)$$

This has the form of a Hamiltonian for three coupled oscillators: (i) the *cavity oscillator*, (ii) the *DW oscillator*, and (iii) the *BDW oscillator* with frequencies ω, ω_D, and ω_B, respectively. Here, the two coupling constants connecting the BDW oscillator to the cavity and DW oscillators are periodically switched on and off or parametrically driven. Interestingly, due to the shaking of the pump, the momenta of the DW and BDW oscillators are also periodically coupled, as seen from the last term in Eq. (8). However, we find that this does not alter the qualitative features of the dynamics, as shown in Fig. 8 in Appendix E.

We initialize the system in the normal state corresponding to having $d = 0$ and $b = 0$, which amounts to the absence of bosons in the excited states $|2\rangle$ and $|3\rangle$, respectively. Note that a small nonzero occupation of the photonic mode $\langle \hat{a} \rangle \equiv a = 10^{-2}$ is necessary to push the system out of the normal phase when it becomes an unstable state [9]. The dynamics is obtained according to Eq. (F4) for varying driving strength f_0 and driving frequency ω_{dr}. A parametric resonance in a linear system corresponding to a bilinear Hamiltonian, such as the simplified toy model (F3), manifests itself as an oscillatory solution with exponentially diverging amplitude. The dotted curves in Figs. 3(a)–3(d) denote the points in the (ω_{dr}, f_0) space, where $(b + b^*)$ exceeds unity within the first 100 driving cycles, signaling a diverging solution (see also Fig. 5). They indicate the regions where the normal phase is unstable towards a different collective phase.

We identify two resonances responsible for the driving-induced destabilization of the normal phase: (i) resonance at the BDW oscillator frequency ω_B and (ii) a sum resonance involving ω_B and the lower polariton frequency ω_{LP} of the atomic modes dressed by the cavity mode forming the lower polariton state [40]. Note that we derive the expression for ω_{LP} within the HP approach and we describe our method for obtaining the lower polariton frequency by exploiting a parametric resonance in Appendix G. The resonance
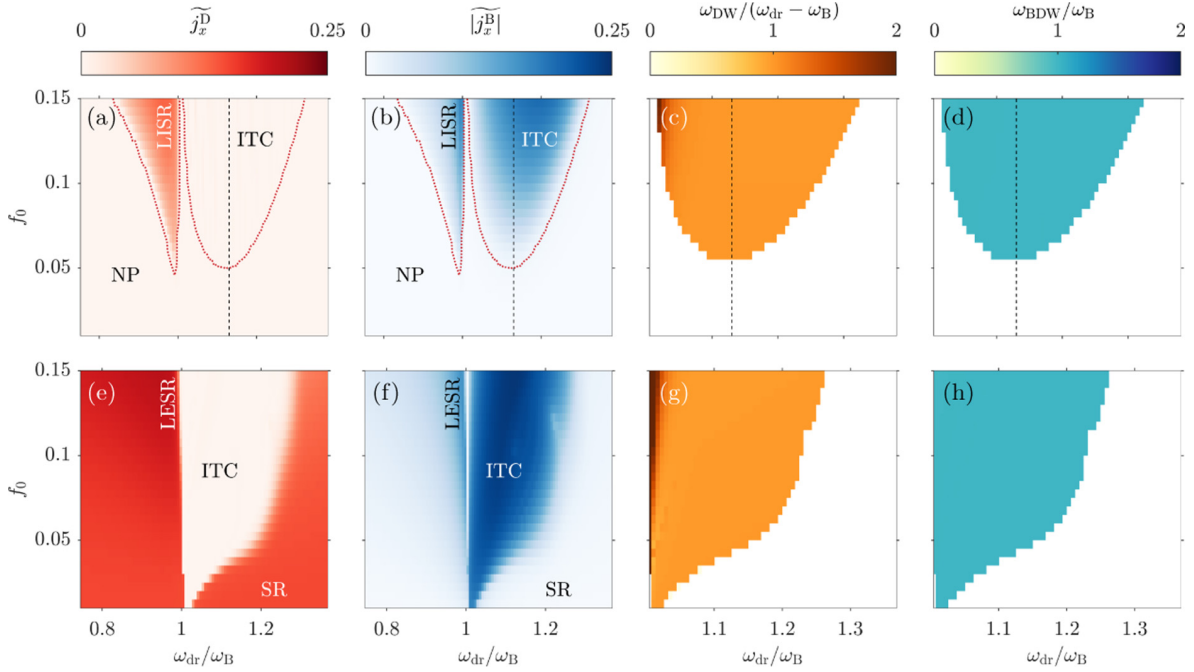
FIG. 3. Dynamical phase diagram for (a)–(d) $\lambda = 0.98\lambda_{cr}$ and (e), (f) $\lambda = 1.02\lambda_{cr}$. Time-averaged (a), (e) $\widetilde{j_x^D}$ and (b), (f) $\widetilde{|j_x^B|}$ taken over 100 driving cycles, $\tau = 100T$, for varying modulation parameters. The dominant or peak frequency in the power spectrum of (c), (g) j_x^D and (d), (h) j_x^B for $\omega_{dr} > \omega_B$. The dotted lines in panels (a) and (b) denote the instability boundary according to the oscillator model. In panels (c), (d), (g), and (h), we are only showing the response frequencies ω_{DW} and ω_{BDW} for parameter sets, which yield $\widetilde{|j_x^B|} > 0.01$ and $\widetilde{j_x^D} < 0$. Note that we are rescaling the response frequencies in panels (c) and (g) to $\omega_{DW}/(\omega_{dr} - \omega_B)$ and it is rescaled in panels (d) and (h) to ω_{BDW}/ω_B. The vertical dashed lines in panels (a)–(d) correspond to the sum frequency $\omega_{sum} = \omega_{LP} + \omega_B$.

frequencies are identified as the driving frequencies with the lowest modulation strength needed to induce an exponential instability. For $\omega_{dr} < \omega_B$, the resonance frequency is close to ω_B. For $\omega_{dr} > \omega_B$, the sum resonance at $\omega_{sum} = \omega_B + \omega_{LP}$ is the main mechanism, as highlighted by the vertical dashed line in Figs. 3(a)–3(d) (see also Fig. 5).
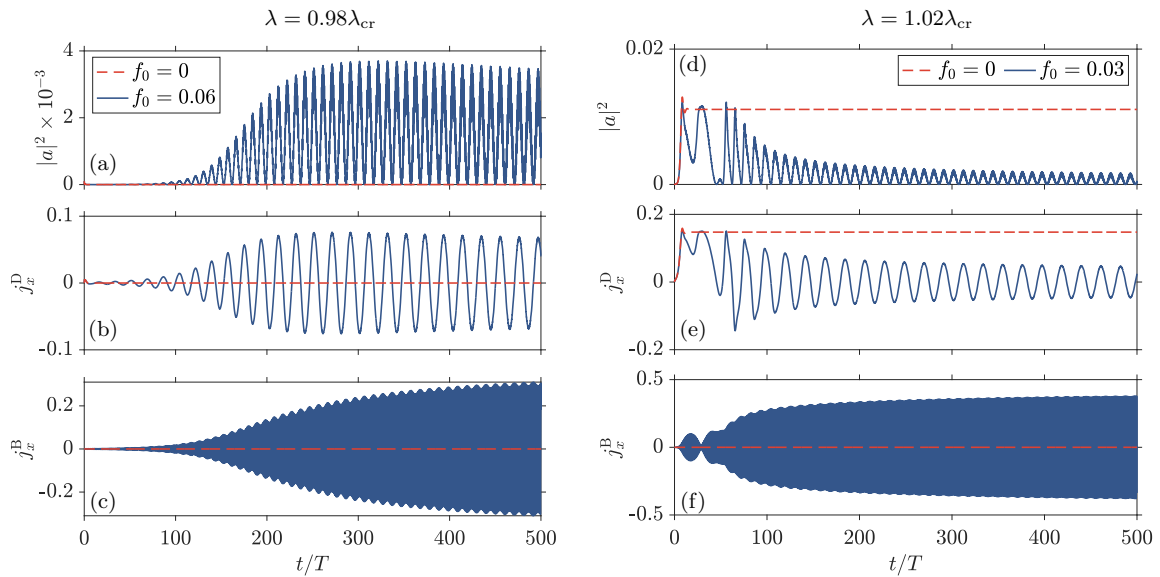
FIG. 4. Comparison between unmodulated and resonantly modulated dynamics for light-matter coupling strengths close to the NP-SR phase of the unmodulated system, (a)–(c) $\lambda = 0.98\lambda_{cr}$ and (d)–(f) $\lambda = 1.02\lambda_{cr}$. The relevant observables are the (a), (d) cavity mode occupation $|a|^2$, and the order parameters (b), (e) j_x^D and (c), (f) j_x^B. The modulation frequency is fixed at $\omega_{dr} = 1.05\omega_B$.
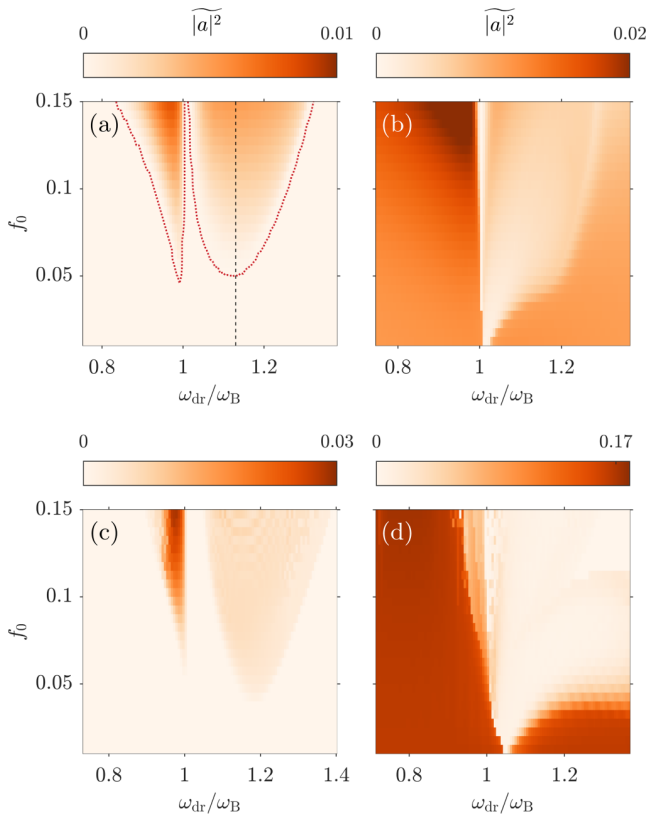
FIG. 5. Time-averaged cavity mode occupation $|a|^2$ taken over 100 driving cycles, $\tau = 100T$, according to (a), (b) the three-level Dicke model and (c), (d) the full atom-cavity model. For the three-level model, the light-matter coupling strengths are (a) $\lambda = 0.98\lambda_{cr}$ and (b) $\lambda = 1.02\lambda_{cr}$. The broken lines denote the instability boundary from the oscillator model. The vertical dashed line in panel (a) corresponds to the sum frequency $\omega_{sum} = \omega_{LP} + \omega_B$ involving the lower polariton frequency ω_{LP}. ω_{LP} has the value $\omega_{LP}/2\pi \approx 1.06$ kHz for this example. For the full atom-cavity model, the pump strengths are (c) $\epsilon_p = 0.96\epsilon_{cr}$ and (d) $\epsilon_p = 1.04\epsilon_{cr}$, which corresponds to $\lambda = 0.98\lambda_{cr}$ and $\lambda = 1.02\lambda_{cr}$, respectively.

B. Dynamical phase diagrams

To further understand the resonant collective phases, we obtain the dynamics of the system. Within the mean-field approximation, we simulate the semiclassical equations of motion shown in Appendix E. Similar to the HP theory in the previous section, we initialize the system in the normal phase with small nonzero occupation of the photonic mode $a = 10^{-2}$, We further choose $j_\mu^\ell = 0$, except for $j_z^D = j_z^B = -1/2$. In addition to the photonic mode occupation $|a|^2$, we are also interested in the x component of the pseudospins j_x^D and j_x^B. Time is in units of the modulation period $T = 2\pi/\omega_{dr}$. The parameters for the simulation are shown in Appendix H.

In Fig. 4, we present exemplary dynamics for resonant modulation, specifically for $\omega_{dr} = 1.05\omega_B$. We choose light-matter coupling strengths close to the phase boundary between the normal and superradiant phases, specifically $\lambda = 0.98\lambda_{cr}$ and $\lambda = 1.02\lambda_{cr}$, respectively. In the absence of driving, $f_0 = 0$, we reproduce the prediction of a normal phase NP and superradiant phase SP from the standard two-level Dicke

model. Periodic driving closed to but blue-detuned from ω_B leads to similar long-time behavior for $\lambda < \lambda_{cr}$ and $\lambda > \lambda_{cr}$. That is, the spin components related to the order parameters in the atom-cavity system, j_x^D and j_x^B, periodically changes their sign concomitant to pulses of light being emitted. The slow subharmonic oscillations in j_x^D, as exemplified in Fig. 4(b), reflects the temporal periodicity of the entire light-matter system. Note that j_x^B rapidly switches sign, as shown in Figs. 4(c) and 4(f). We quantify the dynamical regimes in the system using the response frequencies ω_{DW} and ω_{BDW}, which we define as the frequency at which j_x^D and j_x^B has a maximum in the power spectrum. Considering blue-detuned driving with respect to the BDW oscillator frequency $\omega_{dr} > \omega_B$, we find that the DBDW phase is characterized by fast oscillations of j_x^B at $\omega_{BDW} = \omega_B$ and slow oscillations of j_x^D at $\omega_{DW} = \omega_{dr} - \omega_B$. These observations are valid for both $\lambda < \lambda_{cr}$ and $\lambda > \lambda_{cr}$, as demonstrated in Figs. 3(c), 3(d), 3(g), and 3(h), where the relations $\omega_{DW}/(\omega_{dr} - \omega_B) = 1$ and $\omega_{BDW}/\omega_B = 1$ are satisfied over a wide range modulation parameters. In general, the system's response frequency ω_{DW} is subharmonic and incommensurate with respect to the driving frequency ω_{dr}, underpinning the classification of the DBDW phase as an ITC. Thus, we show that the emergence of the ITC phase is one of the signatures of the parametrically driven three-level Dicke model. In contrast, the system has a harmonic response, meaning that $|a|^2$ and j_x^D have the same response frequency $\omega_{DW} = 2\omega_{dr}$ [34], for combinations of driving parameters outside the dark areas in Figs. 3(c), 3(d), 3(g), and 3(h), including red-detuned driving $\omega_{dr} < \omega_B$.

In the ITC phase for $\omega_{dr} > \omega_B$, the oscillations of j_x^D and j_x^B around zero translate to vanishing time-averaged values,

$$\widetilde{j_x^\ell} = \frac{1}{\tau} \int_0^\tau j_x^\ell dt. \quad (6)$$

This property is visible in the light area in Fig. 3(e). Note, however, that even though $\widetilde{j_x^D} = 0$, the time-averaged cavity mode occupation $\widetilde{|a|^2}$ does not necessarily vanish, especially when j_x^D has nonzero oscillation amplitude, as shown in Figs. 3(a) and 5(a). The normal phase has $j_x^D = 0$ for all times and as such, $|\widetilde{j_x^D}|$ also vanishes, albeit trivially, similar to the ITC phase. Therefore, to distinguish between the normal phase and the ITC phase, we calculate $|\widetilde{j_x^B}|$, a quantity that vanishes for the normal phase and is nonzero for the ITC phase. In Figs. 3(b) and 3(f), it can be seen that the BDW states are resonantly excited not only for the ITC phase in $\omega_{dr} > \omega_B$ but also for red-detuned driving $\omega_{dr} < \omega_B$. We emphasize that the dynamical response for $\omega_{dr} < \omega_B$ remains harmonic, making this phase distinct from the ITC, normal, and superradiant phases.

We now focus on red-detuned driving $\omega_{dr} < \omega_B$ to illustrate the effects of resonantly exciting the BDW states in this case. For $\lambda < \lambda_{cr}$, the normal phase, expected to be dominant in the absence of driving, is suppressed, which then gives rise to a superradiant phase enabled by the excitation of the BDW states. We call this resonant phase for $\lambda < \lambda_{cr}$ and $\omega_{dr} < \omega_B$ the *light-induced superradiant* (LISR) phase. In this phase, the long-time average of the cavity mode occupation $|a|^2$ and j_x^D are both nonzero, similar to the superradiant phase, as seen from the resonance lobe in Figs. 3(a) and 5(a) for $\omega_{dr} < \omega_B$.

However, the occupation of BDW states, demonstrated in Fig. 3(b), distinguishes the LISR phase from the usual SR phase in the undriven case. An analogous effect for $\lambda > \lambda_{cr}$ is the enhancement of the superradiant phase, the stationary phase in the absence of driving. This *light-enhanced superradiant* (LESR) phase is identified by an increase in $|a|^2$ and j_x^D, accompanied by large amplitude oscillations of j_x^B, as shown in Figs. 5(b), 3(e), and 3(f). In addition to the ITC phase, the presence of LISR and LESR phases, depending on λ, is another signature of the driven dissipative three-level Dicke model.

IV. EMULATION USING A SHAKEN ATOM-CAVITY SYSTEM

We now show that the parametrically driven open three-level Dicke model can be emulated by a shaken atom-cavity system. To this end, we first describe the many-body Hamiltonian of the shaken atom-cavity. Then, we present the approximation needed to obtain Eq. (6) from the atom-cavity Hamiltonian.

A. Shaken atom-cavity Hamiltonian

We consider a minimal model for describing the dynamics along the pump and cavity directions of an atom-cavity system schematically depicted in Fig. 1(b). The corresponding many-body Hamiltonian is given by [34]

$$
\begin{aligned}
\hat{H}/\hbar = &-\delta_C \hat{a}^\dagger \hat{a} + \int dy\, dz\, \hat{\Psi}^\dagger(y,z) \bigg[-\frac{\hbar}{2m}\nabla^2 \\
&- \omega_{rec}\epsilon_p \cos^2[ky+\phi(t)] + U_0 \hat{a}^\dagger \hat{a} \cos^2(kz) \\
&- \sqrt{\omega_{rec}|U_0|\epsilon_p}\cos[ky+\phi(t)]\cos(kz)(a^\dagger+a) \bigg] \hat{\Psi}(y,z),
\end{aligned}
$$

(7)

where $\hat{a}$ ($\hat{a}^\dagger$) annihilates (creates) a photon in the single-mode cavity and $\hat{\Psi}(y,z)$ is the bosonic field operator for the atoms with mass m. The pump-cavity detuning is δ_C. The frequency shift per atom is taken to be redshifted, $U_0 < 0$. The pump intensity ϵ_p is measured in units of the recoil energy $E_{rec} = \hbar^2 k^2/2m$, where the wave vector is $k = 2\pi/\lambda_p$. Note that, in Eq. (11), we neglect the effects of short-range collisional interaction. The pump lattice is periodically shaken by introducing a time-dependent phase in the pump mode

$$
\phi(t) = f_0 \sin(\omega_{dr} t),
$$

(8)

where f_0 is the unitless modulation strength and ω_{dr} is the modulation frequency. The characteristic timescale is thus set by the driving period $T = 2\pi/\omega_{dr}$.

The dynamics of the atom-cavity system follows from the Heisenberg-Langevin equations [40,41],

$$
\frac{\partial}{\partial t}\hat{\Psi} = \frac{i}{\hbar}[\hat{H}, \hat{\Psi}],
$$

(9)

$$
\frac{\partial}{\partial t}\hat{a} = \frac{i}{\hbar}[\hat{H}, \hat{a}] - \kappa\hat{a} + \xi,
$$

(10)

where κ is the cavity dissipation rate and the associated fluctuations are captured by the noise term ξ satisfying

$\langle \xi^*(t)\xi(t')\rangle = \kappa\delta(t-t')$. In the mean-field limit of large particle number N, quantum fluctuations are neglected and the bosonic operators can be approximated as c numbers. The dynamics can then be obtained by numerically solving the resulting coupled differential equations corresponding to the equations of motion of the system. This approach and its extension beyond a mean-field approximation have been successfully used to predict and observe various dynamical phases in the transversely pumped atom-cavity system from a driving-induced renormalization of the phase boundary to time crystals [34,42–47].

B. Low-momentum approximation

The atom-cavity system can be mapped onto the Dicke model using a low-momentum approximation. To this end, we assume that the majority of the atoms only occupy the five-lowest momentum modes, namely the zero-momentum mode, $|k_y, k_z\rangle = |0, 0\rangle$, and the states associated with the self-organized checkerboard phase, $|\pm k, \pm k\rangle$. These momentum modes are coupled by the scattering of photons between the pump and cavity fields. This low-momentum approximation is valid close to the phase boundary between the homogeneous BEC phase and the self-organized DW phase.

Resonant shaking has been shown to lead to the emergence of an incommensurate time crystal, where atoms localize at positions between the antinodes of the pump lattice [34,35]. That is, in addition to the spatial mode $\cos(ky)\cos(kz)$ in the DW phase, the atoms are driven into additional states, namely the BDW states, as the atomic distribution acquires an overlap with the spatial mode $\sin(ky)\cos(kz)$. Note that this mode is made available by the periodic shaking of the pump lattice since it explicitly breaks the spatial symmetry along the pump axis. Owing to how the system periodically switches between superpositions of DW and BDW states, we call this dynamical phase as the dynamical BDW (DBDW) phase. Since the DBDW phase has been previously identified as an incommensurate time crystal (ITC), we will use the term DBDW and ITC phase interchangeably.

The atomic field operator is expanded to include the relevant spatial modes

$$
\hat{\Psi}(y,z) = \hat{c}_1 + 2\hat{c}_2 \cos(ky)\cos(kz) + 2\hat{c}_3 \sin(ky)\cos(kz),
$$

(11)

where the c_i are bosonic annihilation and creation operator. We use this expansion in the many-body Hamiltonian (11). Evaluating the integrals within one unit cell and for weak driving $f_0 \ll 1$, we obtain a Hamiltonian in a reduced subspace,

$$
\begin{aligned}
H/\hbar = &-\delta_C \hat{a}^\dagger \hat{a} + 2\omega_{rec}(\hat{c}_2^\dagger \hat{c}_2 + \hat{c}_3^\dagger \hat{c}_3) + \frac{U_0}{2}\hat{a}^\dagger\hat{a}[\hat{c}_1^\dagger \hat{c}_1 \\
&+ \frac{3}{2}(\hat{c}_2^\dagger \hat{c}_2 + \hat{c}_3^\dagger \hat{c}_3)] - \frac{\omega_{rec}\epsilon_p}{4}[2(\hat{c}_1^\dagger \hat{c}_1 + \hat{c}_2^\dagger \hat{c}_2 + \hat{c}_3^\dagger \hat{c}_3) \\
&+ (\hat{c}_2^\dagger \hat{c}_2 - \hat{c}_3^\dagger \hat{c}_3) - 2\phi(t)(\hat{c}_2^\dagger \hat{c}_3 + \hat{c}_3^\dagger \hat{c}_2)] - \frac{\sqrt{\omega_{rec}|U_0|\epsilon_p}}{2} \\
&\times (\hat{a}^\dagger + \hat{a})[(\hat{c}_1^\dagger \hat{c}_2 + \hat{c}_2^\dagger \hat{c}_1) - \phi(t)(\hat{c}_1^\dagger \hat{c}_3 + \hat{c}_3^\dagger \hat{c}_1)].
\end{aligned}
$$

(12)

C. Schwinger boson representation

We transform the bosonic operators in Eq. (12) into collective pseudospin operators through the Schwinger boson representation. The additional spatial mode $\sin(ky)\cos(kz)$ is described by the operator c_3, so the atomic motion is represented as a three-level system. We introduce the pseudospin operators obeying SU(3) algebra via

$$N = \hat{c}_1^\dagger \hat{c}_1 + \hat{c}_2^\dagger \hat{c}_2 + \hat{c}_3^\dagger \hat{c}_3,$$

$$\hat{J}_+^{\mathrm{D}} = \hat{c}_2^\dagger \hat{c}_1, \quad \hat{J}_-^{\mathrm{D}} = \hat{c}_1^\dagger \hat{c}_2, \quad \hat{J}_z^{\mathrm{D}} = \tfrac{1}{2}(\hat{c}_2^\dagger \hat{c}_2 - \hat{c}_3^\dagger \hat{c}_3 - \hat{c}_1^\dagger \hat{c}_1),$$

$$\hat{J}_+^{\mathrm{B}} = \hat{c}_3^\dagger \hat{c}_1, \quad \hat{J}_-^{\mathrm{B}} = \hat{c}_1^\dagger \hat{c}_3, \quad \hat{J}_z^{\mathrm{B}} = \tfrac{1}{2}(\hat{c}_3^\dagger \hat{c}_3 - \hat{c}_2^\dagger \hat{c}_2 - \hat{c}_1^\dagger \hat{c}_1),$$

$$\hat{J}_+^{\mathrm{DB}} = \hat{c}_2^\dagger \hat{c}_3, \quad \hat{J}_-^{\mathrm{DB}} = \hat{c}_3^\dagger \hat{c}_2. \tag{13}$$

This representation suggests that the operators $\hat{J}_\mu^{\mathrm{D}}$ are associated with the DW state while $\hat{J}_\mu^{\mathrm{B}}$ are related to the BDW state. Applying the commutation relations for the bosonic operators $[\hat{c}_m, \hat{c}_n^\dagger] = \delta_{mn}$, we recover the same commutation relations for the pseudospin operators presented in Eq. (A1). That is, we identify $\hat{J}_\mu^{\mathrm{D}} \equiv \hat{J}_\mu^{12}$, $\hat{J}_\mu^{\mathrm{B}} \equiv \hat{J}_\mu^{13}$, and $\hat{J}_\mu^{\mathrm{DB}} \equiv \hat{J}_\mu^{23}$.

Substituting the Schwinger boson representation in Eq. (14) into Eq. (12) yields the driven dissipative three-level Dicke model (6). Within the shaken-atom cavity platform, the effective cavity field frequency is $\omega = (3U_0 N)/4 - \delta_{\mathrm{C}} = U_0 N/4 - \delta_{\mathrm{eff}}$, the effective pump-cavity detuning is δ_{eff}, and the light-matter coupling strength is $\lambda/\sqrt{N} = -\sqrt{\omega_{\mathrm{rec}} \epsilon_{\mathrm{p}} |U_0|}/2$. The pump intensity ϵ_{p} shifts the frequencies of the pair of two-level transitions, $\omega_{\mathrm{D}} = 2\omega_{\mathrm{rec}}(1 - \epsilon_{\mathrm{p}}/8)$ and $\omega_{\mathrm{B}} = 2\omega_{\mathrm{rec}}(1 + \epsilon_{\mathrm{p}}/8)$. We can infer from Eq. (6) that weak periodic shaking effectively leads to a parametric driving of the light-matter coupling between the cavity and the spin associated with the BDW state. With these correspondences, we find that indeed the shaken atom-cavity system can be approximated by the driven three-level Dicke model presented in Eq. (6) and discussed in Sec. III. Moreover, we can identify the order parameters of the self-organized density wave states, namely the DW order parameter $\Theta_{\mathrm{DW}} = \langle \cos(ky)\cos(kz) \rangle = j_x^{\mathrm{D}}$ and the BDW order parameter $\Theta_{\mathrm{BDW}} = \langle \sin(ky)\cos(kz) \rangle = j_x^{\mathrm{B}}$.

D. Comparison with the full atom-cavity model

We compare the dynamics of the cavity mode occupation and the DW order parameter for the full atom-cavity model (11) and the effective three-level model according to Eq. (E2). The parameters for the simulation are shown in Appendix H. For results based on the full atom-cavity model Eq. (11), we numerically determine ϵ_{cr} from the onset of intracavity photon number [34]. Moreover, the BDW oscillator frequency ω_{B} for the full atom-cavity model is extracted from the oscillation frequency of the BDW order parameter Θ_{BDW} [34]. We show in Fig. 5 the time-averaged occupation of the cavity mode $|a|^2$,

$$\widetilde{|a|^2} = \frac{1}{\tau} \int_0^\tau |a|^2 dt, \tag{14}$$

for $\tau = 100T$, as a function of modulation strength f_0 and modulation frequency ω_{dr}. For $\lambda < \lambda_{\mathrm{cr}}$, we obtain a qualitatively similar dynamical phase diagrams for the three-level Dicke model and the full atom-cavity model, as depicted in
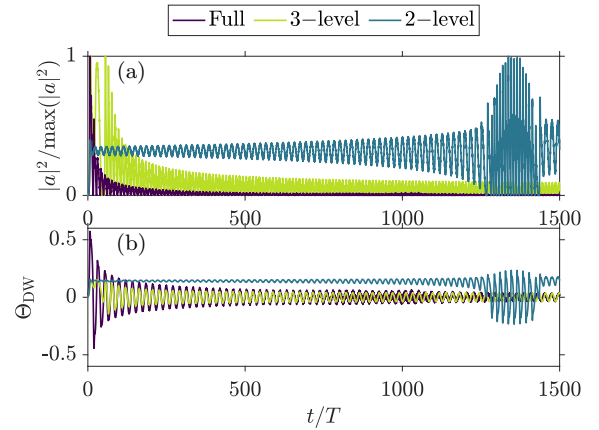
FIG. 6. Comparison of the dynamics between the full atom-cavity model [in purple (black)], three-level [in green (light gray)], and coupled two-level Dicke model [in blue (dark gray)] for the (a) cavity mode occupation and (b) DW order parameter. For the Dicke models, the light-matter coupling strength is $\lambda = 1.02\lambda_{\mathrm{cr}}$. This corresponds to a pump strength of $\epsilon_{\mathrm{p}}/\epsilon_{\mathrm{cr}} = 1.04$ in the full-atom cavity model. The driving parameters are fixed to $f_0 = 0.03$ and $\omega_{\mathrm{dr}} = 1.05\omega_{\mathrm{B}}$.

Figs. 5(a) and 5(c). Therefore, in this regime, the approximation of Eq. (11) via Eq. (6) is applicable. That is, the parametrically driven open three-level Dicke Hamiltonian is realized approximately by the shaken atom-cavity system. Moreover, the instability region from the oscillator model in the thermodynamic limit Eq. (F3) matches the onset of the cavity mode occupation in Fig. 5(a).

For $\lambda > \lambda_{\mathrm{cr}}$, the dark areas in Figs. 5(b) and 5(d) signify that the system has entered the DW or SR phase indicated by a nonvanishing cavity mode occupation, as expected for weak and off-resonant driving. However, the DW phase is suppressed for driving frequencies blue-detuned from ω_{B} as indicated by the relative decrease in the cavity photon number in the light areas in Figs. 5(b) and 5(d). Crucially, the correspondence between Eqs. (11) and (6) breaks down for driving frequencies far-detuned from ω_{B} as inferred from the parameter region $\omega_{\mathrm{dr}} > \omega_{\mathrm{B}}$ in Figs. 5(b) and 5(d). This can be attributed to the occupation of higher momentum modes, specifically $|\pm 2k, 0\rangle$, in the full atom-cavity system [34], which is not captured in the low-momentum expansion (11) utilized in the mapping. Nevertheless, we still find good agreement on the qualitative features for driving frequencies near ω_{B}.
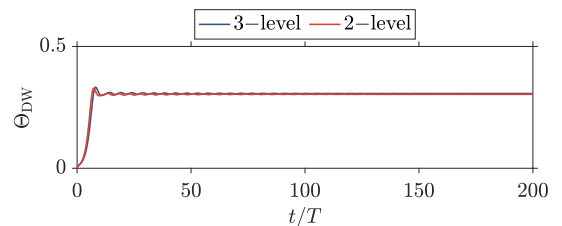
FIG. 7. Dynamics of the density wave order parameter for $\omega_{\mathrm{dr}} = 0.8\omega_{\mathrm{B}}$ and $f_0 = 0.05$. The remaining parameters are the same as in Fig. 6.

We also consider the dynamics according to a coupled two-level Dicke model for the same set of parameters (see Appendix B for details). In Fig. 6, we present the dynamics for $\lambda > \lambda_{cr}$ with a driving frequency blue-detuned with respect to ω_B. The results of the coupled two-level systems clearly do not capture the dynamics of the full atom-cavity system. On the other hand, the three-level Dicke model and the full atom-cavity model predict the same dynamical response, which is a subharmonic motion exhibited as a pulsating photon number [see Fig. 6(a)] and a periodic switching of the sign of the DW order parameter [see Fig. 6(b)]. This further supports our claim that the mapping between the three-level Dicke model and the full-atom cavity system is applicable to $\lambda > \lambda_{cr}$ for as long as the driving frequency is close to ω_B. Note, however, that the coupled two-level systems model and the three-level model agree with each other for off-resonant driving when $j_x^B \approx 0$, as demonstrated in Appendix B.

V. CONCLUSIONS

In this work, we have investigated a three-level Dicke model, and derived its equilibrium phase diagram, which features a normal phase and a superradiant phase. We advanced the model to a driven dissipative system by including a dissipation mechanism via photon loss and a periodic driving process. For this system, we developed the dynamical phase diagram, which shows the phases for varying driving parameters, utilizing analytical and numerical methods. As a central result we characterized the regime of an incommensurate time crystalline state in the phase diagram. Furthermore, we obtained light-enhanced and light-induced superradiant states, in which the equilibrium superradiant state is dynamically stabilized. As a physical system that can be naturally approximated via the three-level Dicke model, we identified a periodically shaken atom-cavity system. While the nonshaken atom-cavity system can be approximated via the standard two-level Dicke model, the shaking induces the atoms to populate additional states that are modeled via a third state in the three-level Dicke model. We note that the LISR and LESR phases display similarities with light-induced [48] and light-enhanced superconductivity [49], for which mechanisms have been proposed that involve the excitation of auxiliary modes, such as phonons [50–52] and Higgs bosons [53], by means of optical pumping. Photoexcitation of the Higgs mode in cuprate superconductors has also been predicted to lead to an incommensurate time crystal [54]. In this work, the BDW state plays the role of such an auxiliary mode, as its excitation [or equivalently, the $|1\rangle \rightarrow |3\rangle$ in Fig. 1(a)] can be used to dynamically control the system to induce or enhance superradiance, or to enter a genuine dynamical order, namely, the incommensurate time crystalline phase. We therefore expand the dynamical control of phases in atom-cavity systems to include light-induced and light-enhanced superradiance, in addition to the previously observed light-enhanced BEC or normal phase [42,43].

Note added. Recently, an example of the driven three-level Dicke model was presented in Ref. [55].

APPENDIX A: THE SU(3) ALGEBRA, GELL-MANN MATRICES, AND CASIMIR CHARGES

$$[\hat{J}_z^{12}, \hat{J}_\pm^{12}] = \pm\hat{J}_\pm^{12}, \quad [\hat{J}_-^{12}, \hat{J}_+^{12}] = 2\hat{J}_z^{12} + \hat{J}_z^{13} + \frac{N}{2},$$

$$[\hat{J}_z^{13}, \hat{J}_\pm^{13}] = \pm\hat{J}_\pm^{13}, \quad [\hat{J}_-^{13}, \hat{J}_+^{13}] = 2\hat{J}_z^{13} + \hat{J}_z^{12} + \frac{N}{2},$$

$$[\hat{J}_\pm^{12}, \hat{J}_\mp^{13}] = \pm\hat{J}_\pm^{23}, \quad [\hat{J}_+^{23}, \hat{J}_-^{23}] = \hat{J}_z^{12} - \hat{J}_z^{13},$$

$$[\hat{J}_z^{12}, \hat{J}_\pm^{23}] = \pm\hat{J}_\pm^{23}, \quad [\hat{J}_z^{13}, \hat{J}_\pm^{23}] = \mp\hat{J}_\pm^{23},$$

$$[\hat{J}_\pm^{12}, \hat{J}_\mp^{23}] = \mp\hat{J}_\pm^{13}, \quad [\hat{J}_\pm^{13}, \hat{J}_\pm^{23}] = \mp\hat{J}_\pm^{12}. \tag{A1}$$

The remaining commutators not listed above vanish. Our choice of pseudospin operators for the SU(3) algebra can be mapped onto the Gell-Mann matrices [31] via

$$F_1 \equiv J_x^{12} = \frac{1}{2}\lambda_1,$$

$$F_2 \equiv J_y^{12} = \frac{1}{2}\lambda_2,$$

$$F_3 \equiv J_z^{12} + \frac{1}{2}J_z^{13} + N/4 = \frac{1}{2}\lambda_3,$$

$$F_4 \equiv J_x^{23} = \frac{1}{2}\lambda_4,$$

$$F_5 \equiv J_y^{23} = \frac{1}{2}\lambda_5,$$

$$F_6 \equiv J_x^{13} = \frac{1}{2}\lambda_6,$$

$$F_7 \equiv -J_y^{13} = \frac{1}{2}\lambda_7,$$

$$F_8 \equiv -\frac{\sqrt{3}}{2}\big(J_z^{13} + N/6\big) = \frac{1}{2}\lambda_8. \tag{A2}$$

Casimir charges

The group SU(3) enjoys two Casimirs, which can be written in matrix form using the Gell-Mann basis as

$$C_1 = \sum_{i=1}^{8} F_i F_i, \tag{A3}$$

$$C_2 = \sum_{j,k,l=1}^{8} d_{jkl} F_j F_k F_l, \tag{A4}$$

with

$$d_{jkl} = \tfrac{1}{4}\mathrm{Tr}(\{\lambda_j, \lambda_k\}\lambda_l). \tag{A5}$$

In our chosen basis, they take the form of

$$\langle C_1 \rangle / N = \frac{1}{12} + \big(j_x^{12}\big)^2 + \big(j_y^{12}\big)^2 + \big(j_z^{12}\big)^2 + \big(j_x^{13}\big)^2 + \big(j_y^{13}\big)^2 + \big(j_z^{13}\big)^2 + \big(j_x^{23}\big)^2 + \big(j_y^{23}\big)^2 + \frac{1}{2}\big(j_z^{12} + j_z^{13} + 2j_z^{12}j_z^{13}\big), \tag{A6}$$

$$
\begin{aligned}
\langle C_2 \rangle / N^{3/2} = \frac{1}{72}\Big\{ &- 18\big(j_y^{12}\big)^2 + 216 j_y^{23}\big(j_y^{12}j_x^{13} - j_x^{12}j_y^{13}\big) + 216 j_x^{23}\big(j_x^{12}j_x^{13} + j_y^{12}j_y^{13}\big) \\
&- \big(1 + 6 j_z^{12}\big)\big[1 + 3 j_z^{12} + 18\big(j_x^{13}\big)^2 + 18\big(j_y^{13}\big)^2\big] - 9 j_z^{13} + 36\big(j_x^{23}\big)^2\big(1 + 3 j_z^{12} + 3 j_z^{13}\big) \\
&+ 36\big(j_y^{23}\big)^2\big(1 + 3 j_z^{12} + 3 j_z^{13}\big) \\
&- 18\big\{\big(j_x^{12}\big)^2\big(1 + 6 j_z^{13}\big) + j_z^{13}\big[6\big(j_y^{12}\big)^2 + j_z^{13} + 2 j_z^{12}\big(2 + 3 j_z^{12} + 3 j_z^{13}\big)\big]\big\}\Big\}. \tag{A7}
\end{aligned}
$$

APPENDIX B: TWO-COMPONENT DICKE MODEL

A modified version of the two-component Dicke model [9,10], which can be realized in a spinor BEC coupled to an optical cavity [16,17], is given by

$$H/\hbar = \omega \hat{a}^\dagger \hat{a} + \omega_1 \hat{J}_z^1 + \omega_2 \hat{J}_z^2 + \frac{2}{\sqrt{N}}(\hat{a}^\dagger + \hat{a})\big(\lambda_1 \hat{J}_x^1 + \lambda_2 \hat{J}_x^2\big). \tag{B1}$$

Note that this has the same form as the three-level Hamiltonian in Eq. (1) except that here, the pseudospin operators fulfill to the SU(2) group algebra with the commutation relations,

$$\big[\hat{J}_z^\ell, \hat{J}_\pm^\ell\big] = \pm\hat{J}_\pm^\ell, \quad [\hat{J}_-^\ell, \hat{J}_+^\ell] = 2\hat{J}_z^\ell, \tag{B2}$$

where $\ell \in \{1, 2\}$. Applying the same mean-field approximation as in Sec. II B, we obtain the following equations of motion consistent with those in Refs. [9,10,16,17],

$$
\begin{aligned}
\frac{da}{dt} &= -(i\omega + \kappa)a - i2\sum_{\ell=1}^{2}\lambda_\ell j_x^\ell, \\
\frac{dj_x^\ell}{dt} &= -\omega_\ell j_y^\ell, \\
\frac{dj_y^\ell}{dt} &= \omega_\ell j_x^\ell - 2\lambda_\ell(a + a^*)j_z^\ell, \\
\frac{dj_z^\ell}{dt} &= 2\lambda_\ell(a + a^*)j_y^\ell. \tag{B3}
\end{aligned}
$$

To obtain the relevant curves in Fig. 6, we propagate the above set of coupled equations with $\omega_1 = \omega_D$, $\omega_2 = \omega_B$, $\lambda_1 = \lambda$, and $\lambda_2 = -\lambda f_0 \sin(\omega_{dr} t)$. The exact values of these parameters are the same as those described in the main text. We present in Fig. 7 a comparison of the dynamics according to the two-component Dicke model and the three-level Dicke model for off-resonant driving.

APPENDIX C: CRITICAL LIGHT-MATTER COUPLING

Using the Hamiltonian in Eq. (3) and the Heisenberg equation in Eq. (D1), we obtain the equations of motion as

$$
\frac{da}{dt} = -(i\omega - \kappa)a - i\lambda_{12}(a_{12}^\dagger + a_{12}) - i\lambda_{13}(a_{13}^\dagger + a_{13}),
$$

$$
\frac{da_{12}}{dt} = -i\omega_{12}a_{12} - i\lambda_{12}(a^* + a),
$$

$$
\frac{da_{13}}{dt} = -i\omega_{13}a_{13} - i\lambda_{13}(a^* + a).
$$

(C1)

We can then construct the matrix M as $\partial_t \vec{v} = M\vec{v}$ to obtain

$$
M = \begin{pmatrix}
\kappa - i\omega & 0 & -i\lambda_{12} & -i\lambda_{12} & -i\lambda_{13} & -i\lambda_{13} \\
0 & \kappa + i\omega & i\lambda_{12} & i\lambda_{12} & i\lambda_{13} & i\lambda_{13} \\
-i\lambda_{12} & -i\lambda_{12} & -i\omega_{12} & 0 & 0 & 0 \\
i\lambda_{12} & i\lambda_{12} & 0 & i\omega_{12} & 0 & 0 \\
-i\lambda_{13} & -i\lambda_{13} & 0 & 0 & -i\omega_{13} & 0 \\
i\lambda_{13} & i\lambda_{13} & 0 & 0 & 0 & i\omega_{13}
\end{pmatrix}.
$$

(C2)

A phase transition occurs if M inherits a zero energy eigenstate [39]. This means, to find the critical light-matter coupling λ, we need to calculate $\det(M) = 0$, giving us

$$
\frac{(\kappa^2 + \omega^2)}{4\omega} = \left(\frac{\lambda_{12}^2}{\omega_{12}} + \frac{\lambda_{13}^2}{\omega_{13}} \right).
$$

(C3)

APPENDIX D: HEISENBERG EQUATIONS OF MOTION

The dynamics of an observable $\hat{O}$ in the dissipative system considered here is governed by the Heisenberg equation

$$
\frac{d\langle\hat{O}\rangle}{dt} = \left\langle \frac{i}{\hbar}[\hat{H}, \hat{O}] + \kappa(2\hat{a}^\dagger \hat{O}\hat{a} - \{\hat{a}^\dagger\hat{a}, \hat{O}\}) \right\rangle.
$$

(D1)

Using the commutation relations Eq. (A1), we get the following equations for the expectation values of relevant operators in the open three-level Dicke model (1):

$$
\frac{d\langle a \rangle}{dt} = -(i\omega + \kappa)\langle a \rangle - i\frac{2}{\sqrt{N}}\left(\lambda_{12}\langle\hat{J}_x^{12}\rangle + \lambda_{13}\langle\hat{J}_x^{13}\rangle\right),
$$

$$
\frac{d\langle\hat{J}_x^{12}\rangle}{dt} = -\omega_{12}\langle\hat{J}_y^{12}\rangle + \frac{\lambda_{13}}{\sqrt{N}}\langle(a^\dagger + a)\hat{J}_{23}^y\rangle,
$$

$$
\frac{d\langle\hat{J}_y^{12}\rangle}{dt} = \omega_{12}\langle\hat{J}_x^{12}\rangle - \frac{\lambda_{12}}{\sqrt{N}}\left[2\langle(a^\dagger + a)\hat{J}_z^{12}\rangle + \langle(a^\dagger + a)\hat{J}_z^{13}\rangle + \langle(a^\dagger + a)N/2\rangle\right] - \frac{\lambda_{13}}{\sqrt{N}}\langle(a^\dagger + a)\hat{J}_x^{23}\rangle,
$$

$$
\frac{d\langle\hat{J}_z^{12}\rangle}{dt} = \frac{2\lambda_{12}}{\sqrt{N}}\langle(a + a^\dagger)\hat{J}_y^{12}\rangle,
$$

$$
\frac{d\langle\hat{J}_x^{13}\rangle}{dt} = -\omega_{13}\langle\hat{J}_y^{13}\rangle - \frac{\lambda_{12}}{\sqrt{N}}\langle(a^\dagger + a)\hat{J}_y^{23}\rangle,
$$

$$
\frac{d\langle\hat{J}_y^{13}\rangle}{dt} = \omega_{13}\langle\hat{J}_x^{13}\rangle - \frac{\lambda_{13}}{\sqrt{N}}\left[2\langle(a^\dagger + a)\hat{J}_z^{13}\rangle + \langle(a^\dagger + a)\hat{J}_z^{12}\rangle + \langle(a^\dagger + a)N/2\rangle\right] - \frac{\lambda_{12}}{\sqrt{N}}\langle(a^\dagger + a)\hat{J}_x^{23}\rangle,
$$

$$
\frac{d\langle\hat{J}_z^{13}\rangle}{dt} = \frac{2\lambda_{13}}{\sqrt{N}}\langle(a + a^\dagger)\hat{J}_y^{13}\rangle,
$$

$$
\frac{d\langle\hat{J}_x^{23}\rangle}{dt} = (\omega_{13} - \omega_{12})\langle\hat{J}_y^{23}\rangle + \frac{\lambda_{12}}{\sqrt{N}}\langle(a^\dagger + a)\hat{J}_y^{13}\rangle + \frac{\lambda_{13}}{\sqrt{N}}\langle(a^\dagger + a)\hat{J}_y^{12}\rangle,
$$

$$
\frac{d\langle\hat{J}_y^{23}\rangle}{dt} = (\omega_{12} - \omega_{13})\langle\hat{J}_y^{23}\rangle + \frac{\lambda_{12}}{\sqrt{N}}\langle(a^\dagger + a)\hat{J}_x^{13}\rangle - \frac{\lambda_{13}}{\sqrt{N}}\langle(a^\dagger + a)\hat{J}_x^{12}\rangle.
$$

(D2)

On the other hand, the equations of motion for the parametrically driven open three-level Dicke model are

$$\frac{d\langle \hat{a} \rangle}{dt} = -(i\omega + \kappa)\langle \hat{a} \rangle - i\frac{2\lambda}{\sqrt{N}}\langle \hat{J}_x^{\mathrm{D}} \rangle + i\phi(t)\frac{2\lambda}{\sqrt{N}}\langle \hat{J}_x^{\mathrm{B}} \rangle,$$

$$\frac{d\langle \hat{J}_x^{\mathrm{D}} \rangle}{dt} = -\omega_{\mathrm{D}}\langle \hat{J}_y^{\mathrm{D}} \rangle - \phi(t)(\omega_{\mathrm{B}} - \omega_{\mathrm{D}})\langle \hat{J}_y^{\mathrm{B}} \rangle - \phi(t)\frac{\lambda}{\sqrt{N}}\langle (a^\dagger + a)\hat{J}_y^{\mathrm{DB}} \rangle,$$

$$\frac{d\langle \hat{J}_y^{\mathrm{D}} \rangle}{dt} = \omega_{\mathrm{D}}\langle \hat{J}_x^{\mathrm{D}} \rangle - \frac{\lambda}{\sqrt{N}}\left[2\langle (a^\dagger + a)\hat{J}_z^{\mathrm{D}} \rangle + \langle (a^\dagger + a)\hat{J}_z^{\mathrm{B}} \rangle + \langle a^\dagger + a \rangle\frac{N}{2} \right]$$
$$+ \phi(t)(\omega_{\mathrm{B}} - \omega_{\mathrm{D}})\langle \hat{J}_x^{\mathrm{B}} \rangle + \phi(t)\frac{\lambda}{\sqrt{N}}\langle (a^\dagger + a)\hat{J}_x^{\mathrm{DB}} \rangle,$$

$$\frac{d\langle \hat{J}_z^{\mathrm{D}} \rangle}{dt} = \frac{2\lambda}{\sqrt{N}}\langle (a + a^\dagger)\hat{J}_y^{\mathrm{D}} \rangle + 2(\omega_{\mathrm{B}} - \omega_{\mathrm{D}})\phi(t)\langle \hat{J}_y^{\mathrm{DB}} \rangle,$$

$$\frac{d\langle \hat{J}_x^{\mathrm{B}} \rangle}{dt} = -\omega_{\mathrm{B}}\langle \hat{J}_y^{\mathrm{B}} \rangle - \phi(t)(\omega_{\mathrm{B}} - \omega_{\mathrm{D}})\langle \hat{J}_y^{\mathrm{D}} \rangle - \frac{\lambda}{\sqrt{N}}\langle (a^\dagger + a)\hat{J}_y^{\mathrm{DB}} \rangle,$$

$$\frac{d\langle \hat{J}_y^{\mathrm{B}} \rangle}{dt} = \omega_{\mathrm{B}}\langle \hat{J}_x^{\mathrm{B}} \rangle + \phi(t)\frac{\lambda}{\sqrt{N}}\left[2\langle (a^\dagger + a)\hat{J}_z^{\mathrm{B}} \rangle + \langle (a^\dagger + a)\hat{J}_z^{\mathrm{D}} \rangle + \langle a^\dagger + a \rangle\frac{N}{2} \right]$$
$$+ \phi(t)(\omega_{\mathrm{B}} - \omega_{\mathrm{D}})\langle \hat{J}_x^{\mathrm{D}} \rangle - \frac{\lambda}{\sqrt{N}}\langle (a^\dagger + a)\hat{J}_x^{\mathrm{DB}} \rangle,$$

$$\frac{d\langle \hat{J}_z^{\mathrm{B}} \rangle}{dt} = -\phi(t)(\omega_{\mathrm{B}} - \omega_{\mathrm{D}})\langle (a + a^\dagger)\hat{J}_y^{\mathrm{B}} \rangle - \frac{4\lambda^2}{U_0 N}\phi(t)\langle \hat{J}_y^{\mathrm{DB}} \rangle,$$

$$\frac{d\langle \hat{J}_x^{\mathrm{DB}} \rangle}{dt} = (\omega_{\mathrm{B}} - \omega_{\mathrm{D}})\langle \hat{J}_y^{\mathrm{DB}} \rangle + \frac{\lambda}{\sqrt{N}}\langle (a^\dagger + a)\hat{J}_y^{\mathrm{B}} \rangle - \phi(t)\frac{\lambda}{\sqrt{N}}\langle (a^\dagger + a)\hat{J}_y^{\mathrm{D}} \rangle,$$

$$\frac{d\langle \hat{J}_y^{\mathrm{DB}} \rangle}{dt} = (\omega_{\mathrm{D}} - \omega_{\mathrm{B}})\langle \hat{J}_x^{\mathrm{DB}} \rangle + \frac{\lambda}{\sqrt{N}}\langle (a^\dagger + a)\hat{J}_x^{\mathrm{B}} \rangle + \phi(t)\frac{\lambda}{\sqrt{N}}\langle (a^\dagger + a)\hat{J}_x^{\mathrm{D}} \rangle + 2(\omega_{\mathrm{B}} - \omega_{\mathrm{D}})\phi(t)\langle \hat{J}_z^{\mathrm{B}} - \hat{J}_z^{\mathrm{D}} \rangle. \tag{D3}$$

APPENDIX E: MEAN-FIELD EQUATIONS OF MOTION

The mean-field equations for the dissipative three-level Dicke model are given by

$$\frac{da}{dt} = -(i\omega + \kappa)a - i2\lambda_{12}j_x^{12} - i2\lambda_{13}j_x^{13},$$

$$\frac{dj_x^{12}}{dt} = -\omega_{12}j_y^{12} + \lambda_{13}(a + a^*)j_{23}^y,$$

$$\frac{dj_y^{12}}{dt} = \omega_{12}j_x^{12} - \lambda_{12}(a + a^*)(2j_z^{12} + j_z^{13} + 1/2) - \lambda_{13}(a + a^*)j_x^{23},$$

$$\frac{dj_z^{12}}{dt} = 2\lambda_{12}(a + a^*)j_y^{12},$$

$$\frac{dj_x^{13}}{dt} = -\omega_{13}j_y^{13} - \lambda_{12}(a + a^*)j_y^{23},$$

$$\frac{dj_y^{13}}{dt} = \omega_{13}j_x^{13} - \lambda_{13}(a + a^*)(2j_z^{13} + j_z^{12} + 1/2) - \lambda_{12}(a + a^*)j_x^{23},$$

$$\frac{dj_z^{13}}{dt} = 2\lambda_{13}(a + a^*)j_y^{13},$$

$$\frac{dj_x^{23}}{dt} = (\omega_{13} - \omega_{12})j_y^{23} + \lambda_{12}(a + a^*)j_y^{13} + \lambda_{13}(a + a^*)j_y^{12},$$

$$\frac{dj_y^{23}}{dt} = (\omega_{12} - \omega_{13})j_y^{23} + \lambda_{12}(a + a^*)j_x^{13} - \lambda_{13}(a + a^*)j_x^{12}. \tag{E1}$$
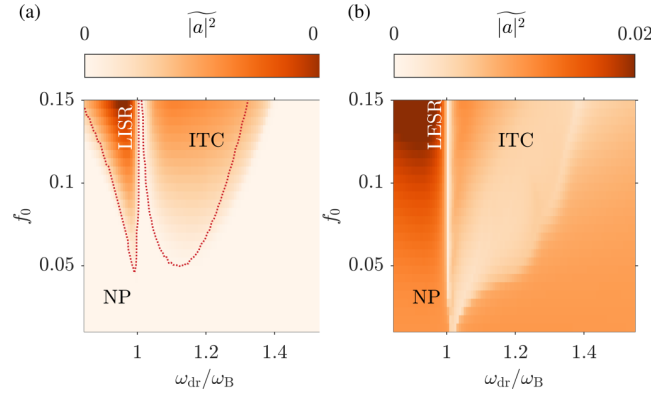
FIG. 8. Time-averaged cavity mode occupation $|a|^2$ taken over 100 driving cycles, $\tau = 100T$. We choose $\omega_D = \omega_B = \omega_{rec}$ while the remaining parameters are the same as those in Figs. 5(a) and 5(b).

For the parametrically driven open three-level Dicke model, the equations of motion are given by

$$\frac{da}{dt} = -(i\omega + \kappa)a - i2\lambda j_x^D + i\phi(t)2\lambda j_x^B,$$

$$\frac{dj_x^D}{dt} = -\omega_D j_y^D - \phi(t)(\omega_B - \omega_D)j_y^B - \phi(t)\lambda(a + a^*)j_y^{DB},$$

$$\frac{dj_y^D}{dt} = \omega_D j_x^D - \lambda(a + a^*)\left(2j_z^D + j_z^B + 1/2\right) + \phi(t)(\omega_B - \omega_D)j_x^B + \phi(t)\lambda(a + a^*)j_x^{DB},$$

$$\frac{dj_z^D}{dt} = 2\lambda(a + a^*)j_y^D + 2(\omega_B - \omega_D)\phi(t)j_y^{DB},$$

$$\frac{dj_x^B}{dt} = -\omega_B j_y^B - (\omega_B - \omega_D)\phi(t)j_y^D - \lambda(a + a^*)j_y^{DB},$$

$$\frac{dj_y^B}{dt} = \omega_B j_x^B + \phi(t)\lambda(a + a^*)\left(2j_z^B + j_z^D + 1/2\right) + \phi(t)(\omega_B - \omega_D)j_x^D - \lambda(a + a^*)j_x^{DB},$$

$$\frac{dj_z^B}{dt} = -\phi(t)2\lambda(a + a^*)j_y^B - 2(\omega_B - \omega_D)\phi(t)j_y^{DB},$$

$$\frac{dj_x^{DB}}{dt} = (\omega_B - \omega_D)j_y^{DB} + \lambda(a + a^*)j_y^B - \phi(t)\lambda(a + a^*)j_y^D,$$

$$\frac{dj_y^{DB}}{dt} = (\omega_D - \omega_B)j_x^{DB} + \lambda(a + a^*)j_x^B + \phi(t)\lambda(a + a^*)j_x^D + 2(\omega_B - \omega_D)\phi(t)\left(j_z^B - j_z^D\right). \tag{E2}$$

In Fig. 8, we demonstrate that the existence of the dynamical phases is independent of the term in the Hamiltonian with j_x^{DB}. That is, the momenta coupling inferred from Eq. (8) does not play a crucial role in the formation of the ITC, LESR, and LISR phases. This suggests that the emergence of these dynamical phases originates from the last term in Eq. (6). To confirm this, we set $\omega_D = \omega_B$ in Fig. 8. For comparison, we show in dotted lines the phase boundary obtained for $\omega_D \neq \omega_B$.

APPENDIX F: HOLSTEIN-PRIMAKOFF TRANSFORMATION

We present a Holstein-Primakoff approximation in the thermodynamic limit, i.e., $N \to \infty$ [5,56]. To capture the correct SU(3) algebra, we use an extended version of the Holstein-Primakoff representation given by [57]

$$\hat{J}_z^{12} = \hat{a}_{12}^\dagger \hat{a}_{12} - N/2, \quad \hat{J}_+^{12} = \hat{a}_{12}^\dagger \sqrt{N - (\hat{a}_{12}^\dagger \hat{a}_{12} + \hat{a}_{13}^\dagger \hat{a}_{13})},$$

$$\hat{J}_-^{12} = \sqrt{N - (\hat{a}_{12}^\dagger \hat{a}_{12} + \hat{a}_{13}^\dagger \hat{a}_{13})}\,\hat{a}_{12},$$

$$\hat{J}_z^{13} = \hat{a}_{13}^\dagger \hat{a}_{13} - N/2, \quad \hat{J}_+^{13} = \hat{a}_{13}^\dagger \sqrt{N - (\hat{a}_{12}^\dagger \hat{a}_{12} + \hat{a}_{13}^\dagger \hat{a}_{13})},$$

$$\hat{J}_-^{13} = \sqrt{N - (\hat{a}_{12}^\dagger \hat{a}_{12} + \hat{a}_{13}^\dagger \hat{a}_{13})}\,\hat{a}_{13},$$

$$\hat{J}_+^{23} = \hat{a}_{12}^\dagger \hat{a}_{13}, \quad \hat{J}_-^{23} = \hat{a}_{13}^\dagger \hat{a}_{12}. \tag{F1}$$

In the $N \to \infty$ limit, we can further approximate the pseudospin operators as

$$\hat{J}_z^D = \hat{a}_{12}^\dagger \hat{a}_{12} - N/2, \quad \hat{J}_+^D = \hat{a}_{12}^\dagger \sqrt{N}, \quad \hat{J}_-^D = \sqrt{N}\,\hat{a}_{12},$$

$$\hat{J}_z^B = \hat{a}_{13}^\dagger \hat{a}_{13} - N/2, \quad \hat{J}_+^B = \hat{a}_{13}^\dagger \sqrt{N}, \quad \hat{J}_-^B = \sqrt{N}\,\hat{a}_{13},$$

$$\hat{J}_+^{DB} = \hat{a}_{12}^\dagger \hat{a}_{13}, \quad \hat{J}_-^{DB} = \hat{a}_{13}^\dagger \hat{a}_{12}. \tag{F2}$$

In an analog fashion for the driven three-level Dicke model we obtain the Hamiltonian with $a_{12} \rightarrow d$ and $a_{13} \rightarrow b$

$$H/\hbar = \omega \hat{a}^\dagger \hat{a} + \omega_D \hat{d}^\dagger \hat{d} + \omega_B \hat{b}^\dagger \hat{b} + \lambda(\hat{a}^\dagger + \hat{a})$$
$$\times [(\hat{d}^\dagger + \hat{d}) - \phi(t)(\hat{b}^\dagger + \hat{b})]$$
$$+ \phi(t)(\omega_B - \omega_D)(\hat{d}^\dagger \hat{b} + \hat{b}^\dagger \hat{d}). \quad \text{(F3)}$$

The mean-field equations of motion for Eq. (F3) are

$$\frac{\partial a}{\partial t} = -(i\omega - \kappa)a - i\lambda(d^* + d) + i\phi(t)\lambda(b^* + b),$$

$$\frac{\partial d}{\partial t} = -i\omega_D d - i\lambda(a^* + a) - i(\omega_B - \omega_D)\phi(t)b,$$

$$\frac{\partial b}{\partial t} = -i\omega_B b + i\phi(t)\lambda(a^* + a) - i(\omega_B - \omega_D)\phi(t)d. \quad \text{(F4)}$$

APPENDIX G: LOWER POLARITON

Consider the standard closed Dicke model

$$\hat{H}/\hbar = \omega \hat{a}^\dagger \hat{a} + \omega_0 \hat{J}_z + \frac{2\lambda}{\sqrt{N}}(\hat{a}^\dagger + \hat{a})(\hat{J}_x). \quad \text{(G1)}$$

In the thermodynamic limit, this can be diagonalized using the Holstein-Primakoff transformation, which leads to two polariton frequencies

$$\omega_{LP,\kappa=0} = \left(\frac{(\omega_0^2 + \omega^2)}{2} - \frac{1}{2}\sqrt{(\omega_0^2 - \omega^2)^2 + 16\lambda^2\omega\omega_0} \right)^{1/2}, \quad \text{(G2)}$$

$$\omega_{UP,\kappa=0} = \left(\frac{(\omega_0^2 + \omega^2)}{2} + \frac{1}{2}\sqrt{(\omega_0^2 - \omega^2)^2 + 16\lambda^2\omega\omega_0} \right)^{1/2}. \quad \text{(G3)}$$

The lower polariton frequency, Eq. (G2), is the upper bound in the presence of dissipation. When $\kappa \neq 0$, the lower polariton frequency can be numerically determined by exploiting the parametric resonance when the light-matter coupling is periodically driven [5,6]:

$$\lambda(t) = \lambda_0[1 + f_0 \sin(\omega_{dr}t)]. \quad \text{(G4)}$$

In the limit $N \rightarrow \infty$, the Hamiltonian can be reduced to a coupled oscillator, whereby the coupling strength is periodic in time. This possesses a parametric resonance manifesting as a resonance lobe centered at the primary resonance, $\omega_{dr} = 2\omega_{LP}$. Thus, we can determine ω_{LP} by mapping the instability region for varying modulation parameters f_0 and ω_{dr}. To this
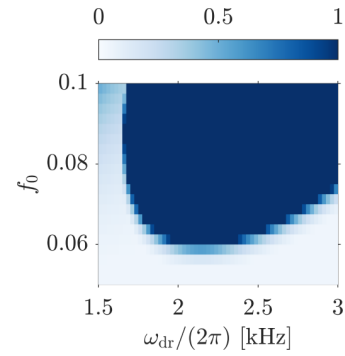
FIG. 9. Maximum value of $(b + b^*)$. The parameters are the same as those in Figs. 3(a)–3(d).

end, we solve the corresponding equations of motion given by

$$i\frac{\partial a}{\partial t} = (\omega - i\kappa)a + \lambda(t)(b^* + b),$$

$$i\frac{\partial b}{\partial t} = \omega_0 b + \lambda(t)(a^* + a). \quad \text{(G5)}$$

The unstable region indicating the parametric resonance is signalled by a diverging $(b + b^*)$, as depicted in Fig. 9. We obtain a lower polariton frequency $\omega_{LP}/2\pi \approx 1.06$ kHz, which is the value used in the sum frequency condition denoted by the vertical line in Figs. 3(a)–(d).

APPENDIX H: PARAMETERS

We consider realistic parameters based on the experimental setup in Ref. [35]. A BEC of $N = 65 \times 10^3$ ^{87}Rb atoms is coupled to a high-finesse optical cavity with a photon loss rate of $\kappa = 2\pi \times 3.6$ kHz. This is very close to the recoil frequency, $\omega_{rec} = 2\pi \times 3.55$ kHz, associated with the standing-wave potential of the pump. The cavity light shift per atom is $U_0 = -2\pi \times 0.36$ Hz. The effective pump-cavity detuning is fixed to $\delta_{eff} = -2\pi \times 18.5$ kHz. We are interested in the two regimes $\lambda < \lambda_{cr}$ and $\lambda > \lambda_{cr}$, where λ_{cr} is the critical light-matter coupling strength needed to enter the DW phase in the absence of modulation, where $\lambda_{cr} = [(\kappa^2 + \omega^2)(\omega_D/\omega)]^{1/2}/2$. By equating the expression for λ_{cr} and λ in terms of the atom-cavity parameters for the two-level Dicke model, we find that the critical pump strength is given by $\epsilon_{cr} = 8(\omega^2 + \kappa^2)/[4N\omega|\Delta_0| + (\omega^2 + \kappa^2)]$.

---

[1] R. H. Dicke, Coherence in spontaneous radiation processes, Phys. Rev. **93**, 99 (1954).

[2] K. Baumann, C. Guerlin, F. Brennecke, and T. Esslinger, Dicke quantum phase transition with a superfluid gas in an optical cavity, Nature (London) **464**, 1301 (2010).

[3] J. Klinder, H. Keßler, M. Wolke, L. Mathey, and A. Hemmerich, Dynamical phase transition in the open Dicke model, Proc. Natl. Acad. Sci. USA **112**, 3290 (2015).

[4] M. Hayn, C. Emary, and T. Brandes, Phase transitions and dark-state physics in two-color superradiance, Phys. Rev. A **84**, 053856 (2011).

[5] V. M. Bastidas, C. Emary, B. Regler, and T. Brandes, Nonequilibrium Quantum Phase Transitions in the Dicke Model, Phys. Rev. Lett. **108**, 043003 (2012).

[6] R. Chitra and O. Zilberberg, Dynamical many-body phases of the parametrically driven, dissipative Dicke model, Phys. Rev. A **92**, 023815 (2015).

[7] Z. Zhiqiang, C. H. Lee, R. Kumar, K. J. Arnold, S. J. Masson, A. S. Parkins, and M. D. Barrett, Nonequilibrium phase transition in a spin-1 Dicke model, Optica **4**, 424 (2017).

[8] M. Soriente, T. Donner, R. Chitra, and O. Zilberberg, Dissipation-Induced Anomalous Multicritical Phenomena, Phys. Rev. Lett. **120**, 183603 (2018).

[9] E. I. Rodríguez Chiacchio and A. Nunnenkamp, Dissipation-Induced Instabilities of a Spinor Bose-Einstein Condensate Inside an Optical Cavity, Phys. Rev. Lett. **122**, 193605 (2019).

[10] B. Buča and D. Jaksch, Dissipation Induced Nonstationarity in a Quantum Gas, Phys. Rev. Lett. **123**, 260401 (2019).

[11] K. C. Stitely, S. J. Masson, A. Giraldo, B. Krauskopf, and S. Parkins, Superradiant switching, quantum hysteresis, and oscillations in a generalized Dicke model, Phys. Rev. A **102**, 063702 (2020).

[12] H. Habibian, A. Winter, S. Paganelli, H. Rieger, and G. Morigi, Bose-Glass Phases of Ultracold Atoms Due to Cavity Backaction, Phys. Rev. Lett. **110**, 075304 (2013).

[13] C. Kollath, A. Sheikhan, S. Wolff, and F. Brennecke, Ultracold Fermions in a Cavity-Induced Artificial Magnetic Field, Phys. Rev. Lett. **116**, 060401 (2016).

[14] F. Mivehvar, F. Piazza, and H. Ritsch, Disorder-Driven Density and Spin Self-Ordering of a Bose-Einstein Condensate in a Cavity, Phys. Rev. Lett. **119**, 063602 (2017).

[15] V. D. Vaidya, Y. Guo, R. M. Kroeze, K. E. Ballantine, A. J. Kollár, J. Keeling, and B. L. Lev, Tunable-Range, Photon-Mediated Atomic Interactions in Multimode Cavity QED, Phys. Rev. X **8**, 011002 (2018).

[16] M. Landini, N. Dogra, K. Kroeger, L. Hruby, T. Donner, and T. Esslinger, Formation of a Spin Texture in a Quantum Gas Coupled to a Cavity, Phys. Rev. Lett. **120**, 223602 (2018).

[17] N. Dogra, M. Landini, K. Kroeger, L. Hruby, T. Donner, and T. Esslinger, Dissipation-induced structural instability and chiral dynamics in a quantum gas, Science **366**, 1496 (2019).

[18] G. Bentsen, I.-D. Potirniche, V. B. Bulchandani, T. Scaffidi, X. Cao, X.-L. Qi, M. Schleier-Smith, and E. Altman, Integrable and Chaotic Dynamics of Spins Coupled to an Optical Cavity, Phys. Rev. X **9**, 041011 (2019).

[19] S. B. Jäger, M. J. Holland, and G. Morigi, Superradiant optomechanical phases of cold atomic gases in optical resonators, Phys. Rev. A **101**, 023616 (2020).

[20] K.-J. Boller, A. Imamoğlu, and S. E. Harris, Observation of Electromagnetically Induced Transparency, Phys. Rev. Lett. **66**, 2593 (1991).

[21] M. Fleischhauer, A. Imamoglu, and J. P. Marangos, Electromagnetically induced transparency: Optics in coherent media, Rev. Mod. Phys. **77**, 633 (2005).

[22] M. O. Scully, S.-Y. Zhu, and A. Gavrielides, Degenerate Quantum-Beat Laser: Lasing without Inversion and Inversion without Lasing, Phys. Rev. Lett. **62**, 2813 (1989).

[23] J. Mompart and R. Corbalán, Lasing without inversion, J. Opt. B: Quantum Semiclassical Opt. **2**, R7 (2000).

[24] U. Gaubatz, P. Rudecki, S. Schiemann, and K. Bergmann, Population transfer between molecular vibrational levels by stimulated Raman scattering with partially overlapping laser fields. A new concept and experimental results, J. Chem. Phys. **92**, 5363 (1990).

[25] N. V. Vitanov, A. A. Rangelov, B. W. Shore, and K. Bergmann, Stimulated Raman adiabatic passage in physics, chemistry, and beyond, Rev. Mod. Phys. **89**, 015006 (2017).

[26] C. C. Sung and C. M. Bowden, Phase transition in the multimode two- and three-level Dicke model (Green's function method), J. Phys. A: Math. Gen. **12**, 2273 (1979).

[27] A. Crubellier, S. Liberman, D. Pavolini, and P. Pillet, Superradiance and subradiance. I. Interatomic interference and symmetry properties in three-level systems, J. Phys. B: At. Mol. Phys. **18**, 3811 (1985).

[28] A. Crubellier and D. Pavolini, Superradiance and subradiance. II. Atomic systems with degenerate transitions, J. Phys. B: At. Mol. Phys. **19**, 2109 (1986).

[29] M. M. Cola, D. Bigerni, and N. Piovella, Recoil-induced subradiance in an ultracold atomic gas, Phys. Rev. A **79**, 053622 (2009).

[30] P. Wolf, S. C. Schuster, D. Schmidt, S. Slama, and C. Zimmermann, Observation of Subradiant Atomic Momentum States with Bose-Einstein Condensates in a Recoil Resolving Optical Ring Resonator, Phys. Rev. Lett. **121**, 173602 (2018).

[31] H. Georgi, *Lie Algebras In Particle Physics from Isospin To Unified Theories* (Taylor & Francis, Boca Raton, 2000).

[32] W. Marciano and H. Pagels, Quantum chromodynamics, Phys. Rep. **36**, 137 (1978).

[33] D. J. Griffiths, *Introduction to Elementary Particles* (Wiley, New York, 2008).

[34] J. G. Cosme, J. Skulte, and L. Mathey, Time crystals in a shaken atom-cavity system, Phys. Rev. A **100**, 053615 (2019).

[35] P. Kongkhambut, H. Keßler, J. Skulte, L. Mathey, J. G. Cosme, and A. Hemmerich, Realization of a periodically driven open Three-Level Dicke model, Phys. Rev. Lett. **127**, 253601 (2021).

[36] J. J. Sakurai and J. Napolitano, *Modern Quantum Mechanics*, 2nd ed. (Cambridge University Press, Cambridge, 2017).

[37] A. Baksic, P. Nataf, and C. Ciuti, Superradiant phase transitions with three-level systems, Phys. Rev. A **87**, 023813 (2013).

[38] F. Dimer, B. Estienne, A. S. Parkins, and H. J. Carmichael, Proposed realization of the Dicke-model quantum phase transition in an optical cavity QED system, Phys. Rev. A **75**, 013804 (2007).

[39] P. Kirton, M. M. Roses, J. Keeling, and E. G. Dalla Torre, Introduction to the Dicke model: From equilibrium to nonequilibrium, and vice versa, Adv. Quantum Technol. **2**, 1800043 (2019).

[40] F. Mivehvar, F. Piazza, T. Donner, and H. Ritsch, Cavity QED with quantum gases: New paradigms in many-body physics, Adv. Phys. **70**, 1 (2021).

[41] H. Ritsch, P. Domokos, F. Brennecke, and T. Esslinger, Cold atoms in cavity-generated dynamical optical potentials, Rev. Mod. Phys. **85**, 553 (2013).

[42] J. G. Cosme, C. Georges, A. Hemmerich, and L. Mathey, Dynamical Control of Order in a Cavity-BEC System, Phys. Rev. Lett. **121**, 153001 (2018).

[43] C. Georges, J. G. Cosme, L. Mathey, and A. Hemmerich, Light-Induced Coherence in an Atom-Cavity System, Phys. Rev. Lett. **121**, 220405 (2018).

[44] H. Keßler, J. G. Cosme, M. Hemmerling, L. Mathey, and A. Hemmerich, Emergent limit cycles and time crystal dynamics in an atom-cavity system, Phys. Rev. A **99**, 053605 (2019).

[45] H. Keßler, J. G. Cosme, C. Georges, L. Mathey, and A. Hemmerich, From a continuous to a discrete time crystal in a dissipative atom-cavity system, New J. Phys. **22**, 085002 (2020).

[46] H. Keßler, P. Kongkhambut, C. Georges, L. Mathey, J. G. Cosme, and A. Hemmerich, Observation of a Dissipative Time Crystal, Phys. Rev. Lett. **127**, 043602 (2021).

[47] C. Georges, J. G. Cosme, H. Keßler, L. Mathey, and A. Hemmerich, Dynamical density wave order in an atom-cavity system, New J. Phys. **23**, 023003 (2021).

[48] D. Fausti, R. I. Tobey, N. Dean, S. Kaiser, A. Dienst, M. C. Hoffmann, S. Pyon, T. Takayama, H. Takagi, and A. Cavalleri, Light-induced superconductivity in a stripe-ordered cuprate, Science **331**, 189 (2011).

[49] W. Hu, S. Kaiser, D. Nicoletti, C. R. Hunt, I. Gierz, M. C. Hoffmann, M. Le Tacon, T. Loew, B. Keimer, and A. Cavalleri, Optically enhanced coherent transport in YBa$_2$Cu$_3$O$_{6.5}$ by ultrafast redistribution of interlayer coupling, Nat. Mater. **13**, 705 (2014).

[50] R. Mankowsky, A. Subedi, M. Först, S. O. Mariager, M. Chollet, H. T. Lemke, J. S. Robinson, J. M. Glownia, M. P. Minitti, A. Frano, M. Fechner, N. A. Spaldin, T. Loew, B. Keimer, A. Georges, and A. Cavalleri, Nonlinear lattice dynamics as a basis for enhanced superconductivity in YBa$_2$Cu$_3$O$_{6.5}$, Nature (London) **516**, 71 (2014).

[51] S. J. Denny, S. R. Clark, Y. Laplace, A. Cavalleri, and D. Jaksch, Proposed Parametric Cooling of Bilayer Cuprate Superconductors by Terahertz Excitation, Phys. Rev. Lett. **114**, 137001 (2015).

[52] J.-i. Okamoto, A. Cavalleri, and L. Mathey, Theory of Enhanced Interlayer Tunneling in Optically Driven High-T_c Superconductors, Phys. Rev. Lett. **117**, 227001 (2016).

[53] G. Homann, J. G. Cosme, J. Okamoto, and L. Mathey, Higgs mode mediated enhancement of interlayer transport in high-T_c cuprate superconductors, Phys. Rev. B **103**, 224503 (2021).

[54] G. Homann, J. G. Cosme, and L. Mathey, Higgs time crystal in a high-T_c superconductor, Phys. Rev. Research **2**, 043214 (2020).

[55] R. Lin, R. Rosa-Medina, F. Ferri, F. Finger, K. Kroeger, T. Donner, T. Esslinger, and R. Chitra, Dissipation-engineered family of nearly dark states in many-body cavity-atom systems, arXiv:2109.00422.

[56] C. Emary and T. Brandes, Chaos and the quantum phase transition in the Dicke model, Phys. Rev. E **67**, 066203 (2003).

[57] M. Wagner, A nonlinear transformation of SU(3)-spin-operators to bosonic operators, Phys. Lett. A **53**, 1 (1975).

2.9 Publication IV: Realization of a Periodically Driven Open Three-Level Dicke Model

P. Kongkhambut, H. Keßler, <u>J. Skulte</u>, L. Mathey, J.G. Cosme A. Hemmerich —
Phys. Rev. Letters 127, 253601 (2021)

Motivation

This work was motivated by the previous proposal to observe an incommensurate time crystal (ITC) in an atom-cavity system during my Bachelor's project and the previous successful observation of a dissipative time crystal with amplitude driving in the same atom-cavity setup. Our goal was to experimentally observe the ITC, to map out the phase diagram for varying the experimentally relevant parameter, and to characterize the phase.

Main findings

In this work, first authored by P. Kongkhambut, we experimentally studied the parametrically driven dissipative three-level Dicke model by emulating it with an atom-cavity system. As shown in the accompanying theoretical paper, we used resonant shaking of the pump field to map our system to the three-level Dicke model. We found two key signatures for the realisation of an incommensurate time crystal (ITC). First, we observed the dynamical switching between the different order states on the relative phase between the pump laser and the emitted cavity light at a small fraction of the driving frequency. Secondly, we showed by measuring the net momentum asymmetry along the pump axis during the drive the emergence of this dynamical phase. With these two observations, together with our theoretical analysis, we showed that this dynamical phase can be classified as an ITC.

Contribution

JGC and I performed the analytical and numerical calculations supervised by LM. PK and HK performed the experiments and data analysis supervised by AH. All authors contributed to the discussion and interpretation of the results, as well as to writing the manuscript.

Realization of a Periodically Driven Open Three-Level Dicke Model

Phatthamon Kongkhambut,[1] Hans Keßler[1,*] Jim Skulte[1,2] Ludwig Mathey,[1,2]
Jayson G. Cosme[3] and Andreas Hemmerich[1,2]

[1]*Zentrum für Optische Quantentechnologien und Institut für Laser-Physik, Universität Hamburg, 22761 Hamburg, Germany*
[2]*The Hamburg Center for Ultrafast Imaging, Luruper Chaussee 149, 22761 Hamburg, Germany*
[3]*National Institute of Physics, University of the Philippines, Diliman, Quezon City 1101, Philippines*

A periodically driven open three-level Dicke model is realized by resonantly shaking the pump field in an atom-cavity system. As an unambiguous signature, we demonstrate the emergence of a dynamical phase, in which the atoms periodically localize between the antinodes of the pump lattice, associated with an oscillating net momentum along the pump axis. We observe this dynamical phase through the periodic switching of the relative phase between the pump and cavity fields at a small fraction of the driving frequency, suggesting that it exhibits a time crystalline character.

Rapid technological advances have elevated cold-atom systems to preeminent platforms for realizing model systems of quantum–many body dynamics [1–6]. An intriguing subclass is hybrid light-matter systems, which are composed of cold atoms coupled to an optical cavity, and display a strongly enhanced light-matter interaction, giving access to the physics of strong light-matter coupling and long-range correlations [7,8]. A specific feature of these platforms is the well controlled dissipation, which allows for fast nondestructive *in situ* monitoring of the system dynamics [8–15]. One of the fundamental models for light-matter interaction is the Dicke model [16,17]. It describes a collection of N two-level systems coupled to a single light mode and displays a phase transition between a normal and a superradiant phase [16]. An open version of the Dicke model with a weak dissipation channel is approximately realized by a Bose-Einstein condensate (BEC) placed in a linear standing wave optical cavity and pumped by an optical standing wave oriented perpendicularly with respect to the cavity axis [10,11,15,18–26]. The normal phase is characterized by a BEC, light shifted by the pump potential, with a homogeneous density distribution along the cavity axis and a small number of photons in the cavity that do not display coherence. The superradiant phase shows a density grating enabling pronounced scattering of photons from the pump into the cavity and vice versa. Various extensions of the standard two-level Dicke model have been proposed and realized using atom-cavity systems, such as the spin-1 Dicke model [27,28] and the two-component Dicke model [29–31], all sharing the coupling of two-level systems to the same monochromatic light mode.

The extension of the Dicke model to the case of three-level systems has been theoretically considered in Refs. [32–34]. A specific example in a ring cavity has been used to experimentally demonstrate subradiance [35].

In the present work, we experimentally realize the periodically driven open three-level Dicke model by shaking the standing wave pump potential in an atom-cavity system as depicted in Fig. 1(a). It has been predicted in Ref. [36] that this enables a dynamical phase, characterized by atoms periodically localizing between the antinodes of the pump lattice, i.e., on the intersite bonds, which has been called dynamical bond density wave (DBDW) phase. This DBDW phase exhibits time crystalline character and is a characteristic signature of the periodically driven open three-level Dicke model. Its experimental observation is the central topic of this work.

We define the three-level Dicke model to describe the interaction between a single quantized light mode and N three-level atoms comprising energy eigenstates $|1\rangle$, $|2\rangle$, and $|3\rangle$ in a V configuration. Its Hamiltonian is

$$H/\hbar = \omega \hat{a}^\dagger \hat{a} + \omega_{12} \hat{J}_z^{12} + \omega_{13} \hat{J}_z^{13}$$
$$+ \frac{2}{\sqrt{N}} (\hat{a}^\dagger + \hat{a})(\lambda_{12} \hat{J}_x^{12} + \lambda_{13} \hat{J}_x^{13}). \quad (1)$$

The bosonic operator $\hat{a}$ ($\hat{a}^\dagger$) annihilates (creates) a photon with frequency ω. The frequency detuning between the lowest energy state $|1\rangle$ and the other two states $|2\rangle$ and $|3\rangle$ are ω_{12} and ω_{13}, respectively. For small detuning ω_{23} between the states $|2\rangle$ and $|3\rangle$, i.e., when $\omega_{23} \ll \omega_{12}, \omega_{13}$, the only relevant light-matter interactions are those that couple state $|1\rangle$ with states $|2\rangle$ and $|3\rangle$, the strengths of which are given by λ_{12} and λ_{13}, respectively. We introduce the pseudospin operators $\hat{J}_\mu^\ell$ with $\ell \in \{12, 13, 23\}$, which are related to the eight generators of the SU(3) group [37]. Note that the Gell-Mann matrices, the standard representation of the SU(3) group, can be obtained by an appropriate superposition of $\hat{J}_\mu^\ell$ [37]. Equation (1) is an extended
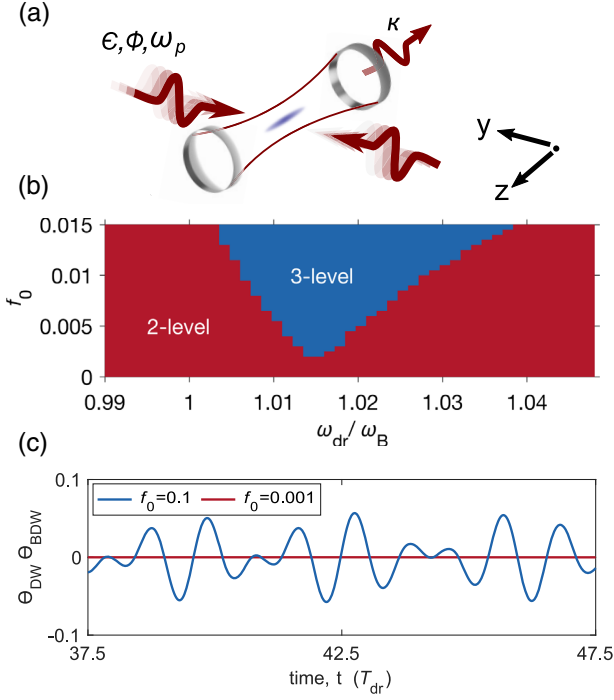
FIG. 1. (a) Schematic of the transversely pumped and shaken atom-cavity system. A sample of cold atoms is placed in a cavity oriented along the z axis. A standing wave potential is periodically shifted along the y axis using phase modulation techniques. (b) Dynamical phase diagram with two distinct regions: In the red area, the dynamics of the system is captured by a two-level Dicke model. In the blue area, a three-level Dicke model is required. (c) Dynamics of the product of the relevant order parameters for strong driving in the three-level Dicke regime (blue) and for weak driving in the two-level Dicke regime (red). The modulation frequency is $\omega_{\mathrm{dr}}/2\pi = 9.4$ kHz and $\omega_B/2\pi = 8$ kHz.

form of the two-component Dicke model [29–31]. However, the latter obeys the SU(2) algebra, while the pseudospin operators in Eq. (1) fulfill the SU(3) algebra, instead.

To implement the three-level Dicke model, we consider atoms in their electronic ground state occupying the following three momentum states forming a V-shaped level structure (see Fig. 1 in Supplemental Material [38]). The ground state is the so called BEC state $|\mathrm{BEC}\rangle$ given by the zero momentum state $|0,0\rangle$ with respect to the yz plane, light shifted by the pump field by an amount $-\epsilon/2$, where ϵ denotes the potential depth of the pump wave [37]. The first excited state is the superposition $\sum_{\nu,\mu\in\{-1,1\}} |\nu\hbar k, \mu\hbar k\rangle$ of the four momentum modes $|\pm \hbar k, \pm \hbar k\rangle$ associated with the yz plane, light shifted by the pump field by an amount $-3\epsilon/4$ (here, k denotes the wave number of the pump field) [37]. In view of its spatially varying density $\propto |\cos(ky)\cos(kz)|^2$, it is denoted as the density wave state $|\mathrm{DW}\rangle$. The light shift for $|\mathrm{DW}\rangle$ is larger compared to that of $|\mathrm{BEC}\rangle$, since the density distribution of $|\mathrm{DW}\rangle$ is localized in the antinodes of the

pump field [37]. The two states $|\mathrm{BEC}\rangle$ and $|\mathrm{DW}\rangle$ span the matter sector of the regular two-level Dicke model. If ϵ exceeds a critical value ϵ_{crt}, $|\mathrm{BEC}\rangle$ acquires an admixture of $|\mathrm{DW}\rangle$. A Bragg grating is thus imprinted upon the density of the $|\mathrm{BEC}\rangle$ state, which via efficient scattering of pump light builds up a coherent intracavity light field. The $|\mathrm{BEC}\rangle$ state, thus dressed by the cavity field, is denoted superradiant phase. In this work, we operate either with $\epsilon < \epsilon_{\mathrm{crt}}$ or with ϵ only very slightly above ϵ_{crt}, such that the additional dressing by the cavity field is zero or negligibly small. The second excited state is associated with the momentum state superposition $\sum_{\nu,\mu\in\{-1,1\}} \nu|\nu\hbar k, \mu\hbar k\rangle$. This state exhibits the smallest light shift $-\epsilon/4$, because its density distribution $\propto |\sin(ky)\cos(kz)|^2$ matches with the nodes of the pump wave [37]. This state is called bond density wave (abbreviated $|\mathrm{BDW}\rangle$) as its density maxima coincide with the bonds between two potential minima of the pump wave. We denote the energy separation between $|\mathrm{DW}\rangle$ and $|\mathrm{BEC}\rangle$ as $\hbar\omega_D$, and that between $|\mathrm{BDW}\rangle$ and $|\mathrm{BEC}\rangle$ as $\hbar\omega_B$, respectively. See Supplemental Material for a more detailed description [38].

In the atom-cavity implementation of the standard Dicke model, $|\mathrm{BDW}\rangle$ is not coupled to $|\mathrm{BEC}\rangle$ and hence can be dropped. To implement a coupling between $|\mathrm{BDW}\rangle$ and $|\mathrm{BEC}\rangle$, the transverse pump lattice is periodically shaken in space [36]. In Ref. [37], we show that the Hamiltonian for the shaken atom-cavity system can be mapped onto a parametrically driven version of the three-level Dicke model.

$$H/\hbar = \omega\hat{a}^\dagger\hat{a} + \hat{J}_z^D\omega_D + \hat{J}_z^B\omega_B + 2\phi(t)(\omega_B - \omega_D)\hat{J}_x^{DB}$$
$$+ \frac{2\lambda}{\sqrt{N}}(\hat{a}^\dagger + \hat{a})[\hat{J}_x^D - \phi(t)\hat{J}_x^B], \qquad (2)$$

where $\phi(t) = f_0 \sin(\omega_{\mathrm{dr}}t)$ is the time-dependent spatial phase of the pump lattice introduced by the shaking protocol, and λ is the overall coupling strength parameter. The pseudospin operators $\hat{J}_\mu^D$ and $\hat{J}_\mu^B$ with $\mu \in \{x, y, z\}$ are directly associated with the $|\mathrm{DW}\rangle$ and the $|\mathrm{BDW}\rangle$ states via the relations to their order parameters $\Theta_{\mathrm{DW}} \equiv \langle\cos(ky)\cos(kz)\rangle = \langle\hat{J}_x^D\rangle$ and $\Theta_{\mathrm{BDW}} \equiv \langle\sin(ky)\cos(kz)\rangle = \langle\hat{J}_x^B\rangle$, respectively. Comparing Eqs. (1) and (2), we identify $\hat{J}_\mu^{12} = \hat{J}_\mu^D$, $\hat{J}_\mu^{13} = \hat{J}_\mu^B$, $\hat{J}_\mu^{23} = \hat{J}_\mu^{DB}$, $\omega_{12} = \omega_D$, $\omega_{13} = \omega_B$, $\lambda_{12} = \lambda$, and a time-dependent light-matter coupling $\lambda_{13} = -\phi(t)\lambda$. Moreover, in Eq. (2), the standing wave potential of the pump introduces an additional albeit negligible term proportional to $\hat{J}_x^{DB}$, which couples $|\mathrm{DW}\rangle$ and $|\mathrm{BDW}\rangle$ [37].

For driving frequencies ω_{dr} slightly above ω_B, the DBDW phase shows periodic oscillations of Θ_{BDW} and Θ_{DW} around zero with frequencies ω_{BDW} and ω_{DW}, respectively. Theory predicts the relation $\omega_{\mathrm{DW}} = \omega_{\mathrm{dr}} - \omega_{\mathrm{BDW}}$ such that ω_{DW} is not an integer fraction of the driving frequency ω_{dr} [36]. This is a hallmark of an incommensurate time crystal [36].

Thus, the long-time average of Θ_{DW} is zero in the three-level Dicke region of the dynamical phase diagram, while it is nonzero in the two-level Dicke region for an initial superradiant phase. This behavior is captured in Fig. 1(b), which shows the time-averaged value of $\langle \hat{J}_x^D \rangle / N \equiv j_x^D$ obtained by solving the equations of motion corresponding to Eq. (2) in the semiclassical limit of a large atom number [37].

The DBDW dynamics may be experimentally studied via the product of the order parameters $\Theta_{DW} \times \Theta_{BDW}$, which can be approximately measured by the normalized occupation imbalance $\Delta \tilde{F} \equiv (F_{+1,\pm1} - F_{-1,\pm1})/(F_{+1,\pm1} - F_{-1,\pm1})_{max}$, where $F_{\pm1,\pm1}$ denotes the population of the momentum state $|\pm\hbar k, \pm\hbar k\rangle$ (see Supplemental Material for details [38]). In the standard Dicke model realized for off-resonant driving, $\Theta_{BDW} \approx 0$ and $\Delta \tilde{F}$ is negligible. On the other hand, for driving frequencies ω_{dr} slightly above ω_B, a beating signal is expected in $\Theta_{DW} \times \Theta_{BDW}$ [see Fig. 1(c)], which can be observed via $\Delta \tilde{F}$. Furthermore, the periodic switching of Θ_{DW} in the three-level model amounts to a periodic switching of the experimentally observable relative phase of the pump and the cavity fields $\varphi \equiv \arg(\langle \hat{a} \rangle)$ between 0 and π.

In our experiment, a BEC of ^{87}Rb atoms is superimposed with the fundamental mode of a high-finesse optical cavity pumped by a retroreflected laser beam at wavelength $\lambda_P = 803$ nm. The resulting optical pump lattice has a depth ϵ and is aligned perpendicular to the cavity axis, as depicted in Fig. 1(a). The cavity has a field decay rate $\kappa = 2\pi \times 3.6$ kHz comparable to the recoil frequency $\omega_{rec} \equiv \hbar k^2 / 2m$ ($m =$ atomic mass), such that the cavity field and the atomic density distribution evolve on similar timescales. This leads to a retarded infinite-range cavity-mediated interaction between the atoms [13]. The system realizes the Dicke phase transition from a homogeneous BEC to a superradiant phase if ϵ exceeds a critical strength. The $\mathbb{Z}_2$ symmetry is spontaneously broken, when the atoms localize at either the even or odd sites of a two dimensional checkerboard optical lattice formed by the interference between the pump and intracavity fields. The two symmetry broken states can be distinguished by the relative phase difference φ between the pump and intracavity light fields using a balanced heterodyne detection of the cavity field. The appearance of the superradiant phase can be detected *in situ* by the observation of a nonzero cavity mode occupation N_P [see red line in Fig. 2(b)], the locking of the relative φ to zero or π [see green line Fig. 2(b)], or in a destructive way through a nonzero occupation of the $\{p_y, p_z\} = \{\pm\hbar k, \pm\hbar k\}$ modes in a momentum spectrum [see Fig. 2(g)].

The experimental sequence proceeds as follows. We prepare the system in the BEC phase or in the superradiant phase close to the phase boundary towards the BEC phase, followed by a 500 μs long waiting period to let the system reach its steady state. Then, we shake the pump potential by modulating the phase of the pump field using an
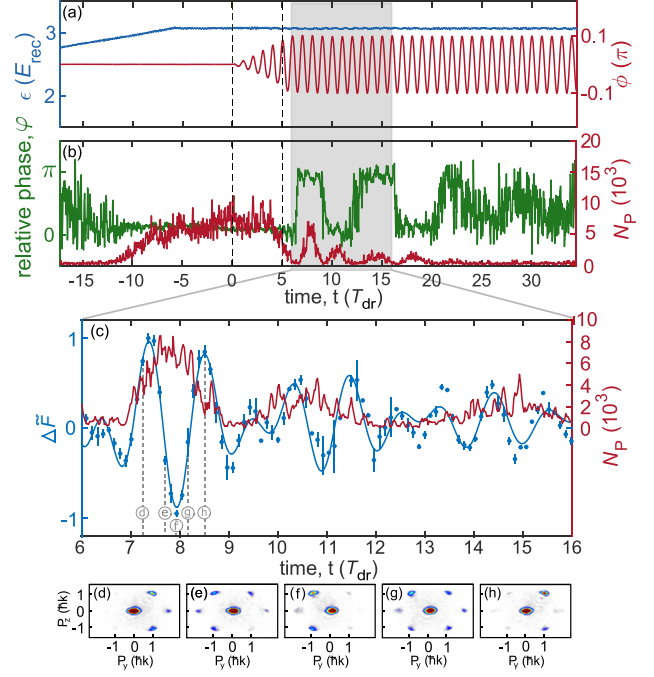
FIG. 2. Single-shot realization of DBDW order. (a) Time sequence for the pump lattice depth (blue) and the phase ϕ of the pump field (red) with modulation strength $f_0 = 0.1\pi$ and a modulation frequency $\omega_{dr} = 11.5$ kHz. (b) Phase difference φ between the pump and intracavity field (green trace) and photon number N_P in the cavity (red trace). The dashed vertical lines mark the time interval during which the modulation strength is increased. The gray shaded area shows the time window for the close-up presented in (c). (c) The red trace repeats the intracavity photon number N_P from (b). The blue data points plot the product $\Theta_{DW} \times \Theta_{BDW}$, approximately given by $\Delta \tilde{F}$ [see also Fig. 1(c)]. Each data point is averaged over five realizations. The solid line shows a fit with a product of two harmonic oscillations. (d)–(h) Single-shot momentum distributions recorded at the times marked in (c).

electro-optical modulator. The modulation strength f_0 is linearly increased to its desired value within 500 μs and kept constant for 6.5 ms. A typical sequence of the pump protocol is presented in Fig. 2(a). Resonant driving induces a switching of the system between the two possible sublattices of the superradiant phase at a frequency ω_{DW} and the intracavity photon number pulsates at a rate of $2\omega_{DW}$. This behavior is exemplified in the green and red curves in Fig. 2(b).

In Fig. 3(a), we plot ω_{DW} as a function of ω_{dr} and average each data point over 100 experimental runs including different modulation strength f_0. The solid gray trace shows a linear fit. We find good agreement with the theoretical prediction $\omega_{DW} = \omega_{dr} - \omega_{BDW}$ of Ref. [36]. In Supplemental Material, we present a similar plot for fixed ω_{dr} and varying f_0 to show that the dependence of ω_{DW} on f_0 is very weak and negligible within the experimental precision [38]. From the linear fit in Fig. 3(a),

(a)

(b)
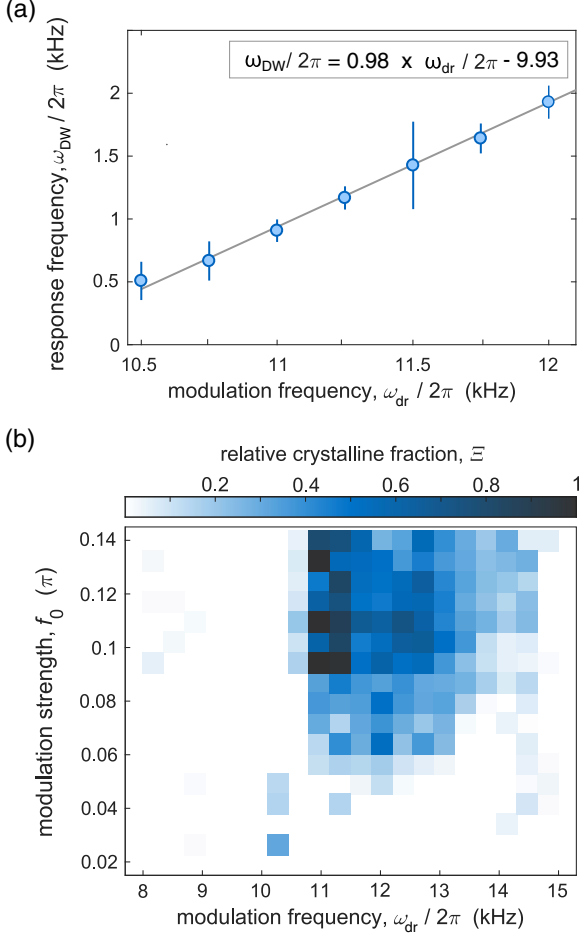
FIG. 3. (a) ω_{DW} is plotted against ω_{dr}. ω_{DW} is extracted by the position of a Gaussian fit of the amplitude spectrum calculated from the measured time evolution of the phase difference between the pump and cavity fields φ. Each data point is averaged over hundreds of realizations with different modulation strength f_0 and fixed ω_{dr}. The gray line is a linear fit yielding the result shown in the plot legend. (b) The relative crystalline fraction Ξ is plotted as a function of the modulation frequency ω_{dr} and strength f_0. The diagram is constructed by dividing the parameter space into 20×16 plaquettes and averaging over multiple experimental runs within each.

we extract the value of the parametric resonance as $\omega_{\mathrm{BDW}} = 9.93 \pm 0.30$ kHz. In Supplemental Material, we also present an alternative protocol for measuring ω_{BDW} from the depletion of the cavity field for resonant modulation [38]. In Fig. 3(b), we present the dynamical phase diagram, highlighting the DBDW order obtained from measuring the relative crystalline fraction Ξ quantified by the color scale. The relative crystalline fraction is a quantity commonly used in studies of time crystals. Here, we define it as the amplitude of the Fourier spectrum, calculated from the relative phase φ, at the expected DW frequency ω_{DW}, rescaled by its maximum value across the parameter space spanned in the phase diagram [15].

The observed DW frequency follows the linear equation $\omega_{\mathrm{DW}} = \xi \times \omega_{\mathrm{dr}} - \omega_{\mathrm{BDW}}$ with ξ determined according to the linear fit in Fig. 3(a) as 0.98, i.e., very close to the expected value of unity. This incommensurate subharmonic response of the system with respect to the modulation frequency ω_{dr} is observed within a broad area of the dynamical phase diagram in Fig. 3(b). In Supplemental Material, we present the robustness of the subharmonic response against temporal noise, which corroborates the classification of this dynamical phase as an incommensurate time crystal.

Finally, we discuss the observed dynamics of the momentum imbalance parameter $\Delta \tilde{F}$ related to the calculations in Fig. 1(c). The oscillation frequencies ω_{DW} and ω_{BDW} are extracted from the data in Fig. 2(c) using $f(t) = \exp(-\tau t) A \sin(\omega_{\mathrm{BDW}} t + \alpha) \sin(\omega_{\mathrm{DW}} t)$ as a fit function. Here, τ is the decay rate of N_P and A is an overall amplitude parameter. This measurement demonstrates a third option for measuring ω_{BDW}. However, since recording the momentum spectra is a destructive measurement, this method is much more time consuming than simply detecting the light leaking out of the cavity, which makes it extremely difficult to explore large areas in the parameter space. Nevertheless, we repeated this measurement for a second set of modulation parameters shown in Supplemental Material [38]. The frequency ω_{BDW} is independent of ω_{dr} and we measure $\omega_{\mathrm{BDW}} = 2\pi \times 9.8 \pm 0.1$ kHz. For a driving frequency of $\omega_{\mathrm{dr}} = 11.5$ kHz, we measure a slow oscillation frequency of $\omega_{\mathrm{DW}} = 2\pi \times 1.8 \pm 0.1$ kHz [see Fig. 2(c)], which agrees well with the theoretical prediction of $\omega_{\mathrm{DW}} = \omega_{\mathrm{dr}} - \omega_{\mathrm{BDW}} = 2\pi \times (11.5 - 9.8)$ kHz $= 2\pi \times 1.7$ kHz.

While we have mostly focused on the case when initially the superradiant state is prepared, we have also confirmed that it is possible to enter the three-level regime heralded by the emergence of the DBDW phase by initializing with the homogeneous BEC or normal phase as exemplified in Fig. 4.

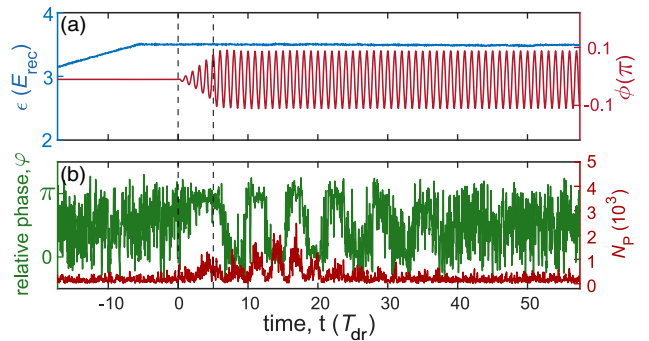FIG. 4. Dynamics in the three-level Dicke regime using an initial homogeneous BEC state. (a) Time sequence for the pump lattice depth (blue) and the phase ϕ of the pump field (red) with modulation strength $f_0 = 0.1\pi$ and a modulation frequency $\omega_{\mathrm{dr}} = 11.5$ kHz. (b) The phase difference φ between the pump and intracavity field is plotted in green and the photon number N_P in the cavity in red.

The finite lifetime of the emergent DBDW phase in our experiment can be mainly attributed to atom losses. Furthermore, we note that our numerical simulations indicate that contact interactions [36] and larger detunings $\omega_{dr} - \omega_B$ [38] decrease the lifetime of the time crystalline response. In the experiment, however, it is difficult to quantitatively separate the effects of atom losses, contact interaction, and detuning from the resonance.

In conclusion, we have realized a periodically driven open three-level Dicke model using a resonantly shaken atom-cavity system. As the main signature of the three-level Dicke model, we have demonstrated the emergence of a dynamical bond density wave phase. When prepared in the three-level Dicke regime, our system realizes an incommensurate time crystal, whereby the atoms periodically self-organize along the bonds of the pump lattice. This advances the understanding of cavity-BEC systems beyond the standard two-level Dicke model, and broadens the scope of dynamically induced many-body states in this and related hybrid light-matter systems.

---

[*]Corresponding author.
hkessler@physnet.uni-hamburg.de

[1] I. Bloch, J. Dalibard, and W. Zwerger, Many-body physics with ultracold gases, Rev. Mod. Phys. **80**, 885 (2008).

[2] I. Bloch, Quantum gases, Science **319**, 1202 (2008).

[3] W. S. Bakr, J. I. Gillen, A. Peng, S. Fölling, and M. Greiner, A quantum gas microscope for detecting single atoms in a Hubbard-regime optical lattice, Nature (London) **462**, 74 (2009).

[4] I. Bloch, J. Dalibard, and S. Nascimbène, Quantum simulations with ultracold quantum gases, Nat. Phys. **8**, 267 (2012).

[5] C. Gross and I. Bloch, Quantum simulations with ultracold atoms in optical lattices, Science **357**, 995 (2017).

[6] L. Bayha, M. Holten, R. Klemt, K. Subramanian, J. Bjerlin, S. M. Reimann, G. M. Bruun, P. M. Preiss, and S. Jochim, Observing the emergence of a quantum phase transition shell by shell, Nature (London) **587**, 583 (2020).

[7] H. Ritsch, P. Domokos, F. Brennecke, and T. Esslinger, Cold atoms in cavity-generated dynamical optical potentials, Rev. Mod. Phys. **85**, 553 (2013).

[8] F. Mivehvar, F. Piazza, T. Donner, and H. Ritsch, Cavity QED with quantum gases: New paradigms in many-body physics, Adv. Phys. **70**, 1 (2021).

[9] A. T. Black, H. W. Chan, and V. V. Vuletic, Observation of Collective Friction Forces due to Spatial Self-Organization of Atoms: From Rayleigh to Bragg Scattering, Phys. Rev. Lett. **91**, 203001 (2003).

[10] K. Baumann, R. Mottl, F. Brennecke, and T. Esslinger, Exploring Symmetry Breaking at the Dicke Quantum Phase Transition, Phys. Rev. Lett. **107**, 140402 (2011).

[11] J. Klinder, H. Keßler, M. Wolke, L. Mathey, and A. Hemmerich, Dynamical phase transition in the open Dicke model, Proc. Natl. Acad. Sci. U.S.A. **112**, 3290 (2015).

[12] H. Keßler, J. Klinder, B. P. Venkatesh, C. Georges, and A. Hemmerich, In situ observation of optomechanical Bloch oscillations in an optical cavity, New J. Phys. **18**, 102001 (2016).

[13] J. Klinder, H. Keßler, C. Georges, J. Vargas, and A. Hemmerich, Bose-Einstein condensates in an optical cavity with sub-recoil bandwidth, Appl. Phys. B **122**, 299 (2016).

[14] C. Georges, J. Vargas, H. Keßler, J. Klinder, and A. Hemmerich, Bloch oscillations of a Bose-Einstein condensate in a cavity-induced optical lattice, Phys. Rev. A **96**, 063615 (2017).

[15] H. Keßler, P. Kongkhambut, C. Georges, L. Mathey, J. G. Cosme, and A. Hemmerich, Observation of a Dissipative Time Crystal, Phys. Rev. Lett. **127**, 043602 (2021).

[16] K. Hepp and E. H. Lieb, On the superradiant phase transition for molecules in a quantized radiation field: The dicke maser model, Ann. Phys. (N.Y.) **76**, 360 (1973).

[17] P. Kirton, M. M. Roses, J. Keeling, and E. G. Dalla Torre, Introduction to the Dicke model: From equilibrium to nonequilibrium, and *vice versa*, Adv. Quantum Technol. **2**, 1800043 (2019).

[18] D. Nagy, G. Szirmai, and P. Domokos, Self-organization of a Bose-Einstein condensate in an optical cavity, Eur. Phys. J. D **48**, 127 (2008).

[19] K. Baumann, C. Guerlin, F. Brennecke, and T. Esslinger, Dicke quantum phase transition with a superfluid gas in an optical cavity, Nature (London) **464**, 1301 (2010).

[20] M. P. Baden, K. J. Arnold, A. L. Grimsmo, S. Parkins, and M. D. Barrett, Realization of the Dicke Model Using Cavity-Assisted Raman Transitions, Phys. Rev. Lett. **113**, 020408 (2014).

[21] F. Piazza and H. Ritsch, Self-Ordered Limit Cycles, Chaos, and Phase Slippage with a Superfluid inside an Optical Resonator, Phys. Rev. Lett. **115**, 163601 (2015).

[22] A. U. J. Lode and C. Bruder, Fragmented Superradiance of a Bose-Einstein Condensate in an Optical Cavity, Phys. Rev. Lett. **118**, 013603 (2017).

[23] H. Keßler, J. G. Cosme, M. Hemmerling, L. Mathey, and A. Hemmerich, Emergent limit cycles and time crystal dynamics in an atom-cavity system, Phys. Rev. A **99**, 053605 (2019).

[24] P. Molignini, L. Papariello, A. U. J. Lode, and R. Chitra, Superlattice switching from parametric instabilities in a driven-dissipative Bose-Einstein condensate in a cavity, Phys. Rev. A **98**, 053620 (2018).

[25] H. Keßler, J. G. Cosme, C. Georges, L. Mathey, and A. Hemmerich, From a continuous to a discrete time crystal in a dissipative atom-cavity system, New J. Phys. **22**, 085002 (2020).

[26] C. Georges, J. G. Cosme, H. Keßler, L. Mathey, and A. Hemmerich, Dynamical density wave order in an atom-cavity system, New J. Phys. **23**, 023003 (2021).

[27] Z. Zhiqiang, C. H. Lee, R. Kumar, K. J. Arnold, S. J. Masson, A. S. Parkins, and M. D. Barrett, Nonequilibrium

phase transition in a spin-1 Dicke model, Optica **4**, 424 (2017).

[28] S. J. Masson, M. D. Barrett, and S. Parkins, Cavity QED Engineering of Spin Dynamics and Squeezing in a Spinor Gas, Phys. Rev. Lett. **119**, 213601 (2017).

[29] E. I. Rodríguez Chiacchio and A. Nunnenkamp, Dissipation-Induced Instabilities of a Spinor Bose-Einstein Condensate inside an Optical Cavity, Phys. Rev. Lett. **122**, 193605 (2019).

[30] B. Buča and D. Jaksch, Dissipation Induced Nonstationarity in a Quantum Gas, Phys. Rev. Lett. **123**, 260401 (2019).

[31] N. Dogra, M. Landini, K. Kroeger, L. Hruby, T. Donner, and T. Esslinger, Dissipation-induced structural instability and chiral dynamics in a quantum gas, Science **366**, 1496 (2019).

[32] C. C. Sung and C. M. Bowden, Phase transition in the multimode two- and three-level Dicke model (Green's function method), J. Phys. A **12**, 2273 (1979).

[33] A. Crubellier, S. Liberman, D. Pavolini, and P. Pillet, Superradiance and subradiance: I. Interatomic interference and symmetry properties in three-level systems, J. Phys. B **18**, 3811 (1985).

[34] A. Crubellier and D. Pavolini, Superradiance and subradiance: II. Atomic systems with degenerate transitions, J. Phys. B **19**, 2109 (1986).

[35] P. Wolf, S. C. Schuster, D. Schmidt, S. Slama, and C. Zimmermann, Observation of Subradiant Atomic Momentum States with Bose-Einstein Condensates in a Recoil Resolving Optical Ring Resonator, Phys. Rev. Lett. **121**, 173602 (2018).

[36] J. G. Cosme, J. Skulte, and L. Mathey, Time crystals in a shaken atom-cavity system, Phys. Rev. A **100**, 053615 (2019).

[37] J. Skulte, P. Kongkhambut, H. Keßler, A. Hemmerich, L. Mathey, and J. G. Cosme, companion paper, Parametrically driven dissipative three-level Dicke model, Phys. Rev. A **104**, 063705 (2021).

[38] See Supplemental Material at http://link.aps.org/supplemental/10.1103/PhysRevLett.127.253601 for details on the experimental setup, the three-level scheme, dependence of the density wave frequency on modulation strength, measurement of parametric resonance using the depletion of intracavity field, and robustness against temporal noise of the dynamical BDW phase.

Supplemental Material for
Realization of a periodically driven open three-level Dicke model

Phatthamon Kongkhambut,[1] Hans Keßler,[1] Jim Skulte,[1,2] Ludwig
Mathey,[1,2] Jayson G. Cosme,[3] and Andreas Hemmerich[1,2]

[1] *Zentrum für Optische Quantentechnologien and Institut für Laser-Physik, Universität Hamburg, 22761 Hamburg, Germany*
[2] *The Hamburg Center for Ultrafast Imaging, Luruper Chaussee 149, 22761 Hamburg, Germany*
[3] *National Institute of Physics, University of the Philippines, Diliman, Quezon City 1101, Philippines*

(Dated: November 1, 2021)

I. EXPERIMENTAL DETAILS

The experimental set-up, as sketched in Fig. 1(a) in the main text, is comprised of a magnetically trapped BEC of $N_a = 65 \times 10^3$ ^{87}Rb atoms, dispersively coupled to a narrow-band high-finesse optical cavity. The cavity field has a decay rate of $\kappa = 2\pi \times 3.6$ kHz, which almost equals the recoil frequency $\omega_{\rm rec} = E_{\rm rec}/\hbar = 2\pi \times 3.55$ kHz. The wavelength of the pump laser is $\lambda_P = 803$ nm, which is red detuned with respect to the relevant atomic transition of ^{87}Rb at 795 nm. The maximum light shift per atom is $U_0 = -2\pi \times 0.36$ Hz. We fix the effective detuning to $\delta_{\rm eff} \equiv \delta_C - (1/2)N_a U_0 = -2\pi \times 18.5$ kHz, where $\delta_C = \omega_P - \omega_C$ is the pump-cavity detuning. A typical experimental sequence starts by preparing the system in the superradiant phase. This is achieved by linearly increasing the pump strength ϵ from zero to its final value $\epsilon_0 = 3.3$ $E_{\rm rec}$ in 10 ms at a fixed effective pump-cavity detuning $\delta_{\rm eff} = -2\pi \times 18.5$ kHz.
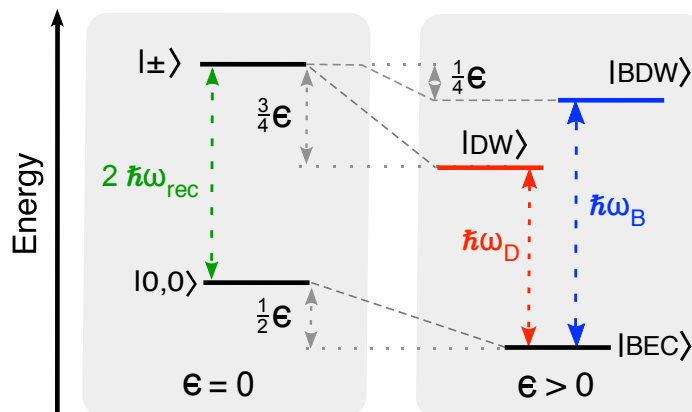
II. THREE-LEVEL SYSTEM

FIG. 1. V-shaped three-level system. On the left, the case of zero pump field strength $\epsilon = 0$ is shown with the zero momentum ground state $|0,0\rangle$ and two degenerate excited states $|+\rangle \equiv \sum_{\nu,\mu \in \{-1,1\}} |\nu\hbar k, \mu\hbar k\rangle$ and $|-\rangle \equiv \sum_{\nu,\mu \in \{-1,1\}} \nu|\nu\hbar k, \mu\hbar k\rangle$ associated with an energy $2\hbar\omega_{\rm rec}$ above that of $|0,0\rangle$ ($\hbar\omega_{\rm rec} =$ recoil energy). For $\epsilon > 0$, these bare states acquire different light-shifts giving rise to the modified states $|{\rm BEC}\rangle$, $|{\rm DW}\rangle$, and $|{\rm BDW}\rangle$. They span a three-level system with the resonance frequencies ω_D and ω_B for the left and right leg of the V-shaped coupling scheme, respectively.

Consider atoms in their electronic ground state. For each atom, a V-shaped three-level system arises as sketched in Fig. 1. For a vanishing pump field $\epsilon = 0$, the ground state is the bare zero momentum state $|0,0\rangle$ and we consider two degenerate excited momentum states given by the even and odd superpositions $|+\rangle \equiv \sum_{\nu,\mu \in \{-1,1\}} |\nu\hbar k, \mu\hbar k\rangle$ and $|-\rangle \equiv \sum_{\nu,\mu \in \{-1,1\}} \nu|\nu\hbar k, \mu\hbar k\rangle$, respectively. Here, $|\pm\hbar k, \pm\hbar k\rangle$ denotes the momentum eigenstates with $\pm\hbar k$ momentum along the pump axis (y-axis) and $\pm\hbar k$ momentum along the cavity axis (z-axis). As shown in Fig. 1, in the presence of a pump field, these states acquire light-shifts of different sizes, giving rise to the three modified states $|{\rm BEC}\rangle$, $|{\rm DW}\rangle$ and $|{\rm BDW}\rangle$. The $|{\rm BEC}\rangle$ state is associated with the zero momentum state $|0,0\rangle$, and hence a homogeneous density distribution. The light-shift for this state is $-\epsilon/2$ with ϵ denoting the potential depth of the pump standing wave [1]. $|{\rm DW}\rangle$ is associated with the bare momentum state $|+\rangle$ and therefore a density distribution proportional to $|\cos(ky)\cos(ky)|^2$. This distribution is localized in the antinodes of the pump wave and thus possesses a larger light-shift $-3\epsilon/4$ [1]. Finally, $|{\rm BDW}\rangle$ is associated with $|-\rangle$ and therefore a density distribution proportional to $|\sin(ky)\cos(ky)|^2$, which matches with the nodes of the pump wave and hence possesses the smallest light-shift $-\epsilon/4$ [1].

The preceding discussion strictly applies, if ϵ remains below a critical value $\epsilon_{\rm crt}$, beyond which the $|{\rm BEC}\rangle$ state undergoes a phase transition to the superradiant state of the regular two-level Dicke model. In particular, above $\epsilon_{\rm crt}$ a coherent intra-cavity field arises, which mixes $|{\rm BEC}\rangle$ and $|{\rm DW}\rangle$ and adds additional light-shifts to these states. In the present work, we operate either below or slightly above $\epsilon_{\rm crt}$, where this additional mixing and the associated

light-shifts are assumed sufficiently small to be neglected.

III. ATOM-CAVITY MODEL

Considering only the pump and cavity directions and neglecting contact interactions between the atoms, the shaken atom-cavity system can be modeled by the many-body Hamiltonian

$$\hat{H}/\hbar = -\delta_{\mathrm{C}}\hat{a}^\dagger\hat{a} + \int dy\,dz\,\hat{\Psi}^\dagger(y,z)\Big[-\frac{\hbar}{2m}\nabla^2 - \omega_{\mathrm{rec}}\epsilon\cos^2(ky+\phi(t)) + U_0\hat{a}^\dagger\hat{a}\cos^2(kz) \tag{1}$$
$$-\sqrt{\omega_{\mathrm{rec}}|U_0|\epsilon_p}\cos(ky+\phi(t))\cos(kz)(a^\dagger+a)\Big]\hat{\Psi}(y,z),$$

where δ_{C} is the pump-cavity detuning, $U_0 < 0$ is the maximum light shift per atom, and ϵ is the pump intensity in units of the recoil energy E_{rec}. This Hamiltonian can be mapped onto the driven open three-level Dicke model (cf. main text) by considering only the five lowest momentum modes of the atoms, $|0,0\rangle$ and $|\pm\hbar k,\pm\hbar k\rangle$, where $k = 2\pi/\lambda_{\mathrm{P}}$ is the wavenumber of the pump (see [1] for details). This assumption is valid when the occupations of higher momentum modes are kept negligible, by initializing the system close to the phase boundary between the homogeneous $|\mathrm{BEC}\rangle$ state and the superradiant phase. The matter sector of the superradiant phase, then mainly consists of the $|\mathrm{BEC}\rangle$ state with a small admixture of the $|\mathrm{DW}\rangle$ state, which exhibits a density modulation $\propto |\sin(ky)\cos(kz)|^2$ and hence, the bosonic atomic field operator can be expanded as $\hat{\Psi}(y,z) \sim \hat{c}_1 + \hat{c}_2\,2\cos(ky)\cos(kz)$ [2]. The Schwinger boson representation can be used to map the transversely pumped atom-cavity Hamiltonian onto the standard two-level Dicke model [2, 3]. The order parameter for the $|\mathrm{DW}\rangle$ state is $\Theta_{\mathrm{DW}} = \langle\cos(ky)\cos(kz)\rangle$ in bosonic operator representation, while it is $\Theta_{\mathrm{DW}} = \langle\hat{J}_x^{\mathrm{D}}\rangle$ in pseudospin representation. In our experiment, periodic shaking allows for occupation of the $|\mathrm{BDW}\rangle$ state, which displays a density modulation $\propto |\sin(ky)\cos(kz)|^2$. The order parameter for $|\mathrm{BDW}\rangle$ is either $\Theta_{\mathrm{BDW}} = \langle\sin(ky)\cos(kz)\rangle$ or $\Theta_{\mathrm{BDW}} = \langle\hat{J}_x^{\mathrm{B}}\rangle$. Taking this into account, the atomic field operator should be extended as $\hat{\Psi}(y,z) \sim \hat{c}_1 + \hat{c}_2\,2\cos(ky)\cos(kz) + \hat{c}_3\,2\sin(ky)\cos(kz)$. The driven three-level Dicke model in the main text can then be obtained using an extended Schwinger boson representation that includes this new mode [1]. The mapping leads to an effective cavity field frequency of $\omega = (3U_0N)/4 - \delta_{\mathrm{C}}$. The strength of the light-matter interaction is $\lambda/\sqrt{N} = -\sqrt{\omega_{\mathrm{rec}}\epsilon_p|U_0|}/2$. Moreover, we obtain $\omega_{\mathrm{D}} = 2\omega_{\mathrm{rec}}(1-\epsilon_{\mathrm{p}}/8)$ and $\omega_{\mathrm{B}} = 2\omega_{\mathrm{rec}}(1+\epsilon_{\mathrm{p}}/8)$ (see Eq. (2) of the main text). These frequency shifts are depicted in Fig. 1.

IV. DEPENDENCE OF THE DENSITY WAVE FREQUENCY ON THE MODULATION STRENGTH

As shown in Fig. 2, the density wave frequency ω_{DW} depends weakly on the modulation strength f_0 but the slope is much smaller as for the dependence on the modulation frequency ω_{dr} and we neglect this effect in the construction of the phase diagram in Fig. 3(b) of the main text. It can be explained as follows. Due to the modulation the atoms are sitting on the slope of the light-induced potential and they effectively feel a slightly weaker pump lattice depth ϵ. This effect increases with increasing f_0. Since the position of the bond density wave resonance ω_{BDW} shifts to lower values for smaller ϵ and $\omega_{\mathrm{DW}} = \omega_{\mathrm{BDW}} - \omega_{\mathrm{dr}}$, the density wave frequency response ω_{DW} increases with increasing modulation strength f_0.

V. MEASURING THE POSITION OF THE PARAMETRIC RESONANCE BY THE DEPLETION OF THE INTRACAVITY FIELD.

As mentioned in the main text, there are three possibilities to measure the position of the bond density wave resonance ω_{BDW}. Firstly, as shown in Fig. 3(a) of the main text, via a linear fit of the density wave frequency response ω_{DW}, and, secondly, from the oscillation of the asymmetry of the momentum modes with negative and positive momentum with respect to the pump direction $F_{+1,\pm1} - F_{-1,\pm1}$. The third method is demonstrated in this paragraph by looking at the depletion of the cavity field in the parameter space spanned by the modulation frequency ω_{dr} and modulation strength f_0. On resonance the intracavity photon number N_{P} depletes fastest for a fixed f_0. To quantify this effect, we divide the parameter space into 20×16 plaquettes. Then, we average $\sum N_{\mathrm{P}}$ in the interval from 2 to 3 ms after starting the modulation, and over multiple experimental runs.
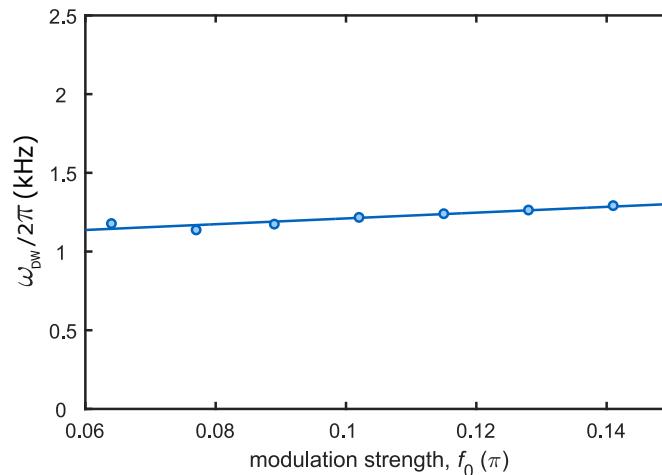
FIG. 2. Response frequency ω_{DW} versus modulation strength. ω_{DW} is plotted against f_0 for fixed $\omega_{\mathrm{dr}} = 2\pi \times 11.5\,\mathrm{kHz}$, using the protocol described in Fig. 3(a) of the main text.
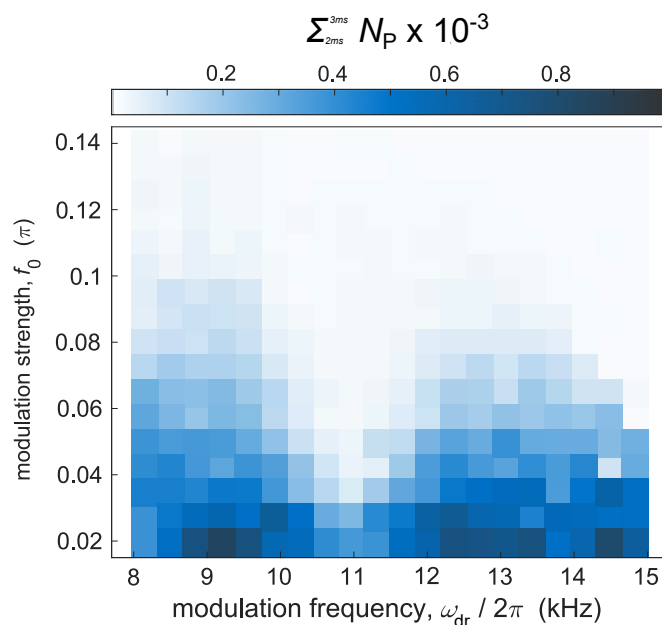
FIG. 3. Sum of N_{P} in the interval from 2 to 3 ms. We follow the protocol described in Fig. 3 of the main text for variable modulation frequencies ω_{dr} and strengths f_0. The color scale parametrizes the sum over the intracavity photon number N_{P} in the interval [2,3] ms after reaching the final modulation strength f_0.

VI. RELATION BETWEEN THE MOMENTUM IMBALANCE AND THE DENSITY WAVE/BOND DENSITY WAVE ORDER PARAMETERS

The density wave and bond density wave order parameters are defined as

$$\Theta_{\mathrm{DW}} = \int \cos(ky)\cos(kz)|\psi(y,z)|^2 dx dy \tag{2}$$

$$\Theta_{\mathrm{BDW}} = \int \sin(ky)\cos(kz)|\psi(y,z)|^2 dx dy \;, \tag{3}$$

FIG. 4. Comparsion between the product of the two order parameters $\Theta_{\mathrm{DW}} \times \Theta_{\mathrm{BDW}}$ and the momentum imbalance ΔF. The modulation strength is $f_0 = 0.1$. (cf. text)

respectively. Using the spatial translation symmetry in the system we expand the atomic field in terms of plane waves as

$$\psi(y,z) = \sum_{n,m} \phi_{n,m} e^{iny} e^{imz} . \tag{4}$$

With this the order parameter can be written in the momentum basis as

$$\Theta_{\mathrm{DW}} = \frac{1}{4} \sum_{n,m} \left(\phi^*_{n+1,m+1} + \phi^*_{n+1,m-1} + \phi^*_{n-1,m+1} + \phi^*_{n-1,m-1} \right) \phi_{n,m} \tag{5}$$

$$\Theta_{\mathrm{BDW}} = \frac{1}{4i} \sum_{n,m} \left(\phi^*_{n+1,m+1} + \phi^*_{n+1,m-1} - \phi^*_{n-1,m+1} - \phi^*_{n-1,m-1} \right) \phi_{n,m} . \tag{6}$$

In the following we will only retain the lowest five momentum modes $\{\phi_{0,0}, \phi_{\pm,\pm}\}$. We approximate the order parameters as

$$\Theta_{\mathrm{DW}} = \frac{1}{4} \left(\phi^*_{+,+} + \phi^*_{+,-} + \phi^*_{-,+} + \phi^*_{-,-} \right) \phi_{0,0} + \text{h.c.} \tag{7}$$

$$\Theta_{\mathrm{BDW}} = \frac{1}{4i} \left(\phi^*_{+,+} + \phi^*_{+,-} - \phi^*_{-,+} - \phi^*_{-,-} \right) \phi_{0,0} + \text{h.c.} . \tag{8}$$

As the momentum modes along the z-direction will stay degenerate, we denote $\phi_{+,\pm} = \phi_+$ and $\phi_{-,\pm} = \phi_-$ and introduce the shorthand notation $\phi_{0,0} = \phi_0$. Then, the order parameter can be written as

$$\Theta_{\mathrm{DW}} = \frac{1}{2} \left(\phi^*_+ + \phi^*_- \right) \phi_0 + \text{h.c.} \tag{9}$$

$$\Theta_{\mathrm{BDW}} = \frac{1}{2i} \left(\phi^*_+ - \phi^*_- \right) \phi_0 + \text{h.c.} . \tag{10}$$
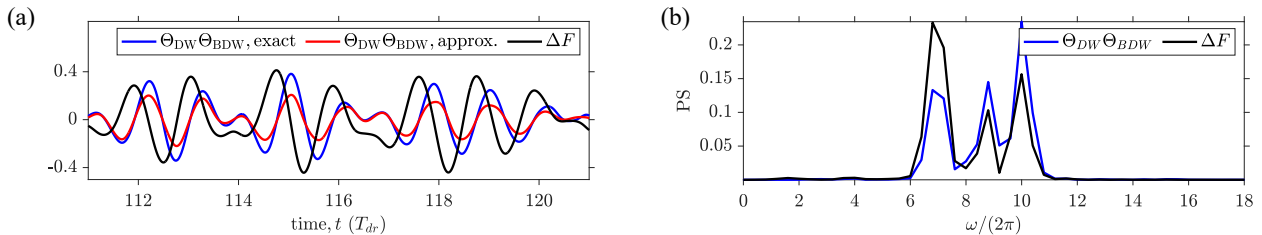
The product of these two order parameters leads to

$$\Theta_{\mathrm{DW}} \times \Theta_{\mathrm{BDW}} = \frac{1}{4i} \left\{ (\phi^*_0)^2 \left((\phi_+)^2 - \phi_-)^2 \right) - (\phi_0)^2 \left((\phi^*_+)^2 - \phi^{*2}_- \right) + 2|\phi_0|^2 \left(\phi^*_- \phi_+ - \phi^*_+ \phi_- \right) \right\} \tag{11}$$

$$= \frac{|\phi_0|^2}{2} \left(|\phi_+|^2 \sin\left(2(\theta_+ - \theta_0)\right) - |\phi_-|^2 \sin\left(2(\theta_- - \theta_0)\right) + 2|\phi_+||\phi_-| \sin\left(\theta_+ - \theta_-\right) \right) , \tag{12}$$

where we used in the last line $\psi_i = |\psi_i| \exp(i\,\theta_i)$. From our numerics, we find that this observable, as measured in the experiment, can be approximated by

$$\Theta_{\mathrm{DW}} \times \Theta_{\mathrm{BDW}} \approx \frac{|\phi_0|^2}{2} \left(|\phi_+|^2 - |\phi_-|^2 \right) \equiv \Delta F . \tag{13}$$

Fig. 4 (a) shows a comparison between the product $\Theta_{\mathrm{DW}} \times \Theta_{\mathrm{BDW}}$ of the two order parameters and the momentum imbalance ΔF. The blue trace shows the exact numerical result. The red trace shows an approximation, if only the five lowest momentum modes are accounted for. To further validate our findings, we compute in Fig. 4 (b) the power spectra of $\Theta_{\mathrm{DW}} \times \Theta_{\mathrm{BDW}}$ and ΔF. Fig. 5 shows that for a small ($f_0 = 0.001$) driving strength $\Theta_{\mathrm{DW}} \times \Theta_{\mathrm{BDW}}$ and ΔF approach zero. Hence, the driven three-level Dicke model regime can only be realized for sufficiently strong driving.
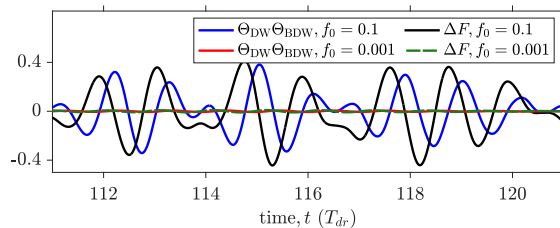
FIG. 5. Comparison of $\Theta_{\mathrm{DW}} \times \Theta_{\mathrm{BDW}}$ and Δ_F for driving strengths $f_0 = 0.1$ and $f_0 = 0.001$, respectively.
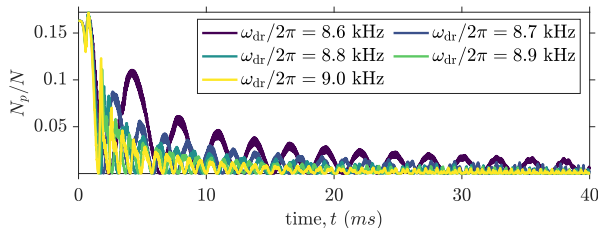
FIG. 6. Decay of the time crystal response for different detunings We choose a modulation strength of $f_0 = 0.05$. The resonance frequency is located at ≈ 8.45 kHz. For larger detunings the time crystal melts more quickly.

VII. LIFETIME OF THE TIME CRYSTALLINE RESPONSE

As was pointed out in [4], the time crystalline response becomes unstable/pre-thermal as one scans further away from the resonance. Using mean-field theory without contact interactions, Fig. 6 shows the decay of the oscillations for different detunings of the driving frequency with respect to the resonance frequency. We note that this effect contributes to the decay observed in the experiment.
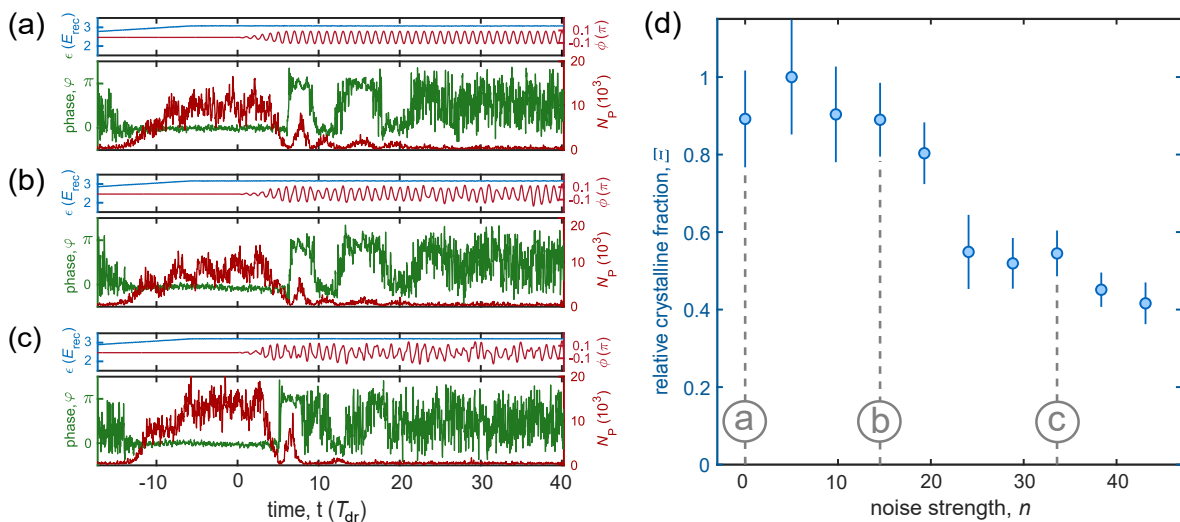
FIG. 7. Robustness of the incommensurate time crystal. (a)-(c) Single-shot experimental runs for the noise strengths marked in subplot (d) with the gray dashed lines. Top panels: single-shot protocols for the pump strength. Bottom panel: corresponding time evolution of the relative phase φ (green trace) and intracavity photon number N_{P} (red trace). (d) Dependence of the relative crystalline fraction Ξ on the noise strength averaged over 10 experimental runs with $f_0 = 0.1\,\pi$ and $\omega_{\mathrm{dr}} = 2\pi \times 11.5\,\mathrm{kHz}$.
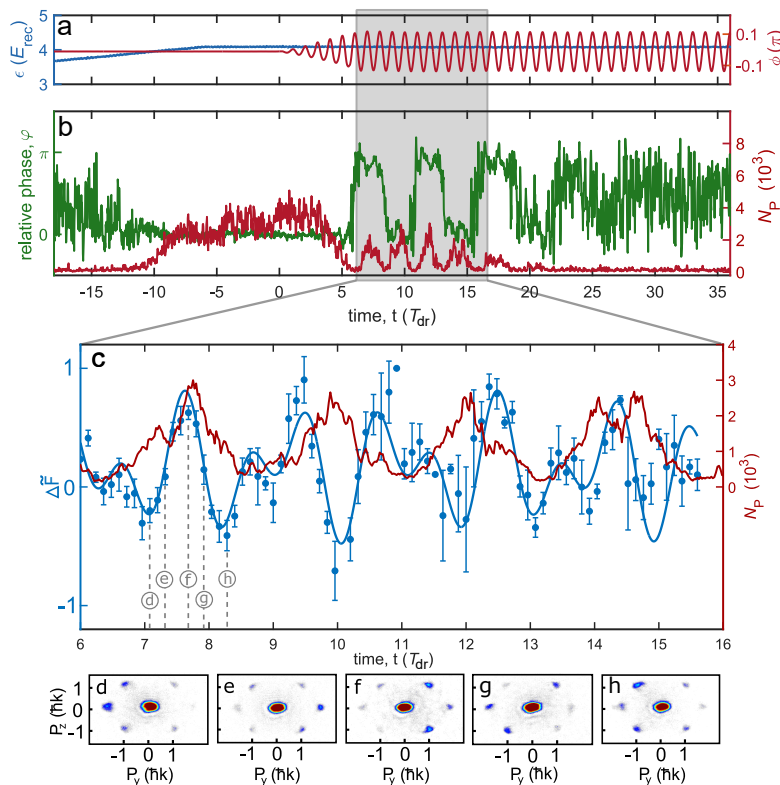
FIG. 8. Single-shot realization of DBDW order. (a) Time sequence for the pump lattice depth (blue) and the phase ϕ of the pump field (red) with modulation strength $f_0 = 0.13\,\pi$ and a modulation frequency $\omega_{\mathrm{dr}} = 12.0\,\mathrm{kHz}$. (b) Phase difference φ between the pump and intracavity field (green trace) and photon number N_{P} in the cavity (red trace). The dashed vertical lines mark the time interval during which the modulation strength is increased. The gray shaded area shows the time window for the zoom presented in (c). (c) The red trace repeats the intracavity photon number N_{P} from (b). The blue data points plot the product $\Theta_{\mathrm{DW}} \times \Theta_{\mathrm{BDW}}$, approximately given by the difference between the number of atoms populating the momentum modes with positive and negative momentum with respect to the pump direction $\Delta\tilde{F} = (F_{+1,\pm1} - F_{-1,\pm1})/(F_{+1,\pm1} - F_{-1,\pm1})_{\mathrm{max}}$ (see also Fig. 1(c) and Fig. 2(c) of the main text). Each data point is averaged over 5 realizations. The solid line shows a fit with a product of two harmonic oscillations. (d)-(h) Single-shot momentum distributions recorded at the times marked in (c).

VIII. ROBUSTNESS AGAINST TEMPORAL PERTURBATIONS.

The robustness against temporal perturbations is one of the main characteristics of time crystalline dynamics. We have tested the stability of the observed bond density wave phase against artificial white noise on the modulation signal with a bandwidth of 20 kHz. The applied noise strength is measured by $n \equiv \sum_{\omega=0}^{2\pi \times 20\ \mathrm{kHz}} |\mathcal{E}_{\mathrm{noisy}}(\omega)| / \sum_{\omega=0}^{2\pi \times 20\ \mathrm{kHz}} |\mathcal{E}_{\mathrm{clean}}(\omega)|$, where $\mathcal{E}_{\mathrm{noisy}}$ ($\mathcal{E}_{\mathrm{clean}}$) is the Fourier spectrum of the pump in the presence (absence) of white noise. Figures 7(d) show how the relative crystalline fraction $\Xi$ changes with increasing noise strength for fixed modulation parameters $f_0 = 0.1$ and $\omega_{\mathrm{dr}} = 11.5\,\mathrm{kHz}$. Note that even for a strongly distorted pump signal, as in Fig. 7(b) the system still switches multiple times between the two sublattices before the intracavity field disappears.

IX. SINGLE-SHOT REALIZATION OF DBDW ORDER FOR $\omega_{\mathrm{dr}} = 12\,\mathrm{KHZ}$

We measured the momentum mode asymmetry for a second parameter set and present the results in Fig. 8. In Fig. 8(c) we used $f(t) = \exp(-\tau t)\, A \sin(\omega_{\mathrm{BDW}} t + \alpha) \sin(\omega_{\mathrm{DW}} t)$ as a fit function. Here, τ is the decay rate of N_{P} and A is an overall amplitude parameter. The fast BDW oscillation frequency is independent of ω_{dr} and we measure $\omega_{\mathrm{BDW}} = 2\pi \times 9.8 \pm 0.1\,\mathrm{kHz}$. We find a slow oscillation frequency of $\omega_{\mathrm{DW}} = 2\pi \times 2.6 \pm 0.1\,\mathrm{kHz}$ (see also Fig. 1(c) and Fig. 2(c) of the main text) for a driving frequency of $\omega_{\mathrm{dr}} = 12.0\,\mathrm{kHz}$, which agrees well with the theoretical prediction of $\omega_{\mathrm{DW}} = \omega_{\mathrm{dr}} - \omega_{\mathrm{BDW}} = 2\pi \times (12.0 - 9.8)\,\mathrm{kHz} = 2\pi \times 2.2\,\mathrm{kHz}$.

[1] J. Skulte, P. Kongkhambut, H. Keßler, A. Hemmerich, L. Mathey, and J. G. Cosme, arXiv:2108.10877 (2021).

[2] F. Mivehvar, F. Piazza, T. Donner, and H. Ritsch, (2021), arXiv:2102.04473.

[3] K. Baumann, C. Guerlin, F. Brennecke, and T. Esslinger, Nature (London) **464**, 1301 (2010).

[4] J. G. Cosme, J. Skulte, and L. Mathey, Phys. Rev. A **100**, 053615 (2019).

2.10 Publication V: Condensate Formation in a Dark State of a Driven Atom-Cavity System

J. Skulte, P. Kongkhambut, S. Rao, L. Mathey, H. Keßler, A. Hemmerich and J.G. Cosme — **Phys. Rev. Letters 130, 163603 (2023)**

Motivation

This work was motivated by the previous study of an incommensurate time crystal (ITC) in an atom-cavity system in our theoretical and experimental work for weak driving. Our goal was to expand our previously introduced three-level Dicke model, such that it can also capture the strong driving physics, that can be found in the experiment and to explore the new emerging phases.

Main findings

In this work, we have demonstrated the formation of a condensate in a dark state of momentum modes for sufficiently strong driving. We mapped the shaken atom-cavity system, without any approximations concerning the driving strength, to an extended three-level Dicke model and compared the dynamical phase diagrams and found good agreement. We further obtained the dynamical phase diagram experimentally and found qualitative agreement as well. Furthermore, we used time-of-flight and photon emission measurements to demonstrate the successful preparation of the condensate in the dark state. The dark state is a superposition of the atomic ground state and excited momentum states that effectively decouples from the light field. This allowed us to show that the cavity coupling and the dark state concept can be used to efficiently produce complex many-body states in open quantum systems.

Contribution

JGC, LM and I conceptualized the work. I performed the analytical and numerical calculations supported by JGC and supervised by LM. PK, SR and HK performed the experiments and data analysis under the supervision by AH. All authors contributed to the discussion and interpretation of the results, as well as to writing the manuscript.

Condensate Formation in a Dark State of a Driven Atom-Cavity System

Jim Skulte[1,2,*], Phatthamon Kongkhambut[1,*], Sahana Rao[1], Ludwig Mathey[1,2], Hans Keßler[1],
Andreas Hemmerich[1,2], and Jayson G. Cosme[3]

[1]*Zentrum für Optische Quantentechnologien und Institut für Laser-Physik, Universität Hamburg, 22761 Hamburg, Germany*
[2]*The Hamburg Center for Ultrafast Imaging, Luruper Chaussee 149, 22761 Hamburg, Germany*
[3]*National Institute of Physics, University of the Philippines, Diliman, Quezon City 1101, Philippines*

We demonstrate the formation of a condensate in a dark state of momentum states, in a pumped and shaken cavity-BEC system. The system consists of an ultracold quantum gas in a high-finesse cavity, which is pumped transversely by a phase-modulated laser. This phase-modulated pumping couples the atomic ground state to a superposition of excited momentum states, which decouples from the cavity field. We demonstrate how to achieve condensation in this state, supported by time-of-flight and photon emission measurements. With this, we show that the dark state concept provides a general approach to efficiently prepare complex many-body states in an open quantum system.

While dissipation is in general perceived as a destructive feature of a quantum system, it can also be utilized to engineer nontrivial states, often in conjunction with driving a system out of equilibrium. A prominent experimental platform for this purpose is ultracold quantum gases coupled to high-finesse optical cavities [1–4], due to the well-controlled dissipative channel resulting from the photon emission out of the cavity. Paradigmatic models of light-matter interaction can be explored, such as the celebrated Dicke model that describes the interaction between N two-level atoms with a single quantized light mode [5]. The driven-dissipative Dicke model, an extension of the standard Dicke model, captures the scenario, when both external driving and dissipation are present [6,7]. A wealth of phases, unique to driven light-matter systems, have been proposed and realized using variations of driven Dicke models, such as the three-level Dicke model [8–20]. In particular, the dissipation channel of the cavity has been utilized to demonstrate the emergence of nonequilibrium or dynamical phases [19,21–35].

An intriguing class of quantum states in light-matter systems, well known in quantum optics, are the so-called dark states [36]. These are superpositions of matter states with relative phases such that the quantum mechanical amplitudes, coupling the different sectors to an irradiated light field, interfere destructively. As a consequence, dark states decouple from the light field. Dark states play a crucial role in physical phenomena, such as stimulated Raman adiabatic passage [37,38], electromagnetically induced transparency [39,40], lasing without inversion [41,42], and combinations of these topics [9,20,43,44]. In conventional quantum optics scenarios, dark states typically arise on a single-particle level. In this Letter, we use the dark state concept in a many-body context,

specifically condensation. Our study suggests how the concept of dark state formation can be utilized in the context of quantum state engineering via dissipation.

In this Letter, we demonstrate in theory and experiment a robust condensate formation in a dark state of a driven atom-cavity system, approximately described by a parametrically driven three-level open Dicke model introduced in Refs. [17,19]. We consider a Bose-Einstein condensate (BEC) prepared in a high-finesse cavity, which is transversely pumped with a shaken one-dimensional optical lattice, as sketched in Fig. 1(a). Previously, we explored the weakly resonantly driven scenario leading to an incommensurate time crystal (ITC) [17,19,26]. Here, technical improvements in our setup allowed us to study theoretically and experimentally the so far unexplored regime of strong driving and a wider range of driving frequencies, which reveals that the ITC has transient character in certain parameter regimes, such that the atoms relax into a dark state of the atom-cavity system eventually.

To understand the dark state and to identify the relevant driving parameters, we employ the time-dependent atom-cavity Hamiltonian in Refs. [17,45] and an approximative parametrically driven three-level Dicke model [17,19], which includes only three atomic modes denoted as $|N\rangle$, $|B\rangle$, and $|D\rangle$, in a plane-wave expansion of the atomic field operator. These modes are illustrated in terms of their momentum components in Fig. 1(b) and form the V-shaped three-level system sketched in Fig. 1(c). The normal state $|N\rangle \equiv |(0,0)\hbar k\rangle$ corresponds to a homogeneous density in real space, wherein all atoms occupy the lowest momentum mode $\{p_y, p_z\} = \{0,0\}\hbar k$ (k is the wave number of the pump field). The pump leads to a light shift of $-\epsilon_p \omega_{rec}/2$, where ϵ_p is the unitless pump intensity and ω_{rec} is the atomic
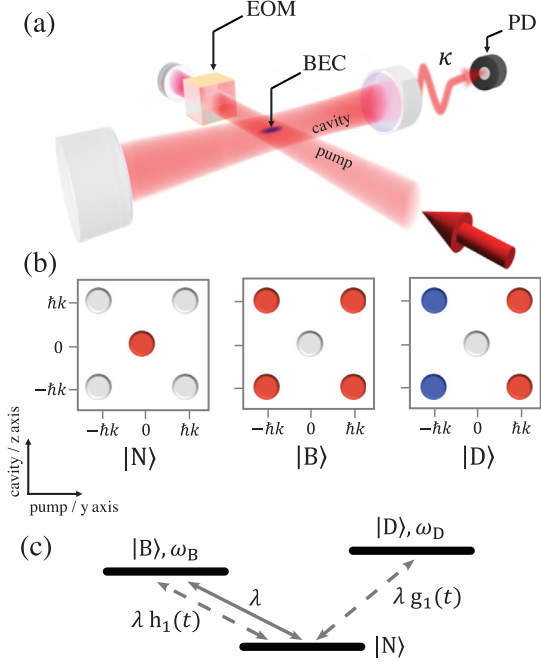
FIG. 1. (a) Sketch of the experimental setup. An electro-optical modulator (EOM) is used to modulate the phase of the pump field, which results in shaking the pump potential. The light leaking out the cavity is detected using a photo diode (PD). (b) Sketch of the momentum distribution of the three relevant superpositions of momentum modes, the normal state $|N\rangle$, the bright state $|B\rangle$, and the dark state $|D\rangle$, which form a three-level Dicke model shown in (c) with the atom-cavity coupling λ and the shaking-induced functions $h_1(t)$ and $g_1(t)$. The colors in (b) represent the phase of the momentum states, where blue indicates a phase shift of π relative to red.

recoil frequency. The bright state $|B\rangle \equiv \sum_{\nu,\mu \in \{-1,1\}} |\nu\hbar k, \mu\hbar k\rangle$ is defined as the in-phase superposition of the $\{\pm 1, \pm 1\}\hbar k$ momentum modes as depicted in Fig. 1(b). The real-space wave function of this state is $\propto \cos(ky)\cos(kz)$, which has even parity with respect to the inversion $(y, z) \rightarrow (-y, -z)$. It exhibits a kinetic energy of $2E_{\text{rec}}$ and is light shifted by the pump wave by $-3\epsilon_p\omega_{\text{rec}}/4$ such that its frequency separation relative to $|N\rangle$ is $\omega_B = (2 - \epsilon_p/4)\omega_{\text{rec}}$. The dark state $|D\rangle \equiv \sum_{\nu,\mu \in \{-1,1\}} \nu|\nu\hbar k, \mu\hbar k\rangle$ is defined as the out-of-phase superposition of the $\{+1, \pm 1\}\hbar k$ and $\{-1, \pm 1\}\hbar k$ momentum modes. In real space, its order parameter is $\propto \sin(ky)\cos(kz)$, which has odd parity under the inversion $(y, z) \rightarrow (-y, -z)$.

The density distributions of the dark state $|D\rangle$ and the bright state $|B\rangle$ both prohibit collective scattering of photons into the cavity. Nonetheless, any admixture of the normal state $|N\rangle$ to the bright state $|B\rangle$ leads to a checkerboard pattern of the atomic density that allows pump photons to scatter into the cavity, which is the reason we refer to $|B\rangle$ as a bright state. Above a critical pump strength, the system forms a superradiant (SR) phase as its stationary state, in which a superposition of $|B\rangle$ and $|N\rangle$

produces a density grating trapped by the intracavity optical lattice composed of the pump and cavity fields. In contrast to $|B\rangle$, the density grating of the dark state $|D\rangle$, due to its odd parity is shifted along the pump direction by a quarter of the pump wavelength, such that the atomic positions coincide with the nodes of the pump lattice, motivating our terminology of bond-density waves in Refs. [17,19]. Hence, even if $|N\rangle$ is admixed to the dark state $|D\rangle$, scattering of pump photons remains suppressed, meaning that for any superposition of the normal and the dark state collective scattering of photons into the cavity cannot occur. The dark state $|D\rangle$ exhibits the same kinetic energy $2E_{\text{rec}}$ as $|B\rangle$, while its light shift due to the pump lattice is only $-\epsilon_p\omega_{\text{rec}}/4$. Thus, its frequency relative to that of $|N\rangle$ is $\omega_D = (2 + \epsilon_p/4)\omega_{\text{rec}}$.

To excite the dark state, we shake the pump lattice by introducing a time-dependent phase in the pump field, $\cos(ky + \phi(t))$, where $\phi(t) = f_0 \sin(\omega_{\text{dr}}t)$, f_0 is the driving strength, and ω_{dr} is the driving frequency. The excitation mechanism is readily understood by means of the three-level Dicke model $\hat{H} = \hat{H}_{\text{stat}} + \hat{H}_{\text{dyn}}$ with a static part,

$$\hat{H}_{\text{stat}}/\hbar = \omega\hat{a}^\dagger\hat{a} + [\omega_B - \Omega(f_0)]\hat{J}_z^B + [\omega_D + \Omega(f_0)]\hat{J}_z^D$$
$$+ \frac{2\lambda}{\sqrt{N_a}}(\hat{a}^\dagger + \hat{a})J_0(f_0)\hat{J}_x^B, \qquad (1)$$

and a dynamical part,

$$\hat{H}_{\text{dyn}}/\hbar = h_2(t)\Delta\omega_{BD}(\hat{J}_z^D - \hat{J}_z^B) + 2g_2(t)\Delta\omega_{BD}\hat{J}_x^{BD}$$
$$+ \frac{4\lambda}{\sqrt{N_a}}(\hat{a}^\dagger + \hat{a})[h_1(t)\hat{J}_x^B - g_1(t)\hat{J}_x^D], \qquad (2)$$

where $\Omega(f_0) = (\epsilon_p\omega_{\text{rec}}/4)[1 - J_0(2f_0)]$, $\Delta\omega_{BD} = (\omega_B - \omega_D)$, $h_m(t) = \sum_{n=1}^{\infty} J_{2n}(mf_0)\cos(2n\omega_{\text{dr}}t)$, $g_m(t) = \sum_{n=1}^{\infty} J_{2n-1} \times (mf_0)\sin[(2n-1)\omega_{\text{dr}}t]$, and $J_n(r)$ is the nth Bessel function of the first kind. The time-dependent terms introduced by the pump lattice shaking are $h_m(t)$ and $g_m(t)$. Details on the derivation of this Hamiltonian are given in the Supplemental Material [45]. The pseudospin operators $\hat{J}_\mu^B$ ($\mu \in \{x, y, z\}$) describe the coupling to the bright state since $\hat{J}_+^B \equiv \hat{J}_x^B + i\hat{J}_y^B = |B\rangle\langle N|$. Accordingly, $\hat{J}_+^D$ is related to the dark state as $\hat{J}_+^D \equiv \hat{J}_x^D + i\hat{J}_y^D = |D\rangle\langle N|$. We see from the last term of Eq. (2) that $|D\rangle$ can be coupled to the cavity mode via the time-dependent shaking of the pump, resulting in a periodic coupling between $|D\rangle$ and $|N\rangle$. Note that the necessary nonzero amplitude $g_1(t)$ can be provided by phase modulation, which breaks the discrete translation symmetry along the pump axis, but not by amplitude modulation. We consider the recoil-resolved regime, i.e., the loss rate of the cavity photons κ is comparable to the recoil frequency ω_{rec}, which for our system is $\omega_{\text{rec}} = 2\pi \times 3.6$ kHz. We emphasize the importance of this regime [48,49] to

protect the dark state from detrimental resonant excitations to higher energy momentum states.

Next, we discuss the dynamics of the system by solving the semiclassical equations of motion of the three-level model Eq. (2) and those of the atom-cavity Hamiltonian [45] including fluctuations due to photon emission out of the cavity. For the three-level model, the dark state occupation is $\langle \hat{J}^D \rangle + 1/2$. For the full atom-cavity model, we apply the following protocol: the pump laser strength is linearly increased within 10 ms, such that we always initially prepare the SR phase. After a holding time of 0.5 ms, the phase of the pump lattice is modulated for 7 driving cycles, starting at $t = t_0$. We choose 7 driving cycles since, as is later seen in the experiment, the dark state occupation N_D is found to equilibrate after 6 driving cycles due to heating [45]. Subsequently, we adiabatically ramp-down the pump strength in 0.5 ms and calculate N_D as the sum of the occupations in the $\{\pm 1, \pm 1\}\hbar k$ modes. The ramp-down is necessary to remove all $\{\pm 1, \pm 1\}\hbar k$ populations, associated with $|B\rangle$ rather than $|D\rangle$, by transferring $|B\rangle$ into $|N\rangle$, which does not affect $|D\rangle$. In Fig. 2, we construct the phase diagrams of the three-level and the full models, plotting N_D for different driving parameters. Our previous work on the emergence of an ITC involved the regime around $\omega_{\mathrm{dr}} \in [1, 1.2] \times \omega_D$ and $f_{0,\mathrm{theory}} < 0.4$ [17,19]. We find qualitative agreement between the numerical simulations of the full atom-cavity system and the driven three-level Dicke model as seen in Fig. 2. Significant occupation of the dark state is observed in a large area of the phase diagram for $\omega_{\mathrm{dr}} > \omega_D$ and also in a small area close to the resonance $\omega_{\mathrm{dr}} \approx \omega_D$. We note that the area in the driving parameter space, where the dark state becomes dynamically occupied, is larger in the full atom-cavity model as compared to the three-level Dicke model. This can be attributed to the $\{0, \pm 2\}\hbar k$ and $\{\pm 2, 0\}\hbar k$ modes,
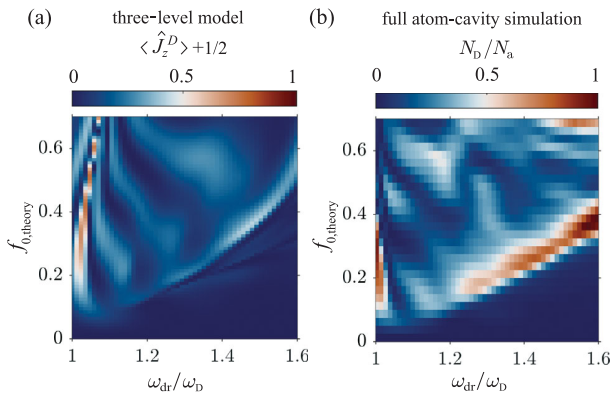
which are neglected in the three-level model [45]. Atoms in these modes may be transferred to the dark state upon scattering photons into the cavity, thus increasing its efficient population. This process competes with a direct resonant transfer of atoms into the second band of the pump wave without scattering photons into the cavity, which impedes efficient population of the dark state as detailed in the Supplemental Material [45]. The respective resonance frequency arises in Fig. 2 for $\omega_{\mathrm{dr}}/\omega_D \approx 1.7$, i.e., slightly outside the shown range.

Next, we employ the truncated Wigner approximation (TWA) to capture the leading-order quantum effects [26,50–52]. We include not only the dissipation due to photon emission out of the cavity but also the associated fluctuations. We further demonstrate that the observed dark state is indeed a finite momentum condensate by calculating the eigenvalues of the single-particle correlation function at equal time, $\langle \Psi(y,z)^\dagger \Psi(y',z') \rangle$, for our full atom-cavity model. This appears in the Penrose-Onsager criterion for condensates, and its largest eigenvalue corresponds to the condensate fraction [53]. We denote the eigenvalues as n_{NO}. We show in Fig. 3(a) the n_{NO} obtained from TWA simulations for the same pump protocol used in Fig. 2(b), but without the final ramp-down of the pump wave. When the system enters the SR phase (at about 5.2 ms), the condensate fragments manifested in the
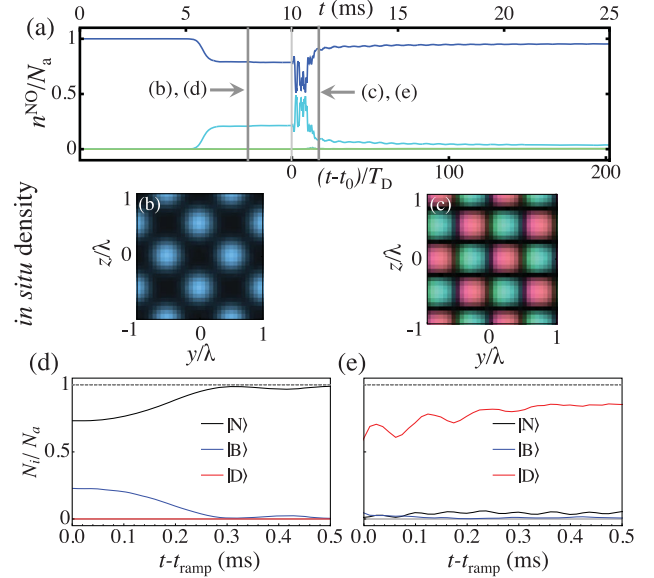
FIG. 3. (a) Simulations of the evolution of the three highest eigenvalues of the single-particle correlation function are shown. Gray dashed and solid vertical lines denote, respectively, the times when the snapshots of the single-particle densities in (b) and (c) are taken. The real-space densities in (b) and (c) are color coded to show the phase of $\Psi(y,z)$. (d),(e) Evolution of the occupations of $|N\rangle$, $|B\rangle$, and $|D\rangle$, while the pump is adiabatically ramped down. Panels (d) and (e), respectively, correspond to initial conditions according to the dashed and solid gray vertical lines in (a).

FIG. 2. (a),(b) Population of the dark state for different driving frequencies ω_{dr} and driving strengths $f_{0,\mathrm{theory}}$. The driving frequency axis is rescaled by the characteristic frequency of the dark state ω_D. (a) The results from the three-level model and (b) the full atom-cavity simulation. The phase diagrams are constructed for 7 driving cycles.

FIG. 4.   Experimental phase diagram of the population of the dark state for different driving frequencies ω_{dr} and driving strengths $f_{0,\mathrm{exp}}$. The driving frequency axis is rescaled by the characteristic frequency of the dark state ω_D. The phase diagram is constructed for 6 driving cycles. (b)–(d) Population of the dark state as a function of the driving cycles for the parameter sets marked by a diamond, a circle, and a rectangle in (a). The population of the dark state is rescaled by the total particle number N_a for different driving cycles derived from time-of-flight (TOF) images in (b)–(d). Examples of TOF images are provided before shaking starts at $t = 0$ (e) and after around 6 driving cycles (f). All TOF images are obtained after an adiabatic ramp-down of the pump wave and ballistic expansion of 25 ms. (g) Time sequence for the pump strength (red) and the phase ϕ of the pump field (blue). (h) Phase difference φ between the pump and intracavity field (blue) and intracavity photon number N_P (red) for the driving parameters marked by a circle in (a).

reduction of the largest eigenvalue and the corresponding increase of the second largest eigenvalue [54]. The real-space density $|\Psi(y, z)|^2$ shown in Fig. 3(b) illustrates the prevailing SR phase at the time indicated by the dashed gray line, before driving starts at $t = t_0$. In Fig. 3(c), we show $|\Psi(y, z)|^2$ at the time indicated by the solid gray line, after driving has acted for about 0.6 ms, indicating a substantial population of the dark state. The zeros (black regions) coincide with the intensity maxima of the pump lattice along the y direction, while there is no significant standing wave potential along the cavity direction. The different colors in Fig. 3(c) denote opposite phases of $\Psi(y, z)$. In Figs. 3(d) and 3(e), 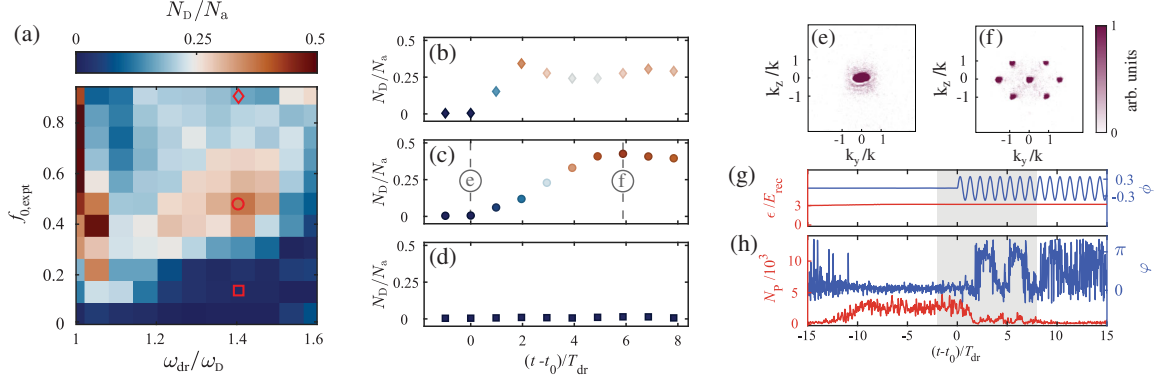we show the occupations of the relevant states as the pump lattice is ramped down at the times indicated by the dashed [Fig. 3(d)] and solid [Fig. 3(e)] gray lines. It can be seen in Fig. 3(d) that for the SR phase [prevailing at the time denoted by the dashed vertical line in Fig. 3(a)] practically all atoms are transferred back to the normal state $|N\rangle$ after the ramp-down. On the other hand, for the driven case in Fig. 3(e), associated with the time indicated by the solid gray line in Fig. 3(a), the dark state $|D\rangle$ has the largest occupation at $t = t_{\mathrm{ramp}}$. After the ramp-down, its occupation increases further, forming a long-lived state, compared to the decay time of the SR state. These results corroborate that the population of the $\{\pm 1, \pm 1\}\hbar k$ modes after the pump is adiabatically switched off is the appropriate observable to quantify the *in situ* occupation of the dark state.

Finally, we experimentally demonstrate driving-induced condensation into a dark state of the atom-cavity system [45]. We present in Fig. 4(a) the resulting experimental phase diagram of the occupation of N_D for varying driving parameters. We find qualitative agreement with the theoretical phase diagrams depicted in Fig. 2. For technical

reasons, such as atom losses, a complete population inversion into the dark state, as seen in the numerical simulations, is not observed in the experiment. We note that there is a slight difference between the numerical and the experimental results for the driving strength needed to populate the dark state. This can possibly be attributed to the pump in the experiment having a nonzero width in frequency space, so that the effective pump power is smaller than it would be for monochromatic pump beam. Therefore, the experimental realization might require a nominally larger pump power than in the theoretical model.

Figures 4(b)–4(d) show the occupation of the dark state for varying numbers of driving cycles and fixed driving frequencies. Each panel corresponds to a value of the driving strength $f_{0,\mathrm{exp}}$ indicated by the red markers in Fig. 4(a). Between the red circular and the red rectangular marker, there is a sharp transition from large occupation of $|D\rangle$ [see also Fig. 4(c)] toward a region where $|D\rangle$ is practically unoccupied [see also Fig. 4(d)]. In the limit of strong driving around the diamond-shaped marker in Fig. 4(a), the dark state becomes highly occupied after only 2 driving cycles, but the occupation number slightly decreases again for larger numbers of driving cycles as shown in Fig. 4(b). This is explained by the excitation of the $|\pm 2\hbar k, 0\rangle$ modes, as discussed below. Each data point is obtained via averaging over 10 TOF images. We also present the corresponding TOF images [see Figs. 4(e) and 4(f)] at two instances of time, i.e., at $t = t_0$ before driving is started and after six driving cycles at $t = t_0 + 6T_{\mathrm{dr}}$ as indicated in Fig. 4(c). These TOF images correspond to the spatial orders calculated in Figs. 3(d) and 3(e). We display the time evolution of the cavity field for a single experimental realization in Fig. 4(h) showcasing the

vanishing intracavity light field as a macroscopic fraction of the atoms occupy the dark state.

For the case depicted in Fig. 4(c), we find that initially N_D increases and saturates beyond 6 driving cycles. The system approaches a steady state because of atom losses before all atoms can be transferred into the dark state. In contrast to the SR phase in Fig. 4(e), the large occupation of the four momentum components $\{\pm 1, \pm 1\}\hbar k$ in Fig. 4(f) in combination with the small intracavity photon number in Fig. 4(h) indicates a large occupation of the dark state $|D\rangle$. Furthermore, a substantial fraction of atoms populates the $\{\pm 2, 0\}\hbar k$ momentum modes as the driving frequency is tuned close to the resonance frequency for excitation to the second band of the pump wave. This process inhibits efficient population of the dark state as is discussed in the Supplemental Material [45]. For reasons explained in Ref. [45], in the experiment, the respective resonance is shifted to $\omega_{\mathrm{dr}}/\omega_D \approx 1.45$, i.e., within the domain shown in Fig. 4(a), acting to suppress the dark state population on the right side of the red circle.

In conclusion, in an atom-cavity system pumped by a periodically shaken standing wave, we have found that in a specific parameter domain, a stationary excited dark state condensate emerges, in which scattering of pump photons into the cavity mode is suppressed. We show that a three-level Dicke model captures this phenomenon qualitatively. Both theoretically and experimentally, we observe that, upon adiabatic ramp-down of the pump wave, the atomic condensate in the dark state is essentially unaffected, while the bright sector of the system undergoes a dynamical phase transition [3]. Our work points out a general approach to form stationary excited many-body states using the concept of dark states known from single-particle quantum optics.

---

[*]These authors contributed equally to this work.

[1] K. Baumann, C. Guerlin, F. Brennecke, and T. Esslinger, Dicke quantum phase transition with a superfluid gas in an optical cavity, Nature (London) **464**, 1301 (2010).

[2] H. Ritsch, P. Domokos, F. Brennecke, and T. Esslinger, Cold atoms in cavity-generated dynamical optical potentials, Rev. Mod. Phys. **85**, 553 (2013).

[3] J. Klinder, H. Keßler, M. Wolke, L. Mathey, and A. Hemmerich, Dynamical phase transition in the open Dicke model, Proc. Natl. Acad. Sci. U.S.A. **112**, 3290 (2015).

[4] V. D. Vaidya, Y. Guo, R. M. Kroeze, K. E. Ballantine, A. J. Kollár, J. Keeling, and B. L. Lev, Tunable-Range, Photon-Mediated Atomic Interactions in Multimode Cavity QED, Phys. Rev. X **8**, 011002 (2018).

[5] R. H. Dicke, Coherence in spontaneous radiation processes, Phys. Rev. **93**, 99 (1954).

[6] P. Kirton, M. M. Roses, J. Keeling, and E. G. Dalla Torre, Introduction to the Dicke model: From equilibrium to nonequilibrium, and vice versa, Adv. Quantum Technol. **2**, 1800043 (2019).

[7] F. Damanet, A. J. Daley, and J. Keeling, Atom-only descriptions of the driven-dissipative Dicke model, Phys. Rev. A **99**, 033845 (2019).

[8] C. C. Sung and C. M. Bowden, Phase transition in the multimode two- and three-level Dicke model (Green's function method), J. Phys. A **12**, 2273 (1979).

[9] M. Hayn, C. Emary, and T. Brandes, Phase transitions and dark-state physics in two-color superradiance, Phys. Rev. A **84**, 053856 (2011).

[10] V. M. Bastidas, C. Emary, B. Regler, and T. Brandes, Nonequilibrium Quantum Phase Transitions in the Dicke Model, Phys. Rev. Lett. **108**, 043003 (2012).

[11] R. Chitra and O. Zilberberg, Dynamical many-body phases of the parametrically driven, dissipative Dicke model, Phys. Rev. A **92**, 023815 (2015).

[12] Z. Zhiqiang, C. H. Lee, R. Kumar, K. J. Arnold, S. J. Masson, A. S. Parkins, and M. D. Barrett, Nonequilibrium phase transition in a spin-1 Dicke model, Optica **4**, 424 (2017).

[13] M. Soriente, T. Donner, R. Chitra, and O. Zilberberg, Dissipation-Induced Anomalous Multicritical Phenomena, Phys. Rev. Lett. **120**, 183603 (2018).

[14] E. I. Rodriguez Chiacchio and A. Nunnenkamp, Dissipation-Induced Instabilities of a Spinor Bose-Einstein Condensate Inside an Optical Cavity, Phys. Rev. Lett. **122**, 193605 (2019).

[15] B. Buča and D. Jaksch, Dissipation Induced Nonstationarity in a Quantum Gas, Phys. Rev. Lett. **123**, 260401 (2019).

[16] K. C. Stitely, S. J. Masson, A. Giraldo, B. Krauskopf, and S. Parkins, Superradiant switching, quantum hysteresis, and oscillations in a generalized Dicke model, Phys. Rev. A **102**, 063702 (2020).

[17] J. Skulte, P. Kongkhambut, H. Keßler, A. Hemmerich, L. Mathey, and J. G. Cosme, Parametrically driven dissipative three-level Dicke model, Phys. Rev. A **104**, 063705 (2021).

[18] L. Broers and L. Mathey, Floquet engineering of non-equilibrium superradiance, SciPost Phys. **14**, 018 (2023).

[19] P. Kongkhambut, H. Keßler, J. Skulte, L. Mathey, J. G. Cosme, and A. Hemmerich, Realization of a Periodically Driven Open Three-Level Dicke Model, Phys. Rev. Lett. **127**, 253601 (2021).

[20] R. Lin, R. Rosa-Medina, F. Ferri, F. Finger, K. Kroeger, T. Donner, T. Esslinger, and R. Chitra, Dissipation-Engineered Family of Nearly Dark States in Many-Body Cavity-Atom Systems, Phys. Rev. Lett. **128**, 153601 (2022).

[21] H. Habibian, A. Winter, S. Paganelli, H. Rieger, and G. Morigi, Bose-Glass Phases of Ultracold Atoms due to Cavity Backaction, Phys. Rev. Lett. **110,** 075304 (2013).

[22] C. Kollath, A. Sheikhan, S. Wolff, and F. Brennecke, Ultracold Fermions in a Cavity-Induced Artificial Magnetic Field, Phys. Rev. Lett. **116,** 060401 (2016).

[23] F. Mivehvar, F. Piazza, and H. Ritsch, Disorder-Driven Density and Spin Self-Ordering of a Bose-Einstein Condensate in a Cavity, Phys. Rev. Lett. **119,** 063602 (2017).

[24] C. Georges, J. G. Cosme, L. Mathey, and A. Hemmerich, Light-Induced Coherence in an Atom-Cavity System, Phys. Rev. Lett. **121,** 220405 (2018).

[25] M. Landini, N. Dogra, K. Kroeger, L. Hruby, T. Donner, and T. Esslinger, Formation of a Spin Texture in a Quantum Gas Coupled to a Cavity, Phys. Rev. Lett. **120,** 223602 (2018).

[26] J. G. Cosme, J. Skulte, and L. Mathey, Time crystals in a shaken atom-cavity system, Phys. Rev. A **100,** 053615 (2019).

[27] N. Dogra, M. Landini, K. Kroeger, L. Hruby, T. Donner, and T. Esslinger, Dissipation-induced structural instability and chiral dynamics in a quantum gas, Science **366,** 1496 (2019).

[28] G. Bentsen, I.-D. Potirniche, V. B. Bulchandani, T. Scaffidi, X. Cao, X.-L. Qi, M. Schleier-Smith, and E. Altman, Integrable and Chaotic Dynamics of Spins Coupled to an Optical Cavity, Phys. Rev. X **9,** 041011 (2019).

[29] S. B. Jäger, M. J. Holland, and G. Morigi, Superradiant optomechanical phases of cold atomic gases in optical resonators, Phys. Rev. A **101,** 023616 (2020).

[30] H. Keßler, P. Kongkhambut, C. Georges, L. Mathey, J. G. Cosme, and A. Hemmerich, Observation of a Dissipative Time Crystal, Phys. Rev. Lett. **127,** 043602 (2021).

[31] C. Georges, J. G. Cosme, H. Keßler, L. Mathey, and A. Hemmerich, Dynamical density wave order in an atom–cavity system, New J. Phys. **23,** 023003 (2021).

[32] R. Rosa-Medina, F. Ferri, F. Finger, N. Dogra, K. Kroeger, R. Lin, R. Chitra, T. Donner, and T. Esslinger, Observing Dynamical Currents in a Non-Hermitian Momentum Lattice, Phys. Rev. Lett. **128,** 143602 (2022).

[33] P. Kongkhambut, J. Skulte, L. Mathey, J. G. Cosme, A. Hemmerich, and H. Keßler, Observation of a continuous time crystal, Science **377,** 670 (2022).

[34] D. Dreon, A. Baumgärtner, X. Li, S. Hertlein, T. Esslinger, and T. Donner, Self-oscillating pump in a topological dissipative atom-cavity system, Nature (London) **608,** 494 (2022).

[35] Z. Zhang, D. Dreon, T. Esslinger, D. Jaksch, B. Buca, and T. Donner, Tunable non-equilibrium phase transitions between spatial and temporal order through dissipation, arXiv:2205.01461.

[36] M. O. Scully and M. S. Zubairy, *Quantum Optics* (Cambridge University Press, Cambridge, England, 1997).

[37] U. Gaubatz, P. Rudecki, S. Schiemann, and K. Bergmann, Population transfer between molecular vibrational levels by stimulated Raman scattering with partially overlapping laser fields. A new concept and experimental results, J. Chem. Phys. **92,** 5363 (1990).

[38] N. V. Vitanov, A. Rangelov, B. W. Shore, and K. Bergmann, Stimulated Raman adiabatic passage in physics, chemistry, and beyond, Rev. Mod. Phys. **89,** 015006 (2017).

[39] M. Fleischhauer, A. Imamoglu, and J. P. Marangos, Electromagnetically induced transparency: Optics in coherent media, Rev. Mod. Phys. **77,** 633 (2005).

[40] K.-J. Boller, A. Imamoğlu, and S. E. Harris, Observation of Electromagnetically Induced Transparency, Phys. Rev. Lett. **66,** 2593 (1991).

[41] M. O. Scully, S.-Y. Zhu, and A. Gavrielides, Degenerate Quantum-Beat Laser: Lasing without Inversion and Inversion without Lasing, Phys. Rev. Lett. **62,** 2813 (1989).

[42] J. Mompart and R. Corbalán, Lasing without inversion, J. Opt. B **2,** R7 (2000).

[43] E. G. Dalla Torre, J. Otterbach, E. Demler, V. Vuletic, and M. D. Lukin, Dissipative Preparation of Spin Squeezed Atomic Ensembles in a Steady State, Phys. Rev. Lett. **110,** 120402 (2013).

[44] A. Piñeiro Orioli, J. K. Thompson, and A. M. Rey, Emergent Dark States from Superradiant Dynamics in Multilevel Atoms in a Cavity, Phys. Rev. X **12,** 011054 (2022).

[45] See Supplemental Material at http://link.aps.org/supplemental/10.1103/PhysRevLett.130.163603 for more details, which includes Refs. [46,47].

[46] M. Abramowitz and I. A. Stegun, *Handbook of Mathematical Functions with Formulas, Graphs, and Mathematical Tables* (Dover, New York, 1964).

[47] J. Keeling, M. J. Bhaseen, and B. D. Simons, Collective Dynamics of Bose-Einstein Condensates in Optical Cavities, Phys. Rev. Lett. **105,** 043001 (2010).

[48] H. Keßler, J. Klinder, M. Wolke, and A. Hemmerich, Optomechanical atom-cavity interaction in the sub-recoil regime, New J. Phys. **16,** 053008 (2014).

[49] J. Klinder, H. Keßler, C. Georges, J. Vargas, and A. Hemmerich, Bose–Einstein condensates in an optical cavity with sub-recoil bandwidth, Appl. Phys. B **122,** 299 (2016).

[50] A. Polkovnikov, Phase space representation of quantum dynamics, Ann. Phys. (Amsterdam) **325,** 1790 (2010).

[51] H. Keßler, J. G. Cosme, M. Hemmerling, L. Mathey, and A. Hemmerich, Emergent limit cycles and time crystal dynamics in an atom-cavity system, Phys. Rev. A **99,** 053605 (2019).

[52] Richelle Jade L. Tuquero, J. Skulte, L. Mathey, and J. G. Cosme, Dissipative time crystal in an atom-cavity system: Influence of trap and competing interactions, Phys. Rev. A **105,** 043311 (2022).

[53] O. Penrose and L. Onsager, Bose-Einstein condensation and liquid helium, Phys. Rev. **104,** 576 (1956).

[54] A. U. J. Lode and C. Bruder, Fragmented Superradiance of a Bose-Einstein Condensate in an Optical Cavity, Phys. Rev. Lett. **118,** 013603 (2017).

Supplemental Material for
Condensate formation in a dark state of a driven atom-cavity system

Jim Skulte,[1,2,*] Phatthamon Kongkhambut,[1,*] Sahana Rao,[1] Ludwig
Mathey,[1,2] Hans Keßler,[1] Andreas Hemmerich,[1,2] and Jayson G. Cosme[3]

[1]*Zentrum für Optische Quantentechnologien and Institut für Laser-Physik, Universität Hamburg, 22761 Hamburg, Germany*
[2]*The Hamburg Center for Ultrafast Imaging, Luruper Chaussee 149, 22761 Hamburg, Germany*
[3]*National Institute of Physics, University of the Philippines, Diliman, Quezon City 1101, Philippines*
(Dated: February 24, 2023)

I. BEC, CAVITY, AND PUMP BEAM PROPERTIES

The experimental setup, as sketched in Fig. 1(a) in the main text, is comprised of a magnetically trapped BEC of $N_a = 4 \times 10^4$ ^{87}Rb atoms, dispersively coupled to a fundamental mode of a narrowband high-finesse optical cavity. The trap creates a harmonic potential with trap frequencies $(\omega_x, \omega_y, \omega_z) = 2\pi \times (119.0, 102.7, 24.7)$ Hz. The corresponding Thomas-Fermi radii of the ensemble are $(r_x, r_y, r_z) = (3.7, 4.3, 18.1)$ μm. These radii are significantly smaller than the size of the Gaussian shaped pump beam, which has a waist of $w_{\text{pump}} \approx 125$ μm. The pump beam is oriented transversally, with respect to the cavity axis, and retro-reflected to form a standing wave. It passes through an electro-optic modulator (EOM) twice. An AC voltage is applied to the EOM to modulate the phase of the pump field, which leads to an effective shaking of the pump lattice potential.

The pump laser is stabilized to the cavity resonance using high bandwidth servo electronics. As a drawback, the pump light is not strictly monochromatic and besides the narrow carrier, the spectrum contains two servo bumps with a frequency shift of roughly ± 2 MHz. We estimate the light power with in these side peaks being about 30% of the total light power. Since this light is far detuned, with respect to the cavity resonance, it cannot contribute to scatter photons into the cavity. In contrast, light of all frequencies contribute to the depth of the standing wave potential, and hence, contributes to the shift of the resonance frequency of the dark state $\omega_D = (2 + \epsilon_p/4) \omega_{\text{rec}}$. Therefore the dark state resonance frequency in the experiment is larger than the one used in our theoretical models.

The cavity field has a decay rate of $\kappa \approx 2\pi \times 3.6$ kHz, which equals the recoil frequency $\omega_{\text{rec}} = E_{\text{rec}}/\hbar = 2\pi \times 3.6$ kHz for ^{87}Rb atoms at the pump wavelength of $\lambda_P = 803.00$ nm. The pump laser is red detuned with respect to the relevant atomic transition of ^{87}Rb at 794.98 nm. The maximum light shift per atom is $U_0 = 2\pi \times 0.4$ Hz.

II. CAVITY FIELD DETECTION

Our experimental system is equipped with two detection setups for the light leaking out of the cavity. On one side of the cavity, we use a single photon counting module (SPCM), which gives access to the intensity of the intracavity field and the associated photon statistics. On the other side of the cavity, a balanced heterodyne detection setup is installed, which uses the pump beam as a local reference. The beating signal of the local oscillator with the light leaking out of the cavity allows for the observation of the time evolution of the intracavity photon number N_P and the phase difference between the pump and the cavity field φ.

III. EXPERIMENTAL PROTOCOL TO OBTAIN THE POPULATION OF THE DARK STATE N_D

To obtain the population of the dark state N_D experimentally, we ramp down the pump laser strength adiabatically within 0.5 ms, similar to the theoretical protocol described in the context of Fig.2(b) in the main text. Subsequently, a ballistic expansion of 25 ms is applied and an absorption image of the resulting density distribution is recorded, time-of-flight (TOF). Finally, N_D is obtained by summing up the occupations around the momentum modes $\{\pm 1, \pm 1\}\hbar k$, in accordance with the findings in Figs.3(d) and Fig.3(e) in the main text.

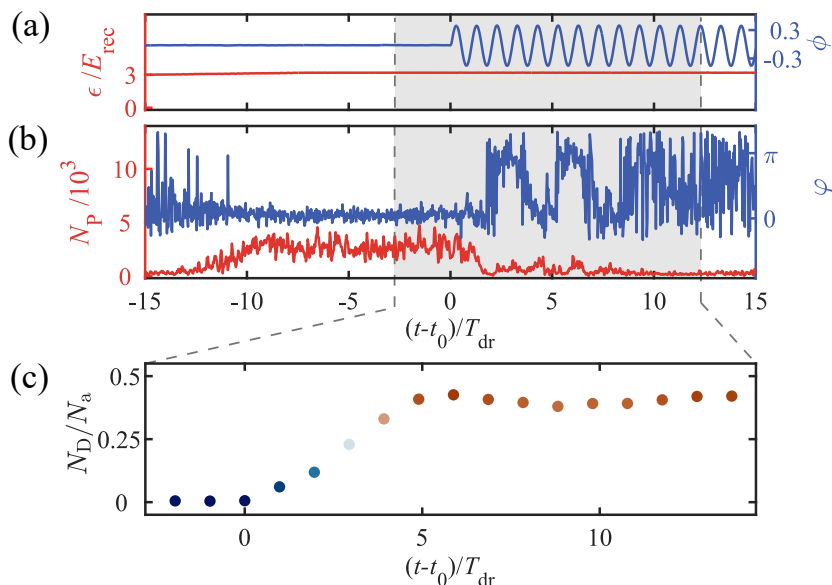*   These authors have contributed equally to this work.

FIG. 1. Typical experimental run. (a) Experimental protocol for the intensity (red) and the phase (dashed blue) of the pump field. (b) In situ number of photons (red) in the cavity N_{P} and the corresponding phase difference φ (blue) between the pump and cavity fields. (c) Population of the dark state rescaled by the total particle number N_{a} (coherent fraction) for different number of driving cycles derived from TOF images.

IV. DYNAMICS DURING A TYPICAL EXPERIMENTAL RUN

Our experimental sequence starts by preparing a BEC and overlap it with the $\mathrm{TEM_{00}}$ mode of our cavity. We linearly increase the pump strength ϵ to its desired value to initialise the system into the self-organized superradiant phase. This is indicated by a finite photon number N_{P} (red trace in Fig. 1(b)) and by the fixed phase difference φ between the pump and cavity fields. At time $t - t_0 = 0$ we switch on the phase modulation of the pump lattice, which leads to a periodic shaking of the optical potential. The system starts to oscillate between the two possible self-organized density patterns, which can be seen by the phase difference φ switching between 0 and π. This is accompanied by an increase in the population of the dark state $N_{\mathrm{D}}/N_{\mathrm{a}}$ until it reaches its maximum value at time $t - t_0 = 5\,T_{\mathrm{dr}}$, where T_{dr} is the driving period. Due to the increasing population of the dark state the atoms step by step decouple from the cavity field and slowly stop scattering photons from the pump into the cavity and vice versa. The photon number N_{P} approaches zero and the light field phase φ shows random values between 0 and 2π. The system is now in a steady state and the population of the dark state, normalized to the total number of coherent atoms $N_{\mathrm{D}}/N_{\mathrm{a}}$, stays constant. Fig. 2(a) shows the dynamics of the relative population of all relevant momentum modes. Fig. 2(b) depicts the corresponding time evolution of N_{a}. As soon as the shaking starts ($t - t_0 = 0$), the total particle number N_{a} drops rapidly due to cavity-field-induced heating. After the atoms are decoupled from the cavity field, the heating rate decreases.

V. COMPARISON OF THE RELATIVE POPULATION OF THE DARK STATE FOR PUMP LIGHT CLOSE AND FAR DETUNED WITH RESPECT TO THE CAVITY RESONANCE

We present in Fig. 3(a),(c) the experimentally obtained phase diagrams showing the population of the dark state with respect to the driving frequency $\omega_{\mathrm{dr}}/\omega_{\mathrm{D}}$ and driving strength f_0. In Figs. 3(b),(d), we show the population of the $\{p_{\mathrm{y}}, p_{\mathrm{z}}\} = \{\pm 2, 0\}\hbar k$ momentum modes for the pump light, close and far detuned with respect to the cavity resonance. For the far detuned case, the cavity is basically inactive and we do not observe population of the dark state, which demonstrates the importance of cavity photons for the excitation of the dark state. Moreover, the parameter range, wherein we observe population of the $\{p_{\mathrm{y}}, p_{\mathrm{z}}\} = \{\pm 2, 0\}\hbar k$ momentum modes, is very similar for both cases, only its amplitude increases for the far detuned case since there are no atoms pumped into the dark state.

As explained in the second paragraph of Sec.I, the dark state frequency is larger in the experiment than in our theoretical models. In our experimental observations, the resonance frequency for excitation of the $\{p_{\mathrm{y}}, p_{\mathrm{z}}\} = \{\pm 2, 0\}\hbar k$ momentum modes lies at $\approx 1.45\,\omega_{\mathrm{dr}}/\omega_{\mathrm{D}}$. In SFig. 3(a), we see that in fact the transfer of atoms into the dark state is suppressed if the $\{\pm 2, 0\}\hbar k$ resonance is approached. Rather, the atoms are transferred into the second band, as shown in SFig. 3(b), without photon scattering into the cavity. The plots in (c) and (d) for large pump-cavity detuning δ_{C} show that no dark state population
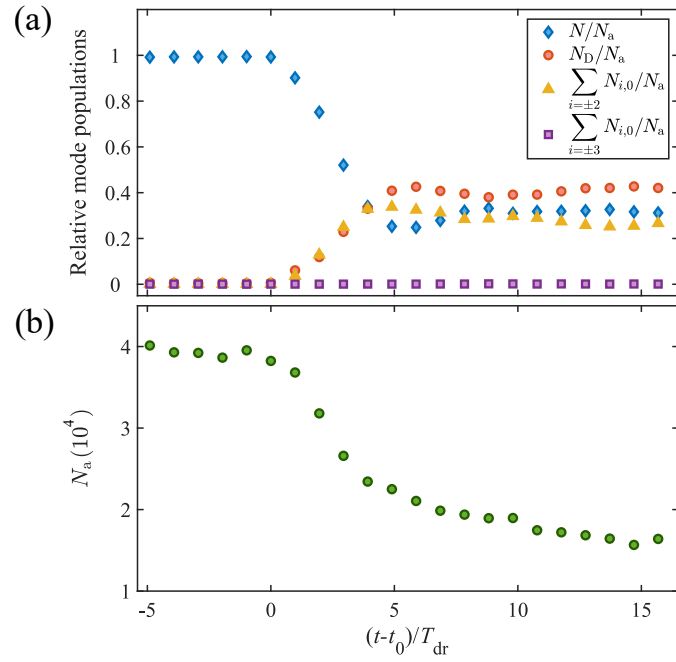
FIG. 2. (a) Time evolution of the population of the relevant momentum modes normalized to the total number of atoms (coherent fraction). (b) Time evolution of the total number of coherent atoms N_a.
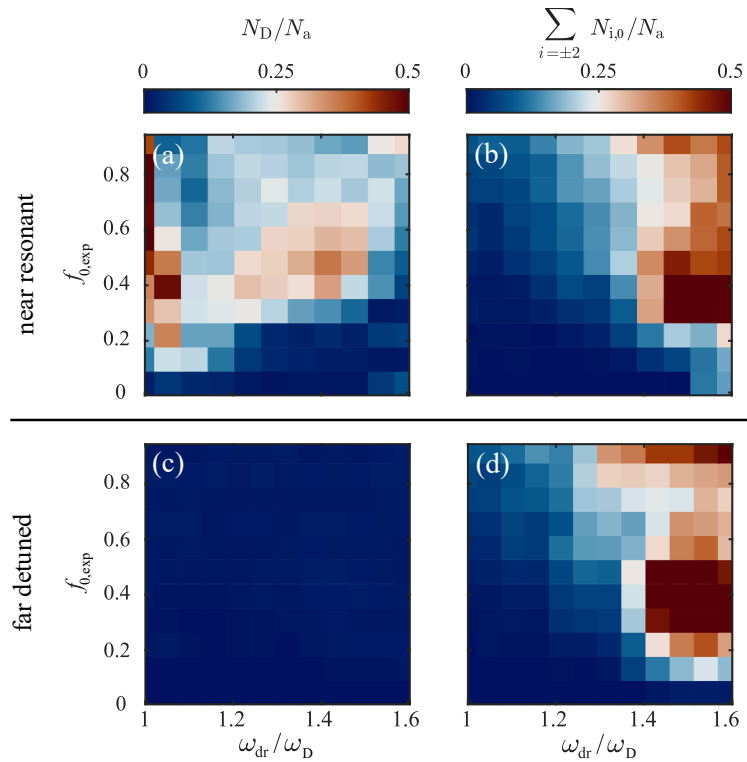
FIG. 3. Relative population of the dark state for different driving frequencies ω_{dr}/ω_D and driving strengths f_0 for (a) the pump light close to resonance ($\delta_C = -2\pi \times 30$ kHz) and (c) far detuned from cavity resonance after six driving cycles. The driving frequency axis is rescaled by the resonance frequency of the dark state ω_D. (b) and (d) show the relative population of the $\{p_y, p_z\} = \{\pm 2, 0\}\hbar k$ momentum modes, which indicates the atoms populating the third band.

arises, while the direct excitation of the $\{\pm 2, 0\}\hbar k$ momentum modes prevails. Finally, in our numerical models, the $\{\pm 2, 0\}\hbar k$ resonance arises at $\approx 1.7\omega_{\mathrm{dr}}/\omega_{\mathrm{D}}$, which lies outside of the range of our simulations.

VI.   ATOM-CAVITY SYSTEM

Our system is well described by the Hamiltonian [1–4]

$$\hat{H}/\hbar = -\delta_{\mathrm{C}}\hat{a}^\dagger\hat{a} + \int dy\,dz\,\hat{\Psi}^\dagger(y, z)\left[-\frac{\hbar}{2m}\nabla^2 - \omega_{\mathrm{rec}}\epsilon_{\mathrm{p}}\cos^2(ky + \phi(t)) + U_0\,\hat{a}^\dagger\hat{a}\cos^2(kz)\right. \tag{1}$$
$$\left. - \sqrt{\omega_{\mathrm{rec}}|U_0|\epsilon_{\mathrm{p}}}\cos(ky + \phi(t))\cos(kz)(a^\dagger + a)\right]\hat{\Psi}(y, z),$$

where δ_{C} is the pump-cavity detuning, and $U_0 < 0$ is the frequency shift of the cavity resonance due to a single atom ($|U_0| = 2\pi \times 0.4\,\mathrm{kHz}$). The phase of the pump field is periodically driven according to $\phi(t) = f_0\sin(\omega_{\mathrm{dr}}t)$ with the modulation index f_0 and the modulation frequency ω_{dr}. Furthermore, $\hat{a}$ ($\hat{a}^\dagger$) is the annihilation (creation) operator for a photon in the single-mode cavity, while $\hat{\Psi}$ ($\hat{\Psi}^\dagger$) is the bosonic annihilation (creation) field operator for the atoms. Here, k denotes the wave number of the pump light, ϵ_{p} is the the pump strength, quantified in terms of the maximal energy depth of the pump lattice in units of the recoil energy $E_{\mathrm{rec}} = \hbar\omega_{\mathrm{rec}}$ with the recoil frequency $\omega_{\mathrm{rec}} = \hbar k^2/2m$, where m is the atomic mass. The experiment operates in the recoil-resolved regime, i.e., the loss rate of the cavity photons κ is smaller than the recoil frequency ω_{rec}. For our system $\omega_{\mathrm{rec}} = 2\pi \times 3.6\,\mathrm{kHz}$. We emphasize the importance of the recoil-resolved regime [5, 6] to excite the atoms into the dark state, as the underlying mechanism relies on a coherent coupling of a limited number of momentum modes.

VII.   PROCESSES FOR POPULATING THE DARK STATE

We briefly discuss the different scattering channels for populating the dark state in our theoretical models, i.e., the three-mode Dicke model and full-atom cavity simulations, and in the experimental setup.

First, we discuss the difference between the full atom-cavity model and the three-level Dicke model. In the full atom-cavity system, we achieve a higher dark state population as compared to the results of the three-mode Dicke model after 7 driving cycles. In the three-mode model, we only consider momentum modes up to $\{p_{\mathrm{y}}, p_{\mathrm{z}}\} = \{\pm 1, \pm 1\}\hbar k$ and neglect the $\{p_{\mathrm{y}}, p_{\mathrm{z}}\} = \{\pm 2, 0\}\hbar k$ modes. However, as can be seen from the last line in the Hamiltonian in Eq. 4, atoms in the $\{p_{\mathrm{y}}, p_{\mathrm{z}}\} = \{\pm 2, 0\}\hbar k$ modes can be transferred into the dark state $|\mathrm{D}\rangle \equiv \sum_{\nu,\mu\in\{-1,1\}}\nu|\nu\hbar k, \mu\hbar k\rangle$. This enhances the dark state population in the full atom-cavity system as compared to the three-mode Dicke model.

Next, we discuss the population of the dark state in the experiment. While the experiment includes the channel for scattering from $\{p_{\mathrm{y}}, p_{\mathrm{z}}\} = \{\pm 2, 0\}\hbar k$ into the dark state, there are additional factors that decrease the efficiency of populating the dark state, i.e., heating and atom loss introduced by phase modulation of the pump wave. The atom loss effectively shifts the critical pump strength required to enter the superradiant phase, as the number of scatterers of photons decreases. Since cavity-photon-mediated interactions are necessary for the transfer of atoms into the dark state, atom loss, which decreases the occupation of the cavity mode, attenuates the process of populating the dark state. Furthermore, in the experiment, as discussed in Sec. I, the additional side lobes of the pump beam frequency spectrum push the dark state resonance towards higher frequencies. This effectively reduces the regime where the dark state can be populated, which is restricted to driving frequencies smaller than the resonance for excitation of the $\{p_{\mathrm{y}}, p_{\mathrm{z}}\} = \{\pm 2, 0\}\hbar k$ momentum modes. The latter resonance gives rise to an efficient transfer of the atoms into the maximum of the second band of the pump wave potential. The relevant driving term in Eq. 1 is $2\phi(t)\sin(2ky)$, which arises by approximating $\cos(ky + \phi(t))^2$ for the case of small driving strengths. We note that the corresponding resonance frequency is light-shifted by the pump beam, however, this effect can be neglected for the relatively shallow pump lattice used in this work.

VIII.   THREE-LEVEL SYSTEM

As first shown in [3], the Hamiltonian in Eq. 1 can be mapped onto a parametrically driven dissipative three level model. Here, to capture the effects for strong driving, where $f_0 \ll 1$ is not fulfilled, we use trigonometric identities and the following

Jacobi-Anger expansions [7]

$$\cos(z\sin(\theta)) = J_0(z) + 2\sum_{n=1}^{\infty} J_{2n}(z)\cos(2n\theta) \tag{2}$$

$$\sin(z\sin(\theta)) = 2\sum_{n=1}^{\infty} J_{2n-1}(z)\cos((2n-1)\theta). \tag{3}$$

The Hamiltonian in Eq. 1 acquires the form

$$\hat{H}/\hbar = -\delta_{\mathrm{C}}\hat{a}^\dagger\hat{a} + U_0\hat{a}^\dagger\hat{a}\int dydz\,\hat{\Psi}^\dagger(y,z)\cos^2(kz)\hat{\Psi}(y,z) \tag{4}$$

$$-\omega_{\mathrm{rec}}\epsilon_{\mathrm{p}}\int dydz\,\hat{\Psi}^\dagger(y,z)\frac{1+\cos(2ky)\left[J_0(2f_0)+2h_2(t)\right]-2\sin(2ky)g_2(t)}{2}\hat{\Psi}(y,z)$$

$$-\sqrt{\omega_{\mathrm{rec}}|U_0|\epsilon_{\mathrm{p}}}(a^\dagger+a)\int dydz\,\hat{\Psi}^\dagger(y,z)\cos(ky)\cos(kz)\left(J_0(f_0)+2h_1(t)\right)\hat{\Psi}(y,z)$$

$$+\sqrt{\omega_{\mathrm{rec}}|U_0|\epsilon_{\mathrm{p}}}(a^\dagger+a)\int dydz\,\hat{\Psi}^\dagger(y,z)\sin(ky)\cos(kz)2g_1(t)\hat{\Psi}(y,z),$$

where we defined $h_2(t) = \sum_{n=1}^{\infty} J_{2n}(2f_0)\cos(2n\omega_{\mathrm{dr}}t)$ and $g_2(t) = \sum_{n=1}^{\infty} J_{2n-1}(2f_0)\sin((2n-1)\omega_{\mathrm{dr}}t)$ and $h_1(t) = \sum_{n=1}^{\infty} J_{2n}(f_0)\cos(2n\omega_{\mathrm{dr}}t)$ and $g_1(t) = \sum_{n=1}^{\infty} J_{2n-1}(f_0)\sin((2n-1)\omega_{\mathrm{dr}}t)$.

Next, the atomic field operator is approximated as

$$\hat{\Psi}(y,z) = \hat{c}_0\psi_0(y,z) + \hat{c}_1\psi_1(y,z) + \hat{c}_2\psi_2(y,z) \tag{5}$$

where $\hat{c}_i$ are bosonic annihilation operator, and $\psi_0(y,z) = 1$, $\psi_1(y,z) = 2\cos(ky)\cos(kz)$ and $\psi_2(y,z) = 2\sin(ky)\cos(kz)$. We note that in applying this approximation we neglect higher momentum mode contributions, e.g. $\cos(2ky)$, which contribute heavily for higher driving frequencies around ~ 14.5 kHz as can be seen in Fig. 3.

Under parity change $y \to -y$ these wave functions transform as

$$\mathcal{P}_y\psi_0(y,z) = \psi_0(-y,z) = +\psi_0(y,z) \tag{6}$$
$$\mathcal{P}_y\psi_1(y,z) = \psi_1(-y,z) = +\psi_1(y,z) \tag{7}$$
$$\mathcal{P}_y\psi_2(y,z) = \psi_2(-y,z) = -\psi_2(y,z)\,. \tag{8}$$

Hence, only ψ_2 gets a minus sign upon application of $\mathcal{P}_y$. Using a Schwinger boson representation, the bosonic operators can be mapped onto pseudo-spin operators to obtain a driven three-level Dicke Hamiltonian

$$H/\hbar = \omega\hat{a}^\dagger\hat{a} + (\omega_{\mathrm{B}} - \Delta_{f_0})\,\hat{J}_z^{\mathrm{B}} + (\omega_{\mathrm{D}} + \Delta_{f_0})\,\hat{J}_z^{\mathrm{D}} + f_2(t)\,(\omega_{\mathrm{B}} - \omega_{\mathrm{D}})\left(\hat{J}_z^{\mathrm{D}} - \hat{J}_z^{\mathrm{B}}\right) + 2g_2(t)\,(\omega_{\mathrm{B}} - \omega_{\mathrm{D}})\,\hat{J}_x^{\mathrm{BD}} \tag{9}$$

$$+ \frac{2\left(\lambda_{f_0} + \eta(t)\right)}{\sqrt{N}}\left(\hat{a}^\dagger + \hat{a}\right)\hat{J}_x^{\mathrm{B}} - \frac{2\zeta(t)}{\sqrt{N}}\left(\hat{a}^\dagger + \hat{a}\right)\hat{J}_x^{\mathrm{D}},$$

where $\omega_{\mathrm{D}} = 2\omega_{\mathrm{rec}}(1 - \frac{\epsilon_{\mathrm{p}}}{8})$, $\omega_{\mathrm{B}} = 2\omega_{\mathrm{rec}}(1 + \frac{\epsilon_{\mathrm{p}}}{8})$, $\Delta_{f_0} = \frac{\epsilon_{\mathrm{p}}\omega_{\mathrm{rec}}}{4}(1 - J_0(2f_0))$, $2\lambda \equiv \sqrt{N_{\mathrm{a}}\epsilon_{\mathrm{p}}\omega_{\mathrm{rec}}|U_0|}$, $\lambda_{f_0} = J_0(f_0)\lambda$, $\eta(t) = 2h_1(t)\lambda$ and $\zeta(t) = 2g_1(t)\lambda$. Expanding this Hamiltonian up to linear order in the driving strength f_0 leads to the parametrically driven dissipative three-level Dicke model presented in [3, 4].

A. Large κ limit

Within our three-level Dicke model we can adiabatically eliminate the light field, if $\kappa \gg \omega_{\mathrm{rec}}$. That is, we assume $\frac{da}{dt} \approx 0$ and solve for a to obtain an atom-only or spin-only like three-level model

$$\hat{H}_{\mathrm{eff}}/\hbar = (\omega_{\mathrm{B}} - \Delta_{f_0})\,\hat{J}_z^{\mathrm{B}} + (\omega_{\mathrm{D}} + \Delta_{f_0})\,\hat{J}_z^{\mathrm{D}} + f_2(t)\,(\omega_{\mathrm{B}} - \omega_{\mathrm{D}})\left(\hat{J}_z^{\mathrm{D}} - \hat{J}_z^{\mathrm{B}}\right) + 2g_2(t)\,(\omega_{\mathrm{B}} - \omega_{\mathrm{D}})\,\hat{J}_x^{\mathrm{BD}} \tag{10}$$

$$- \Lambda\left((J_0(f_0) + 2h_1(t))^2\,\hat{J}_x^{\mathrm{D}}\hat{J}_x^{\mathrm{D}} - (J_0(f_0) + 2h_1(t))\,2g_1(t)\left[\hat{J}_x^{\mathrm{D}}\hat{J}_x^{\mathrm{B}} + \hat{J}_x^{\mathrm{B}}\hat{J}_x^{\mathrm{D}}\right] + 4g_1(t)^2\,\hat{J}_x^{\mathrm{B}}\hat{J}_x^{\mathrm{B}}\right),$$

with $\Lambda = 8\lambda^2\omega/(N(\kappa^2+\omega^2))$. This is the three-level generalisation of the prescription for mapping the standard two-level Dicke model onto the Lipkin-Meshkov-Glick model by adiabatically eliminating the photon dynamics [8]. In Fig. 4, the corresponding phase diagram for varying driving strength and driving frequency is shown for $\lambda = 1.05\,\lambda_{\mathrm{crit}}$. Note, that in a full description of the atom-cavity setup in terms of Eq. 1, a large value of κ would enable the excitation of higher modes, not included here, with the consequence of decoherence and heating.
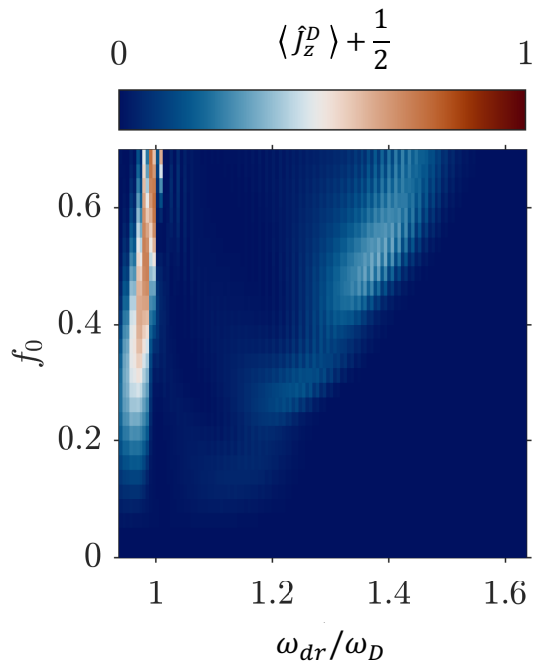
FIG. 4. Population of the dark state for different driving frequencies ω_{dr} and driving strengths f_0 calculated for the Hamiltonian Eq. 10. The driving frequency axis is rescaled by the characteristic frequency of the dark state ω_{D}. The phase diagram is constructed for 7 driving cycles.

IX. DARK STATE CONDENSATION BELOW THE CRITICAL PUMP STRENGTH

Here, we briefly show the dark state condensation starting below the critical pump strength. We ramp up the pump strength to $\epsilon \approx 0.96\,\epsilon_{\mathrm{crit}}$ and start the modulation after 10 ms. In Fig. 5, it can be seen that after the modulation is switched on, the light field builds up before it vanishes again after a large fraction of atoms occupies the dark state as can be seen from the long-time behaviour in Fig. 6. This again highlights the importance of the intra-cavity field for transfering the atoms into the dark state. We note that the transition into the dark state is slower compared to the case starting from the superradiant phase discussed in the main text.
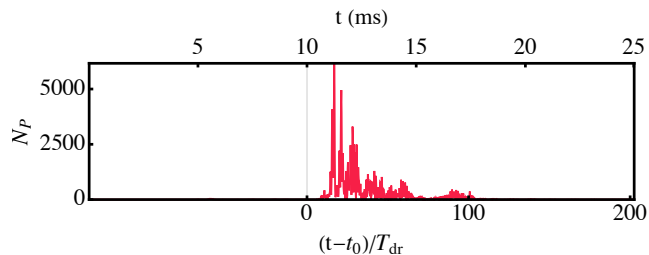
FIG. 5. Number of photons inside the cavity. The periodic drive is switched on at t_0. The parameters are the same as those used in Fig. 4 except for $\epsilon \approx 0.96\,\epsilon_{\mathrm{crit}}$.

X. MODE POPULATION DURING THE RAMP-DOWN PROCESS

Fig. 7 presents the occupation of the sum of the $\{\pm1, \pm1\}\hbar k$ momentum modes, the $|\mathrm{D}\rangle$ as well as the $|\mathrm{N}\rangle$, before, during and after the ramp-down of the pump laser for varying driving strength and driving frequencies rescaled by the characteristic dark state frequency ω_{D}. Before the ramp-down process the population of the $|\mathrm{D}\rangle$ and $|\mathrm{B}\rangle$ cannot be distinguished by summing up the $\{\pm1, \pm1\}\hbar k$ momentum modes in a TOF image. However during the ramp-down the populations of $|\mathrm{B}\rangle$ is transferred back
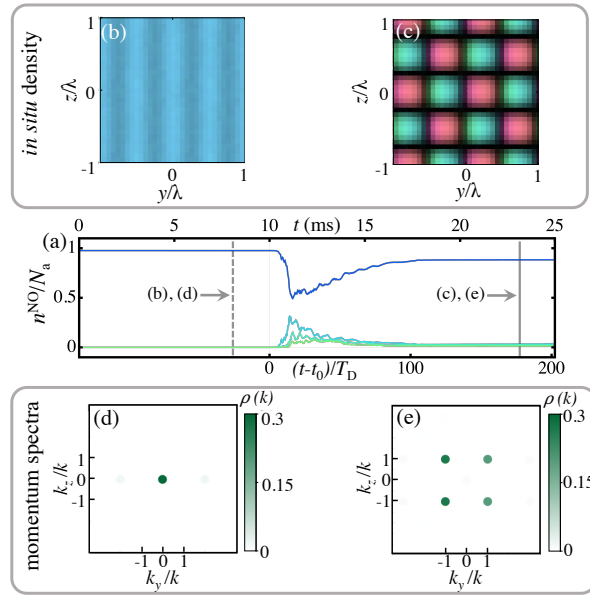
FIG. 6. (a) TWA results for the evolution of the five highest eigenvalues of the single-particle correlation function at equal time (SPCF). Gray vertical lines denote the times when the snapshots of the single-particle density in (b) and (c) are taken. (b), (c) The real space densities are color coded to show the phase within the (y, z)-plane. (d), (e) Momentum spectra at times indicated in (a).

into the $|N\rangle$ and the phase diagram of the population of the $\{\pm 1, \pm 1\}\hbar k$ momentum modes and the population of the dark state $|D\rangle$ are approximately the same. This motivates us to measure the population of $|D\rangle$ using this scheme.

[1] H. Ritsch, P. Domokos, F. Brennecke, and T. Esslinger, Cold atoms in cavity-generated dynamical optical potentials, Rev. Mod. Phys. **85**, 553 (2013).
[2] J. G. Cosme, J. Skulte, and L. Mathey, Time crystals in a shaken atom-cavity system, Phys. Rev. A **100**, 053615 (2019).
[3] J. Skulte, P. Kongkhambut, H. Keßler, A. Hemmerich, L. Mathey, and J. G. Cosme, Parametrically driven dissipative three-level dicke model, Phys. Rev. A **104**, 063705 (2021).
[4] P. Kongkhambut, H. Keßler, J. Skulte, L. Mathey, J. G. Cosme, and A. Hemmerich, Realization of a periodically driven open three-level dicke model, Phys. Rev. Lett. **127**, 253601 (2021).
[5] H. Keßler, J. Klinder, M. Wolke, and A. Hemmerich, Optomechanical atom-cavity interaction in the sub-recoil regime, New Journal of Physics **16**, 053008 (2014).
[6] J. Klinder, H. Keßler, C. Georges, J. Vargas, and A. Hemmerich, Bose–einstein condensates in an optical cavity with sub-recoil bandwidth, Applied Physics B **122**, 299 (2016).
[7] M. Abramowitz and I. A. Stegun, *Handbook of Mathematical Functions with Formulas, Graphs, and Mathematical Tables* (Dover, New York, 1964).
[8] J. Keeling, M. J. Bhaseen, and B. D. Simons, Collective dynamics of bose-einstein condensates in optical cavities, Phys. Rev. Lett. **105**, 043001 (2010).
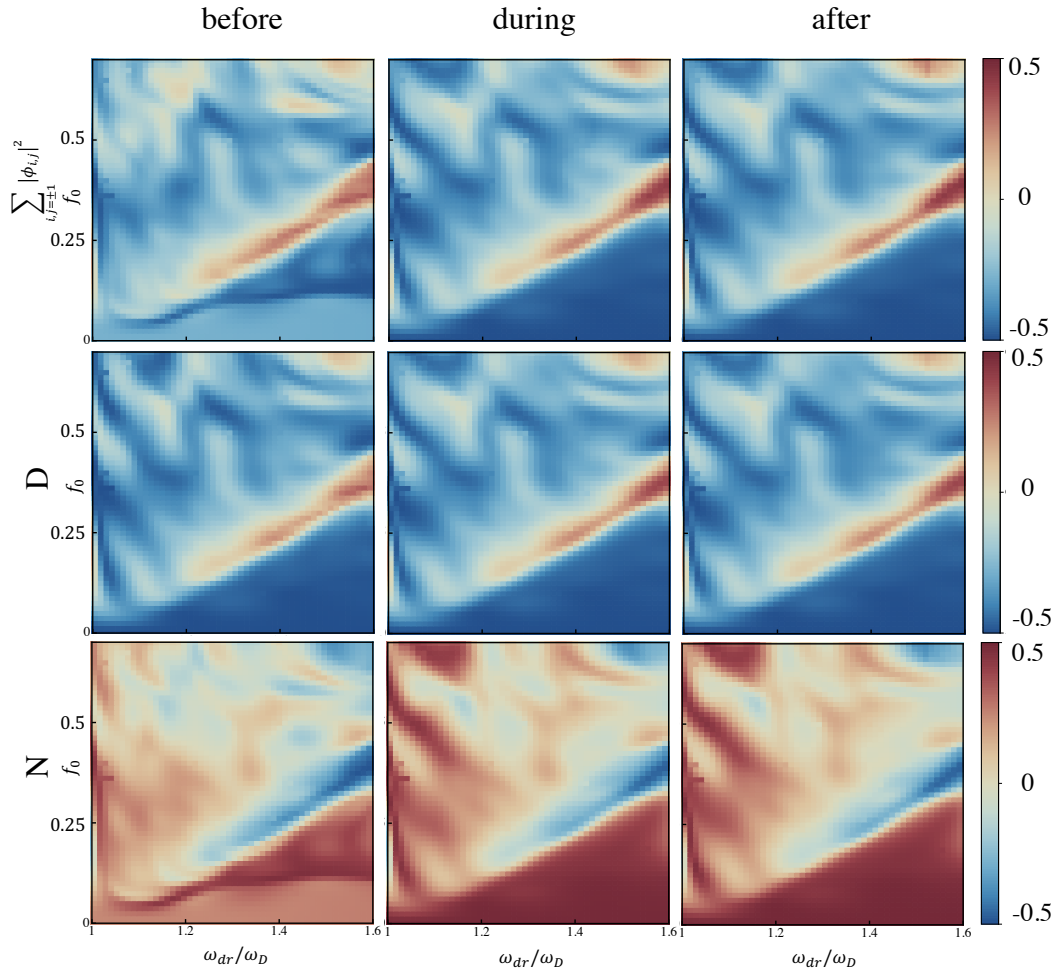
FIG. 7. Population of the $\{\pm1, \pm1\}\hbar k$ momentum modes, the dark state and the ground state for different driving frequencies ω_{dr} and driving strengths f_0. The driving frequency axis is rescaled by the characteristic frequency of the dark state, ω_{D}.

2.11 Publication VI: Observation of a continuous time crystal

P. Kongkhambut, <u>J. Skulte</u>, L. Mathey, J.G. Cosme, A. Hemmerich and H. Keßler
— **Science 377, 670-673 (2022)**

Motivation

This work was motivated by the recent proposal to realise time crystal by Frank Wilczek. While discrete time crystal in closed and open systems have been observed previously, the goal of this paper was to realise and understand the first, so called, continuous time crystal (CTC). Here, the time translational symmetry is spontaneously broken as the systems enters the CTC phase.

Main findings

In this work, first-authored by Phatthamon Kongkhambut, we successfully observed the first CTC. On order to achieve this, a time-independent pump laser was used to enter a limit cycle phase, which is characterised by emergent periodic oscillations in the light-field intensity and the atomic density. We showed that the phase of those oscillations is random for different realisations. Numerically, we showed that this is due to quantum fluctuations in the initial state and stochastical noise stemming from cavity losses. We mapped out the phase diagram and showed the robustness of the CTC against temporal noise in the pump laser intensity. Numerically, we investigated the stability against varying particle numbers. Hence, with all these studies, we successfully showed the first realisation of a continuous time crystal.

Contribution

PK and HK performed the experiments and data analysis. The simulations were performed by me and JGC, supported by LM. The project was designed and supervised by HK and AH. All authors contributed to the discussion and interpretation of the results, conceptualizing of the figures, as well as to writing the manuscript.

QUANTUM DYNAMICS

Observation of a continuous time crystal

Phatthamon Kongkhambut[1], Jim Skulte[1,2], Ludwig Mathey[1,2], Jayson G. Cosme[3], Andreas Hemmerich[1,2]*, Hans Keßler[1]*

Time crystals are classified as discrete or continuous depending on whether they spontaneously break discrete or continuous time translation symmetry. Although discrete time crystals have been extensively studied in periodically driven systems, the experimental realization of a continuous time crystal is still pending. We report the observation of a limit cycle phase in a continuously pumped dissipative atom-cavity system that is characterized by emergent oscillations in the intracavity photon number. The phase of the oscillation was found to be random for different realizations, and hence, this dynamical many-body state breaks continuous time translation symmetry spontaneously. Furthermore, the observed limit cycles are robust against temporal perturbations and therefore demonstrate the realization of a continuous time crystal.

Time crystals are dynamical many-body states that break time translation symmetry in a spontaneous and robust manner (1, 2). The original quantum time crystal envisaged by Wilczek involves a closed many-body system with all-to-all coupling that breaks continuous time translation symmetry by exhibiting oscillatory dynamics in its lowest-energy equilibrium state even though the underlying Hamiltonian is time-independent (1). This would constitute a startling state of matter in motion, fundamentally protected from bringing this motion to a standstill through energy removal. However, a series of no-go theorems have shown that nature prohibits the realization of such time crystals in isolated systems (3–5). The search for time crystals was thus extended to include equilibrium scenarios in periodically driven closed systems (6–8). This has led to realizations of discrete time crystals, which break the discrete time translation symmetry imposed by the external drive (9–17). In such discrete time crystals, during a short initial phase, the drive slightly excites the system until the system decouples from the drive, so that further energy or entropy flow is terminated. The system develops a subharmonic response, an intrinsic oscillation at a frequency slower than that of the drive. Initially, it was argued that dissipation, and hence the use of open systems, must be carefully avoided; then, so-called dissipative discrete time crystals were theoretically predicted (18) and experimentally realized (19–21). As shown in a number of theoretical works (22–24), the use of open systems comes with the unexpected consequence that continuous instead of periodic driving suffices to induce time crystal dynamics. These continuous time crystals (CTCs) realize the spirit of

the original proposal more closely than discrete time crystals and circumvent the no-go theorems through their open character.

Here, we report the observation of a CTC in the form of a limit cycle phase in a continuously pumped dissipative atom-cavity system (Fig. 1A). In classical nonlinear dynamics, the term "limit cycle", coined by Poincaré in a math-

ematical context (25), denotes a closed phase space trajectory, asymptotically approached by at least one neighboring trajectory. Although limit cycles are well-established in classical nonlinear physics (26), there are two essential conditions for limit cycles in open quantum systems to form a CTC. First, the formation of the limit cycle must be associated with spontaneous breaking of continuous time translation symmetry. That is, the relative time phase of the oscillations for repeated realizations takes random values between 0 and 2π. Second, the limit cycle phase is robust against temporal perturbations of technical or fundamental character, such as quantum noise and, for open systems, fluctuations associated with dissipation. The characteristic signature of the CTC presented here is a persistent oscillation of the intracavity intensity and atomic density (Fig. 1, B and C), which complies with the robustness and spontaneous symmetry-breaking criteria (Fig. 1D).

Our experimental setup consists of a Bose-Einstein condensate (BEC) of $N_a \approx 5 \times 10^4$ ^{87}Rb atoms inside a high-finesse optical cavity. The system is transversely pumped with a standing
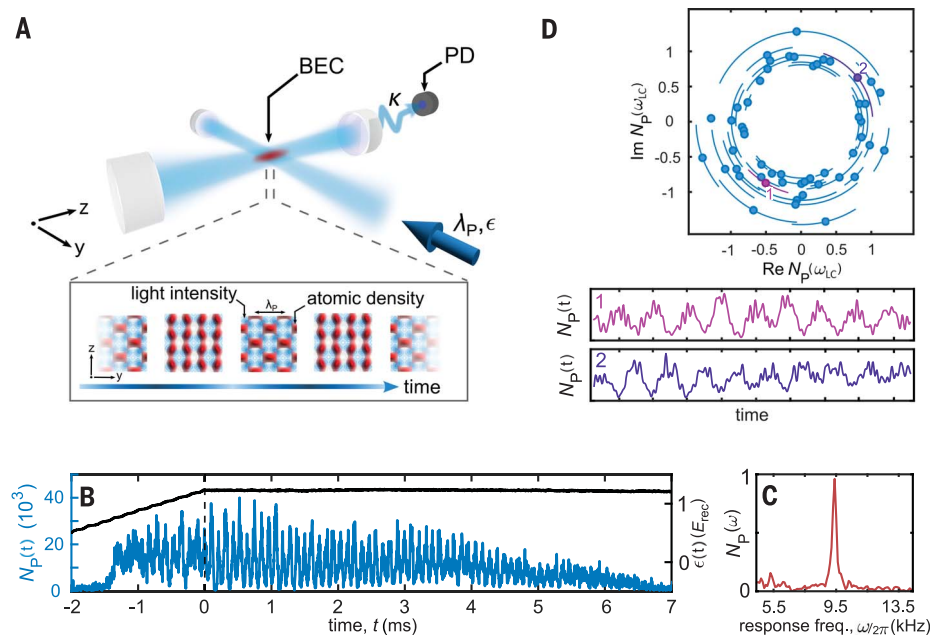
Fig. 1. CTC in an atom-cavity system. (**A**) Schematic drawing of the atom-cavity system pumped transversely with an optical pump lattice, blue detuned with respect to an atomic transition. (Inset) The photon field (blue) and the atomic density (red) of the limit cycle dynamics, based on simulations. The blue color shading of the time axis indicates the intracavity photon number. (**B**) Single experimental realization of the limit cycle phase for $\delta_{eff}/2\pi = -3.8$ kHz and $\varepsilon_f = 1.25$ E_{rec}. The vertical dashed black line indicates the start of the 10 ms holding time, during which the pump strength is held constant. The black line indicates the time trace of the pump strength ε, and the blue line indicates the time evolution of the intracavity photon number $N_P(t)$. (**C**) Normalized and rescaled single-sided amplitude spectrum of N_P calculated from the data shown in (B). (**D**) (Top) Distribution of the time phase in the limit cycle phase for $\delta_{eff}/2\pi = -5.0$ kHz and $\varepsilon_f = 1.25$ E_{rec}. The error bars indicate the phase uncertainty within our discrete Fourier transform resolution of 100 Hz. However, the uncertainty with regard to the radial dimension—the amplitude uncertainty—is negligibly small. For clarity, we removed the errors bars, around 30%, which are overlapping. (Bottom) The evolution of the intracavity photon number for two specific experimental realizations, marked with "1" and "2" at top, which have a time phase difference of almost π.

[1]Zentrum für Optische Quantentechnologien and Institut für Laser-Physik, Universität Hamburg, 22761 Hamburg, Germany. [2]The Hamburg Center for Ultrafast Imaging, 22761 Hamburg, Germany. [3]National Institute of Physics, University of the Philippines, Diliman, Quezon City 1101, Philippines.
*Corresponding author. Email: hemmerich@physnet.uni-hamburg.de (A.H.); hkessler@physnet.uni-hamburg.de (H.K.)

wave field with a wavelength $\lambda_P = 792.55$ nm (Fig. 1A). This wavelength is blue detuned with respect to relevant atomic D_1 transition of ^{87}Rb at a wavelength of 794.98 nm. The cavity operates in the recoil resolved regime (27)—its field decay rate $\kappa = 2\pi \times 3.4$ kHz is smaller than the recoil frequency $\omega_{rec} = 2\pi \times 3.7$ kHz. The cavity resonance frequency ω_c is shifted because of the refractive index of the BEC by an amount of $\delta_- = N_a U_0/2$, where $U_0 = 2\pi \times 1.3$ Hz is the maximal light shift per intracavity photon. We define the effective detuning as $\delta_{eff} \equiv \delta_c - \delta_-$, where $\delta_c \equiv \omega_p - \omega_c$ is the detuning between the pump field frequency ω_p and the resonance frequency of the empty cavity ω_c.

To determine the regime of the CTC, we measured the time dependence of the intracavity photon number $N_P(t)$ that emerges in the protocol given below. We show $N_P(t)$ in Fig. 2A and two derived quantities, the crystalline fraction Ξ and the limit-cycle frequency ω_{LC}, in Fig. 2, B and C, respectively. In our protocol, the intracavity photon number $N_P(t)$ was recorded as we linearly ramped the pump strength ε from 0 to 3.5 E_{rec} within 10 ms, while keeping δ_{eff} fixed. Initially, for weak pump intensities, the BEC phase was stable, and N_P was zero. Above a critical value of ε, the BEC became unstable toward the formation of a self-organized superradiant phase

heralded by a nonzero N_P. This represents a many-body state as the cavity photons mediate a retarded infinite-range interaction between the atoms. Although this superradiant phase transition has been intensively studied for a red-detuned pump (28–31), it has only been realized recently for a blue-detuned pump after its theoretical prediction (32, 33). For blue detuning, the atoms are low-field seeking and localize at the intensity minima of the light field. Nevertheless, the atoms can still self-organize into the superradiant phase, as evident from the large blue areas shown in Fig. 2A. However, the self-organized superradiant phase may become unstable for higher pump strengths because it costs energy for the atoms to localize away from the nodes of the pump lattice. This behavior leads to the disappearance of the self-organized phase for higher pump strengths (32). A phase diagram in fig. S1 in (34) shows a larger range of ε, demonstrating the disappearance of the self-organization for strong pumping. In the recoil-resolved regime, because of the retarded character of the cavity-mediated interaction, we additionally observed the emergence of a new dynamical phase or a limit cycle phase characterized by self-sustained oscillations of N_P as the atoms cycled through different density wave patterns (33, 35). The resolution of the experimental imaging system

is insufficient to observe the real-space density of the cloud; instead, simulations of the evolution of the single-particle density by use of a mean-field model are shown in fig. S3 (34). Physically, the limit cycles can be understood as a competition between opposing energy contributions: one coming from the pump lattice potential, and another coming from the cavity-induced all-to-all interaction between the atoms (33). In the superradiant phase, the cavity-induced interaction energy dominates, and the atoms localize at the antinodes. In the limit cycle phase for sufficiently strong pump intensities, localization of low-field–seeking atoms at the antinodes becomes energetically costly, resulting in a decrease in the density modulations and N_P as the system attempts to go back to the normal homogeneous phase. However, this is unstable toward self-organization because the chosen pump strength already exceeds the critical value, and thus, the cycle starts anew. The regime of recoil-resolution of the cavity, in which the dynamics of the atomic density and the light field evolve with similar time scales, has turned out to be the key ingredient to realize the limit cycle phase. This can be understood by noting that the delayed dynamics of the cavity field, with respect to the atomic density, leads to cavity cooling, which in contrast to broadband cavity
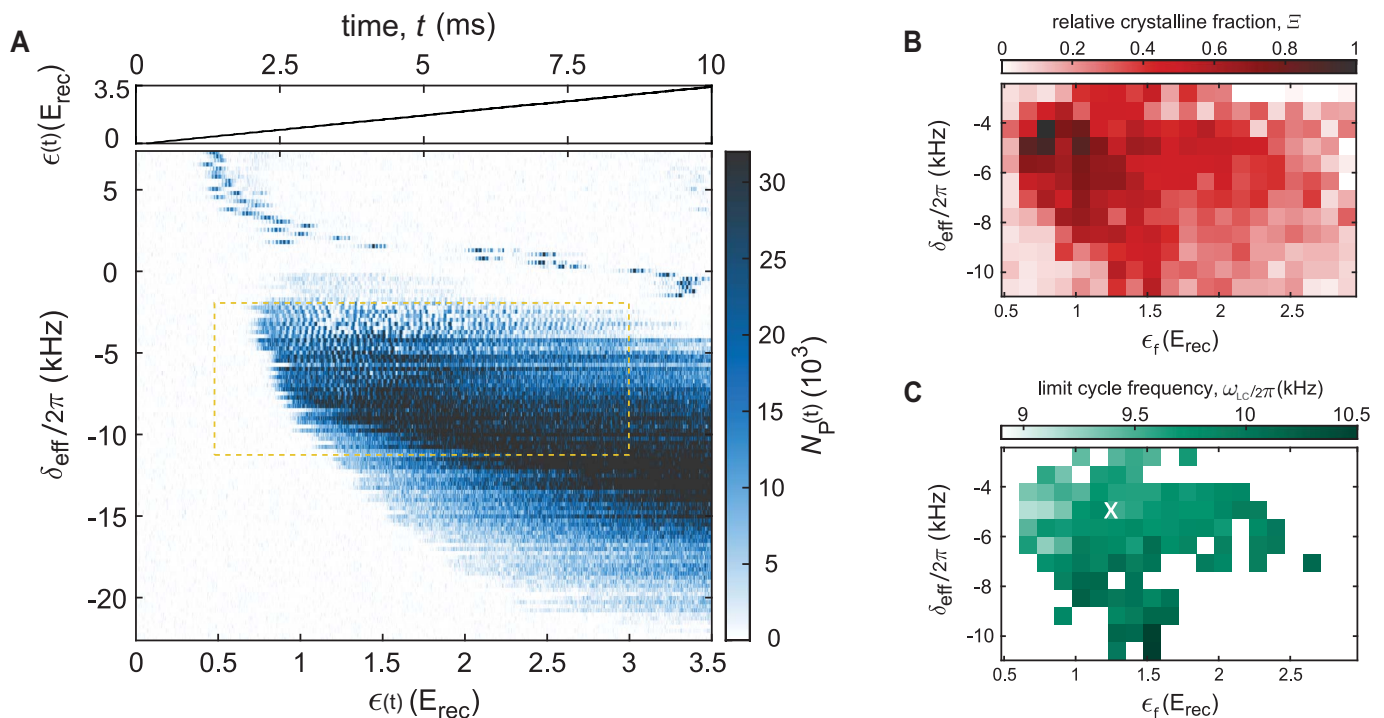
Fig. 2. Determining the time-crystalline regime. (**A**) (Top) Pump strength protocol. (Bottom) The corresponding intracavity photon number N_P as a function of δ_{eff} and ε. The area enclosed by the yellow dashed lines indicates the parameter space spanned in (B) and (C). (**B**) Relative crystalline fraction Ξ and (**C**) limit cycle frequency ω_{LC} plotted versus δ_{eff} and ε_f. To obtain (B) and (C), for fixed δ_{eff}, the pump strength is ramped to its final value ε_f and

subsequently held constant for 10 ms. The relative crystalline fraction Ξ and the corresponding value of ω_{LC} identify the time-crystalline state. The parameter space is divided into 20 by 24 plaquettes and averages across 5 to 10 experimental implementations are produced. The white cross indicates the parameter values $\delta_{eff}/2\pi = -5.0$ kHz and $\varepsilon_f = 1.25\ E_{rec}$. The white area in (C) corresponds to data with Ξ below $1/e$.

setups restricts the atoms to occupy only a small number of momentum modes. This prevents the system from heating up and entering chaotic dynamics. We observed the limit cycle phase in the region shown in Fig. 2A enclosed by the yellow dashed lines. To further highlight the dynamical nature of this phase, we show a typical single-shot realization in Fig. 1, B and C.

Next, we quantitatively identified the area in the parameter space, spanned by the pump strength ϵ and the effective detuning δ_{eff}, where limit cycles can be observed. For fixed δ_{eff}, we linearly ramped ϵ to the desired final value ϵ_f, using the same slope as for the measurement shown in Fig. 2A, and held ϵ constant for 10 ms. The protocol is depicted by the black curve in Fig. 1B. We show in Fig. 1C an example of the normalized and rescaled single-sided amplitude spectrum $N_P(\omega) = \bar{N}_P(\omega)/\bar{N}_{P,\text{max}}(\omega_{\text{LC}})$ obtained from $N_P(t)$ within the holding time window [0,10] ms in Fig. 1B. $\bar{N}_P(\omega)$ is the normalized single-sided amplitude spectrum, and $\bar{N}_{P,\text{max}}(\omega_{\text{LC}})$ is the maximum value of the measured limit cycle amplitude. In the case of pronounced limit cycle dynamics as in Fig. 1C, the single-sided amplitude spectrum shows a distinct peak, with a width associated with the limit cycle lifetime of several milliseconds. The narrowest peaks observed exhibit a e^{-2} width $\Delta\omega \approx 2\pi \times 1.4$ kHz: The limit cycle frequency ω_{LC}, plotted in Fig. 2C, is defined as the frequency of the dominant peak in the single-sided amplitude spectrum within the frequency interval $\Delta_{\text{LC}} = [3.5,15.5] \times 2\pi$ Hz, chosen much larger than $\delta_{\text{LC}} \in [\omega_{\text{LC}} - \Delta\omega/2, \omega_{\text{LC}} + \Delta\omega/2]$. The oscillation frequency of a CTC is not necessarily fixed, and robustness refers to the persistence of the CTC in the thermodynamic limit and for a wide range of system parameters [finite-size effects are discussed in the supplementary materials (*34*)] (*22*). We calculated a common measure for time crystallinity, the crystalline fraction Ξ' (*10*, *11*), as the ratio between the area under the single-sided amplitude spectrum within δ_{LC} and the total area within Δ_{LC}. That is, $\Xi' \equiv \sum_{\omega \in \delta_{\text{LC}}} N_P(\omega)/\sum_{\omega \in \Delta_{\text{LC}}} N_P(\omega)$. The relative crystalline fraction Ξ shown in Fig.

2B is normalized to the maximum crystalline fraction measured in the parameter space explored in this work. Because of the finite lifetime of the BEC, it is difficult to access the long-time behavior of the system, which makes it experimentally challenging to distinguish between the areas of stable limit cycle, chaos, and possible transient phases. Hence, we define a cut-off or threshold value for the relative crystalline fraction, $\Xi_{\text{cut}} = 1/e$, to identify regions with observable limit cycle dynamics. In Fig. 2C, the frequency response of the limit cycle phase is only shown if its relative crystalline fraction is higher than the cut-off value: $\Xi > \Xi_{\text{cut}}$. The experimental lifetime of our time crystal is limited by atom loss. Furthermore, the short-range contact interaction, due to collisions between the atoms, leads to dephasing of the system and hence melting of the time crystal. Simulations that include contact interactions and phenomenological atom loss can be found in the supplementary materials.

The spontaneous symmetry breaking of a many-body system indicates a phase transition. We demonstrated strong evidence that the limit cycle phase emerges through spontaneous breaking of continuous time translation symmetry, and thus, it is a CTC. We repeated the experimental pump protocol shown as the Fig. 1B black line more than 1500 times with fixed $\delta_{\text{eff}}/2\pi = -5.0$ kHz and $\epsilon_f = 1.25\ E_{\text{rec}}$. These parameter values are indicated in Fig. 2C with a white cross. Because of technical instabilities, the number of the atoms in the BEC N_a fluctuates by 5%. This leads to a fluctuating value of δ_{eff} and hence of ω_{LC}. Pictorially, this can be understood by observing that fluctuations in N_a effectively shift the CTC regime in Fig. 2C either up or down. For the parameter values indicated by a white cross in Fig. 2C, the median of ω_{LC} is $\bar{\omega}_{\text{LC}} = 2\pi \times 9.69$ kHz. Our discrete Fourier transform resolution, set by the 10-ms time window, is 100 Hz. Thus, we only considered experimental runs, which yielded response frequencies of $\omega_{\text{LC}} = \bar{\omega}_{\text{LC}} \pm 2\pi \times (50$ Hz). For each single-shot measurement, we obtained the time phase defined as the principal argument $\arg[N_P(\omega_{\text{LC}})]$ of the

Fourier transformed intracavity photon number $N_P(\omega_{\text{LC}})$ evaluated at the limit cycle frequency ω_{LC}. In Fig. 1D, we show the distribution of the observed time phases, which randomly covers the interval [0,2π]. This corroborates the spontaneous breaking of continuous time translation symmetry in the limit cycle phase. In the bottom of Fig. 1D, we show two specific experimental realizations, which have a time phase difference of almost π. Simulations representing the BEC as a coherent state show a range of the response frequency distribution of 300 Hz. Because we post-selected our data far below this limit, the origin of the spread over 2π in the time phase distribution is not due to technical noises but rather to quantum fluctuations. In the supplementary materials, we show a more detailed theoretical analysis to support this argument. The error bars along the angular direction in Fig. 1D indicate the phase uncertainty within 100 Hz of our Fourier limit. The average phase uncertainty is around 0.25π. The uncertainty in the radial direction corresponding to the oscillation amplitude is, however, negligible. Moreover, we removed 30% of the error bars for clarity in Fig. 1D.

Last, we demonstrated the robustness of the limit cycle phase against temporal perturbations, which is a defining feature of time crystals. We introduced white noise onto the pump signal with a bandwidth of 50 kHz. The noise strength is quantified by $n \equiv \sum_{\omega=0}^{2\pi \times 50\ \text{kHz}} |\mathcal{A}_{\text{noisy}}(\omega)|/ \sum_{\omega=0}^{2\pi \times 50\ \text{kHz}} |\mathcal{A}_{\text{clean}}(\omega)| - 1$, where $\mathcal{A}_{\text{noisy}}$ and $\mathcal{A}_{\text{clean}}$ are the single-sided amplitude spectrum of the pump in the presence and absence of white noise, respectively. We chose the parameters $\delta_{\text{eff}}/2\pi = -5.0$ kHz and $\epsilon_f = 1.25\ E_{\text{rec}}$ in the center of the stable limit cycle region, indicated by the white cross in Fig. 2C, and added white noise with varying strengths. In Fig. 3, A and B, top, single-shot realizations of the noisy pump signal are shown for weak and strong noise, respectively. The corresponding dynamics of N_P is shown in Fig. 3, A and B, bottom. In Fig. 3E, we show how increasing the noise strength can "melt" the CTC as inferred by the decreasing relative crystalline fractions calculated from single-sided amplitude spectra, similar to those shown in Fig. 3, C

Fig. 3. Robustness against temporal perturbations. (**A** and **B**) Single experimental runs for noise strengths indicated in (E). (Top) Time traces of the pump strength ϵ. (Bottom) Corresponding dynamics of N_P. (**C** and **D**) Single-sided amplitude spectra of (A) and (B), respectively. (**E**) Relative crystalline fraction for varying noise strength n and fixed $\delta_{\text{eff}}/2\pi = -5.0$ kHz and $\epsilon_f = 1.25\ E_{\text{rec}}$.
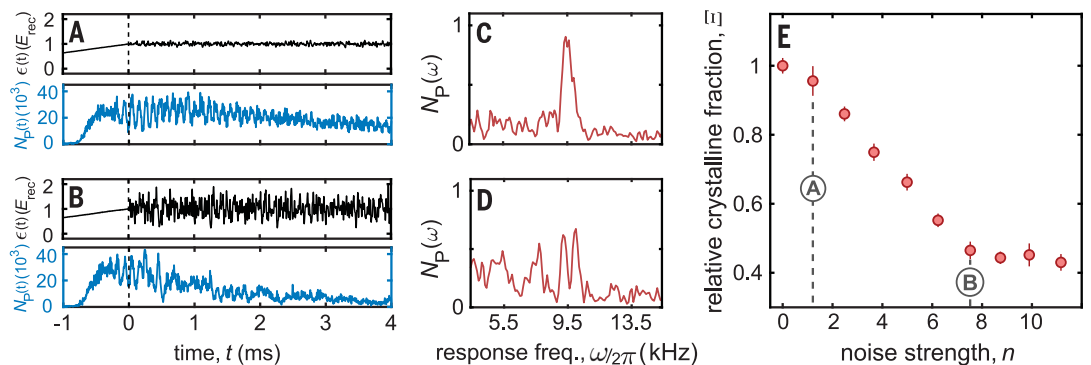
and D. The system takes time to react to the noise, so that a few oscillations can always be observed before decay sets in. This leads to an offset of 0.4 in the crystalline fraction, even for very strong noise. Nevertheless, we found that the limit cycle phase indeed exhibits robust oscillatory behavior over a wide range of the noise strength. This, together with the observation of spontaneous breaking of a continuous time translation symmetry, suggests that the observed limit cycle phase is a CTC.

We have experimentally demonstrated a CTC and provided a theoretical understanding. This class of dynamical many-body states expands the concepts of long-range order and spontaneous symmetry breaking into the time domain and is therefore of fundamental interest. This result, and the precision and control achieved with our atom-cavity platform, paves the way toward a broad and comprehensive study of dynamical many-body states of bosonic or fermionic quantum matter in the strongly correlated regime. For example, an increased atom-photon coupling could generate a new class of time crystals associated with symmetry-broken periodic entanglement. Furthermore, technological applications, such as toward time metrology, can be envisioned.

REFERENCES AND NOTES

1. F. Wilczek, *Phys. Rev. Lett.* **109**, 160401 (2012).
2. A. Shapere, F. Wilczek, *Phys. Rev. Lett.* **109**, 160402 (2012).
3. P. Nozières, *Europhys. Lett.* **103**, 57008 (2013).
4. P. Bruno, *Phys. Rev. Lett.* **111**, 070402 (2013).
5. H. Watanabe, M. Oshikawa, *Phys. Rev. Lett.* **114**, 251603 (2015).
6. D. V. Else, C. Monroe, C. Nayak, N. Y. Yao, *Annu. Rev. Condens. Matter Phys.* **11**, 467–499 (2020).
7. K. Sacha, *Time Crystals* (Springer, 2020).
8. V. Khemani, R. Moessner, S. L. Sondhi, arXiv:1910.10745 [cond-mat.str-el] (2019).
9. J. Zhang *et al.*, *Nature* **543**, 217–220 (2017).
10. S. Choi *et al.*, *Nature* **543**, 221–225 (2017).
11. J. Rovny, R. L. Blum, S. E. Barrett, *Phys. Rev. Lett.* **120**, 180603 (2018).
12. J. Smits, L. Liao, H. T. C. Stoof, P. van der Straten, *Phys. Rev. Lett.* **121**, 185301 (2018).
13. S. Autti, V. B. Eltsov, G. E. Volovik, *Phys. Rev. Lett.* **120**, 215301 (2018).
14. J. O'Sullivan *et al.*, *New J. Phys.* **22**, 085001 (2020).
15. A. Kyprianidis *et al.*, *Science* **372**, 1192–1196 (2021).
16. J. Randall *et al.*, *Science* **374**, 1474–1478 (2021).
17. X. Mi *et al.*, *Nature* **601**, 531–536 (2022).
18. Z. Gong, R. Hamazaki, M. Ueda, *Phys. Rev. Lett.* **120**, 040404 (2018).
19. H. Keßler *et al.*, *Phys. Rev. Lett.* **127**, 043602 (2021).
20. P. Kongkhambut *et al.*, *Phys. Rev. Lett.* **127**, 253601 (2021).
21. H. Taheri, A. B. Matsko, L. Maleki, K. Sacha, *Nat. Commun.* **13**, 848 (2022).
22. F. Iemini *et al.*, *Phys. Rev. Lett.* **121**, 035301 (2018).
23. B. Buča, J. Tindall, D. Jaksch, *Nat. Commun.* **10**, 1730 (2019).
24. H. Keßler, J. G. Cosme, M. Hemmerling, L. Mathey, A. Hemmerich, *Phys. Rev. A* **99**, 053605 (2019).
25. H. Poincaré, *J. Math. Pures Appl.* **7**, 375 (1881).
26. S. H. Strogatz, *Nonlinear Dynamics and Chaos: With Applications to Physics, Biology, Chemistry, and Engineering* (Westview Press, 2015).
27. H. Keßler, J. Klinder, M. Wolke, A. Hemmerich, *New J. Phys.* **16**, 053008 (2014).
28. P. Domokos, H. Ritsch, *Phys. Rev. Lett.* **89**, 253003 (2002).
29. A. T. Black, H. W. Chan, V. Vuletić, *Phys. Rev. Lett.* **91**, 203001 (2003).
30. K. Baumann, C. Guerlin, F. Brennecke, T. Esslinger, *Nature* **464**, 1301–1306 (2010).
31. J. Klinder, H. Keßler, M. Wolke, L. Mathey, A. Hemmerich, *Proc. Natl. Acad. Sci. U.S.A.* **112**, 3290–3295 (2015).
32. P. Zupancic *et al.*, *Phys. Rev. Lett.* **123**, 233601 (2019).
33. F. Piazza, H. Ritsch, *Phys. Rev. Lett.* **115**, 163601 (2015).
34. Supplementary text is available in the supplementary materials.
35. H. Keßler, J. G. Cosme, C. Georges, L. Mathey, A. Hemmerich, *New J. Phys.* **22**, 085002 (2020).
36. P. Kongkhambut *et al.*, Data for "'Observation of a continuous time crystal". Zenodo (2022).

SUPPLEMENTARY MATERIALS

science.org/doi/10.1126/science.abo3382
Materials and Methods
Supplementary Text
Figs. S1 to S7
References (*37*, *38*)

Observation of a continuous time crystal

Phatthamon Kongkhambut, Jim Skulte, Ludwig Mathey, Jayson G. Cosme, Andreas Hemmerich, and Hans Keler

Continuous time crystals

Time crystals are a new dynamical phase of quantum matter resulting from the breaking of time-translation symmetry and the subsequent interplay between interactions forming self-organized phases. To date, discrete time crystals have been observed in periodically driven systems. By contrast, Kongkhambut *et al.* report the observation of spontaneous breaking of a continuous time translation symmetry in an atomic Bose-Einstein condensate inside a high-finesse optical cavity (see the Perspective by LeBlanc). Using a time-independent pump, the authors observed a limit cycle phase that is characterized by emergent periodic oscillations of the intracavity photon number and is accompanied by the atomic density cycling through recurring patterns: a continuous time crystal. —ISO

View the article online
https://www.science.org/doi/10.1126/science.abo3382
Permissions
https://www.science.org/help/reprints-and-permissions

Use of this article is subject to the Terms of service

Science

AAAS

Supplementary Materials for

Observation of a continuous time crystal

Phatthamon Kongkhambut *et al.*

Andreas Hemmerich, hemmerich@physnet.uni-hamburg.de; Hans Keßler, hkessler@physnet.uni-hamburg.de

The PDF file includes:

Materials and Methods
Supplementary Text
Figs. S1 to S7
References

Experimental details

The experimental setup, as sketched in Fig. 1(A) in the main text, is comprised of a magnetically trapped BEC of $N_\mathrm{a} = 5 \times 10^4$ ^{87}Rb atoms, dispersively coupled to a narrowband high-finesse optical cavity. The trap creates a harmonic potential with trap frequencies $\omega = 2\pi \times (119.0, 102.7, 24.7)$ Hz. The cavity field has a decay rate of $\kappa = 2\pi \times 3.4\,\mathrm{kHz}$, which almost equals the recoil frequency $\omega_\mathrm{rec} = E_\mathrm{rec}/\hbar = 2\pi \times 3.7\,\mathrm{kHz}$ for pump wavelength of $\lambda_\mathrm{P} = 792.55\,\mathrm{nm}$. The pump laser is blue detuned with respect to the relevant atomic transition of ^{87}Rb at 794.98 nm. The maximum light shift per atom is $U_0 = 2\pi \times 1.3$ Hz. A typical experimental sequence starts by preparing the BEC and linearly increasing the pump strength ϵ to its desired value ϵ_f and subsequently holding it constant for 10 ms.

Phase diagram for large pump strength range

In Fig. S1A we present a phase diagram, similar to the one shown in Fig. 2A in the main text, but for larger pump strength range. The experimental protocol is the same as for Fig. 2A but the ramp time is increased to 20 ms. For strong pumping the system does not favor anymore the self-organization, since the cost of localizing the atoms at the nodes of the potential exceeds the decrease of energy due to the cavity-mediated coupling. In Fig. S1B the phase difference between the pump and cavity field ϕ is plotted against δ_eff and ϵ. In the self-organized phase, N_P is finite and ϕ locks to either 0 or π and stay constant. In Fig. S1C, we present the amplitude of the Fourier spectrum calculated from the photon number data. The limit cycle region can be identified by a peak in the frequency response around 10 kHz.
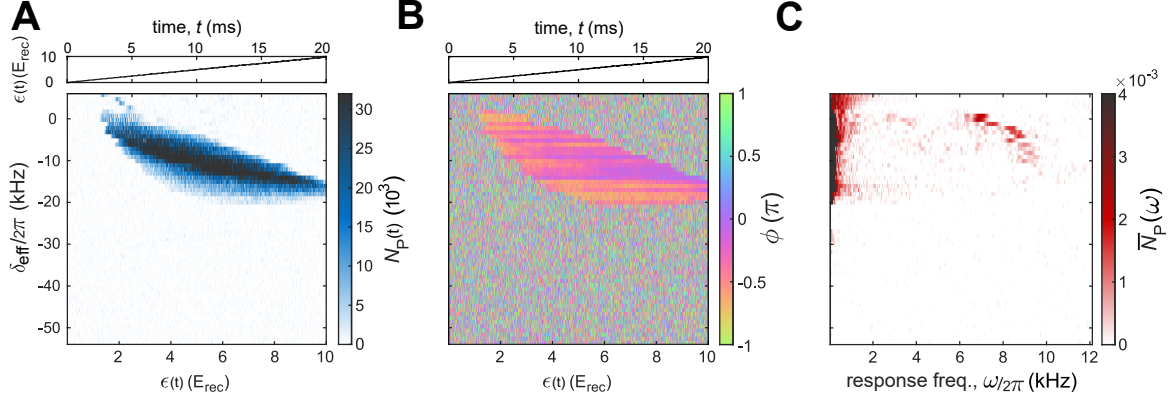
Fig. S1. Phase diagrams for large pump strength range. (**A**) Top panel: Pump strength protocol. Bottom panel: The corresponding intracavity photon number N_P, as a function of the effective detuning δ_eff and pump strength ϵ at a pump wavelength of $\lambda_\mathrm{P} = 792.55\,\mathrm{nm}$. The corresponding light shift per photon is $U_0 = 2\pi \times 1.3\,\mathrm{Hz}$. (**B**) Top panel: Pump strength protocol. Bottom panel: The phase difference between the pump and intracavity field ϕ, as a function of the effective detuning δ_eff and pump strength ϵ. Note, due to technical instabilities of the phase reference, we observe a drift of the phase signal of the cavity field of about 0.02π per ms. (**C**) The single-sided amplitude of the Fourier spectrum calculated using the data of A, as a function of the effective detuning δ_eff.

Atom-Cavity Model

We only consider the pump and cavity directions. The full atom-cavity system can be modeled using the many-body Hamiltonian with four terms describing the cavity, the atoms, and the atom-cavity interactions, given by

$$\hat{H} = \hat{H}_\mathrm{c} + \hat{H}_\mathrm{a} + \hat{H}_\mathrm{aa} + \hat{H}_\mathrm{ac}\,, \tag{1}$$

3

where the cavity contribution is $\hat{H}_c = -\hbar\delta_c\,\hat{a}^\dagger\hat{a}$ and the detuning between the pump and cavity frequencies is $\delta_c < 0$. The cavity mode annihilation and creation operator are denoted by $\hat{a}$ and $\hat{a}^\dagger$. The atomic part is described by

$$\hat{H}_a = \int dydz\,\hat{\Psi}^\dagger(y,z)\left(-\frac{\hbar^2}{2m}\nabla^2 + \mathrm{V}_{\mathrm{ext}}(y,z)\right)\hat{\Psi}(y,z) \tag{2}$$

where the external potential due to the standing wave created by the pump beam is $\mathrm{V}_{\mathrm{ext}}(y,z) = \epsilon_{\mathrm{f}}\cos^2(ky)$ with the potential strength parameter ϵ_{f} and m the mass of an atom. The short-range collisional interaction between the atoms can be captured via

$$\hat{H}_{\mathrm{aa}} = U_{\mathrm{a}}\int dydz\,\hat{\Psi}^\dagger(y,z)\hat{\Psi}^\dagger(y,z)\hat{\Psi}(y,z)\hat{\Psi}(y,z), \tag{3}$$

where $U_{\mathrm{a}} = \sqrt{2\pi}a_{\mathrm{s}}\hbar/ml_{\mathrm{x}}$ is the effective 2D interaction strength with a_{s} the s-wave scattering length and l_{x} the harmonic oscillator length in the x direction. The atom-cavity interaction part is described by

$$\hat{H}_{\mathrm{ac}} = \int dydz\,\hat{\Psi}^\dagger(y,z)\left(\hbar U_0\cos^2(kz)\hat{a}^\dagger\hat{a} + \hbar\sqrt{\hbar\epsilon_{\mathrm{f}}U_0}\cos(ky)\cos(kz)\left[\hat{a}^\dagger + \hat{a}\right]\right)\hat{\Psi}(y,z). \tag{4}$$

The light shift per intracavity photon is denoted by $U_0 > 0$. For our numerical simulations of the dynamics, we use the semiclassical method based on the truncated Wigner approximation (TWA) (37,38). TWA approximates the quantum dynamics by solving the equations of motions over an ensemble of initial states, which are sampled from the initial Wigner distribution. This methods allows us to incorporate the leading order quantum corrections to the meanfield solution. The c number equation for the light field is

$$i\frac{\partial\alpha}{\partial t} = \frac{1}{\hbar}\frac{\partial H}{\partial\alpha^*} - i\kappa\alpha + i\xi = (-\delta_c + U_0\mathcal{B} - i\kappa + i\xi) + \sqrt{\hbar\epsilon_{\mathrm{f}}U_0}\Phi, \tag{5}$$

where we have defined the bunching parameter $\mathcal{B} = \int dydz\,\cos^2(kz)|\psi(y,z)|^2$ and the density wave order parameter that corresponds to a checkerboard ordering $\Phi = \int dydz\,\cos(ky)\cos(kz)|\psi(y,z)|^2$.

4

We further included a decay term proportional to κ in the cavity mode dynamics and the resulting stochastic noise term $\xi(t)$, which is defined via $\langle \xi^*(t)\xi(t') \rangle = \kappa\delta(t - t')$. We obtain the atom-field equations via

$$i\frac{\partial \psi(y, z)}{\partial t} = \frac{1}{\hbar}\frac{\partial H}{\partial \psi^*(y, z)} = \left(-\frac{\hbar}{2m}\nabla^2 + V_{\text{dip}}(y, z) + 2U_{\text{a}}|\psi(y, z)|^2\right)\psi(y, z) \qquad (6)$$

with

$$V_{\text{dip}}(y, z) = \hbar\left(U_0|\alpha|^2\cos^2(kz) + \epsilon_{\text{f}}\omega_{\text{rec}}\cos^2(ky) + \sqrt{\hbar\epsilon_{\text{f}}U_0}\left[\alpha + \alpha^*\right]\cos(ky)\cos(kz)\right). \qquad (7)$$

For the simulations we use the same set of parameters as in the experiment.

Breaking of continuous time translation symmetry

To gain further insights into the continuous time translation symmetry breaking, we consider three different possibilities for including quantum noise in our theory. First, we sample over the full initial Wigner distribution and also include the corresponding stochastic noise ξ corresponding to the cavity-field decay rate κ. Secondly, we include only the sampling of the Wigner distribution of the initial state and ignore the stochastic noise in time due to the fluctuation-dissipation term in the cavity field. Third, we fix the initial state and include stochastic noise in the cavity mode. For each case, we consider 10^3 trajectories but for clearer presentation we only show the first 500 trajectories in Fig. S2(A-C). To obtain Fig. S2(A-C), we use $\delta_{\text{eff}} = -2\pi \times 10.4\,\text{kHz}$ and linearly ramp up the pump strength to its final value $\epsilon_{\text{f}}/\omega_{\text{rec}} = 0.85$ within $10\,\text{ms}$. We compute the fast Fourier transformation between $t_{\text{start}} = 15\,\text{ms}$ and $t_{\text{final}} = 65\,\text{ms}$. We record every $0.00125\,\text{ms}$ and thus, our frequency resolution is limited by $\Delta_{\text{FFT}} = 20\,\text{Hz}$. In Fig. S2A and S2B the limit cycle frequency varies $\pm 150\,\text{Hz}$. For the data set in Fig. S2C, the frequency is fixed. To minimize the fluctuations in the FFT signal due to the offset at $\omega = 0$ we normalize each trajectory by the maximum of the FFT. For better accessibility, after obtaining

5

the data from all trajectories we average over the mean value of all points. The TWA results in Fig. S2A nicely show that all phases between 0 and 2π are realized. The same holds true in Fig. S2B and Fig. S2C. This suggests that the initial quantum noise and stochastic noise from the leaky cavity are sufficient to exhibit the breaking of continuous time translation symmetry.
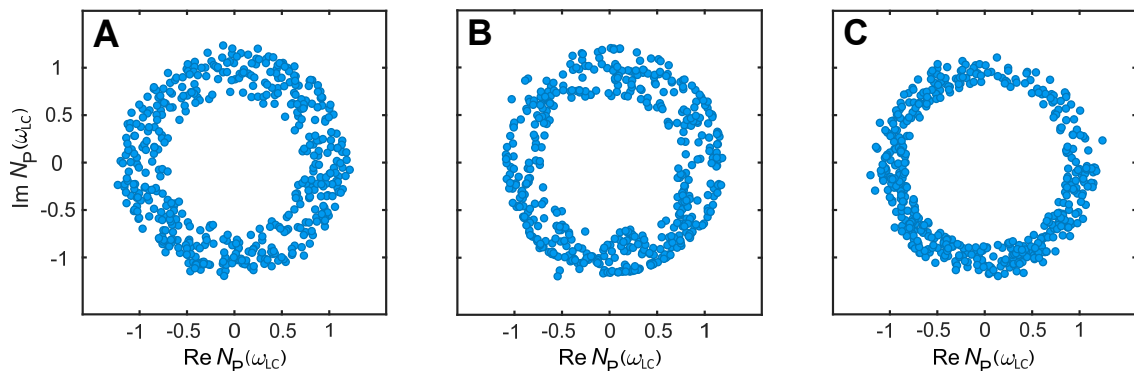
Fig. S2. Distribution of the time phase in the limit cycle phase. TWA simulations including (**A**) both initial quantum noise and stochastic noise, (**B**) only initial quantum noise, and (**C**) only stochastic noise. We use $\delta_{\mathrm{eff}} = -2\pi \times 10.4\,\mathrm{kHz}$ and $\epsilon_{\mathrm{f}}/\omega_{\mathrm{rec}} = 0.85$.

Atom dynamics during one limit cycle

We present the dynamics of the light field and the relevant density wave order parameters for a single exemplary trajectory in the limit cycle phase. We use $\delta_{\mathrm{eff}} = -2\pi \times 10.4\,\mathrm{kHz}$ and a final pump strength of $\epsilon_{\mathrm{f}}/\omega_{\mathrm{rec}} = 0.85$. We ramp up the pump intensity within $10\,\mathrm{ms}$ and present in Fig. S3C the limit cycle dynamics after $20\,\mathrm{ms}$. We find that the only non-zero order parameters are those associated to the chequerboard density wave, $\Phi = \langle \cos(ky)\cos(kz) \rangle$, and to the density waves related to the cavity and pump bunching parameters, $\mathcal{B} = \langle \cos(kz)^2 \rangle$ and $\mathcal{P} = \langle \cos(ky)^2 \rangle$, respectively. Fig. S3C shows the dynamics of the light field and the three order parameters. The oscillations in the dynamics of the atomic field density wave order parameter

lags behind those in the cavity field occupation. In Fig. S3(A-B) and Fig. S3(C-D), the density of the atomic-field is presented. The atoms slosh back and forth from a checkerboard pattern to the minima of the light field intensity.
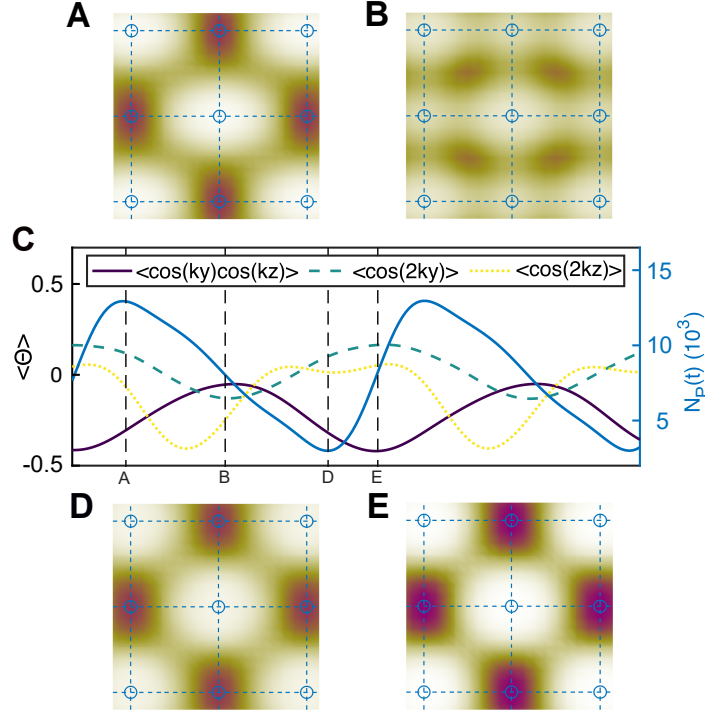
Fig. S3. Numerical results for the limit cycle dynamics. (**A-B**) and (**D-E**) Atomic density distributions for different times during the limit cycle. The gray dashed lines in C indicate the times for which the density distributions are calculated. Horizontal and vertical dashed blue lines mark the extrema of $\cos(ky)$ and $\cos(kz)$, respectively and solid blue circles denote the extrema of the product $\cos(ky)\cos(kz)$, which determines the chequerboard density wave order parameter Φ. **C** Dynamics of the three relevant order parameters and the cavity mode occupation. The vertical dashed lines denote the times when (A-B) and (D-E) are taken. We use $\delta_{\mathrm{eff}} = -2\pi \times 10.4\ \mathrm{kHz}$ and $\epsilon_{\mathrm{f}}/\omega_{\mathrm{rec}} = 0.85$.

Stability against short-range interactions and atom losses

We present the stability of the limit cycles against short-range interactions and phenomenological atom losses. We measure the interaction strengths via the mean-field collisional interaction energy (19)

$$E_{\mathrm{a}} = \frac{U_{\mathrm{a}}}{N_{\mathrm{a}}} \int dy dz \, |\psi_0(y, z)|^4 \tag{8}$$

with the wavefunction of the homogeneous BEC ψ_0. We further add a phenomenological atom loss term to our equations of motion of the form of

$$\frac{dN_{\mathrm{a}}}{dt} = -2\gamma N_{\mathrm{a}} \tag{9}$$

to capture the atom losses in the experiment. To quantify the temporal long-range order we compute the two-point temporal correlation function

$$C(t) = \mathrm{Re}\left(\frac{\langle \hat{a}^\dagger(t) a(t_0) \rangle}{\langle \hat{a}^\dagger(t_0) a(t_0) \rangle} \right). \tag{10}$$

The time t_0 is defined as the time of the first maximum of the limit cycle oscillations after the transition into the superradiant phase.

We present the dynamics of the photon number N_{P} and the nonequal time correlation C in Fig. S4 for different collisional interaction strengths E_{a} and atom loss rates γ. We observe that short-range interactions do not destroy the temporal long range order for weaker collisional interaction energies $E_{\mathrm{a}} = 0.1 \, E_{\mathrm{rec}}$ to strong interactions of $E_{\mathrm{a}} = 0.2 \, E_{\mathrm{rec}}$. However, the combination of strong short-range interactions $E_{\mathrm{a}} = 0.2 \, E_{\mathrm{rec}}$ and atom losses of $\gamma = 40 \, s^{-1}$ lead to a decay of the temporal order similar as observed in the experiment. The loss rate is chosen such that it models the observed atom decay rate in the experiment. We conclude that the main limitation of the limit cycle lifetime stems from atom losses in the experimental set up.
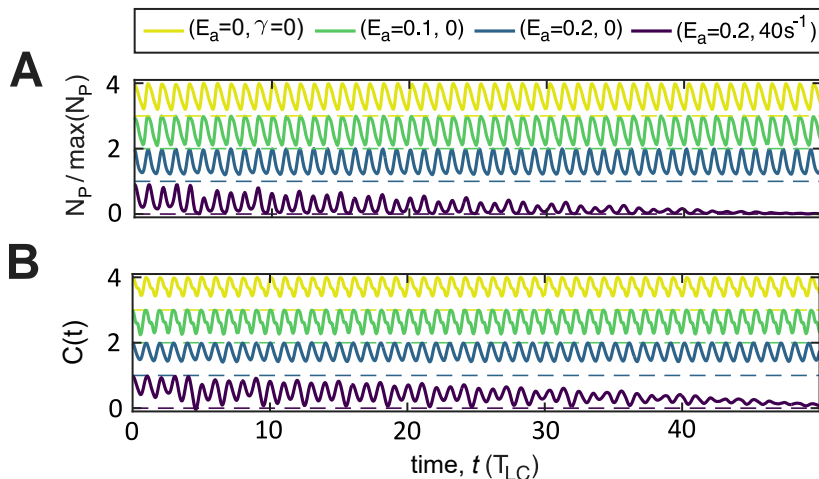
Fig. S4. Numerical results on short-range interactions and atom losses. (**A**) Numerical results on the intracavity photon number N_{P} and (**B**) the corresponding nonequal time correlation C for different contact interaction energies E_{a} and atom losses γ. For better readability, we include an offset of $1, 2, 3$ for the blue, green and yellow trace indicated by the dashed lines. We fix $\delta_{\mathrm{eff}} = -2\pi \times 10.4\,\mathrm{kHz}$.

Stability with respect to pump-atom detuning

The pump-atom detuning is in our system parametrized by the single photon light shift U_0. For all the measurements presented in the main text $U_0 = 2\pi \times 1.3\,\mathrm{Hz}$ is kept constant. To demonstrate robustness with respect to the pump-atom detuning, and hence with respect to U_0, we present in Fig. S5 measurements of self-organization phase diagram for $U_0 = 2\pi \times 1.9\,\mathrm{Hz}$. The limit cycles are indicated by a peak in the Fourier spectrum of the intracavity photon number (Fig. S5C), which can be found for small negative effective pump-cavity detuning $\delta_{\mathrm{eff}}/2\pi$, between -10 and $-20\,\mathrm{kHz}$. This measurement is only an example and we experimentally observe stable limit cycles for different values of U_0.
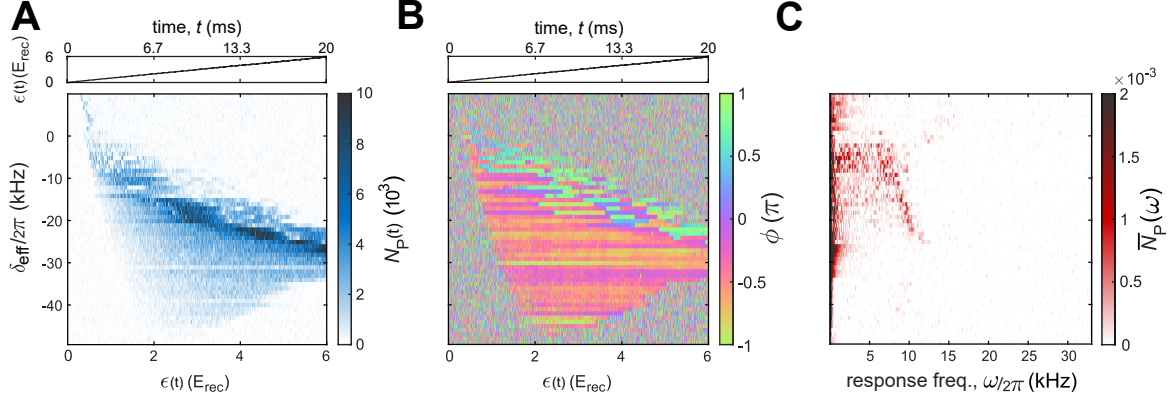
Fig. S5. Phase diagrams for another pump-atom detuning. (**A**) Top panel: Pump strength protocol. Bottom panel: The corresponding intracavity photon number N_{P}, as a function of the effective detuning δ_{eff} and pump strength ϵ at a pump wavelength of $\lambda_{\mathrm{P}} = 793.76\,\mathrm{nm}$. The corresponding light shift per photon is $U_0 = 2\pi \times 1.9\,\mathrm{Hz}$. (**B**) Top panel: Pump strength protocol. Bottom panel: The phase difference between the pump and intracavity field ϕ, as a function of the effective detuning δ_{eff} and pump strength ϵ. (**C**) The single-sided amplitude of the Fourier spectrum calculated using the data of A, as a function of the effective detuning δ_{eff}. Red region around $8 - 10\mathrm{kHz}$ at small negative δ_{eff} indicate a region where limit cycle can be found.

Finite-size effects

We investigate the effects of a finite particle number on the stability of the time crystal. To this end, we compare the mean-field results, which simulate the thermodynamic limit, and the results of single TWA trajectories, which include stochastic noise associated to cavity loss, for different particle numbers. Owing to the cavity-induced all-to-all coupling between the atoms, the thermodynamic limit is expected to be captured by our mean-field theory. We vary the particle number while keeping NU_0 fixed. We obtain the peaks in the dynamics of the intracavity photon number, $\tilde{N}_\mathrm{P}$, to highlight the change in the oscillation amplitude of the limit cycle phase for varying particle number. In Fig. S6A, we show the time evolution of $\tilde{N}_\mathrm{P}/N_\mathrm{a}$ for some exemplary particle numbers using TWA and the MF result corresponding to the thermodynamic limit. It can be seen that as the particle number is increased, the results approach the MF prediction. This means that the temporal dynamics becomes more regular as we increase the particle number N_a towards the thermodynamic limit. To further illustrate this point, we calculate the relative crystalline fraction $\Xi' \equiv \sum_{\omega \in \delta_\mathrm{LC}} N_\mathrm{P}(\omega) / \sum_{\omega \in \Delta_\mathrm{LC}} N_\mathrm{P}(\omega)$. We rescaled the relative crystalline fraction for varying N_a by the value in the thermodynamic limit, i.e., the Ξ' in our mean-field prediction is set to 1 as indicated by the gray dashed line in Fig. S6B. The blue cross marks the typical particle number in our experiment. We find that as N_a is increased, the crystalline fraction approaches the mean-field prediction. This can be understood from the fact that the initial quantum noise and stochastic noise scales with $1/N$ in TWA, meaning that as expected for $N_\mathrm{a} \to \infty$, we recover the thermodynamic limit.
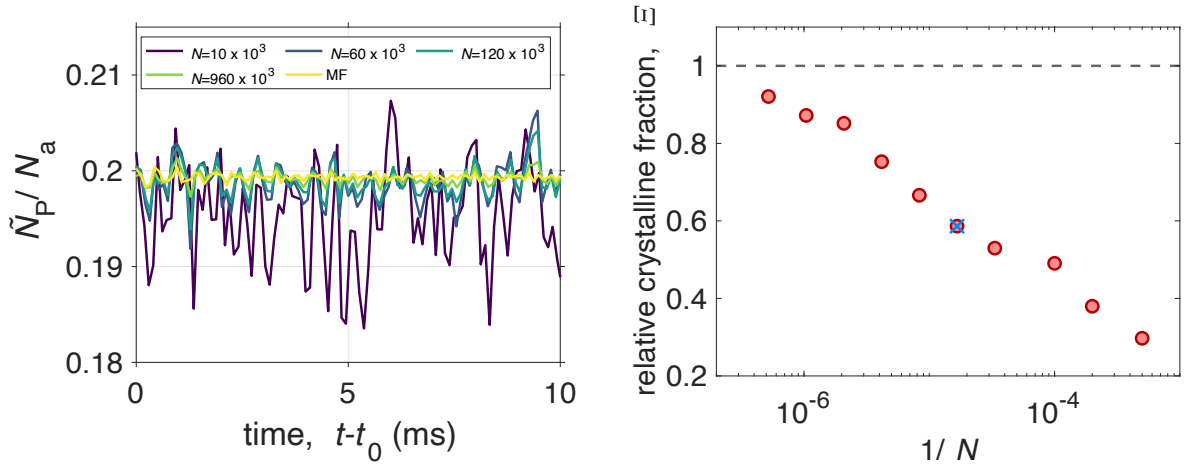
Fig. S6. Numerical results on the stability for different particle numbers (**A**) Results of a single TWA trajectory for the peak height of the intracavity photon number in the limit cycle phase for different particle numbers. (**B**) The relative crystalline fraction for varying particle numbers obtained from single TWA trajectories, which include stochastic noise from the cavity losses. The gray horizontal dashed line represents the mean-field crystalline fraction, which we set to 1 as a benchmark for finite N. The blue cross indicates the particle number, in which the experiment operates. We fix $\delta_{\text{eff}} = -2\pi \times 10.4 \text{ kHz}$ and $NU_0 = 2\pi \times 60 \text{ kHz} = \text{const.}$

Stability against temporal perturbations

The stability of the limit cycle phase against temporal noise can be also explored using our theoretical model. We focus on the mean-field regime to show that the limit cycle phases in the thermodynamic limit exhibit the robustness expected of a continuous time crystal. We add a Gaussian white noise onto the pump signal, which is band-limited to 0.025 GHz. This is set by the integration step size of our stochastic differential equation solver. Note that the noise in the experiment is band-limited to 50 kHz. Examples of the noisy pump signal are shown in Fig. S7A. The noise strength is quantified by a parameter similar to the one in the

experiment, $n \equiv \sum_\omega |\mathcal{A}_{\text{noisy}}(\omega)| / \sum_\omega |\mathcal{A}_{\text{clean}}(\omega)| - 1$, where $\mathcal{A}$ is the Fourier spectrum of the pump signal. In Fig. S7B, we show the peaks in the dynamics of the intracavity photon number, $\tilde{N}_{\text{P}}(t)$, for various noise strengths. We find that increasing the temporal noise strength leads to more irregular oscillations in the limit cycle phase. To further quantify this behaviour, we again obtain the relative crystalline fraction as defined in the previous section. The dependence of the relative crystalline on temporal noise strength n is shown in Fig. S7C. We observe that for small noise strength, the crystalline fraction appears unchanged. The time crystal starts to melt for stronger noise strengths as expected. These numerical results qualitatively agree with the experimental results shown in Fig. 3E and they suggest the robustness of the limit cycle phase in the thermodynamic limit against temporal perturbation.
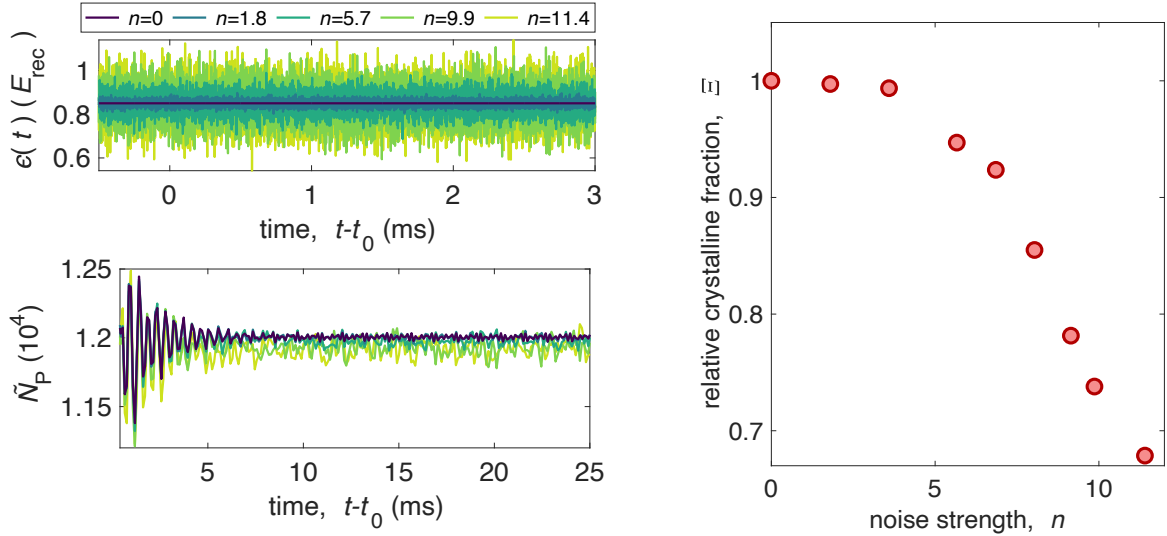
Fig. S7. Numerical results on the stability against temporal noise (**A**) Time dependence of the pump strength ϵ for different noise strengths and (**B**) the corresponding mean-field results for the dynamics of peak height of the intracavity photon number in the limit cycle phase. (**C**) The relative crystalline fraction for different noise strength.

Route to chaos

Our system exhibits a route to chaos, which we have investigated theoretically in a previous study. The full dynamical phase diagram including the chaotic regime can be found in Ref. (24). We find that the limit cycle phase becomes unstable towards chaotic dynamics for large pump strengths. Due to the limited lifetime of the BEC in our experimental setup, it is difficult to experimentally identify such a chaotic phase, which manifests in its characteristic long-time dynamics.

References and Notes

1. F. Wilczek, Quantum time crystals. *Phys. Rev. Lett.* **109**, 160401 (2012). doi:10.1103/PhysRevLett.109.160401 Medline

2. A. Shapere, F. Wilczek, Classical time crystals. *Phys. Rev. Lett.* **109**, 160402 (2012). doi:10.1103/PhysRevLett.109.160402 Medline

3. P. Nozières, EPL. *Europhys. Lett.* **103**, 57008 (2013).

4. P. Bruno, Impossibility of spontaneously rotating time crystals: A no-go theorem. *Phys. Rev. Lett.* **111**, 070402 (2013). doi:10.1103/PhysRevLett.111.070402 Medline

5. H. Watanabe, M. Oshikawa, Absence of Quantum Time Crystals. *Phys. Rev. Lett.* **114**, 251603 (2015). doi:10.1103/PhysRevLett.114.251603 Medline

6. D. V. Else, C. Monroe, C. Nayak, N. Y. Yao, Discrete Time Crystals. *Annu. Rev. Condens. Matter Phys.* **11**, 467–499 (2020). doi:10.1146/annurev-conmatphys-031119-050658

7. K. Sacha, *Time Crystals* (Springer, Cham, 2020).

8. V. Khemani, R. Moessner, S. L. Sondhi, A brief history of time crystals. arXiv:1910.10745 [cond-mat.str-el] (2019).

9. J. Zhang, P. W. Hess, A. Kyprianidis, P. Becker, A. Lee, J. Smith, G. Pagano, I.-D. Potirniche, A. C. Potter, A. Vishwanath, N. Y. Yao, C. Monroe, Observation of a discrete time crystal. *Nature* **543**, 217–220 (2017). doi:10.1038/nature21413 Medline

10. S. Choi, J. Choi, R. Landig, G. Kucsko, H. Zhou, J. Isoya, F. Jelezko, S. Onoda, H. Sumiya, V. Khemani, C. von Keyserlingk, N. Y. Yao, E. Demler, M. D. Lukin, Observation of discrete time-crystalline order in a disordered dipolar many-body system. *Nature* **543**, 221–225 (2017). doi:10.1038/nature21426 Medline

11. J. Rovny, R. L. Blum, S. E. Barrett, Observation of Discrete-Time-Crystal Signatures in an Ordered Dipolar Many-Body System. *Phys. Rev. Lett.* **120**, 180603 (2018). doi:10.1103/PhysRevLett.120.180603 Medline

12. J. Smits, L. Liao, H. T. C. Stoof, P. van der Straten, Observation of a Space-Time Crystal in a Superfluid Quantum Gas. *Phys. Rev. Lett.* **121**, 185301 (2018). doi:10.1103/PhysRevLett.121.185301 Medline

13. S. Autti, V. B. Eltsov, G. E. Volovik, Observation of a Time Quasicrystal and Its Transition to a Superfluid Time Crystal. *Phys. Rev. Lett.* **120**, 215301 (2018). doi:10.1103/PhysRevLett.120.215301 Medline

14. J. O'Sullivan *et al.*, *New J. Phys.* **22**, 085001 (2020).

15. A. Kyprianidis, F. Machado, W. Morong, P. Becker, K. S. Collins, D. V. Else, L. Feng, P. W. Hess, C. Nayak, G. Pagano, N. Y. Yao, C. Monroe, Observation of a prethermal discrete time crystal. *Science* **372**, 1192–1196 (2021). doi:10.1126/science.abg8102 Medline

16. J. Randall, C. E. Bradley, F. V. van der Gronden, A. Galicia, M. H. Abobeih, M. Markham, D. J. Twitchen, F. Machado, N. Y. Yao, T. H. Taminiau, Many-body-localized discrete time crystal with a programmable spin-based quantum simulator. *Science* **374**, 1474–1478 (2021). doi:10.1126/science.abk0603 Medline

17. X. Mi, M. Ippoliti, C. Quintana, A. Greene, Z. Chen, J. Gross, F. Arute, K. Arya, J. Atalaya, R. Babbush, J. C. Bardin, J. Basso, A. Bengtsson, A. Bilmes, A. Bourassa, L. Brill, M. Broughton, B. B. Buckley, D. A. Buell, B. Burkett, N. Bushnell, B. Chiaro, R. Collins, W. Courtney, D. Debroy, S. Demura, A. R. Derk, A. Dunsworth, D. Eppens, C. Erickson, E. Farhi, A. G. Fowler, B. Foxen, C. Gidney, M. Giustina, M. P. Harrigan, S. D. Harrington, J. Hilton, A. Ho, S. Hong, T. Huang, A. Huff, W. J. Huggins, L. B. Ioffe, S. V. Isakov, J. Iveland, E. Jeffrey, Z. Jiang, C. Jones, D. Kafri, T. Khattar, S. Kim, A. Kitaev, P. V. Klimov, A. N. Korotkov, F. Kostritsa, D. Landhuis, P. Laptev, J. Lee, K. Lee, A. Locharla, E. Lucero, O. Martin, J. R. McClean, T. McCourt, M. McEwen, K. C. Miao, M. Mohseni, S. Montazeri, W. Mruczkiewicz, O. Naaman, M. Neeley, C. Neill, M. Newman, M. Y. Niu, T. E. O'Brien, A. Opremcak, E. Ostby, B. Pato, A. Petukhov, N. C. Rubin, D. Sank, K. J. Satzinger, V. Shvarts, Y. Su, D. Strain, M. Szalay, M. D. Trevithick, B. Villalonga, T. White, Z. J. Yao, P. Yeh, J. Yoo, A. Zalcman, H. Neven, S. Boixo, V. Smelyanskiy, A. Megrant, J. Kelly, Y. Chen, S. L. Sondhi, R. Moessner, K. Kechedzhi, V. Khemani, P. Roushan, Time-crystalline eigenstate order on a quantum processor. *Nature* **601**, 531–536 (2022). doi:10.1038/s41586-021-04257-w Medline

18. Z. Gong, R. Hamazaki, M. Ueda, Discrete Time-Crystalline Order in Cavity and Circuit QED Systems. *Phys. Rev. Lett.* **120**, 040404 (2018). doi:10.1103/PhysRevLett.120.040404 Medline

19. H. Keßler, P. Kongkhambut, C. Georges, L. Mathey, J. G. Cosme, A. Hemmerich, Observation of a Dissipative Time Crystal. *Phys. Rev. Lett.* **127**, 043602 (2021). doi:10.1103/PhysRevLett.127.043602 Medline

20. P. Kongkhambut, H. Keßler, J. Skulte, L. Mathey, J. G. Cosme, A. Hemmerich, Realization of a Periodically Driven Open Three-Level Dicke Model. *Phys. Rev. Lett.* **127**, 253601 (2021). doi:10.1103/PhysRevLett.127.253601 Medline

21. H. Taheri, A. B. Matsko, L. Maleki, K. Sacha, All-optical dissipative discrete time crystals. *Nat. Commun.* **13**, 848 (2022). doi:10.1038/s41467-022-28462-x Medline

22. F. Iemini, A. Russomanno, J. Keeling, M. Schirò, M. Dalmonte, R. Fazio, Boundary Time Crystals. *Phys. Rev. Lett.* **121**, 035301 (2018). doi:10.1103/PhysRevLett.121.035301 Medline

23. B. Buča, J. Tindall, D. Jaksch, Non-stationary coherent quantum many-body dynamics through dissipation. *Nat. Commun.* **10**, 1730 (2019). doi:10.1038/s41467-019-09757-y Medline

24. H. Keßler, J. G. Cosme, M. Hemmerling, L. Mathey, A. Hemmerich, Emergent limit cycles and time crystal dynamics in an atom-cavity system. *Phys. Rev. A* **99**, 053605 (2019). doi:10.1103/PhysRevA.99.053605

25. H. Poincaré, *J. Math. Pures Appl.* **7**, 375 (1881).

26. S. H. Strogatz, *Nonlinear Dynamics and Chaos: With Applications to Physics, Biology, Chemistry, and Engineering* Westview press (2015).

27. H. Keßler, J. Klinder, M. Wolke, A. Hemmerich, Optomechanical atom-cavity interaction in the sub-recoil regime. *New J. Phys.* **16**, 053008 (2014). doi:10.1088/1367-2630/16/5/053008

28. P. Domokos, H. Ritsch, Collective cooling and self-organization of atoms in a cavity. *Phys. Rev. Lett.* **89**, 253003 (2002). doi:10.1103/PhysRevLett.89.253003 Medline

29. A. T. Black, H. W. Chan, V. Vuletić, Observation of collective friction forces due to spatial self-organization of atoms: From Rayleigh to Bragg scattering. *Phys. Rev. Lett.* **91**, 203001 (2003). doi:10.1103/PhysRevLett.91.203001 Medline

30. K. Baumann, C. Guerlin, F. Brennecke, T. Esslinger, Dicke quantum phase transition with a superfluid gas in an optical cavity. *Nature* **464**, 1301–1306 (2010). doi:10.1038/nature09009 Medline

31. J. Klinder, H. Keßler, M. Wolke, L. Mathey, A. Hemmerich, Dynamical phase transition in the open Dicke model. *Proc. Natl. Acad. Sci. U.S.A.* **112**, 3290–3295 (2015). doi:10.1073/pnas.1417132112 Medline

32. P. Zupancic, D. Dreon, X. Li, A. Baumgärtner, A. Morales, W. Zheng, N. R. Cooper, T. Esslinger, T. Donner, P-Band Induced Self-Organization and Dynamics with Repulsively Driven Ultracold Atoms in an Optical Cavity. *Phys. Rev. Lett.* **123**, 233601 (2019). doi:10.1103/PhysRevLett.123.233601 Medline

33. F. Piazza, H. Ritsch, Self-Ordered Limit Cycles, Chaos, and Phase Slippage with a Superfluid inside an Optical Resonator. *Phys. Rev. Lett.* **115**, 163601 (2015). doi:10.1103/PhysRevLett.115.163601 Medline

34. Supplementary text is available in the supplementary materials.

35. H. Keßler, J. G. Cosme, C. Georges, L. Mathey, A. Hemmerich, From a continuous to a discrete time crystal in a dissipative atom-cavity system. *New J. Phys.* **22**, 085002 (2020). [doi:10.1088/1367-2630/ab9fc0](doi:10.1088/1367-2630/ab9fc0)

36. P. Kongkhambut *et al.*, Data for "'Observation of a continuous time crystal". Zenodo (2022); doi:10.5281/zenodo.6576125.

37. A. Polkovnikov, Phase space representation of quantum dynamics. *Ann. Phys.* **325**, 1790–1852 (2010). [doi:10.1016/j.aop.2010.02.006](doi:10.1016/j.aop.2010.02.006)

38. J. G. Cosme, J. Skulte, L. Mathey, Time crystals in a shaken atom-cavity system. *Phys. Rev. A* **100**, 053615 (2019). doi:10.1103/PhysRevA.100.053615

2.12 Publication VII: Realizing limit cycles in dissipative bosonic systems

J. Skulte, P. Kongkhambut, H. Keßler, A. Hemmerich, L. Mathey and J.G. Cosme — **accepted to Physical Rev. A (2024)**

Motivation

This work was motivated by the first observation of a continuous time crystal (CTC) in our previous work. The goal of this work was to find an analytical explanation for the previously observed CTC. We have proposed a generic model that captures the limit cycle (LC) transition and used it to find further LC regimes in the atom-cavity system.

Main findings

In this work, we proposed a generic mechanism for generating LC oscillations. The model consists of coupling a linear bosonic model to a dissipative nonlinear bosonic mode. Using a stability analysis, we showed that the LCs appear due to a supercritical Hopf bifurcation. As this phase appears in a many-body context, the LC phase can be classified as a CTC. We showed that this model can be realised for three-level models coupled to a single quantised dissipative light mode as found in atom-cavity systems. By adiabatically eliminating the highest level and further taking the Holstein-Primakoff approximation we arrived at our generic model. Due to this step we obtained the nonlinearity in the form of a Kerr-like interaction term. Using this platform, we experimentally observed, for the first time, LC for an attractive optical pump lattice, thereby confirming our generic model and mapping.

Contribution

JGC, LM and I conceptualized this work. I performed all numerical and analytical studies under the supervision of LM and JGC. PK and HK performed the experiments and data analysis under the supervision by AH. All authors contributed to the discussion and interpretation of the results, as well as to writing the manuscript.

Realizing limit cycles in dissipative bosonic systems

Jim Skulte,[1,2] Phatthamon Kongkhambut,[1] Hans Keßler,[1,3] Andreas Hemmerich,[1,2] Ludwig Mathey,[1,2] and Jayson G. Cosme[4]

[1]*Center for Optical Quantum Technologies and Institute for Quantum Physics, Universität Hamburg, 22761 Hamburg, Germany*
[2]*The Hamburg Center for Ultrafast Imaging, Luruper Chaussee 149, 22761 Hamburg, Germany*
[3]*Physikalisches Institut, Rheinische Friedrich-Wilhelms-Universität, 53115 Bonn, Germany*
[4]*National Institute of Physics, University of the Philippines, Diliman, Quezon City 1101, Philippines*
(Dated: May 19, 2024)

We propose a general mechanism for generating limit cycle (LC) oscillations by coupling a linear bosonic mode to a dissipative nonlinear bosonic mode. By analyzing the stability matrix, we show that LCs arise due to a supercritical Hopf bifurcation. We find that the existence of LCs is independent of the sign of the effective nonlinear interaction. The bosonic model can be realised in three-level systems interacting with a quantised light mode as realised in atom-cavity systems. Using such a platform, we experimentally observe LCs for the first time in an atom-cavity system with attractive optical pump lattice, thereby confirming our theoretical predictions for the minimal model and interactions needed to generate LCs for a class of driven-dissipative systems.

I. INTRODUCTION

A central focus of quantum optics is the understanding of few-level systems coupled to a single photonic mode [1]. A quintessential example is the Dicke model [2, 3], in which a large number of two-level systems are coupled to the same light mode, giving rise to exciting physical phenomena, such as super- and subradiance and the Dicke phase transition. Furthermore, as was pointed out more recently, if this model is extended to incorporate multi-level systems and dissipation, the resulting many-body dynamics can give rise to LCs [4–10] and continuous time crystals (CTCs) [11–18]. LCs are closed phase space trajectories, inherently robust against noise or perturbations in the initial state. They emerge via continuous time translation symmetry breaking, manifesting in an oscillatory motion despite the absence of an explicit time-dependence in their equations of motion. A LC phase in a many-body system with an unbiased distribution of the time phase of its oscillatory motion is a CTC and has been recently demonstrated experimentally in a continuously driven atom-cavity system [16].

In this work, we put forth a model, giving rise to LC oscillations, that can either be understood in terms of a collection of two-level systems coupled to a non-linear photonic mode, or a collection of three-level systems, coupled to a linear photonic mode. The transition between the representations with three- and two-level systems arises by adiabatically eliminating one of the levels in the three-level systems and thereby generating a nonlinearity in the photonic mode. The LC behavior is striking since additional quantum modes beyond the two-level approximation increase the complexity of a quantum system, and thus are expected to support ergodicity in generic systems [19]. To obtain a concrete implementation of LC dynamics, we map our generic model onto an atom-cavity system, and show that the current understanding, that the emergence of LC phases in atom-cavity systems necessarily relies on the use of a repulsive light-shift potential, is incomplete [16, 20–22]. In this paper, we elucidate that the fundamental mechanism is in fact a Kerr-like nonlinearity for the photons, which is induced by a third atomic level, typically neglected in standard Dicke-like models of atom-cavity systems. This nonlinearity
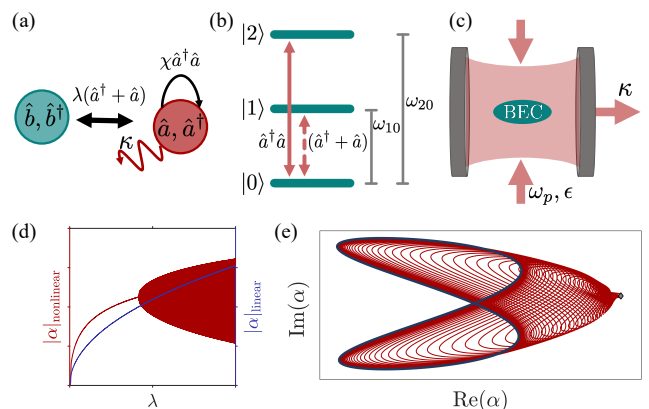
FIG. 1. (a) A bosonic mode (teal) $\hat{b}$ interacts with a dissipative bosonic mode (red) $\hat{a}$ with a nonlinearity proportional to χ and damping κ. The width of the arrows denote the strength of the interactions. (b) Approximate three-level model for (c) a BEC (teal) coupled to a single light mode including single-photon coupling with strength λ and Kerr nonlinearity with strength χ. In (c), the BEC is transversely pumped by a standing wave potential formed by two laser beams and placed inside a high-finesse cavity. The rate of emitted light from the cavity is κ. (d) Exemplary dynamics of the Dicke model and the Dicke model including a Kerr-like nonlinearity for varying coupling strength λ. While the Dicke model reaches a steady state after entering the superradiant phase, the nonlinear Dicke model enters the limit cycle phase for increasing λ. (e) Dynamics of the light field in phase space starting from a fixed point (gray diamond) and relaxing towards the limit cycle (blue line).

can arise irrespective of the sign of the light-shift potential or pump-atom detuning, such that an LC phase may emerge also for negative coupling parameters, which we experimentally demonstrate in this work.

We expect our results to apply to a wide class of systems, wherein the interactions are mediated by a bosonic mode, such as in cavity-magnon systems [23] and superconducting circuits [24, 25], provided that they satisfy the form of the coupling between the modes in our effective bosonic model as schematically depicted in Figs. 1(a) and 1(b). In particular, the Kerr-like nonlinearity needed for the limit cycle to

emerge could originate from either a density- or intensity-dependent coupling of a degree-of-freedom and the dissipative mode. Some examples include a Kerr medium coupled to a cavity field [26] and photon-phonon coupling in cavity-optomechanical systems [27, 28].

The paper is organized as follows. In Sec. II, we discuss the minimal model and use bifurcation theory to explore the instabilities in the system. In Sec. III, we discuss the atom-cavity implementation and present the experimental results showing the emergence of limit cycles in an atom-cavity system with attractive light-shift pump potential. Finally, we conclude in Sec. IV.

II. THEORY

A. General model

We consider a general model describing three bosonic modes (a, b, and c) with the a-mode being dissipative as its occupation decays at a rate of κ. The three-mode Hamiltonian is

$$\hat{H} = \omega_p \hat{a}^\dagger \hat{a} + \omega_{10} \hat{b}^\dagger \hat{b} + \omega_{20} \hat{c}^\dagger \hat{c} + \lambda \left(\hat{a}^\dagger + \hat{a} \right) \left(\hat{b}^\dagger + \hat{b} \right) \quad (1)$$
$$+ \chi \hat{a}^\dagger \hat{a} \left(\hat{c}^\dagger + \hat{c} \right).$$

The natural frequencies of the three modes are ω_p, ω_{10}, and ω_{20}. The b-mode interacts with the a-mode via an amplitude-dependent coupling with strength λ. On the other hand, a density- or intensity-dependent interaction characterized by χ couples the a- and c-modes.

Applying mean-field theory by setting $\langle \hat{a} \rangle = \alpha$, $\langle \hat{b} \rangle = \beta$, $\langle \hat{c} \rangle = \gamma$, and $\langle \hat{A}\hat{B} \rangle \approx \langle \hat{A} \rangle \langle \hat{B} \rangle$, we obtain the following set of equations of motion (EOM) for the three-mode system

$$\frac{d\alpha}{dt} = -i \left[\omega_p - i\kappa + \chi \left(\gamma + \gamma^* \right) \right] \alpha - i\lambda \left(\beta + \beta^* \right) \quad (2)$$
$$\frac{d\beta}{dt} = -i\omega_{10}\beta - i\lambda \left(\alpha + \alpha^* \right)$$
$$\frac{d\gamma}{dt} = -i\omega_{20}\gamma - i\chi \alpha^* \alpha.$$

We can adiabatically eliminate the c-mode for $\omega_{20} \ll \omega_{10}, \omega_p$, such that we approximate $d\gamma/dt \approx 0$ in the last line of Eq. (2). This yields an expression for γ given by

$$\gamma = -\frac{\chi}{\omega_{20}} |\alpha|^2. \quad (3)$$

Using this in the equation for the dissipative mode in the first line of Eq. (2), we obtain an effective two-mode EOM

$$\frac{d\alpha}{dt} = -i \left[\omega_p - 2\frac{\chi^2}{\omega_{20}} |\alpha|^2 - i\kappa \right] \alpha - i\lambda \left(\beta + \beta^* \right)$$
$$\frac{d\beta}{dt} = -i\omega_{10}\beta - i\lambda \left(\alpha + \alpha^* \right), \quad (4)$$

Quantising the remaining modes, an effective Hamiltonian corresponding to Eq. (4) reads

$$\hat{H} = \omega_p \hat{a}^\dagger \hat{a} + \omega_{10} \hat{b}^\dagger \hat{b} + \lambda \left(\hat{a}^\dagger + \hat{a} \right) \left(\hat{b}^\dagger + \hat{b} \right) - \frac{\chi^2}{\omega_{20}} \hat{a}^\dagger \hat{a} \hat{a}^\dagger \hat{a}. \quad (5)$$

Thus, we show that the eliminated mode leads to a Kerr-like nonlinearity for the dissipative boson, which for cavity-QED systems correspond to the cavity photons.

In Fig. 2, we compare the mean-field dynamics for the three-mode model and the two-mode model with the Kerr-like nonlinearity obtained by numerically solving Eqs. (2) and (4), respectively. Here, we fixed the coupling strength to $\lambda = \lambda_{\rm SR}$ with $\lambda_{\rm SR}$ as the critical point signalling the instability of the trivial fixed point $\alpha = \beta = \gamma = 0$. For larger ω_{20} exemplified in Fig. 2(b), the quantitative agreement between the two models improves since the adiabatic elimination of the c-mode hinges on the assumption that $\omega_{20} \ll \omega_{10}, \omega_p$. Nevertheless, we find qualitative agreement for the type of response (i.e., an LC phase) for $\omega_{20} = 4\kappa$, a parameter choice motivated by the experiment that will be discussed later.
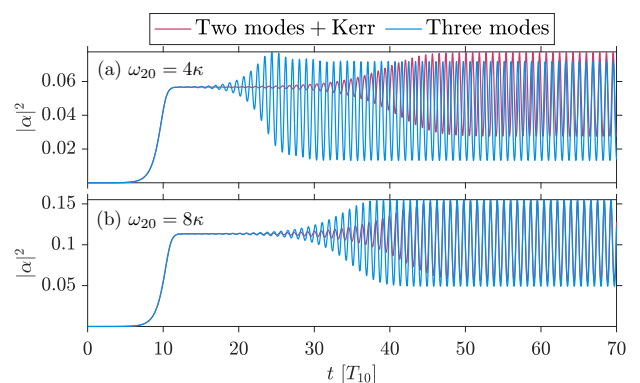
FIG. 2. Comparison of the mean-field dynamics according to the two-mode model with Kerr-like nonlinearity and the three-mode model for (a) $\omega_{20} = 4\kappa$ and (b) $\omega_{20} = 8\kappa$. The coupling strength is fixed to $\lambda = 1.09\lambda_{\rm SR}$. The remaining parameters are $\kappa = \omega_p = \chi/2 = \omega_{10}/2$.

B. Bifurcation theory

To understand the nature of different critical transitions in the system as shown in Fig. 1(d), we employ a stability matrix analysis for fixed points of the semiclassical EOM Eq. (4). The EOM for the three-mode model prior to the adiabatic elimination, Eq. (2), can be recast into $\partial_t \mathbf{X} = \mathbf{F}(\mathbf{X})$ with $\mathbf{X} = \{\alpha, \alpha*, \beta, \beta^*, \gamma, \gamma^*\}$. Numerically solving for the equilibrium or fixed points $\mathbf{X}_0 = \{\alpha_0, \alpha_0^*, \beta_0, \beta_0^*, \gamma_0, \gamma_0^*\}$, such that $\mathbf{F}(\mathbf{X}_0) = 0$, and linearising the EOM around those, we obtain a linearised set of EOM given by

$$\partial_t \delta \mathbf{X} = \mathbf{J}_0 \delta \mathbf{X}, \quad (6)$$

where $\delta_{\mathbf{X}} = (\mathbf{X} - \mathbf{X}_0)$ and $\mathbf{J}_0 = \left.\frac{\partial \mathbf{F}(\mathbf{X})}{\partial \mathbf{X}}\right|_{\mathbf{X}_0}$ is the Jacobian stability matrix. In the case of the three-mode model, the Jacobian matrix is

$$\mathbf{J}_0 = \left.\frac{\partial \mathbf{F}(\mathbf{X})}{\partial \mathbf{X}}\right|_{\mathbf{X}_0} = \begin{pmatrix} -i\left[\omega_p + \chi\left(\gamma_0 + \gamma_0^*\right)\right] - \kappa & 0 & -i\lambda & -i\lambda & -i\chi\alpha_0 & -i\chi\alpha_0 \\ 0 & i\left[\omega_p + \chi\left(\gamma_0 + \gamma_0^*\right)\right] - \kappa & i\lambda & i\lambda & i\chi\alpha_0^* & i\chi\alpha_0^* \\ -i\lambda & -i\lambda & -i\omega_{10} & 0 & 0 & 0 \\ i\lambda & i\lambda & 0 & i\omega_{10} & 0 & 0 \\ -i\chi\alpha_0^* & -i\chi\alpha_0 & 0 & 0 & -i\omega_{20} & 0 \\ i\chi\alpha_0^* & i\chi\alpha_0 & 0 & 0 & 0 & i\omega_{20} \end{pmatrix}. \tag{7}$$

For the two-mode model with Kerr-like nonlinearity described by Eq. (4), applying a similar linearisation leads to the following Jacobian stability matrix

$$\mathbf{J}_0 = \begin{pmatrix} \omega_p - i\kappa - \frac{4|\alpha_0|^2\chi^2}{\omega_{20}} & -\frac{2\alpha_0^2\chi^2}{\omega_{20}} & \lambda & \lambda \\ \frac{2(\alpha_0^*)^2\chi^2}{\omega_{20}} & \frac{4|\alpha_0|^2\chi^2}{\omega_{20}} - i\kappa - \omega_p & -\lambda & -\lambda \\ \lambda & \lambda & \omega_{10} & 0 \\ -\lambda & -\lambda & 0 & \omega_{10} \end{pmatrix}, \tag{8}$$

where $\mathbf{X}_0 = \{\alpha_0, \alpha_0^*, \beta_0, \beta_0^*\}$.

The solutions of Eq. (6) can be written as a superposition of $\exp(\omega_i t)$ with ω_i being the eigenvalues (EVs) of the Jacobian matrix (8). The fixed points are only stable if the real part of all the EVs are negative $\mathrm{Re}(\omega_i) < 0 \, \forall \, i$ [29]. Focusing on the two-mode model with Kerr-like nonlinearity described by the stability matrix in Eq. (8), we present the real and imaginary parts of the EVs of $\mathbf{J}_0$ using the appropriate fixed points in Figs. 3(a) and 3(b), respectively. Exemplary dynamics of the occupation $|\alpha|^2$, which in the atom-cavity platform correponds to the photon number in the cavity, for various phases are shown in Figs. 3(c)-3(e), which we obtain by solving the mean-field EOM of Eq. (12). The parameters are $\kappa = \omega_p = \chi/2 = \omega_{10}/2 = \omega_{20}/4$. We choose $\omega_p = \kappa$ since this corresponds to the weakest light-matter coupling needed to enter the SR phase λ_{SR} for fixed κ, which can be inferred by setting $\partial\lambda_{\mathrm{SR}}/\partial\omega_p = 0$ and solving for ω_p. In Figs. 3(c)-3(e), we use the NP as the initial state and linearly increase the light-matter coupling strength to its finale value within $\approx 150 \, T_{10}$, where $T_{10} = 2\pi/\omega_{10}$. To rule out transient behaviour we only present the dynamics after $600 \, T_{10}$.

In Fig. 3(a), for $\lambda < \lambda_{\mathrm{SR}}$, we use the fixed point $\alpha = \beta = \gamma = 0$ corresponding to the so-called normal phase (NP) and find that, as expected, all $\mathrm{Re}(\omega_i)$ are negative, thereby confirming its stability. The dynamics of the NP is depicted in Fig. 3(c) confirming a steady-state value of $|\alpha|^2 = 0$. Above the critical point λ_{SR}, the NP fixed point acquires an EV with a positive real part (see Appendix A), which suggests an instability of this fixed point manifesting itself as a phase transition from the NP to a superradiant (SR) phase in the context of the Dicke model. This transition is a supercritical pitchfork bifurcation, meaning that the real and imaginary parts of the two

relevant EVs are zero at λ_{SR}. In the SR region highlighted by the pink area in Figs. 3(a) and 3(b), we obtain two new fixed points corresponding to the pair of symmetry broken states in the SR phase. Expanding around the SR fixed points, indeed, we find that they are stable in the SR region as their $\mathrm{Re}(\omega_i)$ are all negative. The time evolution in the SR phase depicted in Fig. 3(d) shows a constant photon occupation.

Our model exhibits a second critical point λ_{LC} at which a supercritical Hopf bifurcation occurs, which signals an instability towards a formation of a LC. The LC region in Figs. 3(a) and 3(b) is depicted in light blue. In contrast to the pitchfork bifurcation, the relevant EVs cross the real axis, while their imaginary parts are nonzero. An exemplary LC dynamics is shown in Fig. 3(e). The photon number oscillates at a frequency given by the imaginary part of the corresponding EVs. For a Hopf bifurcation, the oscillation amplitude of the LCs increases as $\sqrt{\lambda - \lambda_{\mathrm{LC}}}$ [30] and we show that the LCs in this paper follows this scaling behaviour in Appendix B. In Fig. 1(e), we present the photon dynamics in the phase space

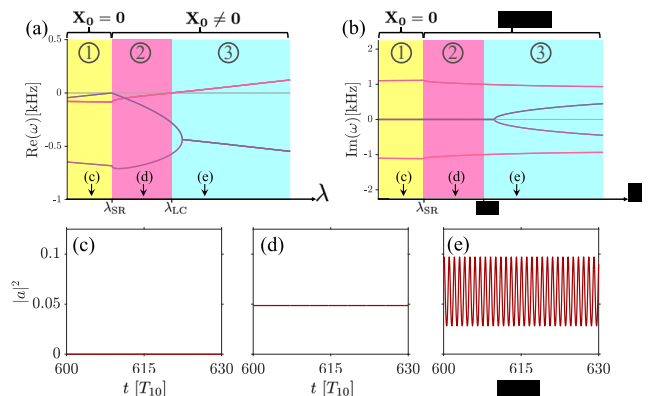FIG. 3. Spectrum and dynamics for the two-mode model with a Kerr-like nonlinearity. (a),(b) Real and imaginary part of the eigenvalues obtained from numerically diagonalizing the stability matrix. Shaded background indicates the different phases: normal phase (yellow (1)), superradiant phase (pink (2)) and limit cycle phase (light blue (3)). (c)-(e) corresponding light field dynamics in each shaded background.

spanned by the real and imaginary parts of the photon field. It demonstrates how the system approaches the stable LC orbit starting from an SR phase marked by the gray diamond. The red curves represent transient oscillations and the blue lines correspond to the final LC orbit. In Appendix B, we show the trajectories of different initial states converging to the same LC orbit, which is a characteristic feature of a limit cycle attractor.

Before we discuss the experimental results, we briefly mention further features of the LCs found in the smaller islands in the phase diagram as shown in Appendix B. Here, an LC phase oscillates between the two fixed points while accumulating a phase in the photon field at integer steps of π. This suggests the presence of a particle current similar to the self-oscillating pumping reported in Ref. [31, 32]. We note that this type of LC is not due to a Hopf bifurcation as the scaling of the LC oscillations amplitude is approximately constant with λ, and therefore inconsistent with the Hopf bifurcation scaling $\sqrt{\lambda - \lambda_{\text{LC}}}$. Exemplary dynamics of the photon number and the phase winding are presented in Appendix B.

III. ATOM-CAVITY IMPLEMENTATION

A. Mapping from the atom-cavity system

In the following, we focus on a specific implementation using an atom-cavity setup [33, 34] as sketched in Fig. 1(c). In the context of LCs and CTCs found in the atom-cavity platform [16], an important implication of our theory is the possibility of observing LCs even for attractive pump field potentials as demonstrated in Fig. 3, which is consistent with the predictions in Ref. [35]. We now show that this is indeed the case for an atom-cavity system operating in the recoil-resolved or good cavity limit $\kappa \sim \omega_{01}$ [36, 37]. The details of the derivation for mapping the atom-cavity Hamiltonian onto the effective model Eq. (12) can be found in Appendix C. In what follows, we will simply sketch the crucial steps. We start from a two-dimensional many-body Hamiltonian [38, 39] neglecting both the trapping potential and contact interactions between the atoms. A study on the influence of inhomogeneous trapping and short-range interactions on a dissipative time crystal in an atom-cavity system reveals the persistence of the time crystalline phase [40]. Next, we expand the atomic field operator in the basis of three momentum excitations of the BEC. The first state in the three-level model $|0\rangle$ is represented by the zero-momentum mode $|p_x, p_y\rangle = |0, 0\rangle$ with an energy $E_0 = 0$. The second level $|1\rangle$ is given by the coherent superposition of $|\pm\hbar k, \pm\hbar k\rangle$ momentum modes with an energy $E_1 = 2\hbar\omega_{\text{rec}}$. The third level $|2\rangle$ corresponds to the coherent superposition of the $|0, \pm 2\hbar k\rangle$ momentum modes along the cavity axis with an energy $E_2 = 4\hbar\omega_{\text{rec}}$. This expansion then leads to the effective three-level model in Fig. 1(b). Similar models have been recently studied in [41–47]. After using an SU(3) representation via the Schwinger boson mapping, we apply the HP approximation [48] to finally obtain Eq. (2).

Now that we have shown that Eq. (2) can be obtained from

the atom-cavity model, one can simply follow the adiabatic elimination discussed in Sec. II to get Eq. (4). Alternatively, we can first derive a nonlinear Dicke model, which can then be approximated as the two-mode model with Kerr-like nonlinearity in the thermodynamic limit, by first adiabatically eliminating the third-level in the few-mode atom-cavity description in Appendix C prior to employing the Schwinger-boson mapping. In doing so, we only need SU(2) spin operators as in the standard Dicke model leading a nonlinear Dicke Hamiltonian

$$\hat{H} = \hat{H}_{\text{Dicke}} + \hat{H}_{\text{Kerr}}, \tag{9}$$

where the Dicke Hamiltonian is

$$\frac{\hat{H}_{\text{Dicke}}}{\hbar} = \omega_p \hat{a}^\dagger \hat{a} + \omega_{10} \sum_{\ell=1}^N \sigma_\ell^z + \frac{2\lambda}{\sqrt{N}} \sum_{\ell=1}^N (\hat{a} + \hat{a}^\dagger)\sigma_\ell^x, \tag{10}$$

with σ_ℓ^μ as the individual SU(2) spin operators. The bosonic operators $\hat{a}$ and $\hat{a}^\dagger$ annihilate and create a photon in the quantised light mode, respectively. The Kerr-like Hamiltonian is

$$\hat{H}_{\text{Kerr}}/\hbar = -\frac{\chi^2}{\omega_{20}}\hat{a}^\dagger \hat{a}\hat{a}^\dagger \hat{a}. \tag{11}$$

We emphasize that while we consider a third level to be the origin of the Kerr nonlinearity, other physical processes generating this nonlinearity will result in the same phenomena, see for example Refs. [26–28]. Introducing $j_\mu = \frac{1}{\sqrt{N}}\langle\sum_\ell \sigma_\ell^\mu\rangle$, with $\mu \in x, y, z$, the EOM for the spin-boson model are given by

$$\begin{aligned}
\frac{d\alpha}{dt} &= -i\left[\omega_p - 2\frac{\chi^2}{\omega_{20}}|\alpha|^2 - i\kappa\right]\alpha - 2i\lambda j_x \\
\frac{dj_x}{dt} &= -\omega_{10}j_y \\
\frac{dj_y}{dt} &= \omega_{10}j_x - 2\lambda(\alpha + \alpha^*)j_z \\
\frac{dj_z}{dt} &= 2\lambda(\alpha + \alpha^*)j_y
\end{aligned} \tag{12}$$

with ω_p is the photon frequency, and ω_{nm} is the level splitting between the atomic states $|n\rangle$ and $|m\rangle$, see Fig.1(b). The light-matter interaction proportional to λ couples the atomic modes with the two lowest energies $|0\rangle$ and $|1\rangle$ as in the standard dipole approximation. Here, we also consider a two-photon coupling between the first and third atomic levels $|0\rangle$ and $|2\rangle$, which we adiabatically eliminate to obtain the Kerr-like nonlinearity for the photonic field. The strength of this nonlinearity is controlled by χ. We included the decay strength κ in the photonic mode equation of motion, which captures the rate at which photons are emitted from the cavity. We apply a Holstein-Primakoff (HP) transformation and include only terms up to linear order in the bosonic operator [42, 49] and obtain precisely the EOM in Eq. (4)

B. Experimental results

We experimentally demonstrate the emergence of a LC phase for an attractive light-shift pump potential in the atom-
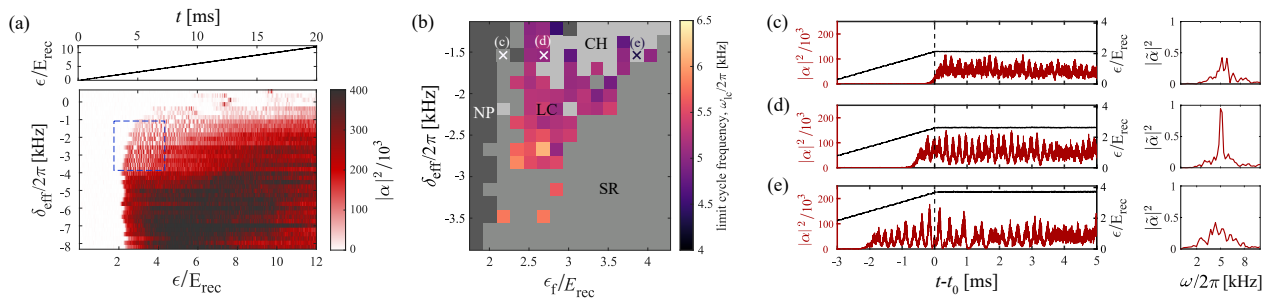
FIG. 4. Experimental data for a red-detuned CTC or LC. (a) Pump strength protocol (top) and the intracavity photon number $|\alpha|^2$ (bottom) for varying the effective cavity field frequency δ_{eff} and linearly ramped pump strength ϵ in units of the recoil energy E_{rec}. The blue dashed box depicts the area of the parameter space further analysed in (b). (b) Phase diagram for varying δ_{eff} and final pump strength ϵ_f. For each plaquette, we linearly ramp the pump strength to ϵ_f while keeping δ_{eff} constant. We categorize the normal phase (NP), superradiant (SR) phase, chaotic phase (CH), and the limit cycle (LC) phase. The colour represents the dominant oscillation frequency in the LC region. (c)-(e) Exemplary dynamics and the resulting power spectrum $\tilde{\alpha}(\omega)$ of the SR, LC, and chaotic phase marked by crosses in (b). t_0 is the time at which the pump strength is fully ramped up and is kept constant.

cavity platform schematically shown in Fig. 1(b). We emphasise that this in contrast to the repulsive light-shift pump potential used in the theoretical prediction [12, 22, 50] and experimental realisation [16] of LCs in the atom-cavity system. That is, we provide here the first experimental observation of a LC or CTC for an attractive light-shift pump potential, which underpins the mechanism put forth by our generic model Eq. (12). That is, the transition from an SR to an LC phase can be understood as a Hopf bifurcation induced by the Kerr nonlinearity χ that gives access to a third level $|2\rangle$ beyond the usual two-level approximation that maps the atom-cavity system onto an open Dicke model.

In our experiment, we place a BEC consisting of $N \approx 4 \times 10^4$ ^{87}Rb atoms inside a high-finesse cavity that is pumped transversely by a retro reflected laser beam, which produces a standing wave potential for the atoms. The pump wavelength used is 803.63 nm, which is red-detuned to the relevant atomic transition at 794.98 nm. The resulting two-photon coupling strength is $\chi/2\pi \approx -6$ kHz. The recoil energy $E_{\text{rec}}/\hbar = 2\pi \times 3.55$ kHz is comparable to the cavity decay rate of $\kappa = 2\pi \times 3.6$ kHz. Thus, the dynamics of the light field and the atoms evolve on the same time scale and influence each other on equal footing. To identify the approximate regime of LCs, we record the photon number $|\alpha|^2$ over 5 ms after the pump strength is slowly ramped up from zero to its final value at a rate of $0.6 \frac{E_{\text{rec}}}{\text{ms}}$. We show the corresponding results for different effective pump-cavity detuning $\delta_{\text{eff}} \sim -\omega_p$ in Fig. 4(a). In addition to the standard NP-SR phase transition [33, 34], we observe oscillatory behaviour for certain values of small $|\delta_{\text{eff}}|$ after entering the SR phase, which is indicative of a LC phase.

We focus on the region enclosed by the dashed blue box in Fig. 4(a). For these combinations of ϵ_f and δ_{eff}, we now ramp up the pump strength with the same rate as before to its desired final value, which is then kept constant, see Appendix D for details on the construction of the phase diagram. The resulting phase diagram is shown in Fig. 4(b). Comparing the overall shape of the experimental LC regime in Fig. 4(b)

and the theoretical results presented in Appendix B, we find qualitative agreement. However, we point out that the approximations applied in our theory lead to a larger area with stable LCs than in the experiment. We further note that, in the experiment, the lifetime of the LCs is limited by atom loss induced by three-body collisions, which essentially reduces the light-matter coupling λ and non-linearity χ, and by the inherent short-range interactions, which has been proposed to make the LC metastable [51]. The atom loss effectively drags the system to the bottom-left region of the phase diagram Fig. 4(b), which brings it back to the NP. In Figs. 4(c)-4(e), we present three exemplary traces of the time evolution of the photon number and their corresponding power spectra, characterizing the chaotic (CH), LC and SR phases marked in Fig. 4(b). Approaching the LC phase boundary from the SR phase, in the intra-cavity photon number versus time, shown in Fig. 4(c), we observe a constant population level of the cavity mode together with noise, with a power spectrum showing a broad peak around the LC-frequency, which we interpret as a precursor of the LC phase (see Appendix D for details). Increasing the pump strength, and thus the light-matter coupling, we observe LC dynamics with a single dominant frequency peak in the power spectrum. Increasing the pump strength even further leads to aperiodic dynamics as seen directly in the time evolution of the photon number, which exhibits a largely broadened power spectrum.

IV. CONCLUSIONS

In conclusion, we have proposed a generic three-mode model and a nonlinear two-mode model that features different types of LCs in a wide range of parameters. We motivate this model as the mean-field approximation of an extended Dicke model, but emphasize that it emerges generically in a broad class of systems. The predominant type of LC in the model arises from a supercritical Hopf bifurcation. The Hamiltonian of this model can be implemented by systems that can be ap-

proximated as coupled bosonic modes using a HP transformation. We show that the existence of LCs are independent of the sign of the Kerr nonlinearity introduced by a two-photon process, which is relevant for the formation of LCs in atom-cavity systems. More specifically, it is the presence of a third mode and its coupling with the density of a dissipative bosonic mode that leads to an effective Kerr-like coupling, which introduces the nonlinearity needed for the emergence of LCs. Using an atom-cavity platform, we experimentally observe for the first time the emergence of stable LCs for attractive or red-detuned pump fields. We map out the phase diagram and find good qualitative agreement with the theoretical results. Our work puts forth a new mechanism for creating LCs and studying nonlinear dynamics in highly controllable quantum systems. We emphasise that our bosonic model Eq. (12) and Eq. (4) is not limited to atom-cavity systems and can be used in a wider class of systems involving boson-mediated interactions and three-level systems, such as cavity-magnon models [23], circuit QED [24, 25], or Rydberg platforms [8, 9].

Appendix A: Spectrum using $\mathbf{X}_0 = 0$

We present in Fig. 5 the spectrum of the Jacobian using the NP fixed point $\mathbf{X}_0 = 0$ for different λ. For $\lambda > \lambda_{\mathrm{SR}}$, the system acquires an EV with $\mathrm{Re}(\omega_i) > 0$ as seen in one of the blue curves in Fig. 5(a). Hence, the NP fixed point becomes unstable.
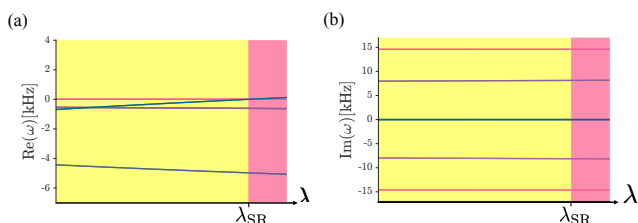
FIG. 5. (a) Real and (b) imaginary parts of the eigenvalues of the stability matrix for the boson-mediated three-level system with the fixed point $\mathbf{X}_0 = 0$. The fixed point $\mathbf{X}_0 = 0$ becomes unstable for $\lambda > \lambda_{\mathrm{SR}}$.

Appendix B: Limit cycle dynamics

1. Amplitude scaling of the LC transition

We show the characteristic scaling of the LC oscillations amplitude as we cross the SR-LC phase transition. For LC stemming from Hopf bifurcations, the amplitude of the LC scales with $\mu = \lambda - \lambda_{\mathrm{LC}}$ as $\mu^{1/2}$ for $\lambda > \lambda_{\mathrm{LC}}$ [30]. We present the scaling as a function of μ in Fig. 6. The scaling agrees well with the theoretical prediction. We attribute deviations from the expeted $\mu^{1/2}$ behaviour to asymmetry in the LC dynamics per cycle. We further note that, while we are very close to the phase transition, numerically its not feasible to zoom in further for even smaller μ as the systems takes too long to approach the corresponding stable LC phase. This could also further lead to deviations from the expected scaling.
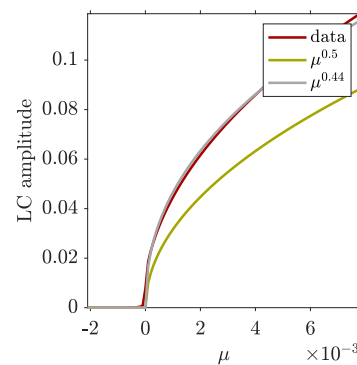
FIG. 6. Scaling of the LC oscillations amplitude on $\mu = \lambda - \lambda_{\mathrm{LC}}$.

2. Different initial states

We present the dynamics of the transient behaviour of the light-field during the transition from a random initial state towards the stable LC orbit. We find that independent of the initial state, the steady state dynamics is the same LC orbit, which is the defining behaviour of LC dynamics. We demonstrate this for three different initial states in Fig. 7.
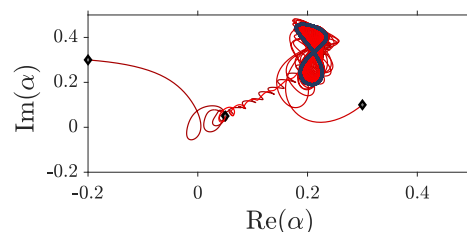
FIG. 7. Dynamics in the phase space of the photon mode α for different initial states (gray diamonds) and their approach towards the limit cycle (blue line).

3. Phase diagram for blue- and red-detuned pump frequencies

Solving the corresponding equations of motion (EOM) allows us to construct the phase diagram in Fig. 8(b) for different combinations of ω_p and λ. The vertical axis is displayed as $-\omega_p/\kappa$ since this is related to the effective detuning between the pump and cavity fields, which is chosen to be negative in atom-cavity experiments. Unless indicated otherwise, we fix the two-photon coupling strength to $\chi/\kappa \approx 4$, which is a typical value in atom-cavity experiments as we will show later. In Fig. 1(d), we only highlight the regimes with stable LCs, although we note that the system also hosts a transition between a normal (NP) and a superradiant (SR) phase at a critical light-matter interaction $\lambda_{\rm SR} = \sqrt{(\kappa^2 + \omega^2)\,\omega_{10}/4\omega}$. We also find chaotic phases marked by irregular dynamics of the photon occupation. We classify a periodic dynamics as a limit cycle if the steady-state amplitude of the oscillations satisfy $\max(|\alpha|^2)/\mathrm{mean}(|\alpha|^2) > 0.02$ and the long-time standard deviation of the oscillation peaks is $\sigma_{|\alpha|^2} < 0.025$. These LC phases are equivalent to the CTCs observed in Ref. [16].
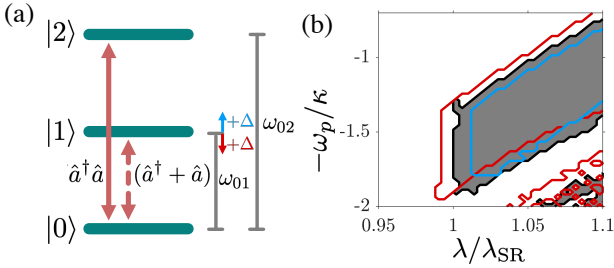
FIG. 8. (a) Three-level model coupled to a single light mode including single-photon coupling with strength λ and two-photon coupling with strength χ. (b) Phase diagram of the three-level model in (a) and Fig1. (c) for varying interaction strengths λ and photon frequencies $\omega_{\rm p}$. Areas enclosed by lines denote a stable limit cycle regime. Black denotes results for the system in (a) without the level dressing of the transverse pump field, while blue and red correspond to blue- and red-detuned pump frequencies relative to ω_{01}, respectively.

The atomic levels can be dressed by the pump field leading to energy shifts $\Delta = \mathrm{sign}(\chi)\epsilon\omega_{\rm rec}/4 = \mathrm{sign}(\chi)\lambda^2/8\omega_{\rm rec}\chi$, where ϵ is the intensity of the pump field and $\omega_{\rm rec}$ is the associated recoil frequency. Neglecting the pump laser dressing in the atom-cavity system means that the frequency splitting be-

tween the $|0\rangle$ and $|1\rangle$ is simply given by the recoil frequency, i.e., $\omega_{01} = 2\omega_{\rm rec}$. A more accurate theory includes such dressing [42, 43], which then adjusts the frequency of $|1\rangle$ depending on the sign of the frequency shift per single atom U_0 as depicted in Fig. 8(a).

In Fig. 8(b) we find two distinct regimes, wherein LCs can emerge. For small ω_p and λ, we find a large area in the phase diagram hosting LCs. In contrast for large ω_p and λ, we find smaller disconnected islands of LCs. We note the energy shift due to the pump dressing Δ simply moves the LC regions without changing their overall shape in the phase diagram. Therefore, our results suggest that the emergence of the LC phase in atom-cavity systems [12, 16, 22] does not hinge on the repulsive nature of the pump $\Delta > 0$. Instead, the effective Kerr-like nonlinearity χ that couples the lowest energy mode to a new third mode is the crucial ingredient for the existence of the LCs or CTCs.

4. Phase-winding limit cycles

For the type of LC found in the small islands shown in Fig. 8, we present the photon number dynamics and the corresponding unwrapped phase in Fig. 9. We find that, in contrast to the LCs discussed in the main text, these LCs pick up a phase of π during each cycle.
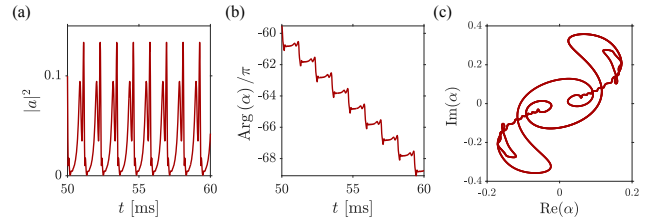
FIG. 9. (a) Light-field dynamics of the photon number, (b) corresponding unwrapped phase of α, and (c) phase space dynamics. The parameters are $\omega_p/\kappa = 1.9$ and $\lambda/\lambda_{\rm SR} = 1.02$.

Appendix C: Mapping from the atom-cavity Hamiltonian

We start from the many-body Hamiltonian describing a transversely pumped BEC inside a high-finesse cavity [16, 38]

$$\hat{H}/\hbar = -\delta_C \hat{a}^\dagger \hat{a} + \int dydz\,\Psi^\dagger(y,z)\left[-\frac{\hbar}{2m}\nabla^2 + \mathrm{sign}\,(U_0)\,\omega_{\rm rec}\epsilon_p \cos^2(ky) \right]\Psi(y,z) \tag{C1}$$

$$+ \Psi^\dagger\left(U_0\hat{a}^\dagger\hat{a}\cos^2(kz) - \sqrt{\omega_{\rm rec}|U_0|\epsilon_p}\cos(ky)\cos(kz)(\hat{a}^\dagger + \hat{a}) \right)\Psi(y,z), \tag{C2}$$

where the pump (cavity) axis is along the $y(z)$-direction, ϵ_p is the pump strength, U_0 is the maximum light-shift per atom,

$\omega_{\rm rec}$ is the recoil frequency, and δ_C is the detuning between

the pump and cavity frequencies. We expand our field operator as

$$\Psi = \psi_0 c_0 + \psi_1 c_1 + \psi_2 c_2 \qquad (C3)$$

with

$$\psi_0 = 1 \qquad (C4)$$
$$\psi_1 = 2\cos(ky)\cos(kz) \qquad (C5)$$
$$\psi_2 = \sqrt{2}\cos(2kz) . \qquad (C6)$$

With this, we obtain the effective Hamiltonian

$$H/\hbar = -\delta_{\mathrm{eff}}\hat{a}^\dagger\hat{a} + \omega_{\mathrm{rec}}\epsilon_p/2 + (\omega_{10} + \Delta)\, c_1^\dagger c_1 + \omega_{20} c_2^\dagger c_2 \qquad (C7)$$

$$+ \frac{U_0}{2}\hat{a}^\dagger\hat{a}\left(\frac{1}{2}c_1^\dagger c_1 + (c_2^\dagger c_0 + c_0^\dagger c_2)/\sqrt{2}\right)$$

$$+ \frac{\lambda}{\sqrt{N}}(\hat{a}^\dagger + \hat{a})\left[(c_0^\dagger c_1 + c_1^\dagger c_0) + (c_1^\dagger c_2 + c_2^\dagger c_1)\sqrt{2}\right] ,$$

where $\lambda/\sqrt{N} = -\omega_{\mathrm{rec}}|U_0|\epsilon_p/2$, $\delta_{\mathrm{eff}} = \delta_C - U_0 N/2 = \delta_C - U/2$, $\Delta = \mathrm{sign}(\chi)\epsilon\omega_{\mathrm{rec}}/4$, $\omega_{10} = \omega_{\mathrm{rec}}$ and $\omega_{20} = 2\omega_{\mathrm{rec}}$. In the following we assume that the the lowest mode is highly occupied. This means we neglect the term $\frac{U_0}{4}a^\dagger a c_1^\dagger c_1$ and $\frac{\lambda}{\sqrt{N}}(a^\dagger + a)(c_1^\dagger c_2 + c_2^\dagger c_1)\sqrt{2}$ as these scale as $1/N$ compared to the other terms and we are interested in the limit $N \gg 1$. We further drop constant energy shifts of the Hamiltonian. Thus, the simplified atom-cavity Hamiltonian is

$$H/\hbar = -\delta_{\mathrm{eff}}\hat{a}^\dagger\hat{a} + (\omega_{10} + \Delta)\, c_1^\dagger c_1 + \omega_{20} c_2^\dagger c_2 \qquad (C8)$$

$$+ \frac{\sqrt{2}U_0}{4}\hat{a}^\dagger\hat{a}\left(c_2^\dagger c_0 + c_0^\dagger c_2\right) + \frac{\lambda}{\sqrt{N}}(\hat{a}^\dagger + \hat{a})\left(c_0^\dagger c_1 + c_1^\dagger c_0\right).$$

Next, we map the three atomic modes to SU(3) spins using the Schwinger-Boson mapping [42] and obtain

$$H/\hbar = -\delta_{\mathrm{eff}}\hat{a}^\dagger\hat{a} + (\omega_{10} + \Delta)\,\hat{J}_z^{01} + \omega_{20}\hat{J}_z^{02} \qquad (C9)$$

$$+ \frac{\sqrt{2}U_0}{4}\hat{a}^\dagger\hat{a}\,\hat{J}_x^{02} + \frac{\lambda}{\sqrt{N}}(\hat{a}^\dagger + \hat{a})\hat{J}_x^{01} .$$

Finally, we use the Holstein-Primakoff representation given by [48]

$$\hat{J}_z^{01} = \hat{b}^\dagger\hat{b} - N/2, \quad \hat{J}_+^{01} = \hat{b}^\dagger\sqrt{N - \left(\hat{b}^\dagger\hat{b} + \hat{c}^\dagger\hat{c}\right)}, \qquad (C10)$$

$$\hat{J}_-^{01} = \sqrt{N - \left(\hat{b}^\dagger\hat{b} + \hat{c}^\dagger\hat{c}\right)}\,\hat{b},$$

$$\hat{J}_z^{02} = \hat{c}^\dagger\hat{c} - N/2, \quad \hat{J}_+^{02} = \hat{c}^\dagger\sqrt{N - \left(\hat{b}^\dagger\hat{b} + \hat{c}^\dagger\hat{c}\right)},$$

$$\hat{J}_-^{02} = \sqrt{N - \left(\hat{b}^\dagger\hat{b} + \hat{c}^\dagger\hat{c}\right)}\,\hat{c},$$

and by retaining terms only up to the lowest order in N, with $\omega_p = -\delta_{\mathrm{eff}}$ and $\chi = \sqrt{2}/4 U_0 N$, we obtain Eq. (1).

Appendix D: Construction of the experimental phase diagram

To construct the phase diagram from the experimental data, we consider the following three quantities to distinguish between the various phases. We consider the average photon number $\overline{|\alpha|^2}$, the standard derivation of the fluctuating photon number divided by the mean photon number $\sigma_{\overline{|\alpha|^2}} = \sigma_{|\alpha|^2}/\overline{|\alpha|^2}$, and the so-called crystalline fraction ξ [16, 52], which is defined via the amplitude of a Gaussian fit around the LC peak in the Fourier transform of the dynamics of the photon number.

We classify trajectories with less then 2×10^3 photons on average detected to be in the normal phase. To further distinguish between the SR phase, limit cycle phase and the chaotic phase, we use the following criteria. If the average photon number is larger then $\overline{|\alpha|^2} > 2 \times 10^3$ and $\xi \leq 1/e \times \max(\xi)$, then the system is classified to be in the SR phase. If the average photon number is larger then $\overline{|\alpha|^2} > 2 \times 10^3$ and $\sigma_{\overline{|\alpha|^2}} > 0.55$, it is in the chaotic/aperiodic phase. Trajectories not falling into one of the previous cases are identified as LC phases.

[1] D. Walls and G. Milburn, *Quantum Optics*, SpringerLink: Springer e-Books (Springer Berlin Heidelberg, 2007).

[2] R. H. Dicke, Coherence in Spontaneous Radiation Processes, Phys. Rev. **93**, 99 (1954).

[3] P. Kirton, M. M. Roses, J. Keeling, and E. G. Dalla Torre, Introduction to the Dicke model: from equilibrium to nonequilibrium, and vice versa, Advanced Quantum Technologies **2**, 1970013 (2019).

[4] C.-K. Chan, T. Lee, and S. Gopalakrishnan, Limit-cycle phase in driven-dissipative spin systems, Phys. Rev. A **91**, 051601 (2015).

[5] E. Owen, J. Jin, D. Rossini, R. Fazio, and M. Hartmann, Quantum correlations and limit cycles in the driven-dissipative Heisenberg lattice, New Journal of Physics **20**, 045004 (2018).

[6] E. Colella, A. Kosior, F. Mivehvar, and H. Ritsch, Open quantum system simulation of faraday's induction law via dynam-

ical instabilities, Physical Review Letters **128**, 10.1103/PhysRevLett.128.070603 (2022).

[7] B. Buča, C. Booker, and D. Jaksch, Algebraic theory of quantum synchronization and limit cycles under dissipation, SciPost Phys. **12**, 097 (2022).

[8] X. Wu, Z. Wang, F. Yang, R. Gao, C. Liang, M. K. Tey, X. Li, T. Pohl, and L. You, Observation of a dissipative time crystal in a strongly interacting Rydberg gas (2023), arXiv:2305.20070 [cond-mat.quant-gas].

[9] K. Wadenpfuhl and C. Adams, Emergence of synchronisation in a driven-dissipative hot Rydberg vapor (2023), arXiv:2306.05188 [physics.atom-ph].

[10] C. Weis, M. Fruchart, R. Hanai, K. Kawagoe, P. B. Littlewood, and V. Vitelli, Exceptional points in nonlinear and stochastic dynamics (2023), arXiv:2207.11667 [nlin.CD].

[11] F. Iemini, A. Russomanno, J. Keeling, M. Schirò, M. Dalmonte, and R. Fazio, Boundary Time Crystals, Phys. Rev. Lett. **121**, 035301 (2018).

[12] H. Keßler, J. G. Cosme, M. Hemmerling, L. Mathey, and A. Hemmerich, Emergent limit cycles and time crystal dynamics in an atom-cavity system, Phys. Rev. A **99**, 053605 (2019).

[13] B. Buča, J. Tindall, and D. Jaksch, Non-stationary coherent quantum many-body dynamics through dissipation, Nature Communications **10**, 1730 (2019).

[14] L. R. Bakker, M. S. Bahovadinov, D. V. Kurlov, V. Gritsev, A. K. Fedorov, and D. O. Krimer, Driven-Dissipative Time Crystalline Phases in a Two-Mode Bosonic System with Kerr Nonlinearity, Phys. Rev. Lett. **129**, 250401 (2022).

[15] M. Krishna, P. Solanki, M. Hajdušek, and S. Vinjanampathy, Measurement-Induced Continuous Time Crystals, Phys. Rev. Lett. **130**, 150401 (2023).

[16] P. Kongkhambut, J. Skulte, L. Mathey, J. G. Cosme, A. Hemmerich, and H. Keßler, Observation of a continuous time crystal, Science **377**, 670 (2022).

[17] T. Liu, J.-Y. Ou, K. MacDonald, and N. Zheludev, Photonic metamaterial analogue of a continuous time crystal, Nature Physics 10.1038/s41567-023-02023-5 (2023).

[18] Y.-H. Chen and X. Zhang, Realization of an inherent time crystal in a dissipative many-body system, Nature Communications **14**, 6161 (2023).

[19] M. P. Zaletel, M. Lukin, C. Monroe, C. Nayak, F. Wilczek, and N. Y. Yao, Colloquium: Quantum and classical discrete time crystals, Rev. Mod. Phys. **95**, 031001 (2023).

[20] J. Keeling, M. Bhaseen, and B. Simons, Collective Dynamics of Bose-Einstein Condensates in Optical Cavities, Phys. Rev. Lett. **105**, 043001 (2010).

[21] M. Bhaseen, J. Mayoh, B. D. Simons, and J. Keeling, Dynamics of nonequilibrium Dicke models, Phys. Rev. A **85**, 013817 (2012).

[22] F. Piazza and H. Ritsch, Self-Ordered Limit Cycles, Chaos, and Phase Slippage with a Superfluid inside an Optical Resonator, Phys. Rev. Lett. **115**, 163601 (2015).

[23] B. Zare Rameshti, S. Kusminskiy, J. Haigh, K. Usami, D. Lachance-Quirion, Y. Nakamura, C.-M. Hu, H. Tang, G. Bauer, and Y. Blanter, Cavity magnonics, Physics Reports **979**, 1 (2022).

[24] C. W. Chang, C. Sabín, P. Forn-Díaz, F. Quijandría, A. M. Vadiraj, I. Nsanzineza, G. Johansson, and C. Wilson, Observation of Three-Photon Spontaneous Parametric Down-Conversion in a Superconducting Parametric Cavity, Phys. Rev. X **10**, 011011 (2020).

[25] F. Minganti, L. Garbe, A. Le Boité, and S. Felicetti, Non-Gaussian superradiant transition via three-body ultrastrong coupling, Phys. Rev. A **107**, 013715 (2023).

[26] J. Larson and T. Mavrogordatos, *The Jaynes–Cummings Model and Its Descendants* (IOP Publishing Ltd, 2021).

[27] M. Aspelmeyer, T. J. Kippenberg, and F. Marquardt, Cavity optomechanics, Reviews of Modern Physics **86**, 1391 (2014).

[28] B. Z. Rameshti, S. V. Kusminskiy, J. A. Haigh, K. Usami, D. Lachance-Quirion, Y. Nakamura, C. M. Hu, H. X. Tang, G. E. Bauer, and Y. M. Blanter, Cavity magnonics (2022).

[29] A. Kosior, H. Ritsch, and F. Mivehvar, Nonequilibrium phases of ultracold bosons with cavity-induced dynamic gauge fields (2022), arXiv:2208.04602 [cond-mat.quant-gas].

[30] S. Strogatz, *Nonlinear Dynamics and Chaos: With Applications to Physics, Biology, Chemistry and Engineering*, Studies in nonlinearity (Westview, 2000).

[31] D. Dreon, X. Baumgärtner, A.and Li, S. Hertlein, T. Esslinger, and T. Donner, Self-oscillating pump in a topological dissipative atom-cavity system, Nature **608**, 494 (2022).

[32] X. Nie and W. Zheng, Nonequilibrium phases of a fermi gas inside a cavity with imbalanced pumping, Phys. Rev. A **108**, 043312 (2023).

[33] K. Baumann, C. Guerlin, F. Brennecke, and T. Esslinger, Dicke quantum phase transition with a superfluid gas in an optical cavity, Nature **464**, 1301 (2010).

[34] J. Klinder, H. Keßler, M. Wolke, L. Mathey, and A. Hemmerich, Dynamical phase transition in the open Dicke model, Proceedings of the National Academy of Sciences **112**, 3290 (2015).

[35] P. Gao, Z.-W. Zhou, G.-C. Guo, and X.-W. Luo, Self-organized limit cycles in red-detuned atom-cavity systems, Phys. Rev. A **107**, 023311 (2023).

[36] H. Keßler, J. Klinder, M. Wolke, and A. Hemmerich, Optomechanical atom-cavity interaction in the sub-recoil regime, New Journal of Physics **16**, 053008 (2014).

[37] J. Klinder, H. Keßler, C. Georges, J. Vargas, and A. Hemmerich, Bose–einstein condensates in an optical cavity with sub-recoil bandwidth, Applied Physics B **122**, 299 (2016).

[38] H. Ritsch, P. Domokos, F. Brennecke, and T. Esslinger, Cold atoms in cavity-generated dynamical optical potentials, Rev. Mod. Phys. **85**, 553 (2013).

[39] J. G. Cosme, J. Skulte, and L. Mathey, Time crystals in a shaken atom-cavity system, Phys. Rev. A **100**, 053615 (2019).

[40] R. J. L. Tuquero, J. Skulte, L. Mathey, and J. G. Cosme, Dissipative time crystal in an atom-cavity system: Influence of trap and competing interactions, Phys. Rev. A **105**, 043311 (2022).

[41] P. Wolf, S. C. Schuster, D. Schmidt, S. Slama, and C. Zimmermann, Observation of subradiant atomic momentum states with bose-einstein condensates in a recoil resolving optical ring resonator, Phys. Rev. Lett. **121**, 173602 (2018).

[42] J. Skulte, P. Kongkhambut, H. Keßler, A. Hemmerich, L. Mathey, and J. G. Cosme, Parametrically driven dissipative three-level Dicke model, Phys. Rev. A **104**, 063705 (2021).

[43] P. Kongkhambut, H. Keßler, J. Skulte, L. Mathey, J. G. Cosme, and A. Hemmerich, Realization of a Periodically Driven Open Three-Level Dicke Model, Phys. Rev. Lett. **127**, 253601 (2021).

[44] R. Lin, R. Rosa-Medina, F. Ferri, F. Finger, K. Kroeger, T. Donner, T. Esslinger, and R. Chitra, Dissipation-Engineered Family of Nearly Dark States in Many-Body Cavity-Atom Systems, Phys. Rev. Lett. **128**, 153601 (2022).

[45] J. Fan and S. Jia, Collective dynamics of the unbalanced three-level Dicke model, Phys. Rev. A **107**, 033711 (2023).

[46] J. Skulte, P. Kongkhambut, S. Rao, L. Mathey, H. Keßler, A. Hemmerich, and J. G. Cosme, Condensate Formation in a Dark State of a Driven Atom-Cavity System, Phys. Rev. Lett. **130**, 163603 (2023).

[47] R. J. Valencia-Tortora, S. P. Kelly, T. Donner, G. Morigi, R. Fazio, and J. Marino, Crafting the dynamical structure of

synchronization by harnessing bosonic multilevel cavity QED, Phys. Rev. Res. **5**, 023112 (2023).

[48] M. Wagner, A nonlinear transformation of SU(3)-spin-operators to bosonic operators, Physics Letters A **53**, 1 (1975).

[49] C. Emary and T. Brandes, Chaos and the quantum phase transition in the Dicke model, Phys. Rev. E **67**, 066203 (2003).

[50] H. Keßler, J. G. Cosme, C. Georges, L. Mathey, and A. Hemmerich, From a continuous to a discrete time crystal in a dissipative atom-cavity system, New Journal of Physics **22**, 085002

(2020).

[51] C. H. Johansen, J. Lang, and F. Piazza, The role of atomic interactions in cavity-induced continuous time crystals (2023), arXiv:2310.16661 [cond-mat.quant-gas].

[52] H. Keßler, P. Kongkhambut, C. Georges, L. Mathey, J. G. Cosme, and A. Hemmerich, Observation of a Dissipative Time Crystal, Phys. Rev. Lett. **127**, 043602 (2021).

2.13 Publication VIII: Observation of a phase transition from a continuous to a discrete time crystal

P. Kongkhambut, J.G. Cosme, <u>J. Skulte</u>, Michelle A. Moreno Armijo, L. Mathey, A. Hemmerich, and H. Keßler — **submitted to Reports on Progress in Physics: Original Research (2024)**

Motivation

This work was motivated by the first observation of a continuous time crystal (CTC) in our previous work and the proposal to use amplitude driving of the pump beam to trigger a phase transition from a CTC to a disspative discrete time crystal (DDTC). The goal of this work was to showcase this transition and show that by doing so the stability and reproducibility of the limit cycle oscillations can significantly be enhanced. A further goal was to use this platform to study classical phenomena occurring in the classical world such as entrainment.

Main findings

In this work, first-authored by Phatthamon Kongkhambut, we have experimentally demonstrated the entrainment of a CTC in an atom-cavity setup. We mapped out the dynamical phase diagram for varying driving strength and driving frequencies and showed the phase locking from an initial random phase to two distinct phases, which shows the transition from a CTC to a DDTC in certain regimes. Comparing our findings to the expected results for classical entrainment we took the first step to bridge between classical and quantum phenomena that occur in bifurcation and synchronisation theory.

Contribution

PK and HK performed the experiments and data analysis supervised by AH. The simulations were performed by JGC, supported by me. JGC and I provided insights into bifurcation theory supervised by LM. All authors contributed to the discussion and interpretation of the results, conceptualizing of the figures, as well as to writing the manuscript.

Observation of a phase transition from a continuous to a discrete time crystal

Phatthamon Kongkhambut,[1] Jayson G. Cosme,[2] Jim Skulte,[1,3] Michelle A. Moreno Armijos,[4] Ludwig Mathey,[1,3] Andreas Hemmerich,[1,3] and Hans Keßler[1,5]

[1]*Zentrum für Optische Quantentechnologien and Institut für Quantenphysik, Universität Hamburg, 22761 Hamburg, Germany*
[2]*National Institute of Physics, University of the Philippines, Diliman, Quezon City 1101, Philippines*
[3]*The Hamburg Center for Ultrafast Imaging, 22761 Hamburg, Germany,*
[4]*Instituto de Física de São Carlos, Universidade de São Paulo, São Carlos, SP 13560-970, Brazil*
[5]*Physikalisches Institut, Rheinische Friedrich-Wilhelms-Universität , 53115 Bonn, Germany*
(Dated: February 20, 2024)

Discrete (DTCs) and continuous time crystals (CTCs) are novel dynamical many-body states, that are characterized by robust self-sustained oscillations, emerging via spontaneous breaking of discrete or continuous time translation symmetry. DTCs are periodically driven systems that oscillate with a subharmonic of the drive, while CTCs are driven continuously and oscillate with a system inherent frequency. Here, we explore a phase transition from a continuous time crystal to a discrete time crystal. A CTC with a characteristic oscillation frequency ω_{CTC} is prepared in a continuously pumped atom-cavity system. Modulating the pump intensity of the CTC with a frequency ω_{dr} close to $2\omega_{\mathrm{CTC}}$ leads to robust locking of ω_{CTC} to $\omega_{\mathrm{dr}}/2$, and hence a DTC arises. This phase transition in a quantum many-body system is related to subharmonic injection locking of non-linear mechanical and electronic oscillators or lasers.

INTRODUCTION

The conceptual idea of time crystals (TCs) was first described as a self-sustaining oscillatory behavior in biological systems Ref. [1], and then established as a dynamical many-body state in physical systems in Refs. [2, 3]. A defining feature of these states is the spontaneous breaking of discrete or continuous time translation symmetry, giving rise to robust oscillatory motion in an extended region of their parameter space. Two distinct scenarios for the emergence of these states are as follows. Firstly, for closed systems, the continuous time translation symmetry (CTTS) can be explicitly broken by a periodic external drive and the remaining discrete time translation symmetry (DTTS) is spontaneously broken by an oscillatory response of the system with a period longer than that of the drive. An ergodicity slowdown mechanism prevents the system from heating up to infinite temperature for long times [4, 5]. This scenario is referred to as a "discrete TC" (DTC). Secondly, a TC state can also arise for open systems coupled to a bath. Similar to the DTC in closed systems, a periodic drive triggers a subharmonic oscillatory motion of the system, resulting in a dissipative DTC. For this state, the appropriately designed coupling to the bath suppresses entropy production. We note that, in contrast to closed systems, in open systems, a TC can also emerge in the absence of periodic driving, resulting in the spontaneous breaking of CTTS. This dynamical state is referred to as a "continuous TC" (CTC) [6–8].

The theoretical conceptualization of TCs in the context of many-body physics was followed by rapid experimental progress. DTCs in nearly closed systems have been realized in arrays of trapped ions, nitrogen vacancy centers, and in a mechanically kicked Bose-Einstein condensate (BEC) [9–11]. Discrete dissipative TCs were demonstrated in a BEC of neutral atoms in an optical cavity [12–15] and in an optical microcavity filled with a Kerr medium [16]. Finally, continuous dissipative TCs were, for example, realized in magnon BECs

[17], BECs of neutral atoms [18], in collections of spins in a semi-conductor matrix [19], in photonic metamaterials [20], or doped crystals [21].

Injection locking (IL) a phenomenon arising if a nonlinear dissipative oscillator in a limit-cycle state [22] is driven externally with a driving frequency ω_{dr}. For sufficiently strong driving, the oscillator locks to the external driving process. This locking can occur at the driving frequency itself, or, more generally, at a rational ratio of the driving frequency [23, 24]. A specific case is subharmonic IL, in which the phase-locking occurs at integer fraction of the driving frequency, i.e. ω_{dr}/n with $n \in \{1, 2, ...\}$. We note that IL is a key phenomenon in electronic circuits, laser systems, and biological systems, such as the circadian rhythms of organisms [25] or the synchronization of flashing of fireflies exposed to a periodically switching torch [26]. In biological systems or mathematical science this phenomenon is referred to as entrainment [22].

RESULTS

In this article, we demonstrate subharmonic IL in the context of time crystals. Here, a limit cycle is provided by a CTC produced in an atom-cavity system, oscillating at a frequency ω_{CTC}. We drive the system with a perturbation with a frequency ω_{dr}, which is close to $2\omega_{\mathrm{CTC}}$. As a result, the CTC locks to the driving frequency, performing an oscillatory motion at $\omega_{\mathrm{dr}}/2$, i.e. at a subharmonic frequency. In the language of time crystals, we realize a non-equilibrium phase transition between a CTC and DTC. In the terminology of laser physics, we establish subharmonic IL in a quantum many-body system.

Our setup is shown in Fig. 1(a). We start with a CTC prepared in an atom-cavity system (cf. Fig. 1(a)) consisting of a BEC located in a high-finesse optical cavity, pumped transversally by an optical standing wave at constant intensity. As reported in Ref. [18], this leads to robust self-sustained oscil-
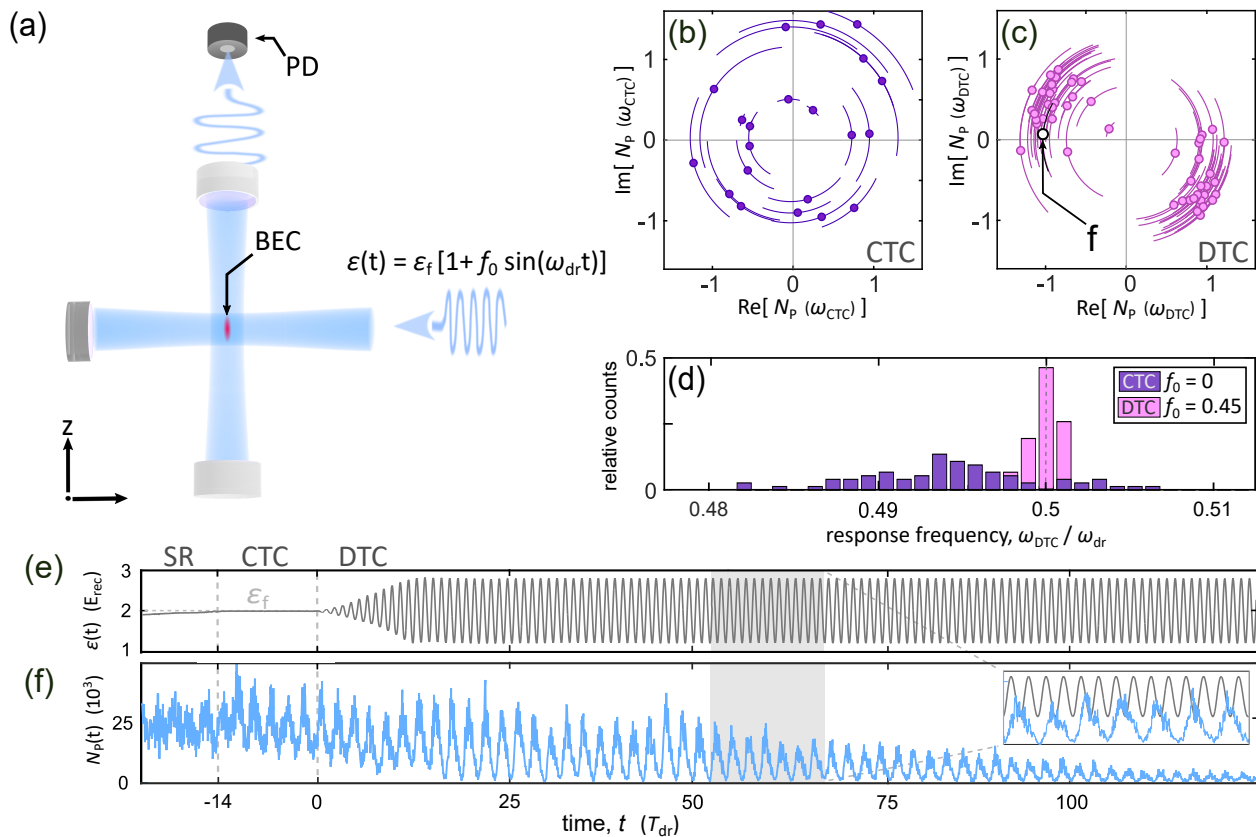
FIG. 1. (a) Schematic drawing of the atom-cavity system periodically pumped transversely with an optical standing wave potential. (b) and (b) Distributions of the time phase of the oscillating intra-cavity photon number $N_P(t)$ at its main response frequency ω_{CTC} (b) for the non-modulated and ω_{DTC} (c) for the modulated case, respectively. The error bars represent the phase uncertainty within the discrete FFT resolution of 100 Hz. The uncertainty with regard to the radial dimension, i.e. the amplitude uncertainty, is negligibly small. Note that the tilt of the two observed phase values by an angle of about $\pi/4$ with respect to modulation signal is due the retardation of the cavity field dynamics due to the small cavity bandwidth. (d) Histogram of the relative number of counts of the response frequency ω_{DTC} in units of the driving frequency $\omega_{dr} = 2\pi \times 22.5$ kHz for the non-modulated ($f_0 = 0$) case in purple (dark) and for the modulated case ($f_0 = 0.45$) in pink (bright), respectively. Here, the same data is used as for B and C, respectively. (e) Pump protocol and (f) the evolution of $N_P(t)$ for a typical experimental realization. Below $t = -14\,T_{dr}$ (first dashed vertical line) $\varepsilon(t)$ is ramped up while the systems is in the SR phase, indicated by a non-zero, non-oscillatory $N_P(t)$. Between $t = -14\,T_{dr}$ and $t = 0\,T_{dr}$, $\varepsilon(t)$ reaches a critical value ε_f and the CTC phase arises, displayed by an oscillatory $N_P(t)$. Above $t = 0\,T_{dr}$ (second dashed vertical line), modulation results in a DTC, indicated by an oscillatory $N_P(t)$ with a significantly lower bandwidth than that of the CTC (cf. d). The inset in F shows a zoom of $\varepsilon(t)$ and $N_P(t)$ for the time interval marked by the gray rectangle. The effective cavity pump detuning is $\delta_{eff} = -2\pi \times 8.2$ kHz and the final pump strength $\varepsilon_f = 2.0\,E_{rec}$ for all measurements presented in the main text.

lations of the intra-cavity photon number $N_P(t)$, which establishes a CTC. Its frequency ω_{CTC} can be associated with the emergence of a limit cycle [7, 27–31]. As seen in Fig. 1(b), the oscillation of the CTC breaks the CTTS. The real and imaginary parts of the Fourier spectrum of $N_P(t)$ at the dominant frequency ω_{CTC} are plotted here for different experimental implementations. The phase values of the Fourier spectra are randomly distributed between 0 and 2π, confirming the expected spontaneous breaking of CTTS.

Next, we modulate the intensity of the pump field $\varepsilon(t)$ at a frequency ω_{dr} close to $2\omega_{CTC}$. The periodic drive breaks the CTTS of the atom-cavity platform such that the modulated system only retains DTTS. Under the influence of the modulation, the system converts into a DTC (cf. Ref. [13]) with an os-

cillation frequency ω_{DTC} approaching $\omega_{dr}/2$, for sufficiently strong driving. In Fig. 1(c), we analyze the Fourier spectra at the emission frequency ω_{DTC} for different experimental implementations. Only two almost equiprobable (49% and 51%) phase values, approximately differing by π, are observed, confirming spontaneous breaking of the DTTS. The modulation, in addition to the observed frequency pulling towards subharmonic response, also gives rise to a line narrowing of the DTC emission as presented in the histogram in Fig. 1(d). This is also seen in Fig. 1(e) and (f), showing that the oscillations observed in $N_P(t)$ become more regular as the modulation sets in at $t = 0$ and the lifetime of the TC extends to more than a hundred driving cycles.
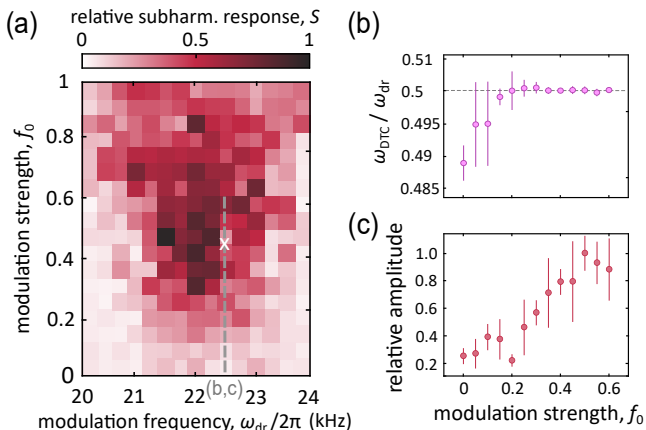
FIG. 2. (a) Relative subharmonic response S versus driving strength f_0 and frequency ω_{dr} for fixed effective detuning $\delta_{\mathrm{eff}} = -2\pi \times 8.2$ kHz and final pump strength $\varepsilon_{\mathrm{f}} = 2.0\, E_{\mathrm{rec}}$. To obtain (a), we ramped the pump strength $\varepsilon(t)$ to its final value ε_{f} for fixed δ_{eff}. After a 0.5 ms long hold time, the driving strength is ramped to its desired value f_0 for selected driving frequency ω_{dr} within 0.5 ms and subsequently held constant for 10 ms. The parameter space is divided into 15 × 18 plaquettes and averaged over 5 to 10 experimental realizations. The white cross indicates the parameter values $f_0 = 0.45$ kHz and $\omega_{\mathrm{dr}} = 2\pi \times 22.5$ kHz, which are used for the measurements in Figs. 1(c-f), Fig. 3 and Fig. 4. (b) Response frequency ω_{DTC} in units of the driving frequency ω_{dr}, plotted versus the driving strength f_0. ω_{DTC} is obtained as the frequency that maximizes a Gaussian fit of the Fourier spectrum of the intra-cavity photon number $N_{\mathrm{P}}(t)$. (c) Relative amplitude of the main spectral component at frequency ω_{DTC}, plotted versus f_0. The plots in (b) and (c) correspond to the path marked in (a) by the gray dashed line. The error bars show the standard deviation and hence represent the shot-to-shot fluctuations.

METHODS

The experimental set-up consists of a Bose-Einstein condensate (BEC) of $N_{\mathrm{a}} = 4 \times 10^4$ ^{87}Rb atoms strongly coupled to a single mode of an optical high-finesse cavity. The system is pumped transversally, perpendicular to the cavity axis at a wavelength $\lambda_{\mathrm{p}} = 791.59$ nm (cf. Fig. 1(a)). The pump light is blue detuned with respect to the relevant atomic transition, the D_1-line of ^{87}Rb at 794.98 nm. The effective pump-cavity detuning is chosen to be negative for all experiments presented and is defined as: $\delta_{\mathrm{eff}} \equiv \delta_c - \delta_-$, where $\delta_c \equiv \omega_{\mathrm{p}} - \omega_{\mathrm{c}}$ is the detuning between the pump field frequency ω_{p} and the cavity resonance frequency ω_{c}, and $\delta_- = \frac{1}{2} N_{\mathrm{a}} U_0$ denotes the collective light shift of the cavity resonance caused by the atomic ensemble for the relevant left circular polarisation mode of the cavity. For the chosen pump wavelength λ_{p}, the light shift per photon is $U_0 = 2\pi \times 0.7$ Hz. The cavity operates in the recoil resolved regime, meaning that the field decay rate of the cavity $\kappa = 2\pi \times 3.2$ kHz, which sets the time scale for the intra-cavity light field dynamics, is comparable to the recoil frequency $\omega_{\mathrm{rec}} = 2\pi \times 3.7$ kHz. The latter sets the time scale for the density distribution of the BEC to adapt to changes of the intra-cavity light field [32, 33]. This
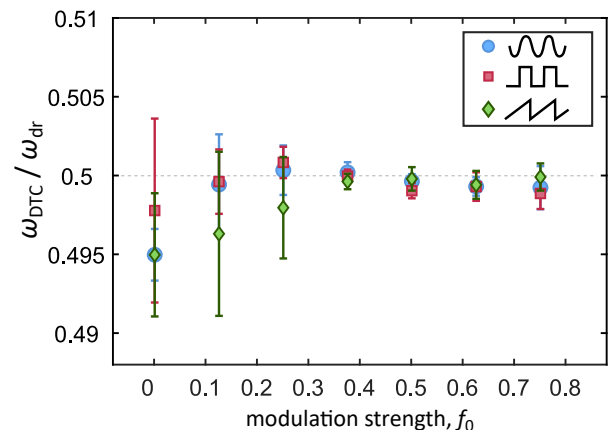
FIG. 3. The blue markers show the response frequency ω_{DTC} in units of the driving frequency ω_{dr} plotted versus the driving strength f_0 for a sinusoidal modulation waveform as used for the measurements presented in Figs. 1, 2, and 4. The error bars show the standard deviation and hence represent the shot-to-shot fluctuations, which are strongly suppressed with increasing value of f_0. The red (square) and green (diamond) markers show the cases of modulation with square wave or sawtooth waveforms, respectively. The experimental protocol is the same as for the measurements in Figs. 2(b,c).

unique regime is a key prerequisite enabling the time crystalline phases [12, 13, 18], which are the starting point of the work presented here. The experimental cycle starts with preparing a CTC. For this, we first prepare the superradiant (SR) phase [33] by linearly increasing the pump-field strength $\varepsilon(t)$. When ε exceeds a critical value, we observe a non-zero intra-cavity photon number N_{P}, indicating that the system is in the SR phase. Increasing $\varepsilon(t)$ further and holding it at a constant value $\varepsilon = \varepsilon_{\mathrm{f}}$, for appropriate settings of δ_{eff} and ε_{f}, causes the system to develop periodic motion, corresponding to a CTC [18]. Subsequently, the pump strength is modulated according to $\varepsilon(t) = \varepsilon_{\mathrm{f}} [1 + f_0 \cos(\omega_{\mathrm{dr}} t)]$ with the mean pump strength ε_{f}, driving strength f_0, and frequency ω_{dr}. If the driving strength f_0 is sufficiently large, the response frequency ω_{DTC} locks to the first subharmonic of ω_{dr} and a DTC is realized (cf. Fig. 1(e,f)).

DISCUSSION

As a first experiment, we identify the optimal parameter values of f_0 and ω_{dr} where the IL of the CTC works most efficiently. We fix the effective detuning $\delta_{\mathrm{eff}} = -2\pi \times 8.2$ kHz and the final pump strength $\varepsilon_{\mathrm{f}} = 2.0\, E_{\mathrm{rec}}$. For these parameters, we observed the strongest subharmonic response while keeping f_0 and ω_{dr} fixed (cf. Fig. 5 in the appendix). The protocol used for the measurement presented in Fig. 2 is as follows. We linearly increase the pump strength $\varepsilon(t)$ to its desired final value $\varepsilon_{\mathrm{f}} = 2.0\, E_{\mathrm{rec}}$ for fixed $\delta_{\mathrm{eff}} = -2\pi \times 8.2$ kHz. This is followed by a waiting time and a linear ramp-up of the
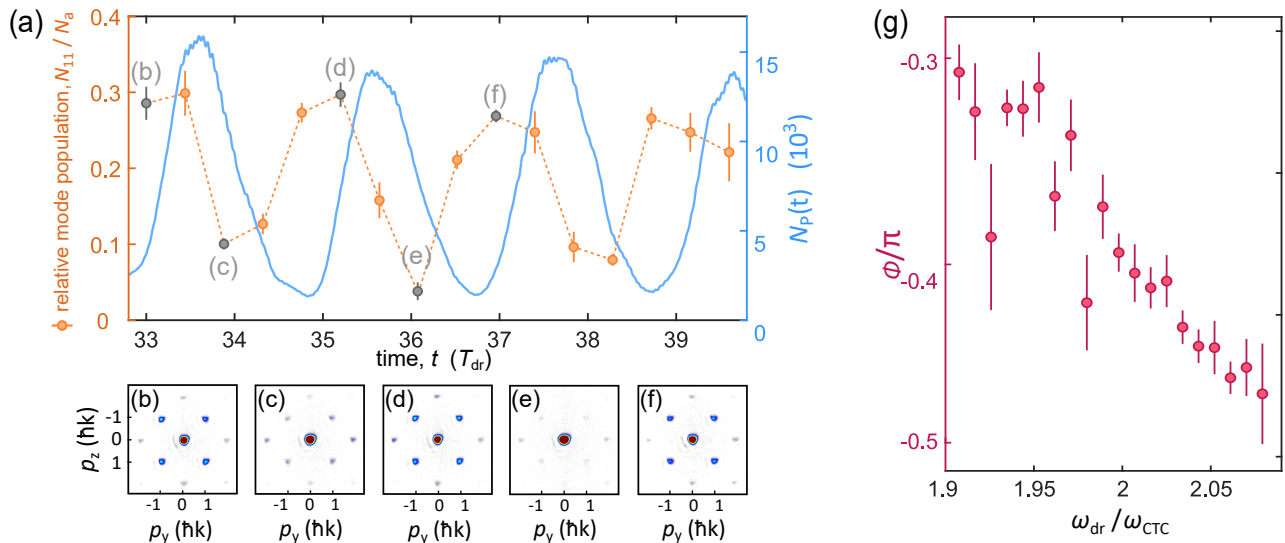
FIG. 4. (a) Blue solid line: intra-cavity photon number $N_P(t)$ averaged over five experimental realizations. Orange and gray markers: relative population of the sum of the four momentum modes $\{p_y, p_z\} = \{\pm 1, \pm 1\}\hbar k$. The dashed orange line connects the data points to guide the eyes. (b-f) Averaged momentum spectra used to obtain the data points marked in (a) by the symbols highlighted in black. We chose the same parameters as for the data presented in Fig. 1. Since the system spontaneously picks one of the two possible time phases, we first extract the time phase as in Fig. 1(c) from a Fourier spectrum and then post-select realizations with similar phase values before averaging. More details about the post-selection process are found in the appendix. (g) Phases of the oscillations of $N_P(t)$. The error bars show statistical errors for averaging over multiple realizations.

driving strength f_0, both with a duration of 0.5 ms. Then, we hold all the pump parameters constant, record $N_P(t)$ during 10 ms, and calculate the Fourier transform $N_P(\omega)$ of $N_P(t)$ (using a Fast Fourier transform method (FFT)). To quantify the degree of IL, we extract the subharmonic response $S = N_P(\omega_{dr}/2)/\text{Max}_{\{\omega_{dr}, f_0\}}[N_P(\omega_{dr}/2)]$, which is the amplitude of the single-sided spectrum at half of the driving frequency $N_P(\omega_{dr}/2)$, normalized to its maximal value observed across the considered portion of the $\{\omega_{dr}, f_0\}$-space.

In Fig. 2(a), we observe a large area showing a strong subharmonic response S. For the optimal choice of δ_{eff} and ε_f (see appendix), S is increased more than fourfold when compared to its value without modulation. The maximal value of S arises for a driving frequency ω_{dr} close to twice the CTC frequency ω_{CTC}, where $\omega_{CTC} \approx 2\pi \times 11$ kHz for the optimal choice of δ_{eff} and ε_f. The optimal driving strength of about $f_0 = 0.45$ exceeds the value predicted in our simulations (cf. appendix), which may be attributed to the limited experimental lifetime and the contact interaction of the BEC, which is not accounted for in the calculations. For increasing f_0, the synchronization happens faster and is more robust in the sense that larger values of the subharmonic response S are observed together with an extension over longer time periods. Based upon the observation of spontaneous breaking of DTTS (cf. Fig. 1(d)) and robustness of the subharmonic response against temporal perturbations of all four pump and modulation parameters ($\delta_{eff}, \varepsilon_f, \omega_{dr}, f_0$), we claim to observe a transition between a CTC and a DTC (see appedix for details). We investigate this transition further for a fixed driv-

ing frequency $\omega_{dr} = 2\pi \times 22.5$ kHz. For each experimental implementation, we obtain the Fourier spectrum as described above, but instead of considering its amplitude at $\omega_{dr}/2$, we fit a Gaussian to extract the dominant response frequency ω_{DTC} as the frequency at the maximum of the Gaussian and its corresponding amplitude. These quantities are plotted versus the driving strength f_0 in Figs. 2(b) and (c), respectively. For increasing f_0, the response frequency ω_{DTC} approaches the value $\omega_{dr}/2$. Each data point is an average of around ten experimental realizations and the error bars in Figs. 2(b,c) indicate the standard deviation, representing shot-to-shot fluctuations. These fluctuations are due to atom number variations in the BEC, originating from a combination of inherent quantum noise and technical instabilities. Interestingly, we find that for sufficiently strong driving, the emergence of the DTC is accompanied by a strong suppression of the shot-to-shot fluctuations of ω_{DTC} (cf. Fig. 2(b)), while at the same time, the relative amplitude of the dominant spectral component at frequency ω_{DTC} increases almost by a factor of 5 (cf. Fig. 2(c)).

To further assess the efficiency of the IL process with respect to frequency pulling and locking, we plot in Fig. 3 the response frequency ω_{DTC}, averaged over about ten experimental realizations, against the driving strength f_0, using three different modulation waveforms: sinusoidal (blue circles), square wave (red squares), and sawtooth (green diamonds). The protocol is otherwise the same as the one described in the previous paragraph. For all three waveforms, ω_{DTC} is pulled towards $\omega_{dr}/2$ for a sufficiently strong driving strength and we observe a plateauing of ω_{DTC} above $f_0 \approx 0.3$. The

shot-to-shot fluctuations, given by the error bars, are seen to significantly decrease as the response locks onto the subharmonic of the drive. Moreover, frequency locking is reached for smaller f_0 when using a square wave or sinusoidal modulation when compared to a sawtooth modulation. This may be explained as follows: the modulation is implemented as $\varepsilon(t) = \varepsilon_\mathrm{f}\left[1 + f_0\, g(t)\right]$, where $g(t)$ denotes one of the three waveforms oscillating between the maximal and minimal values 1 and -1. For this specification of f_0, the amplitude of the fundamental harmonic contribution of the square, sinusoidal, and sawtooth waveforms are $\{4/\pi, 1, 2/\pi\}$, respectively. Hence, when compared to the sinusoidal waveform, the square wave and the sawtooth modulation should produce tighter or weaker locking, respectively. For the square wave, however, the higher harmonic components give rise to increased heating, which reduces the atom-cavity coupling and hence acts to compensate for the tighter locking.

So far, we have restricted ourselves to draw information about the atom-cavity system from analyzing the light field leaking out of the cavity, which serves as a non-destructive monitor for the light-matter dynamics. However, we also have direct access to the matter sector via momentum spectra measured after a $25\,\mathrm{ms}$ long free expansion of the ensemble. This time-of-flight (TOF) technique is destructive, and we need to prepare a new matter sample every time a momentum spectrum is recorded. In the CTC phase, in each experimental realization, the intra-cavity light field and the corresponding matter grating oscillate with a random time phase as a consequence of CTTS breaking (cf. Fig. 1(b)). Hence, averaging over multiple implementations, in order to improve signal-to-noise, washes out the dynamical signatures of the observed momentum distributions. In the DTC regime, only two time phases, differing by π, emerge. These phases can be discriminated by analyzing Fourier spectra according to Fig. 1(c), such that post-selection allows for averaging momentum spectra with the same phase value. With this, we directly observe the dynamics of the atomic matter grating. In Fig. 4(a), the time evolution of $N_\mathrm{P}(t)$ is plotted as a solid blue line, and the time evolution of the sum N_{11} of the populations of the four momentum modes $\{p_\mathrm{y}, p_\mathrm{z}\} = \{\pm 1, \pm 1\}\hbar k$, normalized to the total atom number N_a, is shown by orange and gray markers. In order to obtain N_{11}/N_a, momentum spectra as those shown in Figs. 4(b-f) are recorded, post-selected to only account for similar time phase values, and averaged. We observe an oscillation in the dynamics of N_{11}/N_a at a frequency similar to that of the intra-cavity photon number but notably with a time phase shifted relative to the time phase of $N_\mathrm{P}(t)$. This retardation between the dynamics of the light field and the matter distribution is a key feature of our recoil resolved atom-cavity system [34] and is consistent with simulations using an idealized model for the atom-cavity system (cf. appendix). In Fig. 4(g), the phase of the oscillation of $N_\mathrm{P}(t)$, with respect to the phase of the drive, is plotted versus ω_dr, which is tuned across the resonance $\omega_\mathrm{dr} = 2\,\omega_\mathrm{CTC}$. The observed dissipation-induced change of the phase, when ω_dr is varied, is a characteristic

signature of IL or entrainment. The nearly linear decrease with a negative slope is reproduced by the simulations in the appendix.

CONCLUSION

In conclusion, we have demonstrated dynamical control of a phase transition between two time crystalline phases. Taking the continuous time crystalline phase of a transversally pumped atom-cavity system as a starting point, we have applied external driving at a frequency of approximately twice the frequency of the continuous time crystal. For sufficiently strong driving, the system locks to the external drive in a subharmonic manner, resulting in a discrete time crystal. This phenomenon establishes subharmonic IL of limit cycles of a nonlinear dissipative oscillator in the context of many-body systems. Therefore, we establish a non-trivial interface between classical non-linear dynamics and time crystals, which suggests a vast range of dynamical phenomena to be understood and established in time crystals and related dynamical many-body states.

ACKNOWLEDGMENTS

---

[1] A. T. Winfree, *The Geometry of Biological Time*, Vol. 12 (Springer New York, 2001).

[2] F. Wilczek, Quantum time crystals, Physical Review Letters **109**, 1 (2012).

[3] A. D. Shapere and F. Wilczek, Realization of "time crystal" lagrangians and emergent sisyphus dynamics, arXiv:1708.03348 , 1 (2017).

[4] D. A. Abanin, E. Altman, I. Bloch, and M. Serbyn, Colloquium: Many-body localization, thermalization, and entanglement, Reviews of Modern Physics **91**, 21001 (2019).

[5] M. P. Zaletel, M. Lukin, C. Monroe, C. Nayak, F. Wilczek, and N. Y. Yao, Colloquium: Quantum and classical discrete time crystals, Reviews of Modern Physics **95**, 031001 (2023).

[6] F. Iemini, A. Russomanno, J. Keeling, M. Schirò, M. Dalmonte, and R. Fazio, Boundary time crystals, Physical Review Letters **121**, 35301 (2018).

[7] H. Keßler, J. G. Cosme, M. Hemmerling, L. Mathey, and A. Hemmerich, Emergent limit cycles and time crystal dynamics in an atom-cavity system, Physical Review A **99**, 1 (2019).

[8] B. Buča, J. Tindall, and D. Jaksch, Non-stationary coherent quantum many-body dynamics through dissipation, Nature Communications **10**, 1730 (2019).

[9] J. Zhang, P. W. Hess, A. Kyprianidis, P. Becker, A. Lee, J. Smith, G. Pagano, I. D. Potirniche, A. C. Potter, A. Vishwanath, N. Y. Yao, and C. Monroe, Observation of a discrete time crystal, Nature **543**, 217 (2017).

[10] S. Choi, J. Choi, R. Landig, G. Kucsko, H. Zhou, J. Isoya, F. Jelezko, S. Onoda, H. Sumiya, V. Khemani, C. V. Keyserlingk, N. Y. Yao, E. Demler, and M. D. Lukin, Observation of discrete time-crystalline order in a disordered dipolar many-body system, Nature **543**, 221 (2017).

[11] J. Smits, L. Liao, H. T. Stoof, and P. V. D. Straten, Observation of a space-time crystal in a superfluid quantum gas, Physical Review Letters **121**, 185301 (2018).

[12] H. Keßler, P. Kongkhambut, C. Georges, L. Mathey, J. G. Cosme, and A. Hemmerich, Observation of a dissipative time crystal, Physical Review Letters **127**, 43602 (2021).

[13] P. Kongkhambut, H. Keßler, J. Skulte, L. Mathey, J. G. Cosme, and A. Hemmerich, Realization of a periodically driven open three-level dicke model, Physical Review Letters **127**, 253601 (2021).

[14] B. Zhu, J. Marino, N. Y. Yao, M. D. Lukin, and E. A. Demler, Dicke time crystals in driven-dissipative quantum many-body systems, New Journal of Physics **21**, 10.1088/1367-2630/ab2afe (2019).

[15] J. Skulte, P. Kongkhambut, H. Keßler, A. Hemmerich, L. Mathey, and J. G. Cosme, Parametrically driven dissipative three-level dicke model, Physical Review A **104**, 10.1103/PhysRevA.104.063705 (2021).

[16] H. Taheri, A. B. Matsko, L. Maleki, and K. Sacha, All-optical dissipative discrete time crystals, Nature Communications **13**, 848 (2022).

[17] S. Autti, V. B. Eltsov, and G. E. Volovik, Observation of a time quasicrystal and its transition to a superfluid time crystal, Physical Review Letters **120**, 215301 (2018).

[18] P. Kongkhambut, J. Skulte, L. Mathey, J. G. Cosme, A. Hemmerich, and H. Keßler, Observation of a continuous time crystal, Science **377**, 670 (2022).

[19] A. Greilich, N. E. Kopteva, A. N. Kamenskii, P. S. Sokolov, V. L. Korenev, and M. Bayer, Continuous time crystal in an electron-nuclear spin system: stability and melting of periodic auto-oscillations, arXiv:2303.15989 (2023).

[20] T. Liu, J. Y. Ou, K. F. MacDonald, and N. I. Zheludev, Photonic metamaterial analogue of a continuous time crystal, Nature Physics **19**, 986 (2023).

[21] Y. H. Chen and X. Zhang, Realization of an inherent time crystal in a dissipative many-body system, Nature Communications **14**, 10.1038/s41467-023-41905-3 (2023).

[22] S. H. Strogatz, *Nonlinear Dynamics and chaos* (CRC press, Taylor & Francis Group, 2015).

[23] M. H. Jensen, P. Bak, and T. Bohr, Complete devil's staircase, fractal dimension, and universality of mode-locking structure in the circle map, Physical review Letters **50**, 1637 (1983).

[24] M. H. Jensen, P. Bak, and T. Bohr, Transition to chaos by interaction of resonances in dissipative systems. i. circle maps, Phys. Rev. A **30**, 1960 (1984).

[25] S. Daan and J. Aschoff, The entrainment of circadian systems (Springer US, 2001) pp. 7–43.

[26] F. E. Hanson, J. F. Case, E. Buck, and J. Buck, Synchrony and flash entrainment in a new guinea firefly, Science **174**, 161 (1971).

[27] F. Piazza and H. Ritsch, Self-ordered limit cycles, chaos, and phase slippage with a superfluid inside an optical resonator, Physical Review Letters **115**, 163601 (2015).

[28] H. Keßler, J. G. Cosme, C. Georges, L. Mathey, and A. Hemmerich, From a continuous to a discrete time crystal in a dissipative atom-cavity system, New Journal of Physics **22**, 10.1088/1367-2630/ab9fc0 (2020).

[29] E. Colella, A. Kosior, F. Mivehvar, and H. Ritsch, Open quantum system simulation of faraday's induction law via dynamical instabilities, Physical Review Letters **128**, 10.1103/PhysRevLett.128.070603 (2022).

[30] X. Nie and W. Zheng, Mode softening in time-crystalline transitions of open quantum systems, Physical Review A **107**, 10.1103/PhysRevA.107.033311 (2023).

[31] J. Skulte, P. Kongkhambut, H. Keßler, A. Hemmerich, L. Mathey, and J. G. Cosme, Realizing limit cycles in dissipative bosonic systems, arXiv:2401.05332 (2024).

[32] H. Keßler, J. Klinder, M. Wolke, and A. Hemmerich, Optomechanical atom-cavity interaction in the sub-recoil regime, New Journal of Physics **16**, 53008 (2014).

[33] J. Klinder, H. Keßler, C. Georges, J. Vargas, and A. Hemmerich, Bose-einstein condensates in an optical cavity with sub-recoil bandwidth, Applied Physics B **122**, 765 (2016).

[34] H. Keßler, J. Klinder, B. P. Venkatesh, C. Georges, and A. Hemmerich, In situ observation of optomechanical bloch oscillations in an optical cavity, New Journal of Physics **18**, 102001 (2016).

[35] A. Polkovnikov, Phase space representation of quantum dynamics, Annals of Physics **325**, 1790 (2010).

[36] J. G. Cosme, J. Skulte, and L. Mathey, Time crystals in a shaken atom-cavity system, Physical Review A **100**, 1 (2019).

APPENDIX

Experimental details

The experimental setup, as sketched in Fig. 1(a) in the main text, is comprised of a magnetically trapped BEC of $N_\mathrm{a} = 4 \times 10^4$ ^{87}Rb atoms, dispersively coupled to a narrowband high-finesse optical cavity. The trap creates a harmonic potential with trap frequencies $\omega = 2\pi \times (119.0, 102.7, 24.7)$ Hz. The corresponding Thomas-Fermi radii of the ensemble are $(r_x, r_y, r_z) = (3.7, 4.3, 18.1)$ μm. These radii are significantly smaller than the size of the Gaussian-shaped pump beam, which has a waist of $w_\mathrm{pump} \approx 125$ μm. The pump beam is oriented transversally with respect to the cavity axis and retro-reflected to form a standing wave potential. The cavity field has a decay rate of $\kappa \approx 2\pi \times 3.2$ kHz, which is comparable to the recoil frequency $\omega_\mathrm{rec} = E_\mathrm{rec}/\hbar = 2\pi \times 3.7$ kHz for a pump wavelength of $\lambda_\mathrm{p} = 791.59$ nm. The pump laser

is blue detuned with respect to the relevant atomic transition of ^{87}Rb at 794.98 nm. The maximum light shift per atom is $U_0 = 2\pi \times 0.7$ Hz.

Cavity field detection

Our experimental system is equipped with two detection setups for the light leaking out of the cavity. On one side of the cavity, we use a single photon counting module (SPCM), which provides access to the intensity of the intra-cavity field and the associated photon statistics. On the other side of the cavity, a balanced heterodyne detection setup is installed, which uses the pump beam as a local reference. The beating signal of the local oscillator with the light leaking out of the cavity allows for the observation of the time evolution of the intra-cavity photon number $N_{\mathrm{P}}(t)$ and the phase difference between the pump and the cavity field.

Identifying the optimal pump parameters

The standing wave pump field is characterized by two parameters: the effective pump-cavity detuning δ_{eff} and the time-dependent pump strength $\varepsilon(t)$. The latter follows the equation $\varepsilon(t) = \varepsilon_{\mathrm{f}}[1 + f_0 \cos(\omega_{\mathrm{dr}} t)]$, with the mean pump strength ε_{f} after ramping is completed, the driving strength f_0 and the driving frequency ω_{dr}. Fig. 2(a) in the main text shows the dependence of the subharmonic response S, used to quantify the IL process, for variable modulation parameters f_0 and ω_{dr}. S is the amplitude of the single-sided spectrum at half of the driving frequency, normalized to the maximally observed value. In this section, we hold the driving strength $f_0 = 0.45$ and the driving frequency $\omega_{\mathrm{dr}} = 2\pi \times 22.5$ kHz constant and identify the parameter regime in the space spanned by δ_{eff} and ε_{f} where IL works most efficiently, and hence, S is maximized. In Fig. 5(a), we observe an elliptically shaped island with strong enhancement of S for large negative detunings, compared to the non-modulated case shown in Fig. 5(b). The value of S increases by almost a factor of five for the optimal parameter set. Furthermore, the modulation leads to the suppression of oscillations at small negative δ_{eff}. The white and black crosses indicate an optimized set of parameters, i.e., $\delta_{\mathrm{eff}} = -2\pi \times 8.2$ kHz and $\varepsilon_{\mathrm{f}} = 2.0\,E_{\mathrm{rec}}$, used for the measurements presented in Figs. 1-4 in the main text of this manuscript.

Robustness against temporal perturbations

In this section, we investigate the robustness of the IL process against temporal perturbations applied to all the parameters that characterize the pump field of the periodically driven atom-cavity system, which are δ_{eff}, ε_{f}, and the modulation parameters f_0 and ω_{dr}. For these experiments, we initialize our system in the discrete time crystal (DTC) phase us-
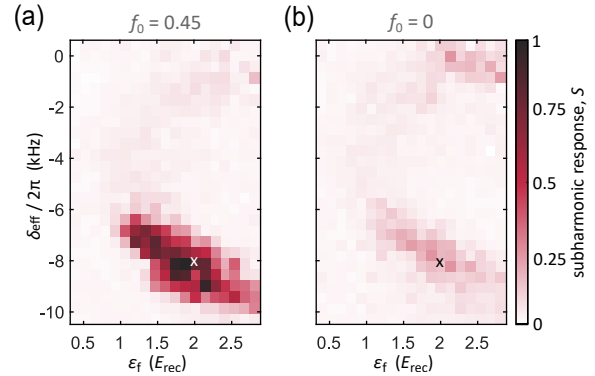
FIG. 5. Subharmonic response S for the modulated (a) and for the non-modulated case (b), plotted versus the effective pump-cavity detuning δ_{eff} and the mean final pump strength ε_{f}. The modulation parameters $\omega_{\mathrm{dr}} = 2\pi \times 22.5$ kHz and $f_0 = 0.45$ are kept constant for the entire measurement. To obtain (a) and (b), we ramp the pump strength ε to its final value ε_{f}, for a fixed δ_{eff}. After a hold time of 0.5 ms at ε_{f}, f_0 is ramped to 0.45 for fixed $\omega_{\mathrm{dr}} = 2\pi \times 22.5$ kHz within 0.5 ms and subsequently held constant for 10 ms. The evolution of $N_{\mathrm{P}}(t)$ is recorded during this time interval and its Fourier spectrum is calculated by a discrete Fast-Fourier-Transformation (FFT) method. The amplitude of the Fourier spectrum at $\omega = 0.5\,\omega_{\mathrm{dr}}$, normalized to the maximally observed value of S, is plotted according to the shown colour code. The parameter space is divided into 21×27 plaquettes and averaged over 5 to 10 experimental realizations. The white and black crosses indicate the parameter values $\delta_{\mathrm{eff}} = -2\pi \times 8.2$ kHz and $\varepsilon_{\mathrm{f}} = 2.0\,E_{\mathrm{rec}}$, which are used for the measurements presented in Figs. 1-4 in the main text of this manuscript.

ing the following protocol: first, we linearly increase the pump strength $\varepsilon(t)$ to its final value $\varepsilon_{\mathrm{f}} = 2.0\,E_{\mathrm{rec}}$ for fixed $\delta_{\mathrm{eff}} = -2\pi \times 8.2$ kHz to prepare our system in the continuous time crystal (CTC) regime. After a waiting time of 0.5 ms, followed by a 0.5 ms ramp of the driving strength to $f_0 = 0.45$ for $\omega_{\mathrm{dr}} = 2\pi \times 22.5$ kHz, we keep all pump parameters constant for 10 ms and separately add white noise with a bandwidth of 50 kHz to each of them. The subharmonic response S for increasing noise strength is plotted in Fig. 6. We observe robustness of the oscillations for nonzero noise strength for all four pump parameters.

IL for fractions of $\omega_{\mathrm{dr}}/\omega_{\mathrm{CTC}}$ close to 1 and 1/2

Next, we investigate the IL process when the ratio between the driving and the intrinsic limit cycle frequencies is close to 1 or 1/2. We prepare the system in the CTC regime, such that its intrinsic frequency is around $\omega_{\mathrm{CTC}} = 2\pi \times 11.10$ kHz. Fig. 7 shows the case of $\frac{\omega_{\mathrm{dr}}}{\omega_{\mathrm{CTC}}} \approx 1$. The experimental protocol and evaluation method are the same as in Figs. 2(b,c) of the main text. However, for the data shown in Fig. 7, we drive at $\omega_{\mathrm{dr}} = 2\pi \times 11.30$ kHz (a,b) and $\omega_{\mathrm{dr}} = 2\pi \times 11.25$ kHz (c,d) to investigate how the CTC is entrained to the driving frequency ω_{dr}. See results in Figs. 7(a,b) and Figs. 7(c,d), re-

FIG. 6. (a) Temporal perturbation of the effective pump-cavity detuning δ_{eff}. The maximum relative noise strength corresponds to adding white noise with an amplitude of $\Delta\delta_{\mathrm{eff,max}} = \pm 2.5\,\mathrm{kHz}$. (b) Temporal perturbation of th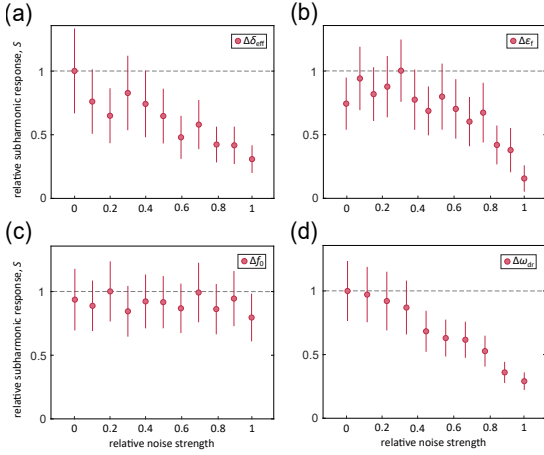e final pump strength ε_{f}. The maximum relative noise strength corresponds to adding white noise with an amplitude of $\Delta\varepsilon_{\mathrm{f,max}} = \pm 0.5\,E_{\mathrm{rec}}$. (c) Temporal perturbation of the driving strength f_0. The maximum relative noise strength corresponds to adding white noise with an amplitude equal to f_0. (d) Temporal perturbation of the driving frequency ω_{dr}. The maximal relative noise strength corresponds to adding white noise with a deviation of $\Delta\omega_{\mathrm{dr}} = 2\pi \times 20\,\mathrm{kHz}$. For all measurements, the bandwidth of the white noise was $50\,\mathrm{kHz}$, $\delta_{\mathrm{eff}} = -2\pi \times 8.2\,\mathrm{kHz}$, $\varepsilon_{\mathrm{f}} = 2.0\,E_{\mathrm{rec}}$, $f_0 = 0.45$, and $\omega_{\mathrm{dr}} = 2\pi \times 22.5\,\mathrm{kHz}$.

spectively.

Fig. 8 shows the IL process when the ratio between the driving and the intrinsic CTC frequencies are close to $1/2$. We drive the CTC at $\omega_{\mathrm{dr}} = 2\pi \times 5.625\,\mathrm{kHz}$ and observe the response frequency ω_{DTC} entrained to twice the driving frequency. The observations in this section emphasize a key feature of nonlinear systems, i.e., their limit cycle frequencies can be entrained to assume any rational fraction of the driving frequency.

Theoretical model

To theoretically model the experimental results, we only include the degrees of freedom along the pump and cavity axes. In doing so, we consider a 2D system and neglect the short-range contact interaction between the atoms. Thereby, the atom-cavity Hamiltonian in second quantized form comprises three contributions, one from the cavity photons, the atoms, and the light matter interactions

$$\hat{H} = \hat{H}_{\mathrm{c}} + \hat{H}_{\mathrm{a}} + \hat{H}_{\mathrm{ac}}. \tag{A1}$$

The Hamiltonian for the single-mode cavity is $\hat{H}_{\mathrm{c}} = -\hbar\delta_c\,\hat{a}^\dagger\hat{a}$, where $\hat{a}$ ($\hat{a}^\dagger$) is the bosonic annihilation (creation) operator for the cavity photons and $\delta_{\mathrm{c}} < 0$ is the detuning between the pump and cavity frequencies. The atomic Hamil-
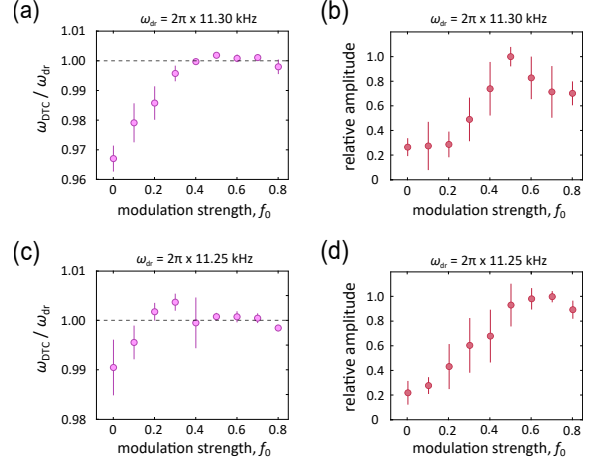
FIG. 7. (a, c) Relative response frequencies ω_{DTC} for driving frequencies $\omega_{\mathrm{dr}} = 11.30\,\mathrm{kHz}$ and $\omega_{\mathrm{dr}} = 11.25\,\mathrm{kHz}$, respectively. The response frequency ω_{DTC} is obtained as the frequency of the dominant spectral component in a Gaussian fit of the Fourier spectrum $N_{\mathrm{P}}(\omega)$. (b, d) Relative amplitude of the dominant spectral component at frequency ω_{DTC}, corresponding to (a) and (c), respectively.
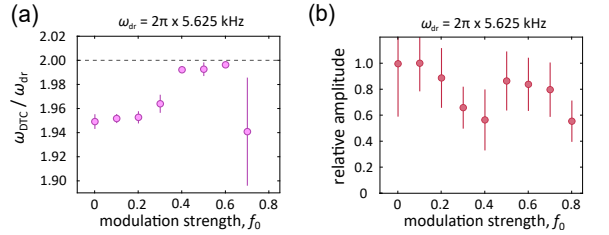
FIG. 8. (a) Relative response frequency ω_{DTC} for the driving frequency $\omega_{\mathrm{dr}} = 5.625\,\mathrm{kHz}$, plotted against the driving strength f_0. ω_{DTC} is obtained as the frequency of the dominant spectral component in a Gaussian fit of the Fourier spectrum $N_{\mathrm{P}}(\omega)$. (b) Corresponding relative amplitude.

tonian is given by

$$\hat{H}_{\mathrm{a}} = \int dy\,dz\,\hat{\Psi}^\dagger(y,z)\left(-\frac{\hbar^2}{2m}\nabla^2 + \mathrm{V}_{\mathrm{ext}}(y,z)\right)\hat{\Psi}(y,z), \tag{A2}$$

where m is the mass of a $^{87}\mathrm{Rb}$ atom, $\mathrm{V}_{\mathrm{ext}}(y,z) = \varepsilon_{\mathrm{f}}\cos^2(ky)$ describes the potential of the standing wave due to the pump beam with its depth characterized by the parameter ε_{f} and its wavelength λ_{p} incorporated in the wave vector $k = 2\pi/\lambda_{\mathrm{p}}$. The bosonic field operators for the atoms are $\hat{\Psi}(y,z)$ and $\hat{\Psi}^\dagger(y,z)$. Finally, the light-matter interaction Hamiltonian is given by

$$\hat{H}_{\mathrm{ac}} = \int dy\,dz\,\hat{\Psi}^\dagger(y,z)$$
$$\left(\hbar U_0\cos^2(kz)\hat{a}^\dagger\hat{a} + \hbar\sqrt{\hbar\varepsilon_{\mathrm{f}}U_0}\cos(ky)\cos(kz)\left[\hat{a}^\dagger + \hat{a}\right]\right)$$
$$\hat{\Psi}(y,z), \tag{A3}$$

where $U_0 > 0$ is the light shift per intra-cavity photon. We assume that the wave number of the cavity field is equal to the wave number k of the pump field.

We simulate the dynamics of the system using a the truncated Wigner approximation (TWA) for open systems [35, 36]. To this end, we first expand the atomic field operators in the basis of plane waves

$$\hat{\Psi}(y, z) = \sum_{n,m} \hat{\phi}_{n,m}^{\dagger} e^{inky} e^{imkz}, \qquad (A4)$$

where the bosonic creation and annihilation operators are $\hat{\phi}_{n,m}^{\dagger}$ and $\hat{\phi}_{n,m}$, respectively. Within the TWA, the operators are treated as c numbers $\hat{a} \rightarrow a$ and $\hat{\phi}_{n,m} \rightarrow \phi_{n,m}$. The semiclassical equations of motion are

$$i\frac{\partial \phi_{n,m}}{\partial t} = \frac{1}{\hbar} \frac{\partial H}{\partial \phi_{n,m}^*}, \qquad (A5)$$

$$i\frac{\partial a}{\partial t} = \frac{1}{\hbar} \frac{\partial H}{\partial a_{n,m}^*} - i\kappa a + i\xi,$$

where the fluctuation strength ξ associated to the cavity field decay follows $\langle \xi^*(t)\xi(t') \rangle = \kappa \, \delta(t - t')$. We initialize both the atomic and photonic modes as coherent states and use the appropriate Wigner distribution to sample the initial state for the time evolution according to Eq. (A5). In doing so, we effectively include the leading order quantum corrections to the mean-field predictions. We consider 10^2 trajectories in our TWA simulations. Furthermore, we use $\delta_{\text{eff}} = -2\pi \times 7$ kHz, $\varepsilon_{\text{f}} = 1.7 \, E_{\text{rec}}$, and $\omega_{\text{dr}} = 2\pi \times 20.5$ kHz. The remaining parameters are the same as those in the experiment.

Finite size effects

To analyze the finite-size behaviour of the system, we vary the particle number N_a for fixed $N_a U_0 = 2\pi \times 28$ kHz. We compare the results of exemplary trajectories within TWA and mean-field theory. The all-to-all couplings of the atoms due to the cavity photons suggest that mean-field theory captures the thermodynamic limit $N_a \rightarrow \infty$, and thus mean-field results provide an idealized scenario for the system. To quantify the stability of the time crystals, we obtain the power spectrum of the intra-cavity photon number $N_P(\omega)$. We then calculate the relative crystalline fraction defined as the ratio between the maximum peak of the power spectrum of the TWA and mean-field results, $\Xi = \max[N_{\text{P,TWA}}(\omega_{\text{DTC}})]/\max[N_{\text{P,MF}}(\omega_{\text{DTC}})]$. This quantifies the stability of the time crystals for finite N_a relative to the idealized mean-field limit, which for the parameters chosen here exhibits stable oscillations at a well-defined frequency.

We present in Fig. 9 the relative crystalline fraction Ξ for different particle numbers N_a. For both driven and undriven cases, the relative crystalline fraction increases Ξ with N_a as it approaches the mean-field prediction in the thermodynamic limit $N_a \rightarrow \infty$. This suggests that the oscillation amplitude of

the time crystals becomes more stable with increasing N_a. For small N_a, in which quantum fluctuations become important, the typical values of Ξ for the undriven system are much less than those for the driven system. This further highlights the capability of periodic driving to enhance the stability of a time crystal. Therefore, in general, the entrained time crystals are more stable than their undriven counterparts.
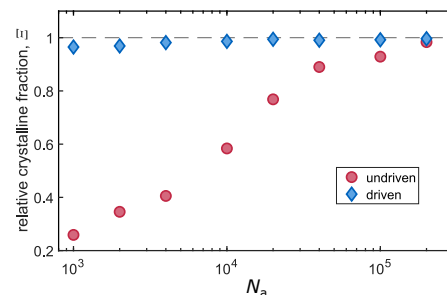
FIG. 9. Relative crystalline fraction Ξ as a function of the particle number N_a for the undriven and driven systems. The parameters are $\delta_{\text{eff}} = -2\pi \times 7$ kHz and $\varepsilon_{\text{f}} = 1.7 \, E_{\text{rec}}$. In the driven case, the driving parameters are $\omega_{\text{dr}} = 2\pi \times 20.5$ kHz and $f_0 = 0.15$. All other parameters are identical with those used in the experiment.

Atom number fluctuations

In the experiment, additional fluctuations from technical noise are present when preparing the initial BEC. To study its consequence on the IL process by the periodic drive, we include artificial noise in the initial particle number in our TWA simulations. Specifically, we increase the fluctuations in the occupation of the lowest momentum mode, the BEC mode, by increasing the standard deviation of the Gaussian distribution used for initial state sampling. In the absence of technical noise, the inherent number fluctuations of a coherent state correspond to a standard deviation of $\sigma_{N_a} = \sqrt{N_a}$. We model the experimentally observed particle number fluctuation by increasing the standard deviation to a value consistent with the experiment, which is $\sigma_{N_a} = 10\sqrt{N_a} = 2 \times 10^3$.

In Fig. 10, we show the numerical results comparing the dominant response frequency ω_{DTC} and its shot-to-shot fluctuations, depicted as error bars, for the ideal case with only the inherent quantum fluctuations of the initial BEC (A) and the case with additional particle number fluctuations due to technical noise (B). The shot-to-shot fluctuations of ω_{DTC} are found to be generally larger when there is additional noise, especially for weak driving. However, we find that IL still works not only with regard to locking the signal to a subharmonic of the drive but also in suppressing the associated shot-to-shot fluctuations, albeit for larger driving strength when compared to the ideal scenario, which only includes the inherent quantum noise.
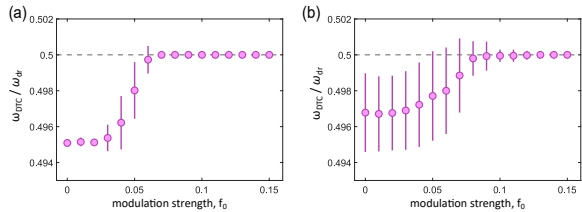
FIG. 10. Numerical results on the influence of atom number fluctuations on the response frequency. The dominant response frequency ω_{DTC} in units of ω_{dr} is plotted versus the driving strength f_0 for a system with (a) only inherent quantum fluctuations and (b) with both quantum and technical noise with a mean atom number $N_{\mathrm{a}} = 40 \times 10^3$ and $\sigma_{N_{\mathrm{a}}} = 10\sqrt{N_{\mathrm{a}}}$.

Time evolution of momentum distribution

In Fig. 11, the time evolution of the sum N_{11} of populations of the four momentum modes $\{p_{\mathrm{y}}, p_{\mathrm{z}}\} = \{\pm 1, \pm 1\}\hbar k$, normalized to the total atom number N_{a}, is shown by the orange line graph. In addition, the time evolution of the intra-cavity photon number $N_{\mathrm{P}}(t)$ is plotted as a solid blue line. In agreement with the experimental findings in Fig. 4(a) of the main text, a delay between both graphs is found, as expected in the recoil resolved regime which presents in our atom-cavity system. The simulation closely follows the experimental protocol for DTC preparation. That is, TWA trajectories are calculated in the momentum basis and post-selected to belong to the same symmetry-broken state of the emerging DTC. The momentum spectrum and thus N_{11} is obtained. The simulation neglects contact interaction and atom loss due to technical heating.
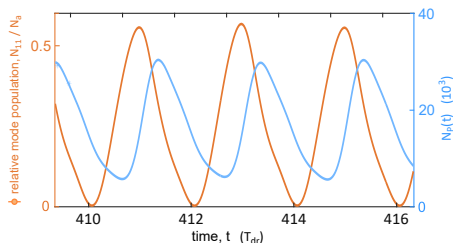
FIG. 11. Numerical simulation of the time evolution of higher order momentum components. The blue solid line plots $N_{\mathrm{P}}(t)$ versus time in units of the oscillation period T_{dr} of the external drive. The orange solid line shows the corresponding time evolution of N_{11}/N_{a}, where N_{11} denotes the sum of the populations of the momentum components $\{p_{\mathrm{y}}, p_{\mathrm{z}}\} = \{\pm 1, \pm 1\}\hbar k$. The mean atom number is $N_{\mathrm{a}} = 40 \times 10^3$.

In Fig. 12, the calculated phases of the oscillations of $N_{\mathrm{P}}(t)$ (magenta markers) and $N_{11}(t)$ (orange markers) are plotted against the driving frequency ω_{dr} varied across the resonance, where $\omega_{\mathrm{dr}} = 2\,\omega_{\mathrm{CTC}}$. The phase of the the drive is defined to be zero. Note that for $\omega_{\mathrm{dr}} = 2\,\omega_{\mathrm{CTC}}$ the time phase of the momentum occupation $N_{11}(t)$ becomes the same as that of the drive, which is a characteristic feature of IL. We find similar monotonously decreasing scaling with ω_{dr} for $N_{11}(t)$ and $N_{\mathrm{P}}(t)$. The photon dynamics $N_{\mathrm{P}}(t)$ show an extra phase lag introduced by the cavity dissipation κ. These findings are compatible with the observations in Fig. 4(g) of the main text.
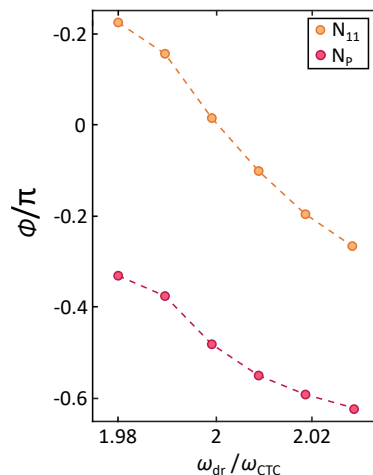
FIG. 12. Phase delays of matter and light sectors after IL. The calculated phases of the oscillations of $N_{\mathrm{P}}(t)$ (magenta markers) and $N_{11}(t)$ (orange markers) are plotted against the driving frequency ω_{dr}.

2.14 Publication IX: Quantum rotation sensor with real-time readout based on an atom-cavity system

J. Skulte, J.G. Cosme and L. Mathey — **submitted to Phys. Rev. Letters (2023)**

Motivation

This work was motivated by the promising properties of atom interferometry, namely the high precision and long-term stability in acceleration and rotation measurements. The applications range from fundamental physics, metrology to inertial navigation. However, current experiments use destructive measurements, which makes them difficult to use for inertial navigation. Our aim was to propose a new setup that overcomes this obstacle and can be used for inertial navigation.

Main findings

In this work, we have proposed to combine the physics of neutral atoms exposed to a Peierls phase induced via external rotation of the setup and the superradiant phase transition as can be found in an atom-cavity system. This allows to build a highly sensitive and fast quantum rotation sensor. Therefore, the atoms are placed in a rectangular array of Bose-Einstein condensates (BEC) coupled to a single quantised light mode. We analytically derived the dependence of the critical light-matter coupling, needed to enter the superradiant phase depending on the external rotational frequency. We suggested different options to increase the accuracy of the sensor. Furthermore, we demonstrated robustness of the sensor against particle number fluctuations, quantum fluctuations in the initial state according to the truncated Wigner approximation, and stochastic noise induced by photon loss in the cavity.

Contribution

I performed all numerical studies supported by JGC under the supervision of LM. I performed the analytical studies together with LM supported by JGC. LM conceptualized this work. All authors contributed to the discussion and interpretation of the results, as well as to writing the manuscript.

Quantum rotation sensor with real-time readout based on an atom-cavity system

Jim Skulte,[1,2] Jayson G. Cosme,[3] and Ludwig Mathey[1,2]

[1]*Zentrum für Optische Quantentechnologien und Institut für Laser-Physik, Universität Hamburg, 22761 Hamburg, Germany*
[2]*The Hamburg Center for Ultrafast Imaging, Luruper Chaussee 149, 22761 Hamburg, Germany*
[3]*National Institute of Physics, University of the Philippines, Diliman, Quezon City 1101, Philippines*
(Dated: March 23, 2023)

Using an atom-cavity platform, we propose to combine the effective gauge phase of rotated neutral atoms and the superradiant phase transition to build a highly sensitive and fast quantum rotation sensor. The atoms in a well-controlled array of Bose-Einstein condensates are coupled to a single light mode of an optical cavity. The photon emission from the cavity indicates changes in the rotation frequency in real time, which is crucial for inertial navigation. We derive an analytical expression for the phase boundaries and use a semi-classical method to map out the phase diagram numerically, which provides the dependence of the photon emission on the rotation. We further suggest to operate the sensor with a bias rotation, and to enlarge the enclosed area, to enhance the sensitivity of the sensor.

Quantum sensing aims to take advantage of the accuracy and long-time stability of quantum platforms, such as ultracold atoms, for new technological applications [1]. While optical Sagnac interferometers are important tools in present day navigation, they can fall short due to limited sensitivity and long-term stability [2]. Atom interferometry emerged as a promising platform to address these issues with high precision rotation and acceleration measurements [3–8]. The applications range from testing fundamental physics [9–11], metrology [12], absolute gravimetry [13, 14] to inertial navigation [15, 16]. So far, the usage of atom interferometers as rotation sensors to measure time-varying signals has been challenging. Each measurement is done destructively, which means that any change in the rotation that occurs during the preparation of the new measurement is not detected. An interleaved operation can be used to increase the repetition rate [17]. However, an accurate rotational measurement of a time-varying rotation with an atom-only interferometry remains challenging, but is crucial if the device is to be used for inertial navigation [18].

Rotating an ultracold atom system creates an artificial gauge field [19–21], which was proposed to study gauge field-driven atom dynamics in a controlled environment and to produce cat states for quantum metrology [20, 22]. A similar setup described by a rotating Bose-Hubbard model has been proposed for rotation sensing [23].

Open quantum systems such as atom-cavity systems [24, 25] allow for a real-time monitoring of the photons emitted out of the cavity. This has been used to in-situ observe phase transitions [26–30]. The precise control of cold atom experiments combined with the inherent cooling of the system due to energy leaking out of the cavity, makes it an ideal platform to study non-equilibrium dynamics [31–38].

In this letter, we propose to build a quantum rotation sensor that allows to measure fast time-varying signals by incorporating atom interferometry, artificial gauge phases in ultracold atoms, and real-time readout of open quantum systems. Specifically, we propose to combine the control of the hopping parameter J by an effective gauge phase, which can be realized by rotations of neutral atoms, and the superradiant (SR) phase transition that can be realized by coupling neu-
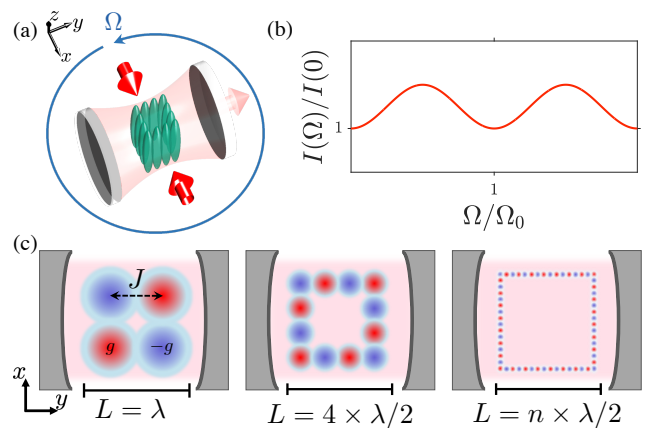
FIG. 1. (a) Sketch of the proposed system. 1D tubes of Bose-Einstein condensates are placed with a separation of $\lambda/2$ in a high-finesse optical cavity. The atoms are transversely pumped by a red-detuned laser beam with wavelength λ that forms a standing wave potential. The effect of an applied rotation around the z-axis at an angular frequency of Ω, as sketched in blue, can be measured in real time through the intensity of the photons transmitted out of the cavity at a rate κ, as shown in (b). (b) A schematic sketch of the measured light field intensity for varying rotational frequencies Ω rescaled by the intensity measured when the system is at rest. (c) Top view of the proposed setup. Red and blue circles denote the sign of the light-matter coupling $\pm g$ at each site. J denotes the tunnelling between neighbouring sites. Using a DMD, a square annulus light potential is applied shown in light blue. From left to right: the proposed setup with increasing area enclosed by the atoms. This allows for an increased frequency sensitivity of the sensor, which scales with the number of array sites, $1/M$.

tral atoms to a single mode cavity with a photon loss rate κ. With this, we propose to create a quantum rotation sensor that possesses both non-destructive detection and real-time observation of precise changes in the external rotational frequency Ω of the system.

Using an mean-field ansatz, we analytically show the dependence of the phase boundary and the intracavity photon number on the rotation, represented by a gauge phase. We fur-

ther use a semi-classical method to numerically determine the phase diagram as a function of the rotation frequency, and the light-matter coupling strengths. We explore the dynamics under dynamical changes of the rotation. These changes can be distinguished dynamically from the inherent quantum noise, which we quantify as the standard deviation of the light field fluctuations. We note that the timescale on which changes of the phase cannot be dynamically distinguished is on the order of the inverse of the hopping parameter, which corresponds to $1/J \approx 5 \times 10^{-4}$ s, for the parameters given below.

A sketch of our proposed sensor is shown in Fig. 1(a) and with a top view depicted in Fig. 1(c). We propose to split a Bose-Einstein condensate of ^{87}Rb atoms into M one-dimensional (1D) tubes and organize them in a two-dimensional square array with a spacing of $\lambda/2$, where λ is the wavelength of the laser beam used to produce the light-matter coupling between the atoms and the cavity. To trap the atoms and produce the atomic array, a DMD can be employed to construct a square annulus potential with barriers running along each side at a periodicity of $\lambda/2$ to produce an atomic array [8, 39]. This system is then placed inside a high finesse cavity with a loss rate κ. In Fig. 1(c), we show schematic diagrams of the desired geometry of the atomic array including the confining potential. The enclosed area can be enlarged leading to an improved frequency sensitivity that scales with $1/L$, a typical strategy done in atom interferometers [7]. This sensor allows to measure changes in the rotational frequency via the light intensity transmitted out of the cavity. The mechanism crucial for the operation is the following. For the SR phase to occur, the light-matter coupling strength needs to exceed the tunnelling energy, which is minimized if all sites have the same population (see Eq. 6). However, the SR phase relies on an imbalance between neighbouring sites as is depicted in red and blue in (c). Rotations of the system lead to an effective gauge field that modifies the tunnelling amplitude. This leads to an effective reduction of the real part of the tunnelling energy, which lowers the critical light-matter coupling needed to enter the SR phase. For a fixed light-matter strength the rotational frequency can now be read off by the light field intensity leaking out of the cavity. This effect is used in our rotational sensor. We note that the sensitivity is further increased with an operation of the sensor close to the phase transition. This allows for small changes in the rotational frequency induce large changes of the photon number, as demonstrated below, due to the strong dependence near the phase transition.

The atomic sector of our system is described by a bosonic field operator $\hat{\Phi}(\mathbf{r})$ and the many-body Hamiltonian

$$\hat{H}_{\mathrm{A}} = \int \hat{\Phi}^{\dagger}(\mathbf{r}) \left(-\frac{\hbar^2 \nabla^2}{2m} - \Omega \hat{L}_z + V(\mathbf{r}) \right) \hat{\Phi}(\mathbf{r}) \, d\mathbf{r}, \quad (1)$$

where the external $\hat{L}_z$ is the angular momentum operator and $V(\mathbf{r})$ is the external potential shaped by a DMD [8, 39]. A DMD can be used to generate a square array of potential wells, such that the atoms are confined with a width of $\lambda/2$ as sketched on Fig. 1(c). We further assume that the external potential will have a periodicity of $\lambda/2$ [8] along the $x-$ and

$y-$direction and is sufficiently weak such that the system remains in the superfluid regime [40]. This condition places a constraint on the length of each side L to be an integer multiple of $\lambda/2$. The cavity photon annihilation (creation) operator is $\hat{a}$ ($\hat{a}^{\dagger}$) and the corresponding Hamiltonian is $\hat{H}_{\mathrm{C}} = \omega \hat{a}^{\dagger} \hat{a}$. The atoms and photons interact according to [24]

$$\hat{H}_{\mathrm{LM}} = \int \hat{\Phi}^{\dagger}(\mathbf{r}) \, \eta \cos(kx) \cos(ky) \left(a + a^{\dagger} \right) \hat{\Phi}(\mathbf{r}) \, d\mathbf{r}, \quad (2)$$

where η the strength of the coupling. We further assume that the potential $V(\mathbf{r})$ is deep enough to neglect next-nearest neighbour tunneling and that the band gap is larger than the rotational energy. With this, we expand the atomic field operators in Wannier orbitals [21]

$$\tilde{W}_i = \exp \left(-\frac{im}{\hbar} \int_{\mathbf{r}_i}^{\mathbf{r}_{i+1}} \mathbf{A}(\mathbf{r}') d\mathbf{r}' \right) W_i(\mathbf{r}), \quad (3)$$

where $\mathbf{A}(\mathbf{r}) = \Omega \, \mathbf{z} \times \mathbf{r}$ is the effective vector potential induced by the rotation.

In the rotating frame, the effective Hamiltonian for the system is given by

$$\hat{H} = \omega \, \hat{a}^{\dagger} a - g \left(\hat{a}^{\dagger} + \hat{a} \right) \sum_{i=1}^{M} (-1)^i \, \hat{n}_i \quad (4)$$
$$- J \exp \left(i\theta \left(\Omega \right) \right) \sum_{i=1}^{M} \left(\hat{b}_i^{\dagger} \hat{b}_{i+1} \right) + \mathrm{h.c.}$$

with the periodic boundary condition $\hat{b}_{M+1} = \hat{b}_1$. J is the tunneling energy between neighboring condensates, and g is the light-matter coupling for the Wannier orbitals. These are defined as $J = \int d\mathbf{r} W_i^* \left[-\frac{\hbar^2 \nabla^2}{2m} + V(\mathbf{r}) \right] W_{i+1}$ and $g = \eta \int d\mathbf{r} W_i^* \cos(kx) \cos(ky) W_i$. The number operator at site i is $\hat{n}_i = \hat{b}_i^{\dagger} \hat{b}_i$, and θ is an effective phase generated by the gauge field $\theta = \int_{x_i}^{x_{i+1}} \mathbf{A}(\mathbf{r}) d\mathbf{r} = \pi^2 n_{\mathrm{s}} \Omega / \omega_{\mathrm{rec}}$. For the four-site model shown in Fig. 1(c), this phase is the same four the four bonds. For larger realizations, shown in Fig. 1(c) as well, the gauge phase will be dependent on the bond. However, the general functionality is retained. The recoil frequency due to the pump is $\omega_{\mathrm{rec}} = \hbar k^2 / 2m$ and we define the number of sites on each side as $n_{\mathrm{s}} = M/4 + 1$. We note that other geometries, e.g. rectangular potentials instead of a square potential, can be used as well. Here, the angle θ will be different for the $x-$ and $y-$axis. However, the functionality is retained for this modification as well, even for the four-site realization. Due to the geometry of the potential and the all-to-all coupling mediated by the cavity light field, all atoms on the even sites experience the same light-field interaction strength, as do the atoms on the odd sites. We determine the phase diagram for the square-shaped four-site realization with a mean-field ansatz. We consider a product state of coherent states as an ansatz

$$|\Psi\rangle = \left(|\psi_-\rangle |\psi_+\rangle \right)^{M/2} |\alpha\rangle \quad (5)$$

where $\psi_\pm$ and α are c-numbers representing the amplitude of the coherent states. ψ_+ (ψ_-) corresponds to the condensate on the odd (even) sites. We compute the energy $E = \langle \Psi | H | \Psi \rangle$, define $\psi_\pm = \sqrt{(N_A \pm \Delta)/M}$ with N_A the total particle number, and find

$$E = \omega |\alpha|^2 - 2g\alpha_r \Delta - 2J \cos\theta \sqrt{N_A^2 - \Delta^2}, \qquad (6)$$

where we denote $\alpha_r \equiv \Re(\alpha)$. By minimizing the energy, we find the critical light-matter coupling strength to be $g_{\text{crit}} = \sqrt{J\omega \cos(\theta)/N_A}$. For an open system with dissipation rate κ, we obtain a modified critical coupling strength,

$$g_{\text{crit}} = \sqrt{\frac{J \cos\theta \, (\omega^2 + \kappa^2)}{N_A \omega}}. \qquad (7)$$

Hence, the critical light-matter coupling strength can be significantly reduced via rotation of the setup, due to the dependence on $\cos(\theta)$. This dependence is the origin of the functionality as a rotation sensor, due to the dependence $\theta = \theta(\Omega)$. A change of Ω results in a change of the emitted light intensity in real time without any destructive measurement.

In the following, we determine the dynamics of the four-site realization via a numerical implementation of the open Truncated Wigner Approximation (TWA) method [29, 41, 42]. The TWA is a semi-classical phase space method, which uses an ensemble of initial states sampled over the corresponding Wigner distribution to predict the quantum dynamics. For the cavity mode, we sample from a Wigner distribution corresponding to a coherent state with $\langle \alpha \rangle = 0$. For the atoms on each site, we sample from a Wigner distribution of a coherent state with $\langle n_i \rangle = N_A/M$. Due to the dissipative nature of the system, we propagate the initial states via stochastic differential equations. The equations of motion are given by the Heisenberg-Langevin equations

$$\frac{d\hat{b}_i}{dt} = i[\hat{H}, \hat{b}_i] \qquad (8)$$

$$\frac{d\hat{a}}{dt} = i[\hat{H}, \hat{a}] - \kappa \hat{a} + \xi \qquad (9)$$

where κ is the cavity dissipation rate and ξ represents the noise associated with the dissipation. The noise fulfills the relation $\langle \xi^*(t')\xi(t) \rangle = \kappa \delta(t - t')$. In the following, we use experimentally realistic parameters [43]. In particular, we consider ^{87}Rb atoms and choose a particle number of $N_A = 60 \times 10^3$ and a recoil energy of $\omega_{\text{rec}} = 2\pi \times 3.5$ kHz, which corresponds to a wavelength of $\lambda \approx 800$ nm. We further assume to be in or near the good cavity or recoil-resolved regime $\omega_{\text{rec}} \approx \kappa = 2\pi \times 5$ kHz. However, we want to stress that our proposed sensor is not limited to operation in this regime. Using a larger κ is also feasible but with the trade-off that the number of photons detected in real time would be less than for smaller κ. For the tunnelling rate, we assume $J = 2\pi \times 2$ kHz.
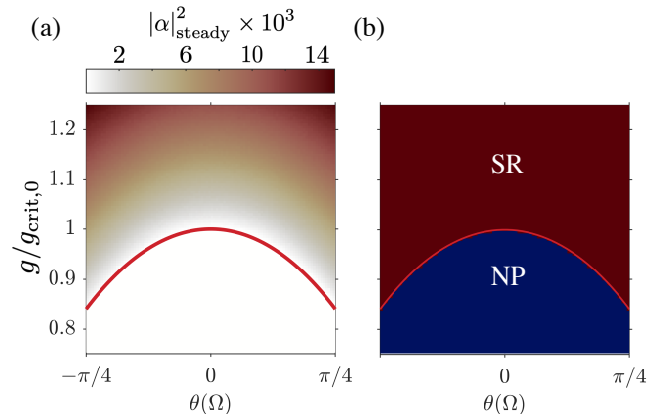

FIG. 2. (a) Steady state light field intensity $|\alpha|^2_{\text{steady}}$ as a function of the rotation frequency and light-matter coupling strength. The light-matter coupling strength is rescaled by the critical value for the non-rotating case. For each data point, we average over 10^3 TWA trajectories. The red curve corresponds to the analytically derived phase boundary in Eq. (7). (b) Phase diagram inferred from (a) using the criterion $|\alpha|^2_{\text{steady}} > 10$ for the superradiant phase.

In Fig. 2(a), we show the TWA results for the steady-state values of the photon number for varying gauge phase θ and light-matter coupling g rescaled by the critical light-matter coupling for the system at rest, $g_{0,\text{crit}} = g_{\text{crit}}(\theta = 0)$. The corresponding phase diagram is presented in Fig. 2(b). The red curve corresponds to the the analytical critical light-matter coupling strength in Eq. (7). We observe that the photon number strongly depends on the phase. In Fig. 2(b), we distinguish between the normal phase (NP), in which there are no cavity photons and no imbalance between the population on the even and odd sites, and the SR phase, in which photons are scattered into the cavity and there is population imbalance between the even and odd sites. We note that for a fixed light-matter coupling the $\mathbb{Z}_2$ symmetry breaking phase transition between the NP and SR phase can be induced by changes in the gauge phase θ which originates from changes in the frequency of the rotation.

In the following, we elaborate on dynamically sensing rotational frequencies in real time. The timescale in which changes of frequencies can be distinguished is roughly $1/J = 5 \times 10^{-4}$ s. This makes the sensor an ideal candidate for inertial navigation, where quick dynamical changes in the the rotational frequency need to be detected. Further, we propose to increase the sensitivity of the sensor by using a bias rotation, i.e. rotating the system at a fixed frequency, so that the signal is the incremental change compared to the bias rotation. In Fig. 3(a), we present TWA results for the light field intensity in red and the corresponding standard deviation in the shaded area. The results are obtained using 10^3 trajectories. The blue line corresponds to the phase θ, which is now modulated in time, as an example for time-dependent behavior. We ramp up the light matter coupling to $g = 1.09 g_{0,\text{crit}}$ within 1 ms at the beginning of each run. Initially the system
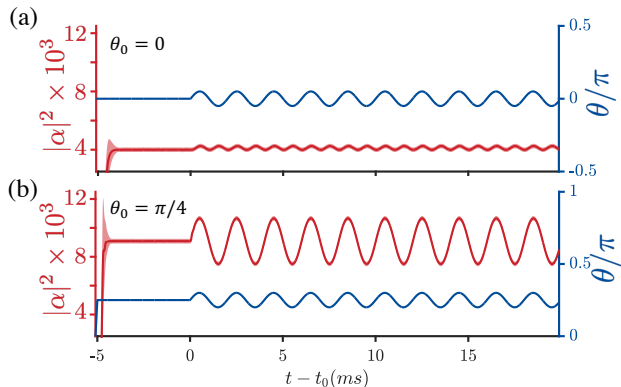
FIG. 3. (a) In blue, the applied phase θ modulated with a sinusoidal drive with strength $\delta_\theta = \pi/20$ and frequency $\omega_{\mathrm{dr}} = 2\pi \times 0.5$ kHz. The dark red line shows the light field intensity derived from 10^3 TWA trajectories. The light red shaded area shows the corresponding standard deviation due to quantum fluctuations within TWA. The system is initialized at rest before driving the system. (b) Same protocol as in (a) but the system is initialized with a phase of $\theta_0 = \pi/4$. In both cases the amplitude change of Ω corresponds to $\omega_{\mathrm{rec}}/(20\pi n_{\mathrm{s}}) = 350$ Hz/n_{s} and we choose $g = 1.09 g_{0,\mathrm{crit}}$.

is at rest, corresponding to $\theta = 0$. After the time t_0 we change the phase via $\theta = \theta_0 + \delta_\theta \sin(\omega_{\mathrm{dr}} t)$ to showcase the dynamical detection of changes in the rotational frequency. We choose $\omega_{\mathrm{dr}} = 0.5$ kHz and $\delta_\theta = \pi/20$ corresponding to a frequency change of $\delta_\Omega = \omega_{\mathrm{rec}}/20\pi n_{\mathrm{s}} = 0.35/n_{\mathrm{s}}$ kHz.

As seen in Fig. 2(a) and Fig. 3(a) for $\theta = 0$, any change in the phase will increase the light intensity. Due to this effect the applied phase change creates a frequency doubling in the light intensity. We emphasize that the magnitude of the relative change in the light field intensity is larger than the standard deviation or uncertainty due to quantum fluctuations. Thus, we can reliably distinguish between the dynamically varying rotational frequencies. In Fig. 3(b), we use the same protocol as in Fig. 3(a) except that for the first 1 ms ramp of the light-matter coupling, the phase θ_0 is also ramped up from 0 to $\pi/4$. This corresponds to rotating the sensor before the sensing starts. Fig. 3(b) shows that the overall photon number is increased for fixed light-matter coupling strength g. Furthermore the response of the system to the changes in the phase is more sensitive as inferred from the larger variations in the photon number compared to Fig. 3(a). For the specific choice of parameters considered here, the sensor must be rotated at approximately $\Omega_0 = \omega_{\mathrm{rec}}/4\pi n_{\mathrm{s}} = 1.75/n_{\mathrm{s}}$ kHz to operate in this regime.

We note that the change of the rotational frequency as depicted in Fig. 3 can still be detected if we assume large particle number fluctuations with the width of $\sigma = 0.1 \times N_{\mathrm{A}}$ in each run of the measurement. This is shown in the supplemental material [44].

Before we conclude, we briefly discuss the influence of parameter choices on the sensitivity of the proposed rotational sensor. In order to prepare a dynamical and sensitive sensor

we want to minimize the ratio $\Delta\Omega$ and τ, where $\Delta\Omega$ is the smallest change in the rotational frequency that can be distinguished from noise and τ is the response time of the sensor. Generally speaking, τ is proportional to $1/J$. Hence, we want to maximize the tunnelling amplitude, while keeping it sufficiently small to avoid exciting atoms into higher bands. To increase the dynamical rotational sensitivity there are two routes one can take. The first is to increase the enclosed area by adding more sites to the array as discussed above, see Fig 1(c). The second choice is to change the platform for implementing the discrete model studied here. Specifically, the spacing between different sites could be increased to decrease ω_{rec}, which means that the system no longer operates in the optical regime but in the near infrared regime instead, for example. This suggests that this mechanism to detect changes in rotational frequencies is not limited to atom-cavity systems, but can be implemented in other light-matter coupled systems, with a different recoil energy of atomic sector and/or which allow to enclose even larger areas. This makes our approach tunable to the desired frequency domain in which the sensor is to operate.

In conclusion, we have presented a new mechanism for dynamical rotational sensing. Our proposed system utilizes the artificial gauge field that neutral atoms experience due to external rotation, and combine it with the superradiant phase transition of an array of atoms coupled to a single mode cavity. This allows for a high precision measurement in real time. We further highlight the possibility that the sensitivity can be increased by increasing the enclosed area of the quantum sensor. A change of $\Delta\theta = \pi/400$ of the gauge field, corresponding to realistic parameters to ≈ 17.5 Hz/M of the rotational frequency, can be measured and distinguished from the cavity noise, where M denotes the total number of sites. We note that the influence of rotation on the superradiant phase transition can be observed in current state-of-the-art atom-cavity experiments [43, 45] using an actuator giving a dynamical twist to the optical table. Our proposal puts forth to create quantum rotational sensors not only for static high precision frequency measurements but also for inertial measurements and navigation, where the ability to measure time-varying signals is crucial.

[1] L. Amico, M. Boshier, G. Birkl, A. Minguzzi, C. Miniatura, L.-C. Kwek, D. Aghamalyan, V. Ahufinger, D. Anderson, N. An-

drei, A. S. Arnold, M. Baker, T. A. Bell, T. Bland, J. P. Brantut, D. Cassettari, W. J. Chetcuti, F. Chevy, R. Citro, S. De Palo, R. Dumke, M. Edwards, R. Folman, J. Fortagh, S. A. Gardiner, B. M. Garraway, G. Gauthier, A. Günther, T. Haug, C. Hufnagel, M. Keil, P. Ireland, M. Lebrat, W. Li, L. Longchambon, J. Mompart, O. Morsch, P. Naldesi, T. W. Neely, M. Olshanii, E. Orignac, S. Pandey, A. Pérez-Obiol, H. Perrin, L. Piroli, J. Polo, A. L. Pritchard, N. P. Proukakis, C. Rylands, H. Rubinsztein-Dunlop, F. Scazza, S. Stringari, F. Tosto, A. Trombettoni, N. Victorin, W. v. Klitzing, D. Wilkowski, K. Xhani, and A. Yakimenko, Roadmap on atomtronics: State of the art and perspective, AVS Quantum Science **3**, 039201 (2021).

[2] H. Lefèvre, *The Fiber-optic Gyroscope*, Artech House optoelectronics library (Artech House, 1993).

[3] D. S. Durfee, Y. K. Shaham, and M. A. Kasevich, Long-term stability of an area-reversible atom-interferometer sagnac gyroscope, Phys. Rev. Lett. **97**, 240801 (2006).

[4] J. H. T. Burke and C. A. Sackett, Scalable bose-einstein-condensate sagnac interferometer in a linear trap, Phys. Rev. A **80**, 061603 (2009).

[5] P. Hamilton, M. Jaffe, J. M. Brown, L. Maisenbacher, B. Estey, and H. Müller, Atom interferometry in an optical cavity, Phys. Rev. Lett. **114**, 100405 (2015).

[6] K. Bongs, M. Holynski, J. Vovrosh, P. Bouyer, G. Condon, E. Rasel, C. Schubert, W. P. Schleich, and A. Roura, Taking atom interferometric quantum sensors from the laboratory to real-world applications, Nature Reviews Physics **1**, 731 (2019).

[7] E. R. Moan, R. A. Horne, T. Arpornthip, Z. Luo, A. J. Fallon, S. J. Berl, and C. A. Sackett, Quantum rotation sensing with dual sagnac interferometers in an atom-optical waveguide, Phys. Rev. Lett. **124**, 120403 (2020).

[8] C. W. Woffinden, A. J. Groszek, G. Gauthier, B. J. Mommers, M. W. J. Bromley, S. A. Haine, H. Rubinsztein-Dunlop, M. J. Davis, T. W. Neely, and M. Baker, Viability of rotation sensing using phonon interferometry in bose-einstein condensates (2022).

[9] R. Bouchendira, P. Cladé, S. Guellati-Khélifa, F. Nez, and F. Biraben, New determination of the fine structure constant and test of the quantum electrodynamics, Phys. Rev. Lett. **106**, 080801 (2011).

[10] J. B. Fixler, G. T. Foster, J. M. McGuirk, and M. A. Kasevich, Atom interferometer measurement of the newtonian constant of gravity, Science **315**, 74 (2007).

[11] R. H. Parker, C. Yu, W. Zhong, B. Estey, and H. Müller, Measurement of the fine-structure constant as a test of the standard model, Science **360**, 191 (2018).

[12] G. Rosi, F. Sorrentino, L. Cacciapuoti, M. Prevedelli, and G. M. Tino, Precision measurement of the newtonian gravitational constant using cold atoms, Nature **510**, 518 (2014).

[13] C. Freier, M. Hauth, V. Schkolnik, B. Leykauf, M. Schilling, H. Wziontek, H.-G. Scherneck, J. Müller, and A. Peters, Mobile quantum gravity sensor with unprecedented stability, Journal of Physics: Conference Series **723**, 012050 (2016).

[14] R. Karcher, A. Imanaliev, S. Merlet, and F. Pereira Dos Santos, Improving the accuracy of atom interferometers with ultracold sources, New Journal of Physics **20**, 113041 (2018).

[15] M. Grewal, A. Andrews, and C. Bartone, *Global Navigation Satellite Systems, Inertial Navigation, and Integration* (Wiley, 2020).

[16] R. Geiger, A. Landragin, S. Merlet, and F. Pereira Dos Santos, High-accuracy inertial measurements with cold-atom sensors, AVS Quantum Science **2**, 024702 (2020).

[17] D. Savoie, M. Altorio, B. Fang, L. A. Sidorenkov, R. Geiger, and A. Landragin, Interleaved atom interferometry for high-sensitivity inertial measurements, Science Advances **4**, eaau7948 (2018).

[18] C. JEekeli, Navigation error analysis of atom interferometer inertial sensor, NAVIGATION **52**, 1 (2005).

[19] R. Bhat, M. J. Holland, and L. D. Carr, Bose-einstein condensates in rotating lattices, Phys. Rev. Lett. **96**, 060405 (2006).

[20] A. M. Rey, K. Burnett, I. I. Satija, and C. W. Clark, Entanglement and the mott transition in a rotating bosonic ring lattice, Phys. Rev. A **75**, 063616 (2007).

[21] A. Nunnenkamp, A. M. Rey, and K. Burnett, Generation of macroscopic superposition states in ring superlattices, Phys. Rev. A **77**, 023622 (2008).

[22] D. W. Hallwood, K. Burnett, and J. Dunningham, Macroscopic superpositions of superfluid flows, New Journal of Physics **8**, 180 (2006).

[23] C. Jiang, Y. Zeng, Q. Qin, Z. Gong, and H. Fu, Quantum sensing of rotation velocity based on bose-hubbard model (2022).

[24] H. Ritsch, P. Domokos, F. Brennecke, and T. Esslinger, Cold atoms in cavity-generated dynamical optical potentials, Rev. Mod. Phys. **85**, 553 (2013).

[25] F. Mivehvar, F. Piazza, T. Donner, and H. Ritsch, Cavity qed with quantum gases: new paradigms in many-body physics, Advances in Physics **70**, 1 (2021).

[26] K. Baumann, C. Guerlin, F. Brennecke, and T. Esslinger, Dicke quantum phase transition with a superfluid gas in an optical cavity, Nature **464**, 1301 (2010).

[27] J. Klinder, H. Keßler, M. Wolke, L. Mathey, and A. Hemmerich, Dynamical phase transition in the open dicke model, Proceedings of the National Academy of Sciences **112**, 3290 (2015).

[28] V. D. Vaidya, Y. Guo, R. M. Kroeze, K. E. Ballantine, A. J. Kollár, J. Keeling, and B. L. Lev, Tunable-range, photon-mediated atomic interactions in multimode cavity qed, Phys. Rev. X **8**, 011002 (2018).

[29] P. Kongkhambut, J. Skulte, L. Mathey, J. G. Cosme, A. Hemmerich, and H. Keßler, Observation of a continuous time crystal, Science **377**, 670 (2022).

[30] D. Dreon, X. Baumgärtner, A.and Li, S. Hertlein, T. Esslinger, and T. Donner, Self-oscillating pump in a topological dissipative atom-cavity system, Nature **608**, 494 (2022).

[31] C. Kollath, A. Sheikhan, S. Wolff, and F. Brennecke, Ultracold fermions in a cavity-induced artificial magnetic field, Phys. Rev. Lett. **116**, 060401 (2016).

[32] F. Mivehvar, F. Piazza, and H. Ritsch, Disorder-driven density and spin self-ordering of a bose-einstein condensate in a cavity, Phys. Rev. Lett. **119**, 063602 (2017).

[33] G. Bentsen, I.-D. Potirniche, V. B. Bulchandani, T. Scaffidi, X. Cao, X.-L. Qi, M. Schleier-Smith, and E. Altman, Integrable and chaotic dynamics of spins coupled to an optical cavity, Phys. Rev. X **9**, 041011 (2019).

[34] S. B. Jäger, M. J. Holland, and G. Morigi, Superradiant optomechanical phases of cold atomic gases in optical resonators, Phys. Rev. A **101**, 023616 (2020).

[35] J. Skulte, P. Kongkhambut, H. Keßler, A. Hemmerich, L. Mathey, and J. G. Cosme, Parametrically driven dissipative three-level dicke model, Phys. Rev. A **104**, 063705 (2021).

[36] R. Rosa-Medina, F. Ferri, F. Finger, N. Dogra, K. Kroeger, R. Lin, R. Chitra, T. Donner, and T. Esslinger, Observing dynamical currents in a non-hermitian momentum lattice, Phys. Rev. Lett. **128**, 143602 (2022).

[37] Z. Zhang, D. Dreon, T. Esslinger, D. Jaksch, B. Buca, and T. Donner, Tunable non-equilibrium phase transitions between spatial and temporal order through dissipation (2022).

[38] D. De Bernardis, Z.-P. Cian, I. Carusotto, M. Hafezi, and

P. Rabl, Light-matter interactions in synthetic magnetic fields: Landau-photon polaritons, Phys. Rev. Lett. **126**, 103603 (2021).

[39] G. Gauthier, I. Lenton, N. McKay Parry, M. Baker, M. J. Davis, H. Rubinsztein-Dunlop, and T. W. Neely, Direct imaging of a digital-micromirror device for configurable microscopic optical potentials, Optica **3**, 1136 (2016).

[40] I. Bloch, J. Dalibard, and W. Zwerger, Many-body physics with ultracold gases, Rev. Mod. Phys. **80**, 885 (2008).

[41] J. G. Cosme, J. Skulte, and L. Mathey, Time crystals in a shaken atom-cavity system, Phys. Rev. A **100**, 053615 (2019).

[42] J. Skulte, P. Kongkhambut, L. Rao, S.and Mathey, H. Keßler, A. Hemmerich, and J. G. Cosme, Condensate formation in a dark state of a driven atom-cavity system (2022).

[43] J. Klinder, H. Keßler, M. R. Bakhtiari, M. Thorwart, and A. Hemmerich, Observation of a superradiant mott insulator in the dicke-hubbard model, Phys. Rev. Lett. **115**, 230403 (2015).

[44] See Supplemental Material for more details on the stability against particle number fluctuations.

[45] R. Landig, L. Hruby, N. Dogra, M. Landini, R. Mottl, T. Donner, and T. Esslinger, Quantum phases from competing short- and long-range interactions in an optical lattice, Nature **532**, 476 (2016).

Supplemental Material for
Quantum rotation sensor with real-time readout based on an atom-cavity system

Jim Skulte,[1,2] Jayson G. Cosme,[3] and Ludwig Mathey[1,2]

[1]*Zentrum für Optische Quantentechnologien and Institut für Laser-Physik, Universität Hamburg, 22761 Hamburg, Germany*
[2]*The Hamburg Center for Ultrafast Imaging, Luruper Chaussee 149, 22761 Hamburg, Germany*
[3]*National Institute of Physics, University of the Philippines, Diliman, Quezon City 1101, Philippines*
(Dated: March 23, 2023)

PARTICLE NUMBER FLUCTUATIONS

To further show the applicability of our detector we assume to have a gaussian particle number distribution with $N = 40000$ and $\sigma = 0.1 \times N$. SFig. 1 we use the same protocol and parameters as discussed in the main text Fig.3(b), but with the new particle number distribution. The change of the rotational frequency can still be distinguished from the fluctuations.
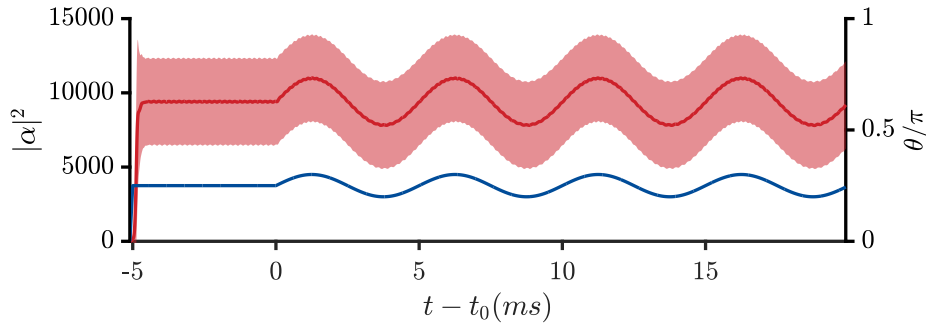
FIG. 1. (a) In blue the applied phase θ modulated using a sinusoidal drive with strength $\delta_\theta = \pi/20$ and frequency $\omega_{\mathrm{dr}} = 2\pi \times 0.5$ kHz. The dark red line shows the light field intensity derived from 10^3 TWA trajectories. The light red shaded area shows the corresponding standard deviation due to quantum fluctuations within TWA. The system is initialized at rest before the drive starts. (b) Same protocol as in (a) but the system is initialized with a phase of $\theta = \pi/4$. In both cases the amplitude change of Ω corresponds to $\omega_{\mathrm{rec}}/(20\pi n_{\mathrm{s}}) = 350$ Hz/n_{s} and we choose $g = 1.09 g_{0,\mathrm{crit}}$.

2.15 Publication X: Equilibrium parametric amplification in Raman-cavity hybrids

H. P. Ojeda Collado, Marios H. Michael, <u>J. Skulte</u>, Angel Rubio and L. Mathey — **submitted to Phys. Rev. Letters (2023)**

Motivation

This work was motivated by the recent experimental advances that showed the possibility to manipulate material properties solely through quantum fluctuations in the light field. The goal of this work was to study precisely such scenarios by coupling a Raman mode to a cavity, where the cavity frequency can be adjusted to control the Raman mode due to the vacuum fluctuations of the cavity light field.

Main findings

In this work, first-authored by H.P. Ojeda Collado, we have shown that for certain resonant conditions the phenomenon of parametric amplification can appear in equilibrium for Raman-cavity hybrid systems. The resonance appears if the cavity frequency is tuned to half of the Raman frequency. Here, the thermal and quantum fluctuations of the Raman mode can enhance the cavity light field. Using numerical and analytical methods, we showed the appearance of what we call an unusual parametric Raman polariton. Using Raman spectroscopy we proposed a scheme to probe our findings and concluded with possible experimental setups that can be used to study this phenomena in more depth experimentally.

Contribution

HPOC conducted all numerical simulations supported by me and supervised by LM. MHM carried out all analytical calculations supported by HPOC. All authors contributed to the discussion and interpretation of the results, as well as to writing the manuscript.

Equilibrium parametric amplification in Raman-cavity hybrids

H. P. Ojeda Collado,[1, 2, *] Marios H. Michael,[3, †] Jim Skulte,[1, 2] Angel Rubio,[3, 4] and Ludwig Mathey[1, 2]

[1]*Center for Optical Quantum Technologies and Institute for Quantum Physics, University of Hamburg, 22761 Hamburg, Germany*
[2]*The Hamburg Center for Ultrafast Imaging, Luruper Chaussee 149, 22761 Hamburg, Germany*
[3]*Max Planck Institute for the Structure and Dynamics of Matter, Luruper Chausse 149, 22761 Hamburg, Germany*
[4]*Center for Computational Quantum Physics, The Flatiron Institute, 162 Fifth Avenue, New York, New York 10010, USA*
(Dated: December 25, 2023)

Parametric resonances and amplification have led to extraordinary photo-induced phenomena in pump-probe experiments. While these phenomena manifest themselves in out-of-equilibrium settings, here, we present the striking result of parametric amplification in equilibrium. In particular, we demonstrate that quantum and thermal fluctuations of a Raman-active mode amplifies light inside a cavity, at equilibrium, when the Raman mode frequency is twice the cavity mode frequency. This noise-driven amplification leads to the creation of an unusual parametric Raman polariton, intertwining the Raman mode with cavity squeezing fluctuations, with smoking gun signatures in Raman spectroscopy. In the resonant regime, we show the emergence of not only quantum light amplification but also localization and static shift of the Raman mode. Apart from the fundamental interest of equilibrium parametric amplification our study suggests a resonant mechanism for controlling Raman modes and thus matter properties by cavity fluctuations. We conclude by outlining how to compute the Raman-cavity coupling, and suggest possible experimental realizations.

Introduction.- Driving condensed matter with light provides a methodology of controlling its properties in an active, dynamic fashion, in contrast to the established, static methods, as reflected in recent scientific studies [1–4]. In this effort, driving matter with laser light has proved to be a remarkably versatile tool in engineering properties of quantum materials such as controlling ferro-electricity [5], magnetism [6–9], superconductivity [10–15], topological features [16] and charge ordering [17, 18]. Even more interestingly, driving with light has provided the possibility to create novel non-equilibrium states. A notable example includes photonic time crystals [19–23], materials exhibiting periodic variation in properties over time that can function as parametric amplifiers for light. Another example is time crystals, denoting a robust, collective dynamical many-body state, in which the response of observables oscillates subharmonically [24–32].

The conceptual approach of dynamical control with light can be extended to the equilibrium domain through cavity-matter hybrids, see e.g. [33–35]. This advancement of control via light involves replacing laser driving by quantum light fluctuations which are strongly coupled to matter through resonant photonic structures, such as cavities [36], plasmonic resonators [37], surfaces hosting surface phonon polaritons [38, 39] and photonic crystals [40]. The feasibility of this approach has been demonstrated experimentally, with examples including manipulation of transport [41], control of superconducting properties [42], magnetism [43], topological features [37] and cavity control of chemical reactivity [44–46].

In this paper, we demonstrate that quantum and thermal *noise* of a Raman-active mode, can amplify cavity fluctuations in equilibrium. We emphasize that parametric amplification generally occurs in driven systems while here we present it in the context of an equilibrium amplification process. This amplification can in turn be used to resonantly control

properties of matter and constitutes a novel method of light control, for Raman-cavity systems.

Our starting point is the nonlinear coupling between Raman active collective modes and light. Here Raman-active modes could be Raman phonons [47], molecular vibrations [13], Higgs modes in superconductors [48–50] and amplitude modes in charge density waves [18] that are even under inversion symmetry, and the electric field of a local cavity mode [51]. Therefore, at leading order, the Raman-light Hamiltonian reads $H_{Raman-light} = \lambda Q E_{cav}^2$ where E_{cav} is the electric field in the cavity, Q is the coordinate of the Raman collective mode and λ is the light-matter coupling. This quadratic coupling includes parametrically resonant processes of the type $\hat{a}^\dagger \hat{a}^\dagger \hat{b} + \hat{a}\hat{a}\hat{b}^\dagger$ where $\hat{a}$ and $\hat{b}$ are the photon and Raman annihilation operators respectively. In the presence of coherent Raman oscillations, $\langle b(t) \rangle = A_0 e^{i\omega_R t}$, at the Raman frequency ω_R, the above coupling leads to exponential growth of the light field when the cavity frequency ω_c satisfies the parametric resonant condition, $2\omega_c = \omega_R$. This observation naturally leads to the question: can a randomly fluctuating field coming from Raman quantum fluctuations also amplify light? We find that the answer is yes which we demonstrate below.

To study this phenomenon, we use an open Truncated-Wigner approximation method (open TWA) [52–54] to simulate the semi-classical dynamics of the Raman-cavity hybrids in the quantum fluctuation regime. We also determine the signatures of equilibrium parametric amplification in Raman spectroscopy (Fig. 1 (a)). We find that a prominent feature of parametric resonance and equilibrium light amplification is the appearance of two Raman polariton branches in Raman spectroscopy as shown in Fig. 1(b). We call this polariton parametric Raman polariton and its formation is attributed to the *nonlinear* process of mixing *squeezed photon fluctuations* with the Raman coordinate. This is substantially different to the

existent polariton panorama where polaritons typically arise from a *linear* coupling between matter degrees of freedom and light [55]. To quantify the coupling between the Raman mode and the cavity, we compute the resonance splitting between the upper and lower parametric Raman polariton. This is a nonlinear extension of the usual Rabi-splitting in the case of infrared active phonon polaritons [36]. We use a frequency dependent Gaussian theory to provide an analytical expression for this splitting as a function of the coupling strength which agrees well with the simulations.

The key features of the parametric Raman polariton are as follows: (i) The vacuum fluctuations of the cavity mode are amplified. (ii) The fluctuations of the Raman are reduced, in response to the amplification of the cavity fluctuations. This corresponds to a localization of the Raman mode. (iii) The average position of the Raman mode is statically shifted due to the cavity fluctuations as shown schematically in Fig. 1(c). These observations suggest that this mechanism can be used to resonantly modify and control both the Raman mode and the cavity in equilibrium. Furthemore we conclude by proposing realistic experimental set-ups where this phenomenon can be observed.

Raman-Cavity Model & Raman spectroscopy.- We consider a model, in which cavity field fluctuations are locally coupled to a Raman coordinate. The Hamiltonian for this system is given by:

$$\frac{H}{\hbar} = \omega_c \hat{a}^\dagger \hat{a} + \omega_R \hat{b}^\dagger \hat{b} + g\left(\hat{b}^\dagger + \hat{b}\right)\left(\hat{a}^\dagger + \hat{a}\right)^2 + \frac{g_4}{4}\left(\hat{a}^\dagger + \hat{a}\right)^4. \quad (1)$$

The cavity creation (annihilation) operator is $\hat{a}^\dagger$ ($\hat{a}$) and ω_c is the cavity frequency. $\hat{b}^\dagger$ and $\hat{b}$ are the creation and annihilation operators for the Raman mode of frequency ω_R and g is the coupling strength between the cavity and Raman mode. To connect these operators to the electric field in the cavity we require that $\hat{E}_{cav}^2 = E_0^2\left(\hat{a} + \hat{a}^\dagger\right)^2$, where E_0^2 is the nonzero quantum noise of the electric field in the cavity that can be measured experimentally [37], while the cavity itself is in equilibrium, $\langle\hat{E}_{cav}\rangle = 0$ and the Raman coordinate is given by $\hat{Q} = \frac{\hat{b}^\dagger + \hat{b}}{\sqrt{2\omega_R}}$. The last term of strength g_4 is an $\hat{E}_{cav}^4$ type of nonlinearity necessary to make the system stable for finite coupling $g < \sqrt{g_4\omega_R}/2$, a condition that is found analytically in the Supplementary Information (SI).

We propose Raman spectroscopy as a natural probe for Raman polaritons (see Fig. 1 (a)). The spectroscopic protocol consists of an incoming probe laser of frequency ω_p that can be scattered to free space as outgoing photons with frequency ω_s after interacting with the Raman medium through a Stimulated Raman Scattering (SRS) (shown schematically in Fig. 1 (a)).

The probe is assumed to be a coherent light-source with an associated electric field $E_p(t) = E_p^0 \sin(\omega_p t)$ whereas the scattered photons are described by the Hamiltonian $H_s/\hbar = \omega_s \hat{a}_s^\dagger \hat{a}_s$. The SRS Hamiltonian can be written as:

$$\frac{H_p}{\hbar} = g_s E_p(t)\left(\hat{b}^\dagger + \hat{b}\right)\left(\hat{a}_s^\dagger + \hat{a}_s\right) \quad (2)$$
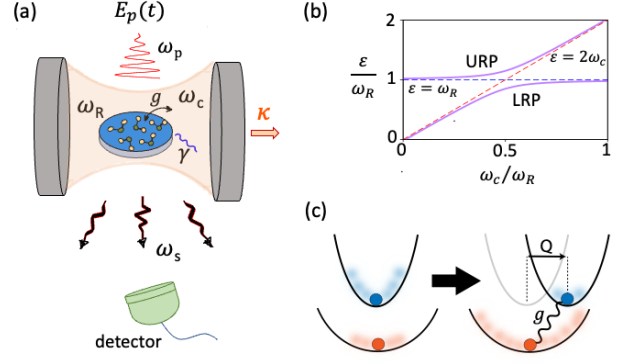

Figure 1. Parametric Raman Polaritons. (a) Sketch of a Raman medium (blue) coupled to a single-photon cavity mode of frequency ω_c (light-red shading) with a constant coupling g. Light can leak out of the cavity at a total decay rate κ while γ represents the damping associated to the Raman mode ω_R. The wavy lines at the top and bottom represent a Raman spectroscopy scheme in which a probe field $E_p(t)$ of frequency ω_p is sent into the sample, and a detector (in green) collects the scattered photons at different frequencies ω_s giving information about the hybrid Raman-cavity system. (b) Representative Raman spectrum (in purple) in which an avoided crossing appears at the resonant condition $\omega_R = 2\omega_c$ indicating the existence of two branches, the upper (URP) and lower (LRP) Raman polaritons. (c) Sketch of how Raman (blue) and cavity (red) properties are modified due to the coupling g. Full circles represent the equilibrium position and shaded regions indicate fluctuations. In the resonant regime the cavity fluctuations are amplified while the Raman mode is statically shifted and localized, i.e. its fluctuations decrease.

where $\hat{a}_s^\dagger$ ($\hat{a}_s$) is the creation (annihilation) operator for scattered photons and g_s the coupling between the Raman mode and photons being scattered. The requirement for weak probing is that $g_s E_p^0$ is much smaller than the magnitude of the energies of the system such as g, as we will choose in the following.

Considering the total Hamiltonian $H_t = H + H_p + H_s$ we derive the corresponding Heisenberg-Langevin equations of motion and use the open TWA method to solve the dynamics. This semi-classical phase-space method captures the lowest order quantum effects beyond mean-field treatment as extensively demonstrated in different contexts [52–54, 56] and consists of sampling the initial states from the corresponding Wigner distribution to take into account the quantum uncertainty. The semiclassical equations of motion for the complex fields a, b and a_s associated with cavity photons, Raman motion and scattered photons operators are given by

$$i\partial_t a = \omega_c a + 2g(a + a^*)(b + b^*) + g_4(a + a^*)^3 \\ - i\kappa a + i\xi_a, \quad (3)$$

$$i\partial_t b = \omega_R b + g(a + a^*)^2 + g_s E_p(t)(a_s + a_s^*) \\ - i\gamma(b - b^*)/2 - \xi_b, \quad (4)$$

$$i\partial_t a_s = \omega_s a_s + g_s E_p(t)(b + b^*) - i\kappa_s a_s + i\xi_s, \quad (5)$$
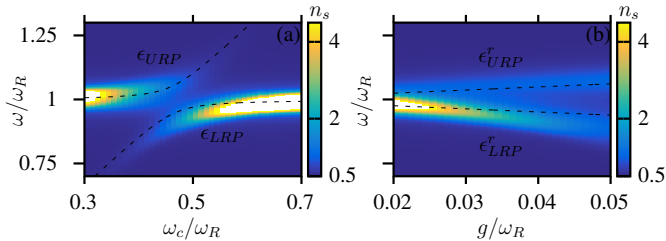
Figure 2. (a) Raman spectra $n_s(\omega)$ for different cavity frequencies ω_c. We consider a probe laser of strength $g_s E_p^0 = 0.04\omega_R$ and frequency $\omega_p = 5\omega_R$ with $g = 0.04\omega_R$, $g_4 = \kappa = \gamma = \kappa_s = 0.01\omega_R$. (b) Raman polariton branches at resonance as a function of the coupling g on resonance, $\bar{\omega}_c = \omega_R/2$. In both panels, the dashed black lines correspond to an analytical solution using a Gaussian approximation theory.

Here κ, γ and κ_s are the decay rates associated with the cavity, Raman and scattered photon field while ξ_a, ξ_b and ξ_s are sources of Gaussian noise obeying the autocorrelation relations $\langle \xi_a^*(t_1)\xi_a(t_2) \rangle = \kappa\delta(t_1 - t_2)$, $\langle \xi_b(t_1)\xi_b(t_2) \rangle = \gamma\delta(t_1 - t_2)$ and $\langle \xi_s^*(t_1)\xi_s(t_2) \rangle = \kappa_s\delta(t_1 - t_2)$. ξ_a and ξ_s are complex-valued whereas ξ_b is real-valued and, along with the damping term, enters only in the equation of motion for the imaginary part of the Raman field which is associated with the momentum of the Raman mode. The choice for the Raman mode is motivated by the Brownian motion in which the frictional force is proportional to the velocity.

We simulate the quantum Langevin Eqs. (3-5) using a stochastic ordinary differential equation (ODE) solver and compute relevant observables in the steady state. To initiate the dynamics we ramp out the coupling g from zero to a finite value and wait for the steady state before turning on the probe field $E_p(t)$ (see SI for details). In particular, we define the Raman spectrum as the number of scattered photons $n_s = |a_s|^2$ as a function of their frequencies which is computed after a certain time of exposure to the probe field (see SI).

Parametric Raman polaritons.- In Fig. 2 (a) we show the Raman spectra $n_s(\omega)$ for different cavity frequencies and a fixed coupling strength where $\omega = \omega_p - \omega_s$ is the Raman shift. Away from resonance we see only one peak at $\omega \approx \omega_R$, which corresponds to the Stokes peak [57, 58] of the Raman mode [59]. Near the resonance at $\omega_c = \omega_R/2$ a second peak appears showing an avoided crossing, which signals the existence of a Raman polariton. To gain insight into the two polariton branches found numerically using the TWA method, we employ a Gaussian approximation. Within this method, outlined in the SI, we find that the two polariton branches arise from resonant coupling between the Raman phonon mode oscillating at ω_R and Gaussian squeezing oscillations of the photon, oscillating at $2\omega_c$ leading to a new hybrid Raman polariton. We have computed analytically the dispersion of the lower and upper Raman polariton branches which are plotted with black dashed lines in Fig. 2(a), showing good agreement with the two numerical peaks in the Raman spectrum (indicated by ϵ_{LRP} and ϵ_{URP}). The exact position

of the avoided crossing is shifted to the left compared to the condition $\omega_c = \omega_R/2$, due to the renormalization of the cavity frequency by nonlinear interactions. Within the Gaussian approximation the effective cavity frequency is found to be $\bar{\omega}_c = \omega_c - 12g^2/\omega_R + 3g_4$ so the improved estimate of the resonance condition is $\bar{\omega}_c = \omega_R/2$.

To quantify the strength of the Raman-cavity coupling, we define the Raman Rabi splitting as the difference between the upper and lower Raman polaritons on resonance, $2\delta = \epsilon_{URP}(\bar{\omega}_c = \omega_R/2) - \epsilon_{LRP}(\bar{\omega}_c = \omega_R/2)$. In Fig. 2(b) we plot the dependence of the Raman polariton branches on resonance $\epsilon_{URP}^r = \epsilon_{URP}(\bar{\omega}_c = \omega_R/2)$ and $\epsilon_{LRP}^r = \epsilon_{LRP}(\bar{\omega}_c = \omega_R/2)$ on the coupling strength g, and overlay the analytical prediction in black dashed lines. The Rabi splitting grows linearly with the coupling strength g and is given analytically by the expression:

$$\delta = \sqrt{2\langle\hat{x}^2\rangle\omega_R}\left(1 - 27g_4\langle\hat{x}^2\rangle^3/2\right)g + \mathcal{O}(g^3). \quad (6)$$

Interestingly, the Gaussian theory suggests that the Rabi splitting could be parametrically enhanced by the cavity quantum fluctuations $\langle\hat{x}^2\rangle$, where $\hat{x} = \frac{a+a^\dagger}{\sqrt{2\omega_c}}$. Perturbatively, $\langle\hat{x}^2\rangle = \frac{1}{2\omega_c} + \mathcal{O}(g^2)$, which is the value we use in Eq. (6) to plot the dashed lines in Fig.2(b).

Equilibrium parametric amplification- While Raman spectroscopy provides experimental evidence for strong Raman-cavity coupling, we now expand the discussion to the equilibrium properties of the Raman polariton system which exhibit equilibrium parametric amplification. This phenomenology corresponds to the amplification of photon fluctuations accompanied by a localization of Raman mode fluctuations, i.e. suppression of fluctuations, depicted schematically in Fig. 1 (c).

To illustrate the modification of each subsystem due to the Raman-cavity coupling, we determine the deviation of the Raman and cavity fluctuations δQ^2 and δx^2 from the uncoupled case given by

$$\delta Q^2 = \frac{\langle\hat{Q}^2\rangle - \langle\hat{Q}^2\rangle_0}{\langle\hat{Q}^2\rangle_0}, \delta x^2 = \frac{\langle\hat{x}^2\rangle - \langle\hat{x}^2\rangle_0}{\langle\hat{x}^2\rangle_0} \quad (7)$$

where $\langle...\rangle$ denotes the expectation value for a finite coupling g and $\langle...\rangle_0$ the expectation value in the absence of coupling and cavity nonlinearities ($g = g_4 = 0$). As in the previous section, $\hat{x} = \frac{\hat{a}^\dagger + \hat{a}}{\sqrt{2\omega_c}}$, is the cavity coordinate which is related to the electric field, $\hat{E}_{cav} = \sqrt{2\omega_c}E_0\hat{x}$, where E_0 is the electric field amplitude of the noise of the cavity mode. Note that also $\delta x^2 = \frac{\langle\hat{E}_{cav}^2\rangle - \langle\hat{E}_{cav}^2\rangle_0}{\langle\hat{E}_{cav}^2\rangle_0}$, and denotes the amplification of the quantum fluctuations in the electric field. To compute these Raman and cavity fluctuations we set the probe field $E_p(t)$ in Eqs. (3-5) to zero and average over steady states of the Langevin equations of motion (see SI for details).

In Fig. 3 we show δQ^2 and δx^2 as well as the Raman coordinate $Q = \langle\hat{Q}\rangle$ for different cavity frequencies and coupling strengths g. In all cases, a clear resonance can
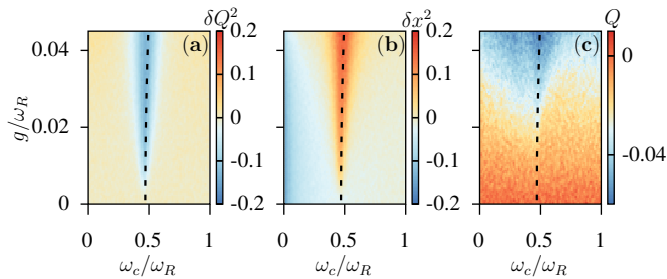
Figure 3. (a), (b) Variation of Raman and cavity fluctuations compared to the uncoupled case $g = 0$ (see text) for different cavity frequencies and coupling strengths g. (c) Raman displacement. The dashed lines represent the parametric resonant condition $\omega_R = 2\bar{\omega}_c$. On resonance, the main features of parametric Raman polaritons appear: localization (a) and shift (c) of the Raman mode in favor of cavity field amplification (b). The decay rates and nonlinear interaction g_4 are the same as in Fig. 2.

be seen around $\omega_c \approx \omega_R/2$ indicating a resonant regime in which both the Raman mode and cavity fluctuations are strongly modified. In this regime, the Raman fluctuations are suppressed by the cavity, $\delta Q^2 < 0$, so the Raman mode is localized while the cavity fluctuations are amplified by the Raman mode $\delta x^2 > 0$. Outside this resonant region the Raman fluctuations are unaffected and remain the same as in free space ($\delta Q^2 \approx 0$). In a similar way, for off-resonant cavity frequencies, quantum vacuum fluctuations remain practically unchanged meaning that the Raman medium barely perturbs the photon field ($\delta x^2 \approx 0$). This observation justifies our choice to consider the coupling of a single cavity mode with a single Raman mode: due to the resonant character of the interaction, we expect that other off-resonant modes do not contribute.

For the parameters used in Fig. 3, on resonance and close to the instability $g \approx \sqrt{g_4\omega_R}/2$, the Raman mode is strongly localized by $\sim 20\%$ compared to the case of Raman fluctuations in free space while the photon field increases by the same amount with respect to the empty cavity case, even though the coupling is only $g \sim 4\%\omega_R$. We would like to emphasize that the coupling values g used in Fig. 2 and Fig. 3 are of the same order of magnitude as the decay rates γ and κ. Therefore the system is between the weak and strong coupling regime but not in the ultrastrong coupling situation ($g > \omega_c$) where these resonant effects may be more pronounced [60].

In Fig. 3 (c) the expectation value of the Raman coordinate Q is shown as a function of coupling strength g and cavity frequency ω_c. A clear shift of the Raman coordinate is observed for large values of g which represents another form of control of the Raman mode by the cavity field. Therefore, the Raman mode is not only localized but also its coordinate is shifted by the quantum vacuum fluctuations. This shift is an off-resonant process and therefore depends only weakly on the parametric resonance compared to the fluctuations in Fig. 3 (a-b).

For the sake of completeness we have also checked that

these parametric resonances in δQ^2, δx^2 and shift in Q survive for stronger nonlinearties g_4 and larger decay rates (see SI).

Experimental platforms.- Our mechanism can be realized in materials hosting Raman phonon modes, coupled resonantly with a Fabry-Pérot cavity in the THz range. Interestingly, the strong coupling regime between infrared phonons and a tunable THz cavity has been experimentally demonstrated [36] opening the door to the study of Raman-active materials in this setup. Possible Raman candidates might be functionalized graphene nanoribbons with Raman activity around 6 THz [61], twisted bilayer graphene with low Raman modes $\lesssim 3$ THz [62] or transition metal dichalcogenides (TMDs) with ultralow breathing and shear modes even below 1 THz due to the weak van der Waals coupling between the layers. All these examples lie in the experimental frequency range of up to ~8 THz in different types of cavities [36, 37, 63, 64].

The Raman-cavity coupling between the cavity mode and the zero-momentum Raman mode can be computed from first principles through the Raman tensor (see SI for derivation) and is given by:

$$\frac{g}{\omega_R} = \frac{\sqrt{N}}{2}\frac{\epsilon_0 E_0^2 V_{cell}}{\omega_R}\tilde{R} \qquad (8)$$

where ϵ_0 is the vacuum permittivity, E_0 is the electric field noise amplitude measured in different photonic structures, V_{cell} is the volume of the unit cell of the material hosting the phonon mode and $N = \frac{V_{samp}}{V_{cell}}$ is the total number of unit cells in the sample of volume V_{samp}. The dimensionless Raman coupling is given by $\tilde{R} \propto \vec{e}_c \cdot \partial_Q \underline{\epsilon}(Q) \cdot \vec{e}_c$ which measures the change in electric permittivity $\underline{\epsilon}$ as a function of a shift of the Raman phonon coordinate $\bar{Q}$ per unit cell, and $\vec{e}_c$ is the polarization vector of the cavity. The electric field noise of a cavity is given by, $E_0 \sim \sqrt{\frac{\omega_c}{\epsilon_0 V_{eff}}}$ [37] and therefore, on parametric resonance $\omega_R = 2\omega_c$, we estimate that $\frac{g}{\omega_R} \sim \frac{\sqrt{V_{samp}V_{cell}}}{V_{eff}}\tilde{R}$.

To circumvent the possible limitation of weak photon-matter coupling g in Fabry-Pérot cavities, due to the small value of V_{cell}/V_{eff}, split-ring resonators (SRRs) cavities could be a solution where large cavity mode volume compression has been experimentally demonstrated. Typically, SRRs are build with cavity frequencies between 0.5-1 THz [63–65] which matches the range of breathing Raman modes of the order of 1 THz in twisted-TMDs like $MoSe_2$ or WSe_2 [66, 67]. Thus the condition $2\omega_c = \omega_R$ can be satisfied. From the above expression we may expect that also the coupling strength will be particularly increased for these twisted bilayer system of triangular lattices for twist angles around 0° or 60°, where the unit cell becomes very large. Considering 10nm x 10nm for the area of the unit cell, $1\ \mu m^2$ for the effective cavity area of SRRs, $g/\omega_R \sim 0.01$ assuming a Raman tensor of the order of 1 as estimated for twisted TMDs using Density Functional Theory (DFT) [67].

Conclusion.- We have presented how parametric resonances in Raman-cavity hybrids can be exploited to

amplify photon quantum noise and localize Raman modes *at equilibrium*. Our study represents a proof of principle of how this nonlinear type of hybridization between Raman modes and photons, at the quantum fluctuation level, gives rise to equilibrium parametric amplification that can be leveraged to control quantum materials. In particular, the cavity control of Raman-active phonons demonstrated here is a crucial step towards cavity-material engineering in more complex systems. Strongly coupled Raman phonons are responsible for superconductivity in K_3C_{60} [68], and statically shifting one of these modes was proposed as a mechanism for photo-induced superconductivity [13, 39]. More broadly, Raman phonons can change lattice symmetries, lift electronic orbital degeneracies [69], gap out gapless electronic systems [70] and manipulate spin-spin interactions [71]. Our work paves the way to new studies on all of these topics and the search of similar equilibrium parametric amplification phenomena in different scenarios such as Higgs-light hybrids in superconducting systems and in the quantum information and quantum sensing realm using the recent three-photon quantum-optics development [72, 73].

---

* hojedaco@physnet.uni-hamburg.de

† marios.michael@mpsd.mpg.de

[1] A. de la Torre, D. M. Kennes, M. Claassen, S. Gerber, J. W. McIver, and M. A. Sentef, "Colloquium: Nonthermal pathways to ultrafast control in quantum materials," Rev. Mod. Phys. **93**, 041002 (2021).

[2] D. N. Basov, R. D. Averitt, and D. Hsieh, "Towards properties on demand in quantum materials," Nature Mater **16**, 1077–1088 (2017).

[3] J. Bloch, A. Cavalleri, V. Galitski, M. Hafezi, and A. Rubio, "Strongly correlated electron–photon systems," Nature **606**, 41 (2022).

[4] D. M. Kennes and A. Rubio, "A New Era of Quantum Materials Mastery and Quantum Simulators In and Out of Equilibrium," in *Sketches of Physics: The Celebration Collection* (Springer International Publishing, Cham, 2023) pp. 1–39.

[5] T. F. Nova, A. S. Disa, M. Fechner, and A. Cavalleri, "Metastable ferroelectricity in optically strained $SrTiO_3$," Science **364**, 1075 (2019).

[6] A. S. Disa, J. Curtis, M. Fechner, A. Liu, A. von Hoegen, M. Först, T. F. Nova, P. Narang, A. Maljuk, A. V. Boris, B. Keimer, and A. Cavalleri, "Photo-induced high-temperature ferromagnetism in $YTiO_3$," Nature **617**, 73 (2023).

[7] F. Siegrist, J. A. Gessner, M. Ossiander, C. Denker, Y. P. Chang, M. C. Schröder, A. Guggenmos, Y. Cui, J. Walowski, U. Martens, J. K. Dewhurst, U. Kleineberg, M. Münzenberg, S. Sharma, and M. Schultze, "Light-wave dynamic control of magnetism," Nature **571**, 240 (2019).

[8] S. Beaulieu, S. Dong, N. Tancogne-Dejean, M. Dendzik, T. Pincelli, J. Maklar, R. Patrick Xian, M. A. Sentef, M. Wolf, A. Rubio, L. Rettig, and R. Ernstorfer, "Ultrafast dynamical Lifshitz transition," Science Advances **7**, eabd9275 (2021).

[9] E. V. Boström, M. Claassen, J. W. McIver, G. Jotzu, A. Rubio, and M. A. Sentef, "Light-induced topological magnons in two-dimensional van der Waals magnets," SciPost Phys. **9**, 061 (2020).

[10] M. Mitrano, A. Cantaluppi, D. Nicoletti, S. Kaiser, A. Perucchi, S. Lupi, P. Di Pietro, D. Pontiroli, M. Riccò, S. R. Clark, D. Jaksch, and A. Cavalleri, "Possible light-induced superconductivity in K_3C_{60} at high temperature," Nature **530**, 461 (2016).

[11] M. Budden, T. Gebert, M. Buzzi, G. Jotzu, E. Wang, T. Matsuyama, G. Meier, Y. Laplace, D. Pontiroli, M. Riccò, F. Schlawin, D. Jaksch, and A. Cavalleri, "Evidence for metastable photo-induced superconductivity in K_3C_{60}," Nat. Phys. **17**, 611 (2021).

[12] E. Rowe, B. Yuan, M. Buzzi, G. Jotzu, Y. Zhu, M. Fechner, M. Först, B. Liu, D. Pontiroli, M. Riccò, and A. Cavalleri, "Giant resonant enhancement for photo-induced superconductivity in K_3C_{60}," (2023), 2301.08633 [cond-mat].

[13] S. Chattopadhyay, C. J. Eckhardt, D. M. Kennes, M. A. Sentef, D. Shin, A. Rubio, A. Cavalleri, E. A. Demler, and M. H. Michael, "Mechanisms for Long-Lived, Photo-Induced Superconductivity," (2023), 2303.15355 [cond-mat, physics:physics].

[14] A. von Hoegen, M. Fechner, M. Först, N. Taherian, E. Rowe, A. Ribak, J. Porras, B. Keimer, M. Michael, E. Demler, and A. Cavalleri, "Amplification of Superconducting Fluctuations in Driven $YBa_2Cu_3O_{6+x}$," Phys. Rev. X **12**, 031008 (2022).

[15] M. H. Michael, A. von Hoegen, M. Fechner, M. Först, A. Cavalleri, and E. Demler, "Parametric resonance of Josephson plasma waves: A theory for optically amplified interlayer superconductivity in $YBa_2Cu_3O_{6+x}$," Phys. Rev. B **102**, 174505 (2020).

[16] J. W. McIver, B. Schulte, F. U. Stein, T. Matsuyama, G. Jotzu, G. Meier, and A. Cavalleri, "Light-induced anomalous Hall effect in graphene," Nat. Phys. **16**, 38 (2020).

[17] A. Kogar, P. E. Zong, A.and Dolgirev, X. Shen, J. Straquadine, Y.Q. Bie, X. Wang, T. Rohwer, I.-C. Tung, Y. Yang, R. Li, J. Yang, S. Weathersby, S. Park, M. E. Kozina, E. J. Sie, H. Wen, P. Jarillo-Herrero, I. R. Fisher, X. Wang, and N. Gedik, "Light-induced charge density wave in $LaTe_3$," Nat. Phys. **16**, 159 (2020).

[18] P. E. Dolgirev, M. H. Michael, A. Zong, N. Gedik, and E. Demler, "Self-similar dynamics of order parameter fluctuations in pump-probe experiments," Phys. Rev. B **101**, 174306 (2023).

[19] M. Lyubarov, Y. Lumer, A. Dikopoltsev, E. Lustig, Y. Sharabi, and M. Segev, "Amplified emission and lasing in photonic time crystals," Science **377**, 425 (2022).

[20] M. H. Michael, M. Först, D. Nicoletti, S. R. Ul Haque, Y. Zhang, A. Cavalleri, R. D. Averitt, D. Podolsky, and E. Demler, "Generalized Fresnel-Floquet equations for driven quantum materials," Phys. Rev. B **105**, 174301 (2022).

[21] M. H. Michael, S. R. Ul Haque, L. Windgaetter, S. Latini, Y. Zhang, A. Rubio, R. D. Averitt, and E. Demler, "Theory of time-crystalline behaviour mediated by phonon squeezing in Ta2NiSe5," (2023), arXiv:2207.08851 [cond-mat.str-el].

[22] S. R. Ul Haque, M. H. Michael, J. Zhu, Y. Zhang,

L. Windgätter, S. Latini, J. P. Wakefield, G. F. Zhang, J. Zhang, A. Rubio, J. G. Checkelsky, E. Demler, and R. D. Averitt, "Terahertz parametric amplification as a reporter of exciton condensate dynamics," (2023), arXiv:2304.09249 [cond-mat.str-el].

[23] P. E. Dolgirev, A. Zong, M. H. Michael, J. B. Curtis, D. Podolsky, A. Cavalleri, and E. Demler, "Periodic dynamics in superconductors induced by an impulsive optical quench," Commun Phys 5, 1 (2022).

[24] D. V. Else, C. Monroe, C. Nayak, and N. Y. Yao, "Discrete Time Crystals," Annual Review of Condensed Matter Physics 11, 467 (2020).

[25] J. Zhang, P. W. Hess, A. Kyprianidis, P. Becker, A. Lee, J. Smith, G. Pagano, I. D. Potirniche, A. C. Potter, A. Vishwanath, N. Y. Yao, and C. Monroe, "Observation of a discrete time crystal," Nature 543, 217 (2017).

[26] S. Choi, J. Choi, R. Landig, G. Kucsko, H. Zhou, J. Isoya, F. Jelezko, S. Onoda, H. Sumiya, V. Khemani, C. von Keyserlingk, N. Y. Yao, E. Demler, and M. D. Lukin, "Observation of discrete time-crystalline order in a disordered dipolar many-body system," Nature 543, 221 (2017).

[27] H. Keßler, P. Kongkhambut, C. Georges, L. Mathey, J. G. Cosme, and A. Hemmerich, "Observation of a Dissipative Time Crystal," Phys. Rev. Lett. 127, 043602 (2021).

[28] P. Kongkhambut, H. Keßler, J. Skulte, L. Mathey, J. G. Cosme, and A. Hemmerich, "Realization of a Periodically Driven Open Three-Level Dicke Model," Phys. Rev. Lett. 127, 253601 (2021).

[29] H. Taheri, A. B. Matsko, L. Maleki, and K. Sacha, "All-optical dissipative discrete time crystals," Nature Communications 13, 848 (2022).

[30] M. P. Zaletel, M. Lukin, C. Monroe, C. Nayak, F. Wilczek, and N. Y. Yao, "Colloquium: Quantum and classical discrete time crystals," Rev. Mod. Phys. 95, 031001 (2023).

[31] H. P. Ojeda Collado, G. Usaj, C. A. Balseiro, D. H. Zanette, and J. Lorenzana, "Emergent parametric resonances and time-crystal phases in driven Bardeen-Cooper-Schrieffer systems," Phys. Rev. Res. 3, L042023 (2021).

[32] H. P. Ojeda Collado, G. Usaj, C. A. Balseiro, D. H. Zanette, and J. Lorenzana, "Dynamical phase transitions in periodically driven Bardeen-Cooper-Schrieffer systems," Phys. Rev. Res. 5, 023014 (2023).

[33] F. Schlawin, D. M. Kennes, and M. A. Sentef, "Cavity quantum materials," Applied Physics Reviews 9 (2022).

[34] J. B. Curtis, M. H. Michael, and E. Demler, "Local fluctuations in cavity control of ferroelectricity," Phys. Rev. Res. 5, 043118 (2023).

[35] M. Ruggenthaler, N. Tancogne-Dejean, J. Flick, H. Appel, and A. Rubio, "From a quantum-electrodynamical light–matter description to novel spectroscopies," Nature Reviews Chemistry 2, 0118 (2018).

[36] G. Jarc, S. Y. Mathengattil, F. Giusti, M. Barnaba, A. Singh, A. Montanaro, F. Glerean, E. M. Rigoni, S. D. Zilio, S. Winnerl, and D. Fausti, "Tunable cryogenic THz cavity for strong light-matter coupling in complex materials," Review of Scientific Instruments 93, 033102 (2022).

[37] F. Appugliese, J. Enkner, G. L. Paravicini-Bagliani, M. Beck, C. Reichl, W. Wegscheider, G. Scalari, C. Ciuti, and J. Faist, "Breakdown of topological protection by cavity vacuum fields in the integer quantum Hall effect," Science 375, 1030–1034 (2022).

[38] K. Lenk, J. Li, P. Werner, and M. Eckstein, "Dynamical mean-field study of a photon-mediated ferroelectric phase transition," Phys. Rev. B 106 (2022).

[39] C. J. Eckhardt, S. Chattopadhyay, D. M. Kennes, E. A. Demler, M. A. Sentef, and M. H. Michael, "Theory of resonantly enhanced photo-induced superconductivity," (2023), 2303.02176 [cond-mat].

[40] A. Baydin, M. Manjappa, S. Subhra Mishra, H. Xu, F. Tay, D. Kim, F. G. G. Hernandez, P. H. O. Rappl, E. Abramof, R. Singh, and J. Kono, "Deep-strong coupling between cavity photons and terahertz to phonons in pbte," in CLEO 2023 (Optica Publishing Group, 2023) p. FF3D.2.

[41] E. Orgiu, J. George, J. A. Hutchison, E. Devaux, J. F. Dayen, B. Doudin, F. Stellacci, C. Genet, J. Schachenmayer, C. Genes, G. Pupillo, P. Samorì, and T. W. Ebbesen, "Conductivity in organic semiconductors hybridized with the vacuum field," Nat Mater 14, 1123–1129 (2015).

[42] A. Thomas, E. Devaux, K. Nagarajan, T. Chervy, M. Seidel, D. Hagenmüller, S. Schütz, J. Schachenmayer, C. Genet, G. Pupillo, and T. W. Ebbesen, "Exploring superconductivity under strong coupling with the vacuum electromagnetic field," (2019), 1911.01459 [cond-mat, physics:quant-ph].

[43] A. Thomas, E. Devaux, K. Nagarajan, G. Rogez, M. Seidel, F. Richard, C. Genet, M. Drillon, and T. W. Ebbesen, "Large enhancement of ferro-magnetism under collective strong coupling of YBCO nanoparticles," Nano Lett. 21, 4365–4370 (2021).

[44] A. Thomas, L. Lethuillier-Karl, K. Nagarajan, R. M. A. Vergauwe, J. George, T. Chervy, A. Shalabney, E. Devaux, C. Genet, J. Moran, and T. W. Ebbesen, "Tilting a ground-state reactivity landscape by vibrational strong coupling," Science 363, 615–619 (2019).

[45] K. Nagarajan, A. Thomas, and T. W. Ebbesen, "Chemistry under vibrational strong coupling," J. Am. Chem. Soc. 143, 16877–16889 (2021).

[46] C. Schäfer, J. Flick, E. Ronca, P. Narang, and A. Rubio, "Shining light on the microscopic resonant mechanism responsible for cavity-mediated chemical reactivity," Nature Communications 13, 7817 (2022).

[47] M. Först, C. Manzoni, S. Kaiser, Y. Tomioka, Y. Tokura, R. Merlin, and A. Cavalleri, "Nonlinear phononics as an ultrafast route to lattice control," Nature Phys 7, 854–856 (2011).

[48] R. Matsunaga, N. Tsuji, H. Fujita, A. Sugioka, K. Makise, Y. Uzawa, H. Terai, Z. Wang, H. Aoki and R. Shimano, "Light-induced collective pseudospin precession resonating with Higgs mode in a superconductor," Science 345, 1145–1149 (2014).

[49] M. Buzzi, G. Jotzu, A. Cavalleri, J. I. Cirac, E. A. Demler, B. I. Halperin, M. D. Lukin, T. Shi, Y. Wang, and D. Podolsky, "Higgs-Mediated Optical Amplification in a Nonequilibrium Superconductor," Phys. Rev. X 11, 011055 (2021).

[50] H. P. Ojeda Collado, J. Lorenzana, G. Usaj, and C. A. Balseiro, "Population inversion and dynamical phase transitions in a driven superconductor," Phys. Rev. B 98, 214519 (2018).

[51] D. M. Juraschek, T. Neuman, J. Flick, and P. Narang, "Cavity control of nonlinear phononics," Phys. Rev. Res. 3, L032046 (2021).

[52] A. Polkovnikov, "Phase space representation of quantum dynamics," Annals of Physics 325, 1790 (2010).

[53] J. G. Cosme, J. Skulte, and L. Mathey, "Time crystals in a shaken atom-cavity system," Phys. Rev. A 100, 053615 (2019).

[54] J. Skulte, P. Kongkhambut, S. Rao, L. Mathey, H. Keßler, A. Hemmerich, and J. G. Cosme, "Condensate Formation in a Dark State of a Driven Atom-Cavity System," Phys. Rev. Lett. 130, 163603 (2023).

[55] D. N. Basov, A. Asenjo-Garcia, P. J. Schuck, X. Zhu,

and A. Rubio, "Polariton panorama," Nanophotonics **10**, 549 (2021).

[56] P. Kongkhambut, J. Skulte, L. Mathey, J. G. Cosme, A. Hemmerich, and H. Keßler, "Observation of a continuous time crystal," Science **377**, 670–673 (2022).

[57] M. Cardona and G.Güntherodt, "Light Scattering in Solids II," Springer-Verlag, Berlin (1982).

[58] P. Brüesch, "Phonons: Theory and Experiments II," Springer-Verlag, Berlin (1986).

[59] Our calculations correspond to the quantum noise limit at zero temperature where only Stokes peaks show up. In the presence of thermal fluctuations, at finite temperature, both Stokes and Anti-stokes peaks appear in the spectrum which we present in the SI for completeness.

[60] A. Frisk Kockum, A. Miranowicz, S. De Liberato, S. Savasta, and F. Nori, "Ultrastrong coupling between light and matter," Nature Reviews Physics **1**, 19 (2019).

[61] I. A. Verzhbitskiy, M. De Corato, A. Ruini, E. Molinari, A. Narita, Y. Hu, M. G. Schwab, M. Bruna, D. Yoon, S. Milana, X. Feng, K. Müllen, A. C. Ferrari, C. Casiraghi, and D. Prezzi, "Raman fingerprints of atomically precise graphene nanoribbons," Nano Lett. **16**, 3442 (2016).

[62] R. He, T.-F. Chung, C. Delaney, C. Keiser, L. A. Jauregui, P. M. Shand, C. C. Chancey, Y. Wang, J. Bao, and Y. P. Chen, "Observation of low energy Raman modes in twisted bilayer graphene," Nano Lett **13**, 3594 (2013).

[63] F. Valmorra, G. Scalari, C. Maissen, W. Fu, C. Schönenberger, J. W. Choi, H. G. Park, M. Beck, and J. Faist, "Low-Bias Active Control of Terahertz Waves by Coupling Large-Area CVD Graphene to a Terahertz metamaterial," Nano Letters **13**, 3193 (2013).

[64] C. Maissen, G. Scalari, F. Valmorra, M. Beck, J. Faist, S. Cibella, R. Leoni, C. Reichl, C. Charpentier, and W. Wegscheider, "Ultrastrong coupling in the near field of complementary split-ring resonators," Phys. Rev. B **90**, 205309 (2014).

[65] G. Scalari, C. Maissen, D. Turčinková, D. Hagenmüller, S. De Liberato, C. Ciuti, C. Reichl, D. Schuh, W. Wegscheider, M. Beck, and J. Faist, "Ultrastrong coupling of the cyclotron transition of a 2d electron gas to a THz metamaterial," Science **335**, 1323 (2012).

[66] K.-Q. Lin, J. Holler, J. M. Bauer, P. Parzefall, M. Scheuck, B. Peng, T. Korn, S. Bange, J. M. Lupton, and C. Schüller, "Large-Scale Mapping of Moiré Superlattices by Hyperspectral Raman Imaging," Advanced Materials **33**, 2008333 (2021).

[67] A. A. Puretzky, L. Liang, X. Li, K. Xiao, B. G. Sumpter, V. Meunier, and D. B. Geohegan, "Twisted MoSe2 Bilayers with Variable Local Stacking and Interlayer Coupling Revealed by Low-Frequency Raman Spectroscopy," ACS Nano **10**, 2736 (2016).

[68] O. Gunnarsson, "Superconductivity in fullerides," Rev. Mod. Phys. **69**, 575–606 (1997).

[69] J. B. Goodenough, "Jahn-Teller Phenomena In Solids," Annual Review of Materials Science **28**, 1 (1998).

[70] Y. Liu, Longxiang Zhang, M. K. Brinkley, G. Bian, T. Miller, and T.-C. Chiang, "Phonon-Induced Gaps in Graphene and Graphite Observed by Angle-Resolved Photoemission," Phys. Rev. Lett. **105**, 136804 (2010).

[71] E. V. Boström, A. Sriram, M. Claassen, and A. Rubio, "Controlling the magnetic state of the proximate quantum spin liquid α-RuCl$_3$ with an optical cavity," npj Computational Materials **9**, 202 (2023).

[72] C. W. Sandbo Chang, C. Sabín, P. Forn-Díaz, F. Quijandría, A. M. Vadiraj, I. Nsanzineza, G. Johansson, and C. M. Wilson, "Observation of Three-Photon Spontaneous Parametric Down-Conversion in a Superconducting Parametric Cavity," Phys. Rev. X **10**, 011011 (2020).

[73] F. Minganti, L. Garbe, A. Le Boité, and S. Felicetti, "Non-Gaussian superradiant transition via three-body ultrastrong coupling," Phys. Rev. A **107**, 013715 (2023).

[74] H. P. Breuer and F. Petruccione, "Open Quantum Systems," Cambridge University Press, Cambridge, U.K. (2002).

[75] L. D. Landau and E. M. Lifshitz, "Mechanics, Course of Theoretical Physics," Butterworth-Heinenann, Oxford, **1** (1976).

[76] L. Liang and V. Meunier, "First-principles Raman spectra of MoS$_2$, WS$_2$ and their heterostructures." Nanoscale **6**, 5394 (2014).

Supplementary Information to "Equilibrium parametric amplification in Raman-cavity hybrids"

Protocols and numerical implementation

We solve the stochastic Heisenberg-Langevin equations of motion introduced in the main text using the truncated Wigner approximation (TWA) method [52, 53]. The equations read

$$\partial_t a = -i\omega_c a - 2ig(a + a^*)(b + b^*) - ig_4(a + a^*)^3 - \kappa a + \xi_a, \tag{S1}$$

$$\partial_t b_r = \omega_R b_i, \tag{S2}$$

$$\partial_t b_i = -\omega_R b_r - g(a + a^*)^2 - 2g_s E_p(t)a_{s,r} - \gamma b_i + \xi_b, \tag{S3}$$

$$\partial_t a_{s,r} = \omega_s a_{s,i} - \kappa_s a_{s,r} + \xi_{s,r}, \tag{S4}$$

$$\partial_t a_{s,i} = -\omega_s a_{s,r} - 2g_s E_p(t)b_r - \kappa_s a_{s,i} + \xi_{s,i}. \tag{S5}$$

where the subscripts r, i denote the real and imaginary part of the field. To initialize the modes we sample from the corresponding Wigner distributions. We assume that all our modes have an expectation value of zero. Hence, the Wigner distribution from which we sample corresponds to a Gaussian distribution with mean zero and standard deviation of $1/2$. For each set of parameter we sample over 15000 trajectories. We further include stochastic delta-correlated noise ξ_a, ξ_b and ξ_s satisfying $\langle \xi_a^*(t_1)\xi_a(t_2)\rangle = \kappa\delta(t_1 - t_2)$, $\langle \xi_b(t_1)\xi_b(t_2)\rangle = \gamma\delta(t_1 - t_2)$ and $\langle \xi_s^*(t_1)\xi_s(t_2)\rangle = \kappa_s\delta(t_1 - t_2)$. Initially we ramp up the Raman-cavity coupling g from zero to its final value at time t_0 as:

$$g(t) = g(\tanh((t - t_0)/\tau) + 1)/2. \tag{S6}$$

We hold this coupling for the rest of the dynamics until the steady state is reached and turn on the probing field at time t_p afterwards. We consider a probing field with an associated electric field $E_p(t) = E_p^0(t)\sin(\omega_p t)$ with

$$E_p^0(t) = E_p^0(\tanh((t - t_p)/\tau) + 1)/2. \tag{S7}$$

Finally, to obtain the Raman spectra, we compute the number of scattered photons $n_s = a_s^* a_s = a_{s,r}^2 + a_{s,i}^2$ at a fixed time $t^* \gg t_p$ by averaging over all the realizations. We take $\omega_R t_0 = 10$ and for the decay rates that we use in the main text $\omega_R t_p \approx 100$ is enough to be in the steady state. We use $\tau = 1/\omega_R$ and checked that same results can be obtained for very different values $\tau = 10/\omega_R$. We choose $\omega_R t^* = 250$ which means the system is under the probing field during a time window $t^* - t_p = 150/\omega_R$. With these parameters we obtain clear Raman spectra.

To compute the modification of cavity and Raman fluctuations; δx^2 and δQ^2, as well as Raman shift Q shown in Fig. 3 of the main text, we drop the probe field ($E_p(t) = 0$) in the equation of motion and solve the dynamics to compute such observables at the steady state $\omega_R t_p \approx 100$.

Raman spectra in the presence of thermal noise

Here we present the Raman spectra for the combined system in the presence of thermal noise associated to both the cavity and Raman mode. In this case we solve the dynamics Eq. (S1)-(S5) but now considering white noises satisfying

$$\langle \xi_a^*(t_1)\xi_a(t_2)\rangle = \kappa \coth(\omega_c/k_B T)\delta(t_1 - t_2), \tag{S8}$$

$$\langle \xi_b(t_1)\xi_b(t_2)\rangle = \gamma \coth(\omega_R/k_B T)\delta(t_1 - t_2) \tag{S9}$$

where k_B is the Boltzmann constant. These autocorrelation relations guarantee the fluctuation-dissipation theorem hold for both subsystem (in the uncoupled case) assuming they are connected to a reservoir at temperature T and considering a Markovian approximation [74].

In Fig. S1(a) we plot the same Raman spectra shown in the main text (in the quantum noise limit) to be contrasted with the Raman spectra in the presence of thermal noise shown in Fig. S1(b). In both cases we show the raw data $n_s(\omega_s)$ instead of $n_s(\omega)$ with $\omega = \omega_p - \omega_s$ being the Raman shift. It allows us to see Stoke and anti-Stoke contributions separately. As discussed in the main text, in the quantum noise limit (Fig. S1(a)), only a Stoke peak appears in the spectra around $\omega_s = \omega_p - \omega_R = 4\omega_R$. In contrast, if thermal noise is added anti-Stoke processes also occur and we find additional peaks around $\omega_s = \omega_p + \omega_R = 6\omega_R$ (see Fig. S1(b)).
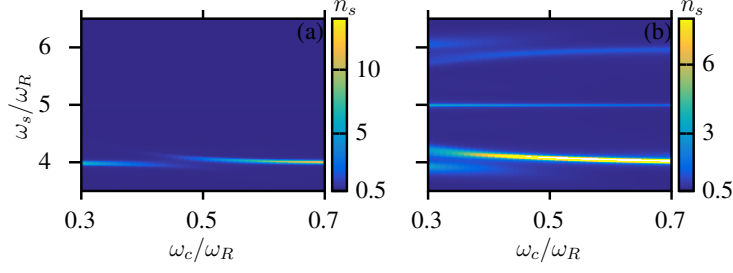
Figure S1. (a) Raman spectra $n_s(\omega_s)$ for different cavity frequencies ω_c in the quantum noise limit. (b) Raman spectra including thermal noise with $k_B T = 2.5\hbar\omega_R$. In both cases we consider a probe laser of strength $g_s E_p^0 = 0.04\omega_R$ and frequency $\omega_p = 5\omega_R$ with $g = 0.04\omega_R$, $g_4 = \kappa = \gamma = \kappa_s = 0.01\omega_R$.

Gaussian theory for cavity fluctuations

The semi-classical Langevin equations of motion, able to capture vacuum fluctuations for bosonic modes are given by the equations (S1)-(S3) where the noise terms, ξ_a and ξ_b are delta-correlated noise, $\langle \xi_a^*(t_1)\xi_a(t_2)\rangle = \kappa\delta(t_1 - t_2)$, $\langle \xi_b(t_1)\xi_b(t_2)\rangle = \gamma\delta(t_1 - t_2)$ and $\langle \xi_a(t_1)\xi_b(t_2)\rangle = 0$. The equations of motion in terms of the frequency Fourier components defined as: $a(\omega) = \int dt e^{i\omega t} a(t)$ and $a(t) = \int \frac{d\omega}{2\pi} e^{-i\omega t} a(\omega)$, are given for the Raman mode by combining equations (S2)-(S3) as:

$$\left(-\omega^2 - i\gamma\omega + \omega_R^2\right) b_r = -g\omega_R \int \frac{d\omega'}{2\pi}(a + a^*)(\omega - \omega')(a + a^*)(\omega') + \omega_R \xi_b(\omega). \tag{S10}$$

Replacing this expression into equation (S1) for the cavity we find:

$$
\begin{aligned}
-i\omega a(\omega) = &-i\omega_c a(\omega) - k a(\omega) + \xi_a(\omega) \\
&- 2ig \int \frac{d\omega'}{2\pi}(a(\omega - \omega') + a^*(\omega' - \omega))\left(\frac{2\omega_R}{-(\omega')^2 - i\gamma\omega' + \omega_R^2} \xi_b(\omega') \right.\\
&\left. - \frac{2g\omega_R}{-(\omega')^2 - i\gamma\omega' + \omega_R^2} \int \frac{d\omega''}{2\pi}(a(\omega' - \omega'') + a^*(\omega'' - \omega'))(a(\omega'') + a^*(-\omega'')) \right) \\
&- ig_4 \int \frac{d\omega' d\omega''}{(2\pi)^2}(a(\omega - \omega') + a^*(\omega' - \omega))(a(\omega' - \omega'') + a^*(\omega'' - \omega')(a(\omega'') + a^*(-\omega'')).
\end{aligned}
\tag{S11}
$$

In the absence of any interactions, $g = g_4 = 0$, the first line recovers the expectation value of the vacuum fluctuations: $\langle \frac{a^*(t)a(t) + a(t)a^*(t)}{2}\rangle = \int \frac{d\omega d\omega'}{(2\pi)^2} e^{it(\omega - \omega')} a^*(\omega)a(\omega') = \int \frac{d\omega}{2\pi} \frac{\kappa}{\kappa^2 + (\omega - \omega_c)^2} = \frac{1}{2}$. To include fluctuations analytically, we use a Gaussian ansatz for the equilibrium fluctuations: $\langle a(t)\rangle = 0$ in equilibrium and $\langle a^*(\omega)a(\omega')\rangle = 2\pi\delta(\omega - \omega')n(\omega)$, $\langle a(\omega)a(\omega')\rangle = 2\pi\delta(\omega + \omega)f(\omega)$ and $\langle b(t)\rangle = b_0$. This form is fixed by symmetry and time-translation invariance in the equilibrium state. The Gaussian approximation ignores higher order non-linear correlations and uses Wick's theorem to derive a self-consistent equations for $n(\omega)$, $f(\omega)$ and b_0. Furthermore, on symmetry grounds the quantities $a(\omega)$ and ξ_b are assumed to be statistically independent to gaussian order. This gives rise to the result:

$$
\begin{aligned}
-i\omega a(\omega) = &-i\omega_c a(\omega) - k a(\omega) + \xi_a(\omega) \\
&i\frac{4g^2}{\omega_R}\left(a(\omega) + a^*(-\omega)\right)\left(\int \frac{d\omega'}{2\pi}\left(2n(\omega') + f(\omega') + f^*(\omega')\right)\right) \\
&i8g^2\left(a(\omega) + a^*(-\omega)\right) \int \frac{d\omega'}{2\pi} \frac{\omega_R}{-(\omega')^2 - i\gamma\omega + \omega_R^2}\left(2n(\omega - \omega') + f(\omega - \omega') + f^*(\omega - \omega')\right) \\
&- i3g_4\left(a(\omega) + a^*(-\omega)\right)\left(\int \frac{d\omega''}{2\pi}\left(2n(\omega') + f(\omega') + f^*(\omega')\right)\right).
\end{aligned}
\tag{S12}
$$

the above result can be compactly re-written in terms of an effective cavity frequency, $\bar{\omega}_c(\omega)$ and a squeezing parameter $\Delta(\omega)$:

$$(-i\omega + \kappa)a(\omega) = -i\bar{\omega}_c(\omega)a(\omega) - i\Delta(\omega)a^*(-\omega) + \xi_a(\omega), \tag{S13}$$

where the effective parameters are given by:

$$
\begin{aligned}
\bar{\omega}_c(\omega) =&\, \omega_c + \left(-\frac{4g^2}{\omega_R} + 3g_4\right)\left(\int \frac{d\omega'}{2\pi}\left(2n(\omega') + f(\omega') + f^*(\omega')\right)\right) \\
&- 8g^2\left(\int \frac{d\omega'}{2\pi}\frac{\omega_R}{-(\omega')^2 - i\gamma\omega' + \omega_R^2}\left(2n(\omega - \omega') + f(\omega - \omega') + f^*(\omega - \omega')\right)\right),
\end{aligned}
\tag{S14}
$$

$$
\begin{aligned}
\Delta(\omega) =&\, \left(-\frac{4g^2}{\omega_R} + 3g_4\right)\left(\int \frac{d\omega'}{2\pi}\left(2n(\omega') + f(\omega') + f^*(\omega')\right)\right) \\
&- 8g^2\left(\int \frac{d\omega'}{2\pi}\frac{\omega_R}{-(\omega')^2 - i\gamma\omega' + \omega_R^2}\left(2n(\omega - \omega') + f(\omega - \omega') + f^*(\omega - \omega')\right)\right).
\end{aligned}
\tag{S15}
$$

The fluctuations are determined through the dependence of $a(\omega)$, $a^*(-\omega)$ to the noise terms $\xi(\omega)$ and $\xi^*(-\omega)$:

$$
\begin{pmatrix} -i\omega + \kappa + i\bar{\omega}_c(\omega) & i\Delta(\omega) \\ -i\Delta(-\omega) & -i\omega + \kappa - i\bar{\omega}_c(-\omega) \end{pmatrix} \cdot \begin{pmatrix} a(\omega) \\ a^*(-\omega) \end{pmatrix} = \begin{pmatrix} \xi_a(\omega) \\ \xi_a^*(-\omega) \end{pmatrix},
\tag{S16}
$$

which leads to:

$$
a(\omega) = \frac{(-i\omega + \kappa - i\bar{\omega}_c(-\omega)\xi_a(\omega) + i\Delta(\omega)\xi_a^*(-\omega)}{\Delta(-\omega)\Delta(\omega) + (-i\omega + \kappa - i\bar{\omega}_c(-\omega)(-i\omega + \kappa + i\bar{\omega}_c(\omega))}.
\tag{S17}
$$

Finally, the ground state fluctuations are found by solving the self consistent equations: $\langle a^*(\omega)a(\omega')\rangle = 2\pi\delta(\omega - \omega')n(\omega)$, $\langle a(\omega)a(\omega')\rangle = 2\pi\delta(\omega + \omega')f(\omega)$.

Renormalized cavity frequency

We explore the normalized cavity frequency quoted in the main text analytically by using perturbation theory in g^2 and g_4. We express the fluctuations as a series expansion, $n(\omega) \approx n_0(\omega) + n_1(\omega)$ and $f(\omega) = f_0(\omega) + f_1(\omega)$, where in the absence of any coupling to the Raman mode, the fluctuations take the form:

$$
n_0(\omega) = \frac{\kappa}{\kappa^2 + (\omega - \omega_c)^2},
\tag{S18}
$$

$$
f_0(\omega) = 0,
\tag{S19}
$$

To leading order in the couplings, the renormalized frequency, $\bar{\omega}_c(\omega)$, and squeezing parameter, $\Delta(\omega)$ are given by:

$$
\bar{\omega}_c(\omega) = \omega_c - \frac{4g^2}{\omega_R} + 3g_4 - 8g^2\frac{\omega_R}{\omega_R^2 - (\omega - \omega_c)^2 - (i\gamma + 2i\kappa)(\omega - \omega_c) + \gamma\kappa + \kappa^2},
\tag{S20}
$$

$$
\Delta(\omega) = -\frac{4g^2}{\omega_R} + 3g_4 - 8g^2\frac{\omega_R}{\omega_R^2 - (\omega - \omega_c)^2 - (i\gamma + 2i\kappa)(\omega - \omega_c) + \gamma\kappa + \kappa^2}
\tag{S21}
$$

for small κ and γ. Similarly, to leading order, the squeezing parameter is given by $\Delta = \Delta(\omega_c) = -\frac{12g^2}{\omega_R} + 3g_4$. Corrections in the frequency of the cavity mode due to the squeezing go as $|\Delta(\omega)|^2 \sim \mathcal{O}(g^4, g_4g^2, g_4^2)$, and corresponds to a higher order contribution. As a result, to leading order in the couplings the cavity response frequency is given by:

$$
\bar{\omega}_c(\omega) = \bar{\omega}_c(\omega = \omega_c) = \omega_c - \frac{12g^2}{\omega_R} + 3g_4.
\tag{S22}
$$

Parametric enhancement of cavity fluctuations

To linear order in g^2 and g_4, the fluctuation functions take the form:

$$
n(\omega) = \frac{\kappa}{\kappa^2 + (\omega - \bar{\omega}_c)^2},
\tag{S23}
$$

$$
f(\omega) = \frac{i\Delta(\omega)}{(i\omega + \kappa - i\omega_c)(-i\omega + \kappa - i\omega_c)(-i\omega + \kappa + i\omega_c)} + \frac{i\Delta(-\omega)}{(-i\omega + \kappa - i\omega_c)(i\omega + \kappa - i\omega_c)(i\omega + \kappa + i\omega_c)}
\tag{S24}
$$

The squeezing term, $f(\omega)$, is resonantly amplified when $\omega_c \approx \omega_R/2$, showing that Gaussian theory can indeed capture the non-trivial equilibrium amplification process. On resonance, perturbation theory breaks down and one should self-consistently solve for $f(\omega)$ and $n(\omega)$. In this Letter, we instead rely on the numerically evaluated solution.

<div align="center">Raman-cavity polariton frequency</div>

As mentioned in the main text, the Raman coherent oscillations linearly hybridized with squeezing fluctuations of the cavity mode. Here for convenience we write the Hamiltonian in the alternative but equivalent form

$$H = \frac{\omega_R^2}{2}\hat{Q}^2 + \frac{\hat{P}^2}{2} + g \times 2\omega_c\sqrt{2\omega_R}\hat{Q}\hat{X}_c^2 + \omega_c^2\frac{\hat{X}_c^2}{2} + \frac{\hat{P}_c^2}{2} + g_4\omega_c^2\hat{X}_c^4 \tag{S25}$$

where the Raman coordinate is defined as $\hat{Q} = \frac{\hat{b}+\hat{b}^\dagger}{\sqrt{2\omega_R}}$, the Raman conjugate momentum as $\hat{P} = \frac{i\sqrt{\omega_R}(\hat{b}^\dagger-\hat{b})}{\sqrt{2}}$, the cavity coordinate as $\hat{X}_c = \frac{\hat{a}+\hat{a}^\dagger}{\sqrt{2\omega_c}}$ and the cavity conjugate momentum as $\hat{P}_c = \frac{i\sqrt{\omega_c}(\hat{a}^\dagger-\hat{a})}{\sqrt{2}}$. In this basis, completing the square in Eq. (S25) the Hamiltonian reads:

$$H = \frac{\omega_R^2}{2}\left(\hat{Q} + g\frac{2\sqrt{2\omega_R}\omega_c}{\omega_R^2}\hat{X}_c^2\right)^2 + \left(g_4\omega_c^2 - \frac{4g^2\omega_c^2}{\omega_R}\right)\hat{X}_c^4 + \frac{\hat{P}^2}{2} + \omega_c^2\frac{\hat{X}_c^2}{2} + \frac{\hat{P}_c^2}{2}, \tag{S26}$$

which leads to the condition for stability quoted in the main text, $g_4 > \frac{4g^2}{\omega_R}$.

The equations of motion for the Raman mode, $\hat{Q}$, and the fluctuations of the cavity mode, $\left(\hat{X}_c^2, \{\hat{X}_c, \hat{P}_c\}, \hat{P}_c^2\right)$ are given by:

$$\frac{d\hat{Q}}{dt} = \hat{P}, \tag{S27}$$

$$\frac{d\hat{P}}{dt} = -\omega_R^2\hat{Q} - g \times 2\omega_c\sqrt{2\omega_R}\hat{X}_c^2, \tag{S28}$$

$$\frac{d\hat{X}_c^2}{dt} = \{\hat{X}_c, \hat{P}_c\}, \tag{S29}$$

$$\frac{d\{\hat{X}_c, \hat{P}_c\}}{dt} = 2\hat{P}_c^2 - 2\omega_c^2\hat{X}_c^2 - 4g \times 2\omega_c\sqrt{2\omega_R}\hat{X}_c^2\hat{Q} - 2g_4 \times 4\omega_c^2\hat{X}_c^4, \tag{S30}$$

$$\frac{d\hat{P}_c^2}{dt} = -\omega_c^2\{\hat{X}_c, \hat{P}_c\} - 2g \times 2\omega_c\sqrt{2\omega_R}\hat{Q}\{\hat{X}_c, \hat{P}_c\} - g_4 \times 4\omega_c^2\{\hat{X}_c^3, \hat{P}_c\} \tag{S31}$$

where $\{\hat{A}, \hat{B}\} = \hat{A}\hat{B} + \hat{B}\hat{A}$ is the anti-commutator. Within a Gaussian approximation theory, the Raman coordinate and cavity fluctuations form a complete system of equations in terms of the variables, $\left\{\langle\hat{Q}\rangle, \langle\hat{P}\rangle, \langle\hat{X}_c^2\rangle, \langle\{\hat{X}_c, \hat{P}_c\}\rangle, \langle\hat{P}_c^2\rangle\right\}$:

$$\frac{d\langle\hat{Q}\rangle}{dt} = \langle\hat{P}\rangle, \tag{S32}$$

$$\frac{d\langle\hat{P}\rangle}{dt} = -\langle\hat{Q}\rangle\omega_R^2 - g \times 2\omega_c\sqrt{2\omega_R}\langle\hat{X}_c^2\rangle, \tag{S33}$$

$$\frac{d\langle\hat{X}_c^2\rangle}{dt} = \langle\{\hat{X}_c, \hat{P}_c\}\rangle, \tag{S34}$$

$$\frac{d\langle\{\hat{X}_c, \hat{P}_c\}\rangle}{dt} = 2\langle\hat{P}_c^2\rangle - 2\omega_c^2\langle\hat{X}_c^2\rangle - 4g \times 2\omega_c\sqrt{2\omega_R}\langle\hat{X}_c^2\rangle\langle\hat{Q}\rangle - 6g_4 \times 4\omega_c^2\langle\hat{X}_c^2\rangle^2, \tag{S35}$$

$$\frac{d\langle\hat{P}_c^2\rangle}{dt} = -\omega_c^2\langle\{\hat{X}_c, \hat{P}_c\}\rangle - 2g \times 2\omega_c\sqrt{2\omega_R}\langle\hat{Q}\rangle\langle\{\hat{X}_c, \hat{P}_c\}\rangle - 3g_4 \times 4\omega_c^2\langle\hat{X}_c^2\rangle\langle\{\hat{X}_c, \hat{P}_c\}\rangle. \tag{S36}$$

To make progress we first compute the equilibrium correlations, $\langle\hat{Q}\rangle = Q_0$, $\langle\hat{X}_c^2\rangle = X_0^2$ and $\langle\hat{P}_c^2\rangle = P_0^2$ within the Gaussian self-consistent approximation theory by taking the derivative of all quantities equal to zero in the above expressions which

produces:

$$Q_0 = -\frac{g \times 2\omega_c\sqrt{2\omega_R}}{\omega_R^2} X_0^2, \tag{S37}$$

$$P_0^2 = \omega_c^2 X_0^2 - 2\frac{(g \times 2\omega_c\sqrt{2\omega_R})^2}{\omega_R^2} X_0^2 + 3g_4 \times 4\omega_c^2 X_0^2, \tag{S38}$$

$$\langle\{X_c, P_c\}\rangle_0 = 0. \tag{S39}$$

Finally, we linearize around the equilibrium, to find the collective modes:

$$\partial_t \delta Q = \delta P, \tag{S40}$$

$$\partial_t \delta P = -\omega_R^2 \delta Q - \left(2g\omega_c\sqrt{2\omega_R}\right)\delta X_c^2, \tag{S41}$$

$$\partial_t \delta X_c^2 = \delta\{X_c, P_c\}, \tag{S42}$$

$$\partial_t \delta\{X_c, P_c\} = -8g\omega_c\sqrt{2\omega_R}X_0^2\delta Q - 2\omega_c^2\left(1 + \left(-16\frac{g^2}{\omega_R} + 24g_4\right)X_0^2\right)\delta X_c^2 + 2\delta P_c^2, \tag{S43}$$

$$\partial_t \delta P_c^2 = \left(-\omega_c^2 - 4g\omega_c\sqrt{2\omega_R}Q_0 - 12g_4\omega_c^2 X_0^2\right)\delta\{X_c, P_c\}. \tag{S44}$$

Considering an oscillating ansatz of the type $X \sim e^{i\omega t}$, we find two distinct solutions corresponding to the hybridized Raman mode with photon fluctuations (Raman polariton branches):

$$\omega_\pm^2 = \frac{1}{2\omega_R}\left(4\omega_c^2\omega_R + \omega_R^3 + 72g_4\omega_c^2\omega_R X_0^2 - 64g^2\omega_c^2 X_0^2\right.$$
$$\left. \pm\sqrt{-16\omega_c^2\omega_R^3\left(-24g^2X_0^2 + 18g_4X_0^2\omega_R + \omega_R\right) + \left(-64g^2X_0^2\omega_c^2 + \left(4 + 72g_4X_0^2\right)\omega_c^2\omega_R + \omega_R^3\right)^2}\right) \tag{S45}$$

Nonlinearities and dissipation effects on the parametric resonances

For the sake of completeness here we show the effects of increasing the nonlinear interaction and decay rates on the parametric resonance discussed in the main text.

Fig. S2 (a-c) shows δQ^2, δx^2 and Q for a larger value of g_4. The main effect is a shift on the parametric resonance to the left while how much localize the Raman mode is, how much it is shifted and how much the cavity field is amplified remain practically the same. This shift to the left results from the analytical resonant condition $\omega_R/2 = \bar{\omega}_c = \omega_c - 12g^2/\omega_R + 3g_4$ which is the dashed line that matches nicely with the numerical TWA simulations (in color). For larger values of couplings g and g_4, not only the linear dependence of the parametric resonance on g_4 is well described by this analytical expression, but also the slow quadratic dependence on g.

In Fig. S2(d-f) we show how by increasing κ and γ four times while keeping g_4 constant, the resonance weakens with the Raman mode being less localized and cavity field less amplified in the steady state. Here the Raman and cavity fluctuations are modified by $\sim 10\%$ in resonance. Also the onset of the resonance is pushed to higher coupling strengths g which is reminiscent of the physics of a periodically driven parametric oscillator in the presence of damping, where a critical amplitude of the external drive is needed to overcome dissipation and get into the zone of amplification [75]. For these larger decay rates the Raman shift decreases and becomes more independent on the cavity frequency (see Fig. S2 (f)).

We have checked that even for stronger nonlinearities (higher value of g_4) and/or strong dissipation the parametric resonance can still be seen so there is a resonant regime in which Raman mode fluctuations decrease in favor of cavity field amplification.

Raman phonon-cavity coupling strength

Following the references [67, 76], Raman phonons are coupled the electric field of light $\vec{E}(x)$ through the Raman tensor $\underline{\underline{R}}$. The Hamiltonian reads

$$H = \int d^3x \frac{\epsilon_0 \vec{E}(x)\cdot\underline{\underline{\epsilon}}(Q)\cdot\vec{E}(x)}{2} \approx H_0 + \epsilon_0\sum_i\frac{\vec{E}_i\cdot\underline{\underline{R}}\cdot\vec{E}_i}{2}Q_i, \tag{S46}$$
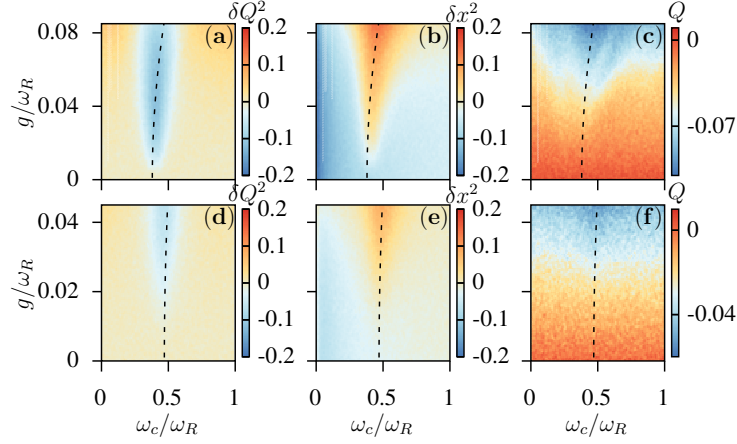
Figure S2. Nonlinearities and dissipation effects on the parametric resonances. (a), (b), (c) The same as Fig. 3 of the main text but increasing the quartic nonlinearity to $g_4 = 0.04\omega_R$ keeping the same decay rates. (d), (e), (f) The same as Fig. 3 but in this case the decay rates have been increased to $\kappa = \gamma = 0.06\omega_R$ keeping the same g_4. Dashed lines are $\omega_R = 2\bar{\omega}_c$.

where ϵ_0 is the vacuum permittivity and $\underline{\epsilon}(Q)$ is the phonon-coordinate dependent polarizability tensor (dielectric tensor). Expanding linearly in the phonon coordinate Q one obtains a first term $H_0 = \int d^3x \frac{\epsilon_0 \vec{E}(x)\cdot\underline{\epsilon}(Q=0)\cdot\vec{E}(x)}{2}$ and the Raman-light coupling which is given by the second term in the right hand side of Eq. (S46). We employ the dipole approximation for the cavity mode where we assume that the electric field is constant over one unit cell and given by $\vec{E}_i = \frac{1}{V_{cell}} \int_{V^i} d^3x \vec{E}(x)$ where V_{cell} is the volume of the unit cell and V^i the volume of the i-th unit cell. The Raman tensor is defined as

$$R_{\alpha\beta} = V_{cell} \sum_{\mu=1}^{N} \sum_{l=1}^{3} \frac{\partial \epsilon_{\alpha\beta}}{\partial r_l(\mu)} \frac{e_l^j(\mu)}{\sqrt{M_\mu}} \tag{S47}$$

where $r_l(\mu)$ is the position of the μth atom along the direction l, $\frac{\partial \epsilon_{\alpha\beta}}{\partial r_l(\mu)}$ is the first derivative of the dielectric tensor over the atomic displacement, $e_l(\mu)$ is the displacement of the μth atom along the direction l of the Raman phonon and M_μ is the mass of the μth atom. Considering that the cavity mode has a constant electric field over the entire sample, $\hat{E}_{cav,i} = E_0 \vec{e}_c (\hat{a} + \hat{a}^\dagger)$, the Raman-light coupling only involves the $q = 0$ phonon. Thus $\sum_i \hat{Q}_i = \sqrt{N}\hat{Q}_{q=0} = \sqrt{N}\frac{\hat{b}+\hat{b}^\dagger}{\sqrt{2\omega_R}}$, where $N = \frac{V_{samp}}{V_{cell}}$ is the total number of unit cells (V_{samp} is the volume of the sample), giving rise to the coupling:

$$\frac{g}{\omega_R} = \frac{\epsilon_0 E_0^2 \sqrt{V_{samp}V_{cell}}}{2\omega_R} \tilde{R}, \tag{S48}$$

$$\tilde{R} = \vec{e}_c \cdot \sum_{\mu=1}^{N} \sum_{l=1}^{3} \frac{\partial \underline{\epsilon}}{\partial r_l(\mu)} \frac{e_l^j(\mu)}{\sqrt{M_\mu}\sqrt{2\omega_R}} \cdot \vec{e}_c, \tag{S49}$$

where $\tilde{R}$ is the dimensionless Raman coupling and $\vec{e}_c$ is the polarization vector of the cavity field. Following references [67, 76] $\tilde{R} \sim 1 - 10$ for TMDs. The electric field of cavities is given by the relationship:

$$E_0^2 = \frac{\omega_c}{\epsilon_0 V_{eff}}, \tag{S50}$$

where on parametric resonance $\omega_c = \omega_R/2$, leading to the final result:

$$\frac{g}{\omega_R} = \frac{1}{4}\tilde{R}\frac{\sqrt{V_{samp}V_{cell}}}{V_{eff}}. \tag{S51}$$

These arguments are rather crude and detailed research needs to be carried out for different cavity designs and Raman-active materials on a case by case basis.

3 Non-equilibrium dynamics in particle-hole symmetric superfluids

Superfluidity can be found in Bose-Einstein condensates (BEC) and in the theory of weakly interaction fermions, called Bardeen-Cooper-Schrieffer (BCS) theory. It describes the property of frictionless flow [221, 222]. To describe such systems, an effective field theory of the form of the Ginzburg-Landau theory of phase transitions can be used [221, 223, 224]. The idea is to use a complex valued scalar field that can vary in space and time to effectively describe the order parameter of the system at sufficiently low temperatures. The equilibrium, as well as the dynamical, properties of the complex scalar field are defined in the effective field theory via a Lagrangian and the overall structure of the effective field theory is determined by the underlying symmetry. The first order contribution for the time dependence in the Lagrangian of the Ginzburg-Landau theory is $i\Psi\partial_t\Psi^*$. This is the dominating term to describe the dynamics of BECs and leads to the well known GP equation. However, some systems obey an approximate particle-hole symmetry, such as BCS systems [170, 225–228] and certain types of neutral atom systems [229–231]. In this case, the leading term for the time dependence is incompatible with the symmetry, as this term is not particle-hole symmetric. As such, the next order term dominates the dynamics. The next order term, $\partial_t\Psi\partial_t\Psi^*$, is indeed particle-hole symmetric and leads to the well-known NLKG equation. This means that this term is unchanged under the transformation of $\Psi \to \Psi^*$.

In this chapter, we will first discuss the NLKG model to describe particle-hole symmetric superfluids, before we start to discuss the low energy modes of the system and finally map our effective field theory including both dynamical terms across the BEC-BCS crossover and while doing that smoothly connect the spectra across the crossover. This is a brief introduction to the effective field theory, that we numerically study in the publication [11]. In publication [11] we discuss the dynamics of vortices for the different dynamical terms. In a manuscript that will be published soon, we use our effective model to describe the spectral results found in the BEC-BCS crossover experiment in the group of Henning Moritz.

For reviews on the BEC-BCS crossover we refer to [221, 222]. For a review and further readings with more examples on the effective field theory we refer to [224, 232]. The discussion in this chapter follows the discussion in the Pekker and Varma review [224] up to the derivation of the low energy modes. Further derivations concerning the parameter fixing of the effective field theory within this section were a collaborative effort with my colleague Lukas Broers. A further discussion about the spectra in confining potentials across the crossover can be found in his PhD thesis.

3.1 Generalised effective superfluid Lagrangian

The effective Lagrangian can be split into a dynamical $\mathcal{L}_{\mathrm{dyn}}$ and a static part $\mathcal{L}_{\mathrm{stat}}$ [11, 224, 226], such that

$$\mathcal{L} = \mathcal{L}_{\mathrm{dyn}} + \mathcal{L}_{\mathrm{stat}}. \tag{3.1}$$

The static part can be written as

$$\mathcal{L}_{\mathrm{stat}} = \frac{\hbar^2}{2m}\partial_{\mathbf{x}}\Psi(\mathbf{x},t)\partial_{\mathbf{x}}\Psi^*(\mathbf{x},t) - r\Psi(\mathbf{x},t)\Psi^*(\mathbf{x},t) + \frac{U}{2}\left(\Psi(\mathbf{x},t)\Psi^*(\mathbf{x},t)\right)^2 \tag{3.2}$$

with m the mass, r a chemical potential like term and U being the contact interaction strength via a density-density coupling. We note that all terms are particle-hole symmetric under the exchange of Ψ and Ψ^* and all terms are standard in the Ginzburg-Landau theory of phase transitions [221, 223, 233]. The dynamical part can be written as

$$\mathcal{L}_{\mathrm{dyn}} = -iK_1\left[\Psi(\mathbf{x},t)^*\partial_t\Psi(\mathbf{x},t) - \Psi(\mathbf{x},t)\partial_t\Psi(\mathbf{x},t)^*\right] - K_2\partial_t\Psi(\mathbf{x},t)\partial_t\Psi(\mathbf{x},t)^* \tag{3.3}$$

with K_1 and K_2 being constants that control the characteristics of the dynamics and will be determined later. We note that K_1 is in the units of $\hbar$ and corresponds to standard, non particle-hole symmetric dynamics as can be found in the GP equation. On the contrary, K_2 leads to particle-hole symmetric dynamics and has the units of $\hbar$ divided by some characteristic frequency ω and leads to the NLKG equation. As mentioned before, effective field theories used to study particle-hole symmetric dynamics need to be symmetric under the exchange of Ψ and Ψ^*. Therefore, $K_1 = 0$ and $K_2 \neq 0$ leads to particle-hole symmetric dynamics.

By use of the Euler-Lagrange equation or by minimizing the action $\mathcal{S} = \int dt \int d\mathbf{x}\mathcal{L}$ one derives the equations of motion as

$$\partial_t\left(-K_2\partial_t + iK_1\right)\Psi(\mathbf{x},t) = \left(-\frac{\hbar^2}{2m}\partial_{\mathbf{x}}^2 - r + U|\Psi(\mathbf{x},t)|^2\right)\Psi(\mathbf{x},t). \tag{3.4}$$

It can be immediately seen that by setting $K_2 = 0$ we recover the GP equation or nonlinear Schrödinger equation, and by setting $K_1 = 0$ we recover the NLKG equation. To gain further insight on the interpretation of the effective field Ψ that is studied and the role of K_1 and K_2 on the dynamics, we can compute the canonical momenta as

$$\Pi(\mathbf{x},t) \equiv \frac{\partial\mathcal{L}}{\partial(\partial_t\Psi)} = -i\frac{K_1}{2}\Psi^*(\mathbf{x},t) - K_2\partial_t\Psi^*(\mathbf{x},t). \tag{3.5}$$

Hence, for the non particle-hole symmetric case the canonical momentum reduces to $\Pi \propto i\Psi^*$ as is known for the GP equation and only for this case the system is fully determined by specifying the field Ψ. For $K_1 = 0$, the canonical momentum becomes $\Pi \propto \partial_t\Psi^*$, which is an independent degree of freedom. In order to specify the system in this case, we do not only need to fix Ψ, but also the canonical momenta Π, as expected for partial differential equations of second order. In the following, we will use

178

Noether's theorem to determine the Noether charge. The theorem can be applied, as the Lagrangian obeys a $U(1)$ symmetry under the exchange of the phase of Ψ. The Noether charge is given by

$$Q = i \int d\mathbf{x} \left(\Pi(\mathbf{x}, t)\Psi(\mathbf{x}, t) - \Pi^*(\mathbf{x}, t)\Psi^*(\mathbf{x}, t) \right)$$
$$= \int d\mathbf{x} \left(K_1 \left| \Psi(\mathbf{x}, t) \right|^2 + i K_2 \left[\Psi^*(\mathbf{x}, t)\partial_t \Psi(\mathbf{x}, t) - \Psi(\mathbf{x}, t)\partial_t \Psi^*(\mathbf{x}, t) \right] \right). \qquad (3.6)$$

The first term of the Noether charge, which is proportional to K_1 conserves the integrated density of the effective field Ψ. In the limit of $K_2 = 0$ this term corresponds to the usual particle number conservation. In this case the effective field can be interpreted as the usual particle probability wave function as is known for Schrödinger physics. For the opposite case, $K_2 = 0$, the density of the field Ψ is not conserved. This signals that in this limit, the field Ψ cannot be interpreted as the particle probability wave function. Rather, the ratio between particles and holes is conserved. However, a particle and a hole can be created as a pair. This can be seen in the bases of the Feshbach-Villars formalism [234] as is shown in the appendix of publication [11]. This can play a crucial difference for the dynamics in these systems. For systems with approximate particle-hole symmetry, both terms K_1 and K_2 can be finite. Here, the interpretation of the field becomes less transparent. It can be understood that some number of the density is conserved, while it is still possible to create pairs of particles and holes. Though, as K_1 becomes the dominant parameter, it costs more and more energy to create a pair. This energy diverges as we approach the GP equation limit and the total particle number is conserved. Fig. 3.1(a) shows the response of the field Ψ at $t = t_0$ as the solid line and the response against a force pushing onto the center as the dashed line. Fig. 3.1(b) sketches the following response of the particle number after this perturbation. We associate non particle-hole dynamics with BEC, the mixed partially particle-hole symmetric case with unitary and the particle-hole symmetric case with BCS like dynamics, in analogy to the BEC-BCS crossover. We see that for the BEC case the fluid is pushed away, while conserving the particle number. This can be interpreted as having an infinitely large compressibility. As we go further along the crossover to particle-hole symmetry the compressibility is lowered, and we cannot only push the fluid away, but can also compress it, hence reduce the particle number. On the BCS side, the compressibility is very low, and we can easily compress the fluid and reduce the particle number. Here, the field rather has the analogy of a gas then a fluid. While this is not quantitative, this already can be interpreted as a new mode that can only appear in particle-hole symmetric models and not in GP equation models, namely the amplitude/Higgs mode. In the following we will always refer to this mode as the amplitude mode. However, we denote that in certain cases, if a gauge field is included, this mode corresponds to the Higgs mode [224].
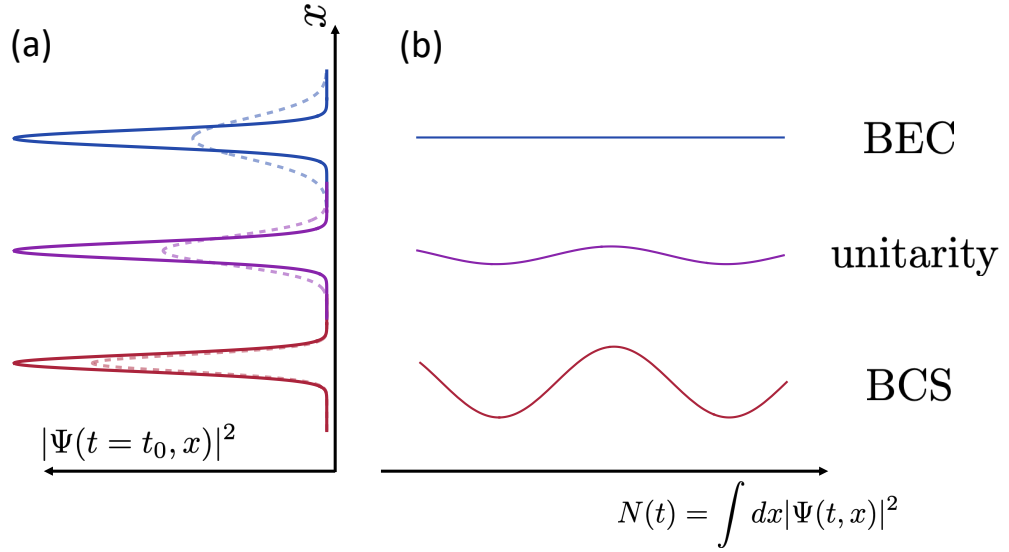
Figure 3.1: Sketch of the response of the order parameter if the density is locally reduced in the center across the crossover. (a) depicts the density profile before (solid line) and after the perturbation (dashed line). For the BEC regime in blue, the unitary regime in purple and the BCS regime in red. (b) depicts the response of the total integrated density after the perturbation. While this is a conserved quantity on the BEC side and the number stays constant, as we move towards the BCS regime, the system can dynamically change this quantity.

3.2 Effective low-energy modes

As the next step, we want to determine the low energy modes of the model. For the limit of $K_2 = 0$ we will recover the well-known Bogoliubov spectra [221] and for $K_1 = 0$ the uncoupled amplitude and phase mode [224].

We will first linearise the equations of motions (EOM) around the steady state solutions, and then separate the imaginary and real parts before taking the Fourier transformation to finally solve the resulting coupled equations to obtain the eigenmodes.

By setting all time derivatives to zero, we obtain the steady state solution as

$$|\Psi_0|^2 = \frac{r}{U}. \tag{3.7}$$

In the next step, we expand our mode around its steady state solution

$$\Psi \approx \Psi_0 + \delta_a + i\psi_0\phi \equiv \psi_0 + \delta_a + i\delta_\phi, \tag{3.8}$$

where we have used the $U(1)$ symmetry of the system to choose the phase to be zero in the steady state. Using this linearised form of the field back in the EOM, and by keeping only the lowest orders in δ_a and δ_ϕ, while separating the real and imaginary

part we obtain

$$-K_2\partial_t^2\delta_a - K_1\partial_t\delta_\phi = 2r\delta_a + \frac{\hbar^2}{2m}q^2\delta_a \tag{3.9}$$

$$-K_2\partial_t^2\delta_\phi - K_1\partial_t\delta_a = \frac{\hbar^2}{2m}q^2\delta_\phi. \tag{3.10}$$

Finally, we take the Fourier transform and arrive at

$$K_2\omega^2\delta_a - i\omega K_1\delta_\phi = 2r\delta_a + \frac{\hbar^2}{2m}q^2\delta_a \tag{3.11}$$

$$K_2\omega^2\delta_\phi + i\omega K_1\delta_a = \frac{\hbar^2}{2m}q^2\delta_\phi. \tag{3.12}$$

Solving for ω we obtain the general result

$$\omega_\phi = \sqrt{\frac{K_1^2 + 2K_2\left(\frac{\hbar^2}{2m}q^2 + r\right) - \sqrt{K_1^4 + 4K_2^2r^2 + 4K_1^2K_2\left(\frac{\hbar^2}{2m}q^2 + r\right)}}{2K_2^2}} \tag{3.13}$$

$$\omega_A = \sqrt{\frac{K_1^2 + 2K_2\left(\frac{\hbar^2}{2m}q^2 + r\right) + \sqrt{K_1^4 + 4K_2^2r^2 + 4K_1^2K_2\left(\frac{\hbar^2}{2m}q^2 + r\right)}}{2K_2^2}}. \tag{3.14}$$

To motivate the naming of this mode as the amplitude mode ω_A and the phase mode ω_ϕ as well as to gain intuition for these modes, we first consider the pure BCS limit ($K_1 = 0$)

$$\omega_\phi \xrightarrow{K_1 \to 0} \sqrt{\frac{\hbar^2}{2mK_2}}|q| \tag{3.15}$$

$$\omega_A \xrightarrow{K_1 \to 0} \sqrt{\frac{2r + \frac{\hbar^2}{2m}q^2}{K_2}} \tag{3.16}$$

and find that indeed in this limit ω_ϕ is a phase or gap free Goldstone mode, while the amplitude mode ω_A becomes gapped [224].
We can also consider the opposite limit, namely $K_2 = 0$. In this case we obtain

$$\omega_\phi \xrightarrow{K_2 \to 0} \frac{\hbar}{K_1}\sqrt{\frac{\frac{\hbar^2}{2m}q^2 + 2r}{2m}}|q|. \tag{3.17}$$

This recovers the well known Bogoliubov spectra for $K_1 = \hbar$ and $r = \mu$.

3.3 Mapping of the effective field theory to the BEC-BCS crossover

In this section we briefly discuss how the effective field theory can be mapped to a specific physical example, namely the BEC-BCS crossover. This is motivated by the collaboration with the group of Henning Moritz, where we quantitatively compared our model to the experimental results. Across the crossover the parameter $\eta \in (-\infty, \infty)$ is used with $\eta \to -\infty$ being the BEC limit, $\eta = 0$ the unitary regime and $\eta \to \infty$ the BCS limit. We determine four physically motivated equations to fix our effective field theory that has four free parameters, namely r, U, K_1 and K_2.

K_1 and K_2 consistency

First, we want to find a relation linking K_1 and K_2 for varying η in the form of

$$K_1 + \alpha(\eta)K_2 = \beta \tag{3.18}$$

with $\alpha(\eta)$ being some parameter in units of $[1/s]$ and β in units of $[Js]$ to be determined. First, we demand that in the limit of $K_2 = 0$ we recover the usual GP equation. Hence, $\beta = \hbar$. For the limit $K_1 = 0$ we are left with

$$\alpha(\eta)K_2 = \hbar. \tag{3.19}$$

For simplicity, we will assume that $\alpha(\eta)$ is constant along the crossover, $\alpha(\eta) = \alpha$. We note that this is a choice and can be seen as the lowest order approximation. With this, we can use that in the BCS limit the speed of sound is given by $v_s^{\text{BCS}} = \sqrt{E_{\text{F}}/m} \equiv \sqrt{\hbar^2/2mK_2}$ [221], see Eq. 3.13. We deduce that in the limit of BCS $K_2^{\text{BCS}} = \hbar^2/2E_{\text{F}}$. Hence, $\alpha = 2\frac{E_{\text{F}}}{\hbar}$ and we arrive at our final relation for K_1 and K_2

$$K_1 + 2\frac{E_{\text{F}}}{\hbar}K_2 = \hbar. \tag{3.20}$$

Amplitude mode

Next, we expand the amplitude mode in 3.13 up to zeroth order in $|q|$ and find

$$\omega_{\text{A}} = \sqrt{\frac{2(\hbar - \frac{2E_F K_2}{\hbar})^2 + 4K_2 r}{2K_2^2}} + \mathcal{O}(q^1). \tag{3.21}$$

We demand that this mode is associated with the amplitude mode as can be found in the BEC-BCS crossover. The frequency of this mode is in the lowest order given by $2\Delta/\hbar$ [224], which can be expressed using the Fermi energy and the parameter η as $2\Delta/\hbar = 4E_{\text{F}}/\hbar e^{-\eta}$. With this we obtain the relation

$$\omega_{\text{A}}(K_1, K_2, r, q=0) \equiv \frac{2\Delta}{\hbar} = \frac{4E_{\text{F}}}{\hbar}e^{-\eta}, \tag{3.22}$$

where we have already inserted the relation between K_1 and K_2 to eliminate K_1.

Speed of sound

We expand the phase mode up to linear order in $|q|$ and find

$$\omega_\phi = \hbar^2 \sqrt{\frac{r}{m}} \sqrt{\frac{1}{\left(\hbar^2 - 2E_F K_2\right)^2 + 2\hbar^2 K_2 r}} |q| + \mathcal{O}(q^2). \tag{3.23}$$

We define the speed of sound as $v_s = (\partial \omega_\phi / \partial q)|_{q=0}$. We map this to the speed of sound v_s^{QMC} that has been calculated in [235] using the quantum Monte Carlo method (QMC) for the BEC-BCS crossover. Furthermore, we find the relation

$$\left.\frac{\partial \omega_\phi(K_1, K_2, r, q)}{\partial q}\right|_{q=0} = \sqrt{\frac{r}{m}} \sqrt{\frac{\hbar^4}{\left(\hbar^2 - 2E_F K_2\right)^2 + 2\hbar^2 K_2 r}} \equiv v_s^{\mathrm{QMC}}. \tag{3.24}$$

Equilibrium density

Finally, we use the equilibrium density to obtain the 4th relation to fix the free parameter in our effective field theory. In our model, the equilibrium density is computed by $n_0 = r/U$. By setting this value to the condensed fraction across the BEC-BCS crossover [236] we obtain

$$n_0 = r/U \equiv \frac{n_{2d}}{2} \frac{\pi/2 + \arctan(x^{-1})}{x^{-1} + \sqrt{1 + x^{-2}}} \tag{3.25}$$

with $x = \Delta/\mu$. μ is taken from the QMC results in [235].
Tab. 3.3 summarizes our findings. By solving these four equations for our four free parameter for each η along the crossover we fix our effective field theory.

K_1, K_2 consistency	$K_1 + 2\frac{E_F}{\hbar} K_2 \equiv \hbar$
Amplitude mode	$\omega_A(K_1, K_2, r, q = 0) \equiv \frac{2\Delta}{\hbar} = \frac{4E_F}{\hbar} e^{-\eta}$
Speed of sound	$\left.\frac{\partial \omega_\phi(K_1, K_2, r, q)}{\partial q}\right|_{q=0} \equiv v_s^{\mathrm{QMC}}$
Equilibrium density	$\frac{r}{U} \equiv n_0^{\mathrm{QMC}}$

Table 3.1: The table is summarising the equations to fix our parameter in the field theory across the BEC-BCS crossover.

In Fig. 3.2 we show example dependencies for the four parameter across the crossover. We have chosen parameters accordingly to the experiment by the group of Henning Moritz and the QMC results from [235]. We choose $\omega_z = 2\pi \times 8.7$ kHz, $E_F = 1.6 \times \hbar\omega_z$. U is not shown as it can be simply computed via $U = r/n_0$ and follows the form of r. It can be seen that K_1 and K_2 quickly change as η changes sign. Thus, as expected for $\eta < 0$ the dynamics is dominated by K_1 and is approximately particle-hole symmetric for $\eta > 0$.
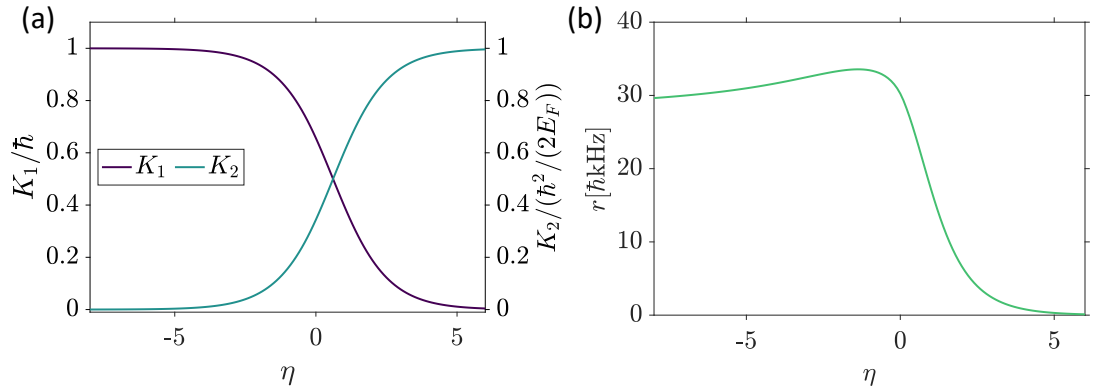
Figure 3.2: The effective parameters are shown across the crossover. (a) K_1 and K_2 in units of $\hbar$ and $\hbar^2/2E_\mathrm{F}$, respectively. (b) r in units of $\hbar$ kHz. It can be seen that there is a rapid change of the parameter as η changes sign.

3.4 Effective two-mode model

We fix our parameter for a two-dimensional free superfluid across the BEC-BCS crossover. We are interested in the case of having an additional third direction with strong spatial confinement. For simplicity, we assume that there are no excitations within the two-dimensional plane, and we are left with considering an effective one dimensional case with a deep harmonic trap. In the following we briefly sketch how we obtain the two-mode model used starting from the effective one-dimensional case. To simplify the model, we eliminate the trapping direction z. We assume that the harmonic trap is sufficiently deep such that we can expand our wavefunction in the lowest three eigenstates of the trap along the z-direction. We further assume that the contact interaction is small enough such that it can be seen as a small perturbation around the idealised eigenstates of the harmonic oscillator without contact interactions. Furthermore, we have checked numerically that the first excited state is empty and as we drive the system periodically by changing the strength of the laser beam, which translates into changes of the trap depth, the parity is conserved such that the first excited state stays empty throughout the simulation. Hence, we further approximate the system and only consider the ground and second excited state of the harmonic oscillator. We can expand the wavefunction as

$$\Psi(x,y,z) = \frac{1}{L_x L_y} \left[f_0(z)\alpha_0 + f_2(z)\alpha_2 \right] \tag{3.26}$$

with the harmonic oscillator (HO) eigenfunctions f_i

$$f_i(z) = \frac{1}{\sqrt{2^n n!}} \left(\frac{m\omega_z}{\hbar\pi} \right)^{1/4} e^{-\frac{m\omega_z}{2\hbar}x^2} H\left(n, \sqrt{\frac{m\omega_z}{\hbar}} x \right) \tag{3.27}$$

with $H(n,x)$ being the n-th hermitian Hermite polynomial. Using this ansatz for the wavefunction and by evaluating the integrals over space for the Lagrange density, we

obtain the new effective Lagrangian as

$$\int d^3r \mathcal{L}_{\mathrm{dyn}} = -K_2 \left(\partial_t \alpha_0 \partial_t \alpha_0^* + \partial_t \alpha_2 \partial_t \alpha_2^* \right) + i K_1 \left\{ \left(\alpha_0^* \partial_t \alpha_0 - \alpha_0 \partial_t \alpha_0^* \right) + \left(\alpha_2^* \partial_t \alpha_2 - \alpha_2 \partial_t \alpha_2^* \right) \right\}$$

(3.28)

and

$$
\begin{aligned}
\int d^3r \mathcal{L}_{\mathrm{stat}} = {} & \frac{\hbar \omega_z}{2} \left(\alpha_0^* \alpha_0 + 5\alpha_2^* \alpha_2 + \frac{b(t)}{2} \left[\alpha_0^* \alpha_0 + 5\alpha_2^* \alpha_2 + \frac{\sqrt{2}}{2} \left(\alpha_2^* \alpha_0 + \alpha_0^* \alpha_2 \right) \right] \right) \\
& - r(\alpha_0^* \alpha_0 + \alpha_2^* \alpha_2) \\
& + \frac{U}{2} \frac{1}{16} \sqrt{\frac{M\omega_z}{\pi\hbar}} \left[12\sqrt{2}\alpha_2^* \alpha_0^* \alpha_2 \alpha_0 + 8\sqrt{2}\alpha_0^* \alpha_0^* \alpha_0 \alpha_0 + \frac{41}{8}\sqrt{2}\alpha_2^* \alpha_2^* \alpha_2 \alpha_2 \right] \\
& + \frac{U}{2} \frac{1}{16} \sqrt{\frac{M\omega_z}{\pi\hbar}} \left[\left(-8\alpha_0^* \alpha_0^* \alpha_2 \alpha_0 + \alpha_2^* \alpha_2^* \alpha_2 \alpha_0 + 3\sqrt{2}\alpha_2^* \alpha_2^* \alpha_0 \alpha_0 \right) + \mathrm{h.c.} \right],
\end{aligned}
$$

(3.29)

where we introduced $\omega_z(t)^2 = \omega_z^2 + a(t)$ and $a(t) = b\omega_z^2 \sin(\omega_{\mathrm{dr}} t)$ to include periodic driving of the harmonic potential. Finally, we obtain the equations of motion

$$\partial_t \left(-K_2 \partial_t + i K_1 \right) \alpha_0 = \left(-\tilde{r} + \frac{\hbar\omega_z}{2} \left[1 + b(t) \right] \right) \alpha_0 + b(t) \frac{\sqrt{2}\hbar\omega_z}{4} \alpha_2$$

(3.30)

$$+ \frac{U}{2} \frac{1}{16} \sqrt{\frac{M\omega_z}{\pi\hbar}} \left[12\sqrt{2}\alpha_2^* \alpha_2 \alpha_0 + 16\sqrt{2}\alpha_0^* \alpha_0 \alpha_0 - 16\alpha_0^* \alpha_2 \alpha_0 - 8\alpha_2^* \alpha_0 \alpha_0 + \alpha_2^* \alpha_2 \alpha_2 + 6\sqrt{2}\alpha_0^* \alpha_2 \alpha_2 \right]$$

$$\partial_t \left(-K_2 \partial_t + i K_1 \right) \alpha_2 = \left(-\tilde{r} + 5\frac{\hbar\omega_z}{2} \left[1 + b(t) \right] \right) \alpha_2 + b(t) \frac{\sqrt{2}\hbar\omega_z}{4} \alpha_0$$

(3.31)

$$+ \frac{U}{2} \frac{1}{16} \sqrt{\frac{M\omega_z}{\pi\hbar}} \left[12\sqrt{2}\alpha_0^* \alpha_2 \alpha_0 + \frac{41}{4}\sqrt{2}\alpha_2^* \alpha_2 \alpha_2 - 8\alpha_0^* \alpha_0 \alpha_0 + 2\alpha_2^* \alpha_2 \alpha_0 + \alpha_0^* \alpha_2 \alpha_2 + 6\sqrt{2}\alpha_2^* \alpha_0 \alpha_0 \right].$$

In our numerics we choose $b \ll 1$ to ensure that we only probe the mode structure by our drive without distorting it. We further add a phenomenological small dissipative channel to prevent the system from heating and to reach a steady state within finite time. We have also used this model to obtain the lowest order mean field shift added to the analytical results of the harmonic oscillator during the K_1 to K_2 crossover as is discussed in the PhD thesis of Lukas Broers and in the supplemental material of the manuscript, which will be published soon. Our numerical results as well as a comparison with the experimental results by the group of Henning Moritz can be found in the manuscript in preparation with further details on our numerical protocol in the supplemental material.

3.5 Publication XI: Vortex and soliton dynamics in particle-hole-symmetric superfluids

J. Skulte, L. Broers, J.G. Cosme and L. Mathey — **Phys. Rev. Res. 3, 043109 (2021)**

Motivation

This work was motivated by the recent findings of chaotic phases in driven high-TC superconductors. The model studied, can be seen as an analog model of superconductors without the gauge field. The aim of this work was to use a nonlinear particle-hole symmetric (PHS) superfluid, namely the nonlinear Klein-Gordon equation, to study turbulence and chaos. As the first primer towards this goal, we studied the dynamics of single topological defects as vortices and the instability of a soliton decaying into single vortices and compared this dynamics to the dynamics of a Bose-Einstein condensate using the Gross–Pitaevskii equation.

Main findings

In this work, we have proposed a scheme to induce topological defects in PHS superfluids with the example of the Bardeen-Cooper-Schrieffer phase in ultracold neutral atoms experiments. For this study we used the NLKG equation and compared our results to the GP equation that is widely used to study BEC dynamics. We showed that the dynamics of vortices is qualitatively distinct for PHS superfluids and showed numerically and analytically the absence of the Magnus force. We further obtained results for varying charges, which can be interpreted as smoothly connecting both ends of the BEC-BCS crossover. Finally, we pointed out experimental signatures to distinguish the GP equation and NLKG equation dynamics.

Contribution

My contribution to this work consisted of conceptualizing and creating the pseudo-spectral code in C++ using MPI, together with LB. I performed the analytical calculations, as well as the numerical studies supported by LB. JGC and LB assisted me in analyzing the numerical results and in writing the manuscript. All of this was done under the supervision of LM. All authors contributed to the discussion and interpretation of the results, as well as to writing the manuscript.

Vortex and soliton dynamics in particle-hole-symmetric superfluids

Jim Skulte [1,2] Lukas Broers [1] Jayson G. Cosme [3] and Ludwig Mathey[1,2]

[1]*Zentrum für Optische Quantentechnologien und Institut für Laserphysik, Universität Hamburg, 22761 Hamburg, Germany*
[2]*The Hamburg Centre for Ultrafast Imaging, Luruper Chaussee 149, 22761 Hamburg, Germany*
[3]*National Institute of Physics, University of the Philippines, Diliman, Quezon City 1101, Philippines*

We propose to induce topological defects in particle-hole-symmetric superfluids, with the prime example of the Bardeen-Cooper-Schrieffer state of ultracold atoms, and detect their time evolution and decay. We demonstrate that the time evolution is qualitatively distinct for particle-hole-symmetric superfluids and point out that the dynamics of topological defects is strongly modified in particle-hole-symmetric fluids. We obtain results for different charges and compare them with the standard Gross-Pitaevskii prediction for Bose-Einstein condensates. We highlight the observable signatures of the particle-hole symmetry in the dynamics of decaying solitons and subsequent vortices.

I. INTRODUCTION

The presence or absence of particle-hole symmetry in a physical system is a fundamental property pervading its dynamical properties. Particle-hole symmetry is realized in Lorentz invariant theories such as the standard model of elementary physics [1], low-energy effective models close to quantum criticality [2], and the famous Bardeen-Cooper-Schrieffer (BCS) theory of superconductivity [3,4].[1] We note that the order parameter dynamics of high-T_c superconductors can be described by an effective particle-hole-symmetric theory, which allows for exploring the dynamics of the Higgs/amplitude mode [5–8]. Similarly, in ultracold neutral atoms the emergence of an effective particle-hole symmetry has been predicted theoretically [9,10] and confirmed experimentally [11,12]. Recently, amplitude oscillations of the order parameter in the Bose-Einstein condensate (BEC) to BCS crossover have been reported [13], suggesting the presence of approximate particle-hole symmetry.

The dynamics of topological defects, such as solitons and quantized vortices, derives from and exemplifies the properties of the underlying quantum fluid. The stability of solitons has been discussed extensively for the nonlinear Schrödinger equation or Gross-Pitaevskii (GP) equation [14–18]. Zakharov and Rubenchik coined the term snaking to refer to the characteristic bending of solitons prior to their decay.

Snaking is a manifestation of the Magnus force. This has been discussed for neutral bosonic systems within the GP equation [19–25], in the BEC-BCS crossover [26–28], and in superconductors [29,30].

We propose to determine the influence of particle-hole symmetry on the dynamics of topological defects in two-dimensional neutral superfluids. We focus on the BCS state as our primary example, but our results hold for any approximately particle-hole-symmetric system, e.g., bosons in an optical lattice near unit filling [12]. For this purpose we present the similarities and differences in the dynamics of topological defects in the absence and presence of particle-hole symmetry. We also compare the dynamics of the particle-hole-symmetric theory for zero and nonzero Noether charge, corresponding to a balanced mixture of particles and holes and an imbalanced mixture of particles and holes, respectively. We find that the case with nonzero charge is reminiscent of the dynamics of the GP equation. On the other hand, for vanishing charge, in which the number of particles and holes is balanced, we show that vortices do not experience any Magnus force. This leads to a soliton decay without snaking, setting it apart from soliton dynamics in non-particle-hole-symmetric fluids, such as BECs. To induce soliton dynamics of the quantum fluid in the BCS limit, we propose to imprint a soliton on the BEC side of the crossover in the presence of a potential barrier. As the next step, we propose to ramp the fluid adiabatically across the crossover into the BCS limit while keeping the barrier potential up. Finally, the barrier potential is ramped to zero, to induce the soliton dynamics. This protocol of initializing the dynamics enables imprinting of the phase pattern with an off-resonant optical pulse, whereas direct phase imprinting in the particle-hole-symmetric limit is prohibited. We note that this statement holds only for an exact particle-hole-symmetric case. In experiments such as those in Ref. [27], particle-hole symmetry is only approximately realized. That is, the appropriate effective

---

[1]Due to the close connection between relativistic Lorentz invariance and particle-hole symmetry, models that are particle-hole symmetric are also sometimes referred to as relativistic models.
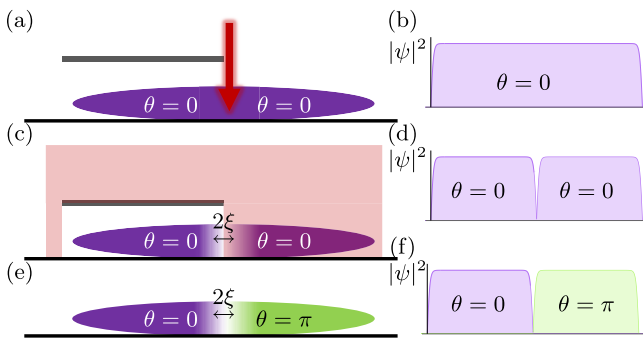
FIG. 1. Schematic representation of (a), (c), and (e) the proposed protocol to imprint a soliton and (b), (d), and (f) the corresponding density profiles $|\psi|^2$ and phase distributions θ. (a) A narrow laser sheet is applied to a quantum fluid on the BEC side of the crossover to create a density depletion in the condensate. (b) and (d) The quantum fluid is split into two subsystems with a relative phase of zero. (c) Next a π pulse is applied to half of the condensate to create (e) and (f) the phase pattern of a dark soliton. Next the interaction is adiabatically changed across the crossover deep into the BCS side. The narrow laser sheet separating the two subsystems is removed, which triggers the soliton dynamics. Here ξ is the healing length of the condensate.

action is expected to have both $K_1 \partial_t$ and $K_2 \partial_t^2$ contributions, as we discuss below. The $K_1 \partial_t$ term allows the phase imprinting as it is the dominant term in the BEC regime. The proposed protocol is displayed in Fig. 1.

II. SYSTEM

We consider a low-energy effective models of the form [3]

$$
\begin{aligned}
S = \int d^2x \, dt \bigg(& K_2 (\partial_t \psi)(\partial_t \bar{\psi}) - iK_1 (\partial_t \psi) \bar{\psi} \\
& - \frac{1}{m} \nabla \bar{\psi} \nabla \psi - \mu |\psi|^2 + \frac{g}{2} |\psi|^4 + V_{\text{ext}} |\psi|^2 \\
& - i\mu_Q [(\partial_t \bar{\psi})\psi - \bar{\psi} \partial_t \psi] \bigg),
\end{aligned}
\tag{1}
$$

where $K_{1,2}$ are the above-mentioned parameters that determine the time dependence, μ is the square root of the gap energy, which has the dimensions of a mass term, g is the contact interaction strength, and V_{ext} is the externally applied potential. A similar effective field theory has been proposed and discussed to model the BEC-BCS crossover in [31–34]. We include a Lagrange multiplier μ_Q to fix the Klein-Gordon charge (7) (discussed below). By setting $K_2 = 0$, $K_1 = 1$, and $\mu_Q = 0$, we recover the GP equation

$$
i\partial_t \psi(\mathbf{x}, t) = \frac{\nabla^2}{2m} \psi(\mathbf{x}, t) + V(|\psi|^2)\psi(\mathbf{x}, t),
\tag{2}
$$

where $V[|\psi(\mathbf{x}, t)|^2] = \mu - g|\psi(\mathbf{x}, t)|^2 + V_{\text{ext}}(\mathbf{x})$. We refer to a condensate described by the GP equation as a GP fluid. This equation is manifestly not particle-hole symmetric under the exchange $\psi \leftrightarrow \bar{\psi}$. On the other hand, particle-hole symmetry is fulfilled in the action (1) by setting $K_1 = 0$ and $K_2 \neq 0$.

We introduce a dimensionless representation via $\psi = \tilde{\psi}/\xi$, $\nabla = \tilde{\nabla}/\xi$, $\partial_t = c_s/\xi \tilde{\partial}_t$, and $V = \mu \tilde{V}$, where ξ is the healing length of the fluid and c_s the speed of sound. This leads to the modified nonlinear Klein-Gordon (NLKG) equation

$$
\partial_{\tilde{t}}^2 \tilde{\psi}(\mathbf{x}, t) = \tilde{\nabla}^2 \tilde{\psi}(\mathbf{x}, t) + \tilde{V}(|\tilde{\psi}|^2)\tilde{\psi}(\mathbf{x}, t) + i\mu_Q \partial_{\tilde{t}} \tilde{\psi}(\mathbf{x}, t).
\tag{3}
$$

We refer to condensates evolving according to the NLKG equation as Klein-Gordon (KG) fluids. In the following we drop the tilde. We trap the fluid using a box potential of the form

$$
V_{\text{ext}}(\mathbf{x}) = V_0 \{1 + \tanh[(|\mathbf{x}| - r_0)/\xi]\}.
\tag{4}
$$

We note that this model is a relativistic BEC [35–37] and a similar equation has been proposed to model cold dark matter [38–40] and relativistic boson stars [41–43].

In the following we show the influence of particle-hole symmetry on the dynamics of topological defects. For the KG fluid, we introduce the canonical momentum $\Pi(x, t) = \partial_t \bar{\psi}(x, t) + i\mu_Q \bar{\psi}(x, t)$ to obtain two coupled first-order partial differential equations

$$
\partial_t \psi(\mathbf{x}, t) = \bar{\Pi}(\mathbf{x}, t) + i\mu_Q \psi(\mathbf{x}, t),
\tag{5}
$$

$$
\partial_t \Pi(\mathbf{x}, t) = \nabla^2 \bar{\psi}(\mathbf{x}, t) + V(|\psi|^2)\bar{\psi}(\mathbf{x}, t) - i\mu_Q \Pi(\mathbf{x}, t).
\tag{6}
$$

A crucial feature of a KG fluid is that the particle number $N = \int |\psi(\mathbf{x}, t)|^2 dx$ is not conserved, in contrast to a GP fluid. Instead, in the KG fluid, the Noether charge

$$
Q = -i \int [\bar{\Pi}(\mathbf{x}, t)\bar{\psi}(\mathbf{x}, t) - \Pi(\mathbf{x}, t)\psi(\mathbf{x}, t)] d^2x
\tag{7}
$$

is conserved. The Noether charge Q can be thought of as the difference of particles and holes in the system. That is, a zero Noether charge describes the situation with an equal number of particles and holes. An intuitive example for illustrating the Noether charge is a system of interacting bosons in an optical lattice with unit filling. An excitation corresponds to exciting one atom out of the lattice side and leaving behind a hole. Thus, the Noether charge stays unchanged as the same number of particles and hole were created. Another possible excitation is to excite the atom out of the lattice and further removing it from the system, which leaves a hole behind. The system then slightly goes away from unit filling as there is now an imbalance between the number of holes and particles and this corresponds to an effective nonzero Noether charge. Another example can be envisioned in the BCS regime for nonzero temperature. Here a rf knife can be used to remove some of the atoms occupying the Bogoliubov modes, leading to an imbalance between particle and hole excitations.

We apply the Madelung transformation to the field and the canonical momentum, in which the field ψ is written in an amplitude-phase representation

$$
\psi(\mathbf{x}, t) = A(\mathbf{x}, t) \exp[i\theta(\mathbf{x}, t)],
\tag{8}
$$

$$
\Pi(\mathbf{x}, t) = \left(\frac{\dot{A}(\mathbf{x}, t)}{A(\mathbf{x}, t)} + i[\mu_Q - \dot{\theta}(\mathbf{x}, t)] \right) \psi(\mathbf{x}, t),
\tag{9}
$$

and obtain the continuity equation and particle-hole-symmetric Euler equation

$$\partial_t \rho_{\mathrm{KG}} + \frac{\mu_Q}{2} \partial_t \rho_S = -\nabla(\rho_S \mathbf{u}), \tag{10}$$

$$\left(\frac{\rho_{\mathrm{KG}}}{\rho_S} + \frac{\mu_Q}{2} \right) \partial_t \mathbf{u} = \mathbf{u}\nabla\mathbf{u} + \frac{\nabla \rho_S}{2\rho_0} - \frac{\nabla}{2}\left(\frac{\square \sqrt{\rho_S}}{\sqrt{\rho_S}} \right), \tag{11}$$

where we introduce the GP density $\rho_S = A^2$, the KG density $\rho_{\mathrm{KG}} = A^2 \partial_t \theta$, the velocity $\mathbf{u} = \nabla\theta$, and the box operator $\square = \partial_t^2 - \nabla^2$. In this representation, the charge simplifies to $Q = \int \rho_{\mathrm{KG}} dx$. In the particle-hole-symmetric Euler equations there is a prefactor $\rho_{\mathrm{KG}}/\rho_S$ in front of the time derivative of the velocity field $\partial_t \mathbf{u}$. This prefactor depends on the charge Q. This is a crucial difference to the GP Euler equation where this prefactor is always 1.

The particle-hole-symmetric Euler equation (11) has two quantum pressure terms. One term is due to the kinetic energy of the condensate and is proportional to $\frac{\nabla^2 \sqrt{\rho_S}}{\sqrt{\rho_S}}$. It is the zero-point motion of the condensate and becomes dominant if the condensate has spatial variations on short length scales [44]. The second is proportional to $\frac{\partial_t^2 \sqrt{\rho_S}}{\sqrt{\rho_S}}$ and originates from the second-order time derivative. It only exists for particle-hole-symmetric condensates.

We present the local velocity field around a single vortex. Therefore, we transform into the Feshbach-Villars basis, which translates the NLKG to coupled GP equations for the particles and antiparticles, respectively [45]

$$\psi = \frac{1}{\sqrt{2}}(\psi^{\mathrm{p}} + \psi^{\mathrm{a}}), \tag{12}$$

$$\Pi = \frac{i}{\sqrt{2}}(\psi^{\mathrm{a}} - \psi^{\mathrm{p}}). \tag{13}$$

Next we expand the field around the vortex core position r_0 with the amplitude A^{i} and phase θ^{i} [see Eqs. (8) and (9)] and propagate the location of the vortex core using the equations of motion and compare the new location with the previous location to obtain the local velocity field (for a detailed discussion and derivation see [46–48]). For the two velocity fields we obtain

$$v^{\mathrm{a}} = -\frac{(-i, 1)^{\mathrm{T}} \cdot \nabla(A^{\mathrm{p}} + A^{\mathrm{a}}) + (A^{\mathrm{p}} + A^{\mathrm{a}})(1, i)^{\mathrm{T}} \cdot \nabla\theta}{A^{\mathrm{a}}}, \tag{14}$$

$$v^{\mathrm{p}} = \frac{(-i, 1)^{\mathrm{T}} \cdot \nabla(A^{\mathrm{p}} + A^{\mathrm{a}}) + (A^{\mathrm{p}} + A^{\mathrm{a}})(1, i)^{\mathrm{T}} \cdot \nabla\theta}{A^{\mathrm{p}}}, \tag{15}$$

where the spatial plane (x, y) is represented as the complex plane $z = x + iy$. Translating this back into the (ψ, Π) basis, we obtain

$$v^{\psi} = \frac{1}{\sqrt{2}}(v^{\mathrm{p}} + v^{\mathrm{a}}) = \sqrt{2}\left(1 - \frac{A^{\mathrm{a}}}{A^{\mathrm{p}}} \right) v^{\mathrm{p}}. \tag{16}$$

For $Q \neq 0$ we have $A^{\mathrm{a}} \neq A^{\mathrm{p}}$, which means that we obtain a nonzero velocity field. In this case the velocity is proportional to the velocity obtained for GP fluids [47]. For $Q = 0$, we have $A^{\mathrm{p}} = A^{\mathrm{a}}$ and $N^{\mathrm{p}} = N^{\mathrm{a}}$, with N^{i} the total number of particles/antiparticles. For this balanced scenario the local velocity field vanishes precisely as shown in Fig. 2. As pointed out before and as can be seen from Eq. (16), for a finite charge
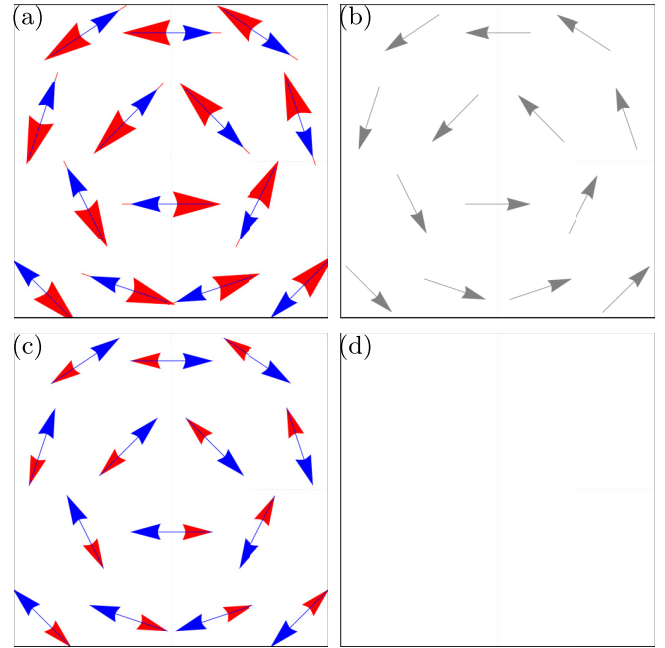

FIG. 2. Schematic sketch of (a) and (c) the local velocity fields of the particles (blue) and antiparticles (red) and (b) and (d) the resulting total local velocity field for the ψ field (gray). (a) An unbalanced mixture of particles and antiparticles with a finite charge Q leads to (b) a nonzero effective velocity field for the ψ field. (c) A balanced mixture of particles and antiparticles with a vanishing charge Q leads to (d) a vanishing effective velocity field for the ψ field.

Q corresponding to an imbalance between particles and antiparticles, the magnitudes of the velocity fields are different [see Fig. 2(a)], which results in a nonzero velocity field for the KG fluid ψ [see Fig. 2(b)]. In contrast, for a balanced mixture the local velocity field magnitudes are the same [see Fig. 2(c)] and due to the opposite direction of the velocity fields the velocity field of the KG fluid vanishes [see Fig. 2(d)].

III. NUMERICAL RESULTS

To expand on our analytical predictions and to propose an experimental setup to detect vortex dynamics of KG fluids, we simulate the equations using the pseudospectral method [49] for both the GP and KG fluids. We set the ratio between the chemical potential μ and the contact interaction g to $\mu/g = 10/\xi^2$. In the following we express all length scales in units of ξ. Our simulations are discretized in a 256×256 grid. We choose $r_0/\xi = 25$, where r_0 is half of the box size, as defined in Eq. (4), and resolve ξ with three grid points. The phase and density distribution for snapshots in real time are shown for a GP fluid [see Fig. 3(a)] and for a KG fluid with vanishing charge [see Fig. 3(c)]. Circles (KG fluid with $Q = 0$) and diamonds (GP fluid) in red correspond to a phase winding of $+1$, while blue corresponds to -1 [see Fig. 3(b)]. The gray arrows show the flow of time in the figure. It can be seen that for a dipole distance $d_{12} > 2\xi$ in the GP fluid the dipole will start to propel forward perpendicular to the dipole axis and will not annihilate. In contrast, the KG vortex dipoles will move along the dipole axis and annihilate each other, due to the absence
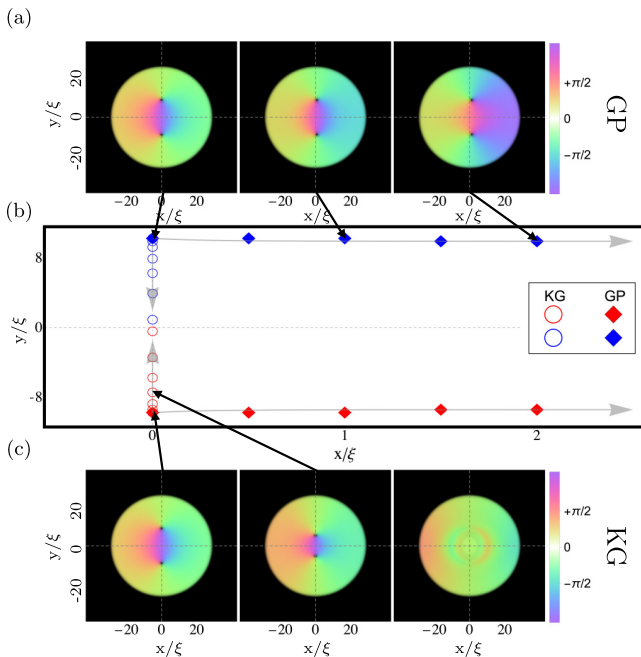
FIG. 3. Dynamics of vortex dipole pairs in a GP and a KG fluid. The phase and the density of (a) the GP fluid and (c) the KG fluid are shown. (b) The symbols display the locations of the vortices and antivortices in red and blue, respectively, of the GP fluid (diamonds) and the KG fluid (circles), and difference times. The snapshots of (a) and (c) are indicated via black arrows. The gray arrows indicate the movement of the vortices in time.

of a velocity field. Related observations of vortex dynamics were reported in Ref. [50]. We note that the particle-hole symmetry is the origin of this qualitatively distinct behavior from GP fluid dynamics. We propose that the data from a future experimental realization of our proposal could be used to numerically fit the ratio of K_1 and K_2 for different interaction strengths. This links our proposal to the parameters used in the universal effective action of such systems.

To investigate the influence of the particle-hole symmetry on the soliton dynamics, we initialize the condensate with a modified Thomas-Fermi profile [44], as described in the Supplemental Material [48], for a box potential in Eq. (4) with $V_0 = 10$ and $r_0 = 30$ for the GP (KG) fluid and start with a soliton imprinted in the fluid. We let the condensate relax using the imaginary-time propagation [51] extended to particle-hole-symmetric fluids [48]. For the KG fluids, we set the initial canonical momentum as $\Pi = i\frac{\mu_Q}{2}\psi$ with $\mu_Q \in \mathbb{R}$, resulting in a charge of $Q = \mu_Q N$. Furthermore, we add 1% white noise on the initial condensate density to study the stability of solitons.

The system is propagated in time according to Eqs. (2), (5), and (6). At lowest order, the Higgs mode and the Goldstone mode decouple in a particle-hole-symmetric theory [3]. Within this approximation, this initial state only induces the dynamics of the Goldstone mode. However, this approximation fails in soliton and vortex solutions. For the same parameters μ and g, the healing length is twice as large in the KG case compared to GP equation due to the difference in the prefactor of the kinetic energy.

In Fig. 4 we present the real-time dynamics of the complex field ψ shaded from white to black corresponding to decreasing amplitude, i.e., black regions denote areas with vanishing $|\psi|$. The phase of the wave function is represented as color. The wave function is normalized for each snapshot such that the maximum value is set to unity to make it easier to compare GP and KG results.

In the GP fluid, we observe the established soliton instability in Figs. 4(a)–4(c) [16] and the motion of trapped vortices in Figs. 4(c)–4(e) [23,47]. The vortices move towards the edge of the condensate. As they approach the edge, they experience a net force and move along the trap boundary as depicted in Figs. 4(d) and 4(e) [23]. The behavior of the KG fluid with $Q \neq 0$ is similar. As displayed in Figs. 4(f)–4(j), the soliton decays into vortices, which then move around the condensate. Similar to the GP fluid, as the phase rotates in Figs. 4(f)–4(j), the vortices experience a net force leading to their motion along the trap boundary as seen in Figs. 4(i)–4(j).

In contrast, for the KG fluid with $Q = 0$, the soliton decays into vortices that are located along the soliton axis, as shown in Figs. 4(k)–4(m). Similar results have been found in [28]. Moreover, we find that the vortices are not rotating as displayed in Figs. 4(m)–4(o), which is consistent with Eqs. (14) and (16) and Fig. 3. When the vortices reach the trap boundary, they evaporate into the thermal cloud as shown in Figs. 4(n) and 4(o).

IV. CONCLUSION

In conclusion, we have shown that by measuring the density profile of a two-dimensional condensate after imprinting a soliton in a particle-hole-symmetric superfluid, such as a BCS state of neutral particles, it is possible to test the effective low-energy theoretical description of the system. We have shown analytically and numerically that for particle-hole-symmetric superfluids with vanishing Noether charge, the Magnus force is absent. This allows for a dipole pair of vortices to approach each other without transverse motion and to annihilate, reminiscent of a recent observation in Ref. [50]. Another consequence of the vanishing Magnus force is that a soliton does not bend as it decays into vortices. Probing these effects experimentally will reveal how well particle-hole symmetry is realized in the dynamics of superfluids or whether the non-particle-hole-symmetric term, the first-order derivative in time, is the dominant contribution in the effective theory. This is crucial in understanding the notion of turbulence in particle-hole-symmetric fluids such as superconductors. Our work reveals that turbulence in a BCS superconductor and its scaling laws might deviate from Kolmogorov scaling laws [52], which apply to classical systems as well to GP fluids. We note that our predictions could be experimentally confirmed using refined experimental technique, such as *in situ* observations of two-dimensional Fermi liquids when probing the BEC-BCS crossover in neutral atoms [53,54] or the well-controlled imprinting of vortex dipole pairs [50].
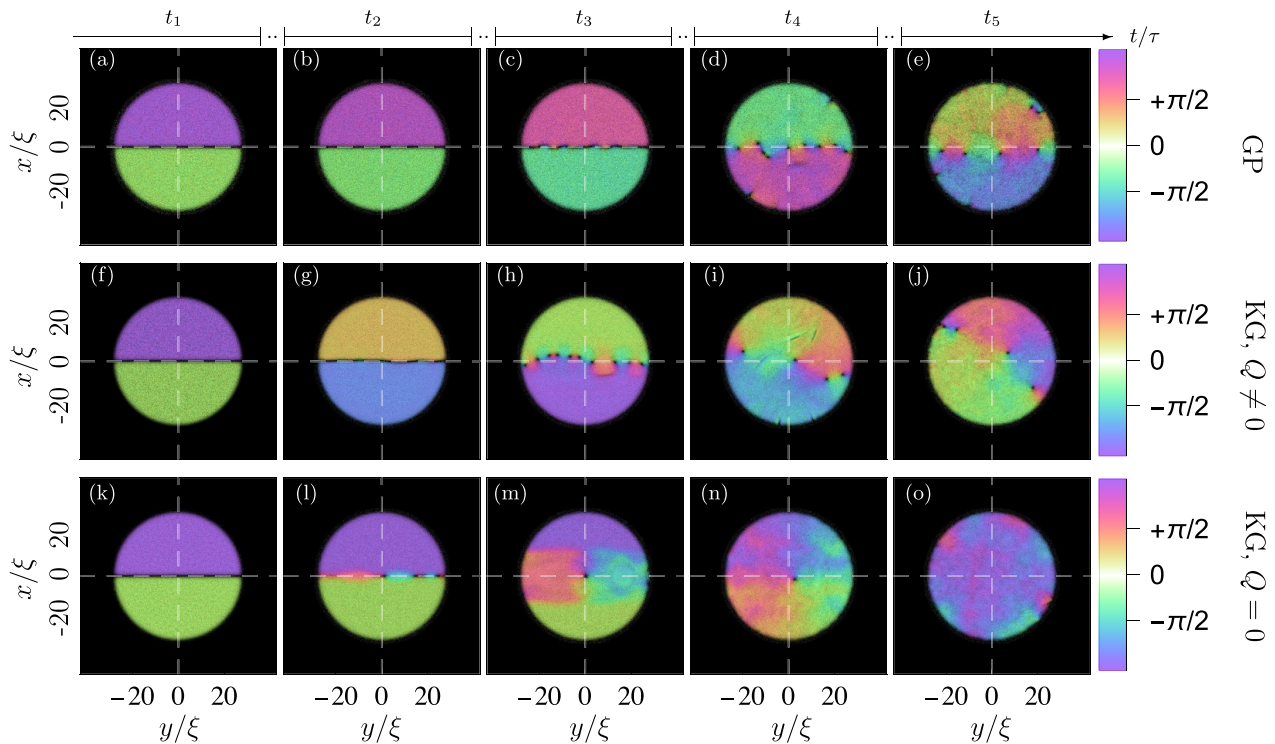
FIG. 4. Overview of the soliton instability for the three distinct cases corresponding to (a)–(e) the GP results, (f)–(j) the KG results with $Q \neq 0$, and (k)–(o) the KG results with $Q = 0$. For a better comparison between the GP and KG results the ψ field density is normalized such that the maximum value is set to unity in each snapshot. The shading of the plots ranging from black to white visualizes the magnitude of the field $|\psi|$, while the colormap indicates the phase. (a), (f), and (k) Initial soliton seeded with white noise. (b), (g), and (l) Soliton bending. (c), (h), and (m) Vortices appearing after the soliton decay. The long-time dynamics of the vortices inside the trap are presented in (d), (i), and (n) and in (e), (j), and (o). White dashed lines indicate the soliton axis and the perpendicular axis. The spatial length is expressed in terms of the healing length ξ. A movie showing the dynamics is presented in the Supplemental Material [48].

[1] S. Weinberg, *The Quantum Theory of Fields* (Cambridge University Press, Cambridge, 2013), Vol. 2.

[2] S. Sachdev, *Quantum Phase Transitions*, 2nd ed. (Cambridge University Press, Cambridge, 2011).

[3] D. Pekker and C. Varma, Amplitude/Higgs modes in condensed matter physics, Annu. Rev. Condens. Matter Phys. **6**, 269 (2015).

[4] C. M. Varma, Higgs boson in superconductors, J. Low Temp. Phys. **126**, 901 (2002).

[5] G. Homann, J. G. Cosme, and L. Mathey, Higgs time crystal in a high-T_c superconductor, Phys. Rev. Res. **2**, 043214 (2020).

[6] G. Homann, J. G. Cosme, J. Okamoto, and L. Mathey, Higgs mode mediated enhancement of interlayer transport in high-T_c cuprate superconductors, Phys. Rev. B **103**, 224503 (2021).

[7] Z. Dai and P. A. Lee, Photo-induced superconducting-like response in strongly correlated systems, Phys. Rev. B **104**, 054512 (2021).

[8] Z. Dai and P. A. Lee, Superconducting-like response in driven systems near the Mott transition, arXiv:2106.08354.

[9] E. Altman and A. Auerbach, Oscillating Superfluidity of Bosons in Optical Lattices, Phys. Rev. Lett. **89**, 250404 (2002).

[10] L. Pollet and N. Prokof'ev, Higgs Mode in a Two-Dimensional Superfluid, Phys. Rev. Lett. **109**, 010401 (2012).

[11] J. Léonard, A. Morales, P. Zupancic, T. Donner, and T. Esslinger, Monitoring and manipulating Higgs and Goldstone modes in a supersolid quantum gas, Science **358**, 1415 (2017).

[12] M. Endres, T. Fukuhara, D. Pekker, M. Cheneau, P. Schauss, C. Gross, E. Demler, S. Kuhr, and I. Bloch, The 'Higgs' amplitude mode at the two-dimensional superfluid/Mott insulator transition, Nature (London) **487**, 454 (2012).

[13] A. Behrle, T. Harrison, J. Kombe, K. Gao, M. Link, J. S. Bernier, C. Kollath, and M. Köhl, Higgs mode in a strongly interacting fermionic superfluid, Nat. Phys. **14**, 781 (2018).

[14] V. E. Zakharov and A. M. Rubenchik, Instability of waveguides and solitons in nonlinear media, Sov. Phys.—JETP **38**, 494 (1974).

[15] C. A. Jones, S. J. Putterman, and P. H. Roberts, Motions in a Bose condensate. V. Stability of solitary wave solutions of non-linear Schrodinger equations in two and three dimensions, J. Phys. A: Math. Gen. **19**, 2991 (1986).

[16] J. Brand and W. P. Reinhardt, Solitonic vortices and the fundamental modes of the "snake instability": Possibility of

observation in the gaseous Bose-Einstein condensate, Phys. Rev. A **65**, 043612 (2002).

[17] A. Muñoz Mateo and J. Brand, Chladni Solitons and the Onset of the Snaking Instability for Dark Solitons in Confined Superfluids, Phys. Rev. Lett. **113**, 255302 (2014).

[18] P. G. Kevrekidis, I. Danaila, J.-G. Caputo, and R. Carretero-González, Planar and radial kinks in nonlinear Klein-Gordon models: Existence, stability, and dynamics, Phys. Rev. E **98**, 052217 (2018).

[19] N.-E. Guenther, P. Massignan, and A. L. Fetter, Quantized superfluid vortex dynamics on cylindrical surfaces and planar annuli, Phys. Rev. A **96**, 063608 (2017).

[20] L. A. Toikka and J. Brand, Asymptotically solvable model for a solitonic vortex in a compressible superfluid, New J. Phys. **19**, 023029 (2017).

[21] B. Jackson, J. F. McCann, and C. S. Adams, Vortex line and ring dynamics in trapped Bose-Einstein condensates, Phys. Rev. A **61**, 013604 (1999).

[22] S. A. McGee and M. J. Holland, Rotational dynamics of vortices in confined Bose-Einstein condensates, Phys. Rev. A **63**, 043608 (2001).

[23] D. E. Sheehy and L. Radzihovsky, Vortices in spatially inhomogeneous superfluids, Phys. Rev. A **70**, 063620 (2004).

[24] J. Denschlag, J. E. Simsarian, D. L. Feder, C. W. Clark, L. A. Collins, J. Cubizolles, L. Deng, E. W. Hagley, K. Helmerson, W. P. Reinhardt, S. L. Rolston, B. I. Schneider, and W. D. Phillips, Generating solitons by phase engineering of a Bose-Einstein condensate, Science **287**, 97 (2000).

[25] S. Burger, K. Bongs, S. Dettmer, W. Ertmer, K. Sengstock, A. Sanpera, G. V. Shlyapnikov, and M. Lewenstein, Dark Solitons in Bose-Einstein Condensates, Phys. Rev. Lett. **83**, 5198 (1999).

[26] M. W. Zwierlein, J. R. Abo-Shaeer, A. Schirotzek, C. H. Schunck, and W. Ketterle, Vortices and superfluidity in a strongly interacting Fermi gas, Nature (London) **435**, 1047 (2005).

[27] M. J. H. Ku, W. Ji, B. Mukherjee, E. Guardado-Sanchez, L. W. Cheuk, T. Yefsah, and M. W. Zwierlein, Motion of a Solitonic Vortex in the BEC-BCS Crossover, Phys. Rev. Lett. **113**, 065301 (2014).

[28] W. Van Alphen, H. Takeuchi, and J. Tempere, Crossover between snake instability and Josephson instability of dark solitons in superfluid fermi gases, Phys. Rev. A **100**, 023628 (2019).

[29] J. Bardeen and M. J. Stephen, Theory of the motion of vortices in superconductors, Phys. Rev. **140**, A1197 (1965).

[30] P. Ao and D. J. Thouless, Berry's Phase and the Magnus Force for a Vortex Line in a Superconductor, Phys. Rev. Lett. **70**, 2158 (1993).

[31] S. N. Klimin, J. Tempere, and J. T. Devreese, Finite-temperature effective field theory for dark solitons in superfluid Fermi gases, Phys. Rev. A **90**, 053613 (2014).

[32] S. N. Klimin, J. Tempere, G. Lombardi, and J. T. Devreese, Finite temperature effective field theory and two-band superfluidity in Fermi gases, Eur. Phys. J. B **88**, 122 (2015).

[33] G. Lombardi, W. Van Alphen, S. N. Klimin, and J. Tempere, Soliton-core filling in superfluid Fermi gases with spin imbalance, Phys. Rev. A **93**, 013614 (2016).

[34] W. Van Alphen, G. Lombardi, S. N. Klimin, and J. Tempere, Dark soliton collisions in superfluid Fermi gases, New J. Phys. **20**, 053052 (2018).

[35] S. Fagnocchi, S. Finazzi, S. Liberati, M. Kormos, and A. Trombettoni, Relativistic Bose-Einstein condensates: A new system for analogue models of gravity, New J. Phys. **12**, 095012 (2010).

[36] H. E. Haber and H. A. Weldon, Thermodynamics of an Ultra-relativistic Ideal Bose Gas, Phys. Rev. Lett. **46**, 1497 (1981).

[37] M. Grether, M. de Llano, and G. A. Baker, Bose-Einstein Condensation in the Relativistic Ideal Bose Gas, Phys. Rev. Lett. **99**, 200406 (2007).

[38] K. Huang, H.-B. Low, and R.-S. Tung, Scalar field cosmology II: Superfluidity, quantum turbulence, and inflation, Int. J. Mod. Phys. A **27**, 1250154 (2012).

[39] J. Magaña, T. Matos, A. Suárez, and F. J. Sánchez-Salcedo, Structure formation with scalar field dark matter: The field approach, J. Cosmol. Astropart. Phys. **2012**, 003 (2012).

[40] C. Xiong, M. R. Good, Y. Guo, X. Liu, and K. Huang, Relativistic superfluidity and vorticity from the nonlinear Klein-Gordon equation, Phys. Rev. D **90**, 125019 (2014).

[41] M. Colpi, S. L. Shapiro, and I. Wasserman, Boson Stars: Gravitational Equilibria of Self-Interacting Scalar Fields, Phys. Rev. Lett. **57**, 2485 (1986).

[42] P.-H. Chavanis and T. Harko, Bose-Einstein condensate general relativistic stars, Phys. Rev. D **86**, 064011 (2012).

[43] A. Suárez and P.-H. Chavanis, Hydrodynamic representation of the Klein-Gordon-Einstein equations in the weak field limit: General formalism and perturbations analysis, Phys. Rev. D **92**, 023510 (2015).

[44] C. J. Pethick and H. Smith, *Bose-Einstein Condensation in Dilute Gases*, 2nd ed. (Cambridge University Press, Cambridge, 2008).

[45] H. Feshbach and F. Villars, Elementary relativistic wave mechanics of spin 0 and spin 1/2 particles, Rev. Mod. Phys. **30**, 24 (1958).

[46] O. Törnkvist and E. Schröder, Vortex Dynamics in Dissipative Systems, Phys. Rev. Lett. **78**, 1908 (1997).

[47] A. J. Groszek, D. M. Paganin, K. Helmerson, and T. P. Simula, Motion of vortices in inhomogeneous Bose-Einstein condensates, Phys. Rev. A **97**, 023617 (2018).

[48] See Supplemental Material at http://link.aps.org/supplemental/10.1103/PhysRevResearch.3.043109 for a movie.

[49] W. Bao, D. Jaksch, and P. A. Markowich, Numerical solution of the Gross-Pitaevskii equation for Bose-Einstein condensation, J. Comput. Phys. **187**, 318 (2003).

[50] W. J. Kwon, G. D. Pace, K. Xhani, L. Galantucci, A. M. Falconi, M. Inguscio, F. Scazza, and G. Roati, Sound emission and annihilations in a programmable quantum vortex collider, arXiv:2105.15180.

[51] C. Barenghi and N. G. Parker, *A Primer on Quantum Fluids* (Springer, Cham, 2016).

[52] A. Kolmogorov, The local structure of turbulence in incompressible viscous fluid for very large Reynolds numbers, Dokl. Akad. Nauk SSSR **30**, 301 (1941).

[53] K. Hueck, N. Luick, L. Sobirey, J. Siegl, T. Lompe, and H. Moritz, Two-Dimensional Homogeneous Fermi Gases, Phys. Rev. Lett. **120**, 060402 (2018).

[54] L. Sobirey, N. Luick, M. Bohlen, H. Biss, H. Moritz, and T. Lompe, Observation of superfluidity in a strongly correlated two-dimensional Fermi gas, Science **372**, 844 (2021).

<div align="center">

Supplemental Material for
Vortex and soliton dynamics in particle-hole symmetric superfluids

</div>

<div align="center">

Jim Skulte,[1,2] Lukas Broers,[1] Jayson G. Cosme,[3] and Ludwig Mathey[1,2]

[1]*Zentrum für Optische Quantentechnologien and Institut für Laserphysik, Universität Hamburg, 22761 Hamburg, Germany*
[2]*The Hamburg Center for Ultrafast Imaging, Luruper Chaussee 149, 22761 Hamburg, Germany*
[3]*National Institute of Physics, University of the Philippines, Diliman, Quezon City 1101, Philippines*

</div>

<div align="center">

CONTENTS

</div>

<div align="center">

I. FESHBACH-VILLARS FORMALISM

</div>

We want to rewrite the KG equations in a Hamiltonian form of

$$i\partial_t \Psi = H\Psi \ . \tag{1}$$

This can be done via the so called Feshbach-Villars formalism [1]. The Klein-Gordon equation reads

$$\partial_t^2 \psi(r,t) = \nabla^2 \psi(x,t) + V\left(|\psi|^2\right)\psi(r,t) + i\mu_{\rm Q}\partial_t\psi \ . \tag{2}$$

The conjugate momentum is defined as $\Pi = \frac{\partial \mathcal{L}}{\partial(\partial_t\psi)} = \partial_t\bar{\psi} + i\mu_Q\bar{\psi}$. The equations of motion read

$$\partial_t\psi = \bar{\Pi} + i\mu_Q\psi \tag{3}$$

$$\partial_t\Pi = \nabla^2\bar{\psi}(x,t) + V\left(|\psi|^2\right)\bar{\psi}(r,t) - i\mu_{\rm Q}\Pi. \tag{4}$$

The Feshbach-Villars particles or also sometimes called the particles $\psi^{\rm p}$ and antiparticles/holes $\psi^{\rm a}$ are introduced as the following linear combination of the conjugate momentum and the KG field ψ

$$\psi^{\rm p/a} = \frac{1}{\sqrt{2}}\left(\psi \pm i\Pi\right) \ . \tag{5}$$

That is, we can write

$$\psi = \frac{1}{\sqrt{2}}(\psi^{\rm p} + \psi^{\rm a}) \tag{6}$$

$$\Pi = \frac{i}{\sqrt{2}}(\psi^{\rm a} - \psi^{\rm p}) \ . \tag{7}$$

Note that the conserved charge Q in this basis simplifies to the difference between two positive definite densities as

$$Q = \int d^2x \left(|\psi^{\rm p}| - |\psi^{\rm a}|^2\right) \ . \tag{8}$$

The equations read

$$i\partial_t \psi^{\mathrm{p}} = -\frac{\nabla^2}{2}(\psi^{\mathrm{a}} + \psi^{\mathrm{p}}) - (\mu_{\mathrm{Q}} + \mu)\psi^{\mathrm{p}} - V\psi^{\mathrm{p}} + \frac{g}{4}|(\psi^{\mathrm{a}} + \psi^{\mathrm{p}})|^2(\psi^{\mathrm{a}} + \psi^{\mathrm{p}}) \tag{9}$$

$$i\partial_t \psi^{\mathrm{a}} = +\frac{\nabla^2}{2}(\psi^{\mathrm{a}} + \psi^{\mathrm{p}}) + (\mu_{\mathrm{Q}} + \mu)\psi^{\mathrm{a}} + V\psi^{\mathrm{a}} - \frac{g}{4}|(\psi^{\mathrm{a}} + \psi^{\mathrm{p}})|^2(\psi^{\mathrm{a}} + \psi^{\mathrm{p}}) \ . \tag{10}$$

II. LOCAL VELOCITY FIELD

A. ψ and Π basis

We start by denoting our field and the canonical momentum as

$$\psi(r, t = 0) \equiv \psi_{r,0} = P(\vec{z} - \vec{z}_0)\, A \exp(i\theta) \ , \tag{11}$$

$$\Pi(r, t = 0) \equiv \Pi_{r,0} = \bar{P}(\vec{z} - \vec{z}_0)\left(\dot{A} + iA\left[\mu_{\mathrm{Q}} - \dot{\theta}\right]\right)\exp(-i\theta) \tag{12}$$

where $P((x,y)^{\mathrm{T}}) = x + iy$ and the vortex core position is located at $\vec{z}_0 = (x_0, y_0)^{\mathrm{T}}$. Note that $A(r,t)$ and $\theta(r,t)$ are real valued and smoothly varying functions of space and time. This field features a vortex, where $P(\vec{z} - \vec{z}_0)$ captures both the phase winding and the condensate density around the vortex core. We can propagate the field for an infinitesimally small Δt according to the Klein-Gordon equation as:

$$\psi_{r,\Delta_t} \equiv \psi_{r,0} + \Delta t\left(\bar{\Pi}_{r,0} + i\mu_{\mathrm{Q}}\psi_{r,0}\right) \ , \tag{13}$$

$$\Pi_{r,\Delta_t} \equiv \Pi_{r,0} + \Delta t\left(\nabla^2 \bar{\psi}_{r,0} + V\left(|\psi_{r,0}|^2\right)\bar{\psi}_{r,0} - i\mu_{\mathrm{Q}}\Pi_{r,0}\right) \ . \tag{14}$$

Using $\nabla\bar{z} = (1, -i)^{\mathrm{T}} = \vec{e}_x - i\vec{e}_y$ and $\nabla^2 z = 0$, we obtain

$$\nabla^2 \bar{\psi}_{r,0} = [\bar{P}(\vec{z} - \vec{z}_0)\nabla^2 A + 2(1, -i)^{\mathrm{T}} \cdot \vec{\nabla}A - 2i\{\bar{P}(\vec{z} - \vec{z}_0)\vec{\nabla}A + A\,(1, -i)^{\mathrm{T}}\} \cdot \vec{\nabla}\theta$$
$$+ \bar{P}(\vec{z} - \vec{z}_0)A\{-i\nabla^2\theta - (\vec{\nabla}\theta)^2\}]\exp(i\theta) \ . \tag{15}$$

The canonical momentum in Eq. (12) vanishes at the vortex core position $\vec{z}_0$ at $t = 0$. Thus, we can write the new vortex core position as $\vec{z}_{\Delta t} = \vec{z}_0 + \vec{v}\Delta t$ after the small time Δt, where the canonical momentum still vanishes. Evaluating $\bar{\Pi}(z_{\Delta t}, \Delta t)$, and demanding it to be zero while only keeping lowest order terms in Δt, we obtain

$$0 \approx \bar{\Delta}z\left(\dot{A} - iA(\dot{\theta} - \mu_{\mathrm{Q}})\right) + \Delta t\left(2(1, -i)^{\mathrm{T}} \cdot \vec{\nabla}A + 2A\,(1, i)^{\mathrm{T}} \cdot \vec{\nabla}\theta\right) \ , \tag{16}$$

where we used $\bar{P}(\vec{z}_{\Delta t} - \vec{z}_0) = \bar{\Delta}z$. We rearrange this and take the complex conjugate to obtain an expression for the velocity as

$$P(\vec{v}) \equiv \frac{\Delta z}{\Delta t} = -2\frac{(1, -i)^{\mathrm{T}} \cdot \vec{\nabla}A - A\,(i, 1)^{\mathrm{T}} \cdot \vec{\nabla}\theta}{\dot{A} + iA(\dot{\theta} - \mu_{\mathrm{Q}})} \ . \tag{17}$$

Similarly, the velocity field for the GP fluid can be obtained as [2, 3]

$$P(\vec{v}) \equiv \frac{\Delta z}{\Delta t} = (-i, 1)^{\mathrm{T}} \cdot \vec{\nabla}A + A\,(1, i)^{\mathrm{T}} \cdot \vec{\nabla}\theta \ . \tag{18}$$

The discussion changes if we choose $\Pi = 0$, $(Q = 0)$ as the initial state. The derivation holds up to Eq. (16). From this equation we obtain

$$0 \approx \Delta t\left(2(1, -i)^{\mathrm{T}} \cdot \vec{\nabla}A + 2A\,(1, i)^{\mathrm{T}} \cdot \vec{\nabla}\theta\right) \ . \tag{19}$$

As $\Delta t \neq 0$ we deduce that

$$\left(2(1, -i)^{\mathrm{T}} \cdot \vec{\nabla}A + 2A\,(1, i)^{\mathrm{T}} \cdot \vec{\nabla}\theta\right) = 0 \ . \tag{20}$$

Hence, there is no dynamics up to lowest order for the canonical momentum Π and the field ψ as can be seen from plugging this result into (14).

B. Particle and antiparticle basis

In the following we will redo the steps as before but now using the particle and antiparticle fields to obtain a physical explanation of the vanishing velocity field for the zero charge case.
We denote our fields as

$$\psi^{a/p}(r, t = 0) \equiv \psi^{a/p}_{r,0} = P\left(\vec{z} - \vec{z_0}\right) A^{a/p} \exp\left(i\theta\right) \ , \tag{21}$$

where we have assumed that the two fields stay in phase. Note that for the choice of $A^a = A^p$ the Noether charge is vanishing. For small times Δt the fields can be propagated in time via

$$\psi^{a/p}_{r,\Delta_t} \equiv \psi^{a/p}_{r,0} \mp i\Delta t \left(\frac{\nabla^2}{2}(\psi^a_{r,0} + \psi^p_{r,0}) - (\mu_Q + \mu)\psi^{a/p}_{r,0} + \frac{g}{4}|(\psi^a_{r,0} + \psi^p_{r,0})|^2(\psi^a_{r,0} + \psi^p_{r,0})\right) \ . \tag{22}$$

By performing the same steps as for the ψ and Π basis we obtain for the local velocity fields

$$P(\vec{v^p}) = \frac{(-i, 1)^T \cdot \vec{\nabla}(A^p + A^a) + (A^p + A^a)\,(1, i)^T \cdot \vec{\nabla}\theta}{A^p} \tag{23}$$

$$P(\vec{v^a}) = -\frac{(-i, 1)^T \cdot \vec{\nabla}(A^p + A^a) + (A^p + A^a)\,(1, i)^T \cdot \vec{\nabla}\theta}{A^a} \ . \tag{24}$$

We note that $\vec{v^p} A^p = -\vec{v^a} A^a$ and hence

$$\vec{v^p} = -\frac{A^a}{A^p} \vec{v^a} \ . \tag{25}$$

The velocity field of the ψ field can be recovered by the linear superposition as

$$\vec{v^\psi} = \frac{1}{\sqrt{2}}\left(\vec{v^p} + \vec{v^a}\right) = \sqrt{2}\left(1 - \frac{A^a}{A^p}\right)\vec{v^p} \ . \tag{26}$$

We can understand the vanishing local velocity of the total field ψ at vanishing Noether charge $A^p = A^a$ as the result of two counter rotating fields consisting of the particle and antiparticle field. This results is in a similar spirit as the zero magnetization results for two component spinors in [4].

III. THOMAS-FERMI-APPROXIMATION

In order to find steady state solutions we demand that $\partial_t \psi = 0$ and $\partial_t \Pi = 0$, while neglecting the kinetic energy. This approximation is justified for large particle numbers and repulsive interactions [5]. We obtain the two equations

$$0 = \bar{\Pi} + i\mu_Q \psi \tag{27}$$

$$0 = \left(V(x) - \mu + g|\psi|^2\right) \bar{\psi}(r, t) - i\mu_Q \Pi. \tag{28}$$

We find for the region, where $V(x) \leq (\mu + \mu_Q^2)$

$$|\psi(x)|^2 = \frac{\mu + \mu_Q^2 - V(x)}{g} \tag{29}$$

$$\Pi(x) = -i\mu_Q \bar{\psi}(x) \tag{30}$$

and $\psi = \Pi = 0$ otherwise. The boundary of the fluid is at $V(x) = (\mu + \mu_Q^2)$.

IV. IMAGINARY TIME METHOD FOR PARTICLE-HOLE SYMMETRIC FLUIDS

The particle-hole symmetry enforces the energy spectrum to be symmetric around $E = 0$. We will follow the same line of arguments as in [6]. For Schrödinger like equations the fields can be propagated via

$$\psi^{p/a}(x, t + \Delta t) = e^{-i\Delta t H}\psi^{p/a}(x, t) \ . \tag{31}$$

Expanding the fields in energy modes as $\psi^{\mathrm{p/a}}(x,t) = \sum_m a_m^{p/a}(t)\phi_m^{p/a}(x)$, we obtain

$$\psi^{\mathrm{p/a}}(x,t+\Delta t) = \sum_m a_m^{p/a}(t)\phi_m^{p/a}(x)e^{\mp i\Delta t E_m} \tag{32}$$

To ensure that the wavefunction decays into the lowest energy state we rotate Δt for the particles and antiparticles as $\Delta t \to \mp i\Delta t$. By doing so we obtain

$$\psi^{\mathrm{p/a}}(x,t+\Delta t) = \sum_m a_m^{p/a}(t)\phi_m^{p/a}(x)e^{-\Delta t E_m} \ . \tag{33}$$

After each propagating step we fix the total number

$$N^{p/a} = \int d^2x |\psi^{\mathrm{p/a}}|^2 \ , \tag{34}$$

which ensures that the total charge Q stays constant.

[1] H. Feshbach and F. Villars, Elementary relativistic wave mechanics of spin 0 and spin 1/2 particles, Rev. Mod. Phys. **30**, 24 (1958).
[2] O. Törnkvist and E. Schröder, Vortex Dynamics in Dissipative Systems, Physical Review Letters **78**, 1908–1911 (1997).
[3] A. J. Groszek, D. M. Paganin, K. Helmerson, and T. P. Simula, Motion of vortices in inhomogeneous Bose-Einstein condensates, Phys. Rev. A **97**, 023617 (2018).
[4] A. M. Turner, Mass of a spin vortex in a bose-einstein condensate, Phys. Rev. Lett. **103**, 080603 (2009).
[5] C. J. Pethick and H. Smith, *Bose–Einstein Condensation in Dilute Gases*, 2nd ed. (Cambridge University Press, 2008).
[6] C. Barenghi and N. G. Parker, A Primer on Quantum Fluids, SpringerBriefs in Physics 10.1007/978-3-319-42476-7 (2016).

4 Conclusion and Outlook

In this thesis, we have discussed various non-equilibrium phases in both atom-cavity systems [1–10] and particle-hole symmetric superfluids [11]. We have shown how dissipation can stabilise new emergent phases in light-matter coupled systems. First, we have studied the stability of a dissipative TC against spatial confinement and contact interactions [1], as well as against different dissipation strengths [2]. It is worth pointing out that while contact interactions and strong spatial confinement often destabilise the time crystalline phase and should be avoided in experiments, dissipation can actually stabilies the TCs. It increases the robustness against noise in the drive and increases the TC regime within the phase diagram. We have provided insights into the proposal of an incommensurate TC [52] by modelling the systems with a toy-model [3,4] capturing the effect. The reduced model allowed us to find analytical insights into the resonance conditions for this phenomenon and to explore the physics for applying a stronger drive [5]. Together with the group of Andreas Hemmerich, we have been able to observe limit cycles in an ultracold atom experiment and together with further analysis and our theoretical simulations have been able to show that this LC can be understood as the first realisation of a CTC [6]. Following up on this work, we have found a generalised minimal model to describe these previous findings [7] by the use of a stability analyses and suggested other platforms, which can be reduced to similar minimal models hosting the same kind of limit cycle for certain parameter regimes. We have further showed by adding a periodic drive the first realisation of a transition from a CTC to a DTC by measuring the phase delay between the driving field and the light field oscillations. In the language of nonlinear physics we have, for the first time, demonstrated entrainment in a quantum gas experiment [8]. We have contributed to the field of atomtronics by using our knowledge about the cavity-BEC platform to propose a new rotation sensor [9], which translates changes in the external rotations applied to changes in the number of photons leaking out of the cavity. We have used numerical methods as well as analytical tools to estimate the sensitivity, which can be achieved using realistic parameter from existing experiments. Further, we have shown how a resonantly tuned cavity can be used to manipulate active Raman modes [10] and discuss various platforms to observe this phenomenon.

Finally, we have studied the influence of particle-hole symmetry on the dynamics in superfluids as shown in publication [11] and find, due to the missing Magnus force for the particle-hole symmetric case, qualitatively different dynamics for two attractive vortices next to each other. We also applied this method to the BEC-BCS crossover. We have used QMC data to fit our effective field parameter to the experiment and found great agreement between the collective modes across the crossover.

Outlook

In the previous section I summarized the results during my PhD. In this section I would like to briefly highlight some potential follow-up research topics and trends.

After the first realisation of a limit cycle in a quantum simulator [6], many experiments have followed [151, 152, 237] and successfully realised limit cycle in their experiments. Two possible explorations seem to be within reach. First, while all of these experiments used some quantum simulator, they all have in common that they operate in a regime with large atom numbers. It would be interesting to push the systems to small atom numbers, where quantum effects become crucial and dominant. First theoretical work towards this direction has been done in [192–194, 238–240], but to the best of my knowledge, experimental studies are still lacking. It would be interesting to measure the Feigenbaum constant [191, 241] in a purely quantum system to see, if there is any modification due to quantum mechanics or if this universal constant is unchanged. This can be studied by measuring the recurrence rate of period-doubling bifurcations towards chaotic dynamics. We recently did first steps towards this direction in a joint project with the group of Andreas Hemmerich and Jayson Cosme, and a manuscript is currently in preparation. We have shown by the use of Floquet-multiplier that further bifurcations can be studied for stronger light-matter coupling strength with the use of our proposed toy model in publication [7]. Likewise, we discuss how the type of bifurcation can be altered from a period-doubling bifurcation to a Neimark-Sacker bifurcation by change of the level spacing between the two lower energy states. We find that for the two-dimensional scenario studied in the experiment that a Neimark-Sacker bifurcation is present and confirm this prediction by the first study of the Neimark-Sacker bifurcation in an ultracold gas experiment.

Secondly, it might be fruitful to study many coupled LCs. This will allow studying quantum synchronisation [242,243] in a very controlled way. It would be interesting to see how these networks compare to classical systems, which are naturally non-reciprocal [244]. Further, these networks might be used for some sort of quantum machine learning inspired from neuroscience [186], where the nonlinearities are within each subsystem containing a limit cycle and the connection between subsystems can be linear a priori. These networks relate to echo state networks [245, 246] and their exploration both numerical and experimental might be promising. The use of tweezer arrays inside of cavities as has been recently reported in [247] can be a useful tool to carry out these studies.

Another promising research line could be the further exploration of quantum sensors using atom-cavity systems like our proposed sensor in publication [9]. It might be worth considering different platforms with different, possibly more favorably, parameters for sensing in certain frequency regimes. I believe that this platform, together with our results on LC, is a promising platform to build early warning signals working close to the Hopf bifurcation [172, 248–250].

Finally, I would like to highlight our approach to use the NLKG equation to describe complicated systems as the BEC-BCS crossover. While by no means we are able to capture the full glory of the system, by adding a symmetry, namely the particle-hole symmetry on the BCS side, one is able to describe certain aspects of the collective exci-

tation spectrum very successfully. Our approach highlights how different spatial modes can be used to design the collective mode structure within the crossover. Further, this approach, after mapping the parameter to the experiment, as we did for the BEC-BCS crossover, could be used in other physical systems with an approximate particle-hole symmetry.

Acknowledgements

My thesis would not have been possible without the contributions and support of the following people.

First of all, I would like to thank my supervisor Ludwig for his seemingly endless energy and passion for physics, which has always motivated me. The discussions have always been inspiring and I have learnt a lot from those along the way, not only in physics, but have also helped me to grow personally.

I would also like to thank my dear colleague and friend Jayson for his great support at all stages of my PhD. Our discussions and collaborations have been a key driver of my research.

I would also like to thank my experimental collaborators, especially Andreas, Hans and Popla. I have always enjoyed our discussions and your perspectives have certainly helped me to sharpen my understanding of physics.

Furthermore, my PhD would not have been the same without the colleagues in Ludwig's group. Many thanks to Lukas, Nico and the whole 206 office, who have always made working in the office something special.

I would also like to thank my friends at the Institute, with whom I have had a lot of coffee breaks over the years.

Special thanks to my parents for their unconditional and sheer unlimited support.

Most of all I would like to thank Vanessa for making my life complete.

Bibliography

[1] R.J.L. Tuquero, J. Skulte, L. Mathey, and J.G. Cosme. Dissipative time crystal in an atom-cavity system: Influence of trap and competing interactions. *Phys. Rev. A*, 105:043311, Apr 2022.

[2] J.G. Cosme, J. Skulte, and L. Mathey. Bridging closed and dissipative discrete time crystals in spin systems with infinite-range interactions. *Physical Review B*, 108(2), July 2023.

[3] J. Skulte, P. Kongkhambut, H. Keßler, A. Hemmerich, L. Mathey, and J.G. Cosme. Parametrically driven dissipative three-level dicke model. *Phys. Rev. A*, 104:063705, Dec 2021.

[4] P. Kongkhambut, H. Keßler, J. Skulte, L. Mathey, J. G. Cosme, and A. Hemmerich. Realization of a periodically driven open three-level dicke model. *Phys. Rev. Lett.*, 127:253601, Dec 2021.

[5] J. Skulte, P. Kongkhambut, S. Rao, L. Mathey, H. Keßler, A. Hemmerich, and J.G. Cosme. Condensate formation in a dark state of a driven atom-cavity system. *Phys. Rev. Lett.*, 130:163603, Apr 2023.

[6] P. Kongkhambut, J. Skulte, L. Mathey, J.G. Cosme, A. Hemmerich, and H. Keßler. Observation of a continuous time crystal. *Science*, 377(6606):670–673, 2022.

[7] J. Skulte, P. Kongkhambut, H. Keßler, A. Hemmerich, L. Mathey, and J.G. Cosme. Realizing limit cycles in dissipative bosonic systems, 2024.

[8] P. Kongkhambut, J.G. Cosme, J. Skulte, M.A. Moreno Armijos, L. Mathey, A. Hemmerich, and H. Keßler. Observation of a phase transition from a continuous to a discrete time crystal, 2024.

[9] J. Skulte, J.G. Cosme, and L. Mathey. Quantum rotation sensor with real-time readout based on an atom-cavity system, 2023.

[10] H.P. Ojeda Collado, M.H. Michael, J. Skulte, A. Rubio, and L. Mathey. Equilibrium parametric amplification in raman-cavity hybrids, 2023.

[11] J. Skulte, L. Broers, J.G. Cosme, and L. Mathey. Vortex and soliton dynamics in particle-hole-symmetric superfluids. *Phys. Rev. Res.*, 3:043109, Nov 2021.

[12] S.H. Strogatz. *Nonlinear Dynamics and Chaos: With Applications to Physics, Biology, Chemistry and Engineering.* Studies in nonlinearity. Westview, 2000.

[13] A.T. Winfree. Biological rhythms and the behavior of populations of coupled oscillators. *Journal of Theoretical Biology*, 16(1):15–42, 1967.

[14] R.M. May. Limit cycles in predator-prey communities. *Science*, 177(4052):900–902, 1972.

[15] Y.A. Kuznetsov. *Elements of Applied Bifurcation Theory (2nd Ed.)*. Springer-Verlag, Berlin, Heidelberg, 1998.

[16] R.P. Feynman. Simulating physics with computers. *International Journal of Theoretical Physics*, 21(6):467–488, 1982.

[17] I. Bloch, J. Dalibard, and S. Nascimbène. Quantum simulations with ultracold quantum gases. *Nature Physics*, 8(4):267–276, 2012.

[18] K.B. Davis, M.-O. Mewes, M.R. Andrews, N.J. van Druten, D.S. Durfee, D.M. Kurn, and W. Ketterle. Bose-einstein condensation in a gas of sodium atoms. *Phys. Rev. Lett.*, 75:3969–3973, Nov 1995.

[19] M.H. Anderson, J.R. Ensher, M.R. Matthews, C.E. Wieman, and E.A. Cornell. Observation of bose-einstein condensation in a dilute atomic vapor. *Science*, 269(5221):198–201, 1995.

[20] I. Bloch. Ultracold quantum gases in optical lattices. *Nature Physics*, 1(1):23–30, 2005.

[21] D. Jaksch and P. Zoller. The cold atom hubbard toolbox. *Annals of Physics*, 315(1):52–79, 2005. Special Issue.

[22] Sanpera A. Ahufinger V. Damski B. Sen(De) A. Lewenstein, M. and U. Sen. Ultracold atomic gases in optical lattices: mimicking condensed matter physics and beyond. *Advances in Physics*, 56(2):243–379, 2007.

[23] C. Gross and Bloch. I. Quantum simulations with ultracold atoms in optical lattices. *Science*, 357(6355):995–1001, 2017.

[24] M. Greiner, O. Mandel, T. Esslinger, T.W. Hänsch, and I. Bloch. Quantum phase transition from a superfluid to a mott insulator in a gas of ultracold atoms. *Nature*, 415(6867):39–44, 2002.

[25] S. Sachdev. *Quantum Phase Transitions*. Cambridge University Press, 2 edition, 2011.

[26] M. Srednicki. *Quantum field theory*. Cambridge University Press, 1 2007.

[27] F. Strocchi. *Symmetry Breaking in Quantum Systems*, pages 115–122. Springer Berlin Heidelberg, Berlin, Heidelberg, 2008.

[28] F. Schlawin, D.M. Kennes, and M.A. Sentef. Cavity quantum materials. *Applied Physics Reviews*, 9(1):011312, 02 2022.

[29] J. Bloch, A. Cavalleri, V. Galitski, M. Hafezi, and A. Rubio. Strongly correlated electron–photon systems. *Nature*, 606(7912):41–48, 2022.

[30] D.M. Kennes and A. Rubio. *A New Era of Quantum Materials Mastery and Quantum Simulators In and Out of Equilibrium*, pages 1–39. Springer International Publishing, 2023.

[31] J. Struck, C. Ölschläger, M. Weinberg, P. Hauke, J. Simonet, A. Eckardt, M. Lewenstein, K. Sengstock, and P. Windpassinger. Tunable gauge potential for neutral and spinless particles in driven optical lattices. *Phys. Rev. Lett.*, 108:225304, May 2012.

[32] T. Oka and S. Kitamura. Floquet engineering of quantum materials. *Annual Review of Condensed Matter Physics*, 10:387–408, 2019.

[33] F. Harper, R. Roy, M.S. Rudner, and S.L. Sondhi. Topology and broken symmetry in floquet systems. *Annual Review of Condensed Matter Physics*, 11:345–368, 2020.

[34] M. Nuske, L. Broers, B. Schulte, G. Jotzu, S.A. Sato, A. Cavalleri, A. Rubio, J. W. McIver, and L. Mathey. Floquet dynamics in light-driven solids. *Phys. Rev. Res.*, 2:043408, Dec 2020.

[35] A.T. Winfree. *When time breaks down : the three-dimensional dynamics of electrochemical waves and cardiac arrhythmias*. Princeton University Press, Princeton, N.J., 1987.

[36] F. Wilczek. Quantum time crystals. *Phys. Rev. Lett.*, 109:160401, Oct 2012.

[37] A. Shapere and F. Wilczek. Classical time crystals. *Phys. Rev. Lett.*, 109:160402, Oct 2012.

[38] C.W.S. Chang, C. Sabín, P. Forn-Díaz, F. Quijandría, A.M. Vadiraj, I. Nsanzineza, G. Johansson, and C.M. Wilson. Observation of three-photon spontaneous parametric down-conversion in a superconducting parametric cavity. *Phys. Rev. X*, 10:011011, Jan 2020.

[39] F. Minganti, L. Garbe, A. Le Boité, and S. Felicetti. Non-gaussian superradiant transition via three-body ultrastrong coupling. *Phys. Rev. A*, 107:013715, Jan 2023.

[40] B. Zare Rameshti, S. Viola Kusminskiy, J.A. Haigh, K. Usami, D. Lachance-Quirion, Y. Nakamura, C.-M. Hu, H.X. Tang, G.E.W. Bauer, and Y.M. Blanter. Cavity magnonics. *Physics Reports*, 979:1–61, 2022. Cavity Magnonics.

[41] M. Mitrano, A. Cantaluppi, D. Nicoletti, S. Kaiser, A. Perucchi, S. Lupi, P. Di Pietro, D. Pontiroli, M. Riccò, S. R. Clark, D. Jaksch, and A. Cavalleri. Possible light-induced superconductivity in k3c60 at high temperature. *Nature*, 530(7591):461–464, 2016.

[42] G. Homann, J.G. Cosme, and L. Mathey. Parametric control of meissner screening in light-driven superconductors. *New Journal of Physics*, 24(11):113007, Nov 2022.

[43] K. Baumann, C. Guerlin, F. Brennecke, and T. Esslinger. Dicke quantum phase transition with a superfluid gas in an optical cavity. *Nature*, 464(7293):1301–1306, 2010.

[44] J. Klinder, H. Keßler, M. Wolke, L. Mathey, and A. Hemmerich. Dynamical phase transition in the open dicke model. *Proceedings of the National Academy of Sciences*, 112(11):3290–3295, 2015.

[45] A.T. Black, H.W. Chan, and V. Vuletić. Observation of collective friction forces due to spatial self-organization of atoms: From rayleigh to bragg scattering. *Phys. Rev. Lett.*, 91:203001, Nov 2003.

[46] V.D. Vaidya, Y. Guo, R.M. Kroeze, K.E. Ballantine, A.J. Kollár, J. Keeling, and B.L. Lev. Tunable-range, photon-mediated atomic interactions in multimode cavity qed. *Phys. Rev. X*, 8:011002, Jan 2018.

[47] X. Zhang, Y. Chen, Z. Wu, J. Wang, J. Fan, S. Deng, and H. Wu. Observation of a superradiant quantum phase transition in an intracavity degenerate fermi gas. *Science*, 373(6561):1359–1362, 2021.

[48] V. Helson, T. Zwettler, F. Mivehvar, E. Colella, K. Roux, H. Konishi, H. Ritsch, and J.-P. Brantut. Density-wave ordering in a unitary fermi gas with photon-mediated interactions. *Nature*, 618(7966):716–720, 2023.

[49] F. Mivehvar, F. Piazza, T Donner, and H. Ritsch. Cavity qed with quantum gases: new paradigms in many-body physics. *Advances in Physics*, 70(1):1–153, 2021.

[50] H. Ritsch, P. Domokos, F. Brennecke, and T. Esslinger. Cold atoms in cavity-generated dynamical optical potentials. *Rev. Mod. Phys.*, 85:553–601, Apr 2013.

[51] J.G. Cosme, C. Georges, A. Hemmerich, and L. Mathey. Dynamical control of order in a cavity-bec system. *Phys. Rev. Lett.*, 121:153001, Oct 2018.

[52] J.G. Cosme, J. Skulte, and L. Mathey. Time crystals in a shaken atom-cavity system. *Phys. Rev. A*, 100:053615, Nov 2019.

[53] H. Keßler, J. Klinder, M. Wolke, and A. Hemmerich. Optomechanical atom-cavity interaction in the sub-recoil regime. *New Journal of Physics*, 16(5):053008, May 2014.

[54] J. Klinder, H. Keßler, C. Georges, J. Vargas, and A. Hemmerich. Bose–einstein condensates in an optical cavity with sub-recoil bandwidth. *Applied Physics B*, 122(12):299, 2016.

[55] P.B. Blakie, A.S. Bradley, M.J. Davis, R.J. Ballagh, and C.W. Gardiner. Dynamics and statistical mechanics of ultra-cold bose gases using c-field techniques. *Advances in Physics*, 57(5):363–455, 2008.

[56] A. Polkovnikov. Phase space representation of quantum dynamics. *Annals of Physics*, 325(8):1790–1852, 2010.

[57] A.C. Mathey, C.W. Clark, and L. Mathey. Decay of a superfluid current of ultra-cold atoms in a toroidal trap. *Phys. Rev. A*, 90:023604, Aug 2014.

[58] J. G. Cosme and O. Fialko. Thermalization in closed quantum systems: Semiclassical approach. *Phys. Rev. A*, 90:053602, Nov 2014.

[59] O.L. Acevedo, A. Safavi-Naini, J. Schachenmayer, M.L. Wall, R. Nandkishore, and A.M. Rey. Exploring many-body localization and thermalization using semiclassical methods. *Phys. Rev. A*, 96:033604, Sep 2017.

[60] W.K. Wootters. A wigner-function formulation of finite-state quantum mechanics. *Annals of Physics*, 176(1):1–21, 1987.

[61] J. Schachenmayer, A. Pikovski, and A.M. Rey. Many-body quantum spin dynamics with monte carlo trajectories on a discrete phase space. *Phys. Rev. X*, 5:011022, Feb 2015.

[62] K. Nagao, Y. Takasu, Y. Takahashi, and I. Danshita. Su(3) truncated wigner approximation for strongly interacting bose gases. *Phys. Rev. Res.*, 3:043091, Nov 2021.

[63] C.D. Mink, D. Petrosyan, and M. Fleischhauer. Hybrid discrete-continuous truncated wigner approximation for driven, dissipative spin systems. *Phys. Rev. Res.*, 4:043136, Nov 2022.

[64] J. Huber, A.M. Rey, and P. Rabl. Realistic simulations of spin squeezing and cooperative coupling effects in large ensembles of interacting two-level systems. *Phys. Rev. A*, 105:013716, Jan 2022.

[65] C. Gardiner and P. Zoller. *Quantum Noise: A Handbook of Markovian and Non-Markovian Quantum Stochastic Methods with Applications to Quantum Optics*. Springer Series in Synergetics. Springer, 2004.

[66] J. Schwinger. *Angular Momentum*, pages 149–181. Springer Berlin Heidelberg, Berlin, Heidelberg, 2001.

[67] S. Okubo. Algebraic identities among U (n) infinitesimal generators. *Journal of Mathematical Physics*, 16(3):528–535, Mar 1975.

[68] M. Hayn, C. Emary, and T. Brandes. Phase transitions and dark-state physics in two-color superradiance. *Phys. Rev. A*, 84:053856, Nov 2011.

[69] T. Holstein and H. Primakoff. Field dependence of the intrinsic domain magnetization of a ferromagnet. *Phys. Rev.*, 58:1098–1113, Dec 1940.

[70] M. Wagner. A nonlinear transformation of su(3)-spin-operators to bosonic operators. *Physics Letters A*, 53(1):1–2, 1975.

[71] A. Klein and E.R. Marshalek. Boson realizations of lie algebras with applications to nuclear physics. *Rev. Mod. Phys.*, 63:375–558, Apr 1991.

[72] C. Emary and T. Brandes. Chaos and the quantum phase transition in the dicke model. *Phys. Rev. E*, 67:066203, Jun 2003.

[73] V.M. Bastidas, C. Emary, B. Regler, and T. Brandes. Nonequilibrium quantum phase transitions in the dicke model. *Phys. Rev. Lett.*, 108:043003, Jan 2012.

[74] J. Larson and T. Mavrogordatos. *The Jaynes–Cummings Model and Its Descendants: Modern research directions.* IOP Publishing, Dec 2021.

[75] R.H. Dicke. Coherence in spontaneous radiation processes. *Phys. Rev.*, 93:99–110, Jan 1954.

[76] G. Ferioli, A. Glicenstein, I. Ferrier-Barbut, and A. Browaeys. A non-equilibrium superradiant phase transition in free space. *Nature Physics*, 19(9):1345–1349, 2023.

[77] N.E. Rehler and J.H. Eberly. Superradiance. *Phys. Rev. A*, 3:1735–1751, May 1971.

[78] S. Inouye, A.P. Chikkatur, D.M. Stamper-Kurn, J. Stenger, D.E. Pritchard, and W. Ketterle. Superradiant rayleigh scattering from a bose-einstein condensate. *Science*, 285(5427):571–574, 1999.

[79] J.P. Clemens, L. Horvath, B.C. Sanders, and H.J. Carmichael. Collective spontaneous emission from a line of atoms. *Phys. Rev. A*, 68:023809, Aug 2003.

[80] S.J. Masson and A. Asenjo-Garcia. Universality of dicke superradiance in arrays of quantum emitters. *Nature Communications*, 13(1):2285, 2022.

[81] S. Cardenas-Lopez, S. J. Masson, Z. Zager, and A. Asenjo-Garcia. Many-body superradiance and dynamical mirror symmetry breaking in waveguide qed. *Phys. Rev. Lett.*, 131:033605, Jul 2023.

[82] F. Haake, M.I. Kolobov, C. Fabre, E. Giacobino, and S. Reynaud. Superradiant laser. *Phys. Rev. Lett.*, 71:995–998, Aug 1993.

[83] D. Meiser, J. Ye, D.R. Carlson, and M.J. Holland. Prospects for a millihertz-linewidth laser. *Phys. Rev. Lett.*, 102:163601, Apr 2009.

[84] D. Meiser and M.J. Holland. Steady-state superradiance with alkaline-earth-metal atoms. *Phys. Rev. A*, 81:033847, Mar 2010.

210

[85] J. G. Bohnet, Z. Chen, J. M. Weiner, D. Meiser, M.J. Holland, and J.K. Thompson. A steady-state superradiant laser with less than one intracavity photon. *Nature*, 484(7392):78–81, 2012.

[86] M.A. Norcia and J.K. Thompson. Cold-strontium laser in the superradiant crossover regime. *Phys. Rev. X*, 6:011025, Mar 2016.

[87] K. Debnath, Y. Zhang, and K. Mølmer. Lasing in the superradiant crossover regime. *Phys. Rev. A*, 98:063837, Dec 2018.

[88] T. Laske, H. Winter, and A. Hemmerich. Pulse delay time statistics in a superradiant laser with calcium atoms. *Phys. Rev. Lett.*, 123:103601, Sep 2019.

[89] K. Hepp and E.H. Lieb. Equilibrium statistical mechanics of matter interacting with the quantized radiation field. *Phys. Rev. A*, 8:2517–2525, Nov 1973.

[90] K. Hepp and E.H. Lieb. On the superradiant phase transition for molecules in a quantized radiation field: the dicke maser model. *Annals of Physics*, 76(2):360–404, 1973.

[91] Y.K. Wang and F.T. Hioe. Phase transition in the dicke model of superradiance. *Phys. Rev. A*, 7:831–836, Mar 1973.

[92] H.J. Carmichael, C.W. Gardiner, and D.F. Walls. Higher order corrections to the dicke superradiant phase transition. *Physics Letters A*, 46(1):47–48, 1973.

[93] F.T. Hioe. Phase transitions in some generalized dicke models of superradiance. *Phys. Rev. A*, 8:1440–1445, Sep 1973.

[94] R. Chitra and O. Zilberberg. Dynamical many-body phases of the parametrically driven, dissipative dicke model. *Phys. Rev. A*, 92:023815, Aug 2015.

[95] Z. Zhiqiang, C. Hui Lee, R. Kumar, K.J. Arnold, S.J. Masson, A.S. Parkins, and M.D. Barrett. Nonequilibrium phase transition in a spin-1 dicke model. *Optica*, 4(4):424–429, Apr 2017.

[96] M. Soriente, T. Donner, R. Chitra, and O. Zilberberg. Dissipation-induced anomalous multicritical phenomena. *Phys. Rev. Lett.*, 120:183603, May 2018.

[97] E.I.R. Chiacchio and A. Nunnenkamp. Dissipation-induced instabilities of a spinor bose-einstein condensate inside an optical cavity. *Phys. Rev. Lett.*, 122:193605, May 2019.

[98] B. Buča and D. Jaksch. Dissipation induced nonstationarity in a quantum gas. *Phys. Rev. Lett.*, 123:260401, Dec 2019.

[99] K.C. Stitely, S.J. Masson, A. Giraldo, B. Krauskopf, and S. Parkins. Superradiant switching, quantum hysteresis, and oscillations in a generalized dicke model. *Phys. Rev. A*, 102:063702, Dec 2020.

[100] L. Broers and L. Mathey. Floquet engineering of non-equilibrium superradiance. *SciPost Phys.*, 14:018, 2023.

[101] L. Broers and L. Mathey. Robustness of the floquet-assisted superradiant phase and possible laser operation, 2023.

[102] K. Rzażewski, K. Wódkiewicz, and W. Żakowicz. Phase transitions, two-level atoms, and the A^2 term. *Phys. Rev. Lett.*, 35:432–434, Aug 1975.

[103] J.M. Knight, Y. Aharonov, and G.T.C. Hsieh. Are super-radiant phase transitions possible? *Phys. Rev. A*, 17:1454–1462, Apr 1978.

[104] I. Bialynicki-Birula and K. Rzażewski. No-go theorem concerning the superradiant phase transition in atomic systems. *Phys. Rev. A*, 19:301–303, Jan 1979.

[105] K. Rzągewski and K. Wódkiewicz. Stability of matter interacting with photons. *Phys. Rev. A*, 43:593–594, Jan 1991.

[106] P. Domokos and H. Ritsch. Collective cooling and self-organization of atoms in a cavity. *Phys. Rev. Lett.*, 89:253003, Dec 2002.

[107] F. Dimer, B. Estienne, A.S. Parkins, and H.J. Carmichael. Proposed realization of the dicke-model quantum phase transition in an optical cavity qed system. *Phys. Rev. A*, 75:013804, Jan 2007.

[108] D. Nagy, G. Kónya, G. Szirmai, and P. Domokos. Dicke-model phase transition in the quantum motion of a bose-einstein condensate in an optical cavity. *Phys. Rev. Lett.*, 104:130401, Apr 2010.

[109] P. Nataf and C. Ciuti. No-go theorem for superradiant quantum phase transitions in cavity qed and counter-example in circuit qed. *Nature Communications*, 1(1):72, 2010.

[110] S. Genway, W. Li, C. Ates, B. P. Lanyon, and I. Lesanovsky. Generalized dicke nonequilibrium dynamics in trapped ions. *Phys. Rev. Lett.*, 112:023603, Jan 2014.

[111] A. Safavi-Naini, R.J. Lewis-Swan, J.G. Bohnet, M. Gärttner, K.A. Gilmore, J.E. Jordan, J. Cohn, J.K. Freericks, A.M. Rey, and J.J. Bollinger. Verification of a many-ion simulator of the dicke model through slow quenches across a phase transition. *Phys. Rev. Lett.*, 121:040503, Jul 2018.

[112] J. Keeling, M.J. Bhaseen, and B.D. Simons. Collective dynamics of bose-einstein condensates in optical cavities. *Phys. Rev. Lett.*, 105:043001, Jul 2010.

[113] P. Kirton, M.M. Roses, J. Keeling, and E.G. Dalla Torre. Introduction to the Dicke Model: From Equilibrium to Nonequilibrium, and Vice Versa. *Adv. Quantum Technol.*, 2(1-2):1800043, 2019.

[114] F. Damanet, A.J. Daley, and J. Keeling. Atom-only descriptions of the driven-dissipative dicke model. *Phys. Rev. A*, 99:033845, Mar 2019.

[115] H.J. Lipkin, N. Meshkov, and A.J. Glick. Validity of many-body approximation methods for a solvable model: (i). exact solutions and perturbation theory. *Nuclear Physics*, 62(2):188–198, 1965.

[116] N. Meshkov, A.J. Glick, and H.J. Lipkin. Validity of many-body approximation methods for a solvable model: (ii). linearization procedures. *Nuclear Physics*, 62(2):199–210, 1965.

[117] A.J. Glick, H.J. Lipkin, and N. Meshkov. Validity of many-body approximation methods for a solvable model: (iii). diagram summations. *Nuclear Physics*, 62(2):211–224, 1965.

[118] S. Morrison and A.S. Parkins. Collective spin systems in dispersive optical cavity qed: Quantum phase transitions and entanglement. *Phys. Rev. A*, 77:043810, Apr 2008.

[119] S. Morrison and A.S. Parkins. Dynamical quantum phase transitions in the dissipative lipkin-meshkov-glick model with proposed realization in optical cavity qed. *Phys. Rev. Lett.*, 100:040403, Jan 2008.

[120] G. Engelhardt, V.M. Bastidas, C. Emary, and T. Brandes. ac-driven quantum phase transition in the lipkin-meshkov-glick model. *Phys. Rev. E*, 87:052110, May 2013.

[121] A. Russomanno, F. Iemini, M. Dalmonte, and R. Fazio. Floquet time crystal in the lipkin-meshkov-glick model. *Phys. Rev. B*, 95:214307, Jun 2017.

[122] Y. Zhou, S.-L. Ma, B. Li, X.-X. Li, F.-L. Li, and P.-B. Li. Simulating the lipkin-meshkov-glick model in a hybrid quantum system. *Phys. Rev. A*, 96:062333, Dec 2017.

[123] M.H. Muñoz Arias, K. Chinni, and P.M. Poggi. Floquet time crystals in driven spin systems with all-to-all p-body interactions. *Phys. Rev. Res.*, 4:023018, Apr 2022.

[124] C.C. Sung and C.M. Bowden. Phase transition in the multimode two- and three-level dicke model (green's function method). *Journal of Physics A: Mathematical and General*, 12(11):2273, Nov 1979.

[125] A. Crubellier, S. Liberman, D. Pavolini, and P. Pillet. Superradiance and subradiance. i. interatomic interference and symmetry properties in three-level systems. 18(18):3811, Sep 1985.

[126] A. Crubellier and D. Pavolini. Superradiance and subradiance. ii. atomic systems with degenerate transitions. 19(14):2109, Jul 1986.

[127] M.M. Cola, D. Bigerni, and N. Piovella. Recoil-induced subradiance in an ultracold atomic gas. *Phys. Rev. A*, 79:053622, May 2009.

[128] P. Wolf, S.C. Schuster, D. Schmidt, S. Slama, and C. Zimmermann. Observation of subradiant atomic momentum states with bose-einstein condensates in a recoil resolving optical ring resonator. *Phys. Rev. Lett.*, 121:173602, Oct 2018.

[129] R. Lin, R. Rosa-Medina, F. Ferri, F. Finger, K. Kroeger, T. Donner, T. Esslinger, and R. Chitra. Dissipation-engineered family of nearly dark states in many-body cavity-atom systems. *Phys. Rev. Lett.*, 128:153601, Apr 2022.

[130] J. Fan and S. Jia. Collective dynamics of the unbalanced three-level dicke model. *Phys. Rev. A*, 107:033711, Mar 2023.

[131] D. Jaksch, C. Bruder, J.I. Cirac, C.W. Gardiner, and P. Zoller. Cold bosonic atoms in optical lattices. *Physical Review Letters*, 81(15):3108–3111, Oct 1998.

[132] C. Maschler, I.B. Mekhov, and H. Ritsch. Ultracold atoms in optical lattices generated by quantized light fields. *The European Physical Journal D*, 46(3):545–560, 2008.

[133] R. Landig, L. Hruby, N. Dogra, M. Landini, R. Mottl, T. Donner, and T. Esslinger. Quantum phases from competing short- and long-range interactions in an optical lattice. *Nature*, 532(7600):476–479, 2016.

[134] P. Nozières. Time crystals: Can diamagnetic currents drive a charge density wave into rotation? *Europhysics Letters*, 103(5):57008, Sep 2013.

[135] P. Bruno. Impossibility of spontaneously rotating time crystals: A no-go theorem. *Phys. Rev. Lett.*, 111:070402, Aug 2013.

[136] H. Watanabe and M. Oshikawa. Absence of quantum time crystals. *Phys. Rev. Lett.*, 114:251603, Jun 2015.

[137] C.W. von Keyserlingk and S.L. Sondhi. Phase structure of one-dimensional interacting floquet systems. ii. symmetry-broken phases. *Phys. Rev. B*, 93:245146, Jun 2016.

[138] V. Khemani, A. Lazarides, R. Moessner, and S.L. Sondhi. Phase structure of driven quantum systems. *Phys. Rev. Lett.*, 116:250401, Jun 2016.

[139] D.V. Else, B. Bauer, and C. Nayak. Floquet time crystals. *Phys. Rev. Lett.*, 117:090402, Aug 2016.

[140] N.Y. Yao, A.C. Potter, I.-D. Potirniche, and A. Vishwanath. Discrete time crystals: Rigidity, criticality, and realizations. *Phys. Rev. Lett.*, 118:030401, Jan 2017.

[141] J. Zhang, P.W. Hess, A. Kyprianidis, P. Becker, A. Lee, J. Smith, G. Pagano, I.-D. Potirniche, A.C. Potter, A. Vishwanath, N.Y. Yao, and C. Monroe. Observation of a discrete time crystal. *Nature*, 543(7644):217–220, 2017.

[142] S. Choi, J. Choi, R. Landig, G. Kucsko, H. Zhou, J. Isoya, F. Jelezko, S. Onoda, H. Sumiya, V. Khemani, C. von Keyserlingk, N.Y. Yao, E. Demler, and M.D. Lukin. Observation of discrete time-crystalline order in a disordered dipolar many-body system. *Nature*, 543(7644):221–225, 2017.

[143] H. Keßler, P. Kongkhambut, C. Georges, L. Mathey, J.G. Cosme, and A. Hemmerich. Observation of a dissipative time crystal. *Phys. Rev. Lett.*, 127:043602, Jul 2021.

[144] H. Taheri, A.B. Matsko, L. Maleki, and K. Sacha. All-optical dissipative discrete time crystals. *Nature Communications*, 13(1):848, 2022.

[145] F. Piazza and H. Ritsch. Self-ordered limit cycles, chaos, and phase slippage with a superfluid inside an optical resonator. *Phys. Rev. Lett.*, 115:163601, Oct 2015.

[146] F. Iemini, A. Russomanno, J. Keeling, M. Schirò, M. Dalmonte, and R. Fazio. Boundary time crystals. *Phys. Rev. Lett.*, 121:035301, Jul 2018.

[147] B. Buča, J. Tindall, and D. Jaksch. Non-stationary coherent quantum many-body dynamics through dissipation. *Nature Communications*, 10(1):1730, 2019.

[148] H. Keßler, J.G. Cosme, M. Hemmerling, L. Mathey, and A. Hemmerich. Emergent limit cycles and time crystal dynamics in an atom-cavity system. *Phys. Rev. A*, 99:053605, May 2019.

[149] T. Liu, J.-Y. Ou, K.F. MacDonald, and N.I. Zheludev. Photonic metamaterial analogue of a continuous time crystal. *Nature Physics*, 19(7):986–991, 2023.

[150] Y.-H. Chen and X. Zhang. Realization of an inherent time crystal in a dissipative many-body system. *Nature Communications*, 14(1):6161, 2023.

[151] K. Wadenpfuhl and C.S. Adams. Emergence of synchronization in a driven-dissipative hot rydberg vapor. *Phys. Rev. Lett.*, 131:143002, Oct 2023.

[152] A. Greilich, N.E. Kopteva, A.N. Kamenskii, P.S. Sokolov, V.L. Korenev, and M. Bayer. Robust continuous time crystal in an electron–nuclear spin system. *Nature Physics*, 2024.

[153] J. Rovny, R.L. Blum, and S.E. Barrett. Observation of discrete-time-crystal signatures in an ordered dipolar many-body system. *Phys. Rev. Lett.*, 120:180603, May 2018.

[154] Z. Gong, R. Hamazaki, and M. Ueda. Discrete time-crystalline order in cavity and circuit qed systems. *Phys. Rev. Lett.*, 120:040404, Jan 2018.

[155] B. Zhu, J. Marino, N.Y. Yao, M.D. Lukin, and E.A. Demler. Dicke time crystals in driven-dissipative quantum many-body systems. *New Journal of Physics*, 21(7):073028, Jul 2019.

[156] P. Nurwantoro, R. W. Bomantara, and J. Gong. Discrete time crystals in many-body quantum chaos. *Phys. Rev. B*, 100:214311, Dec 2019.

[157] A. Lazarides, S. Roy, F. Piazza, and R. Moessner. Time crystallinity in dissipative floquet systems. *Phys. Rev. Res.*, 2:022002, Apr 2020.

[158] A. Kyprianidis, F. Machado, W. Morong, P. Becker, K.S. Collins, D.V. Else, L. Feng, P.W. Hess, C. Nayak, G. Pagano, N.Y. Yao, and C. Monroe. Observation of a prethermal discrete time crystal. *Science*, 372(6547):1192–1196, 2021.

[159] A. Pizzi, J. Knolle, and A. Nunnenkamp. Higher-order and fractional discrete time crystals in clean long-range interacting systems. *Nature Communications*, 12(1):2341, 2021.

[160] J. Randall, C.E. Bradley, F.V. van der Gronden, A. Galicia, M.H. Abobeih, M. Markham, D.J. Twitchen, F. Machado, N.Y. Yao, and T.H. Taminiau. Many-body–localized discrete time crystal with a programmable spin-based quantum simulator. *Science*, 374(6574):1474–1478, 2021.

[161] M. Krishna, P. Solanki, M. Hajdušek, and S. Vinjanampathy. Measurement-induced continuous time crystals. *Phys. Rev. Lett.*, 130:150401, Apr 2023.

[162] R.D. Jara Jr., D.F. Salinel, and J.G. Cosme. Theory of parametric resonance for discrete time crystals in fully-connected spin-cavity systems, 2024.

[163] J. Smits, L. Liao, H.T.C. Stoof, and P. van der Straten. Observation of a space-time crystal in a superfluid quantum gas. *Phys. Rev. Lett.*, 121:185301, Oct 2018.

[164] S. Autti, V.B. Eltsov, and G.E. Volovik. Observation of a time quasicrystal and its transition to a superfluid time crystal. *Phys. Rev. Lett.*, 120:215301, May 2018.

[165] H. Keßler, J.G. Cosme, C. Georges, L. Mathey, and A. Hemmerich. From a continuous to a discrete time crystal in a dissipative atom-cavity system. *New Journal of Physics*, 22(8):085002, Aug 2020.

[166] C. Booker, B. Buča, and D. Jaksch. Non-stationarity and dissipative time crystals: spectral properties and finite-size effects. *New Journal of Physics*, 22(8):085007, Aug 2020.

[167] K. Giergiel, T. Tran, A. Zaheer, A. Singh, A. Sidorov, K. Sacha, and P. Hannaford. Creating big time crystals with ultracold atoms. *New Journal of Physics*, 22(8):085004, Aug 2020.

[168] A. Kuroś, R. Mukherjee, W. Golletz, F. Sauvage, K. Giergiel, F. Mintert, and K. Sacha. Phase diagram and optimal control for n-tupling discrete time crystal. *New Journal of Physics*, 22(9):095001, Sep 2020.

216

[169] L.R. Bakker, M.S. Bahovadinov, D.V. Kurlov, V. Gritsev, A.K. Fedorov, and D.O. Krimer. Driven-dissipative time crystalline phases in a two-mode bosonic system with kerr nonlinearity. *Phys. Rev. Lett.*, 129:250401, Dec 2022.

[170] G. Homann, J. G. Cosme, and L. Mathey. Higgs time crystal in a high-T_c superconductor. *Phys. Rev. Res.*, 2:043214, Nov 2020.

[171] H.P. Ojeda Collado, G. Usaj, C.A. Balseiro, D.H. Zanette, and J. Lorenzana. Emergent parametric resonances and time-crystal phases in driven bardeen-cooper-schrieffer systems. *Phys. Rev. Res.*, 3:L042023, Nov 2021.

[172] A. Cabot, F. Carollo, and I. Lesanovsky. Continuous sensing and parameter estimation with the boundary time crystal. *Phys. Rev. Lett.*, 132:050801, Jan 2024.

[173] K. Sacha and J. Zakrzewski. Time crystals: a review. *Reports on Progress in Physics*, 81(1):016401, Nov 2017.

[174] V. Khemani, R. Moessner, and S.L. Sondhi. A brief history of time crystals, 2019.

[175] E.V. Else, C. Monroe, C. Nayak, and N.Y. Yao. Discrete time crystals. *Annual Review of Condensed Matter Physics*, 11(1):467–499, 2020.

[176] M.P. Zaletel, M. Lukin, C. Monroe, C. Nayak, F. Wilczek, and N.Y. Yao. Colloquium: Quantum and classical discrete time crystals. *Rev. Mod. Phys.*, 95:031001, Jul 2023.

[177] M. Först, C. Manzoni, S. Kaiser, Y. Tomioka, Y. Tokura, R. Merlin, and A. Cavalleri. Nonlinear phononics as an ultrafast route to lattice control. *Nature Physics*, 7(11):854–856, 2011.

[178] D.M. Juraschek, T. Neuman, J. Flick, and P. Narang. Cavity control of nonlinear phononics. *Phys. Rev. Res.*, 3:L032046, Aug 2021.

[179] S. Chattopadhyay, C.J. Eckhardt, D.M. Kennes, M.A. Sentef, D. Shin, A. Rubio, A. Cavalleri, E. A. Demler, and M.H. Michael. Mechanisms for long-lived, photo-induced superconductivity, 2023.

[180] R. Matsunaga, N. Tsuji, H. Fujita, A. Sugioka, K. Makise, Y. Uzawa, H. Terai, Z. Wang, H. Aoki, and R. Shimano. Light-induced collective pseudospin precession resonating with higgs mode in a superconductor. *Science*, 345(6201):1145–1149, 2014.

[181] H.P.O. Collado, J. Lorenzana, G. Usaj, and C.A. Balseiro. Population inversion and dynamical phase transitions in a driven superconductor. *Phys. Rev. B*, 98:214519, Dec 2018.

[182] M. Buzzi, G. Jotzu, A. Cavalleri, J.I. Cirac, E.A. Demler, B.I. Halperin, M.D. Lukin, T. Shi, Y. Wang, and D. Podolsky. Higgs-mediated optical amplification in a nonequilibrium superconductor. *Phys. Rev. X*, 11:011055, Mar 2021.

[183] W. Bührer and P. Brüesch. *Phonons: Theory and Experiments II: Experiments and Interpretation of Experimental Results.* Springer Series in Solid-State Sciences. Springer Berlin Heidelberg, 1986.

[184] S. Felicetti, J.S. Pedernales, I.L. Egusquiza, G. Romero, L. Lamata, D. Braak, and E. Solano. Spectral collapse via two-phonon interactions in trapped ions. *Phys. Rev. A*, 92:033817, Sep 2015.

[185] L. Garbe, P. Wade, F. Minganti, N. Shammah, S. Felicetti, and F. Nori. Dissipation-induced bistability in the two-photon dicke model. *Scientific Reports*, 10(1), Aug 2020.

[186] E.M. Izhikevich. *Dynamical Systems in Neuroscience: The Geometry of Excitability and Bursting.* The MIT Press, Jul 2006.

[187] M. Ospeck, V.M. Eguíluz, and M.O. Magnasco. Evidence of a hopf bifurcation in frog hair cells. *Biophysical Journal*, 80(6):2597–2607, 2001.

[188] S. Camalet, T. Duke, F. Jülicher, and J. Prost. Auditory sensitivity provided by self-tuned critical oscillations of hair cells. *Proceedings of the National Academy of Sciences*, 97(7):3183–3188, 2000.

[189] M.W. Hirsch, S. Smale, and R.L. Devaney. *Differential equations, dynamical systems, and an introduction to chaos.* Academic Press San Diego, CA, 2004.

[190] M.R. Roussel. *Nonlinear Dynamics.* 2053-2571. Morgan and Claypool Publishers, 2019.

[191] A. Kosior, H. Ritsch, and F. Mivehvar. Nonequilibrium phases of ultracold bosons with cavity-induced dynamic gauge fields. *SciPost Phys.*, 15:046, 2023.

[192] T.E. Lee and H.R. Sadeghpour. Quantum synchronization of quantum van der pol oscillators with trapped ions. *Phys. Rev. Lett.*, 111:234101, Dec 2013.

[193] S. Walter, A. Nunnenkamp, and C. Bruder. Quantum synchronization of a driven self-sustained oscillator. *Phys. Rev. Lett.*, 112:094102, Mar 2014.

[194] S. Dutta and N.R. Cooper. Critical response of a quantum van der pol oscillator. *Phys. Rev. Lett.*, 123:250401, Dec 2019.

[195] L. Ben Arosh, M.C. Cross, and R. Lifshitz. Quantum limit cycles and the rayleigh and van der pol oscillators. *Phys. Rev. Res.*, 3:013130, Feb 2021.

[196] C.W. Wächtler and G. Platero. Topological synchronization of quantum van der pol oscillators. *Phys. Rev. Res.*, 5:023021, Apr 2023.

[197] F.E. Hanson, J.F. Case, E. Buck, and J. Buck. Synchrony and flash entrainment in a new guinea firefly. *Science*, 174(4005):161–164, 1971.

[198] S. Daan and J. Aschoff. *The Entrainment of Circadian Systems.* Springer US, 2001.

[199] N.M. Kondratiev, V.E. Lobanov, A.E. Shitikov, R.R. Galiev, D.A. Chermoshentsev, N.Y. Dmitriev, A.N. Danilin, E.A. Lonshakov, K.N. Min'kov, D.M. Sokol, S.J. Cordette, Y.-H. Luo, W. Liang, J. Liu, and I.A. Bilenko. Recent advances in laser self-injection locking to high-q microresonators. *Frontiers of Physics*, 18(2):21305, 2023.

[200] M.H. Jensen, P. Bak, and T. Bohr. Complete devil's staircase, fractal dimension, and universality of mode- locking structure in the circle map. *Phys. Rev. Lett.*, 50:1637–1639, May 1983.

[201] M.H. Jensen, P. Bak, and T. Bohr. Transition to chaos by interaction of resonances in dissipative systems. i. circle maps. *Phys. Rev. A*, 30:1960–1969, Oct 1984.

[202] L. Amico, M. Boshier, G. Birkl, A. Minguzzi, C. Miniatura, L.-C. Kwek, D. Aghamalyan, V. Ahufinger, D. Anderson, N. Andrei, A.S. Arnold, M. Baker, T.A. Bell, T. Bland, J.P. Brantut, D. Cassettari, W.J. Chetcuti, F. Chevy, R. Citro, S. De Palo, R. Dumke, M. Edwards, R. Folman, J. Fortagh, S.A. Gardiner, B.M. Garraway, G. Gauthier, A. Günther, T. Haug, C. Hufnagel, M. Keil, P. Ireland, M. Lebrat, W. Li, L. Longchambon, J. Mompart, O. Morsch, P. Naldesi, T.W. Neely, M. Olshanii, E. Orignac, S. Pandey, A. Pérez-Obiol, H. Perrin, L. Piroli, J. Polo, A.L. Pritchard, N.P. Proukakis, C. Rylands, H. Rubinszstein-Dunlop, F. Scazza, S. Stringari, F. Tosto, A. Trombettoni, N. Victorin, W. von Klitzing, D. Wilkowski, K. Xhani, and A. Yakimenko. Roadmap on atomtronics: State of the art and perspective. *AVS Quantum Science*, 3(3):039201, 2021.

[203] L. Amico, D. Anderson, M. Boshier, J.-P. Brantut, L.-C. Kwek, A. Minguzzi, and W. von Klitzing. Colloquium: Atomtronic circuits: From many-body physics to quantum technologies. *Rev. Mod. Phys.*, 94:041001, Nov 2022.

[204] L.C. Kwek. Atomtronics: Towards Sensors and Devices with Ultracold Atoms and Optical Lattices. Talk presented at New Advances in Quantum Information Science And Quantum Technology Samarkand, Uzbekistan, 2019.

[205] H. Lefèvre. *The Fiber-optic Gyroscope.* Artech House optoelectronics library. Artech House, 1993.

[206] D.S. Durfee, Y.K. Shaham, and M.A. Kasevich. Long-term stability of an area-reversible atom-interferometer sagnac gyroscope. *Phys. Rev. Lett.*, 97:240801, Dec 2006.

[207] J.H.T. Burke and C.A. Sackett. Scalable bose-einstein-condensate sagnac interferometer in a linear trap. *Phys. Rev. A*, 80:061603, Dec 2009.

[208] P. Hamilton, M. Jaffe, J.M. Brown, L. Maisenbacher, B. Estey, and H. Müller. Atom interferometry in an optical cavity. *Phys. Rev. Lett.*, 114:100405, Mar 2015.

[209] K. Bongs, M. Holynski, J. Vovrosh, P. Bouyer, G. Condon, E. Rasel, C. Schubert, W.P. Schleich, and A. Roura. Taking atom interferometric quantum sensors from the laboratory to real-world applications. *Nature Reviews Physics*, 1(12):731–739, 2019.

[210] E.R. Moan, R.A. Horne, T. Arpornthip, Z. Luo, A J. Fallon, S.J. Berl, and C.A. Sackett. Quantum rotation sensing with dual sagnac interferometers in an atom-optical waveguide. *Phys. Rev. Lett.*, 124:120403, Mar 2020.

[211] C.W. Woffinden, A.J. Groszek, G. Gauthier, B.J. Mommers, M.W. J. Bromley, S.A. Haine, H. Rubinsztein-Dunlop, M.J. Davis, T.W. Neely, and M. Baker. Viability of rotation sensing using phonon interferometry in bose-einstein condensates, 2022.

[212] J.B. Fixler, G.T. Foster, J.M. McGuirk, and M.A. Kasevich. Atom interferometer measurement of the newtonian constant of gravity. *Science*, 315(5808):74–77, 2007.

[213] R. Bouchendira, P. Cladé, S. Guellati-Khélifa, F. Nez, and F. Biraben. New determination of the fine structure constant and test of the quantum electrodynamics. *Phys. Rev. Lett.*, 106:080801, Feb 2011.

[214] R.H. Parker, C. Yu, W. Zhong, B. Estey, and H. Müller. Measurement of the fine-structure constant as a test of the standard model. *Science*, 360(6385):191–195, 2018.

[215] C. Freier, M. Hauth, V. Schkolnik, B. Leykauf, M. Schilling, H. Wziontek, H.-G. Scherneck, J. Müller, and A. Peters. Mobile quantum gravity sensor with unprecedented stability. *Journal of Physics: Conference Series*, 723(1):012050, Jun 2016.

[216] R. Karcher, A. Imanaliev, S. Merlet, and F. Pereira Dos Santos. Improving the accuracy of atom interferometers with ultracold sources. *New Journal of Physics*, 20(11):113041, Nov 2018.

[217] D. Savoie, M. Altorio, B. Fang, L. A. Sidorenkov, R. Geiger, and A. Landragin. Interleaved atom interferometry for high-sensitivity inertial measurements. *Science Advances*, 4(12):eaau7948, 2018.

[218] R. Geiger, A. Landragin, S. Merlet, and F. Pereira Dos Santos. High-accuracy inertial measurements with cold-atom sensors. *AVS Quantum Science*, 2(2):024702, 2020.

[219] M.S. Grewal, A.P. Andrews, and C.G. Bartone. *Global Navigation Satellite Systems, Inertial Navigation, and Integration*. Wiley, 2020.

[220] C. Jekeli. Navigation error analysis of atom interferometer inertial sensor. *NAVIGATION*, 52(1):1–14, 2005.

220

[221] H.T.C. Stoof, D.B.M. Dickerscheid, and K. Gubbels. *Ultracold Quantum Fields.* Springer, Feb 2009.

[222] C.J. Pethick and H. Smith. *Bose–Einstein Condensation in Dilute Gases.* Cambridge University Press, 2 edition, 2008.

[223] V.L. Ginzburg and L.D. Landau. On the Theory of superconductivity. *Zh. Eksp. Teor. Fiz.*, 20:1064–1082, 1950.

[224] D. Pekker and C.M. Varma. Amplitude/higgs modes in condensed matter physics. *Annual Review of Condensed Matter Physics*, 6(1):269–297, 2015.

[225] C. M. Varma. Higgs boson in superconductors. *Journal of Low Temperature Physics*, 126(3):901–909, 2002.

[226] G. Homann, J.G. Cosme, J. Okamoto, and L. Mathey. Higgs mode mediated enhancement of interlayer transport in high-T_c cuprate superconductors. *Phys. Rev. B*, 103:224503, Jun 2021.

[227] Z. Dai and P.A. Lee. Superconductinglike response in a driven gapped bosonic system. *Phys. Rev. B*, 104:054512, Aug 2021.

[228] Z. Dai and P.A. Lee. Superconducting-like response in driven systems near the mott transition. *Phys. Rev. B*, 104(24), Dec 2021.

[229] E. Altman and A. Auerbach. Oscillating superfluidity of bosons in optical lattices. *Phys. Rev. Lett.*, 89:250404, Dec 2002.

[230] L. Pollet and N. Prokof'ev. Higgs mode in a two-dimensional superfluid. *Phys. Rev. Lett.*, 109:010401, Jul 2012.

[231] M. Endres, T. Fukuhara, D. Pekker, M. Cheneau, P. Schauß, C. Gross, E. Demler, S. Kuhr, and I. Bloch. The 'higgs'amplitude mode at the two-dimensional superfluid/mott insulator transition. *Nature*, 487(7408):454–458, 2012.

[232] M. Faccioli and L. Salasnich. Spontaneous symmetry breaking and higgs mode: Comparing gross-pitaevskii and nonlinear klein-gordon equations. *Symmetry*, 10(4), 2018.

[233] B. Rosenstein and D. Li. Ginzburg-landau theory of type ii superconductors in magnetic field. *Rev. Mod. Phys.*, 82:109–168, Jan 2010.

[234] H. Feshbach and F. Villars. Elementary relativistic wave mechanics of spin 0 and spin 1/2 particles. *Rev. Mod. Phys.*, 30:24–45, Jan 1958.

[235] H. Shi, S. Chiesa, and S. Zhang. Ground-state properties of strongly interacting fermi gases in two dimensions. *Phys. Rev. A*, 92:033603, Sep 2015.

[236] L. Salasnich. Condensate fraction of a two-dimensional attractive fermi gas. *Phys. Rev. A*, 76:015601, Jul 2007.

[237] D. Dreon, A. Baumgärtner, X. Li, S. Hertlein, T. Esslinger, and T. Donner. Self-oscillating pump in a topological dissipative atom–cavity system. *Nature*, 608(7923):494–498, 2022.

[238] N. Lörch, E. Amitai, A. Nunnenkamp, and C. Bruder. Genuine quantum signatures in synchronization of anharmonic self-oscillators. *Phys. Rev. Lett.*, 117:073601, Aug 2016.

[239] E. Amitai, M. Koppenhöfer, N. Lörch, and C. Bruder. Quantum effects in amplitude death of coupled anharmonic self-oscillators. *Phys. Rev. E*, 97:052203, May 2018.

[240] I. Yusipov and M.V. Ivanchenko. Quantum neimark-sacker bifurcation. *Scientific Reports*, 9(1):17932, 2019.

[241] K.T. Alligood, T.D. Sauer, and J.A. Yorke. *Chaos: An Introduction to Dynamical Systems*. Textbooks in Mathematical Sciences. Springer New York, 2000.

[242] A. Roulet and C. Bruder. Quantum synchronization and entanglement generation. *Phys. Rev. Lett.*, 121:063601, Aug 2018.

[243] M. Koppenhöfer, C. Bruder, and A. Roulet. Quantum synchronization on the ibm q system. *Phys. Rev. Res.*, 2:023026, Apr 2020.

[244] M. Fruchart, R. Hanai, P.B. Littlewood, and V. Vitelli. Non-reciprocal phase transitions. *Nature*, 592(7854):363–369, 2021.

[245] H. Jaeger. The "echo state" approach to analysing and training recurrent neural networks-with an erratum note'. *Bonn, Germany: German National Research Center for Information Technology GMD Technical Report*, 148, Jan 2001.

[246] D. Verstraeten, B. Schrauwen, M. D'Haene, and D. Stroobandt. An experimental unification of reservoir computing methods. *Neural Networks*, 20(3):391–403, 2007. Echo State Networks and Liquid State Machines.

[247] Z. Yan, J. Ho, Y.-H. Lu, S.J. Masson, A. Asenjo-Garcia, and D.M. Stamper-Kurn. Superradiant and subradiant cavity scattering by atom arrays. *Phys. Rev. Lett.*, 131:253603, Dec 2023.

[248] M. Scheffer, J. Bascompte, W.A. Brock, V. Brovkin, S.R. Carpenter, V. Dakos, H. Held, E.H. van Nes, M. Rietkerk, and G. Sugihara. Early-warning signals for critical transitions. *Nature*, 461(7260):53–59, 2009.

[249] F. Grziwotz, C.-W. Chang, V. Dakos, E.H. van Nes, M. Schwarzländer, O. Kamps, M. Heßler, I.T. Tokuda, A. Telschow, and C.H. Hsieh. Anticipating the occurrence and type of critical transitions. *Science Advances*, 9(1):eabq4558, 2023.

[250] J. Zhang, Z.-K. Liu, L.-H. Zhang, B. Liu, Z.-Y. Zhang, S.-Y. Shao, Q. Li, H.-C. Chen, Y. Ma, T.-Y. Han, Q.-F. Wang, C.S. Adams, D.-S. Ding, and B.-S. Shi. Early warning signals of the tipping point in strongly interacting rydberg atoms, 2024.

Eidesstattliche Versicherung

Hiermit versichere ich an Eides statt, die vorliegende Dissertationsschrift selbst verfasst und keine anderen als die angegebenen Hilfsmittel und Quellen benutzt zu haben.

Hamburg, den ___29.05.2024___

_____

Unterschrift des Doktoranden